Utilisation of radiocarbon and tephrochronology to constrain the oceanic circulation in the Southeast Pacific Ocean during the last 20,000 years

Consuelo Martínez Fontaine

université PARIS-SACLAY

Utilisation of radiocarbon and tephrochronology to constrain the oceanic circulation in the Southeast Pacific Ocean during the last 20,000 years

Utilisation du radiocarbone et de la téphrochronologie pour contraindre la circulation océanique dans l'Océan Pacifique Sud-est depuis les dernières 20,000 années

Thèse de doctorat de l'université Paris-Saclay

École doctorale n° 579 : Sciences mécaniques et énergétiques, matériaux et géosciences (SMEMAG)
Spécialité de doctorat: Terre solide : géodynamique des enveloppes supérieures, paléobiosphère
Unité de recherche : Université Paris-Saclay, CNRS, GEOPS, 91405, Orsay, France
Graduate School: Géosciences, climat, environnement et planètes.
Référent: Faculté des sciences d'Orsay

Thèse présentée et soutenue à Orsay, le 23 novembre 2021 par

Consuelo MARTÍNEZ FONTAINE

Composition du Jury

Xavier QUIDELLEUR Directeur adjoint école doctorale SMEMAG, Laboratoire GEOPS, Université Paris-Saclay	Président
Andrea BURKE Professeure associée, University of St Andrews	Rapporteure & Examinatrice
Samuel JACCARD Professeur, Université de Lausanne	Rapporteur & Examinateur
Ricardo DE POL HOLZ Chercheur associé, GAIA-Antarctica, Universidad de Magallanes	Examinateur

Direction de la thèse

Giuseppe SIANI Professeur, Université Paris-Saclay	Directeur de thèse
Elisabeth MICHEL Chercheuse, Laboratoire des Sciences du Climat et de l'Environnement LSCE	Co-encadrante de thèse

Álvaro AMIGO RAMOS Directeur du service National de Vigilance Volcanique du Chili	Invité

Thèse de doctorat

NNT : 2021UPASJ019

This thesis was financed by Chilean National Agency of Research and Development (ANID) by its financial support through Becas Chiles, Doctorado en el Extranjero Convocatoria 2017.

Acknowledgements

I thank everyone that was a part of this journey, which was transformative, full of suffering, hard work, teachings and joy.

To my family, for supporting me during this period which was also hard for them, especially for my parents that suffered seeing me suffer, but who found joy in my joy and pride in this achievement. To my sister and brother whom I love and miss very much.

To Giuseppe and Elisabeth, thank you for teaching me the ways of science, you've given me tools which I hope I can put in the service of Chile's development. Thank you for being good people and understanding when I needed some time to re adjust. For welcoming me in your house and developing more than just a work relationship. Whenever you go to Chile you and your families are very welcome in my house for a homemade pisco sour and maybe some coastal upwelling-sea food.

To my Berlin family who gave me love and party energy when I was drained and who welcomed me in their house which I call my own. Without you I would have probably quitted the PhD.

To the people in LSCE and GEOPS who very happily teached me the lab techniques and were open to discuss science ☺: Gulay, Fatima, Patricia, Will, Guillaume, Chiara, Julius, Serge. And to the nice people in the lab who made it easier to live the cultural transition, in particular to Elisabeth Teca, in whom I finally found someone to really share this experience (and to eat lunch with), without you it would most definitely had been a different/worse experience.

To all the people involved in the database project, especially to Chiara who showed me a new world from which I hope to continue to learn in the future, and to Vanessa, who didn't even know me and has been so key to this project, who I now call my friend and with whom I hope to continue to work in advancing a science that helps solve the very real problems of the times we live in. To Guillaume, Karen and the people from SERNAGEOMIN who believe in the project and in my work and have really supported it through these years ☺ even if it takes a long time :S

To Dharma, my dear friend and colleague, a ray of sunshine in this dark world, who always inspires me to be better and with whom I trust we can build a better Chile.

To my friends in Ile-de-France, I love you and I couldn't have done it without you in my life, I hope you'll go to Chile one day.

To the suppliers from les Ulis, who always provided a quality service and who I thank for much of my work and my mental health.

"Last but not least, I wanna thank me for believing in my self, for doing all this hard work, for having no days off, for never quitting".

Introduction

The last few decades have been marked by a growing concern regarding climate change. All over the world the effects of global warming and associated climate change are being experienced: prolonged droughts (e.g. Chile (Garreaud et al., 2019) and Australia (Cai et al., 2014)); extreme heatwaves (e.g. Western Europe in 2003, 2019 (García-Herrera et al., 2010; Vautard et al., 2020) and Eastern Europe in 2010 (e.g. Barriopedro, 2011)); heavy precipitation events (e.g. China in 2016 (Sun & Miao, 2018), Pakistan in 2010 (Hong et al., 2011)); and global glacier retreat (e.g. Jenkins et al., 2018 King et al., 2020; Solomina et al., 2015;). If humanity wants to adapt to this changing world, it is essential to understand the climate system and the impact human activities have on it. This task is currently undertaken by scientists worldwide and summarized by the Intergovernmental Panel on Climate Change (IPCC) through periodic assessments on climate change and recommendations to mitigate and adapt to it (e.g. IPCC, 2021).

In this attempt to better understand the climate system, marine sediment cores have supplied valuable information. By analyzing the chemical composition of the sediment at different depths in marine cores, changes in global ice volume, sea level, and dust supply to the Southern Ocean during the last ~5 million years (MA) have been reconstructed. These records, have revealed that –at least during the last ~2 MA– earth's climate has oscillated cyclically between two contrasting states: a glacial (cold) state, lasting either ~40 or ~100 kilo years (ka); and an interglacial (warm) state, lasting between ~10–20 ka (e.g. Elderfield et al., 2012; Lisiecki and Raymo, 2005; Martínez-García 2011;Rohling et al., 2014). Additionally, by analyzing the chemical composition of ancient bubbles trapped in ice cores, we have come to know that during these glacial–interglacial cycles, the temperature of the atmosphere and the amount of ice in Antarctica varied in phase with atmospheric CO_2, at least during the last ~850 thousand years (Figure 1.1; Bereiter et al., 2014; Higgins et al., 2015; Lüthi et al., 2008), highlighting the strong relationship between glacial–interglacial cycles and atmospheric CO_2.

Carbon is distributed on earth in different reservoirs (e.g. the ocean, the atmosphere, vegetation, the soil, etc.), where it can be found forming different chemical compounds (e.g. CO_2, CO_3^{2-}, CH_4, organic matter). Each of these reservoirs contains a different amount of carbon and exchanges it with the other reservoirs at different rates. For example, the atmosphere contains (so far) ~870 gigatons of carbon (GtC) as CO_2, CH_4 and CO, whereas vegetation contains ~2000 GtC as organic carbon, and the ocean ~38,000 GtC as inorganic carbon (CO_2, HCO_3^-, CO_3^{-2}, H_2CO_3) and dissolved organic carbon (IPCC, 2021 and references therein). Every year, ~130 GtC of carbon go from the atmosphere into vegetation by photosynthesis, whereas ~60 GtC go back to the atmosphere through plant respiration and another ~60 GtC through the decomposition of organic matter. The second most important annual flux of carbon into the atmosphere occurs at the ocean surface. Every year, ~78 GtC are *released* to the atmosphere, whereas ~80 GtC *ente*r

the surface ocean, from where it is transported to deeper depths, making it the second most important *sink* of atmospheric carbon at present (IPCC, 2021 and references therein). Since the industrial revolution, the burning of fossil fuels has transferred carbon from rocks and sediment into the atmosphere at an unprecedented rate, adding an extra ~445 ± 20 GtC in ~270 years (IPCC, 2021). In order to understand the effect this abrupt increase in atmospheric carbon might have on climate, it is necessary to understand the mechanisms that drive the exchanges between the different carbon reservoirs, how these mechanisms interact in time and how they ultimately determine climate. This is the study subject of the "Carbon cycle" and is key when understanding climate change and finding solutions to adapt to it.

One period in time that might give us some insight into the Carbon cycle is the last transition between a glacial and an interglacial state, often referred to as Termination I or "the last deglaciation", which occurred between ~18,000 and 11,000 calendar years Before the Present (cal ka BP, Figure 1.1). During the last deglaciation, ice sheets in Antarctica, Greenland, North America, Eurasia and Patagonia decreased extensively (Davies et al., 2020; Dyke, 2004; Hughes et al., 2015; RAISED consortium et al., 2014), at the same time as atmospheric CO_2 in Antarctica rose abruptly from ~190 to 270 ppm (Barnola et al., 1987; Marcott et al., 2014; Monnin et al., 2001) and global temperatures increased ~3.5° C (Shakun et al., 2012; Tierney et al., 2020). Thus raising the question of **what reservoirs and mechanisms were involved in this –relatively fast– transfer of carbon into the atmosphere, provoking the transition from a glacial to an interglacial state?** Proxy evidence[1] from different areas of the world oceans indicate that, during the last glacial period (just before the last deglaciation), a larger amount of carbon was stored in the deep ocean (e.g. Allen et al., 2015; Anderson et al., 2019; Jaccard et al., 2009; de la Fuente et al., 2017; Rae et al., 2018; Sikes et al., 2017). Furthermore, reconstructions of CO_2 pressure at the surface ocean, indicate that during the last deglaciation, more CO_2 than at present would have been *released* to the atmosphere in the Southern Ocean and the Equatorial East Pacific Ocean (Martínez-Botí et al., 2015). This, together with additional proxy evidence (e.g. Anderson et al., 2009; Pichevin et al., 2009; Siani et al., 2013), has led to the hypothesis that the ocean has an important role in the regulation of glacial–interglacial cycles by *storing* carbon during glacial states (thus decreasing the amount of atmospheric CO_2) and *releasing* it to the atmosphere during interglacials (thus increasing the amount of atmospheric CO_2).

[1] Proxy evidence refers to estimations of climatological parameters in the past. When some parameter cannot be directly measured, for example the temperature of the ancient ocean, some other parameter is quantified which records variations the parameter of interest. For example, in the ocean the chemistry of micro fossils of phytoplankton, such as foraminifera or diatoms, is often used as a proxy for sea water temperature (e.g. Elderfield et al., 2017).

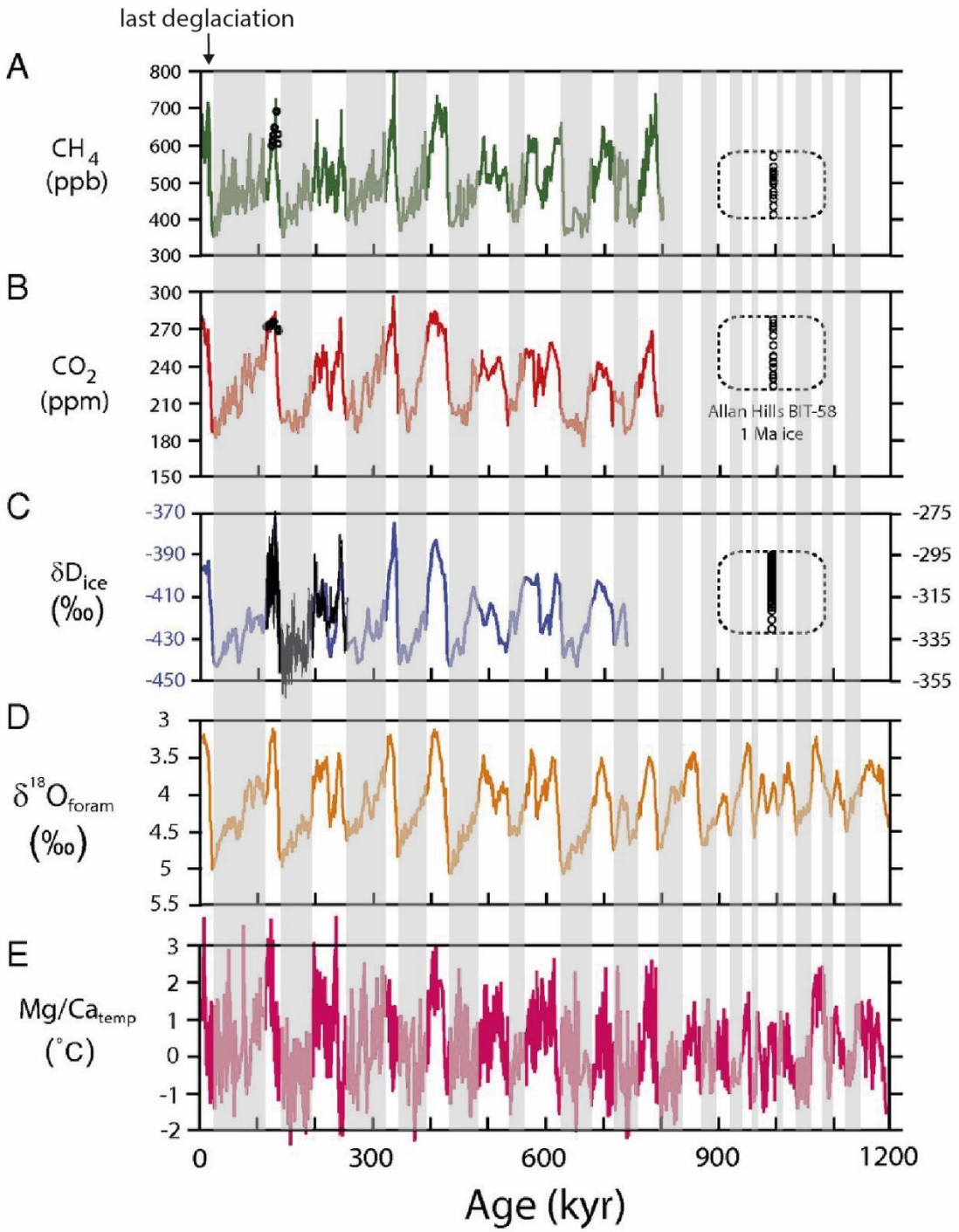

Figure 1.1 Records showing glacial–interglacial signals. The colder periods (glacials) are grey shaded. Records of atmospheric variations of CH_4 (A), CO2 (*B*), and δD (a proxy for temperature, *C*), from records in Antarctica: Vostok/EPICA Dome C (green, red and blue curves; Jouzel et al., 2007; Elderfield et al., 2012; Lüthi et al., 2008; Bereiter et al., 2015, respectively) and Allan Hills Blue Ice Area (black circles; Higgins et al., 2015). (E) Benthic $\delta^{18}O$ stack (Lisiecki & Raymo, 2005). (F) Deep ocean temperature based on foraminiferal Mg/Ca (Bereiter et al., 2012). Modified from Higgins et al. (2015).

The exact areas of the ocean where this *store/release* of carbon would have taken place, and the mechanisms leading to it, are still being debated. First of all, because of the high complexity of the climate system, where different mechanisms interact through a series of feedbacks, making it difficult to estimate their relative importance in modifying atmospheric CO_2. For example, among the potential mechanisms

invoked to explain the store/release of carbon in/from the deep ocean, it is hypothesized that changes in oceanic circulation would result in a deep glacial ocean which was more isolated from the atmosphere than at present, thus accumulating more carbon. Today, most carbon is stored in the deep ocean (>1,000 m depth), where it accumulates over time as organic matter produced at the surface ocean sinks and decomposes, releasing carbon and nutrients back into the water. When this deep water is transported to the surface, it exchanges CO_2 with the atmosphere, releasing part of this accumulated carbon. Thus, a more isolated deep ocean would accumulate more carbon over time. At the same time, this change in oceanic circulation is explained by paleoceanographers as changes in other climatic features, such as the position and intensity of the Southerly Westerly Winds –an intense band of westerly winds blowing above the Southern Ocean, all the way around Antarctica (section 1.1.2)– (Anderson et al., 2009; Denton et al., 2010; Toggweiler, 1999); and/or the extension of Antarctic sea ice (Adkins, 2013; Ferrari et al., 2014; Keeling & Stephens, 2001; Stephens & Keeling, 2000; Watson & Naveira-Garabato, 2006). Both these mechanisms would modulate the degree of gas exchange between deep waters and the atmosphere in the Southern Ocean, one of the main areas where deep waters upwell to the surface and exchange gases with the atmosphere today (e.g. Sloyan & Rintoul, 2001; Webb & Suginohara, 2001). Additionally, it is proposed that not only the rate of this exchange would change in time, but also the amount of carbon that is effectively transported from the surface to the deep ocean. In particular, it has been proposed that variations in nutrient availability at the surface ocean would regulate the biological productivity there, and consecutively the organic matter sinking to the deep ocean. In turn, the amount of nutrients at the surface ocean could be regulated by changes in oceanic circulation or from non–oceanic sources, such as iron *fertilization* by dust transport in the atmosphere (e.g. Kohfeld et al., 2005; Pichevin et al., 2009; Sigman & Boyle, 2000). Even more, it has also been hypothesized that the accumulation of carbon in the deep ocean during the late glacial could result from increased submarine *production* of CO_2 during periods of enhanced volcanism in oceanic ridges, as a response to lower sea levels during glacial states (Crowley et al., 2015; Lund & Asimow, 2011; Tolstoy, 2015). Very likely, all these mechanisms –and many more– interact through a series of feedbacks resulting in what is called the last deglaciation, and proxy records reflect changes in not one, but in an ensemble of these mechanisms. This is the complexity of the climate system and the study of past climates.

Disentangling the complexity of the climate system –and in particular the mechanisms driving the hypothesized *store/release of* carbon from the ocean during the last deglaciation– is additionally complicated by the scarcity of data available in vast areas of the ocean (e.g. Lauvset et al., *in preparation*), both at present –which is the reference from which paleoceanographic records are interpreted– and in the past. The oceanographic and paleoceanographic information currently available is not enough to resolve the spatial complexity in some parts of the ocean, for example in the equator (e.g. Bostock et al., 2010), nor is enough to make statistically robust inferences about regional climatic processes, for

example regarding the carbon storage in the deep ocean during the last late glacial period. The latter can be aided by producing more information, beginning by less researched areas of the global ocean. One such area is the Southeast Pacific (and the Southeast Pacific sector of the Southern Ocean), an interesting area of study as there circulate water masses *formed* both in the Southern Ocean and in the Equatorial East Pacific Ocean (section 1.1.1; Figure 1.2). These are important areas where CO_2 is exchanged between the atmosphere and the deep ocean at present (e.g. Gruber et al., 2018; Mikaloff Fletcher et al., 2007; Takahashi et al., 2009; Wu et al., 2019), and which have been indicated to have had an important role in the store/release of carbon from the ocean during the last deglaciation (e.g. Anderson et al., 2009; Martínez-Botí et al., 2013; Siani et al., 2013). Thus, understanding how (and if) the circulation of water masses in the Southeast Pacific changed since the late glacial, might shed some light into the mechanisms regulating the exchange of carbon between the ocean and the atmosphere. In this context, the first objective of this thesis (developed in chapter 2 and 5) is:

To characterize changes in the ventilation of intermediate and deep water masses in the Southeast Pacific Ocean during the last ~20,000 years.

For this, I studied nine marine sediment cores retrieved in the Chilean continental margin, between ~500 and ~3,300 m, and ~31° and 49° S (Figure 1.2). New and previously analyzed radiocarbon (^{14}C) ages of planktic and benthic foraminifera are used as proxy of the ventilation ages (the time a water mass has been isolated from the atmosphere) of intermediate (~500–1,000 m) and deep waters (>1,000 m) in the Southeast Pacific during the last ~20,000 years (details in section 1.2.1.1). Changes in oceanic circulation in the Southeast Pacific are then interpreted from these records together with previously published radiocarbon information in the area (De Pol-Holz et al., 2010; Siani et al., 2013).

Another important limitation to robustly asses *how* these proposed mechanisms interact to explain the observed atmospheric CO_2 records, are the differences in resolution and levels of certitude of chronologies in the atmosphere compared to those in the ocean. For the deglaciation, atmospheric records of ice cores in Antarctica are available with resolutions as low as a couple of decades and chronological uncertainties below 150 years, determined from annual layer counting (WAIS Divide Project Members, 2013; Marcott et al., 2014). In contrast, oceanic records in marine sediment cores generally have lower resolution, of a few hundred years, and their chronologies are less constrained (section 1.2.1.2; e.g. Heaton et al., 2020). For example, during the last deglaciation, atmospheric records show abrupt increases in CO_2 of ~15 ppm in a ~100 years. Meanwhile, no paleoceanographic record has the resolution and chronological precision necessary to robustly identify the origin of these CO_2 pulses. Thus, there is still work to be done to ameliorate chronologies in the ocean to better understand the Carbon cycle. In order to better constrain the chronologies of the marine sediment cores studied in this thesis, the second objective (developed in chapters 4 and 5) is to:

Use tephrochronology together with stable isotopes ($\delta^{18}O$, $\delta^{13}C$) stratigraphy in marine sediment cores to better constrain chronologies in the Southeast Pacific Ocean during the last ~20,000 years.

Tephrochronology identifies the remains of specific explosive eruptions (tephra) in different sites and environments (e.g. the continent, the ocean, lakes, glaciers) and with this information it reconstructs the eruptive history of volcanic centers (details in chapters 3 and 4). By identifying tephras which have been dated on land, in the marine sediment cores, we evaluate if they allow to better constrain the marine chronologies (details in section 1.2.1.2 and chapter 5). Because the study area is adjacent to two very active volcanic zones: the Southern and Austral Volcanic Zones of the Andes (section 1.1.3), there is great potential of using tephrochronology to ameliorate marine chronologies in the area.

Chapter 1

1.1 Study area

1.1.1 Southeast Pacific and the southeast pacific sector of the Southern Ocean

The marine sediment cores studied in this thesis (cores GeoB 7149-2, GeoB 7163-7, GeoB 7162-6, SO161-22SL, GeoB 7167-6, MD07-3100, MD07-3098, MD07-3119 and MD07-3081) were retrieved in the Chilean continental margin between ~31° S and ~49° S (Figure 1.2), which corresponds to the transition between the Southeast Pacific Ocean and the Southern Ocean. There, water masses formed in the Southern Ocean are transported north into the Pacific Ocean (Subantarctic Surface Water (SAAW), Subantarctic Mode Waters, Antarctic Intermediate Water (AAIW) and Circumpolar Deep Water (LCDW)); and water masses formed in the Equatorial East Pacific (Equatorial Subsurface Water (ESSW)) and North Pacific (Pacific Deep Water (PDW)), are transported south towards the Southern Ocean. In oceanography, a water mass corresponds to a body of water which has distinct physical (e.g. T°, salinity, density) and geochemical (e.g. ^{14}C, phosphate, silicate) characteristics, which derive from a common *formation* process and consecutive circulation path. From their formation areas, water masses are transported through the world oceans by currents and diffusive transport (Talley et al., 2013), and as they circulate in different areas, their geochemical composition is modified by different processes. Among these: mixing with other water masses, variations in biological productivity, hydrothermal activity or continental processes, such as input from rivers; all of which leave a particular geochemical imprint on water. Oceanographic missions since the ~1960's have sampled and analyzed the physical and chemical characteristics of the world oceans, allowing to identify the global distribution of water masses and begin to understand the processes driving their formation and circulation. Here, the distribution of water masses in the study area is done by looking at the GLODAP v2 2021 compilation of oceanographic data (Lauvset et al., *in preparation*), together with a compilation of the Southeast Pacific Ocean (Figure 1.2, Reyes-Macaya et al., *submitted*). The interpretation of the paleoceanographic records produced in this thesis, are later interpreted in terms of changes in the formation and/or circulation of the intermediate and deep water masses *bathing* the sites where the marine sediment cores here studied were retrieved (chapter 2 and 5).

The study area is highly influenced by processes occurring in the Southern Ocean. This ocean corresponds to the portion of the global ocean located around Antarctica and bounded to the north by the Subtropical Front. The Subtropical Front is a latitudinal band at which surface temperature and salinity change fast from colder/less saline waters to the south (associated with processes in the Southern Ocean), to warmer/more saline waters to the north (associated with processes in the equator and subtropical latitudes). This ocean connects the Pacific, Atlantic and Indian Oceans through the Antarctic Circumpolar

Current, an eastward flowing current that carries surface, intermediate, deep and abyssal waters all the way around Antarctica. One of the most relevant processes occurring in the Southern Ocean, in particular with respect to the *store/release of* carbon from the deep ocean, is the upwelling of deep waters. At the surface, the eastward flowing water driven by the Antarctic Circumpolar Current, is pushed northward by the effect of the Southerly Westerly Winds blowing above it (e.g. Marshall & Speer, 2012; Wyrtki, 1961; Gordon, 1971; Toggweiler and Samuels, 1993). This continuous transport of surface waters to the north is balanced by the upward flow of deep waters to the surface. The intense winds at the surface ocean then favor gas exchange between the newly upwelled deep waters and the atmosphere, *ventilating* the deep ocean.

The southern tip of South America reaches ~56° S, thus being the southernmost continental extremity on earth on the planet, excluding Antarctica, and as such, it *interrupts* the Antarctic Circumpolar Current in its flow from the Pacific into the Atlantic Ocean. At the surface, east flowing waters *bump into* South America, deviating some of the flow to the north along the Chilean margin, and some to the south rejoining the Antarctic Circumpolar Current main flow (Figure 1.2). Because of the latter, Southern Ocean–like conditions at the surface ocean reach further north in the Southeast Pacific (~30° S) than in any other part of the world. In contrast, at deep and abyssal depths, the Antarctic Circumpolar Current is bounded by bathymetry, and in the study area is particularly constrained by the Chile Rise (~50° S; Figure 1.2). Thus, the limit between the Southern Ocean and the Southeast Pacific in the surface, close to the continent, is not very clear , and both "Southeast Pacific sector of the Southern Ocean" or "Southeast Pacific" are used to refer to this area.

In the following, the characteristics of water masses identified in the study area are described, together with the mechanisms proposed in the literature to explain their formation.

1.1.1.1 Subantarctic Surface Water

Subantarctic Surface Water (SAAW, SASW or SSW) is a surface water found in the Southern Ocean, between the Subtropical Front to the north, and the Polar Front to the south. This water mass is identified by low salinities and high levels of oxygen and intermediate levels of phosphate, which in the Chilean continental margin are observed between ~54° S and ~30° S, from the surface until ~100 m depth (Figure 1.2, Strub et al., 1998; Silva et al., 2009; Reyes-Macaya et al., *submitted*). The characteristics of SAAW are given by the upwelling of deep waters in the Southern Ocean to the surface, and their consecutively circulation around Antarctica driven by the Antarctic Circumpolar Current. When deep waters upwell, they bring high phosphate, low oxygen waters into the surface. While these waters are being transported around Antarctica, they exchange gases with the atmosphere (aided by the high velocities of the Southerly Westerly Winds above them), rising their oxygen contents. At the same time, biological productivity at the surface utilizes part if its initial phosphate content, resulting in intermediate values. Finally, relative low salinities are given by high precipitation and sea–ice meltwater inputs,

freshening surface waters (McCartney, 1977). In the studied area, salinities are particularly low because of additional fresh water input from Patagonia (Bostock et al., 2013).

SAAW is transported east around Antarctica by the Antarctic Circumpolar Current, which as mentioned before, encounters the South American continent at ~43° S. There, it separates in a northern branch, the Peru–Chile Current, also known as the Humboldt Current, which transport SAAW until ~30° S; and the Cape Horn current, which transports it south and east through the Drake Passage into the Atlantic Ocean. SAAW is present at the surface at the retrieving sites of all the cores studied in this thesis.

1.1.1.2 Equatorial Subsurface Water

Underneath surface waters, the Equatorial Subsurface Water (ESSW) is transported south from the Equatorial East Pacific (EEP) by the Peru–Chile Undercurrent along the South American margin (Silva et al., 2009; Silva & Fonseca, 1983; Strub et al., 1998; Wooster & Gilmartin, 1961; Wyrtki, 1967), and at ~80°W by the Perú–Chile Countercurrent (Silva et al., 2009). It can be identified as a subsurface salinity maximum, phosphate maximum and oxygen minimum, between ~200 m and 600 m depth (Figure 1.1), and from ~10° S to ~39°S (Wooster & Gilmartin, 1961; Llanillo et al., 2013; Garcia et al., 2013; Vargas et al., 2021; Reyes-Macaya et al., *submitted*), though not further than ~100 km from the coast (Silva et al., 2009). The high salinity of the ESSW is interpreted as derived from a slow southward flow from the equator, where evaporation exceeds precipitation. The oxygen minima and phosphate, in the other hand, derive from its flow south along the South American margin, where it is constantly brought to the surface by coastal upwelling. When the ESSW upwells, it brings nutrients such as phosphate and silicate to the surface, sustaining high marine productivity in the area. When these organisms die, they decompose on its way down the water column, a process which utilizes oxygen and returns phosphate and silicate to the water. This process is constantly recycling nutrients and using oxygen, explaining the observed characteristics of ESSW. Permanent coastal upwelling in the Southeast Pacific brings ESSW to the surface north of ~35° S (Strub et al., 1998).

1.1.1.3 Antarctic Intermediate Water

Antarctic Intermediate Water (AAIW) is a water mass flowing at intermediate depths of the ocean, characterized by having relatively low salinity, low phosphate and high oxygen contents. In the Southeast Pacific, it is identified between ~400 m and 1,200 m depth, from ~55° S until ~25° S (Reyes-Macaya et al., *submitted*; Silva et al., 2009; Johnson, 1973; Reid, 1965; Tsuchiya & Talley, 1996, 1998). The relatively high oxygen and low phosphate contents of AAIW, derive from the same initial process as SAAW: the upwelling of deep waters in the Southern Ocean and their modification as they flow around Antarctica. For reasons that are still debated (for a more detailed discussion on AAIW formation, see Bostock et al., 2013), part of this water mass sinks to intermediate depths of the Southern Ocean, from where it is transported north to lower latitudes in the Pacific, Atlantic, and Indian oceans (Bostock et al., 2013; McCartney, 1977; Piola & Gordon, 1989). AAIW formation occurs in many areas of the Southern Ocean,

from which the Southeast Pacific has been indicated as the main modern formation area (e.g., Bostock et al., 2013; McCartney, 1977, 1982; Talley, 1996, 1999). From there, it circulates to the north to enter the south Pacific subtropical gyre circulation and to the east through the Drake Passage into the Atlantic Ocean (Talley, 2013; Tomczak & Godfrey, 2003). Cores GeoB 7163-7, GeoB 7162-6 and 22SL where retrieved in the upper boundary, core and lower boundary of the AAIW, respectively.

1.1.1.4 Circumpolar Deep Water

Circumpolar Deep Water (CDW) corresponds to the subsurface flow of the Antarctic Circumpolar Current. At the same time as CDW circulates east around Antarctica, it is upwelled to the surface in the Southern Ocean being the precursor of SAAW, AAIW and Antarctic Bottom Water (section 1.1.1.4). CDW can be divided in Upper Circumpolar Deep Water (UCDW) and Lower Circumpolar Deep Water (LCDW). UCDW is recognized as a relative oxygen minimum (Cater et al., 2008), which results from the southward transport of Pacific Deep Water (section 1.1.1.4) into the Southern Ocean, where it encounters the Antarctic Circumpolar Current (Carter et al., 2008). In the study area, UCDW can be found south of ~54° S, between ~1,400 m and 2,500 m depth. Underneath UCDW, LCDW is recognized as a salinity maximum. This high salinity derives from North Atlantic Deep Water (NADW) entering the Antarctic Circumpolar Current in the South Atlantic, together with newly formed high–salinity deep waters around Antarctica. A portion of LCDW is transported northward by deep western boundary currents in the Atlantic, Indian and Pacific Oceans (Whitworth et al., 1999; Sloyan and Rintoul, 2001; Sloyan, 2005). In this northward path, LCDW very likely reaches the North Pacific to be part of the formation of PDW (Holzer et al., 2021; Koshlyakov & Tarakanow, 2004). In the study area, LCDW can be found south of ~54° S at depths below ~2,500 m, north of ~54° S, it can be identified at depths higher than ~3,500 m, recognized by relatively high oxygen contents with respect to PDW. There, probably a mix of Antarctic Bottom Water (AABW) and LCDW is transported to the North Pacific to form PDW (Holzer et al., 2021; Koshlyakov & Tarakanow, 2004; Talley, 2013). Core MD07-3119 (46.08° S, 76.1° W, 2500 m) was retrieved in the boundary between UCDW and PDW, and core MD07-3081 (49.42° S, 76.96° W, 3273 m) was retrieved in the boundary between PDW and LCDW (Figure 1.2).

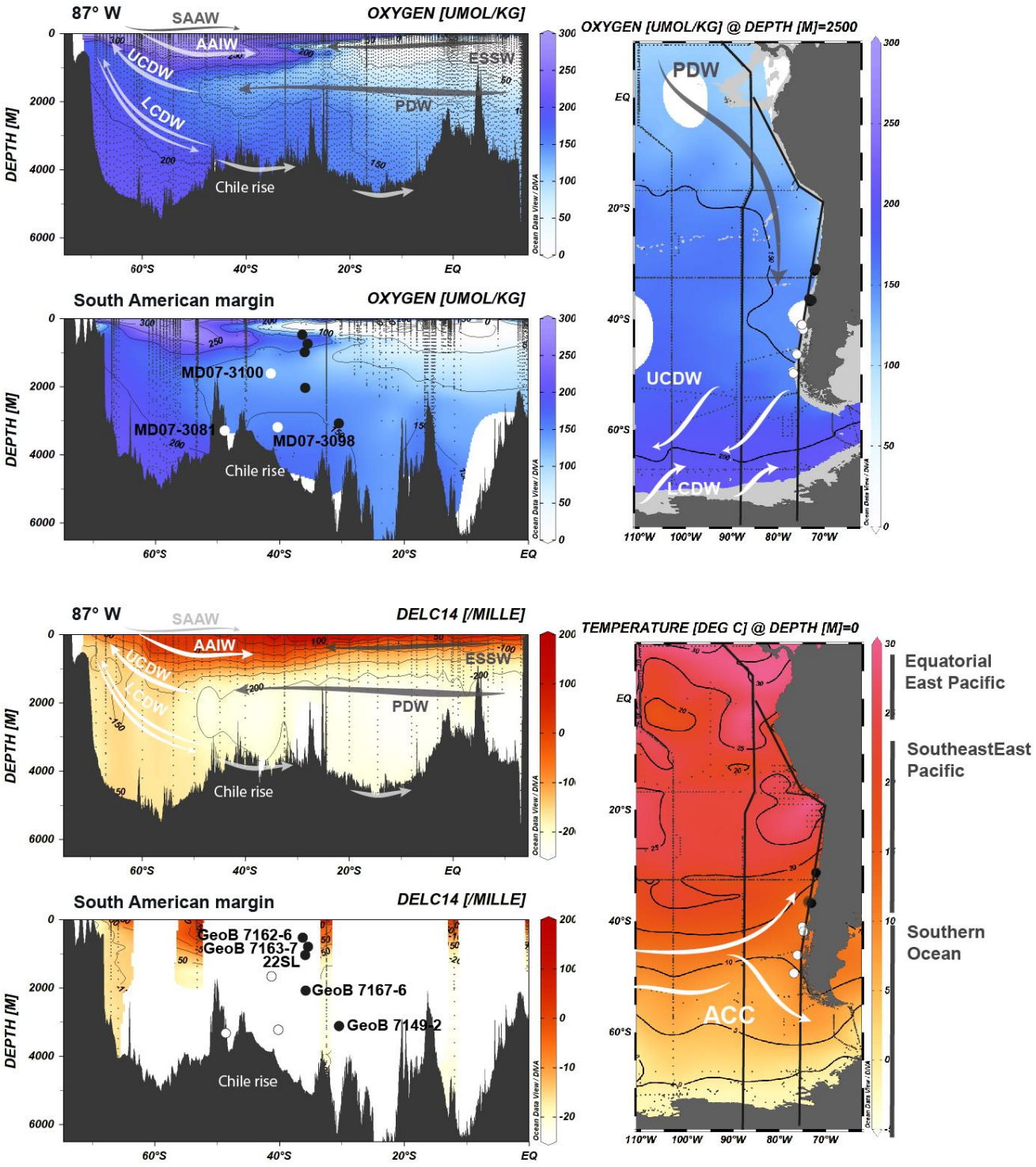

Figure 1.2 Water mass distributions in the Southeast Pacific and position of the marine sediment cores studied in the thesis. The postion of the ections is illustrated in the maps to the right All sections produced in ODV with the GLODAPv2.2021 collection (Lauvset et al., in preparation).

1.1.1.5 Pacific Deep Water

Pacific Deep Water (PDW) is the oldest water mass in the modern ocean, i.e. the water mass that has been *isolated* from the atmosphere for the longest time, with estimated ventilation ages of ~1,500–2,000 years (Kumamoto et al., 2007). It is characterized by high nutrient contents (phospahte, silicate) and low oxygen and radiocarbon contents (see section 1.2.1.1 for more details on radiocarbon). These characteristics derive from its isolation from the atmosphere for long periods of time, during which deep waters accumulate nutrients and loose oxygen during the remineralization of organic matter. The exact formation mechanisms of this water mass are not well understood, however, is thought to derive from a mixture of deep and abyssal waters (a mixture of CDW, AABW and NADW) transported north from the Southern Ocean, upwelling to the mid–depths of the North Pacific Ocean; together with intermediate waters: AAIW and North Atlantic Intermediate Water, which would down well to mid–depths. PDW is much older than any of the water masses from which it is thought to derive. It has been proposed that the transport out of the North Pacific to the Southern Ocean, would be diffusion rather than advection controlled, which would explain the *aging* of PDW in the North Pacific. The latter can be understood as the mid–depths of the North Pacific being a more *stagnant* area of the ocean, where water takes a long time to circulate. In the study area, PDW can be identified between ~1,000–3,500 m, from the North Pacific until ~50° S, where it is transported south to upwell in the Southern Ocean, being one of the precursors of SAAW and AAIW. Core MD07-3100 (41.60° S, 74.95° W, 1609 m depth) was retrieved in the upper limit of PDW, near the boundary with AAIW; cores MD07-3098 (40.93° S, 75.03° W, 3055 m).

Because of the position of the marine sediment cores near the boundaries of deep water masses, it is expected that, if their formation and/or circulation varied since the late glacial, these changes would be observed in the studied cores.

1.1.1.6 Antarctic Bottom Water

This water mass is not found in the study area, however it is indicated to have had an important role in the accumulation of carbon in the deep ocean in the late glacial period (e.g. Adkins, 2013; Keeling & Stephens, 2001), and as such –for the objectives of this thesis–it is relevant to understand its formation and distribution in the modern ocean. AABW is characterized by its high neutral density, derived from an ensemble of processes occurring in the Southern Ocean (Carter et al., 2008). Among these, the formation of sea ice around Antarctica, which leaves behind highly saline waters; at the same time, the freezing and melting of water at temperatures around 0° C, which results in super cold–highly saline waters. These processes and others, result in waters denser than surrounding ocean, which subduct into abyssal depths. A *pure* version of this water mass is not found far from the Southern Ocean, as it mixes with CDW in its circulation to abyssal depths and to lower latitudes, in the Pacific, Atlantic and Indian Oceans.

1.1.2 Southerly Westerly Winds

A very important climatic feature in the study area are the Southerly Westerly Winds (SWW). These are strong eastward blowing winds present all the way around Antarctica. Their latitudinal extension and intensity changes seasonally: in summer they are more intense and concentrated in a narrower band between ~50–55 °S; whereas in winter their distribution is wider, reaching until ~35° S in South America, but velocities are lower. These winds have a strong influence both in the oceanic circulation in the Southeast Pacific and Southern Ocean, as in the climate in Patagonia, the southernmost area of South America (south of ~40° S). On top of its seasonal variability, the SWW display a decadal–to–centennial variability in its latitudinal position, referred to as the Southern Annular Mode. In a positive (negative) phase of the Southern Annular Mode, SWW are closer (farther) from Antarctica. As air masses blow east above the Pacific Ocean, their water vapor content increases. When these encounter the Andean cordillera, the air is forced to ascend and as it does, it cools down, and they precipitate. This process is the main the precipitation source in Chile south of ~33° S (Garreaud et al., 2013), and in southern Patagonia it sustains the remnants of the Patagonian Ice Sheet: the northern and southern Patagonian Ice Field (Campos de Hielo Norte y Campos de Hielo Sur). The strong relationship between precipitation in Patagonia and the position of the SWW has been used to track latitudinal and intensity variations of SWW since the late glacial, by studying vegetation variations (e.g. Moreno et al., 2012). These studies indicate that at ~20 cal ka BP, the position of the SWW was ~5° to the north of its present day position.

The position of the SWW also modulates coastal upwelling in the Chilean continental margin, which brings ESSW to the surface. The western boundary of South America is characterized by strong northward winds, running parallel to the coast line north of ~35° S. This wind *pushes* the surface water northward, while the rotation of earth deviates it west. This pushes surface away from the coast, which brings deeper waters (ESSW) to the surface. At latitudes where SWW are present, however, the wind direction in the coast is eastward, which pushes water into de continent, impeding coastal upwelling. Broadly, the latter results in permanent upwelling north of 35° S; seasonal upwelling between ~35–40° S, because of the presence of SWW in austral summer; and no upwelling south of ~40° S, because of permanent presence of SWW.

Finally, the SWW also modulate upwelling of deep waters around Antarctica and aid the sea–air gas exchange at the surface in the Southern Ocean. Both the position and intensities of the SWW are associated with the net upwelling of deep waters in the Southern Ocean. It has been indicated that a southward position of the SWW coincident with the ACC is the most favorable for deep water upwelling (Marshall & Speer, 2012). Meanwhile, in a northward position of the SWW, the ACC is less strong and the surface oceanic circulation is instead dominated by eddy circulation. In this context, the effect of the SWW is less effective in pushing water north, and consequently in upwelling deep waters. Because of this

reason, and as mentioned before, the position of the SWW has been indicated to have been part of the store/release mechanisms associated with the last glacial–interglacial transition.

1.1.3 Geological context

As mentioned before, the studied cores where retrieved in the Chilean continental margin, adjacent to Patagonia. There, two very active volcanic zones are present: the Southern and Austral Volcanic Zone of the Andes. The Southern Volcanic Zone of the Andes, extends from Tupungatito volcano (~33° S) to Hudson volcano (~46° S) and is the result of the subduction of the Nazca plate under the South American plate (a more comprehensive description can be accessed in chapter 4). This subduction also is responsible for the uprising of the Andean Cordillera. During the Last Glacial Maximum (~26,000–20,000 years BP), a glacial casquet occupied the Andes south of ~38° S (Davies et al., 2020). The erosion and retreat of this glacial casquet resulted in numerous proglacial lakes, fjords and islands south of 38° S. All the cores here studied were retrieved in the open ocean, however during the last deglaciation, surface waters at the core retrieving sites were affected by the melt of the Patagonian casquet, as already observed by Haddam et al. (2018) is core MD07-3100.

1.2 Methods overview

1.2.1 Stable isotopes ($\delta^{18}O$, $\delta^{13}C$) stratigraphy

As mentioned before, water masses have particular geochemical imprints which derive from the different processes leading to their formation and from the circulation paths they follow through the global oceans (Figure 1.2). In oceanography, the chemical species which provide relevant information on these processes are called *tracers.* In order to interpret how oceanic circulation might have changed in the past, paleoceanographers reconstruct variations in these tracers in different parts of the global ocean. To do so, they often study deep sea corals and/or marine sediment cores, which correspond to paleoceanographic *archives*. In this thesis, I studied the downcore variations in radiocarbon ages and stable isotope ratios ($\delta^{18}O$, $\delta^{13}C$) of planktic and benthic foraminifera, in nine marine sediment cores. Here, ^{14}C, $\delta^{18}O$ and $\delta^{13}C$ are the tracers which are interpreted in terms of variations in oceanic circulation (details below). The principle behind this, is that sediment that accumulates in the bottom ocean contains information about variations in the water above it. This sediment is composed of detrital particles (such as rock fragments, volcanic ash, clay, etc.) and the remains of organisms that once lived in the water above it (such as foraminifera, diatoms, coccolithophores, etc). When living organisms die, their bodies sink to the bottom ocean and become part of the sediment. There, the remains of planktonic organisms contain information about the surface waters they once lived in (e.g. planktonic foraminifera), whereas benthic organism record information about bottom water and/or pore water (e.g. benthic foraminifera). The composition of the sediment that is continuously buried in the bottom ocean varies in time, reflecting changes occurring in the ocean (e.g. increase/decrease of biological productivity, a different water mass

circulating in the surface or bottom ocean), and on land (e.g. more or less sedimentary input by rivers, dust and/or volcanic eruptions). These changes are *recorded* in the sediment, and by analyzing the characteristics of the marine sediment at different depths of the cores, we can reconstruct for example, how a particular oceanic tracer varied in the past.

Before interpreting changes in the characteristics of the sediments in the marine cores in terms of oceanic circulation variations, it is necessary to evaluate whether these sediments were deposited in situ or not. Ideally, the studied marine sediment cores correspond to sediment deposited continuously and in situ, thus effectively representing variations in the surface and bottom water above the core retrieving sites. In the studied area, marine sediments are not unlikely to be remobilized as the Chilean continental margin is relatively narrow, with steep slopes and recurrent seismic activity, derived from the subduction of the Nazca plate below the Sudamerican plate (Contreras-Reyes, 2018). At the same time, to begin to study the marine sediment cores, it is very important to have an initial reference of the time frame they represent. This will allow first of all to identify the intervals of the cores to be analyzed, in this case the portion between the last late glacial and the core top. Additionally, it allows to have an idea on the sediment accumulation rate of the cores, i.e. the time it takes for a given thickness of sediment to accumulate. This is important because, depending on the aim of the study and the accumulation rate, the sampling spacing is determined. Stable isotope ($\delta^{18}O$) stratigraphies, of marine sediment cores are a very useful tool to evaluate the time frame the cores span, and whether or not the sediment has been deposited in situ or not. In this thesis I used them with this purpose. However, the same information can be interpreted in terms of oceanic circulation (e.g. Haddam et al., 2018).

$\delta^{18}O$ corresponds to the ratio of the stable isotopes of oxygen ^{18}O and ^{16}O measured in a particular sample, versus a reference value. Most of the oxygen on the earth corresponds to ^{16}O (~99.8%), whereas the ^{18}O represents about ~.2%. These two isotopes of oxygen are distributed on different reservoirs in different proportions and move between them at different rates. For example, when water evaporates, H_2O containing ^{16}O will preferentially evaporate because it is lighter than H_2O containing ^{18}O. In contrast, when water precipitates, H_2O with ^{18}O will precipitate first. Broadly speaking, most of the water evaporation occurs in the equator, and from there water moves poleward precipitating, and again evaporating, several times in its way to the Arctic and Antarctica. This process leaves waters at the equator depleted in ^{16}O (thus having higher $\delta^{18}O$ values), and waters in the poles and ice caps enriched in ^{16}O (thus having lower $\delta^{18}O$ ratios). Following this principle, if relatively more water precipitates and is *stored* in ice caps, the overall $\delta^{18}O$ value of the ocean will increase. On the contrary, as these ice caps melt, the $\delta^{18}O$ of the ocean will decrease, as ^{16}O from ice caps goes into the ocean. Because of this property, $\delta^{18}O$ analyzed in ice and marine sediment cores is used as a proxy to interpret global ice volume changes in the past. These records have revealed cyclical changes during the last ~2 MA (Figure 1.1), the glacial—interglacial cycles. This is a global signal that is recorded by planktonic and benthonic

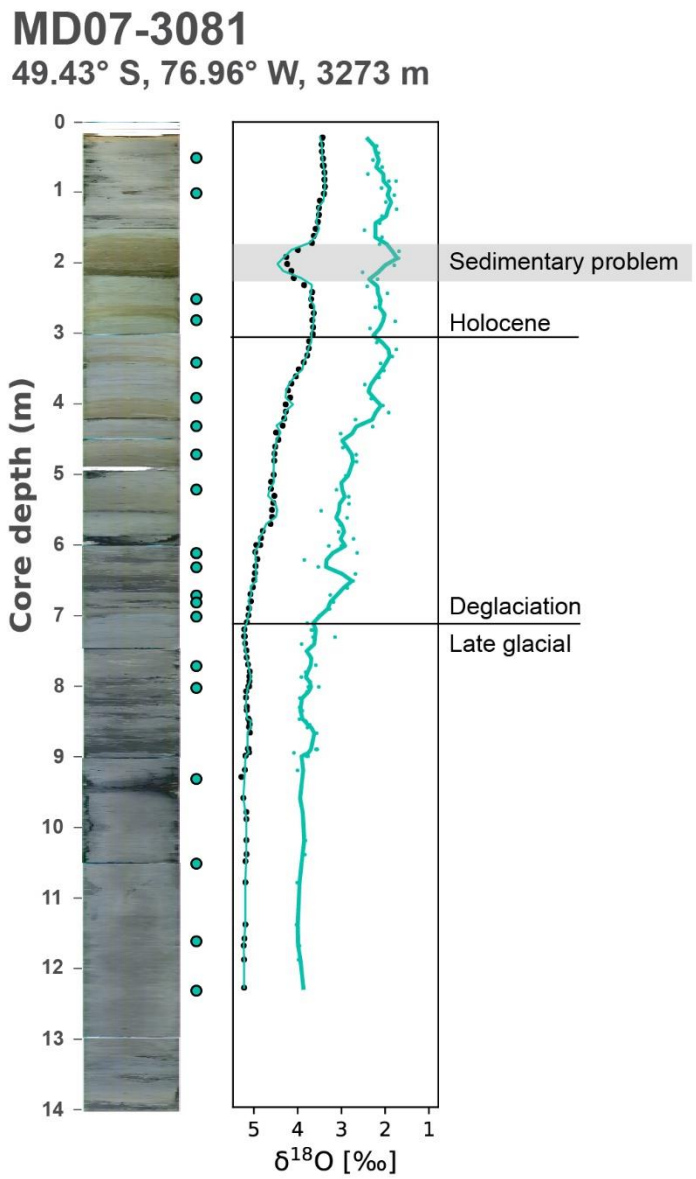

Figure 1.3 Stable isotope ($\delta^{18}O$) stratigraphy of core MD07-3081. The curve allows to have a first order evaluation of the time frame the core represents, by recording transitions associated with climatic periods (late glacial, deglaciation, Holocene). Curve with black dots corresponds to analysis in benthic foraminifera *Uvigerina peregrina*, and the turquoise line to the three point moving average. Curve with turquoise dots corresponds to planktic foraminifera *Globigerina bulloides*. To the left, a composite image of the core.

foraminifera which form part of the marine core sediment. By analyzing the $\delta^{18}O$ of planktic and benthic foraminifera *picked* at different depths of marine sediment cores, the $\delta^{18}O$ of surface and bottom waters in the core retrieving site can be reconstructed. Even though local processes can affect the $\delta^{18}O$ recorded by the foraminifera, the signal of global ice volume is generally observable and can be used as a reference to understand the time interval the cores represent. In this thesis, I used previously produced $\delta^{18}O$ records in cores MD07-3098, MD07-3100, MD07-3119 and MD07-3081 to identify the portion of the cores containing the last deglaciation, and discriminate between relevant climatic periods (an example in Figure 1.3).

Additionally, the fact that the $\delta^{18}O$ is a global signal, can be used to identify portions of marine sediment cores which might have been remobilized. For example, if a landslide occurs and results in older sediments being deposited above modern sediments. In this case, if the sediments are old enough to have a different $\delta^{18}O$ value, the down core δ^{18} curve will reveal this re transported sediment as anomalous $\delta^{18}O$ values (Figure 1.3). In the study area, this is particularly true for benthic foraminifera $\delta^{18}O$. Because these cores were retrieved adjacent to the remains of the Patagonian ice sheet, the planktic foraminifera $\delta^{18}O$ was affected by its melting during the deglaciation (Haddam et al., 2018). And so, the global ice volume signal is overprinted by the local melt signal. The benthic foraminifera $\delta^{18}O$ signal, on the other hand, is more stable as is less affected by surface processes such as fresh water inputs or evaporation. Thus, in order to identify the portions of the cores where sediments where probably remobilized, I looked at the benthic foraminifera curves and identified intervals with sedimentary problems in cores M07-3098 and MD07-3081. The portions with problems were not analyzed for radiocarbon or tephrochronology.

Another broadly utilized stable isotope ratio, in paleooceanography is $\delta^{13}C$ ratios of planktic and benthic foraminifera. As $\delta^{18}O$, $\delta^{13}C$ corresponds to the ratio between two stable isotopes of carbon: ^{13}C (~1.1%) and ^{12}C (~98.9%), measured in a given sample, with respect to a reference value. The information provided by the down core $\delta^{13}C$ values of planktic and benthic foraminifera is complementary to that of $\delta^{18}O$, and generally both ratios are analyzed at the same time in a given sample. The $\delta^{13}C$ of ocean water is controlled mainly by two processes: photosynthesis/respiration of organic matter and air–sea gas exchange. On the one hand, the photosynthesis of living organisms in the surface ocean uses preferentially ^{12}C, leaving surface waters with relatively higher $\delta^{13}C$ values. When these organisms die, they sink and in their way down they decompose and ^{12}C is reincorporated to the water column. Because of this, the longer a water mass has been isolated from the atmosphere, the lower its $\delta^{13}C$. When these waters upwell to the surface, they exchange gases with the atmosphere and its $\delta^{13}C$ is modified again. This process is temperature–dependent and so, surface waters in the equator have higher $\delta^{13}C$ than surface waters in the pole. Water masses present in the Southeast Pacific Ocean display very contrasting $\delta^{13}C$ values (e.g. Reyes-Macaya et al., submitted) and thus $\delta^{13}C$ can be used as a tracer for water mass circulation changes. In particular, I used the $\delta^{13}C$ of planktic foraminifera *Globigerina bulloides*, to interpret changes in coastal upwelling at different latitudes in the Chilean continental margin. As mentioned before, coastal upwelling north of ~40° S brings *older/* $\delta^{13}C$–depleted ESSW to the surface. This will have an effect on the radiocarbon ages of planktic foraminifera, and thus in the marine core chronologies (details in section 1.2.1.2). So the information provided by planktic foraminifera $\delta^{13}C$ is very valuable, by being able to record variations in coastal upwelling. Benthic foraminifera $\delta^{13}C$, in the other hand, represents variations in the circulation of intermediate and deep waters, and so is complementary to the information provided by the benthic foraminifera ^{14}C ages.

The downcore analysis of $\delta^{18}O$ and/or $\delta^{13}C$ of planktic and benthic foraminifera, and its stratigraphic implications, corresponds to the *stable isotope stratigraphy*.

1.2.2 Radiocarbon

In this thesis, I use radiocarbon ages of benthic foraminifera as a tracer of the time a determined water mass has been isolated from the atmosphere. From this, variations in the circulation of intermediate and deep waters in the Southeast Pacific, during the last 20,000 years, are interpreted (chapters 2 and 5). This is relevant in the context of understanding the mechanisms of store/release of carbon in the ocean, as the longest a water mass is isolated from the atmosphere, the more carbon it accumulates through remineralization of organic matter. Thus, it is possible to roughly interpret changes in carbon storage of a water mass from its ^{14}C content.

^{14}C is a radioactive isotope of carbon, naturally produced in the upper atmosphere. There, a series of reactions are initiated by the irruption of high–energy cosmic rays. One of the products of these reactions are free neutrons, which when emitted to the atmosphere collide with ^{14}N atoms. The result of this collision adds an extra neutron and removes a proton from ^{14}N, resulting in a ^{14}C atom. This way, ^{14}C is produced in the atmosphere where it *enters* the carbon cycle. There, it reacts to form different carbonated species (e.g. CO2, CH4, etc.) that are, for example, incorporated in living organisms by photosynthesis or go into the ocean by air–sea gas exchange. This newly produced ^{14}C is unstable (radioactive) and thus, given a certain amount of time, it transforms back into ^{14}N. The rate at which this process occurs is quantified by the "half–life", which is a measure of the time it takes for an initial quantity of a radioactive element (in this case radiocarbon) to reduce in half. The accepted half–life or ^{14}C is 5,730 ± 40 years (Godwin, 1962).

As many other radioactive isotopes, the fact that ^{14}C transforms at a fixed rate can be used as a way of timing different processes involving carbon species and to estimate the age of materials composed of carbon. Radiocarbon can be analyzed either as a geochemical component of, for example the atmosphere or the ocean, in which case it is generally reported as $\Delta^{14}C$ [‰]. $\Delta^{14}C$ is a measure of the level of enrichment or depletion of a sample with respect to a reference value, which represents the ^{14}C of the atmosphere of the year 1950 a.d. (Stuiver and Polach, 1997). On the other hand, when ^{14}C is analyzed in order to estimate the age of materials, it is reported as a "conventional ^{14}C age" (from here on ^{14}C age), which is different from the *absolute* age, often called the "calendar age". In order to estimate the calendar age of a material from its ^{14}C content, it would be necessary to either: quantify the daughter product of the decay of ^{14}C (i.e. ^{14}N) or alternatively, know the initial quantity of ^{14}C in the sample.

With this information then it is possible to estimate how much time has passed to explain the amount of ^{14}C remaining in the sample. Unfortunately, it is not possible to quantify the daughter product of ^{14}C of a sample (i.e. ^{14}N) because it is either not retained in the material to be dated, or even if it does, as ^{14}N is a

very abundant element on earth, it is not possible to distinguish the original ^{14}N from the one produced by radioactive decay. Alternatively, it is not possible either to estimate the original amount of ^{14}C of a sample, as the amount of radiocarbon in the atmosphere, and thus in other reservoirs, varies in time (and space). First of all, changes in the magnetic field of earth can derive in changes in the production rate of ^{14}C, by modulating the amount of cosmic rays entering the upper atmosphere (Laj et al., 2002). Additionally, atmospheric ^{14}C is proposed to change because of the exchange of carbon between different

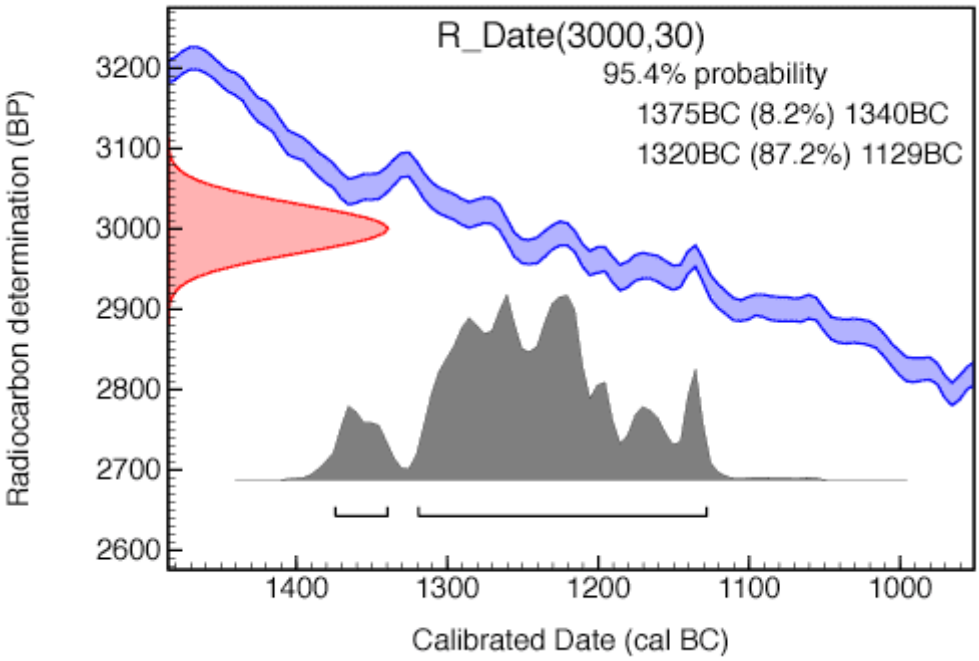

Figure 1.4 Calibration of a radiocarbon age (in the example 3,000 ± 30 ^{14}C years BP, red curve). The resulting calendar age distribution corresponds to the grey curve. The uncertainty derived from the calibration can be communicated as a 95.4% confidence interval of 1375–1320 cal years BC. Imagen and calibration by OxCal 4.4 (Bronk Ramsey, 2009) using IntCal20 (Reimer et al., 2020)

reservoirs. In fact, during the last deglaciation, an atmospheric ^{14}C drop in ~190‰ has been proposed to be associated with the release of the old carbon from the deep ocean reservoir (Broecker and Barker, 2007). Because of this, the conventional ^{14}C age is calculated, which represents the time it would have to pass for a reference value (0.95* ^{14}C activity of oxalic acid in 1950 a.d.) to decrease its ^{14}C content, to the amount analyzed in the sample (Stuiver & Polach, 1977). This ^{14}C age is then compared with a calibration curve, which pairs ^{14}C ages with calendar ages. The curve is *built* by dating materials which can be dated by ^{14}C and by an independent method by which absolute calendar ages can be obtained (e.g. tree rings). Because the amount of radiocarbon in the atmosphere has changed in time, many calendar ages can have similar ^{14}C ages. Thus, when a ^{14}C age is calibrated, it is not assigned one calendar age, but the probability of corresponding to one or many intervals of calendar ages (Figure 1.4). The construction of the calibration curve is an international effort which integrates tree ring records, speleothems, plants

macrofossils, among other. Periodically, an updated calibration curve is published, the last of which corresponds to IntCal20 (Reimer et al., 2020). Because the ^{14}C content of the atmosphere is not homogeneous, two calibration curves are produced by the international community: IntCal20, which represents the content of the Northern Hemisphere; and SHCal20, the Southern Hemisphere (Hogg et al., 2020). Thus, when calibrating ages in the Southern Hemisphere, the latter should be used.

1.2.1.1 Benthic foraminifera ^{14}C dating as a proxy for deep water ventilation changes

As already mentioned, ^{14}C is produced in the atmosphere, from where it enters the ocean by air–sea gas exchange at the surface. In some areas of the global ocean, the water at the surface is continuously being subducted to deeper depths, where they begin a subsurface circulation. When the latter occurs, water stops exchanging ^{14}C with the atmosphere and thus begins to *lose* its radiocarbon content over time. Thus, waters containing less ^{14}C, have generally been isolated the longest from the atmosphere and so, its ^{14}C content can be used as a tracer to estimate the time a water mass has been isolated from the atmosphere. Nevertheless, other processes can also modify the ^{14}C of a water mass, such as submarine production of CO_2 from hydrothermal sources, or mixing with water masses with different initial ^{14}C contents.

In the modern ocean, the radiocarbon content of sea water is sometimes analyzed and is reported as $\Delta^{14}C$ [‰]. At present, negative $\Delta^{14}C$ values are found in intermediate (~500–1000 m), deep (1000–3000 m) and abyssal waters (>3000 m), derived from long periods of time being isolated from the atmosphere, whereas positive values are found in surface and in upper layers of intermediate waters (Figure 1.2). The latter is a result of anthropogenic production of ^{14}C in the atmosphere during bomb–tests in the 1960's. These tests liberated a high amount of free neutrons into the atmosphere, increasing atmospheric $\Delta^{14}C$ from ~0 ‰ in the 1950's, to ~1000‰ in 1963–1964 A.D. The entrance of this "extra" ^{14}C in the carbon cycle, altering "natural values", for example in surface and intermediate waters, has been termed *the bomb effect*. It is important to keep this in mind when interpreting the $\Delta^{14}C$ of the ocean, as the absolute differences in $\Delta^{14}C$ of the different water masses in the present cannot be use as reference to interpret changes in the past. Different approaches have reproduced pre–bomb oceanic $\Delta^{14}C$ values (Kumamoto et al., 2011; Key et al., 2004; Devries and Holzer et al., 2019), estimating it from other tracers correlated with ^{14}C, such as silicate concentration, alkalinity and apparent oxygen utilization. However, there is no consensus on the accuracy of these estimates. Still, the relative $\Delta^{14}C$ values of water can still give us information on the circulation of different water masses. In particular, in the Southeast Pacific, the most detailed ^{14}C information available corresponds to a transect at 87° W (Figure 1.2), from which the main water masses described in section 1.1.1 are distinguishable, except for ESSW. From this, it is clear that the water mass with the least amount of ^{14}C in the modern ocean is PDW, which derives from its formation away from the surface at the mid-depths of the North Pacific Ocean (Talley et al., 2013; Holzer et al., 2021). In contrast, AAIW has relatively high ^{14}C contents, which derive from its formation at the surface, in the presence of intense SWW that favor sea–air gas exchange and which has incorporated some of the

bomb effect ^{14}C. CDWs on the other hand, have lower ^{14}C than AAIW but higher than PDW, indicating less exchange with the atmosphere during its formation than the former. From this, if oceanic circulation was different in the past, for example modulating the exchange of gases with the atmosphere, it is expected to be reflected in the ^{14}C of the content of the ocean.

But how we can reconstruct the radiocarbon content of sea water in the past?

As said before, the study of ancient climate (paleoclimate) and ancient oceanography (paleoceanography) uses proxy records to reconstruct important climatic variables that cannot be directly measured. In this case, I use ^{14}C ages of planktic and benthic foraminifera as a proxy for ^{14}C content of intermediate and deep waters in the last 20,000 years. Foraminifera are unicellular organisms that live in the ocean or lakes, and form their tests (similar to shells) out of the carbonate (CO_3^-) and calcium (Ca^+) of the water they live in, a process called *calcification*. Foraminifera are though to calcify in equilibrium with the carbon in the surrounding sea water, thus they *register* the ^{14}C content of the sea water they live in. Planktonic foraminifera live in the surface ocean (from the surface down to ~400 m depths); whereas benthic foraminifera can live either just above the sediment (epibenthic foraminifera) or within the sediment (infaunal benthic foraminifera). When they die, planktonic foraminifera sink to the bottom of the ocean, and in their way down, some of them dissolve, whereas another portion makes it to the bottom ocean, joining living and dead benthic foraminifera at the bottom. In time, this results in foraminifera–bearing sediment accumulation which holds information on the variation of ^{14}C in the column water: planktonic foraminifera register changes in surface waters; whereas benthonic foraminifera, register changes in bottom waters.

In order to estimate the variation of ^{14}C content of deep waters in time, marine sediment cores are sampled at specific depths, from where benthic foraminifera are identified and collected for radiocarbon dating (a method often called *picking*). If a calendar age is assigned (see below) to the depths where benthic foraminifera where sampled, then the $\Delta^{14}C$ of deep waters in the past can be estimated by the following expression (Adkins and Boyle's (1997) definition derived from Stuiver and Polach (1977)):

$$\Delta^{14}C = \left(\frac{e^{-\frac{^{14}C\ age}{8,033}}}{e^{-\frac{cal\ age}{8,266}}} - 1 \right) 1000‰$$

Where ^{14}C age corresponds to the age of benthic foraminifera, and cal age to the calendar age assigned to the depth dated by benthic foraminifera. I use this approach to estimate variations in the ventilation of intermediate and deep waters in the Southeast Pacific during the last ~20,000 years.

1.2.1.2 Planktic foraminifera ^{14}C dating for marine core chronologies

As previously mentioned, if we want to understand how the atmosphere and the ocean interacted during the last deglaciation, it is necessary to better constrain the chronologies of paleoceanographic records. Their estimated calendar ages need to be more accurate and precise, and all the uncertainties in their estimations need to be accounted for and communicated. Additionally, in order to estimate $\Delta^{14}C$ variations of intermediate and deep waters in the past, it is also essential to precisely constrain the calendar ages of benthic foraminifera ^{14}C dates. For the time span studied in this thesis, chronologies for marine sediment cores are generally obtained by either: aligning stratigraphic records of the marine sediment cores (e.g. $\delta^{18}O$, Diffusive Spectral Rreflectance) to stratigraphic records of –precisely dated– ice cores (e.g. $\delta^{18}O$; Marchitto et al., 2007), a method called *tuning* or *wiggle matching*; by calibrating ^{14}C ages of planktonic foraminifera picked at different depths of marine sediment cores (e.g. De Pol-Holz et al., 2010); or by a mixture of both (e.g. Bova et al., 2018). Alternatively, another valuable paleoceanographic archive are deep sea corals. In contrast to marine sediment cores, deep sea corals can be absolutely dated by U–Th (e.g. Burke & Robinson, 2011; Chen et al., 2015), and additionally dated by ^{14}C, thus allowing to precisely estimate $\Delta^{14}C$ variations in the ocean in the past. Unfortunately, marine sediment cores cannot be dated by an absolute technique and subsequently their chronologies are less constrained. In the one hand, tuning is less precise as it relies, in that changes in the ocean and the sea are synchronous, which might not be the case, thus using this technique introduces an uncertainty which is not quantitatively accounted for. Additionally, it relies in identifying abrupt changes in the stratigraphic records of marine sediment cores (the *wiggles*), used as reference to synchronize them with ice core records. This abrupt change might not be present in the marine stratigraphy because their signal has been overprinted by local processes, or because the resolution of the marine stratigraphy is not enough to record these abrupt changes. In this case, the tuning introduces an additional error which is not accounted for quantitatively. On the other hand, the uncertainties in chronologies obtained by calibrating ^{14}C ages of planktic foraminifera, are associated mainly to two reasons. First of all, as already mentioned, ^{14}C ages are not calendar ages, instead they must be calibrated in order to estimate the calendar age they correspond to. Because the calibration curves are constantly being updated (e.g. IntCal09 (Reimer et al., 2009), IntCal13 (Reimer et al., 2013), IntCal20 (Reimer et al., 2020)), so will the calibrated calendar age estimates, thus chronologies must be updated regularly. Additionally, even if the curve did not change, because the amount of ^{14}C in the atmosphere varies in time, the same ^{14}C age might correspond not to one, but to several intervals of calendar ages. This constitutes an intrinsic error of the method, which is accounted for quantitatively when ^{14}C ages are calibrated (e.g. by using the software http://calib.org/calib/; Stuiver et al., 2021). Additionally, planktic foraminifera ^{14}C ages cannot be directly calibrated by curves such as IntCal20 or SHCal20, instead they must be corrected by an –a priori– unknown quantity before: the ^{14}C age difference between the atmosphere and the surface ocean (see

below), which introduces an additional source of uncertainty to calendar age estimates using this technique.

As already mentioned, ^{14}C is produced in the atmosphere, from where it enters the surface ocean by air–sea gas exchange. The efficiency of this exchange is modulated by different factors, for example by the wind intensity, which favors the exchange; the temperature, colder (warmer) waters impede (enhance) exchange; by how much time water stays at the surface ocean exchanging gas with the atmosphere, a longer time resulting in ^{14}C contents in surface ocean closer to that in the atmosphere; and by the initial ^{14}C content of the water, waters with lower ^{14}C contents will take a longer time reach an equilibrium with the atmosphere. Because of the bomb effect, we do not know exactly the degree of disequilibrium between surface waters and the atmosphere. However simulations on pre–bomb ocean indicate values lower than the atmosphere everywhere in the ocean (e.g. Khatiwala et al., 2018).

Thus, in order to obtain their true calendar age, marine ^{14}C ages must be first corrected by its difference with the contemporary atmosphere, called *marine surface reservoir age* (from here on Rs = $^{14}C_{water}$ - $^{14}C_{atmosphere}$). Because of the heterogeneities of the world ocean (such as: variations in temperature, wind velocities, residence time in the surface, initial ^{14}C of the water), Rs vary spatially; and because of the evolution of the climate system in time, they also vary in time. Thus, in order to correctly calibrate a planktonic foraminifera ^{14}C age, it is necessary to correct it for an appropriated Rs ($^{14}C_{corrected\ age}$ = $^{14}C_{measured\ age}$ + Rs).

Estimations of both modern and past variations in Rs worldwide are very scarce (e.g. Siani et al., 2013; Sikes & Guilderson, 2016; Zhao et al., 2018). In lack of any reference for modern or past variations of Rs, planktonic foraminifera ^{14}C ages are often corrected by constant Rs, or they are calibrated by marine calibration curves (the last of which is Marine20 (Heaton et al. , 2020). The latter introduces an uncertainty that is rarely quantitatively accounted for and thus, the interpretation of these records can change a lot over time, as new Rs estimates become available and chronologies of marine sediment cores are updated (e.g. De Pol-Holz et al., 2010; Martínez Fontaine et al., 2019). Alternatively, variations of Rs in different areas of the modern and past ocean have been estimated by different techniques (e.g. refs). When this is the case, however, generally not every depth where ^{14}C ages are analyzed has a corresponding Rs estimate, and thus assumptions on Rs variations over time must also be made in order to correct the planktic foraminifera ^{14}C age. For the time span studied in this thesis, Rs estimates are available for the last ~10 ka cal BP in Southeast Pacific at ~18° S (Fontugne et al., 2004) and ~32° S (Carré et al., 2004). These Rs have been estimated as the difference of contemporary mollusk and charcoal remains found in archaeological sites in the South American west coast. Additionally, Rs estimates for the deglaciation and Holocene have been produced by tephrochronology, i.e. by identifying remains of specific eruptions in marine sediment cores, which have been dated on land by ^{14}C, in core MD07-3088

(~46° S, Siani et al., 2013). Thus, any chronology for marine sediment cores based on ^{14}C ages in the Southeast Pacific, must make important assumptions on how Rs changed in the past.

Before the beginning of this thesis, radiocarbon dates in benthic and planktic foraminifera and stable isotope stratigraphy had been obtained for five cores in the SEP (GeoB 7149-2, GeoB 7163-7, GeoB 7162-6, SO161-22SL and GeoB 7167-6), retrieved between ~500 and ~3000 m depth, at ~31° S and ~36° S. These cores hold valuable information on the ventilation of intermediate and deep waters during the last 20 ka, however, they lack of in situ estimation of Rs in the past. In the second chapter of this thesis, I explore how stable isotope stratigraphy ($\delta^{13}C$), together with the ^{14}C ages of planktic foraminifera can give us information in the past variation of Rs in areas where no Rs estimates are available. Then, multiple chronologies and corresponding $\Delta^{14}C$ are produced for each core, taking into consideration the range of possible Rs given the available information in the area. This work putted forward the fact that ideally some reference of in situ Rs variations must be available for producing robust chronologies. In particular, in the Southeast Pacific Rs vary latitudinally because of different upwelling regimes at different latitudes bringing more or less *older* subsurface waters to the surface; and because the latitudinal distribution of these upwelling regimes has probably also varied in time. This work thus motivated the second main objective of this thesis, that is to use tephrochronology in marine sediment cores to improve chronologies in the Southeast Pacific. The idea behind this is that by identifying the remains of specific explosive volcanic eruptions (tephra), which have been dated by ^{14}C on land, Rs variation at the core retrieving sites can be estimated. In order to accomplish this task, and because the two volcanic zones adjacent to the core retrieving sites have been very active during the last ~20,000 years, first a compilation of previous information of volcanic activity in the study area is produced: the TephraDataBase, described in chapter three. In chapter four, the methodology to identify remains of volcanic eruptions in marine sediment cores is detailed, and the TephraDataBase is used as a reference to robustly identify specific eruptions in marine sediment cores MD07-3100 and MD07-3098. A similar approach was followed to identify the tephrochronological record of MD07-3081, which is described in the supplementary material of chapter five. Finally, in chapter five, new Rs for the Southeast Pacific are estimated at depths were specific eruptions could be robustly identified. These Rs, together with stable isotope stratigraphies are then used to produce marine core chronologies in cores MD07-3100, M07-3098 and MD07-3081. Because Rs information in the past is still scarce, the methodology to assign Rs to depths where no Rs has been estimated is also discussed in chapter five. Finally, variations in the ventilation of intermediate and deep waters in the Southeast Pacific since the late glacial are interpreted, integrating $\Delta^{14}C$ estimations in the marine sediment cores at ~31° S, ~36° S (chapter 2), ~41° S, ~46°S and ~49°S.

1.3 References

Adkins, J., & Boyle, E. 1997. Changing atmospheric Δ14C and the record of deep water paleo-ventilation ages. Paleoceanography, 12 (3), 337–344. https://doi.org/10.1029/97PA00379

Adkins, J. 2013. The role of deep ocean circulation in setting glacial climates. *Paleoceanography*, 28 (3), 539–561. https://doi.org/10.1002/palo.20046

Allen, K. A., Sikes, E. L., Hönisch, B., Elmore, A. C., Guilderson, T. P., Rosenthal, Y. & Anderson, R. F. 2015. Southwest Pacific deep water carbonate chemistry linked to high southern latitude climate and atmospheric CO2 during the Last Glacial Termination. *Quaternary Science Reviews*, 122, 180–191. https://doi.org/10.1016/j.quascirev.2015.05.007

Anderson, R. F., Ali, S., Bradtmiller, L. I., Nielsen, S. H. H., Fleisher, M. Q., Anderson, B. E. & Burckle, L. H. 2009. Wind–Driven Upwelling in the Southern Ocean and the Deglacial Rise in Atmospheric CO2. *Science*, 323 (5920), 1443–1448. https://doi.org/10.1126/science.1167441

Anderson, R. F., Sachs, J. P., Fleisher, M. Q., Allen, K. A., Yu, J., Koutavas, A. & Jaccard, S. L. 2019. Deep-sea oxygen depletion and ocean carbon sequestration during the last ice age. *Global Biogeochemical Cycles*, 33, 301–317. https://doi.org/10.1029/2018GB006049

Barnola, J. M., Raynaud, D., Korotkevich, Y. S., & Lorius, C. (1987). Vostok ice core provides 160,000-year record of atmospheric CO2. *Nature*, 329, 408–414. https://doi.org/10.1038/329408a0

Barriopedro, D., Erich M. Fischer, Jürg Luterbacher, Ricardo M. Trigo & Ricardo García-Herrera. 2011. The Hot Summer of 2010: Redrawing the Temperature Record Map of Europe. *Science*, 332 (6026), 220–224. https://doi.org/10.1126/science.1201224

Bereiter, B., Eggleston, S., Schmitt, J., Nehrbass-Ahles, C., Stocker, T. F., Fischer, H., Kipfstuhl, S., & Chappellaz, J. 2014. Revision of the EPICA Dome C CO2 record from 800 to 600 kyr before present, *Geophysical Research Lett*ers, 42, 542–549, https://doi.org/10.1002/2014GL061957

Bostock, H., Sutton, P., Williams, M. & Opdyke, B. 2013. Reviewing the circulation and mixing of Antarctic Intermediate Water in the South Pacific using evidence from geochemical tracers and Argo float trajectories. *Deep Sea Research, Part I*, 73, 84–98. https://doi.org/10.1016/j.dsr.2012.11.007

Bostock, H. C., Opdyke, B. N. & Williams, M. J. M. 2010. Characterising the intermediate depth waters of the Pacific Ocean using δ13C and other geochemical tracers. *Deep Sea Research Part I: Oceanographic Research Papers,* 57 (7), 847–859. https://doi.org/10.1016/j.dsr.2010.04.005

Bronk Ramsey, C. 2009. Bayesian analysis of radiocarbon dates. *Radiocarbon*, 51 (1), 337–360. https://doi.org/10.1017/S0033822200033865

Cai, W., Santoso, A., Wang, G., Weller, E., Wu, L., Ashok, K., Matsumoto, Y. & Yamagata, T. 2014: Increased frequency of extreme Indian Ocean Dipole events due to greenhouse warming. *Nature*, 510(7504), 254–258. http://doi.org/10.1038/nature13327

Carter,L. McCave, I. N. & Williams, .M. J. M. 2008. Chapter 4 Circulation and Water Masses of the Southern Ocean: A Review, in F. Florindo & M. Siegert, *Developments in Earth and Environmental Sciences* (Volume 8, pp. 88–114), Elsevier. https://doi.org/10.1016/S1571-9197(08)00004-9.D

Contreras-Reyes E. 2018. *Structure and Tectonics of the Chilean Convergent Margin from Wide-Angle Seismic Studies: A Review.* In: Folguera A. et al. (eds) The Evolution of the Chilean-Argentinean Andes. Springer Earth System Sciences. Springer, Cham. https://doi.org/10.1007/978-3-319-67774-3_1

Crowley, J., Katz, R. F., Huybers, P., Langmuir, C., & Park, S. 2015. Glacial cycles drive variations in the production of oceanic crust. Science, 347 (6227), 1237–1240. https://doi.org/10.1126/science.1261508

Davies, B.J., Darvill, C.M., Lovell, H., Bendle, J.M., Dowdeswell, J.A., Fabel, D., García, J.L., Geiger, A., Glasser, N.F., Gheorghiu, D.M., Harrison, S., Hein, A.S., Kaplan, M.R., Martin, J.R.V., Mendelova, M., Palmer, A., Pelto, M., Rodés, Á., Sagredo, E.A., Smedley, R.K., Smellie, J.L., Thorndycraft, V.R., 2020. The evolution of the Patagonian Ice Sheet from 35 ka to the present day (PATICE). *Earth-Science Rev*iews 204, Article: 103152. https://doi.org/10.1016/j.earscirev.2020.103152

Denton, G. H., Anderson, R. F., Toggweiler, J. R., Edwards, R. L., Schaefer, J. M. & Putnam, A. E. 2010. The Last Glacial termination. *Science*, 328 (5986), 1652–1656. https://doi.org/10.1126/science.1184119

De Pol-Holz, R., Keigwin, L., Southon, J., Hebbeln, D., & Mohtadi, M. 2010. No signature of abyssal carbon in intermediate waters off Chile during deglaciation. *Nature Geoscience*, 3 (3), 192–195. https://doi.org/10.1038/NGEO745

de la Fuente, M., Calvo, E., Skinner, L., Pelejero, C., Evans, D., Müller, W. & Cacho, I. 2017. The evolution of deep ocean chemistry and respired carbon in the Eastern Equatorial Pacific over the last deglaciation. *Paleoceanography*, 32, 1371–1385. https://doi.org/10.1002/2017PA003155

Dyke, A. S. 2004. An outline of North American deglaciation with emphasis on central and northern Canada. In Ehlers, J. et al. (Eds.), *Quaternary Glaciations–Extent and Chronology—Part II: North America, Developments in Quaternary Science*, 373–424, Elsevier. https://doi.org/10.1016/S1571-0866(04)80209-4

Elderfield, H., Ferretti, P., Greaves, M., Crowhurst, S., McCave, I. N., Hodell, D. & Piotrowski, A. M. 2012. Evolution of Ocean Temperature and Ice Volume Through the Mid-Pleistocene Climate Transition, *Science*, 337 (6095), 704–709, https://doi.org/10.1126/science.1221294

EPICA Community Members. One-to-one coupling of glacial climate variability in Greenland and Antarctica. *Nature*, 444, 195–198 (2006). https://doi.org/10.1038/nature05301

Ferrari, R., Jansen, M. F., Adkins, J. F., Burke, A., Stewart, A. L., & Thompson, A. F. 2014. Antarctic sea ice control on ocean circulation in present and glacial climates. Proceedings of the National Academy of Sciences of the United States of America, 111 (24), 8753–8758. https://doi.org/10.1073/pnas.1323922111

García-Herrera R., Díaz J., Trigo R. M., Luterbacher J. & Fischer E. M. 2010. A review of the European summer heat wave of 2003. *Critical Reviews in Environmental Science and Technology*, 40, 267–306. https://doi.org/10.1080/10643380802238137

Garreaud, R. D., Boisier, J. P., Rondanelli, R., Montecinos, A., Sepúlveda, H. H., Veloso-Aguila, D. 2019. The Central Chile Mega Drought (2010–2018): A climate edynamis perspective. *International Journal of Climatology*, 40 (1), 421–439. https://doi.org/10.1002/joc.6219

Garreaud, R., Lopez, P., Minvielle, M., Rojas, M., 2013. Large-scale control on the Patagonian climate. *Journal of Climate*. 26, 215e230. https://doi.org/10.1175/JCLI-D-12-00001.1

Gordon, A. 1971. Oceanography of Antarctic waters, in Antarctic Oceanology I, Antarctic Research Series, vol. 15, edited by J. L. Reid, pp. 169– 203, AGU, Washington, D. C. https://doi.org/10.1029/AR015p0169

Godwin, H. 1962. Half-life of Radiocarbon. *Nature*, 195, 984. https://doi.org/10.1038/195984a0

Gruber, N., Landschützer, P., & Lovenduski, N.S. 2018. The Variable Southern Ocean Carbon Sink. Annual review of marine science, 11, 159-186. https://doi.org/10.1146/annurev-marine-121916-063407

Heaton, T. J., Köhler, P., Butzin, M., Bard, E., Reimer, R. W., Austin, W. E. N., Ramsey, C. B., Grootes, P. M., Hughen, K. A., Kromer, B., Reimer, P. J., Adkins, J., Burke, A., Cook, M. S., Olsen, J. & Skinner, L. C. MARINE20—THE MARINE RADIOCARBON AGE CALIBRATION CURVE (0–55,000 CAL BP). Radiocarbon, 62 (4), 779–820. https://doi.org/10.1017/RDC.2020.68

Higgins, J. A., Kurbatov, A. V.,Spaulding, N. E.,Brook, E.,Introne, D. S.,Chimiak, L. M.,Yan, Y.,Mayewski, P. A. & Bender, M. L. 2015. Atmospheric composition 1 million years ago, *Proceedings of the National Academy of Sciences*, 112 (22), 6887–6891; https://doi.org/10.1073/pnas.1420232112

Holzer, M., DeVries, T. & de Lavergne, C. 2021. Diffusion controls the ventilation of a Pacific Shadow Zone above abyssal overturning. *Nature Communications,* 12, Article: 4348. https://doi.org/10.1038/s41467-021-24648-x

Hong, C., Hsu, H., Lin, N. & Chiu, H. 2011. Roles of European blocking and tropical–extratropical interaction in the 2010 Pakistan flooding. *Geophysical Research Letters*, 38 (13), Article L13806. https://doi.org/10.1029/2011GL047583

Hogg, A., Heaton, T., Hua, Q., Palmer, J., Turney, C., Southon, J., Bayliss, A., Blackwell, P. G., Boswijk, G., Ramsey, C. B., Pearson, C., Petchey, F., Reimer, P., Reimer, R., … Wacker, L. 2020. SHCal20 Southern Hemisphere Calibration, 0–55,000 Years cal BP. *Radiocarbon,* 62(4), 759-778. https://doi.org/10.1017/RDC.2020.59

Hughes, A. L., Gyllencreutz, R., Lohne, Ø. S., Mangerud, J. & Svendsen, J. I. 2015. The last Eurasian ice sheets–a chronological database and time-slice reconstruction, DATED-1. *Boreas*, 45 (1), 1–45. https://doi.org/10.1111/bor.12142

IPCC, 2021: Climate Change 2021: The Physical Science Basis. Contribution of Working Group I to the Sixth Assessment Report of the Intergovernmental Panel on Climate Change [Masson-Delmotte, V., P. Zhai, A. Pirani, S.L. Connors, C. Péan, S. Berger, N. Caud, Y. Chen, L. Goldfarb, M.I. Gomis, M. Huang, K. Leitzell, E. Lonnoy, J.B.R. Matthews, T.K. Maycock, T. Waterfield, O. Yelekçi, R. Yu, and B. Zhou (eds.)]. Cambridge University Press. In Press.

Jaccard, S.L., Galbraith, E.D.,Sigman, D.M.,Haug, G.H.,Francois, R.,Pedersen, T.F.,Dulski, P. & Thierstein, H.R. 2009. Subarctic Pacific evidence for a glacial deepening of the oceanic respired carbon pool. *Earth and Planetary Science Letters*, 277 (1–2), 156–165, https://doi.org/10.1016/j.epsl.2008.10.017

Jenkins, A., Shoosmith, D., Dutrieux, P., Jacobs, S., Kim, T. W., Lee, S. H., Ha, H. K. & Stammerjohn, S. 2018: West Antarctic Ice Sheet retreat in the Amundsen Sea driven by decadal oceanic variability. *Nature Geoscience*, 11, 733–738 https://doi.org/10.1038/s41561-018-0207-4

Johnson, R. E. 1973. Antarctic intermediate water in the South Pacific Ocean. In R. Fraser (Ed.), Oceanography of the South Pacific (pp. 55–69). Wellington, New Zealand: New Zealand National Commission for UNESCO.

Jouzel, J., Masson-Delmotte, V., Cattani, O., Dreyfus, G., Falourd, S., Hoffmann, G., Minster, B., Nouet, J., Barnola, J. M., Chappellaz, J., Fischer, H., Gallet, J. C., Johnsen, S., Leuenberger, M., Loulergue, L., Luethi, D., Oerter, H., Parrenin, F., Raisbeck, G., Raynaud, D., Schilt, A., Schwander, J., Selmo, E., Souchez, R., Spahni, R., Stauffer, B., Steffensen, J. P., Stenni, B., Stocker, T. F., Tison, J. L., Werner, M.& Wolff, E. W.. 2007. Orbital and Millennial Antarctic Climate Variability over the Past 800,000 Years. *Science*, 317 (5839), 793–796. https://doi.org/10.1126/science.1141038

Khatiwala, S., Graven, H., Payne, S. & Heimbach, P. 2018. Changes to the Air-Sea Flux and Distribution of Radiocarbon in the Ocean Over the 21st Century. *Geophysical Research Letters*, 45 (11) , 5617–5626. https://doi.org/10.1029/2018GL078172

Keeling, R., & Stephens, B. 2001. Antarctic sea ice and the control of Pleistocene climate instability. Paleoceanography, 16(1), 112–131. https://doi.org/10.1029/2000PA000529

King, M. D., Howat, I. M., Candela, S.G., Noh, M. J., Jeong, S., Noël, B. P. Y., van den Broeke, M. R., Wouters, B. & Negrete, A. 2020. Dynamic ice loss from the Greenland Ice Sheet driven by sustained glacier retreat. *Communications Earth & Environment* 1, Article 1. https://doi.org/10.1038/s43247-020-0001-2

Kohfeld, K. E., Le Quéré, C., Harrison, S. P., & Anderson, R. F. 2005. Role of marine biology in glacial-interglacial CO2 cycles. Science, 308 (5718), 74–78. https://doi.org/10.1126/science.1105375

Koshlyakov, M. & Tarakanow, R. Y. 2004. Pacific deep water in the Southern Ocean. *Oceanology*, 44 (3), 299–314.

Kumamoto, K. 2007. Radiocarbon-based circulation age of the world oceans. *Journal of geophysical research*, *112*, Article: C909004. https://doi.org/10.1029/2007JC004095

Laj, C., Kissel, C., Mazaud, A., Michel, E., Muscheler, R., Beer, J. 2002. Geomagnetic field intensity, North Atlantic Deep Water circulation and atmospheric Δ14C during the last 50 kyr. *Earth and Planetary Science Letters*, 200 (1–2), 177–190. https://doi.org/10.1016/S0012-821X(02)00618-0

Lauvset, S. K., Lange, N., T. Tanhua, H. Bittig, Are Olsen, A. Kozyr, M. Álvarez , S. Becker, P. J. Brown, B. R. Carter, L. Cotrim da Cunha, R. A. Feely, S. van Heuven, M. Hoppema, M. Ishii, E. Jeansson , S. Jutterström, S. D. Jones, M. K. Karlsen, C. Lo Monaco, P. Michaelis, A. Murata, F. F. Pérez, B. Pfeil, C. Schirnick , R. Steinfeldt, T. Suzuki, B. Tilbrook, A. Velo, R. Wanninkhof, R. J. Woosley & R. M. Key. An updated version of the global interior ocean biogeochemical data product, GLODAPv2.2021, in preparation for Earth Syst. Sci. Data.

Lisiecki, L. E. & Raymo, M. E. 2005. A Pliocene-Pleistocene stack of 57 globally distributed benthic $\delta^{18}O$ records, *Paleoceanography*, 20 (1), Article PA1003, https://doi.org/10.1029/2004PA001071

Lund, D. & Asimow, P. 2011. Does sea level influence mid-ocean ridge magmatism on Milankovitch timescales? *Geochemistry, Geophysics, Geosystems,* 12 (12), Article: Q12009. https://doi.org/10.1029/2011GC003693

Luthi, D., M. Le Floch, B. Bereiter, T. Blunier, J.-M. Barnola, U. Siegenthaler, D. Raynaud, J. Jouzel, H. Fischer, K. Kawamura, and T.F. Stocker. 2008. High-resolution carbon dioxide concentration record

650,000-800,000 years before present. Nature, 453, 379–382 https://doi.org/10.1038/nature06949

Marcott, S. A., Bauska, T. K., Buizert, C., Steig, E. J., Rosen, J. L., Cuffey, K. M., Fudge, T. J., Severinghaus, J. P., Anh, J., Kalk, M. L., McConnell, J. R., Sowers, T., Taylor, K. C., White, W. C. J. & Brook, E. J. 2014. Centennial-scale changes in the global carbon cycle during the last deglaciation. *Nature*, 514, 616–619. https://doi.org/10.1038/nature13799

Martínez-Botí, M. A., Marino, G., Foster, G. L., Ziverti, P., Henehan, M. J., Rae, J. W. B., et al. (2015). Boron isotope evidence for oceanic carbon dioxide leakage during the last deglaciation. *Nature*, 518(7538), 219–222. https://doi.org/10.1038/nature14155

Martínez-Garcia, A., Rosell-Melé, A., Jaccard, S., Geibert, W., Sigman, D. M. & Haug, G. H. 2011. Southern Ocean dust–climate coupling over the past four million years. *Nature*, 476, 312–315. https://doi.org/10.1038/nature10310

Marshall, J. & Speer, K. 2012. Closure of the meridional overturning circulation through Southern Ocean upwelling. *Nature Geosciences*, 5, 171–180. https://doi.org/10.1038/ngeo1391

McCartney, M. S. 1977. Subantarctic mode water. Deep-Sea Research, 24, 103–119.

McCartney, M. S. 1982. The subtropical recirculation of mode waters. *Journal of Marine Research*, 40(Supplement), 427–464.

Mikaloff Fletcher, S. E., Gruber, N., Jacobson, A. R., Gloor, M., Doney, S. C., Dutkiewicz, S.,, Gerber, M., Follows, M., Joos, F., Lindsay, K., Menemenlis, D., Mouchet, A., Müller, S. A. & Sarmiento, J. L. 2007. Inverse estimates of the oceanic sources and sinks of natural CO2 and the implied oceanic carbon transport. *Global Biogeochemical Cycles*, 21 (1), Article: GB1010. https://doi.org/10.1029/2006GB002751

Monnin, E., Indermühle, A., Dällenbach, A., Flückiger, J., Stauffer, B., Stocker, T., Raynaud, D. & Barnola, J. 2001. Atmospheric CO_2 concentrations over the Last Glacial Maximum. *Science*, 291(5501), 112–114. https://doi.org/10.1126/science.291.5501.112

Moreno, P.I., Villa-Martínez, R., Cardenas, M.L., Sagredo, E. a, 2012. Deglacial changes of the southern margin of the southern westerly winds revealed by terrestrial records from SW Patagonia (52 S). Quat. Sci. Rev. 41, 1e21. https://doi.org/10.1016/j.quascirev.2012.02.002

Parrenin, F., Masson-Delmotte, V., Köhler, P., Raynaud, D., Paillard, D., Schwander, J., Barbante, C., Landais, A., Wegner & A., Jouzel, J. 2013. Synchronous Change of Atmospheric CO_2 and Antarctic Temperature During the Last Deglacial Warming. *Science*, 339 (6123), 1060–1063. https://doi.org/10.1126/science.1226368

Petit, J., Jouzel, J., Raynaud, D. et al. 1999. Climate and atmospheric history of the past 420,000 years from the Vostok ice core, Antarctica. *Nature*, 399, 429–436. https://doi.org/10.1038/20859

Pichevin, L. E., Reynolds, B. C., Ganeshram, R. S., Cacho, I., Pena, L., Keefe, K. & Ellam, R. M. 2009. Enhanced carbon pump inferred from relaxation of nutrient limitation in the glacial ocean. *Nature*, 459, 1114–1117. https://doi.org/10.1038/nature08101

Piola, A. R. & Gordon, A. I. 1989. Intermediate water in the southwestern South Atlantic. Deep-Sea Research, 36 (1), 1–16. https://doi.org/10.1016/0198-0149(89)90015-0

RAISED Consortium et al. 2014. A community-based geological reconstruction of Antarctic Ice Sheet deglaciation since the Last Glacial Maximum. *Quaternary Science Reviews*, 100, 1–9. https://doi.org/10.1016/j.quascirev.2014.06.025

Reid, J. L. 1965. Intermediate waters of the Pacific Ocean. In The Johns Hopkins Oceanographic Studies, No. 2. Baltimore, United States of America: The Johns Hopkins Press. 85 p. https://doi.org/10.4319/lo.1966.11.2.0313

Reimer, P., Austin, W., Bard, E., Bayliss, A., Blackwell, P., Bronk Ramsey, C., Butzin, M., Cheng, H., Edwards, R. L., Friedrich, M., Grootes, P. M., Guilderson, T. P., Hajdas, I., Heaton, T. J., Hogg, A. G., Hughen, K. A., Kromer, B., Manning, S. W., Muscheler, R., G Palmer, J. G., ... Talamo, S. 2020. The IntCal20 Northern Hemisphere Radiocarbon Age Calibration Curve (0–55 cal kBP). *Radiocarbon*, 62 (4), 725-757. https://doi.org/10.1017/RDC.2020.41

Reimer, P. J., Bard, E., Bayliss, A., Beck, J. W., Blackwell, P. G., Ramsey, C. B., et al. 2013. INTCAL13 and MARINE13 radiocarbon age calibration curves 0–50,000 years cal BP. *Radiocarbon*, 55(4), 1869–1887. https://doi.org/10.2458/azu_js_rc.55.16947

Reimer, P., Baillie, M., Bard, E., Bayliss, A., Beck, J., Blackwell, P., ... Weyhenmeyer, C. (2009). IntCal09 and Marine09 Radiocarbon Age Calibration Curves, 0–50,000 Years cal BP. Radiocarbon, 51(4), 1111-1150. https://doi.org/10.1017/S0033822200034202

Reyes-Macaya, D., Hebbeln, D., Mohtadi, M., Hoogakker, B., Martínez-Méndez, G., Llanillo, P. J., Gayo, E. M., Troncoso, M., Farias, L., Crasse, P., McCorkle, D. C., Leng, M., Cornejo-D'Ottone, M., Carhuapoma, W., Graco, M., De Pol Holz, R., Fernandez, C., Narvaez, D., Cordova, K., Lange, C. B., Ulloa, O., Vargas, C. A. *submitted.* Isotopic characterization of water masses from the South-East Pacific: Paleoceanography implications.

Rohling, E., Foster, G. L., Grant, K. M., Marino, G., Roberts, A. P., Tamisiea, M. E. & Williams, F. 2014. Sea-level and deep-sea-temperature variability over the past 5.3 million years. *Nature* 508, 477–482. https://doi.org/10.1038/nature13230

Shakun, J., Clark, P., He, F., Marcott, S. A., Mix, A. C., Liu, Z., Otto-Bliesner, B., Sschmittner, A. & Bard, E. 2012. Global warming preceded by increasing carbon dioxide concentrations during the last deglaciation. Nature 484, 49–54. https://doi.org/10.1038/nature10915

Siani, G., Michel, E., De Pol-Holz, R., DeVries, T., Lamy, F., Carel, M., Isguder, G., Dewilde, F. & Lourantou, A. 2013. A. Carbon isotope records reveal precise timing of enhanced Southern Ocean upwelling during the last deglaciation. *Nature Communications*, 4, Article 2758. https://doi.org/10.1038/ncomms3758

Sigman, D. M., & Boyle, E. A. 2000. Glacial/interglacial variations in atmospheric carbon dioxide. Nature, 407, 859–869. https://doi.org/10.1038/35038000

Sikes, E.L, Allen, K.A. & Lund, D. 2017. Enhanced $\delta^{13}C$ and $\delta^{18}O$ differences between the South Atlantic and South Pacific during the last glaciation: The deep gateway hypothesis. *Paleoceanography*, 32, 1000–1017. https://doi.org/10.1002/2017PA003118

Sikes, E., & Guilderson, T. 2016. Southwest Pacific Ocean surface reservoir ages since the last glaciation: Circulation insights from multiple-core studies. *Paleoceanography and Paleoclimatology*, 3 (2), 298–310. https://doi.org/10.1002/2015PA002855

Silva, N., Rojas, N., & Fedele, A. 2009. Water masses in the Humboldt Current System: Properties, distribution, and the nitrate deficit as a chemical water mass tracer for Equatorial Subsurface Water off Chile. *Deep-Sea Research II*, 56, 1004–1020. https://doi.org/10.1016/j.dsr2.2008.12.013

Sloyan, B. M. 2005. Antarctic bottom and lower circumpolar deep water circulation in the eastern Indian Ocean. *Journal of Geophysical Research*, 111 (C2), Article: C02006. https://doi.org/10.1029/2005JC003011

Sloyan, B. M. & Rintoul, S. R. 2001. The Southern Ocean limb of the global deep overturning circulation. *Journal of Physical Oceanography*. 31 (1), 1431–73. https://doi.org/10.1175/1520-0485(2001)031<0143:TSOLOT>2.0.CO;2

Solomina, O. N., Bradley, R. S., Hodgson, D. A., Ivy-Ochs, S., Jomelli, V., Mackintosh, A. N., Nesje, A., Owen, L. A., Wanner, H., Wiles, G. C., Young, N. E. 2015. Holocene glacier fluctuations. *Quaternary Science Reviews*, 111 (1), 9–34. https://doi.org/10.1016/j.quascirev.2014.11.018

Stenni, B., Buiron, D., Frezzotti, Albani, S., Barbante, C., Bard, E., Barnola, J. M., Baroni, M., Baumgartner, M., Bonazza, M., Capron, E., Castellano, E., Chappellaz, J., Delmonte, B., Falourd, S., Genoni, L., Iacumin, P., Jouzel, J., Kipfstuhl, S., Landais, A., Lemieux-Dudon, B., Maggi, V., Masson-Delmotte, V., Mazzola, C., Minster, B., Montagnat, M., Mulvaney, R., Narcisi, B., Oerter, H., Parrenin, F., Petit, J. R.,

Ritz, C., Scarchilli, C., Schilt, A., Schüpbach, S., Schwander, J., Selmo, E., Severi, M., Stocker, T. F.& Udisti, R.. 2011. Expression of the bipolar see-saw in Antarctic climate records during the last deglaciation. *Nature Geoscience*, 4, 46–49. https://doi.org/10.1038/ngeo1026

Stephens, B. S., & Keeling, R. F. 2000. The influence of Antarctic sea ice in glacial-interglacial CO2 variations. *Nature*, 404, 171–174. https://doi.org/10.1038/35004556

Strub,P., Mesías, J., Montecino, V., Rutllant, J. & Salinas, S. 1998. Coastal ocean circulation off western South America. In: Robinson, A., Brink, K. (Eds.), The Sea, The Global Coastal Ocean, vol.11. Wiley, NewYork, pp.272–313.

Stuiver, M., & Polach, H. 1977. Reporting of 14C data. *Radiocarbon*, 19 (3), 355–363. https://doi.org/10.1017/S0033822200003672

Sun, Q., & Miao, C. 2018. Extreme Rainfall (R20mm, RX5day) in Yangtze–Huai, China, in June–July 2016: The Role of ENSO and Anthropogenic Climate Change, *Bulletin of the American Meteorological Society*, *99* (1), S102-S106. https://doi.org/10.1175/BAMS-D-17-0091.1

Takahashi, T., Sutherland, S. C., Wanninkhof, R., Sweeney, C., Feely, R. A., Chipman, D. W., Hales, B., Friederich, G., Chavez, F., Sabine, C., Watson, A., Bakker, D. C. E., Schuster, U., Metzl, N., Yoshikawa-Inoue, H., Ishii, M., Midorikawa, T., Nojiri, Y. … de Baar, H. J. W. 2009. Climatological mean and decadal change in surface ocean pCO_2 , and net sea-air 849 CO2 flux over the global oceans. *Deep-Sea Research Part II: Topical Studies in Oceanography*, 56 (8–10), 554–577. https://doi.org/10.1016/j.dsr2.2008.12.009

Talley, L. D. 1996. Antarctic Intermediate Water in the South Atlantic. In G. Wefer, W. H. Berger, G. Siedler, & D. J. Webb (Eds.), The South Atlantic: Present and past circulation, (pp. 219–238). New York, United States of America: Springer. https://doi.org/10.1007/978-3-642-80353-6_11

Talley, L. D. 1999. Some aspects of ocean heat transport by the shallow, intermediate and deep overturning circulations. In P. U. Clark, R. S. Webb, & L. D. Keigwin (Eds.), Mechanisms of Global Climate Change at Millennial Time Scales, Geophysical Monograph Series (Vol. 112, pp. 1–22). United States of America: American Geophysical Union. https://doi.org/10.1029/GM112p0001

Talley, L.D. 2013. Closure of the global overturning circulation through the Indian, Pacific, and Southern Oceans: Schematics and transports. *Oceanography* 26 (1), 80–97, https://doi.org/10.5670/oceanog.2013.07

Tierney, J.E., Zhu, J., King, J., Malevich, S. B., Hakim, G. J. & Poulsen, C. J.. 2020. Glacial cooling and climate sensitivity revisited. Nature 584, 569–573. https://doi.org/10.1038/s41586-020-2617-x

Toggweiler, J. R. & B. Samuels. 1993. New radiocarbon constraints on the upwelling of abyssal water to the ocean's surface, in The Global Carbon Cycle, edited by M. Heimann, NATO ASI Ser., Ser. I, vol. 15, pp. 333– 366, Springer, New York. https://doi.org/10.1007/978-3-642-84608-3_14

Toggweiler, J. R. 1999. Variation of atmospheric CO2 by ventilation of the ocean's deepest water. *Paleoceanography*, 14 (5), 571–588. https://doi.org/10.1029/1999PA900033

Tomczak, M. & Godfrey, J. 2003. Regional oceanography: An introduction. Delhi: Daya Publishing House. https://doi.org/10.1002/joc.3370150511

Tolstoy, M. 2015. Mid-ocean ridge eruptions as a climate valve. *Geophysical Research Letters*, 42, 1346–1351. https://doi.org/10.1002/2014GL063015

Tsuchiya, M., & Talley, L. 1996. Water-property distribution along an eastern Pacific hydrographic section at 135°W. Journal of Marine Research, 54 (3), 541–564. https://doi.org/10.1357/0022240963213583

Tsuchiya, M., & Talley, L. 1998. A Pacific hydrographic section at 881W: Water-property distribution. Journal of Geophysical Research, 103 (C6), 12899–12918. https://doi.org/10.1029/97JC03415

van der Werf, G. R., Randerson, J. T., Giglio, L., van Leeuwen, T. T., Chen, Y., Rogers, B. M., Mu, M., van Marle, M. J. E., Morton, D. C., Collatz, G. J., Yokelson, R. J. & Kasibhatla, P. S. 2017. Global fire emissions estimates during 1997–2016, Earth System Science Data, 9 (2), 697–720. https://doi.org/10.5194/essd-9-697-2017

Vautard, R., Aalst, M., Boucher, O., Drouin, A., Haustein, K., Kreienkamp, F., van Oldenborgh, G. J., Otto, F. E. L., Ribes, A., Robin, Y., Schneider, M., Soubeyroux, J., Stott, P., Seneviratne, S. I., Vogel, M. M. & Wehner, M. 2020a. Human contribution to the record-breaking June and July 2019 heat waves in Western Europe. *Environmental Research Letters*, 15, Article 094977. https://doi.org/10.1088/1748-9326/aba3d4

WAIS Divide Project Members. 2013. Onset of deglacial warming in West Antarctica driven by local orbital forcing. *Nature*, 500 (7463), 440-4. https://doi.org/10.1038/nature12376

Watanabe, O., Jouzel, J., Johnsen, S., Parrenin, F., Shoji, H. & Yoshida, N. 2003. Homogeneous climate variability across East Antarctica over the past three glacial cycles. *Nature*, 422, 509–512. https://doi.org/10.1038/nature01525

Watson, A. J., & Naveira Garabato, A. C. 2006. The role of Southern Ocean mixing and upwelling in glacial-interglacial atmospheric CO2 change. Tellus Series B: *Chemical and Physical Meteorology*, 58 (1), 73–87. https://doi.org/10.1111/j.1600-0889.2005.00167.x

Webb, D. J. & Suginohara, N. 2001. Chapter 4.2 The interior circulation of the ocean. International Geophysics, 77, 205–214. https://doi.org/10.1016/S0074-6142(01)80120-0

Whitworth III, T., Warren, B.A, Nowlin, W. D., Rutz, S. B., Pillsbury, R.D. & Moore, M.I. 1999. On the deep western-boundary current in the Southwest Pacific Basin. *Progress in Oceanography*, 43 (1), 1–54. https://doi.org/10.1016/S0079-6611(99)00005-1

Wu, Y., Hain, M. P., Humphreys, M. P., Hartman, S., & Tyrrell, T. 2019. What drives the latitudinal gradient in open-ocean surface dissolved inorganic carbon concentration? *Biogeosciences*, 16 (13), 2661–2681. https://doi.org/10.5194/bg-16-2661-2019

Wyrtki, K. 1961. The thermohaline circulation in relation to the general circulation in the oceans. *Deep Sea Research (1953)*, 8 (1), 39–64, https://doi.org/10.1016/0146-6313(61)90014-4

Zhao, N., & Keigwin, L. D. 2018. An atmospheric chronology for the glacial-deglacial Eastern Equatorial Pacific. *Nature Communications*, 9 (1), 3077. https://doi.org/10.1038/s41467-018-05574-x

Chapter 2: Preliminary ventilation changes in the Southeast Pacific during the last 20,000 years, and finding appropriate Rs for marine core chronologies

Chapter 2 corresponds to a work that started before the beginning of this thesis, but which was developed in great part, and published (Martínez Fontaine et al., 2019; full reference in the supplementary material of this chapter), during the first two years of this PhD. It corresponds to a study of five sediment cores retrieved along the Chilean continental margin by the German R/V Sonne. Planktic and benthic foraminifera were picked and prepared for radiocarbon dating and stable isotopes analysis by Dharma Reyes-Macaya and Ricardo de Pol-Holz. As this information was already available, my undergraduate degree study consisted in using it to better understand the oceanic circulation changes in the Southeast Pacific during the last deglaciation. In doing this work, a very important problem I encountered was obtaining robust chronologies for the marine sediment cores. In particular because no previous work on Rs variations were available for the latitudes where they were retrieved. In that area, latitudinal Rs variations can be very important, because of seasonal coastal upwelling. This coastal upwelling is largely controlled by the annual latitudinal migration of the SWW, which is additionally thought to have changed in the past (details in Chapter 2, section "4. Age models"). Because of the latter, I started my PhD by using the available planktic foraminifera stable isotopes stratigraphy in the cores I was studying to evaluate how the surface waters at the core retrieving sites might have varied in the past. To do this, I compared these records with previously published planktonic foraminifera stable isotope stratigraphy in marine sediment cores in the study area that had complementary chronological constraints. By doing this, I inferred that important variations in Rs affected the surface waters at the core retrieving sites. However, in lack of robust constraints in the cores to complement this inference, this work proved to hold big uncertainties in the chronologies of the cores and several age models where produced for each core in order to account for these uncertainties. This work, which was developed in great part during the PhD, motivated the use of stable isotopes together with tephrochronology in order to more robustly assess the chronologies in the Southeast Pacific Ocean since the late glacial.

Paleoceanography and Paleoclimatology

RESEARCH ARTICLE
10.1029/2019PA003613

Ventilation of the Deep Ocean Carbon Reservoir During the Last Deglaciation: Results From the Southeast Pacific

Consuelo Martínez Fontaine[1,3,4], Ricardo De Pol-Holz[2], Elisabeth Michel[3], Giuseppe Siani[4], Dharma Reyes-Macaya[5], Gema Martínez-Méndez[5], Tim DeVries[6], Lowell Stott[7], John Southon[8], Mahyar Mohtadi[5], and Dierk Hebbeln[5]

[1]Departamento de Geología, Universidad de Chile, Santiago, Chile, [2]Centro de Investigación GAIA-Antárctica (CIGA) and Network for Extreme Environments Research (NEXER), Universidad de Magallanes, Punta Arenas, Chile, [3]Laboratoire des Sciences du Climat et de l'Environnement (LSCE), Laboratoire mixte CNRS-CEA, Gif-sur-Yvette Cedex, France, [4]Geoscience Paris Sud (GEOPS) Universities of Paris Sud and Paris-Saclay, CNRS, Orsay, France, [5]MARUM, Center for Marine Environmental Sciences, University of Bremen, Bremen, Germany, [6]Earth Research Institute, University of California, Santa Barbara, CA, USA, [7]Department of Earth Sciences, University of Southern California, Los Angeles, CA, USA, [8]Earth System Science Department, University of California, Irvine, CA, USA

Key Points:
- New foraminifer ^{14}C records are presented, spanning from 540 to 3,100 m water depth along the Chilean Margin
- Waters at ~2,000 m were between 50% and 80% more depleted in $\Delta^{14}C$ than waters at ~1,500 m when compared to modern values
- Intermediate water records suggest that during the deglaciation, there was a deeper penetration of Antarctic Intermediate Water in the Pacific

Supporting Information:
- Supporting Information S1
- Table S1
- Table S2

Correspondence to:
R. De Pol-Holz,
ricardo.depol@umag.cl

Citation:
Martínez Fontaine, C., De Pol-Holz, R., Michel, E., Siani, G., Reyes-Macaya, D., Martínez-Méndez, G., et al. (2019). Ventilation of the deep ocean carbon reservoir during the last deglaciation: results from the southeast pacific. *Paleoceanography and Paleoclimatology*, *34*. https://doi.org/10.1029/2019PA003613

Received 26 MAR 2019
Accepted 9 OCT 2019
Accepted article online 7 NOV 2019

Abstract Coeval changes in atmospheric CO_2 and ^{14}C contents during the last deglaciation are often attributed to ocean circulation changes that released carbon stored in the deep ocean during the Last Glacial Maximum (LGM). Work is being done to generate records that allow for the identification of the exact mechanisms leading to the accumulation and release of carbon from the oceanic reservoir, but these mechanisms are still the subject of debate. Here we present foraminifera ^{14}C data from five cores in a transect across the Chilean continental margin between ~540 and ~3,100 m depth spanning the last 20,000 years. Our data reveal that during the LGM, waters at ~2,000 m were 50% to 80% more depleted in $\Delta^{14}C$ than waters at ~1,500 m when compared to modern values, consistent with the hypothesis of a glacial deep ocean carbon reservoir that was isolated from the atmosphere. During the deglaciation, our intermediate water records reveal homogenization in the $\Delta^{14}C$ values between ~800 and ~1,500 m from ~16.5–14.5 ka cal BP to ~14–12 ka cal BP, which we interpret as deeper penetration of Antarctic Intermediate Water. While many questions still remain, this process could aid the ventilation of the deep ocean at the beginning of the deglaciation, contributing to the observed ~40 ppm rise in atmospheric pCO_2.

1. Introduction

The ocean is thought to play an important role in the variations of atmospheric pCO_2 over glacial-interglacial cycles. During the last deglaciation, a ~75 ppm rise in atmospheric pCO_2 (Barnola et al., 1987; Marcott et al., 2014; Monnin et al., 2001) occurred synchronously with a ~190 ± 10‰ drop in atmospheric $\Delta^{14}C$ (Reimer et al., 2013). Due to its large content of mobile carbon and the time scale of its overturning, the deep ocean is considered the most likely source of a ^{14}C-depleted CO_2 reservoir that would be transferred to the atmosphere during the last deglaciation (Broecker & Barker, 2007). Different hypotheses have been called upon to explain the ocean's role in changing atmospheric CO_2 concentrations and for the exact source area and mechanism controlling this release of depleted $^{14}CO_2$. Among these are changes in oceanic circulation leading to the formation of an isolated deepwater carbon reservoir (Adkins, 2013; Ferrari et al., 2014; Keeling & Stephens, 2001, Keeling, 2007; Toggweiler, 1999; Stephens & Keeling, 2000; Watson & Naveira Garabato, 2006), changes in the biological pump efficiency in capturing atmospheric CO_2 (e.g., Duchamp-Alphonse et al., 2018; Kohfeld et al., 2005; Pichevin et al., 2009; Sigman & Boyle, 2000), release of ^{14}C-dead CO_2 from clathrate deposits due to changes in the temperature of the ocean (Stott & Timmermann, 2011), and increased production of ^{14}C-dead CO_2 associated with higher magmatism in ocean ridges during periods of low sea level, such as the last glacial period (Crowley et al., 2015; Lund & Asimow, 2011; Tolstoy, 2015).

Evidence of the deep ocean as the source of the atmospheric ^{14}C decline has been found in marine sediment cores throughout the oceans. Widespread evidence of moderately ^{14}C-depleted deep waters (>2,000-m depth) during the late glacial period (25–10 ka BP) has been found in the North Pacific (NP; Galbraith

Paleoceanography and Paleoclimatology 10.1029/2019PA003613

et al., 2007; Rae et al., 2014), South West Pacific (SWP; Ronge et al., 2016; Sikes et al., 2016), Equatorial East Pacific (EEP; De la Fuente et al., 2015; Keigwin & Lehman, 2015; Umling & Thunell, 2017), and Southern Ocean (SO; Burke & Robinson, 2012; Chen et al., 2015; Skinner et al., 2010). These records are consistent with the hypothesis of an isolated deep ocean reservoir during the Last Glacial Maximum (LGM) associated with increased sea ice extent around Antarctica (Adkins, 2013; Ferrari et al., 2014; Keeling & Stephens, 2001; Stephens & Keeling, 2000; Watson & Naveira Garabato, 2006). Additionally, extremely ^{14}C-depleted values have been found in deepwater sediment cores dating from the LGM in the SWP (Ronge et al., 2016; Sikes et al., 2016; Skinner et al., 2015) and East Pacific Rise (EPR; Ronge et al., 2016) and during the deglaciation in intermediate water cores in the EEP (Bova et al., 2018; Stott et al., 2009), Baja California (Lindsay et al., 2015; Marchitto et al., 2007), and Arabian Sea (Bryant et al., 2010). It has been hypothesized that these extremely ^{14}C-depleted waters are due to a breakdown in deep ocean stratification at the beginning of the deglaciation, and the subsequent transfer of a ^{14}C-depleted water mass to intermediate waters, particularly to Subantarctic Mode Water (SAMW) and Antarctic Intermediate Water (AAIW) as seen in ^{13}C records of planktonic foraminifera (Spero & Lea, 2002). However, evidence of this mechanism closer to the formation areas of intermediate and deep waters has not been found (e.g., Burke & Robinson, 2012; De Pol-Holz et al., 2010; Rose et al., 2010). An alternative hypothesis suggests that the extremely ^{14}C-depleted deepwater records of the SWP and EPR (Ronge et al., 2016) stem from enhanced local ^{14}C-dead CO_2 production in oceanic ridges during glacial periods. This hypothesis is supported by independent evidence of enhanced undersea volcanism during the last deglacial period, driven by lower sea level and reduced pressure in the deep ocean (Crowley et al., 2015; Lund & Asimow, 2011; Tolstoy, 2015).

While it is important to identify the mechanisms leading to the formation of the glacial deep ocean carbon reservoir, it is equally important to understand the mechanisms associated with its release to the atmosphere. During the last deglaciation, the SO and the EEP registered changes suggesting that both areas had a key role in the ventilation of the CO_2-rich/^{14}C-depleted deep ocean reservoir. Carbon isotope and opal flux records reveal sustained conditions of increased upwelling and/or decreased stratification between the upper and deep oceanic circulation cells in the SO during the deglaciation, diminishing only during the Antarctic Cold Reversal (ACR; Anderson et al., 2009; Siani et al., 2013). At the same time, boron isotope records suggest enhanced outgassing of CO_2 in both the SO and EEP during the deglaciation (Martínez-Botí et al., 2015). In addition, tephrochronology records indicate high ^{14}C Surface Reservoir ages (R_S) in the SO at the beginning of the deglaciation, suggesting upwelling of ^{14}C-depleted water to the surface (Siani et al., 2013; Sikes & Guilderson, 2016; Sikes et al., 2016; Sikes et al., 2000; Skinner et al., 2015). Meanwhile, in the Galapagos platform, R_S estimated by tuning between different records (Bova et al., 2018; De la Fuente et al., 2015; Umling & Thunell, 2017) yield R_S even higher than in the SO. In contrast, the EEP region along the south American margin, the R_S obtained by tuning (Bova et al., 2018) and by wood-planktic foraminifera pairs (Zhao & Keigwin, 2018) yield generally lower values. In conclusion, the exact mechanism(s) of carbon release remains highly debated, and more work is still needed to understand the details of oceanic circulation changes, from the LGM into the Holocene, that control this ventilation.

The Southeast Pacific (SEP) is a key region for testing these hypotheses since it is influenced by water masses originating in the SO, the EEP, and the NP (Figure 1). Our studied area therefore captures the different signals propagating from each of these regions, potentially allowing us to distinguish the local processes occurring in the SO and EEP from those in the NP. So far only two cores have been studied in the SEP using ^{14}C to interpret ventilation changes (Figure 1): core SO161-22SL (from now on 22SL, ~1,000 m, ~36°S; De Pol-Holz et al., 2010) and core MD07-3088 (~1,500 m, ~46°S; Siani et al., 2013). Based on carbon isotope data and tephrochronology estimates of R_S, Siani et al. (2013) inferred enhanced upwelling in the Pacific area of the SO during the last deglaciation and found ^{14}C-depleted waters during the LGM (~350‰ Δ^{14}C lower than the contemporary atmosphere) in line with a large number of deep cores in the Pacific Ocean (De la Fuente et al., 2015; Galbraith et al., 2007; Keigwin & Lehman, 2015; Rae et al., 2014; Ronge et al., 2016; Sikes et al., 2016; Skinner et al., 2015; Umling & Thunell, 2017).

These two locations capture only a narrow depth range (Figure 1), which could have missed the core of intermediate waters and potentially the ^{14}C-depleted deepwater reservoir. In order to obtain a more complete picture of the ventilation history in the SEP during the last deglaciation, we here report ^{14}C ages of planktic and benthic foraminifera and stable isotope (δ^{13}C) measurements in planktic foraminifera, from

Paleoceanography and Paleoclimatology 10.1029/2019PA003613

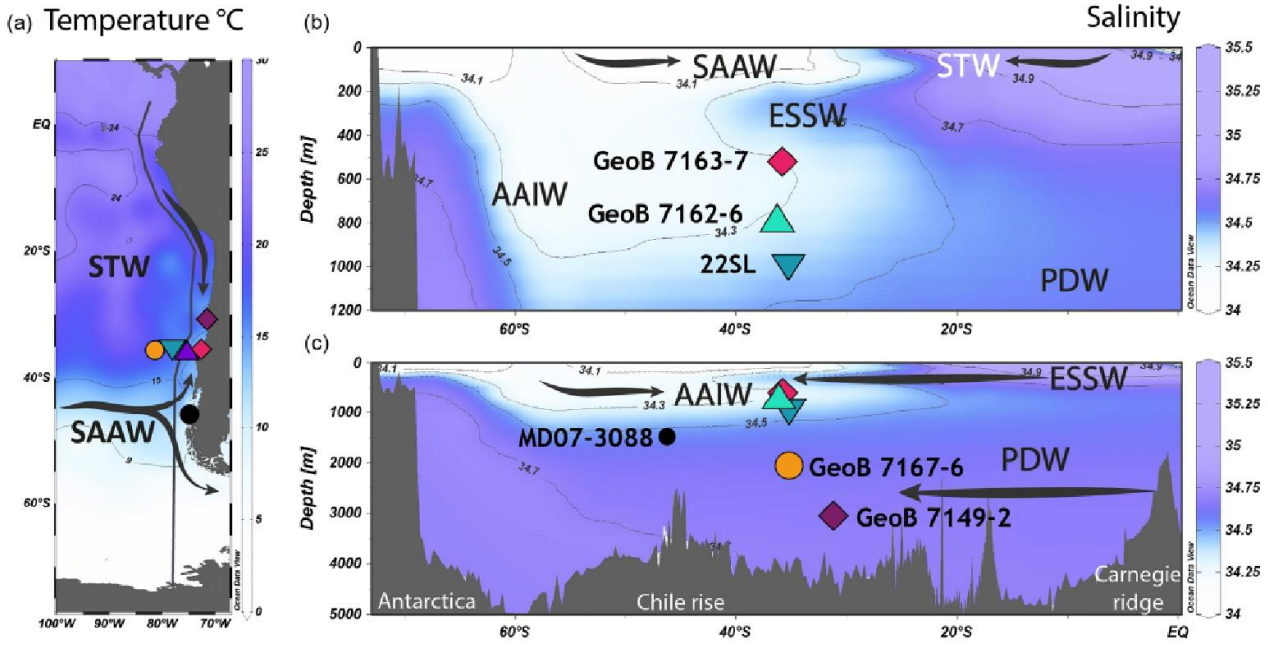

Figure 1. (a) Position of the studied cores (Table S3) and core MD07-3088 (Siani et al., 2013) in a sea surface temperature map. Also presented are the surface water masses in the area: Subantarctic Water (SAAW), transported by the Antarctic Circumpolar Current, and Subtropical Water (STW), transported by the Perú-Chile Countercurrent; (b) main water masses discussed in the text indicated by the salinity distribution obtained from gridded WOCE data (Gouretski & Koltermann, 2004) along the transect shown in gray in (a) in depths from 0 to 1,200 m; (c) same as (b) but between 0- and 5,000m depth. Visualization is based on Ocean Data View (Schlitzer, 2018). All studied core sites are indicated by the respective colored symbols. AAIW = Antarctic Intermediate Water; ESSW = Equatorial Subsurface Water; PDW = Pacific Deep Water.

five sediment cores, including new ^{14}C ages for core 22SL. This new set of marine sediment cores spans from ~31°S to 36°S and ~540 to 3,100 m water depth along the Chilean continental margin (Figure 1), providing a more complete perspective of ventilation and water mass changes during glacial-interglacial cycles.

2. Oceanographic Setting

The SEP is influenced by water masses originating in the SO, the EEP, and the NP (Figure 1). Subantarctic Water (SAAW), SAMW, and AAIW form in the SO; Equatorial Subsurface Water (ESSW) in the EEP; and Pacific Deep Water (PDW) originates in the NP and North Atlantic, primarily. SAAW is found along the Chilean margin from ~52°S to ~28°S (Silva et al., 2009) from the surface to ~100 m depth. It originates from upwelled water in the Antarctic divergence zone (Tomczak & Godfrey, 2003) and is advected by the Antarctic Circumpolar Current (ACC) until it encounters the American continent between ~42°S and 48°S where it divides in two branches, the southward flowing Cape Horn Current and the northward flowing Peru-Chile Current or Humboldt Current (Silva & Neshyba, 1977, 1980; Strub et al., 1998). Northward of ~28°S, the surface layer is occupied by Subtropical Water (STW), advected southward by the Peru-Chile Countercurrent (PCCC, Strub et al., 1998).

Underneath surface waters, the ESSW is transported from the EEP to the south (Figure 1) by the Peru-Chile Undercurrent along the Chilean margin (Silva et al., 2009; Silva & Fonseca, 1983; Strub et al., 1998; Wooster & Gilmartin, 1961; Wyrtki, 1967) and at ~80°W by the PCCC (Silva et al., 2009). Its core is characterized by a subsurface salinity maximum at ~250 m depth (Figure 1), which can still be identified at ~48°S, though not further than ~100 km from the coast (Silva et al., 2009). The ESSW is also characterized by low oxygen content, derived from the advection of waters from the Oxygen Minimum Zone of the EEP.

Information on ^{14}C content in the water column for the region is scarce. The most detailed record is station P06-E11 (~32.5°S) from the World Ocean Circulation Experiment-Hydrographic Program (Kumamoto et al., 2011).

Paleoceanography and Paleoclimatology 10.1029/2019PA003613

Because of the "bomb effect," which doubled the ^{14}C content of the atmosphere in the 1950s and 1960s, the amounts of ^{14}C have been modified from the surface down to ~1,500 m in the SEP. However, prebomb $\Delta^{14}C$ values has been estimated from silicate concentrations, alkalinity, and apparent oxygen utilization by Kumamoto et al. (2011), which is here used as reference for depths shallower than 1,500 m (Figure S2 in the supporting information).

SAMW and AAIW originate in the SO and, in the SEP, have very similar characteristics (McCartney, 1977). In particular, AAIW ventilates intermediate waters from ~400 to 1,000 m depth with its core at ~600 m (Silva et al., 2009), easily identified as a salinity minimum (Figure 1; Johnson, 1973; Reid, 1965; Tsuchiya & Talley, 1996, 1998). Both SAMW and AAIW presently form in various areas of the SO, where recently upwelled deep waters subduct into intermediate depths ventilating the thermocline in the Pacific, Atlantic, and Indian oceans (Bostock et al., 2013; McCartney, 1977; Piola & Gordon, 1989). The exact subduction and formation mechanisms of these water masses are still debated (see Bostock et al., 2013, for a more detailed discussion on AAIW formation and Sloyan et al., 2010, for SAMW and AAIW). The SEP has been indicated as the main modern source of AAIW (e.g., Bostock et al., 2013; McCartney, 1977, 1982; Talley, 1996, 1999); from there it circulates to the north to enter the south Pacific subtropical gyre circulation and to the east through the Drake Passage into the Atlantic Ocean (Talley, 2013; Tomczak & Godfrey, 2003). The prebomb $\Delta^{14}C$ estimate for the depths bathed by AAIW in the SEP ranges between approximately −150‰ and approximately −100‰ $\Delta^{14}C$ (Figure S2).

Off Chile, at depths deeper than ~1,200 m, the PDW circulates to the south (Silva et al., 2009). PDW is the most ^{14}C-depleted water mass in the modern ocean, with $\Delta^{14}C$ values in the SEP between approximately −150‰ and −230‰ $\Delta^{14}C$ (Kumamoto et al., 2011). The formation of PDW is associated with sluggish mixing processes between Antarctic Bottom Water (AABW), AAIW, and recirculated North Atlantic Deep Water (NADW) along their way to the north Pacific (Talley, 2013; Tomczak & Godfrey, 2003); from there PDW circulates back south and is recognized by low ^{14}C and high nutrient contents.

3. Materials and Methods

Marine sediment cores GeoB 7167-6, GeoB 7163-7, GeoB 7162-6, GeoB 7149-2, and 22SL (Figure 1) were retrieved by the German r/v Sonne during expeditions SONNE 156 (Hebbeln and cruise participants, 2001) and SONNE 161 (Wiedicke-Hombach et al., 2002). Cores GeoB 7167-6, GeoB 7163-7, GeoB 7162-6, and 22SL were obtained at ~36°S, off Concepción, where sedimentation rates are very high (~40 cm/kyr) due to high terrestrial input derived from rivers (Hebbeln et al., 2007). Core GeoB 7149-2 was recovered at ~31°S off Puerto Oscuro. Despite being adjacent to the semidesert areas of the "Norte Chico," sedimentation rates at GeoB 7149-2 are relatively high, varying between 20 and 40 cm/kyr due to quasi-perennial upwelling-driven marine productivity (De Pol-Holz et al., 2007).

The planktic foraminifera species—*N. dutertrei*, *N. pachyderma* (syn) (i.e., *N. pachyderma*), *N. pachyderma* (dex) (i.e., *N. incompta)*, *G. bulloides*, and *G. inflata*—and the benthic foraminifera species—*Uvigerina sp.* and *Brizalina sp.*—were handpicked for monospecific dating when possible. Otherwise, mixed planktic foraminifera (*N. pachyderma* (syn), *N. pachyderma* (dex), *N. dutertrei*, and *G. bulloides*) and mixed benthic foraminifera (*Uvigerina sp.*, *Bolivina sp.*, *Angulogerina sp.*, *Globocassidulina sp.*, and *Dentalina sp.*) were measured. Foraminifer abundances limited the time span and resolution of some of the ^{14}C and ^{13}C records. Detailed information on each sample is provided in Table S1. All ^{14}C measurements were carried out at the Keck Carbon Cycle Accelerator Mass Spectrometer facility at the University of California, Irvine, except for published data from core 22SL (De Pol-Holz et al., 2010), dated at the National Ocean Science Accelerator Mass Spectrometer facility at the Woods Hole Oceanographic Institution. Briefly, samples were leached by 10% of their mass using HCl in order to remove any secondary (younger) carbonate and then hydrolyzed with 85% H_3PO_4 under vacuum. Finally, all samples were graphitized using Fe as a catalyst in the presence of H_2. All ^{14}C dates are shown in Table S1 and plotted in Figure S1.

Stable isotopes of carbon ($\delta^{13}C$) were obtained for the planktic foraminifera *Globigerina bulloides* every 5 cm, where possible, in the size range >212 μm, in cores GeoB 7163-6, GeoB 7167-6, 22SL, and GeoB 7149-2. Additionaly, *N. dutertrei* was measured in core GeoB 7149-2. Analyses were performed at the MARUM Stable Isotope Laboratory on a Thermo Finnigan MAT 252 mass spectrometer linked online to a

Paleoceanography and Paleoclimatology 10.1029/2019PA003613

CarboKiel-II carbonate preparation device. Long-term standard deviation was monitored through the internal laboratory standard Solnhofen Limestone (SHK) with errors estimated in 0.05‰ V-PDB for $\delta^{13}C$. Isotope values were calibrated to the Vienna Pee dee Belemnite scale with the NBS-19 standard. Results are presented in Table S2.

4. Age Models

Correcting planktic foraminifera ^{14}C ages for a constant R_S has been broadly utilized as a method to produce marine sediment core chronologies (e.g., De Pol-Holz et al., 2010; Kaiser et al., 2008; Lamy et al., 2004). However, the assessment of precise R_S has demonstrated that these can vary greatly during the Holocene (Carré et al., 2015; Latorre et al., 2017) but especially during the late glacial and last deglaciation (Siani et al., 2013; Sikes & Guilderson, 2016; Sikes et al., 2000; Sikes et al., 2016; Skinner et al., 2015). In particular, Siani et al. (2013) demonstrated the varying nature of the R_S in the SEP between ~15 and 2 ka cal BP, using tephrochronology in core MD07-3088 (~46°S) and obtaining R_S values ranging between 790 ± 160 years and 1,320 ± 95 years. In order to obtain robust chronologies, we assess R_S changes at ~36°S and ~31°S since the LGM.

In the modern SEP, R_S ages result from a combination of SAAW or STW (Figure 1) with relatively ^{14}C-depleted ESSW (Figure S2), which is brought to the surface by coastal upwelling (Strub et al., 1998). Broadly, three different coastal upwelling regimes exist, which are controlled by the position of the Southerly Westerly Winds (SWW): (i) south of ~39°S, the permanent presence of SWW inhibits upwelling; thus, R_S there are controlled mainly by the presence of SAAW; (ii) between ~35°S and 39°S, coastal upwelling is seasonal, because of the latitudinal shift of the SWW to the south in Austral summer allowing coastal upwelling to occur; (iii) north of ~35°S, coastal upwelling is permanent, and the highest R_S are found in this area (Carré et al., 201; Ingram & Southon, 1996; Merino-Campos et al., 2019; Ortlieb et al., 2011; Taylor & Berger, 1967). These different domains of upwelling can also be observed in $\delta^{13}C$ measurements in planktic foraminifera in the modern SEP. At present, *G. bulloides* is interpreted to live in the surface mixed layer and prefer upwelling conditions, in the SEP (Marchant et al., 1998) and elsewhere (Bemis et al., 1998; Fairbanks et al., 1982; Ortiz et al., 1995; Sautter & Thunell, 1991). On the other hand, *N. pachyderma* (dex) has been suggested to prefer a more stratified surface layer (Marchant et al., 1998; Mortyn & Charles, 2003; Ortiz et al., 1995, 1996; Sautter & Thunell, 1991). Between ~39°S and 46°S, both species yield similar values (Figure S2), consistent with a lack of upwelling, whereas between ~24°S and 35°S, $\delta^{13}C$ values of *G. bulloides* are ~1.5‰ lighter than *N. pachyderma* (dex), consistent with persisting upwelling conditions in this area (Mohtadi et al., 2005). As a result, $\delta^{13}C$ records of *G. bulloides* are expected to reflect differences in R_S at ~46°S, ~36°S, and ~31°S resulting from differing contributions of SAAW and ESSW due to variations in the intensity of coastal upwelling along the margin. Additionally, R_S variations in the past may have occurred because of changes in the ^{14}C signature of the upwelled waters and/or because of modifications in habitat preferences of planktonic foraminifera.

To assess the relative contribution of SAAW to R_S at ~36°S and ~31°S in the past, we compare the *G. bulloides* $\delta^{13}C$ records of this study versus core MD07-3088 at ~46°S. *G. bulloides* $\delta^{13}C$ in core MD07-3088 is interpreted to represent the SAAW end member because of its position directly influenced by the ACC and no coastal upwelling (Strub et al., 1998). In order to assess how R_S varies with latitude, the $\delta^{13}C$ records are plotted against their planktic conventional ^{14}C ages (Figure 2). Similar trends are observed at ~36°S and ~46°S (Figure 2d), with a distinct "W"-shaped trend in both latitudes but not at ~31°S. However, from ~15 ^{14}C ka BP, $\delta^{13}C$ values of *G. bulloides* at ~36°S become relatively lower than at ~46°S, similar to what is observed today (Figure S2). In addition, between ~13 and 11 ^{14}C ka BP (gray interval in Figure 2), values at ~36°S appear to lag ~500–700 ^{14}C years behind the $\delta^{13}C$ of *G. bulloides* at ~46°S.

In the SEP, the deglaciation is characterized by abrupt changes in surface water properties that have been interpreted as a reorganization of water masses and fronts (e.g., Haddam et al., 2018; Kaiser et al., 2008; Mohtadi et al., 2008), associated with the meridional migration of the SWW to the south and/or changes in its distribution and intensity. The transition from higher to lower $\delta^{13}C$ at ~36°S (22SL) from ~16 to 14 ^{14}C ka BP (Figure 2d) is consistent with the migration of the SWW to the south at the beginning of the deglaciation (Denton et al., 2010; Mohtadi et al., 2008; Moreno et al., 1999) allowing the onset of seasonal

Paleoceanography and Paleoclimatology 10.1029/2019PA003613

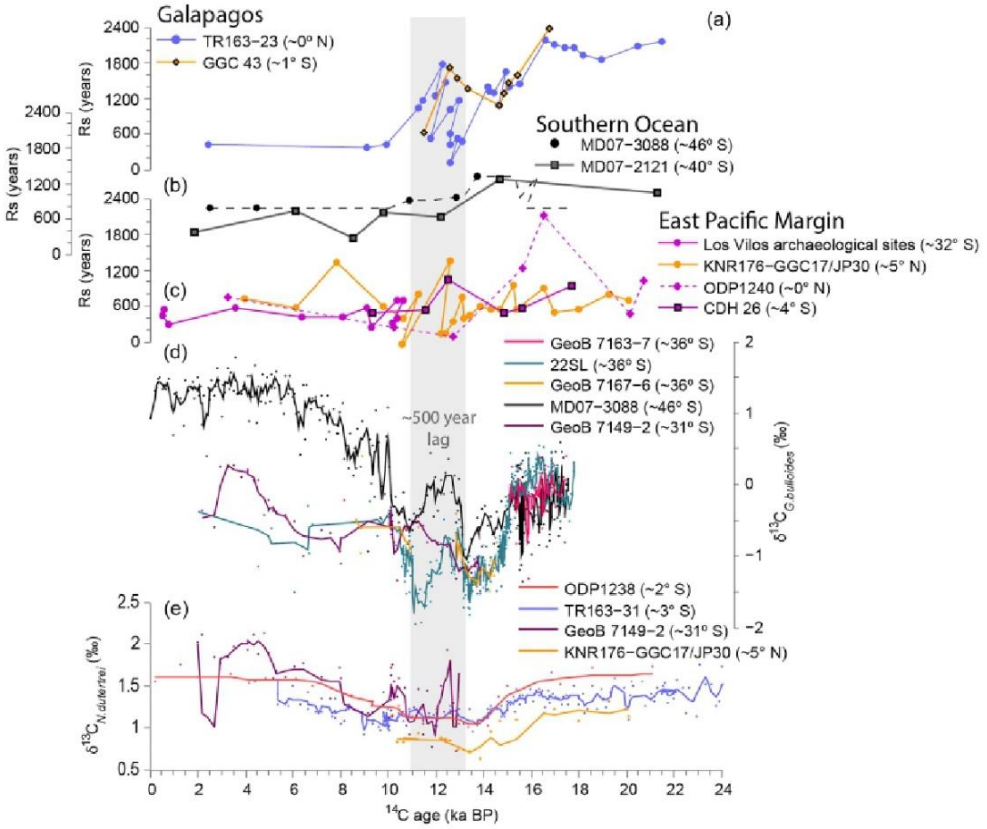

Figure 2. Comparison of records in the South East Pacific with records in the Southern Ocean and Equatorial East Pacific against ^{14}C age of planktic foraminifera, rather than calendar age. In order to do this, the ^{14}C dates were interpolated to obtain ^{14}C estimates for the depths in which only ^{13}C was measured. For depths where more than one planktic foraminifera specie was dated, the mean at each depth was used as references for the interpolation. R_S estimates in (a) Galapagos platform: core TR163-23 (0.41°S, 92.16°W, 2,730 m; Umling & Thunell, 2017), from tuning with Greenland Ice Core Chronology GICC05 and core GGC 43 (1°15.13′S, 89°41.07′S, 617 m; Bova et al., 2018); (b) the Southern Ocean, from tephrochronology in core MD07-3088 in the South East Pacific sector (41°S, 74°W, 1,536 m; Siani et al., 2013; symbols are the measured R_S while the black line corresponds to the interpolated values) and core MD97-2121 (40°22.935′S, 177°59.68′E, 2,314 m; Skinner et al., 2015) the South West Pacific sector; (c) the East Pacific margin, at ~32°S obtained from paired mollusk shells and charcoal fragments from archeological sites near Los Vilos (Carré et al., 2015); in core CDH 26 (3°59.16′S, 81°18.52′W, 1,023 m; Bova et al., 2018) from tuning with EPICA Dome C and in core KNR176-GGC17/JP30 (5.02°N, 77.63°W, 707 m; Zhao & Keigwin, 2018) from wood-planktic foraminifera pairs. (d) *G. bulloides* $\delta^{13}C$ from cores used in this study and core MD07-3088 (Siani et al., 2013), the lines correspond to smoothed 3-point moving averages of the original data (small symbols). (e) *N. dutertrei* $\delta^{13}C$ in the Equatorial East Pacific: core TR163-31 (3°37.2′S, 83°58′W, 3,210 m; Patrick & Thunell, 1997) and ODP site 1238 (1°52.2′S, 82°46.8′W, 2,203 m; Martínez-Botí et al., 2015) compared with *N. dutertrei* $\delta^{13}C$ GeoB 7149-2; the lines correspond to smoothed 3-point moving averages of the original data (small symbols). Gray interval: ~500 years lag between the $\delta^{13}C$ record at ~46°S and ~36°S discussed in the text.

upwelling at this latitude, thus establishing a situation similar to what is observed today (Figure S2). In addition, between ~13 and 11.5 ^{14}C ka BP not only does $\delta^{13}C$ become relatively more depleted but also radiocarbon dates of planktic foraminifera are consistently older at ~36°S than at ~46°S. These observations are consistent with upwelling of older ESSW at 36°S between ~13 and 11.5 ^{14}C ka.

To observe how the R_S of the ESSW endmember changed, we use a broad range of cores in the EEP either with R_S assessments or stable isotope records. These cores are thought to record changes in the Equatorial Undercurrent (EUC), which feeds the ESSW (Brink et al., 1983; Lukas, 1986; Toggweiler et al., 1991). The comparison is based in measurements done on the deep-dwelling planktic foraminifera *N. dutertrei*, as they are thought to represent the geochemistry of the EUC (Fairbanks et al., 1982; Spero & Lea, 2002). The

Paleoceanography and Paleoclimatology 10.1029/2019PA003613

observed lag between ~13 and 11.5 ^{14}C ka BP (gray interval in Figure 2) implies R_S ages ~500–700 ^{14}C years older at ~36°S than at ~46°S under the assumption that the "W"-shaped trend in both δ^{13}C records should be contemporaneous. When compared with other EEP records, the SO shows, in general, lower Rs values (Figures 2a–2c). The higher R_S in the EEP is probably the result of the extremely ^{14}C-depleted intermediate waters observed in this area (Bova et al., 2018; Stott et al., 2009), which would be even older than contemporaneous deep waters upwelling in the SO (Figures 6 and S4).

Since there is a lot of uncertainty on how much these source areas influenced each of our sites, four age models, each assigning different R_S to planktic foraminifera ^{14}C ages were built for each core accounting for four possible scenarios: (a) Surface water from SAAW was advected north of 46°S reaching as far north as 31°S throughout the considered period, and thus, R_S values from core MD07-3088 are applied to all studied cores; (b) between ~13 and 11 ^{14}C ka BP the upwelling of ^{14}C-depleted ESSW increases the R_S at ~36°S (22SL, GeoB 7167–6, and GeoB 7162–6), and thus, equatorial R_S from core TR163-23 are assigned for this interval to cores at ~36°S; (c) no changes occur in R_S, and thus, constant values, equivalent to the modern mean in the closest latitude with available information (Merino-Campos et al., 2019), are assigned; (d) at ~31°S (Geob 7149-2) exclusively equatorial waters flow in the whole interval, and thus, for ages older than ~11 ka ^{14}C BP, R_S from core TR163–23 (~0°N) are assigned, and for ages younger, R_S ages from ~32°S are assigned (Carré et al., 2015). See Table S2 for a summary.

After assigning the relevant R_S to each planktic foraminifera ^{14}C age, the age models for each core were generated using the Bacon algorithm (Blaauw & Christen, 2011). We then calculated the Δ^{14}C of deep and intermediate waters following Adkins and Boyle's (1997) definition derived from Stuiver and Polach (1977),

$$\Delta^{14}C = \left(\frac{e^{-\frac{^{14}C\ age}{8,033}}}{e^{-\frac{cal\ age}{8,266}}} - 1 \right) 1,000‰,$$

for each age model. The resulting Δ^{14}C values are presented in Figure 3 with their respective 1σ and 2σ envelopes.

In addition, the simulated variation of Δ^{14}C at each depth was obtained by a modern circulation model constrained by observations of temperature, salinity, CFC-11, and prebomb Δ^{14}C (DeVries, 2014). The model takes into account variations in the atmospheric ^{14}C and CO_2 concentration using the gas exchange formulation of DeVries and Primeau (2010; their equations B.6 and B.7). This formulation states that the gas exchange piston velocity for Δ^{14}C is proportional to the ratio of atmospheric pCO_2 to surface ocean DIC. To a first approximation we assume a globally uniform surface ocean DIC that varies with pCO_2 according to a buffer factor of 10 (i.e., a 10% change in atmospheric pCO_2 translates to a 1% change in DIC) in a modern oceanic circulation scenario. This model simulation thus approximates the expected Δ^{14}C that would arise in a scenario of constant (modern) ocean circulation and gas exchange piston velocity matching the observed modern Δ^{14}C relatively well at the core locations (Figure 3). For the model calculations, we used atmospheric ^{14}C concentration from the IntCal13 curve (Reimer et al., 2013), and atmospheric pCO_2 from ice core reconstructions (Marcott et al., 2014; Monnin et al., 2001), and air-sea piston velocity from the OCMIP-2 protocol, reduced by 20% globally in light of recent estimates (Sweeney et al., 2007). Deviations from the modeled Δ^{14}C can be interpreted as arising from changes in ocean circulation, changes in air-sea gas exchange due to changes in wind speed or sea ice cover, or from neglected sources and/or sinks of ^{14}C such as inputs of ^{14}C-dead carbon from hydrothermal vents. The model displays a slight positive bias of ~25–30‰ relative to the modern core-top Δ^{14}C values, which is likely due to the simplifications of the air-sea gas exchange parameterization. This positive bias is corrected for when comparing the modeled and observed variations in Δ^{14}C.

5. Results

With the exception of age models using constant R_S (age model *c*), there is general agreement between the different age models and derived Δ^{14}C values (Figures 3 and S3). These age models represent the different scenarios depicted in section 4 and the most likely R_S given our current knowledge of the area. For cores

Paleoceanography and Paleoclimatology 10.1029/2019PA003613

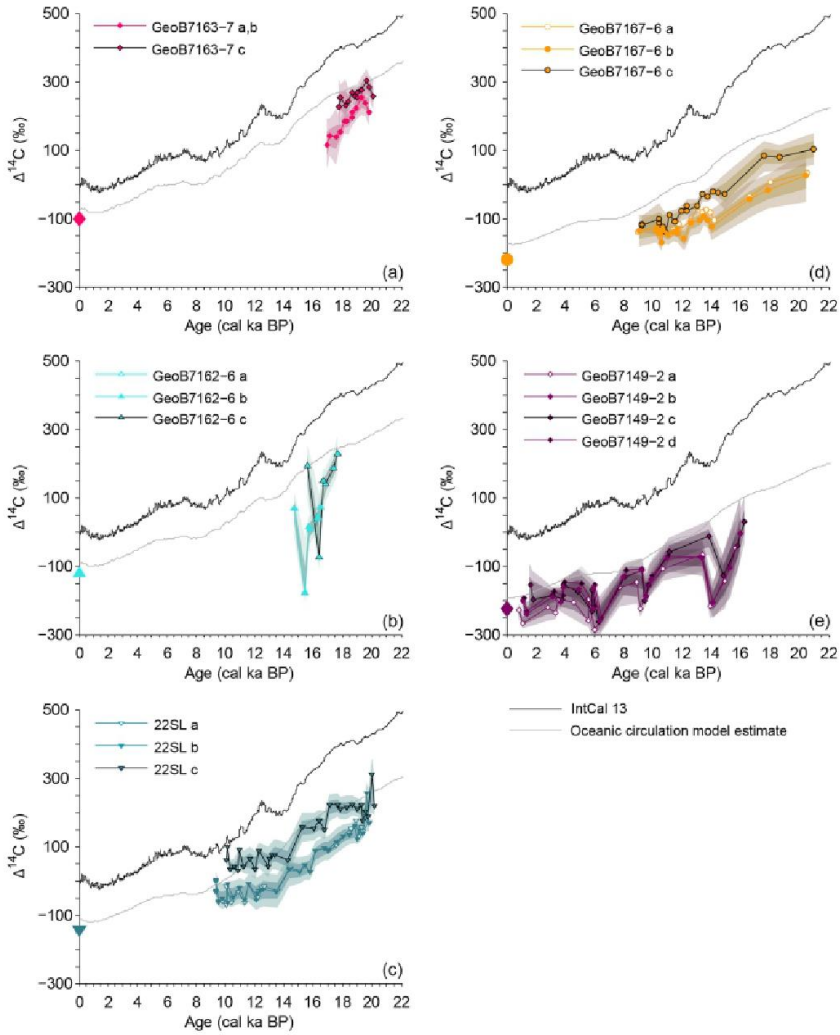

Figure 3. $\Delta^{14}C$ estimates for the cores in this study with their corresponding 1σ (dark) and 2σ (light) envelopes, which take into account errors in ^{14}C dating of benthic foraminifera and calendar ages estimates, from the different age model scenarios discussed in the text: (a) Surface water from SAAW was advected north of 46°S reaching as far north as 31°S throughout all the considered period, and thus, the R_S from core MD07-3088 are applied to all studied cores; (b) between ~13 and ~11 ^{14}C ka BP, the upwelling of ^{14}C-depleted ESSW increases the R_S at ~36°S (22SL, GeoB 7167–6, GeoB 7162–6), and thus, equatorial R_S from core TR163-23 are assigned for this interval to cores at ~36°S; (c) no changes occur in R_S, and thus, constant values, equivalent to the modern mean in the closest latitude with available information (Merino-Campos et al., 2019), are assigned; (d) at ~31°S (Geob 7149-2) exclusively equatorial waters flow in the whole interval, and thus, for ages older than ~11 ka ^{14}C BP, R_S from core TR163–23 (~0°N) are assigned, and for ages younger, R_S ages from ~32°S are assigned (Carré et al., 2015). Also plotted are the atmospheric $\Delta^{14}C$ (black line, Reimer et al., 2013), the modeled $\Delta^{14}C$ at each depth accounting for changes in atmospheric $\Delta^{14}C$ and CO_2 (gray curves), and the modern $\Delta^{14}C$ from station P06-E11 (Kumamoto et al., 2011).

at ~36°S, age models *a* and *b* yield virtually identical results, and the discussion is based on age model *b*, which takes into account a lag observed in the $\delta^{13}C$ records between ~36°S and ~46°S (Figure 2). Core GeoB 7149-2 presents more variability among the different age models during the Holocene. However, as described in section 4, R_S ages at ~31°S are probably lower than those for core MD07-3088, in agreement with values estimated at ~32°S (Carré et al., 2015). Consequently, the discussion for core GeoB 7149-2 is based on the results obtained with age model *d*.

Paleoceanography and Paleoclimatology 10.1029/2019PA003613

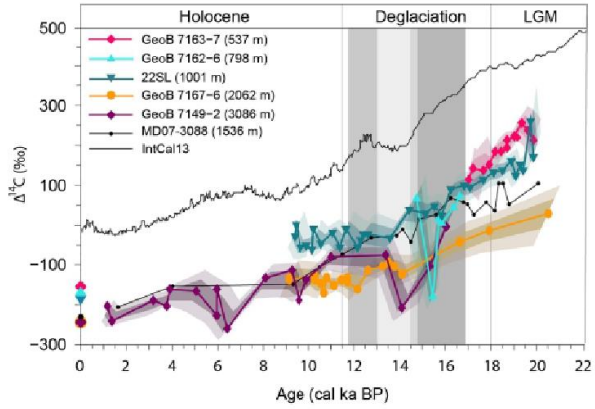

Figure 4. $\Delta^{14}C$ variations in intermediate and deep waters in the South East Pacific since the Last Glacial Maximum, from cores in this study with their corresponding 1σ (dark) and 2σ (light) envelopes, which take into account errors in ^{14}C dating of benthic foraminifera and calendar ages estimates. Also plotted are core MD07-3088, in the South East Pacific sector of the Southern Ocean (Siani et al., 2013), the atmospheric $\Delta^{14}C$ variation IntCal13 (black line, Reimer et al., 2013), and the modern $\Delta^{14}C$ estimate from station P06-E11 (~32°S) at each core depth (Kumamoto et al., 2011).

Additional information is provided by the modeled $\Delta^{14}C$ change at each depth (Figures 3 and 5), which is a reference on how the ^{14}C content of the water would change accounting only for changes in atmospheric pCO_2 and its ^{14}C content. The modeled $\Delta^{14}C$ is in general agreement with the modern data, with values ~20–30‰ $\Delta^{14}C$ higher than the modern in all cores except from GeoB 7167-6, which presents a difference of ~50 ‰ $\Delta^{14}C$ (Figure 3). In order to better visualize how much of the obtained $\Delta^{14}C$ in each core would not be accounted by changes in atmospheric pCO_2 and its ^{14}C content, the difference between the $\Delta^{14}C$ obtained with the selected age models and the modeled $\Delta^{14}C$ is also presented (Figure 5), corrected by the difference between the modern modeled value and the modern value (Figure S2). In Figure 5, a deviation from zero implies changes in oceanic circulation, in air-sea gas exchange (unrelated to pCO_2 changes, which are already accounted for in the model) and/or geologic input of ^{14}C-dead CO_2. Also, similar deviations from zero at the different analyzed depths imply that the relative amount of ^{14}C between them was similar to the modern.

During the LGM, $\Delta^{14}C$ records from all cores in the SEP are more depleted in ^{14}C with respect to the contemporaneous atmosphere than they are in the Holocene (Figure 4). The observed minus modeled $\Delta^{14}C$ is predominantly negative during the LGM (Figure 5), suggesting that the depleted ^{14}C values result from slower ventilation or older reservoir ages, rather than from changes in atmospheric ^{14}C or pCO_2. The variation of ^{14}C with depth is similar to the modern ocean above ~1,500 m (Figures 4 and 5) suggesting similar water column structures during the LGM and early Holocene (Figure 4), though with slightly more ventilated waters at ~540 m. Meanwhile, at ~2,000 m the only available data point is the most depleted both compared with the atmosphere and the modeled values, in agreement with a broad range of deepwater records (Figure 7). Unfortunately, there are no contemporaneous data points at ~1,500 and ~2,000 m for the glacial in the SEP; however, we can at least obtain the difference between the mean values at each depth, which is ~66‰ $\Delta^{14}C$ (Figure 4) whereas the modern difference is ~20‰ $\Delta^{14}C$. This difference also stands when comparing with the simulated $\Delta^{14}C$ values at each depth (Figure 5a), where waters at ~2,000 m are ~25‰ more depleted with respect to the simulated estimated than at ~1,500 m. The above information suggests a more ^{14}C-depleted and stratified deep glacial ocean, in particular below ~1,500 m.

Between ~19 and 17 ka cal BP, the $\Delta^{14}C$ signature of waters at ~1,000, ~1,500, and ~2,000 m maintains a stable offset from the modeled estimate (Figure 5). At ~540 m, however, $\Delta^{14}C$ values become rapidly more ^{14}C depleted at ~19 ka cal BP, decreasing from a mean difference with waters at ~1,000 m of ~54‰ $\Delta^{14}C$ in the LGM to ~29‰ $\Delta^{14}C$ in the early deglaciation (~17 ka; Figure 4). Between ~16.5 and 14.8 ka cal BP, intermediate waters at ~800 and ~1,000 m become more ^{14}C depleted with respect to the atmosphere and model; meanwhile, waters at ~1,500 m become more ventilated, reaching similar values to those found at ~800 and ~1,000 m until ~14.8 ka cal BP (Figure 4). At ~800 m, waters reach an extremely ^{14}C depleted minimum of ~460‰ $\Delta^{14}C$ lower than the contemporary atmosphere and ~350‰ $\Delta^{14}C$ lower than the modeled estimate. Between ~18 ka cal BP and ~14 ka cal BP, the only data point available at deep waters at ~2,000 m remains as ^{14}C depleted from the model as during the LGM (Figure 5), with a difference from the contemporary atmosphere of approximately −380‰ $\Delta\Delta^{14}C$. At ~3,000 m, values are both more ^{14}C enriched (~16 ka cal BP) and more 14C depleted (~14 ka cal BP) than at ~2,000 m, and a decreasing trend is observed between ~16 and 14 ka cal BP, reaching a minimum of approximately −400‰ $\Delta\Delta^{14}C$ at ~14 ka cal BP.

Around ~14.5 ka cal BP, benthic foraminifer $\Delta^{14}C$ offsets from the model measured at water depths between 1,000 and 3,000 m briefly return to LGM values; waters at ~1,500 m are more poorly ventilated (larger offset), while waters at ~800 and ~1,000 m are better ventilated (smaller offsets). Between ~13.5 and 10.5 ka cal BP intermediate waters at ~1,000 and 1,500 m return to a situation similar to what is observe between ~16.5 and ~14.5 ka cal BP, whereas deep waters at ~2,000 and ~3,000 m become rapidly ventilated at ~13 ka cal BP. In particular, waters at ~2,000 m go from a $\Delta\Delta^{14}C$ of −320‰ at ~14 ka cal BP to −280‰ at ~13.5 ka cal BP and at ~3,000 m from −400‰ $\Delta\Delta^{14}C$ at ~14 ka cal BP to −270 at ~13.3 ka cal BP. Between ~13.5 and 12.5 ka cal

Paleoceanography and Paleoclimatology 10.1029/2019PA003613

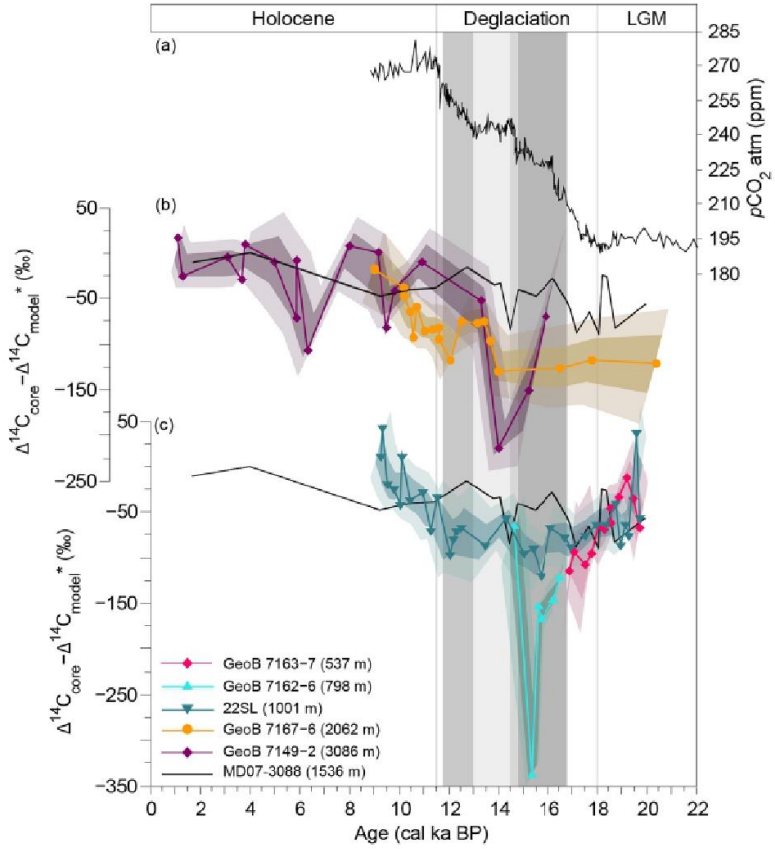

Figure 5. (a) Atmospheric pCO_2 from West Antarctic Ice Sheet Divide ice core (Marcott et al., 2014). (b) Deviation of the obtained $\Delta^{14}C$, in cores in the South East Pacific, from the modeled estimate, corrected by the difference between the modern modeled estimate and the modern natural $\Delta^{14}C$ at each depth (Kumamoto et al., 2011). Also plotted are their corresponding 1σ (dark) and 2σ (light) envelopes, which take into account errors in ^{14}C dating of benthic foraminifera and calendar ages estimates and the error associated with the model.

BP, waters at ~2,000 m stay relatively well ventilated and at ~12.1 ka cal BP decrease its $\Delta\Delta^{14}C$ in about 40‰; from there they become increasingly better ventilated until the end of the record around 9 ka cal BP. At ~10 ka cal BP, all records with available information reach values similar to modern, and the difference with the modeled estimates is close to zero.

6. Discussion

6.1. Last Glacial Maximum

The obtained $\Delta^{14}C$ data at ~2,000 m show a depletion from the contemporary atmosphere of approximately −410‰ (Figure 4), which agrees with a broad range of other deepwater records (Figure 6): approximately −310‰ to −600‰ in the SWP (Ronge et al., 2016; Sikes et al., 2016), approximately −400‰ to −540‰ in the SA (Skinner et al., 2010), approximately −370‰ to −500‰ in the NP (Galbraith et al., 2007; Rae et al., 2014), and approximately −400‰ to −480‰ in the EEP (De la Fuente et al., 2015; Umling & Thunell, 2017). These glacial deep ocean values show relatively larger depletion than modern data but not as extremely ^{14}C-depleted values as observed in the SWP and EPR, where ^{14}C contents were between approximately −900‰ to −1,000‰ lower than the contemporary atmosphere (Ronge et al., 2016). Therefore, the new SEP ^{14}C data contribute to the idea that the widespread situation during the LGM was a relatively ^{14}C-depleted deep ocean with only localized extreme depletions. Above these depths, at ~1,500 m, values are ~66‰ $\Delta^{14}C$ higher than the point at ~2,000 m, a difference three times higher than

Paleoceanography and Paleoclimatology 10.1029/2019PA003613

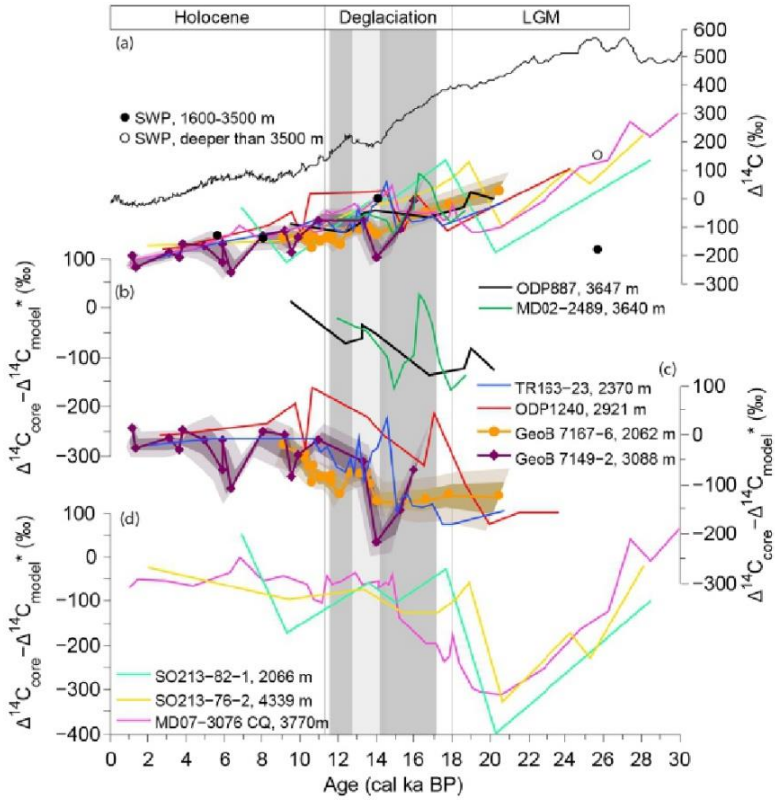

Figure 6. (a) $\Delta^{14}C$ variations in deep waters in the Pacific Ocean and South Atlantic along with the atmospheric $\Delta^{14}C$ variation IntCal13 (black line; Reimer et al., 2013). South West Pacific mean values at depths between 1,600–3,500 m and deeper than 3,500 m (Sikes et al., 2016) together with cores described in (b), (c), and (d), which correspond to the deviation of the $\Delta^{14}C$ in deep waters from the modeled estimate, corrected by the difference between the modern modeled estimate and the modern $\Delta^{14}C$ at each depth from GLODAPv2 (Key et al., 2015). (b) North Pacific: ODP887 (54.4°N, 148.5°W, 3,647 m; Galbraith et al., 2007), MD02-2489 (54.4°N, 149°W, 3,640 m, Rae et al., 2014); (c) Equatorial East Pacific: ODP1240 (0°N, 86.5°W, 2,921 m; De la Fuente et al., 2015), TR163-23 (0.4°N, 92.2°W, 2,730 m; Umling & Thunell, 2017), and South East Pacific records GeoB 7167-6 and GeoB 7149-2 from this study. (d) South West Pacific (Ronge et al., 2016): SO213-82-1 (45.8°S, 176.6°E), PS75/100-4 (45.8°S, 177.1°E, 2,498 m); SO213-76-2 (46.2°S, 178°E, 4,339 m), and South Atlantic (Skinner et al., 2010): MD07-3076 CQ (44°4.46′S, 14°12.47′W, 3,770 m).

modern (Figure 4). In contrast, the relative $\Delta^{14}C$ values at ~540, ~1,000, and ~1,500 m suggest a glacial structure similar to the modern ocean (Figure 4), though with relatively more ventilated waters at ~540 m.

The observed structure is consistent with the idea of a more stratified deep glacial ocean (e.g., Burke & Robinson, 2012; Ronge et al., 2016; Sikes et al., 2017) in which less ventilated deep waters and increased carbon storage were associated to a stronger geochemical divide between middepth and deep waters (Toggweiler, 1999). Different hypotheses have been called upon to explain the observed changes in the glacial ocean (Adkins, 2013; Ferrari et al., 2014; Keeling & Stephens, 2001; Watson & Naveira Garabato, 2006). These hypotheses have in common the importance of sea ice extension, controlling gas exchange between deep waters and the atmosphere (Ferrari et al., 2014; Stephens & Keeling, 2000) and/or by modulating the production and density of deep SO waters (Adkins, 2013; Keeling & Stephens, 2001; Watson & Naveira Garabato, 2006). During the late glacial, freshening of surface waters in the SO would be diminished by the presence of more extensive sea ice, blocking precipitation (Keeling & Stephens, 2001), and/or decreasing sea ice melt water supply (Adkins, 2013; Keeling & Stephens, 2001). This, together with a colder water column, would result in production of denser deep waters in the SO (Adkins, 2013; Watson & Naveira Garabato, 2006), where density would be salt, rather than temperature controlled, as observed in pore water chloride (Adkins et al., 2002). This would decrease isopycnal mixing between southern sourced deep waters

Paleoceanography and Paleoclimatology 10.1029/2019PA003613

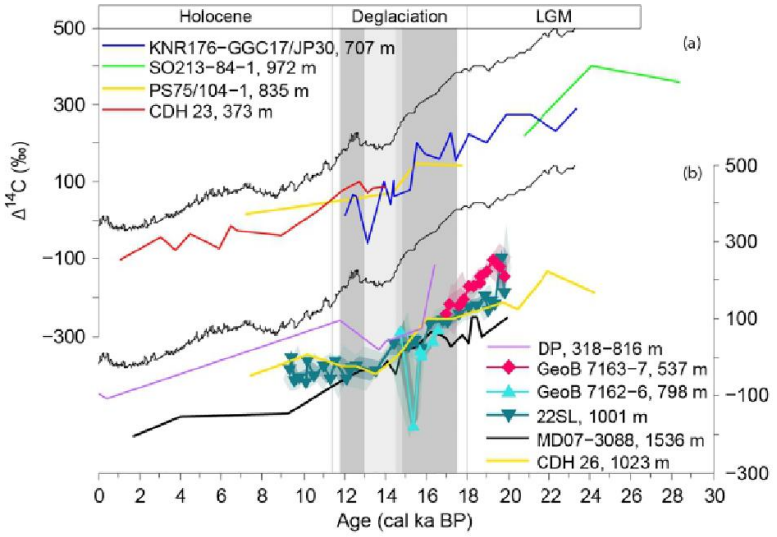

Figure 7. $\Delta^{14}C$ variations in intermediate waters in the Pacific Ocean and Drake Passage along with the atmospheric $\Delta^{14}C$ variation IntCal13 (black line, Reimer et al., 2013). (a) Records where no decreased ventilation is observed during the deglaciation: KNR176-GGC17/JP30 (5.02°N, 77.63°W; Zhao & Keigwin, 2018); SO213-84-1 (45°123′S; 174°58′E; Ronge et al., 2016); PS75/104-1 (44°77′S, 174°52′E; Ronge et al., 2016); CDH 23 (3°44 to 95′S, 81°08.05′W; Bova et al., 2018). (b) Records interpreted as deeper convection of the AAIW during the deglaciation, as indicated in the text: Corals in the Drake Passage (DP) between 318 and 816 m (Burdwood Bank; Burke & Robinson, 2012); MD07-3088 (46°S, 75°W; Siani et al., 2013); CDH 26 (3°59.16′S, 81°18.52′W; Bova et al., 2018).

and NADW, a mechanism that today helps ventilate the deep ocean (Adkins, 2013). Additionally, Ferrari et al. (2014) proposed that the depth of the waters upwelling in the SO would be controlled by the latitude at which the Antarctic divergence occurs, given by the zero-buoyancy boundary. This, in turn would be bounded to the quasi permanent sea ice extent (Ferrari et al., 2014), which is thought to have extended north during the LGM (Gersonde et al., 2005; Otto-Bliesner et al., 2007). When the zero buoyancy boundary moves northward along with sea ice, deep waters that were previously upwelling north of it, thus forming intermediate waters, upwell south of it, forming deep and abyssal deep waters instead. This would enhance carbon and nutrient trapping in the Southern Ocean (Primeau et al., 2013; Holzer et al., 2014), further contributing to a buildup of respired carbon in an isolated Southern-sourced water mass in the deep ocean. Ferrari et al. (2014) estimate that a northern extent of the quasi permanent sea ice would shoal the depth of the isopycnes upwelling in the divergence zone by ~500 m, consistent with findings in the Atlantic and Pacific Oceans (e.g., Sikes et al., 2017). This would have a double effect in the ventilation of the deep ocean. On the one hand, a larger proportion of the deep ocean would upwell south of the zero-buoyancy boundary under quasi permanent sea ice, where the extent of gas exchange with the atmosphere is decreased (Stephens & Keeling, 2000). On the other hand, the shoaling of the upwelled waters would additionally act to diminish the ventilation of abyssal waters since topography-driven turbulent mixing across isopycnals is higher below the reach of seamounts and mid-ocean ridges, near ~2,000-m depth (Figure 1; Adkins, 2013; Ferrari et al., 2014) and waters below this depth would upwell to the south of the divergence zone during the LGM. Additionally, it has been suggested that a northern position of the SWW during the glacial would result in less upwelling of warmer waters, reinforcing the development of the sea ice, thus working together with the previously described processes to develop the isolated deepwater reservoir (Toggweiler et al., 2006).

The high contrast in ^{14}C content of waters at ~1,000, ~1,500, and ~2,000 m observed in the SEP, much higher than today, with waters at ~2,000 m especially ^{14}C depleted, argues in favor of decreased mixing between waters above and below this depth. The latter would result from decreased ventilation of the deep ocean and a lesser contribution of deep waters in the formation of intermediate waters consisting with the aforementioned glacial picture. However, the glacial information provided here is not able to distinguish to what extent each of the previously described mechanisms is responsible.

Paleoceanography and Paleoclimatology 10.1029/2019PA003613

6.2. Deglaciation

The first change with respect to the ventilation of water masses in the SEP during the deglaciation is the decreased ventilation of intermediate waters (Figures 4, 5, and 7). These changes begin before the deglaciation, around ~19.5 ka cal BP, but become more rapid at ~18.5 ka cal BP at ~540 m, followed by a further depletion at ~800 and ~1,000 m between ~16.5 and 14.5 ka cal BP, while waters at ~1,500 m become better ventilated during the same period. The homogenization of ^{14}C values in the water column in the SEP could be explained by deeper convection of AAIW in the SO during the deglaciation, as proposed by Ronge et al. (2015) in the SWP and Haddam (2016) in the SEP. In fact, a similar change to least ventilated intermediate waters is observed in $\Delta^{14}C$ in the East Pacific margin (Bova et al., 2018) and in the DP (Burke & Robinson, 2012) at depths bathed by southern sourced intermediate waters. Additionally, these changes are paralleled by a shift to $\delta^{13}C$ enriched values between ~16.5 and 14 ka cal BP at ~1,500 m in the SEP (Siani et al., 2013) and at ~1,200 m in the SWP (Sikes et al., 2016) and in the East Pacific margin at ~1,000 m (Bova et al., 2018), which is consistent with increased presence of AAIW at these depths. Around this time, increasing ventilation in deepwater records is also observed in the SA (Skinner et al., 2010), SWP (Ronge et al., 2016; Sikes et al., 2016), EEP (De la Fuente et al., 2015; Umling & Thunell, 2017), and NP (Galbraith et al., 2007; Rae et al., 2014), though not all records show the same trend and timing (Figure 6), maybe denoting local effects and/or inconsistencies in the chronologies of the records. Notably, no increase in ventilation is observed in the SEP in deep waters at ~2,000 m; furthermore, at ~3,000 m even decreased ventilation is observed, a trend contrary to what is observed in most deep ocean records (Figure 6). Unfortunately, no data are available for the whole interval at ~2,000 m to enable a thorough comparison with ~3,000 m waters. The origin of the observed ventilation changes at ~3,000 m is puzzling; they might represent local processes such as reinvigorated mixing of the deep ocean advecting stagnant ^{14}C-depleted deep waters to ~3,000 m or ^{14}C dead-CO_2 injected directly from hydrothermal vents (Judd, 2003), which is likely to have happened due to the numerous active ridges in the area (Beaulieu et al., 2013). Notably, the observed decrease is coeval with the decrease in $\Delta^{14}C$ of intermediate waters in the Galapagos platform (Figure S4), which is thought to be sourced in the NP (Bova et al., 2018). However, this is not observed in deepwater records in the NP or EEP. Thus, the origin for the observed trend remains unknown. A comparable situation is found in waters at ~800 m depth, where one data point displays extremely ^{14}C-depleted values. This situation is not observed in other southern sourced intermediate waters but is similar to what has been observed in Baja California (Lindsay et al., 2015; Marchitto et al., 2007). We have confidence in this value since the ^{14}C dating in this core was performed on the abundance peaks in an area with high sedimentation rates and the resulting value is much larger than the 1σ envelope in all age models (Figure 3). However, given the available information, it is difficult to interpret this particular data point, since a Southern Ocean seems unlikely. Nevertheless, the overall less ventilated and vertically expanded AAIW, together with a generally better ventilated deep ocean between 16.5 and 14.5 ky cal BP, is consistent with an oceanic source for the observed steep decrease in atmospheric ^{14}C at this time (Broecker & Barker, 2007). The ^{14}C records presented here further suggest the ^{14}C-depleted carbon was ventilated from depth in the Southern Ocean.

M.

At shallower intermediate depths (~540 m), we observe a steep decrease in the ^{14}C content earlier in the deglaciation at ~18.5 ka cal BP, around the time of the initial increase in atmospheric pCO_2 in Antarctica (Figure 5; Marcott et al., 2014). A possible explanation relating these observations is sea ice retreat allowing deeper waters to be ventilated and feed the formation of AAIW, as proposed by Ferrari et al. (2014). However, constraints on sea ice extent are very scarce and thus is not yet possible to draw any conclusions on this matter. On the other hand, the decrease in the ^{14}C content at ~800 and ~1,000 m depth, associated with the onset of the inferred deeper convection of AAIW at ~16.5 ka cal BP, is consistent with increased upwelling (Anderson et al., 2009; Siani et al., 2013) and surface water pCO_2 (Martínez-Botí et al., 2015) in the SO. In addition, a migration of the SWW to the south has also been proposed during this time (e.g., Denton et al., 2010; Mohtadi et al., 2008; Moreno et al., 1999) and is inferred from the planktic $\delta^{13}C$ trends in the SEP here presented, as depicted in section 4 (Figure 2). As previously stated, a southern position of the SWW is proposed to increase upwelling of deep waters in the SO (Toggweiler et al., 2006), which might translate to more AAIW formation and sea ice retreat. Unfortunately, even in the modern ocean AAIW formation is not clearly understood (Bostock et al., 2013; McCartney, 1977; Piola & Gordon, 1989; Sloyan et al., 2010), thus, the relation between these processes remains to be clarified. However, recent simulations indicate that the recorded glacial-interglacial changes in carbon species (CO_2, ^{14}C, and ^{13}C) in both the atmosphere and

Paleoceanography and Paleoclimatology 10.1029/2019PA003613

the ocean could be explained by intensification of the SWW resulting in more AABW and AAIW production (Menviel et al., 2018). An intensification of the SWW would result in steeper isopycnals, allowing AAIW to reach deeper depths near its formation zone, explaining higher $\Delta^{14}C$ values observed in core MD07-3088 and in turn ventilating deeper waters, explaining lower $\Delta^{14}C$ at ~800 and ~1,000 m (Figure 4). Additionally, according to the simulation by Menviel et al. (2018), this deeper convection could allow for an initial upwelling of low-alkalinity intermediate waters, which would be responsible for the observed abrupt CO_2 increase in the atmosphere at ~16 ka cal BP.

The inferred deeper convection of AAIW is interrupted by a brief return to glacial conditions at the beginning of the ACR, in which intermediate waters at ~800 and ~1,000 m become better ventilated and at ~1,500 m less ventilated. This return to a shallower AAIW is brief, and the homogenized ^{14}C values are again observed between ~13.5 and 10.5 ka cal BP. A similar behavior is observed in sea surface pCO_2 in the SO (Martínez-Botí et al., 2015), and both are consistent with the ventilation of deep waters in the SEP at ~2,000 and ~3,000 m. However, these changes are contrasted by constant atmospheric $\Delta^{14}C$ and pCO_2 (Figures 4 and 5). The latter might be explained by problems in the chronology of the records, or it might reflect that even if this process is taking place, it is not dominating the atmospheric signature. Alternatively, from the comparison with deepwater records in Figure 6, it seems plausible that even if deeper convection in the SO was occurring at this time, the larger part of the isolated deepwater reservoir would have been already ventilated; thus, no important increase in atmospheric pCO_2 would have occurred.

The latter might seem inconsistent with the observed increased in atmospheric pCO_2 in ~30 ppm between ~13 and 11.5 ka cal BP. However, it has been proposed that this increase in atmospheric pCO_2 was related to the outgassing in the EEP rather than in the SO (Bova et al., 2018; Martínez-Botí et al., 2015). Extremely ^{14}C-depleted records have been found in the EEP at intermediate water depths (Bova et al., 2018; Stott et al., 2009) and in Baja California (Lindsay et al., 2015; Marchitto et al., 2007) during the deglaciation. Additionally, CO_2 outgassing in the EEP has been reconstructed by Martínez-Botí et al. (2015), which is similar to the observed outgassing in the SO during Heinrich Stadial 1, but ~70 ppm higher during the Younger Dryas (YD). This, together with increased upwelling in the EEP during the YD (Bova et al., 2018), would result in the ventilation of the extremely ^{14}C-depleted intermediate waters and is proposed to be an important contributor to the observed rise in $pCO2$ (Bova et al., 2018; Martínez-Botí et al., 2015). In addition, simulations indicating the SWW as an important factor in atmospheric pCO_2 increase during the deglaciation only account for ~40 ppm (Menviel et al., 2018; Toggweiler et al., 2006).

Finally, around ~10 ka cal BP the available ^{14}C data indicate the establishment of the current structure, homogeneous deep waters below ~1,500 m, and better ventilated waters above, reaching similar values to the modeled $\Delta^{14}C$ (Figures 4 and 5). The divergence of values at ~1,000 and ~1,500 m with the onset of the Holocene could be interpreted as the end of the conditions that were favoring the deeper convection of the AAIW.

7. Conclusions

The SEP benthic radiocarbon records presented in this study indicate a deepening of AAIW convection during the beginning of the last deglaciation (Haddam, 2016; Ronge et al., 2015). These changes could spur the ventilation of glacial carbon-rich deep waters, contributing to the observed ~40 ppm increase in atmospheric pCO_2 during Heinrich Stadial 1 (Menviel et al., 2018; Toggweiler et al., 2006). This finding of enhanced convection associated with the release of CO_2 through Southern Ocean water masses is consistent with numerous other studies (e.g., Anderson et al., 2009; Bostock et al., 2013; Sloyan et al., 2010), further solidifying this interpretation. The mechanisms for the enhanced convection of AAIW at the beginning of the deglaciation are a subject of debate but could be related to changes in the southern hemisphere westerly winds (e.g., Chiang et al., 2014), perhaps associated with declining Antarctic sea ice extent (Keeling & Stephens, 2001).

During the Younger-Drays period (~13–11 ka cal BP) atmospheric pCO_2 increased by ~30 ppm, but our radiocarbon records suggest a relatively stable pattern of ventilation in the SEP. This suggests that the SO was not the pivotal region for ventilating the second pulse of CO_2 to the atmosphere. Instead, other regions such as the EEP may have provided the conduit for these old waters to the atmosphere, as supported by several radiocarbon records (Stott et al., 2009; Bova et al., 2018; Martínez-Botí et al., 2015).

We observe similarities between our records and those from the EEP (Bova et al., 2018; Stott et al, 2008) both in intermediate and deep waters (Figure S4) that suggest EEP dynamics impact conditions on the Chilean Margin as far south as 46°S and therefore further afield than generally thought. However, the complexity of EEP dynamics, compounded by problems in core chronologies, makes it difficult to draw definitive conclusions on links between the two regions. Future work toward a greater understanding of the interplay between the EEP and SEP is therefore necessary, particularly given that both regions likely play an important role in regulating carbon release from the deep ocean to the atmosphere.

Acknowledgments
We are indebted to the staff of the Keck radiocarbon facility at the University of California, Irvine. We also thank Dra. Silvana Collado, Paola Cárdenas, Andrea Iturra, and Víctor Merino-Campos for laboratory assistance. This work was partially funded by FONDECYT Grants 11100281 and 1140536, Iniciativa Científica Milenio NC-120066, Fondap 15110009 (CR)^2, and ECOS-SUD/CONICYT C15U04. All the data used in this study can be found in the PANGAEA repository (through this link: https://doi.pangaea.de/10.1594/PANGAEA.907746). We also would like to thank the reviewers for the comments on the manuscript, which have enriched the discussion and broaden our view on the issue here addressed.

References

Adkins, J. (2013). The role of deep ocean circulation in setting glacial climates. *Paleoceanography*, *28*, 539–561. https://doi.org/10.1002/palo.20046

Adkins, J., & Boyle, E. (1997). Changing atmospheric $\Delta^{14}C$ and the record of deep water paleo-ventilation ages. *Paleoceanography*, *12*(3), 337–344. https://doi.org/10.1029/97PA00379

Adkins, J. F., MacIntyre, K., & Schrag, D. P. (2002). The Salinity, Temperature, and delta $\delta^{18}O$ of the Glacial Deep Ocean. *Science*, *298*(5599), 1769–1773. https://doi.org/10.1126/science.1076252

Anderson, R. F., Ali, S., Bradtmiller, L. I., Nielsen, S. H. H., Fleisher, M. Q., Anderson, B. E., & Burckle, L. H. (2009). Wind-driven upwelling in the Southern Ocean and the deglacial rise in atmospheric CO_2. *Science*, *323*(5920), 1443–1448. https://doi.org/10.1126/science.1167441

Barnola, J. M., Raynaud, D., Korotkevich, Y. S., & Lorius, C. (1987). Vostok ice core provides 160,000-year record of atmospheric CO_2. *Nature*, *329*, 408–414. https://doi.org/10.1038/329408a0

Beaulieu, S. E., Baker, E. T., German, C. R., & Maffei, A. (2013). An authoritative global database for active submarine hydrothermal vent fields. *Geochemistry, Geophysics, Geosystems*, *14*, 4892–4905. https://doi.org/10.1002/2013GC004998

Bemis, B. E., Spero, H. J., Bijma, J., & Lea, D. W. (1998). Reevaluation of the oxygen isotopic composition of planktonic foraminifera: Experimental results and revised paleotemperature equations. *Paleoceanography*, *13*(2), 150–160. https://doi.org/10.1029/98PA00070

Blaauw, M., & Christen, A. (2011). Flexible paleoclimate age-depth models using an autoregressive gamma process. *Bayesian Analysis*, *6*(3), 457–c474. https://doi.org/10.1214/11-BA618

Bostock, H., Sutton, P., Williams, M., & Opdyke, B. (2013). Reviewing the circulation and mixing of Antarctic Intermediate Water in the South Pacific using evidence from geochemical tracers and Argo float trajectories. *Deep Sea Research, Part I*, *73*, 84–98. https://doi.org/10.1016/j.dsr.2012.11.007

Bova, S. C., Herbert, T. D., & Altabet, M. A. (2018). Ventilation of northern and southern sources of aged carbon in the eastern equatorial Pacific during the Younger Dryas rise in atmospheric CO_2. *Paleoceanography and Paleoclimatology*, *33*, 1151–1168. https://doi.org/10.1029/2018PA003386

Brink, K. H., Halpern, D., Huyer, A., & Smith, R. L. (1983). The physical environment of the Peru upwelling system. *Progress in Oceanography*, *12*(3), 285–305. https://doi.org/10.1016/0079-6611(83)90011-3

Broecker, W., & Barker, S. (2007). A 190 ‰ drop in atmosphere's $\Delta^{14}C$ during the "Mystery Interval" (17.5 to 14.5 kyr). *Earth and Planetary Science Letters*, *256*(1–2), 90–99. https://doi.org/10.1016/j.epsl.2007.01.015

Bryant, S. P., Marchitto, T. M., & Lehman, S. J. (2010). The release of ^{14}C–depleted carbon from the deep ocean during the last deglaciation: Evidence from the Arabian Sea. *Earth and Planetary Science Letters*, *298*(1–2), 244–254. https://doi.org/10.1016/j.epsl.2010.08.025

Burke, A., & Robinson, L. F. (2012). The Southern Ocean's Role in Carbon Exchange During the Last Deglaciation. *Science*, *335*(6068), 557–561. https://doi.org/10.1126/science.1208163

Carré, M., Jackson, D., Maldonado, A., Chase, B., & Sachs, P. (2015). Variability of ^{14}C reservoir age and air-sea flux of CO_2 in the Perú-Chile upwelling region during the past 12,000 years. *Quaternary Research*, *85*(1), 87–93. https://doi.org/10.1016/j.yqres.2015.12.002

Chen, T., Robinson, L. F., Burke, A., Southon, J., Spooner, P., Morris, P. J., & Hong Chin, N. (2015). Synchronous centennial abrupt events in the ocean and atmosphere during the last deglaciation. *Science*, *349*(6255), 1537–1541. https://doi.org/10.1126/science.aac6159

Chiang, J. C. H., Lee, S., Putnam, A. E., & Wang, X. (2014). South Pacific Split Jet, ITCZ shifts, and atmospheric North-South linkages during abrupt climate changes of the last glacial period. *Earth and Planetary Science Letters*, *406*, 233–246. https://doi.org/10.1016/j.epsl.2014.09.012

Crowley, J., Katz, R. F., Huybers, P., Langmuir, C., & Park, S. (2015). Glacial cycles drive variations in the production of oceanic crust. *Science*, *347*(6227), 1237–1240. https://doi.org/10.1126/science.1261508

De la Fuente, M., Skinner, L., Calvo, E., Pelejero, C., & Cacho, I. (2015). Increased reservoir ages and poorly ventilated deep waters inferred in the glacial Eastern Equatorial Pacific. *Nature Communications*, *6*, 7420. https://doi.org/10.1038/ncomms8420

De Pol-Holz, R., Keigwin, L., Southon, J., Hebbeln, D., & Mohtadi, M. (2010). No signature of abyssal carbon in intermediate waters off Chile during deglaciation. *Nature Geoscience*, *3*(3), 192–195. https://doi.org/10.1038/NGEO745

De Pol-Holz, R., Ulloa, O., Lamy, F., Dezileau, L., Sabatier, P., & Hebbeln, D. (2007). Late Quaternary variability of sedimentary nitrogen isotopes in the eastern South Pacific Ocean. *Paleoceanography*, *22*, PA2207. https://doi.org/10.1029/2006PA001308

Denton, G. H., Anderson, R. F., Toggweiler, J. R., Edwards, R. L., Schaefer, J. M., & Putnam, A. E. (2010). The Last Glacial termination. *Science*, *328*(5986), 1652–1656. https://doi.org/10.1126/science.1184119

DeVries, T. (2014). The oceanic anthropogenic CO_2 sink: Storage, air-sea fluxes, and transports over the industrial era. *Global Biogeochemical Cycles*, *28*, 631–647. https://doi.org/10.1002/2013GB004739

DeVries, T., & Primeau, F. (2010). An improved method for estimating water-mass ventilation age from radiocarbon data. *Earth and Planetary Science Letters*, *295*(3–4), 367–378. https://doi.org/10.1016/j.epsl.2010.04.011

Duchamp-Alphonse, S., Siani, G., Michel, E., Beaufort, L., Gally, Y., & Jaccard, S. L. (2018). Enhanced ocean-atmosphere carbon partitioning via the carbonate pump during the last deglacial. *Nature Communications*, *9*(1), 2396. https://doi.org/10.1038/s41467-018-04625-7

Fairbanks, R. G., Sverdlove, M., Free, R., Wiebe, P. H., & Bé, A. W. H. (1982). Vertical distribution and isotopic fractionation of living planktonic foraminifera from the Panama Basin. *Nature*, *298*, 841–844. https://doi.org/10.1038/298841a0

Ferrari, R., Jansen, M. F., Adkins, J. F., Burke, A., Stewart, A. L., & Thompson, A. F. (2014). Antarctic sea ice control on ocean circulation in present and glacial climates. *Proceedings of the National Academy of Sciences of the United States of America*, *111*(24), 8753–8758. https://doi.org/10.1073/pnas.1323922111

Galbraith, E. D., Jaccard, S. L., Pedersen, T. F., Sigman, D. M., Haug, G. H., Cook, M., et al. (2007). Carbon dioxide release from the North Pacific Abyss during the last deglaciation. *Nature*, *449*(7164), 890–893. https://doi.org/10.1038/nature06227

Gersonde, R., Crosta, X., Abelmann, A., & Armand, L. (2005). Sea-surface temperature and sea ice distribution of the Southern Ocean at the EPILOG Last Glacial Maximum—A circum-Antarctic view based on siliceous microfossil records. *Quaternary Science Reviews*, *24*(7–9), 869–896. https://doi.org/10.1002/2014GB004929

Gouretski, V., & Koltermann, K. P. (2004). WOCE global hydrographic climatology (Tech. Rep. 35). Hamburg, Germany: Berichte des Bundesamtes fur Seeschifffahrt und Hydrographie.

Haddam, N. (2016). Rôle de l'Océan Austral dans les Variations Climatiques Rapides de la Dernière Transition Glaciaire-Holocène: Approche Géochimique et Micropaléontologique (Doctoral Thesis). Retrieved from Researchgate. Université Paris-Saclay, France.

Haddam, N. A., Siani, G., Michel, E., Kaiser, J., Lamy, F., Duchamp-Alphonse, S., et al. (2018). Changes in latitudinal sea surface temperature gradients along the Southern Chilean margin since the last glacial. *Quaternary Science Reviews*, *194*, 62–76. https://doi.org/10.1016/j.quascirev.2018.06.023

Hebbeln, D., & cruise participants (2001). PUCK, Report and preliminary results of RV SONNE Cruise SO-156, Valparaíso (Chile) - Talcahuano (Chile), March 29 - May 14, 2001. Bremen, Germany. Berichte, Fachbereich Geowissenschaften, Universität Bremen No. 279.

Hebbeln, D., Lamy, F., Mohtadi, M., & Echtler, H. (2007). Tracing the impact of glacial-interglacial climate variability on erosion of the southern Andes. *Geology*, *35*(2), 131–134. https://doi.org/10.1130/G23243A.1

Holzer, M., Primeau, F. W., DeVries, T., & Matear, R. (2014). The Southern Ocean silicon trap: Data-constrained estimates of regenerated silicic acid, trapping efficiencies, and global transport paths. *Journal of Geophysical Research: Oceans*, *119*(1), 313–331. https://doi.org/10.1002/2013jc009356

Ingram, B., & Southon, J. (1996). Reservoir ages in eastern Pacific coastal and estuarine waters. *Radiocarbon*, *38*(3), 573–582. https://doi.org/10.1017/S0033822200030101

Johnson, R. E. (1973). Antarctic intermediate water in the South Pacific Ocean. In R. Fraser (Ed.), *Oceanography of the South Pacific* (pp. 55–69). Wellington, New Zealand: New Zealand National Commission for UNESCO.

Judd, A. G. (2003). The global importance and context of methane escape from the seabed. *Geo-Marine Letters*, *23*(3–4), 147–154. https://doi.org/10.1007/s00367-003-0136-z

Kaiser, J., Schefuss, E., Lamy, F., Mohtadi, M., & Hebbeln, D. (2008). Glacial to Holocene changes in sea surface temperature and coastal vegetation in north central Chile: High versus low latitude forcing. *Quaternary Science Reviews*, *27*(2122), 2064–2075. https://doi.org/10.1016/j.quascirev.2008.08.025

Keeling, R. (2007). Deglaciation mysteries. *Science*, *316*(5830), 1440–1441. https://doi.org/10.1126/science.1142326

Keeling, R., & Stephens, B. (2001). Antarctic sea ice and the control of Pleistocene climate instability. *Paleoceanography*, *16*(1), 112–131.

Keigwin, L. D., & Lehman, S. J. (2015). Radiocarbon evidence for a possible abyssal front near 3.1 km in the glacial equatorial Pacific Ocean. *Earth and Planetary Science Letters*, *425*, 93–104. https://doi.org/10.1016/j.epsl.2015.05.025

Key, R.M., A. Olsen, S. van Heuven, S. K. Lauvset, A. Velo, X. Lin et al. (2015). Global Ocean Data Analysis Project, Version 2 (GLODAPv2). ORNL/CDIAC-162, NDP-093. Carbon Dioxide Information Analysis Center, Oak Ridge National Laboratory, US Dept. of Energy, Oak Ridge, Tennessee. https://doi.org/10.3334/CDIAC/OTG.NDP093_GLODAPv2.

Kohfeld, K. E., Le Quéré, C., Harrison, S. P., & Anderson, R. F. (2005). Role of marine biology in glacial-interglacial CO_2 cycles. *Science*, *308*(5718), 74–78. https://doi.org/10.1126/science.1105375

Kumamoto, Y., Murata, A., Watanabe, S., & Fukasawa, M. (2011). Temporal and spatial variations on bomb-produced radiocarbon along BEAGLE2003 lines—Revisits of WHP P06, A10, and I03/I04 in the Southern Hemisphere Oceans. *Progress in Oceanography*, *89*(1–4), 49–60. https://doi.org/10.1016/j.pocean.2010.12.007

Lamy, K., Kaiser, J., Ninnemann, U., Hebbeln, D., Arz, H. W., & Stoner, J. (2004). Antarctic timing of surface water changes off Chile and Patagonian ice sheet response. *Science*, *304*(5679), 1959–1962. https://doi.org/10.1126/science.1097863

Latorre, C., De Pol-Holz, R., Carter, C., & Santoro, C. (2017). Using archaeological shell middens as a proxy for past local coastal upwelling in northern Chile. *Quaternary International*, *427*(A), 128–136. https://doi.org/10.1016/j.quaint.2015.11.079

Lindsay, C. M., Lehman, S. J., Marchitto, T. M., Ortiz, J. D. (2015). The surface expression of radiocarbon anomalies near BajaCalifornia during deglaciation. *Earth and Planetary Science Letters*, *422*, 67–74. https://doi.org/10.1016/j.epsl.2015.04.012

Lukas, R. (1986). The termination of the equatorial undercurrent in the eastern Pacific. *Progress in Oceanography*, *16*(2), 63–90. https://doi.org/10.1016/0079-6611(86)90007-8

Lund, D., & Asimow, P. (2011). Does sea level influence mid-ocean ridge magmatism on Milankovitch timescales? *Geochemistry, Geophysics, Geosystems*, *12*, Q12009. https://doi.org/10.1029/2011GC003693

Marchant, M., Hebbeln, D., & Wefer, G. (1998). Seasonal flux patterns of planktic foraminifera in the Peru-Chile Current. *Deep Sea Research, Part I*, *45*(7), 1161–1185. https://doi.org/10.1016/S0967-0637(98)00009-0

Marchitto, T., Scott, J., Ortiz, J., Flückiger, J., & van Green, A. (2007). Marine radiocarbon evidence for the mechanism of deglacial atmospheric CO_2 rise. *Science*, *316*(5830), 1456–1459. https://doi.org/10.1126/science.1138679

Marcott, S. A., Bauska, T. K., Buizert, C., Steig, E. J., Rosen, J. L., Cuffey, K. M., et al. (2014). Centennial-scale changes in the global carbon cycle during the last deglaciation. *Nature*, *514*(7524), 616–619. https://doi.org/10.1038/nature13799

Martínez-Botí, M. A., Marino, G., Foster, G. L., Ziverti, P., Henehan, M. J., Rae, J. W. B., et al. (2015). Boron isotope evidence for oceanic carbon dioxide leakage during the last deglaciation. *Nature*, *518*(7538), 219–222. https://doi.org/10.1038/nature14155

McCartney, M. S. (1977). Subantarctic mode water. *Deep-Sea Research*, *24*, 103–119.

McCartney, M. S. (1982). The subtropical recirculation of mode waters. *Journal of Marine Research*, *40*(Supplement), 427–464.

Menviel, L., Spence, P., Yu, J., Chamberlain, M. A., Matear, R. J., Meissner, K. J., & England, M. H. (2018). Southern Hemisphere westerlies as a driver of the early deglacial atmospheric CO_2 rise. *Nature Communications*, *9*(1), 2503. https://doi.org/10.1038/s41467-018-04876-4

Merino-Campos, V., De Pol-Holz, R., Southon, J., Latorre, C., & Collado-Fabbri, S. (2019). Marine radiocarbon reservoir age along the Chilean continental margin. *Radiocarbon*, *61*(1), 1–16. https://doi.org/10.1017/RDC.2018.81

Mohtadi, M., Hebbeln, D., & Marchant, M. (2005). Upwelling and productivity along the Peru-Chile Current derived from faunal and isotopic compositions of planktic foraminifera in surface sediments. *Marine Geology*, *216*(3), 107–126. https://doi.org/10.1016/j.margeo.2005.01.008

Mohtadi, M., Rossel, P., Lange, C. B., Pantoja, S., Böning, P., Repeta, D. J., et al. (2008). Deglacial pattern of circulation and marine productivity in the upwelling region off central south Chile. *Earth and Planetary Science Letters*, *272*(1-2), 221–230. https://doi.org/10.1016/j.epsl.2008.04.043

Monnin, E., Indermühle, A., Dällenbach, A., Flückiger, J., Stauffer, B., Stocker, T., et al. (2001). Atmospheric CO_2 concentrations over the Last Glacial Maximum. *Science*, *291*(5501), 112–114. https://doi.org/10.1126/science.291.5501.112

Moreno, P. I., Lowell, T. V., Jacobson, G. L. Jr., & Denton, G. H. (1999). Abrupt vegetation and climate changes during the Last Glacial Maximum and last termination in the Chilean Lake District: A case study from Canal de la Puntilla (41°S). *Geografiska Annaler*, *81*(A), 285–311.

Mortyn, P. G., & Charles, C. D. (2003). Planktic foraminiferal depth habitat and $\delta^{18}O$ calibrations: Plankton tow results from the Atlantic sector of the Southern Ocean. *Paleoceanography*, *18*(2), 1037. https://doi.org/10.1029/2001PA000637

Ortiz, J. D., Mix, A. C., & Collier, R. W. (1995). Environmental control of living symbiotic and asymbiotic foraminifera of the California Current. *Paleoceanography*, *10*(6), 987–1009.

Ortiz, J. D., Mix, A. C., Rugh, W., Watkins, J. M., & Collier, R. W. (1996). Deep-dwelling planktonic foraminifera of the northeastern Pacific Ocean reveal environmental control of oxygen and carbon isotopic disequilibria. *Geochimica et Cosmochimica Acta*, *60*(22), 4509–4523. https://doi.org/10.1016/S0016-7037(96)00256-6

Ortlieb, L., Vargas, G., & Saliège, J. F. (2011). Marine radiocarbon reservoir effect along the northern Chile–southern Peru coast (14–24°S) throughout the Holocene. *Quaternary Research*, *75*(1), 91–103. https://doi.org/10.1016/j.yqres.2010.07.018

Otto-Bliesner, B. L., Hewitt, C. D., Marchitto, T. M., Brady, E., Abe-Ouchi, A., Crucifix, M., et al. (2007). Last Glacial Maximum ocean thermohaline circulation: PMIP2 model intercomparisons and data constraints. *Geophysical Research Letters*, *34*, LI2706. https://doi.org/10.1029/2007GL029475

Patrick, A., & Thunell, R. C. (1997). Tropical Pacific sea surface temperatures and upper water column thermal structure during the Last Glacial Maximum. *Paleoceanography*, *12*(5), 649–657.

Pichevin, L. E., Reynolds, B. C., Ganeshram, R. S., Cacho, I., Pena, L., Keefe, K., & Ellam, R. M. (2009). Enhanced carbon pump inferred from relaxation of nutrient limitation in the glacial ocean. *Nature*, *459*(7250), 1114–1117. https://doi.org/10.1038/nature08101

Piola, A. R., & Gordon, A. L. (1989). Intermediate water in the southwestern South Atlantic. *Deep-Sea Research*, *36*(1), 1–16. https://doi.org/10.1016/0198-0149(89)90015-0

Primeau, F. W., Holzer, M., & DeVries, T. (2013). Southern Ocean nutrient trapping and the efficiency of the biological pump. *Journal of Geophysical Research: Oceans*, *118*, 2547–2564. https://doi.org/10.1002/jgrc.20181

Rae, J. W. B., Sarnthein, M., Foster, G. L., Ridgwell, A., Grootes, P. M., & Elliott, T. (2014). Deep water formation in the North Pacific and deglacial CO_2 rise. *Paleoceanography*, *29*, 645–667. https://doi.org/10.1002/2013PA002570

Reid, J. L. (1965). Intermediate waters of the Pacific Ocean. In *The Johns Hopkins Oceanographic Studies, No. 2*. Baltimore, United States of America: The Johns Hopkins Press. 85 p. https://doi.org/10.4319/lo.1966.11.2.0313

Reimer, P. J., Bard, E., Bayliss, A., Beck, J. W., Blackwell, P. G., Ramsey, C. B., et al. (2013). INTCAL13 and MARINE13 radiocarbon age calibration curves 0–50,000 years cal BP. *Radiocarbon*, *55*(4), 1869–1887. https://doi.org/10.2458/azu_js_rc.55.16947

Ronge, T., Tiedemann, R., Lamy, F., Köhler, P., Allway, B. V., Pol-Holz, D., et al. (2016). Radiocarbon constraints on the extent ad evolution of the South Pacific glacial carbon pool. *Nature Communications*, *7*(1), 11487. https://doi.org/10.1038/ncomms11487

Ronge, T. A., Steph, S., Tiedemann, R., Prange, M., Merkel, U., Nürnberg, D., & Kuhn, G. (2015). Pushing the boundaries: Glacial/interglacial variability of intermediate and deep waters in the southwest Pacific over the last 350,000 years. *Paleoceanography*, *30*, 23–38. https://doi.org/10.1002/2014PA002727

Rose, K., Sikes, E., Guilderson, T., Shane, P., Hill, T., Zahn, R., & Spero, H. (2010). Upper-ocean-to-atmosphere radiocarbon offsets imply fast deglacial carbon dioxide release. *Nature*, *466*(7310), 1093–1097. https://doi.org/10.1038/nature09288

Sautter, L. R., & Thunell, R. C. (1991). Planktonic foraminiferal response to upwelling and seasonal hydrographic conditions: Sediment trap results from San Pedro Basin, Southern California Bight. *Journal of Foraminiferal Research*, *21*(4), 347–363. https://doi.org/10.2113/gsjfr.21.4.347

Schlitzer, R. (2018). Ocean Data View software. http://odv.awi.de/.

Siani, G., Michel, E., De Pol-Holz, R., DeVries, T., Lamy, F., Carel, M., et al. (2013). A. Carbon isotope records reveal precise timing of enhanced Southern Ocean upwelling during the last deglaciation. *Nature Communications*, *4*(1), 2758. https://doi.org/10.1038/ncomms3758

Sigman, D. M., & Boyle, E. A. (2000). Glacial/interglacial variations in atmospheric carbon dioxide. *Nature*, *407*(6806), 859–869. https://doi.org/10.1038/35038000

Sikes, E., & Guilderson, T. (2016). Southwest Pacific Ocean surface reservoir ages since the last glaciation: Circulation insights from multiple-core studies. *Paleoceanography and Paleoclimatology*, *3*, 298–310. https://doi.org/10.1002/2015PA002855

Sikes, E. L., Allen, K. A., & Lund, D. (2017). Enhanced $\delta^{13}C$ and $\delta^{18}O$ differences between the South Atlantic and South Pacific during the last glaciation: The deep gateway hypothesis. *Paleoceanography*, *32*, 1000–1017. https://doi.org/10.1002/2017PA003118

Sikes, E. L., Cook, M. S., & Guilderson, T. P. (2016). Reduced deep ocean ventilation in the southern Pacific Ocean during the Last Glaciation persisted into the deglaciation. *Earth and Planetary Science Letters*, *438*, 130–138.

Sikes, E. L., Samson, C. R., Guilderson, T. P., & Howard, W. R. (2000). Old radiocarbon ages in the southwest Pacific Ocean during the last glacial period and deglaciation. *Nature*, *405*(6786), 555–559. https://doi.org/10.1038/35014581

Silva, N., & Fonseca, T. R. (1983). Geostrophic component of the oceanic flow off northern Chile. In P. Arana (Ed.), *Recursos Marinos del Pacifico, Escuela de Ciencias del Mar*, (pp. 59–70). Valparaíso, Chile, Universidad Católica de Valparaíso.

Silva, N., & Neshyba, S. (1977). Corrientes superficiales frente a la costa austral de Chile. *Ciencia y Tecnologia del Mar*, *3*, 37–42.

Silva, N., & Neshyba, S. (1980). Masas de agua y circulación geostrófica frente a la costa de Chile Austral. *Serie Cientifica, Instituto Antártico Chileno*, *25*(26), 5–32.

Silva, N., Rojas, N., & Fedele, A. (2009). Water masses in the Humboldt Current System: Properties, distribution and the nitrate deficit as a chemical water mass tracer for Equatorial Subsurface Water off Chile. *Deep Sea Research, Part II*, *56*(16), 1004–1020. https://doi.org/10.1016/j.dsr2.2008.12.013

Skinner, L., Fallon, S., Waelbroeck, C., Michel, E., & Barker, S. (2010). Ventilation of the deep Southern Ocean and deglacial CO_2 rise. *Science*, *328*(5982), 1147–1151. https://doi.org/10.1126/science.1183627

Skinner, L., McCave, I. N., Carter, L., Fallon, S., Scrivner, A. E., & Primeau, F. (2015). Reduced ventilation and enhanced magnitude of the deep Pacific carbon pool during the last glacial period. *Earth and Planetary Science Letters*, *411*, 45–52. https://doi.org/10.1016/j.epsl.2014.11.024

Sloyan, B. M., Talley, L. D., Chereskin, K., Fine, R., & Holte, J. (2010). Antarctic intermediate water and subantarctic mode water formation in the Southeast Pacific: The role of turbulent mixing. *Journal of Physical Oceanography*, *40*, 1558–1574. https://doi.org/10.1175/2010JPO4114.1

Spero, H. J., & Lea, D. W. (2002). The cause of carbon isotope minimum events on Glacial Terminations. *Science*, *296*(5567), 522–525. https://doi.org/10.1126/science.1069401

Stephens, B. S., & Keeling, R. F. (2000). The influence of Antarctic sea ice in glacial-interglacial CO_2 variations. *Nature*, *404*(6774), 171–174. https://doi.org/10.1038/35004556

Stott, L., Southon, J., Timmermann, A., & Koutavas, A. (2009). Radiocarbon age anomaly at intermediate water depth in the Pacific Ocean during the last deglaciation. *Paleoceanography*, *24*, PA2223. https://doi.org/10.1029/2008PA001690

Stott, L. D., & Timmermann, A. (2011). Hypothesized link between glacial/interglacial atmospheric CO_2 cycles and storage/release of CO_2-rich fluids from deep-sea sediments. In R. Harunur, L. Polyak, & E. Mosley-Thompson (Eds.), *Abrupt climate change: Mechanisms, patterns, and impacts geophysical monograph series*, (Vol. 193, pp. 123–138). United States of America: American Geophysical Union. https://doi.org/10.1029/2010GM001052

Strub, P., Mesias, J., Montecino, V., Rutllant, J., & Salinas, S. (1998). Coastal ocean circulation off western South America Coastal Segment (6,E). In A. Robinson, & K. Brink (Eds.), *The Sea, The Global Coastal Ocean*, (Vol. 11, pp. 272–313). New York: Wiley.

Stuiver, M., & Polach, H. (1977). Reporting of ^{14}C data. *Radiocarbon*, *19*(3), 355–363. https://doi.org/10.1017/S0033822200003672

Sweeney, C., Gloor, E., Jacobson, A. R., Key, R. M., McKinley, G., Sarmiento, J. L., & Wanninkhof, R. (2007). Constraining global air-sea gas exchange for CO_2 with recent bomb ^{14}C measurements. *Global Geochemical Cycles*, *21*, GB2015. https://doi.org/10.1029/2006GB002784

Talley, L. D. (1996). Antarctic Intermediate Water in the South Atlantic. In G. Wefer, W. H. Berger, G. Siedler, & D. J. Webb (Eds.), *The South Atlantic: Present and past circulation*, (pp. 219–238). New York, United States of America: Springer. https://doi.org/10.1007/978-3-642-80353-6_11

Talley, L. D. (1999). Some aspects of ocean heat transport by the shallow, intermediate and deep overturning circulations. In P. U. Clark, R. S. Webb, & L. D. Keigwin (Eds.), *Mechanisms of Global Climate Change at Millennial Time Scales*, *Geophysical Monograph Series* (Vol. 112, pp. 1–22). United States of America: American Geophysical Union. https://doi.org/10.1029/GM112p0001

Talley, L. D. (2013). Closure of the global overturning circulation through the Indian, Pacific, and Southern Oceans: Schematics and transports. *Oceanography*, *26*(1), 80–97. https://doi.org/10.5670/oceanog.2013.07

Taylor, R., & Berger, R. (1967). Radiocarbon content of marine shells from the Pacific coast of central and South America. *Science*, *158*(3805), 1180–1182. https://doi.org/10.1126/science.158.3805.1180-a

Toggweiler, J. R. (1999). Variation of atmospheric CO_2 by ventilation of the ocean's deepest water. *Paleoceanography*, *14*(5), 571–588.

Toggweiler, J. R., Dixon, K., & Broecker, W. S. (1991). The Peru upwelling and the ventilation of the South Pacific thermocline. *Journal of Geophysical Research*, *96*(C11), 20467–20497. https://doi.org/10.1029/91JC02063

Toggweiler, J. R., Russell, J. L., & Carson, S. R. (2006). Midlatitude westerlies, atmospheric CO_2, and climate change during the ice ages. *Paleoceanography*, *21*, PA2005. https://doi.org/10.1029/2005PA001154

Tolstoy, M. (2015). Mid-ocean ridge eruptions as a climate valve. *Geophysical Research Letters*, *42*, 1346–1351. https://doi.org/10.1002/2014GL063015

Tomczak, M., & Godfrey, J. (2003). *Regional oceanography: An introduction*. Delhi: Daya Publishing House. https://doi.org/10.1002/joc.3370150511

Tsuchiya, M., & Talley, L. (1996). Water-property distribution along an eastern Pacific hydrographic section at 135°W. *Journal of Marine Research*, *54*(3), 541–564. https://doi.org/10.1357/0022240963213583

Tsuchiya, M., & Talley, L. (1998). A Pacific hydrographic section at 881W: Water-property distribution. *Journal of Geophysical Research*, *103*(C6), 12899–12918. https://doi.org/10.1029/97JC03415

Umling, N. E., & Thunell, R. C. (2017). Synchronous deglacial thermocline and deep water ventilation in the eastern equatorial Pacific. *Nature Communications*, *8*(1), 1–10. https://doi.org/10.1038/ncomms14203

Watson, A. J., & Naveira Garabato, A. C. (2006). The role of Southern Ocean mixing and upwelling in glacial-interglacial atmospheric CO_2 change. *Tellus Series B: Chemical and Physical Meteorology*, *58*(1), 73–87. https://doi.org/10.1111/j.1600-0889.2005.00167.x

Wiedicke-Hombach M., Andruleit H., Balmaceda G., Bruns A., Contardo X., Cramer B. et al. (2002). SO161 – 5 SPOC (Subduction Processes off Chile) Geologie – Geochemie – Wärmestrom, BGR.

Wooster, W. S., & Gilmartin, M. (1961). The Perú-Chile undercurrent. *Journal of Marine Research*, *19*(3), 97–122.

Wyrtki, K. (1967). Circulation and water masses in the eastern equatorial Pacific Ocean. *International Journal of Oceanography and Limnology*, *1*(2), 117–147.

Zhao, N., & Keigwin, L. D. (2018). An atmospheric chronology for the glacial-deglacial Eastern Equatorial Pacific. *Nature Communications*, *9*(1), 3077. https://doi.org/10.1038/s41467-018-05574-x

2.2 Supplementary material

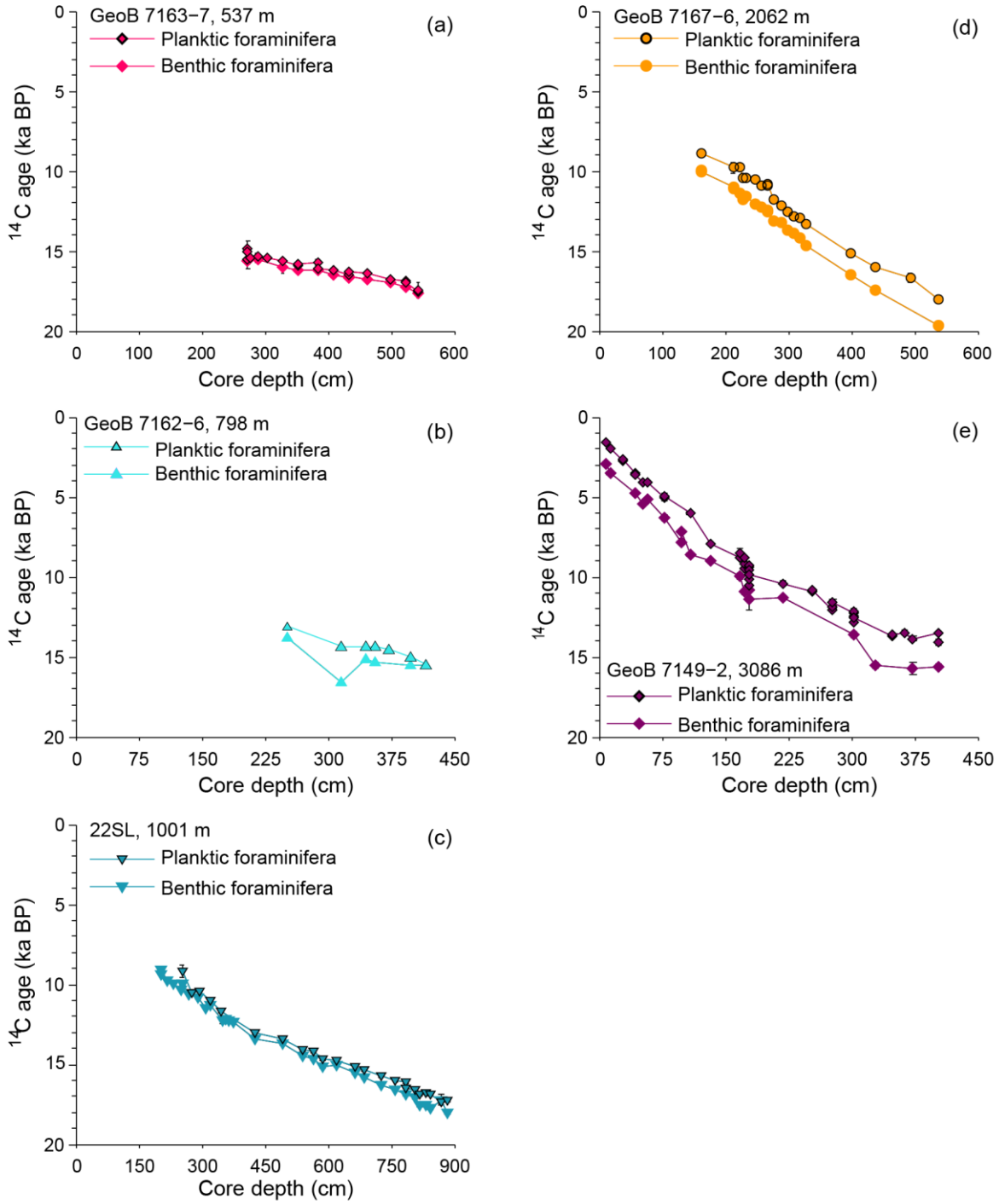

Figure S1 Planktonic and benthonic foramifera uncalibrated ^{14}C ages against core depth. Detailed information in Table S1.

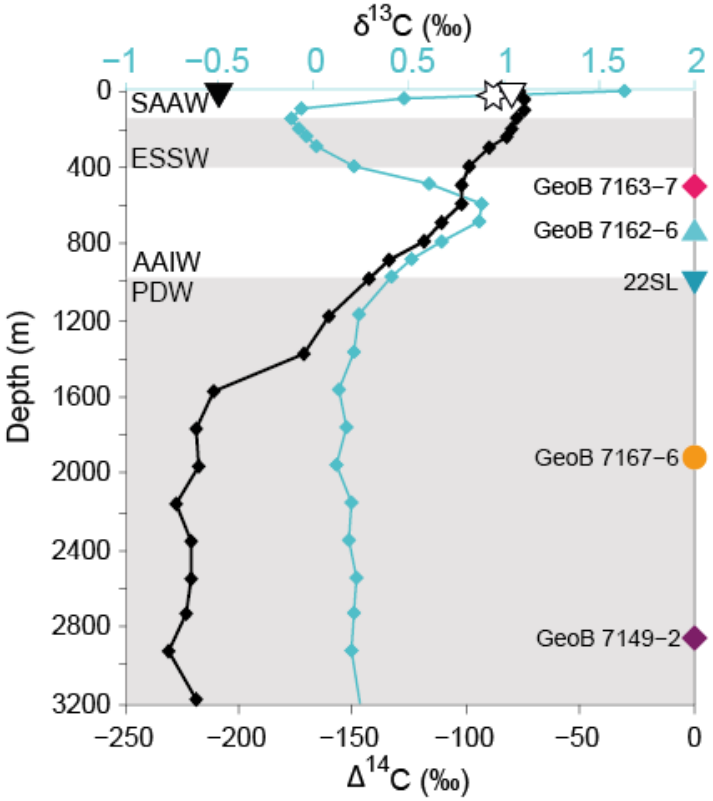

Figure S2 Modern $\delta^{13}C$ (turquoise) and $\Delta^{14}C$ (black) water column data from station P06-E11 (32° 29.64' S, 72° 42.66' W; Kumamoto et al., 2011). For depths shallower than ~1500 m, the ^{14}C coresponds to a natural $\Delta^{14}C$ estimate, based on silicate concentrations, alkalinity and apparent oxygen utilization, deeper than ~1500 m values are the direct mesures Also indicated in the figure are the mean modern $\delta^{13}C$ measured in *G. bulloides* and *N. pachyderma* (dex) in the South East Pacific between ~24–46° S (Mohtadi et al., 2005) and the depth of the studied cores. Black triangle: *G. bulloides* north of ~35° S, white triangle: *G. bulloides* south of ~39° S; white star: *N. pachyderma* (dex) between ~24–35° S and 39–46° S. SAAW: Subantarctic Water; ESSW: Equatorial Subsurface Water; AAIW: Antarctic Intermediate Water; PDW: Pacific Deep Water.

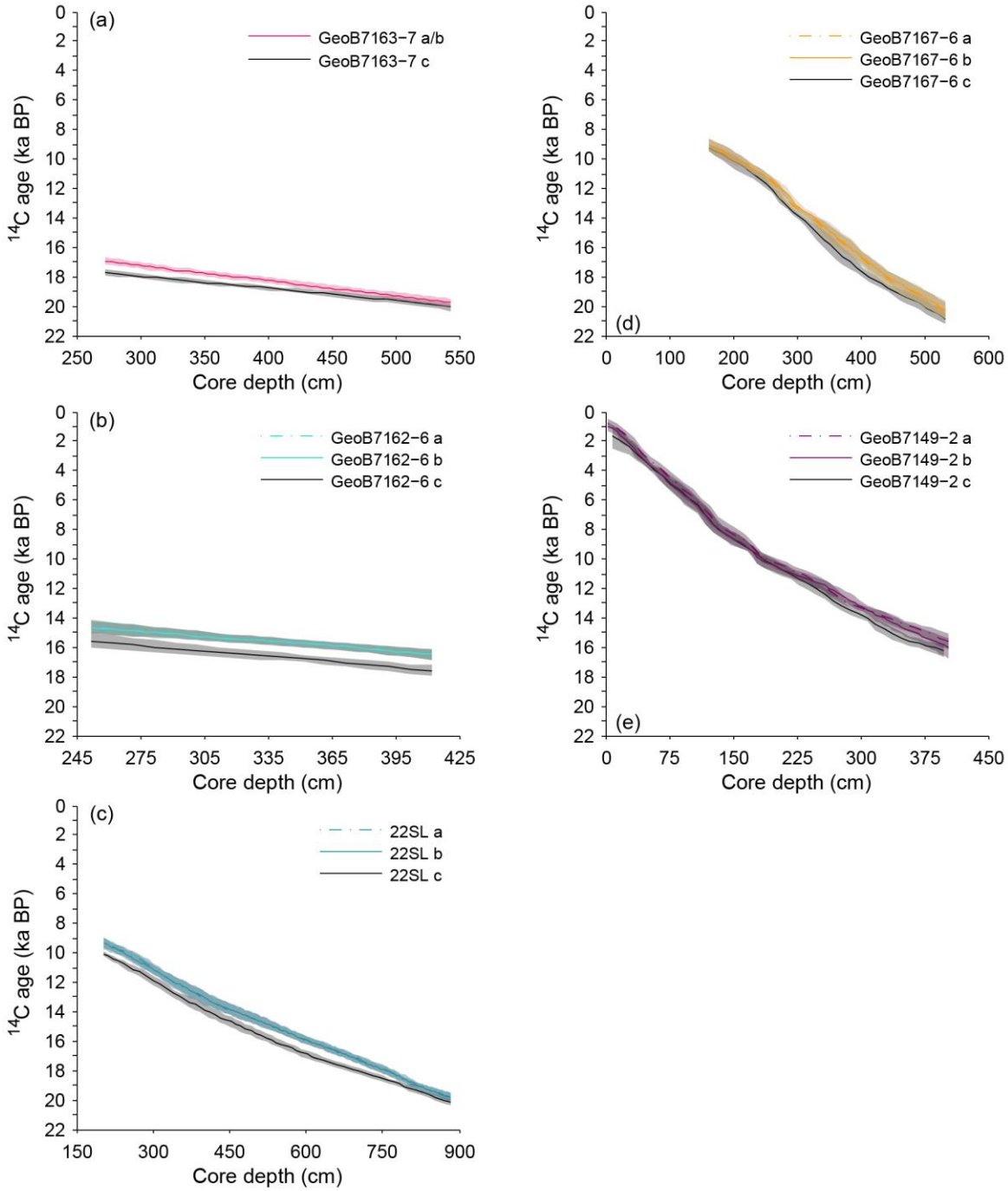

Figure S3. Resulting age models for the cores in this study, obtained using the Bacon algorithm (Blaauw & Christen, 2011) by assigning different ^{14}C Surface Reservoir ages (R_S) to the planktonic foraminifera ^{14}C ages, as described in the Age Model section of the main text: a) surface water from SAAW was advected north of 46° S reaching as far north as 31° S throughout all the considered period, and thus the R_S from core MD07-3088 are applied to all studied cores; b) between ~13 and ~11 ^{14}C ka BP the upwelling of 14C–depleted ESSW increases the R_S at ~36° S (22SL, GeoB 7167–6, GeoB 7162–6) and thus equatorial R_S from core TR163-23 are assigned for this interval to cores at ~36° S; c) no changes occur in R_S and thus constant values, equivalent to the modern mean in the closest latitude with available information (Merino–Campos et al., 2019) are assigned; d) at ~31° S (Geob 7149-2) exclusively equatorial waters flow in the whole interval, and thus for ages older than ~11 ka ^{14}C BP, RS from core TR163–23 (~0° N) are assigned and for ages younger, R_S ages from ~32° S are assigned (Carré et al., 2015). The colored line corresponds to the wmean and its corresponding 1σ envelope is plotted, derived from the Bacon.

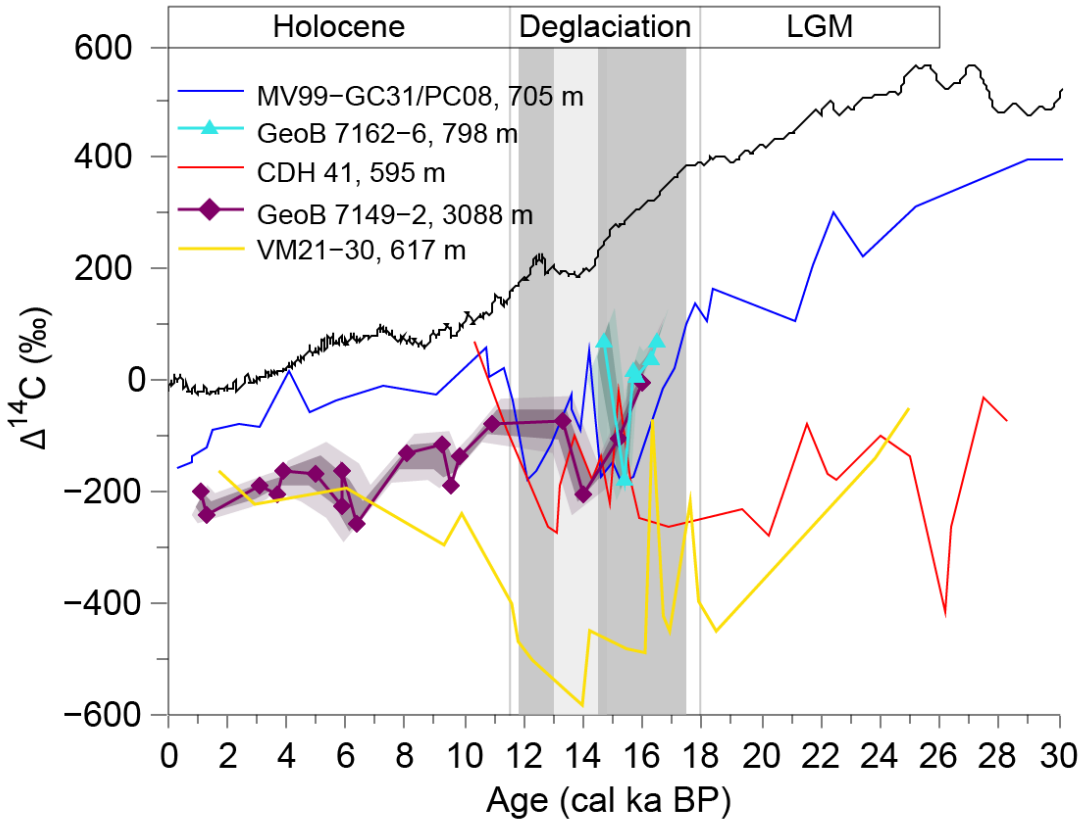

Figure S4 Comparison of $\Delta^{14}C$ in intermediate and deep water from the South East Pacific (this study) with core MV99-MC19/GC31/PC08 in Baja California (23.5° N, 111.6° W, 705 m; Marchitto et al., 2007) and cores Equatorial East Pacific: CDH 41 (1°15.94' S, 89° 41.88' W, 595 m; Bova et al., 2018) and VM21-30 (1°13'S, 89°41'W, Stott et al., 2009). Also plotted is the atmospheric $\Delta^{14}C$ (Reimer et al., 2013).

Table S1 Planktonic and benthonic radiocarbon dates for all cores, calendar and $\Delta^{14}C$ obtained according to the text.

Table S2 $\delta^{13}C$ measurements presented in Figure S2. Ages marked with an * correspond to the original ^{14}C ages, whereas the rest are the extrapolated ages.

Table S3 Cores location

Core	Latitude	Longitude	Depth (m)
GeoB 7149-2	31°29.14'S	72°00.00'W	3086
GeoB 7163-7	36°25.54'S	73°35.73'W	537
GeoB 7167-6	36°27.19'S	73°55.50'W	2062
GeoB 7162-6	36°32.52'S	73°40.02'W	798
22SL	36°13.26'S	73°40.50'W	1001

Table S4 Reservoir ages used in different age models described in the text.

Age model	**>13 ka 14C**	**13-11 ka 14C**	**<11 ka 14C**
a	Rs from MD07-3088	Rs from MD07-3088	Rs from MD07-3088
b	Rs from MD07-3088	Rs from TR163-23	Rs from MD07-3088
c	Rs modern	Rs modern	Rs modern
d (core GeoB 7149-2)	Rs from TR163-23	Rs from TR163-23	Rs from ~32° S
Age model	**>13 ka 14C**	**13-11 ka 14C**	**<11 ka 14C**
a	Rs from MD07-3088	Rs from MD07-3088	Rs from MD07-3088
b	Rs from MD07-3088	Rs from TR163-23	Rs from MD07-3088
c	Rs modern	Rs modern	Rs modern
d (core GeoB 7149-2)	Rs from TR163-23	Rs from TR163-23	Rs from ~32° S

2.2.1 References

Martínez Fontaine, C., De Pol-Holz, R., Michel, E., Siani, G., Reyes-Macaya, D., Martínez-Méndez, G., DeVries, T., Stott, L., Southon, J., Mohtadi, M., Hebbeln, D., 2019. Ventilation of the Deep Ocean Carbon Reservoir During the Last Deglaciation: Results From the Southeast Pacific. Paleoceanogr. Paleoclimatology 34, 2080–2097. https://doi.org/10.1029/2019PA003613

Chapter 3: Tephrochronology dataset of the Southern (33–46° S) and Austral (49–55° S) Volcanic Zones of the Andes and exploration tools

As mentioned before, one important conclusion of the work developed in chapter 2 is that in order to better constrain the chronologies of marine sediment cores in the Southeast Pacific, it is important to estimate Rs variations in the past. The aim of my PhD was to follow up the reconstruction of the circulation changes in the Southeast Pacific Ocean during the last ~20,000 years, extending the study area with southern cores. And thus, in order to obtain more robust chronologies for the cores I was going to study, it was necessary to estimate Rs variation at the latitudes were these cores were retrieved (~41° S and ~49° S). One approach to do this is tephrochronology, a tool that had already been used by Siani et al. (2013) to estimate Rs variations at 46° S in the Chilean continental Margin. Because of the presence of active volcanic centers belonging to the Southern and Austral Volcanic Zones of the Andes, adjacent to the study area, tephrochronology has great potential for ameliorating chronologies for marine sediment cores retrieved in the Chilean continental margin.

The first work I developed was gathering information about previous tephrochronology and volcanology work in the region. In particular which volcanoes had had eruptions during the last 20,000 years, how many eruptions had them had, if these eruptions were dated or not, analyzed by geochemistry or not, etc. All of this with the aim of identifying the volcanoes and particular eruptions responsible for the volcanic ashes identified in the southern marine sediment cores (MD07-3100, MD07-3098 and MD07-3081). In developing this task, I encountered various obstacles such as different names given to the same eruptive event, data not being standardized, not being able to access raw data, missing information, for example the position of the samples, etc. With the help of Chiara Marmo, ingénieure de recherche at GEOPS laboratory, I compiled a set of tephrochronological and volcanological data to make them FAIR (Findable, Accesible, Interoperable, Reusable; Wilkinson et al., 2016).

Chapter 3 corresponds to the description of the dataset I compiled in order to be able to identify the source of the volcanic remains found in the marine sediment cores. But not only that. The problem of the FAIRness of the tephrochronological data in the Southern and Austral Zones of the Andes grows as new and more information is produced and every researcher using tephrochronological data in the region encounters similar problems to integrate the bulk of available information. With this in mind, I developed a work which tries to help moved forward in this regard. In order to do this, collaborating with Chiara Marmo and Vanessa Araya, former post doc and current professor at INRIA (Institut national de recherche en sciences et technologies du numérique), we began developing a web application with the aim of creating visualizations that will help future users of the dataset make sense of it, help the discovery

of information, and which will assist in custom downloading data in the dataset. This work is in progress and it is possible to access the explorer at: http://varaya.cl:3001/. This work was done in collaboration with the Chilean Geology and Mining agency: SERNAGEOMIN through the National Volcanic Vigilance Network department and with the kind collaboration and support of the tephrochronology community working in that area. The idea is that in the future the dataset and explorer are managed by SERNAGEOMIN, and that new information can be added to it, moving forward to making this data more FAIR.

Tephrochronology dataset of the Southern (33–46° S) and Austral (49–55° S) Volcanic Zones of the Andes and exploration tools

Consuelo Martínez Fontaine[a, b*], Vanessa Araya[b], Chiara Marmo[c], Guillaume Delpech[a], Karen Fontijn[d], Giuseppe Siani[a]

[a]Géoscience Paris Saclay (GEOPS) Université Paris-Saclay, CNRS UMR 8148, 91405 Orsay, France

[b]Laboratoire des Sciences du Climat et de l'Environnement (LSCE), Laboratoire mixte CNRS-CEA, Avenue de la Terrasse, 91198 Gif-sur-Yvette Cedex, France

[c]

[d]Department of Geosciences Environment and Society, Université Libre de Bruxelles

*Corresponding author: Consuelo Martínez Fontaine, Geoscience Paris Sud (GEOPS) Université Paris-Saclay, CNRS UMR 8148, 91405 Orsay, France; E-mail: consuelo.martinez-fontaine@universite-paris-saclay.fr

3.1 Introduction

Tephrochronology is the discipline of geosciences which uses the deposits of explosive volcanic eruptions as stratigraphic and chronological markers. By identifying the pyroclastic remains of specific eruptions (tephras) in different sites, tephrochronology helps reconstruct the eruptive history of volcanic centers: the magnitude of their eruptions, their recurrence in time and the dispersion of its products. At the same time, tephras can be viewed as regional stratigraphic tie points. If a specific tephra is identified in different paleoenvironmental archives (e.g. paleoclimatological, paleoceanographic, archaeological), their chronologies can be synchronized, which is essential when interpreting the evolution of complex systems in time, such as the climate.

The Southern (SVZ, 33–46° S) and Austral (AVZ, 49–55° S) volcanic Zones of the Andes are two very active volcanic zones, where so far ~65 volcanic centers have been identified which have had recurrent explosive activity in historical times (e.g. Llaima, Villarrica, Puyehue-Cordón Caulle, Calbuco, Hudson and Lautaro volcanic centers) or during the last ~20,000 years (e.g. Mocho-Choshuenco, Michinmahuida and Mount Burney volcanic centers). In these regions, tephrochronology has a great potential of use, for example by helping reconstruct the eruptive history of these volcanic centers, essential in the production of volcanic hazard maps. This task is currently undertaken by the Chilean Geology and Mining agency: SERNAGEOMIN through the National Volcanic Vigilance Network department, who rely on their own surveys as well as scientific publications in tephrochronology and volcanology to produce them (e.g. Bertin et al., 2018). On the other hand, tephrochronology has the potential of ameliorating chronologies of paleoenvironmental archives in Patagonia, essential for reconstructing the climatic evolution of this zone which plays an important role in the regulation of the climate system at a global scale. For example, lacustrine and marine sediment cores can give us information on changes in the positon and intensity of the Southerly Westerly Winds (e.g. Menviel et al., 2018; Toggweiler, Russell, & Carson, 2006) and upwelling in the Southern Ocean (Anderson et al., 2009; Siani et al., 2013), thought to be important factors controlling glacial–interglacial transitions.

In the last four decades, tephrochronology together with volcanology have importantly increased our understanding of the eruptive history of the SVZ and AVZ, revealing higher recurrence and explosivity of many volcanic centers than previously thought (e.g. Chaitén and Michinmahuida volcanoes (Amigo et al., 2013; Watt et al., 2013b; Moreno et al., 2015; Alloway et al., 2017, Martínez Fontaine et al., 2021)). It has also become apparent that there are still many under researched active volcanic centers in the area, such as Yanteles and Corcovado (López-Escobar et al., 1993; Naranjo and Stern, 2004) for which no eruptions have been robustly identified jet. In parallel, this work has begun to unveil a very intricate tephrochronological record in the area, given by the close proximity of the volcanic centers together with the high recurrence of explosive volcanic activity (e.g. Alloway, Pearce, et al., 2017; Fontijn et al., 2016; Watt et al., 2011; Weller, De Porras, Maldonado, Méndez, & Stern, 2017). Disentangling this intricate

record is hampered by the very similar geochemical composition of the products of many volcanic centers, which makes it difficult to identify their source; additionally, the high uncertainties associated with the age estimates of the tephra deposits further hinders their correlation.

At present, the available tephrochronological and volcanological information for the SVZ and AVZ can be found dispersed in journals, government (SERNAGEOMIN) publications and personal collections, which vary greatly in formats. This, together with the increased data stream associated with the development of analytical techniques (such as Electron Microprobe analysis (EMP)), makes the integration of the data produced by different actors (researchers and the government), and consecutively its interpretation, increasingly harder. A great amount of time is invested by every researcher and government employee to find, standardize and integrate this information before even interpreting it. This increasing need for organization of the tephrochronological and volcanological data in the region, is an issue that has already been addressed in previous publications (Alloway et al., 2017a, 2017b; Fontijn et al., 2016, 2014). Here we address it by compiling a dataset integrating tephrochronology and volcanology information on 32 volcanic centers and 132 eruptions in the SVZ and AVZ; and developing an online platform which provides tools for the exploration of the dataset and custom downloading the data. The latter aims to be a step towards making this data FAIR (Findable, Accessible, Interoperable and Reusable; Wilkinson, Dumontier, & Aalbersberg, 2016) by providing a standardized data structure from which to build upon.

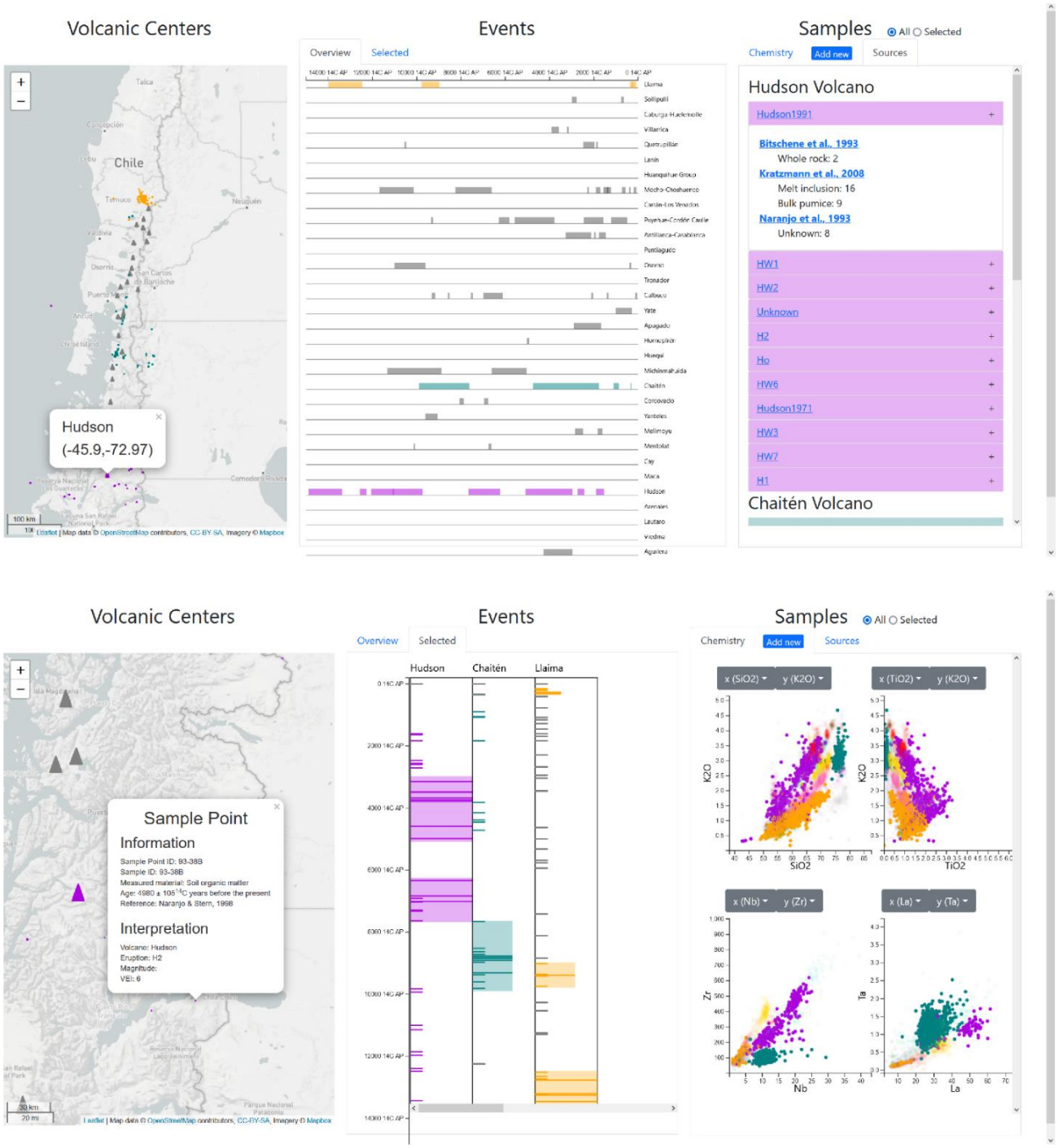

Figure 3.1 Screenshots of the exploration tool (for the moment you can access it at http://varaya.cl:3001/), showing different visualizations of the data in the database. In the screenshots, volcanoes Hudson, Llaima and Chaitén have been selected.

3.2 Methods

3.2.1 Interviews

Because this tool aims to aid the wide and heterogeneous community using tephrochronology in the SVZ and AVZ, a series of interviews were conducted in order to characterize their work. However small, the interviewed sample represents to some extent the diversity in the tephrochronological community in the area. Three researchers on volcanology and paleoceanography and a team of 16 people from the National Volcanic Vigilance Network where interviewed between June and August of 2020. Each interview lasted between one and three hours and had as objective understanding their everyday tasks when using tephrochronological data in their work. In particular to understand: what questions they try to answer using tephrochronology; what data they use for accomplishing this task; where do they obtain the data from; how they organize and visualize it; and the problems they encounter when developing these tasks. A summary of the answers can be viewed in Table S3.1. This information aided the development of the dataset structure and the explorer.

3.2.2 Data collection

Tephrochronological and volcanological information on 32 active volcanic centers from the SVZ and AVZ, between Llaima (~38.7° S) and Mount Burney (~52.3° S) was collected from seventy-three scientific publications published in peer reviewed journals, six publications from SERNAGEOMIN, and two doctoral theses. These correspond to ~130 different eruptive events and ~16,500 sample analyses. Here, active volcanic centers are considered as those for which evidence of volcanic activity occurring during the last ~20,000 years has been identified. This time frame is considered taking into account that, for the volcanic centers here considered, tephrochronological evidence older than ~20,000 years has been largely eroded by the presence of the Patagonian Ice Sheet, which covered most of the Andes south of ~38° S during the last glacial period (~20,000 –60,000 years before present; (Davies et al., 2020). The data was obtained either directly from the publication tables, text and supplementary material, or alternatively through private requests to the authors when the data discussed in the publication was not readily available. The authors were informed of the purpose of the data request beforehand.

3.2.3 Major element standardization

The major element composition of volcanic products (e.g. lava, glass shards, bulk tephra) is often utilized in tephrochronology to discriminate between the potential sources of the studied pyroclastic deposits. Major elements correspond to the geochemical elements found more abundantly in rocks, which compositions are expressed in weight percentage (wt%) of oxides: SiO_2, TiO_2, Al_2O_3, FeO, Fe_2O_3, MnO, MgO, CaO, Na_2O, K_2O, P_2O_5. Ideally, the sum of the analyzed major elements composition would approach 100% and the difference would account for volatile content in the sample, for example H_2O, CO_2, SO_2, which can derive from different degrees of post depositional hydration. Additionally, Cl (also a volatile) is sometimes analyzed and usually considered with major/minor elements. In order to being able to

compare the major element composition of different volcanic deposits, the analyzed compositions are generally normalized to a 100% volatile–free basis.

In this context, special attention must be taken regarding how Iron (Fe) is presented in the original publications in order to normalize the samples by a comparable amount. Fe can exist in volcanic rocks in two states of oxidation (Fe^{2+} forming FeO and Fe^{3+} forming Fe_2O_3), which exist in different proportions in different types of rocks. Most analytical techniques employed to analyze volcanic rocks are not able to distinguish between these two states of Fe, and thus Fe is presented in most publications as a *total* Fe value, although this is not always communicated. For example, when volcanic glass shards are analyzed by EMP, Fe might be presented as FeO, FeOT or FeO*, all of which correspond to total Fe as FeO. In contrast, when bulk tephra are analyzed by X-ray fluorescence (XRF) or Inductively Coupled Plasma – Optical Emission Spectrometry (ICP-OES), it might be presented as Fe_2O_3 or Fe_2O_3T, which correspond to total Fe as Fe_2O_3. Additionally, other techniques as Atomic Absorption Spectroscopy and wet chemical analysis (titration) can discriminate between Fe^{2+} and $Fe^{3+,}$ however they are not commonly used. In this case, publications calculate the total Fe as FeOT = FeO + 0.899*Fe_2O_3, as Fe_2O_3T = 1.1*FeO + Fe_2O_3 or even as FeO + Fe_2O_3. At present, most of the major element analyses are done with EMP which can analyze smaller size materials than previous methods. For example, 30 individual glass shards can be analyzed from one sample for which only one bulk observation would be obtained if analyzing by XRF. The latter clearly reflects in the dataset, where analyses obtained with EMP correspond to ~90% of the major element observations. Because of the latter, the normalization in the dataset and in the exploration tool is done taking into account Fe as FeOT for calculating the volatile–free analytical total (i.e. the sum of major elements before normalizing). When FeOT is not directly presented in the original publication, it is calculated either as: FeO + 0.899Fe_2O_3, when both FeO and Fe_2O_3 have been analyzed (~3% of major element observations); or as 0.899Fe_2O_3T, when Fe has been analyzed as Fe_2O_3T (~5% of major element observations). In order to save the original data and its heterogeneity, Fe is described in the dataset by four attributes: FeO, Fe_2O_3, FeOT and Fe_2O_3T, and only the original data is filled. Both the original and normalized data can be downloaded.

3.3.4 Data Visualization: Development of the Exploration Tool

Given the requirements extracted from the interviews with the domain experts, we decided to build a light visualization tool, which can be easily installed in a local environment. This will allow researchers to have more control of it and even make modifications of it if needed.

The tool was developed in Javascript, using node.js[2] as the back-end environment. For the visualization components, we used the Leaflet library[3] for the map, D3.js[4] for the timelines, and dc.js[5] with Crossfilter[6] for chemical scatterplots. The database is originally delivered as an CSV file, but in order to allow fast queries in the visualization, we exported it to a SQLite[7] database that is accessed from node.js. This transformation also includes precomputed queries that help with the performance of the tool.

3.3 Data records

Broadly, tephrochronology identifies deposits of explosive eruptions in the stratigraphic record, samples and characterizes them physically and chemically, and based on this characterization and the comparison with available volcanological and tephrochronological information, it proposes a volcanic source and ideally a particular eruptive event for the identified deposit. The dataset follows this structure, it corresponds to a collection of observations and/or analyses of tephrochronological and volcanological samples. Because each element in the collection corresponds to an individual observation/analysis of a sample, many elements in the dataset can correspond to the same sample (Figure 3.1). In concrete, the data is contained in two .csv files. In the main file (from now on TephraDataSet) each observation of a sample (row) can be characterized by 80 attributes (columns), which might be grouped by the type of information they provide (Figure 3.1, Table 3.1). The first group corresponds to Identification attributes, which is further subdivided in ID, Position, Reference and Analysis attributes. The second group corresponds to the actual observations of the sample or Characterization attributes, which correspond to information used to answer to the questions of: volcanic source of the sample, specific event it corresponds to, magnitude of this event and dispersion of its products. In particular, the Characterization attributes give information on the Stratigraphy of the samples (stratigraphic position and age estimates), their Physical characteristics (color, thickness and grain size) and their Geochemical composition (major and trace elements, isotope ratios). A third group of attributes correspond to the Interpretation attributes, the volcanic source of the deposit: Volcano; the specific eruptive event at the origin of the products: Event; and its Magnitude and Volcanic Explosivity Index (VEI). The fact that these attributes are Interpretation attributes is relevant in tephrochronology because tephra can be found far away from its volcanic source, and identifying it might not be trivial. In fact, in many cases the volcanic source of tephras contained in the dataset have been questioned and re interpreted over time (e.g. tephra identified by Naranjo & Stern (2004) whose source in Corcovado and Yanteles volcanoes has been questioned in later publications such as Amigo et al. (2013) and Alloway et al. (2017)). A final group of attributes

[2] https://nodejs.org/
[3] https://leafletjs.com/
[4] https://d3js.org/
[5] https://dc-js.github.io/dc.js/
[6] https://crossfilter.github.io/crossfilter/
[7] https://www.sqlite.org

corresponds to Flags and Comments. Data can be flagged for seven type of reasons (Table 3. 2), in every case the type of flag is indicated under Flag attribute and the particular situation is detailed under Flag Description. Comments corresponds to additional information that can help interpret the data.

The second .csv file (from now on MeasurementRuns) is part of the Geochemical composition attributes and it corresponds to information used to evaluate the quality and comparability of the analyses performed by different authors (Figure 3.1). The geochemistry of samples is analyzed in batches, in the dataset each batch corresponds to a different MeasurementRun. Ideally, the MeasurementRun corresponding to each SampleObservation in the TephraDataSet file is detailed in the MeasurementRuns file, thus linking both files. The MeasurementRuns file contains information to characterize each batch analysis: the analytical conditions during the analysis (beam size, accelerating voltage and beam current); as well as information on the secondary standards analyzed along with the samples, an information used to assess the comparability of analyses performed in different laboratories. Multiple secondary standards are analyzed several times in each MeasurementRun and the number of analyses (n), mean value and standard deviation for each analyzed element, as well as the analytical totals, are reported in the literature and included in the dataset.

As mentioned before, the dataset includes data from seventy three scientific publications published in peer reviewed journals, full list in the supplementary .The two files of the dataset and the explorer are hosted in the ESPRI server (Ensemble de Service Pour la Recherche) of the IPSL (Institute Pierre-Simon Laplace), France. ESPRI provides the storage space for the dataset as well as the platforms of distribution of scientific data. The major element composition of the dataset can be downloaded both normalized or not. If normalized, the Total corresponds to the sum of major elements and LOI before normalization.

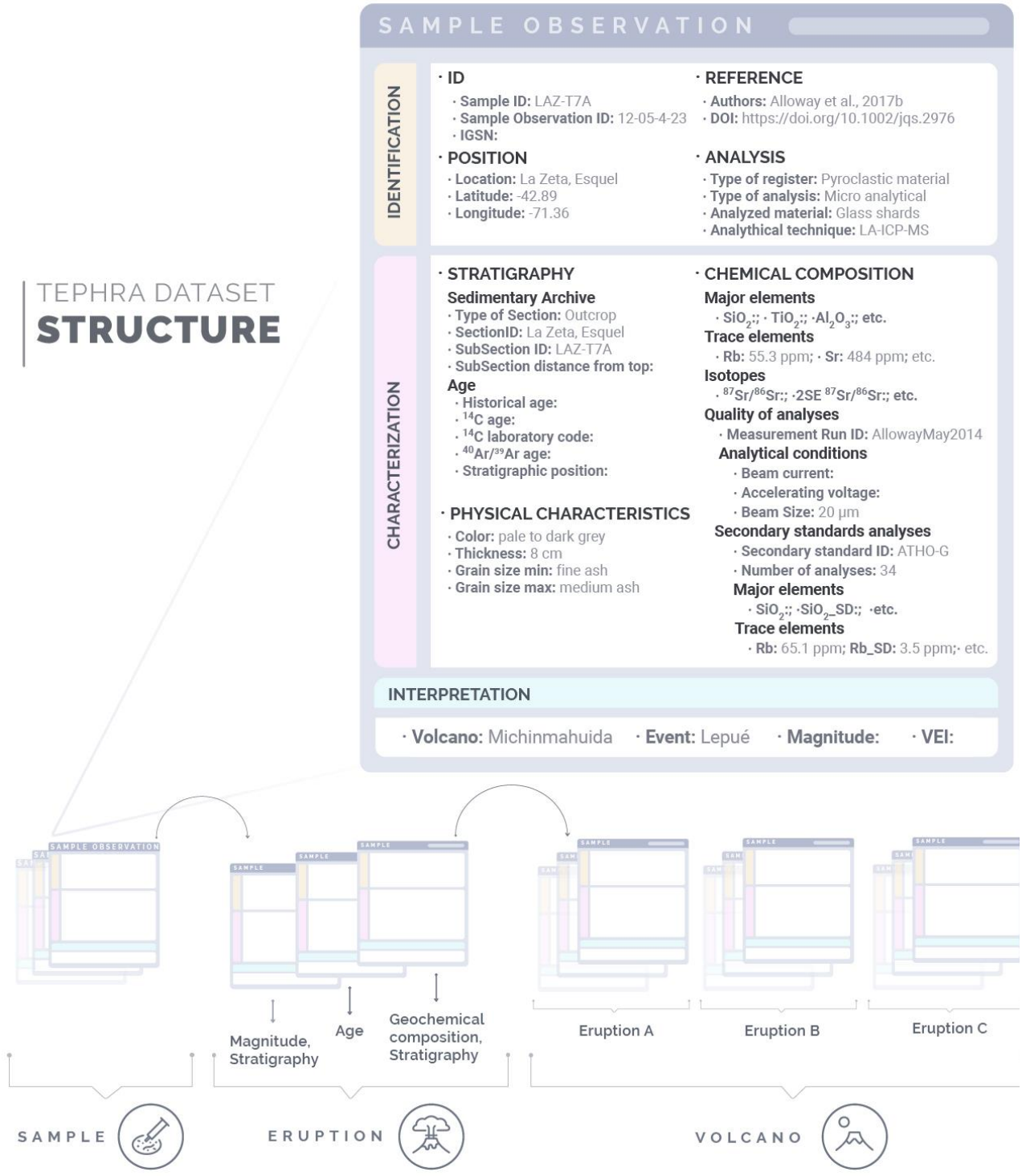

Figure 3.2. Dataset structure, using information from sample LAZ-T7A (Alloway et al. 2017b) as an example. The Flag and comment attributes are not illustrated.

Table 3.1. Detailed description of the attributes in the dataset.

		Dataset attributes	Unit	Description
Identification	**ID**	**Sample ID**		Name given in the original publication to the sample. In cases where this information was not provided by the authors, or two samples had the same Sample ID, a new Sample ID is given and indicated by a Flag "SampleID_Issue".
		Sample Observation ID		Name given to a specific observation/analysis of a sample. In cases when there is only one observation/analysis in a sample, the Sample ID and Sample Observation ID coincide.
		ISGN		International GeoSample Number. It corresponds to a specific identifier for earth samples.
	Position	**Location**		Name of the place where the sample was obtained, as indicated in the original publication.
		Latitude, Longitude	Decimal degrees	Latitude and Longitude where the sample was obtained. This information was obtained either directly from the text or the maps of the publication if provided. When this information could not be obtained even contacting authors, a position equal to the volcanic center is provided, which is indicated by a Flag "Position_Issue".
	Reference	**Authors**		APA style reference of the publication from where the sample information was published, e.g. "Martínez Fontaine et al., 2021".
		DOI		Digital Object Identifier of the publication where the sample information is published. In some cases the DOI link is broken so it is not included. In these cases this is indicated by a Flag "DOI_Issue".
	Analysis	**Type of register**		Type of material sampled. It might correspond to: “Organic matter”, “Pyroclastic material” or “Effusive material”.
		Type of analysis		Whether the analysis performed in the sample correspond to "Bulk" (e.g. when bulk tephra is analyzed) or "Micro Analytical" (e.g. when individual glass shards are analyzed).
		Analytical technique		Laboratory techniques employed to analyze the samples. The names of the analytical techniques are abbreviated (e.g. Electron Microprobe analysis as EMP).
		Analyzed material		Specific material analyzed (e.g. "Charcoal", "Glass shards", "Lava").
Characterization	**Stratigraphy**	**Sedimentary archive**	**Type of Section**		Type of sedimentary archive where the sample was obtained from (e.g. "Outcrop", "Lacustrine core", "Archaeological site").
			Section ID		Name given to the sedimentary archive in the original publication.
			SubSection ID		Name given to the specific portion of the sedimentary archive where the sample was obtained.
			SubSection distance from top	cm	When available, distance from top of the Sub Section.

		Age	**Historical age**	years AD	Year AD when the eruption producing the deposit occurred.
			Age ^{14}C	^{14}C years BP	^{14}C years BP of organic matter associated to a specific tephra.
			Age ^{14}C error	years BP	Analytical error for the ^{14}C age.
			^{14}C LabCode		Specific code assigned by each radiocarbon laboratory to each sample. Usually different to Sample ID and Sample Observation ID.
			Stratigraphic position		Position of the organic matter analyzed for ^{14}C age, relative to the tephra deposit it is associated to. It might be: Above, Below or Within the deposit. If additional information is given in the publication, then it is also indicated under this attribute.
			$^{40}Ar/^{39}Ar$ age	kilo years	$^{40}Ar/^{39}Ar$ age estimate of volcanic products.
			$^{40}Ar/^{39}Ar$ age error	kilo years	Analytical error of the $^{40}Ar/^{39}Ar$ age estimate.
	Physical properties		**Deposit Color**		Observed color of the tephra deposit sampled. Different from the color of the particular components of the deposits, e.g. the glass shards.
			Deposit Thickness	cm	Thickness of the tephra deposit sampled.
			Grain Size min	mm or description	Minimum grain size of the sampled deposit reported by the authors. In the original publications this information is not standardize and it can be presented as either categorical or numerical, i.e. "fine ash" or “0.625 mm”.
			Grain Size max	mm or description	Maximum gran size of the deposit reported by the authors. In the original publications this information is not standardize and it can be presented as either categorical or numerical, i.e. "fine ash" or “0.625 mm”.
	Geochemical composition	**Major elements**	**SiO_2, TiO_2, Al_2O_3, FeO, Fe_2O_3, Fe_2O_3T, FeOT, MnO, MgO, CaO, Na_2O, K_2O, P_2O_5, Cl**	wt%	Major element composition of the analyzed volcanic products. Both the raw and volatile–free normalized dataset can be accessed. However it must be noted that ~14% of the Sample Observations analyzed for major elements are already published normalized and with no information of the Total, thus the *raw* data cannot be accessed.
			LOI	wt%	Loss on Ignition. A measure of the amount of volatiles in the sample.
			Total	wt%	*Raw* dataset: Sum of the non–normalized analyzed major elements and LOI, as indicated in the original publication. Normalized dataset: Sum of the non–normalized analyzed major elements and LOI taking into account FeOT as *total* Fe.
		Trace elements	**Rb, Sr, Y, Zr, Nb, Cs, Ba, La, Ce, Pr, Nd, Sm, Eu, Gd, Tb, Dy, Ho, Er, Tm, Yb,**	ppm	Trace element concentrations of the analyzed volcanic products.

			Lu, Hf, Ta, Pb, Th, U		
		Isotopes	**$^{87}Sr\_^{86}Sr$**		Ratio of isotopes of strontium: $^{87}Sr/^{86}Sr$.
			2SE_$^{87}Sr_^{86}Sr$		Analytical 2σ error for the $^{87}Sr/^{86}Sr$ ratio.
			$^{143}Nd\_^{144}Nd$		Ratio of isotopes of neodymium: $^{143}Nd/^{144}Nd$.
			2SE_$^{143}Nd_^{144}Nd$		Analytical 2σ error interval for the $^{143}Nd/^{144}Nd$ ratio.
		Quality of analyses	**Measurement Run ID**		Label given to the batch of analyses which share the same analytical conditions and secondary standard analyses.
			Analytical conditions	**Beam Size**	μm	For EMP data: size of electron beam used during analysis. For glass analysis, this is usually widened from a point source.
				Accelerating Voltage	kV	For EMP data: accelerating voltage used during analysis.
				Beam Current	nA	For EMP data: electron beam current used during analysis. For glass analysis, this is usually lowered relative to analyses of hard materials.
			Secondary standard analyses	**Standard ID**		Secondary standard analyzed along with the samples.
				n		Number of analyzes performed to the same secondary standard during the same Measurement Run.
				SiO_2: U	wt%, ppm	Mean value of the "n" analyzes for each element and/or Total for each secondary standard in each Measurement Run.
				SD_SiO_2 : SD_ U		Standard deviation of the "n" analyses for each secondary standard in each Measurement Run.
Interpretation			**Volcano**		Volcanic center indicated as the source of the volcanic deposit sampled. If the volcanic source of the deposit has been questioned or re assessed, it is indicated with a "VolcanicSource_Issue" flag.
			Event		Name given to the specific eruptive event producing the sampled volcanic deposit. When the name given to a specific eruption has changed in time, it is indicated under "EventName_Issue" flag.
			Magnitude		Magnitude of the eruptive Event (Pyle, 2000; 2015) associated with the sampled volcanic deposit, as estimated in the original publication. Different publications might estimate different Magnitudes for the same event.
			VEI		Volcanic Explosivity Index (VEI; Newhall and Self, 1982) of the eruptive Event associated with the sampled volcanic deposit, as estimated in the original publication. Different publications might estimate different VEIs for the same event.
Flags			**Flag**		Indication of the type of issue(s) associated with different attributes of the data, detailed in Table 3.2. Data might be flagged by more than one issue.

	Flag Description		Description of the particular situation why data is flagged. When data is flagged by different type of flags, the description is preceded by the type of flag it corresponds to. For example "SampleID_Issue: No Sample ID is provided by the authors. DOI_issue: no DOI has been assigned to the publication."
Comments			Additional information that can help interpret data that doesn't fall under any other attribute.

3.4 Technical validation

The tephrochronological work utilizes very heterogeneous type of information to identify the source of the remains of explosive eruptions and to consequently characterize the eruptive activity of volcanic centers. Because of the latter, an important part of the technical validation of tephrochronological data is understanding if this very heterogeneous information is comparable or not. A first order evaluation of the comparability of data is qualitatively, which can be illustrated, for example, by taking a closer look at radiocarbon dating of tephras. Because pyroclastic products cannot be directly dated with sufficient precision to discriminate between eruptions, organic matter associated with the deposits are dated instead. For instance, a charcoal piece found within the deposit can be dated to estimate the age of the eruption, as it is assumed to be the result of hot pyroclastic material burning living trees. Alternatively, if no charcoal is found within the tephra, soil either above or below the deposit might be dated. However, the age of the soil might not represent the age of the deposit, as soil above might take years to develop and soil below might incorporate older organic matter. In these cases, these ages are interpreted as minimum and maximum ages, respectively. Thus, in order to correctly interpret what the radiocarbon ages represent, it is important to have access to all this information, and not only the radiocarbon age estimate and its analytical error. A similar situation occurs with geochemical compositions of pyroclastic versus effusive products or bulk versus micro analytical analyses, as they represent different processes. In the dataset, this information is contained in the Analysis attributes: Type of register (effusive material, pyroclastic material, organic matter), Type of analysis (micro analytical, bulk), Analyzed Material (e.g. lava, pumice, wood), Analytical technique (e.g. EMP, XRF, ICPMS); and additionally, the Stratigraphic Position attribute, which indicate the stratigraphic position of the dated organic matter relative to the pyroclastic deposit.

The heterogeneity of data also expresses in the major element analyses. As mentioned before, different publications might present Fe in different ways, which must be standardize in order to being able to compare the data. Additionally, different publications might analyze different major elements. In particular, less abundant major elements might or might not be analyzed (Figure 3.2) because of the increased amount of time employed to analyze them versus the information they provide. In particular: Cl (not analyzed in ~72% of the Sample Observations analyzed for major elements), P_2O_5 (not analyzed in ~25% of the cases) and/or MnO (not analyzed ~6% of the cases) are not always analyzed and thus the normalization, even when standardizing Fe, does not represent exactly the same. However, because of the relatively small concentrations of these elements in the volcanic products in the dataset (Cl between 0.001 and 0.6 wt%; P_2O_5 between 0.0001 and 1.78 wt%; MnO between 0 and 0.6 wt%), the normalized concentration of elements is expected to vary little with respect to an *ideal* case where all major elements are analyzed. Here this is tested by re–normalizing the samples, where major elements were analyzed and the analytical total was published, by a new analytical total which does not include Cl, P_2O_5 or MnO.

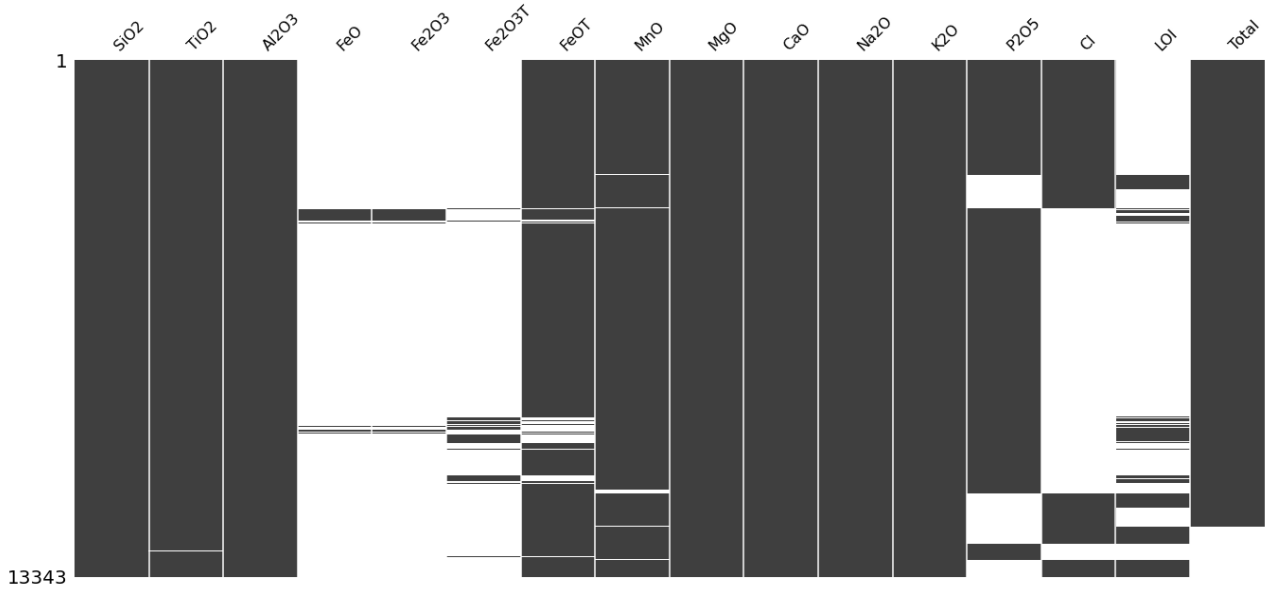

Figure 3.3. Hetereogeneity of the analyzed major elements contained in the dataset. In the figure the vertical axis corresponds to the Sample Observations. In this case, 13,343 Sample Observations correspond to major element analyses.

Then, this difference is compared with the 95%CL interval of the secondary standards analyzed along with the samples. Because ~40% of the sample observations analyzed for major elements for which the analytical total was published, were not published along with the secondary standards analyses, here all samples observations are compared with all the secondary standard analyzed along with the remaining ~60% of the Sample Observations. However, the detailed comparison for each Measurement run can be accessed in the code availability section. In all cases except for SiO_2 and Al_2O_3, the difference between the normalizations is lower than the 95%CL of secondary standards analyzed along with the samples (Figure

3.3, S1, S2). In the case of SiO_2 and Al_2O_3 for some the samples the difference is higher than the 95%CL (Figure 3.3 a, b), however it is difficult to estimate the number because the information of the analyzed secondary standards is not available for all samples, as previously mentioned. Nevertheless, in ~99% of the sample observations the difference is lower than 0.5 wt% for SiO_2 and lower than 0.13 wt% for Al_2O_3.

In order to correctly interpret the available information, it is also very important to understand the quality of the data, i.e. being able to assess the accuracy, precision and making sure that the analyzed products are not altered. In the case of radiocarbon ages, $^{40}Ar/^{39}Ar$ ages and isotope analyses $^{87}Sr/^{86}Sr$ and $^{143}Nd/^{144}Nd$, an analytical error is directly provided from the laboratories, which allows to understand the analytical precision of the data. In the case of the geochemical composition, however, assessing this is less direct and in the dataset this can be done by looking at different attributes. In the first place, a quality assessment can be done through the LOI and Total attributes. As mentioned before, ideally, the analytical total (sum of major elements and LOI) should approach 100 wt%. Lower Totals can result from analytical problems (e.g. surface roughness of the samples, poor sample positioning, loss of alkalis), from post depositional hydration (i.e. alteration of the volcanic products) or from a pre depositional characteristic of the analyzed volcanic products (e.g. subduction magmas, as in the SVZ and AVZ, are relatively hydrated). Thus, Totals lower than 100 wt% and or higher LOIs do not necessarily reflect poor quality analyses or alteration of the samples, but can also reflect characteristics of the volcanic environment. Because of the latter, there is no consensus regarding acceptable Totals and thus in the dataset this value is stocked, when presented in the literature (~86% of the Sample Observations analyzed for major elements are published along with the analytical Totals) for the user to judge. However, it must be noted that for 95% of the Sample Observations, the Total is between 95 and 102 wt%, whereas the LOI is between -3 and 5 wt%. Also, samples with Totals lower than 90 wt% were not included in the dataset.

Additionally, a quality control of the geochemical composition analyses of the samples can be done by looking at the analytical conditions attributes (Beam size, Accelerating voltage, Beam current), when the analyses have been performed by EMP. This information allows for a first order evaluation of how comparable the results are.

An information of great value for assessing the quality of the geochemical composition analyses are the composition of the secondary standards, analyzed along with the samples. Samples are analyzed for geochemistry in batches, in each batch multiple secondary standards (generally no more than three or four) are analyzed several times along with the samples to evaluate the comparability of the analyses performed in different laboratories and estimate their precision and accuracy. This information can be presented in publications as the mean analyzed value for each element of interest for each secondary standard analyzed, along with their respective standard deviation and the number of analyzes performed (n). Alternatively, in some publications all performed analyzes are presented, from which the latter

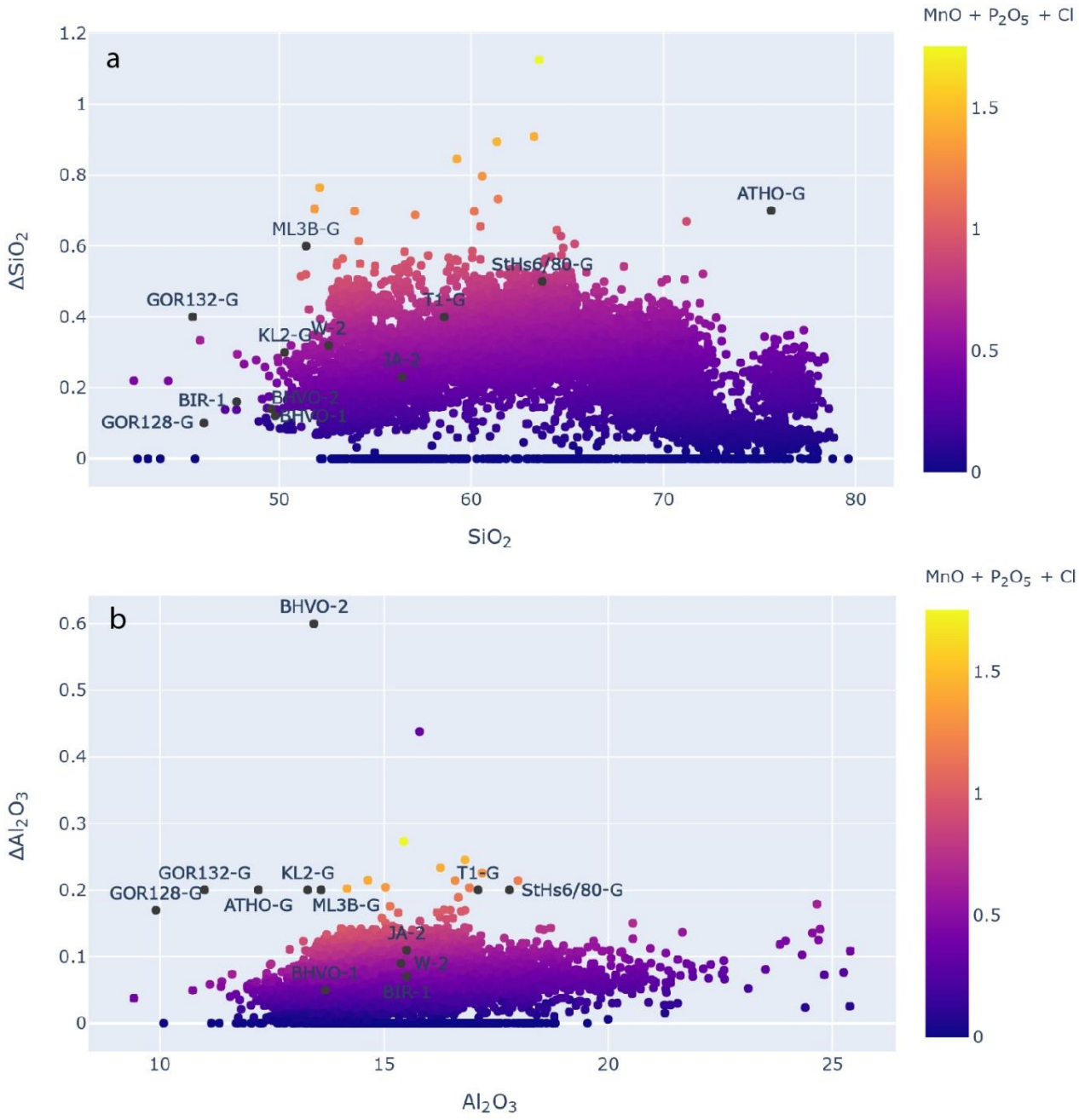

Figure 3.4. Assessment of the impact of normalizing by analytical totals considering different major elements. Δ= Normalized value considering the analytical total as the sum of all analyzed major elements – Normalized value considering the analytical total withouth Mn0, P_2O_5 and Cl. The composition of secondary standards analyzed along with the samples are also shown and indicated in the figure, the y value in this case corresponds to the 95%CL. Only secondary standards with certified values are shown: GOR128-G, GOR132-G, KL2-G, ML3B-G, T1-G, StHs6/80-G, ATHO-G (Jochum et al., 2006), NISTSRM610 (Jochum et al., 2011), AGV-2, BIR-1, BHVO-1, BHVO-2, BCR-2, JA-1, JA-2, W-2 (Jochum et al., 2016), S-Y, OREAS184, OREAS700.

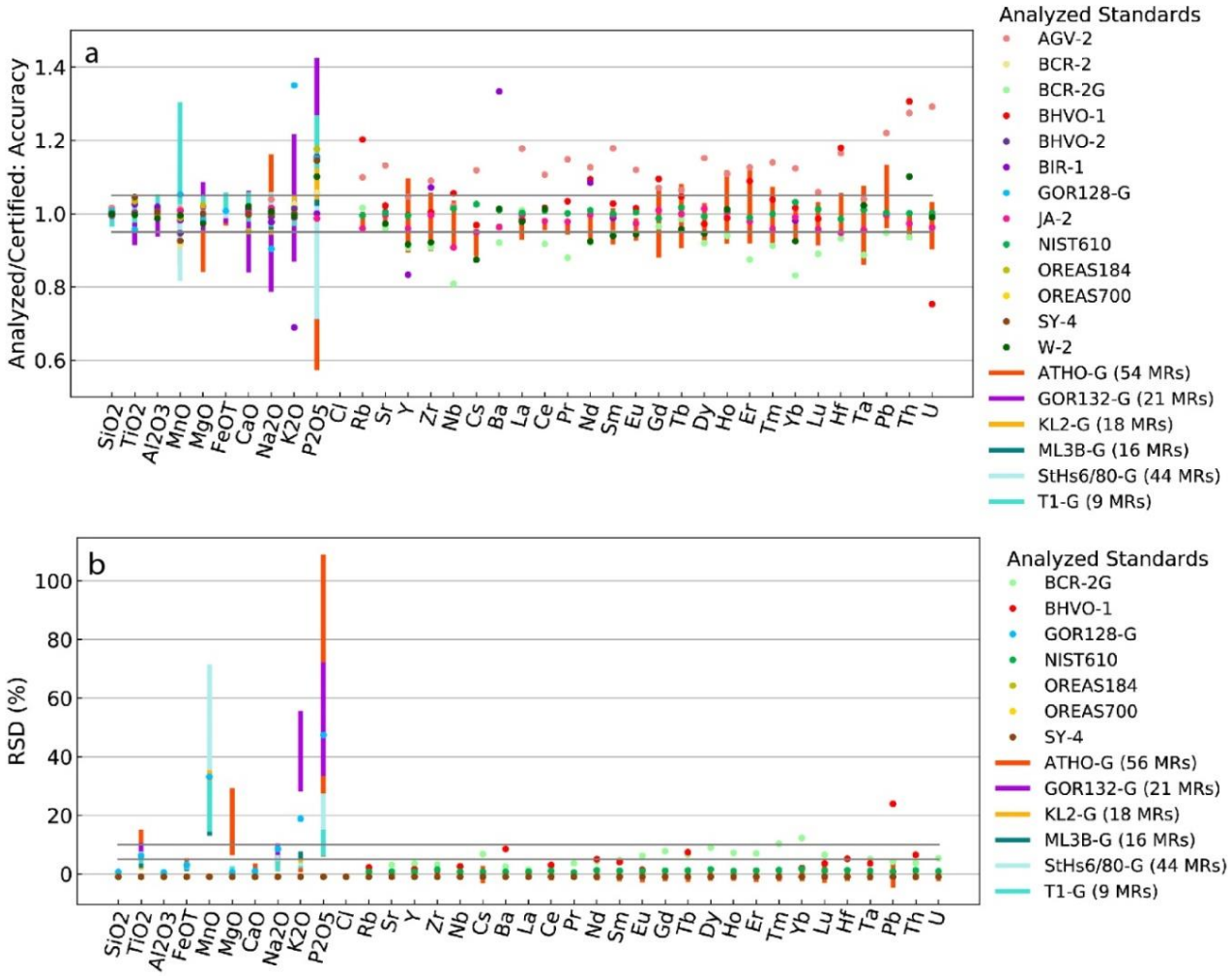

Figure 3.5. Assessment of the overal quality of the geochemical data in the dataset. a: Accuracy of the geochemical analyses, calculated as mean analyzed value of a particular secondary standard/certified value. b: Precision of the geochemical analyses, calculated as mean/std analyzed value of a particular secondary standard. In order to better visualize the information, when the same secondary standard is analyzed in more than three Measurement Runs, the mean and standard deviation were obtained and plotted as a vertical line and the number of Measurement runs are indicated in the legend as MRs. Otherwise the values are indicated as dots. Bold horiontal lines corresponds to 0.95 and 1.05 values for the accuracy and 5 and 10% for the precision. Only secondary standards with certified values are shown: GOR128-G, GOR132-G, KL2-G, ML3B-G, T1-G, StHs6/80-G, ATHO-G (Jochum et al., 2006), NISTSRM610 (Jochum et al., 2011), AGV-2, BIR-1, BHVO-1, BHVO-2, BCR-2, JA-1, JA-2, W-2 (Jochum et al., 2016), S-Y, OREAS184, OREAS700.

parameters can be obtained. In the dataset, this information is stocked as the mean and standard deviation values together with the number of analyses n, when this information was provided, either in the original publication or through private request to the authors. From the total of Sample Observations corresponding to major and trace elements compositions, for ~61.5% (10,209 Sample Observations), it was possible to obtain the full information, whereas in ~1.5% of the cases (134 Sample Observations) only the mean analyzed values were published. In order for this information to be actually comparable, it is important that certified values of the secondary standards are available in order to compare the obtained values with them and estimate the accuracy of the analyses. From the thirty three secondary

standards analyzed in the publications on the dataset, certified values are available for nineteen of them: GOR128-G, GOR132-G, KL2-G, ML3B-G, T1-G, StHs6/80-G, ATHO-G (Jochum et al., 2006), NISTSRM610 (Jochum et al., 2011), AGV-2, BIR-1, BHVO-1, BHVO-2, BCR-2, JA-1, JA-2, W-2 (Jochum et al., 2016), S-Y (), OREAS184, OREAS700 (). The latter corresponds to ~53 % of the Samples Observations analyzed for geochemistry, and ~52% has the full information (mean, standard deviation and n). For these Measurement Runs, accuracy can be estimated as the relative standard deviation (RSD) estimated as the mean analyzed value versus the certified value (Figure 3.4a) and the precision as the mean versus the standard deviation (Figure 3.4b). The accuracy estimates and precision plots and values for each of the Measurement runs or for the whole dataset can be produced and accessed in the code availability section. Overall, maximum accuracies and precisions are observed for SiO_2, which range between ~0.95 and ~1.02, and ~0.09% and 1.54%, respectively; and minimum accuracies and precisions for P_2O_5, which range between ~0.16 and ~2.00, and between 3% and 206%.

Finally, because of the very heterogeneous sources of information in the dataset, some issues were encountered when gathering the data and trying to standardize it. These issues are categorized in the Flag attribute and the particular situation is described under Flag Description. Seven type of issues where identified and are described in Table 3.2.

Table 3.2. Detail of Flag attribute values.

Type of Flag	Description
SampleID_Issue	This flag is assigned when: a Sample ID or Sample Observation ID is not given in the original publication; when the same Sample ID or Sample Observation ID is given to two analyses in the same or in different publication; or when different Sample IDs or Sample Observation IDs are given to the same sample in different publications.
Position_Issue	This flag is assigned when: the sample position could not be assessed because it is not made explicit in the publication and was not provided upon request to the co authors; or when it was obtained from the map in the original publications.
Age_Issue	This flag is assigned when: the age estimate is considered by the authors as an outlier with respect to other age estimates for the same eruptive event; or it is said to represent either younger or older age because of contamination with older/younger organic matter.
VolcanicSource_Issue	This flag is assigned when: the deposit has been indicated as sourced from different volcanic centers in different publications; when the geochemistry is somewhat different from the proposed source; when the authors suggest a volcanic source for the deposit with some doubt.
Geochemistry_Issue	This flag is assigned when: the authors indicate that the analyzed material might be altered; analyzed glass shards are highly microlitic and thus the geochemical composition approximates a bulk analysis rather than micro analytical; when the Total in the dataset is not the same as the Total published by the authors, because the published Total does not correspond to the sum of the major element analyses; when the data are said to be normalized in the original publication but the Total does not add to 100% and thus are here re-normalized; when it is not made explicit in the publication if the FeO or Fe2O3 presented correspond to *total* Fe, but is inferred from the analytical techniques.
EventName_Issue	This flag is assigned when: different names have been assigned to the same eruptive event in different publications; the same sample has been correlate to different eruptive events by different authors; the authors indicate that two eruptions cannot be differentiated and thus the assigned event might be one or the other; based on information on the dataset a correlation with a specific tephra or deposit is proposed.

DOI_Issue	This flag is assigned when: no DOI has been assigned to the publication; the DOI link is broken.

3.5 Usage notes

The explorer can be access at the moment at: http://varaya.cl:3001/

Data can be downloaded either with major elements normalized or not, and either the whole data set or the data corresponding to a selection of specific volcanoes and/or events. In order to do this, a download tab in the upper part of the explorer will be implemented, with the buttons download "raw" or "normalized" and "all" or "selected".

3.6 Code availability

The code to normalize the raw data and to reproduce the analyses in Figures 3.4 and 3.5 (for the whole dataset or for particular Measurement Runs) can be accessed for the moment at: https://github.com/consuelola/TephraDataBase/ in the Notebooks file as "Normalizing.ipynb", "CheckNormalizations.ipynb" and "UncertaintyAndStandards.ipynb".

3.7 References

Abarzúa A. M. & Moreno P. I. 2008. Changing fire regimes in the temperate rainforest region of southern Chile over the last 16,000 yr. *Quaternary Research,* 69 (1), 62–71. https://doi.org/10.1016/j.yqres.2007.09.004

Abarúa A. M., Villagrán C. & Moreno P. I. 2004. Deglacial and postglacial climate history in east-central Isla Grande de Chiloé, southern Chile (43°S). *Quaternary Research,* 62 (1), 49–59. https://doi.org/10.1016/j.yqres.2004.04.005

Alloway, B. V., Moreno, P.I., Pearce, N.J.G., De Pol-Holz, R., Henríquez, W.I., Pesce, O.H., Sagredo, E., Villarosa, G. & Outes, V. 2017a. Stratigraphy, age and correlation of Lepué Tephra: a widespread c. 11 000 cal a BP marker horizon sourced from the Chaitén Sector of southern Chile. *Journal of Quaternary Science*. 32 (6), 795–829. https://doi.org/10.1002/jqs.2976

Alloway, B. V., Pearce, N.J.G., Moreno, P.I., Villarosa, G., Jara, I., De Pol-Holz, R. & Outes, V. 2017b. An 18,000 year-long eruptive record from Volcán Chaitén, northwestern Patagonia: Paleoenvironmental and hazard-assessment implications. *Quaternary Science Reviews*. 168, 151–181. https://doi.org/10.1016/j.quascirev.2017.05.011

Alloway, B. V., Pearce, N.J.G., Villarosa, G., Outes, V. & Moreno, P.I. 2015. Multiple melt bodies fed the AD 2011 eruption of Puyehue-Cordón Caulle, Chile. *Scientific Reports*, 5, Article: 17589. https://doi.org/10.1038/srep17589

Amigo, Á., Lara, L.E. & Smith, V.C. 2013. Holocene record of large explosive eruptions from Chaitén and Michinmahuida Volcanoes, Chile. *Andean Geology*, 40 (2), 227–248. https://doi.org/10.5027/andgeov40n2-a03

Bertin, L., Moreno, H. & Becerril, L., 2018. *Peligros del Campo Volcánico Carrán-Los Venados, Región de los Ríos.* Servicio Nacional de Geología y Minería, Carta Geológica de Chile, Serie Geológica Ambiental, 33, 1–90, Santiago.

Bertrand, S., Castiaux, J. & Juvigné, E. 2008. Tephrostratigraphy of the late glacial and Holocene sediments of Puyehue Lake (Southern Volcanic Zone, Chile, 40°S). *Quaternary Research*. 70 (3), 343–357. https://doi.org/10.1016/j.yqres.2008.06.001

Bitschene, P., Arias, N., Arizmendia, A., Giacosa, R., Grizinik, M., Fernández, M., Márquez, M. & Nillni, A. 1993. Vulcanology and enviromental impact of the August 1991 eruption of the Hudson Vulcano (Patagonian Andes; Chile). *Zentralblatt Geologie u. Paläontologie*. Stuttgart. H 1-2: 493-500.

Bouvet de Maisonneuve, C., Dungan, M. A., Bachmann, O. & Burgisser, A. 2012. Insights into shallow magma storage and crystallization at Volcán Llaima (Andean Southern Volcanic Zone, Chile). *Journal of Volcanology and Geothermal Research*. 211–212, 76–91. https://doi.org/10.1016/j.jvolgeores.2011.09.010

Brahm, R., Parada, M. A., Morgado, E., Contreras, C. & McGee, L. E. 2018. Origin of Holocene trachyte lavas of the Quetrupillán volcanic complex, Chile: Examples of residual melts in a rejuvenated crystalline mush reservoir. *Journal of Volcanology and Geothermal Research*, 357, 163–176. https://doi.org/10.1016/j.jvolgeores.2018.04.020

Bucchi, F., Lara, L. E. & Gutiérrez, F. 2015. The Carrán–Los Venados volcanic field and its relationship with coeval and nearby polygenetic volcanism in an intra-arc setting. *Journal of Volcanology and Geothermal Research*, 308, 70-81. https://doi.org/10.1016/j.jvolgeores.2015.10.013

Carel, M., Siani, G. & Delpech, G. 2011. Tephrostratigraphy of a deep-sea sediment sequence off the south Chilean margin: New insight into the Hudson volcanic activity since the last glacial period. *Journal of Volcanology and Geothermal Research,* 208 (3–4), 99–111. https://doi.org/10.1016/j.jvolgeores.2011.09.011

Casati, E., D'Amico, M., Šefrna, L., Trombino, L., Tunesi, A. & Previtali, F. 2019. Geo-pedological contribution to the reconstruction of Holocene activity of Chaitén volcano (Patagonia, Chile). Journal of South American Earth Sciences, 94, Article: 102222. https://doi.org/10.1016/j.jsames.2019.102222

Clapperton C. M., Sugden D. E., Kaufman D. S. & McCulloch R. D. 1995. The last glaciation in central Magellan Strait, southernmost Chile. *Quaternary Research*, 44 (2), 133–148. https://doi.org/10.1006/qres.1995.1058

Costantini, L., Pioli, L., Bonadonna, C., Clavero, J. & Longchamp, C. 2011. A Late Holocene explosive mafic eruption of Villarrica volcano, Southern Andes: The Chaimilla deposit, *Journal of Volcanology and Geothermal Research*, 200 (3–4), 143–158. https://doi.org/10.1016/j.jvolgeores.2010.12.010

Del Carlo, P., Di Roberto, A., D'Orazio, M., Petrelli, M., Angioletti, A., Zanchetta, G., Maggi, V., Daga, R., Nazzari, M. & Rocchi, S., 2018. Late Glacial-Holocene tephra from southern Patagonia and Tierra del Fuego (Argentina, Chile): A complete textural and geochemical fingerprinting for distal correlations in the Southern Hemisphere. Quaternary Science Reviews, 195 (1), 153–170. https://doi.org/10.1016/j.quascirev.2018.07.028

D'Orazio, M., Innocenti, F., Manetti, P., Tamponi, M., Tonarini, S., González-Ferrán, O., Lahsen, A. & Omarini, R. 2003. The Quaternary calc-alkaline volcanism of the Patagonian Andes close to the Chile triple junction: geochemistry and petrogenesis of volcanic rocks from the Cay and Maca volcanoes (~45°S, Chile). *Journal of South American Earth Sciences*, 16 (4), 219–242. https://doi.org/10.1016/S0895-9811(03)00063-4

Fontijn, K., Rawson, H., Van Daele, M., Moernaut, J., Abarzúa, A.M., Heirman, K., Bertrand, S., Pyle, D.M., Mather, T.A., De Batist, M., Naranjo & J.A., Moreno, H., 2016. Synchronisation of sedimentary records using tephra: A postglacial tephrochronological model for the Chilean Lake District. *Quaternary Science Reviews*. 137, 234–254. https://doi.org/10.1016/j.quascirev.2016.02.015

Futa K. & Stern C. R. 1988. Sr and Nd isotopic and trace element compositions of Quaternary volcanic centers of the southern Andes. *Earth and Planetary Science Letters*, 88 (3–4), 253–262. https://doi.org/10.1016/0012-821X(88)90082-9

Geoffroy, C. A., Alloway, B. V., Amigo, Á., Parada, M. A., Gutierrez, F., Castruccio, A., Pearce, N. J. G., Morgado, E. & Moreno, P.I., 2018. A widespread compositionally bimodal tephra sourced from Volcán Melimoyu (44°S, Northern Patagonian Andes): Insights into magmatic reservoir processes and opportunities for regional correlation. *Quaternary Science Reviews,* 200, 141–159. https://doi.org/10.1016/j.quascirev.2018.09.034

Gerlach, D.C., Frey, F.A., Moreno-Roa, H. & López-Escobar, L. 1988. Recent Volcanism in the Puyehue–Cordon Caulle Region, Southern Andes, Chile (40.5°S): Petrogenesis of Evolved Lavas. *Journal of Petrology,* 29 (2), 333–382. https://doi.org/10.1093/petrology/29.2.333

Haberle, S.G. & Lumley, S.H. 1998. Age and origin of tephras recorded in postglacial lake sediments to the west of the southern Andes, 44°S to 47°S. *Journal of Volcanology and Geothermal Research*, 84 (3–4), 239–256. https://doi.org/10.1016/S0377-0273(98)00037-7

Harambour, S. V. 1988. Sobre et hallazgo del mítico volcán Reclus, ex Mano del diablo, Hielo Patagónico Sur, Magallanes, Chile. *Revista Geológica de Chile*, 15 (2), 173–179.

Heusser, C. J. 1995. Three late Quaternary pollen diagrams from Southern Patagonia and their palaeoecological implications. *Palaeageography, Palaeoclimatology. Palaeoecology,* 118 (1–2), 1–24. https://doi.org/10.1016/0031-0182(94)00138-X

Heusser, C. J., Heusser, L. E. & Hausser A. 1989. A 12,000 yr B.P. tephra layer at Bahia Inutile (Tierra del Fuego, Chile). *Anales del Instituto de la Patagonia*, 19 (1), 39–49.

Heusser, C. J., Heusser, L. E., Lowell, T.V., Moreira, A. & Moreira, S. 2000. Deglacial palaeoclimate at Puerto del Hambre, subantarctic Patagonia, Chile. *Journal of Quaternary Science*, 15 (2), 101–114. https://doi.org/10.1002/(SICI)1099-1417(200002)15:2<101::AID-JQS500>3.0.CO;2-Y

Hickey-Vargas, R.L., Moreno Roa, H., López-Escobar, L. & Frey, F.A. 1989. Geochemical variations in Andean basaltic and silicic lavas from the Villarrica-Lanin volcanic chain (39.5° S): an evaluation of source heterogeneity, fractional crystallization and crustal assimilation. *Contributions to Mineralogy and Petrology*. 103, 361–386. https://doi.org/10.1007/BF00402922

Jacques, G., Hoernle, K., Gill, J., Wehrmann, H., Bindeman, I. & Lara, L.E., 2014. Geochemical variations in the Central Southern Volcanic Zone, Chile (38–43°S): The role of fluids in generating arc magmas. *Chemical Geology,* 371, 27–45. https://doi.org/10.1016/j.chemgeo.2014.01.015

Kilian, R., Hohner, M., Biester, H., Wallrabe-Adams, H.J., Stern, C.R. 2003. Holocene peat and lake sediment tephra record from the southernmost Chilean Andes (53-55°S). *Revista Geológica de Chile* 30 (1), 47–64. http://dx.doi.org/10.4067/S0716-02082003000100002

Kratzmann, D.J., Carey, S., Scasso, R. & Naranjo, J.A., 2008. Compositional variations and magma mixing in the 1991 eruptions of Hudson volcano, Chile. *Bulletin of Volcanology*. 71, Article: 419. https://doi.org/10.1007/s00445-008-0234-x

Lara, L. E., Naranjo, J. A. & Moreno, H. 2004. Lanín volcano (39.5°S), Southern Andes: geology and morphostructural evolution. *Revista Geológica de Chile*, 31 (2), 241–257. https://doi.org/10.4067/S0716-02082004000200004

Lara, L.E., Moreno, H., Naranjo, J.A., Matthews, S. & Pérez de Arce, C., 2006. Magmatic evolution of the Puyehue-Cordón Caulle Volcanic Complex (40° S), Southern Andean Volcanic Zone: From shield

to unusual rhyolitic fissure volcanism. *Journal of Volcanology and Geothermal Research*, 157 (4), 343–366. https://doi.org/10.1016/j.jvolgeores.2006.04.010

Lara, L. E. & Moreno, H. 2006. *Geología del complejo volcánico Puyehue-Cordón Caulle, Región de Los Lagos*. Servicio Nacional de Geología y Minería, Carta Geológica de Chile, Serie Geológica Básica, 99, Escalara 1:50.000, Santiago.

Lohmar, 2008. Pétrologie des grands dépôts d'ignimbrites des volcans Villarrica (Licán et Pucón) et Llaima (Ignimbrite Curacautín), dans les Andes du Sud (Chili). PhD Thesis, Université Blause Pascal - Clermont Ferrand II, France.

Lohmar, S., Parada, M., Gutiérrez, F., Robin, C. & Gerbe, M. C. 2012. Mineralogical and numerical approaches to establish the pre-eruptive conditions of the mafic Licán Ignimbrite, Villarrica Volcano (Chilean Southern Andes). *Journal of Volcanology and Geothermal Research*, 235–236, 55–69, https://doi.org/10.1016/j.jvolgeores.2012.05.006

López-Escobar, L., Parada, M.A., Moreno, H., Frey, F.A. & Hickey-Vargas, R.L., 1992. A contribution to the petrogenesis of Osorno and Calbuco volcanoes, Southern Andes (41°00'-41°30'S): a comparative study. *Revista Geológica de Chile,* 19 (2), 211–226.

López-Escobar, L., Kilian, R., Kempton, P.D. & Tagiri, M., 1993. Petrography and geochemistry of Quaternary rocks from the Southern Volcanic Zone of the Andes between 41°30′ and 46°00′S, Chile. *Revista Geológica de Chile*, 20, 33–55.

López-Escobar, L., Parada, M.A., Hickey-Vargas, R.L., Frey, F.A., Kempton, P.D. & Moreno, H., 1995. Calbuco Volcano and minor eruptive centers distributed along the Liquiñe-Ofqui Fault Zone, Chile (41°–42° S): contrasting origin of andesitic and basaltic magma in the Southern Volcanic Zone of the Andes. *Contributions to Mineralogy and Petrology*, 119, 345–361. https://doi.org/10.1007/BF00286934

Martínez Fontaine, C., Siani, G., Delpech, G., Michel, E., Villarosa, G., Manssouri, F. & Nouet, J. 2021. Post–glacial tephrochronology record off the Chilean continental margin (~41° S). *Quaternary Science Reviews,* 261, Article: 106928. https://doi.org/10.1016/j.quascirev.2021.106928

Mayr, C., Smith, R.E., García, M.L., Massaferro, J., Lücke, A., Dubois, N., Maidana, N., I., Meier, W. J-H., Wissel, H. & Zolitschka, B. 2019. Historical eruptions of Lautaro Volcano and their impacts on lacustrine ecosystems in southern Argentina. *Journal of Paleolimnology*, 62, 205–221. https://doi.org/10.1007/s10933-019-00088-y

Mella, M, 2008. Petrogêneses do complexo vulcânico Yate (42, 30ºS), Andes do Sul, Chile. Tese de Doutorado, Instituto de Geociências, Universidade de São Paulo, São Paulo. https://doi.org/10.11606/T.44.2009.tde-04032009-091537

Moreno P. I. & León A.L. 2003. Abrupt vegetation changes during the last glacial to Holocene transition in mid-latitude South America. *Journal of Quaternary Science,* 18 (18), 787–800. https://doi.org/10.1002/jqs.801

Moreno, P.I., Alloway, B. V., Villarosa, G., Outes, V., Henríquez, W.I., De Pol-Holz, R. & Pearce, N.J.G., 2015. A past-millennium maximum in postglacial activity from Volcán Chaitén, southern Chile. Geology 43 (1), 47–50. https://doi.org/10.1130/G36248.1

Moreno PI. 2004. Millennial-scale climate variability in northwest Patagonia over the last 15000 yr. *Journal of Quaternary Science,* 19 (1), 35–47. https://doi.org/10.1002/jqs.813

Moreno, H., Lara, L. & Orozco, G. 2010. *Geología del Volcán Osorno, Región de Los Lagos*. Servicio Nacional de Geología y Minería, Carta Geológica de Chile, Serie Geológica Básica, 126, 1–31, Santiago.

Morgado, E., Parada, M.A., Contreras, C., Castruccio, A., Gutiérrez, F. & McGee, L.E. 2015. Contrasting records from mantle to surface of Holocene lavas of two nearby arc volcanic complexes: Caburgua-Huelemolle Small Eruptive Centers and Villarrica Volcano, Southern Chile. *Journal of Volcanology and Geothermal Research*. 306, 1–16. https://doi.org/10.1016/j.jvolgeores.2015.09.023

Morgado, E., Morgan, D.J., Harvey, J., Parada, M.Á., Castruccio, A., Brahm, R., Gutiérrez, F., Georgiev, B. & Hammond, S.J. 2019. Localised heating and intensive magmatic conditions prior to the 22–23 April 2015 Calbuco volcano eruption (Southern Chile). *Bulletin of Volcanology*. 81, Article: 24. https://doi.org/10.1007/s00445-019-1280-2

Motoki, A., Orihashi, Y., Naranjo, J. A., Hirata, D., Skvarca, P. & Anma, R. 2006. Geologic reconnaissance of Lautaro Volcano, Chilean Patagonia. *Revista Geológica de Chile*, 33 (1), 177–187. http://doi.org/10.4067/S0716-02082006000100008

Naranjo, J.A. & Moreno, H. 1991. Actividad explosiva postglacial en el volcan Llaima, Andes del Sur (38° 45'S). *Revista Geológica de Chile*, 18, 69–80.

Naranjo, J.A., Moreno, H. & Banks, N.G. 1993. *La erupción del volcán Hudson en 1991 (46°S), Región XI, Aisén, Chile*. Servicio Nacional Geología y Minería Boletín 44, 1–50.

Naranjo, J.A. & Moreno, H. 2005. *Geología del Volcán Llaima, Región de la Araucanía.* Servicio Nacional de Geología y Minería, Carta Geológia de Chile, Serie Geología Básica, 88, 1-33, Escala 1:50.000, Santiago.

Naranjo, J.A., Singer, B.S., Jicha, B.R., Moreno, H. & Lara, L.E. 2017. Holocene tephra succession of Puyehue-Cordón Caulle and Antillanca/Casablanca volcanic complexes, southern Andes (40–41°S). *Journal of Volcanology and Geothermal Research,* 332, 109–128. https://doi.org/10.1016/j.jvolgeores.2016.11.017

Naranjo, J.A. & Stern, C.R. 2004. Holocene tephrochronology of the southernmost part (42°30'-45°S) of the Andean Southern Volcanic Zone. *Revista Geológica de Chile,* 31 (2), 225–240. https://doi.org/10.4067/S0716-02082004000200003

Naranjo, J.A., Stern, C.R. 1998. Holocene explosive activity of Hudson Volcano, southern Andes. *Bulletin of Volcanology* 59, 291–306. https://doi.org/10.1007/s004450050193

Newhall, C.G. and Self, S. 1982. The Volcanic Explosivity Index (VEI) An Estimate of Explosive Magnitude for Historical Volcanism. *Journal of Geophysical Research: Oceans*, 87, 1231-1238. http://dx.doi.org/10.1029/JC087iC02p01231

Pesce, O. H. & Moreno, P. I. 2014. Vegetation, fire and climate change in central-east Isla Grande de Chiloé (43°S) since the Last Glacial Maximum, northwestern Patagonia. *Quaternary Science Reviews,* 90, 143–157. https://doi.org/10.1016/j.quascirev.2014.02.021

Pyle, D. 2000. LENTZ, H. M., III. 1999. The Volcano Registry. Names, Locations, Descriptions and Histories for Over 1500 Sites. *Geological Magazine*, 137 (1), 97-106. https://doi.org/10.1017/S0016756800383662

Pyle, D. 2015. Chapter 13 – Sizes of Volcanic Eruptions. In H. Sigurdsson (Eds.), *The Encyclopedia of Volcanoes (Second Edition)* (pp. 257-264), Academic Press. https://doi.org/10.1016/B978-0-12-385938-9.00013-4

Rawson, H., Keller, T., Fontijn, K., Pyle, D. M., Mather, T.A., Smith, V.C. & Naranjo, J. A. 2016. Compositional variability in mafic arc magmas over short spatial and temporal scales: Evidence for the signature of mantle reactive melt channels. *Earth and Planetary Science Letters*. 456, 66–77. https://doi.org/10.1016/j.epsl.2016.09.056

Rawson, H., Naranjo, J. A., Smith, V. C., Fontijn, K., Pyle, D. M., Mather, T. A. & Moreno, H. 2015. The frequency and magnitude of post-glacial explosive eruptions at Volcán Mocho-Choshuenco, southern Chile. *Journal of Volcanology and Geothermal Research*, 299, 103–129. https://doi.org/10.1016/j.jvolgeores.2015.04.003

Reubi, O., Bourdon, B., Dungan, M.A., Koornneef, J.M., Sellés, D., Langmuir, C.H. & Aciego, S. 2011. Assimilation of the plutonic roots of the Andean arc controls variations in U-series disequilibria

at Volcán Llaima, Chile. *Earth and Planetary Science Letters*, 303 (1–2), 37–47. https://doi.org/10.1016/j.epsl.2010.12.018

Schindlbeck, J.C., Freundt, A. & Kutterolf, S. 2014. Major changes in the post-glacial evolution of magmatic compositions and pre-eruptive conditions of Llaima Volcano, Andean Southern Volcanic Zone, Chile. *Bulletin of Volcanology*. 76, Article : 830. https://doi.org/10.1007/s00445-014-0830-x

Sellés, D. & Moreno, H. 2011. *Geología del Volcán Calbuco*. Servicio Nacional de Geología y Minería, Carta Geológica de Chile, Serie Geológica Básica, 130, Escala 1:50.000, Santiago.

Simmons, I., McGarvie, D., Cortés, J., Calder, E. & Pavez, A. 2020. Holocene volcanism at the Quetrupillán Volcanic Complex (39°30' S, 71°43' W), southern Chile. *Volcanica*, 3 (1), 115–137. https://doi.org/10.30909/vol.03.01.115137

Singer, B.S., Jicha, B.R., Harper, M.A., Naranjo, J.A., Lara, L.E. & Moreno, H., 2008. Eruptive history, geochronology, and magmatic evolution of the Puyehue-Cordón Caulle volcanic complex, Chile. *GSA Bulletin,* 120 (5–6), 599–618. https://doi.org/10.1130/B26276.1

Smith, R.E., Smith, V.C., Fontijn, K., Gebhardt, A.C., Wastegård, S., Zolitschka, B., Ohlendorf, C., Stern, C. & Mayr, C. 2019. Refining the Late Quaternary tephrochronology for southern South America using the Laguna Potrok Aike sedimentary record. *Quaternary Science Reviews*. 218, 137–156. https://doi.org/10.1016/j.quascirev.2019.06.001

Stern, C. R., Moreno, P. I., Villa-Martínez, R., Sagredo, E. A., Prieto, A. & Labarca, R. 2011. Evolution of ice-dammed proglacial lakes in Última Esperanza, Chile: implications from the late-glacial R1 eruption of Reclús volcano, Andean Austral Volcanic Zone. *Andean Geology*, 38 (1), 82–97.

Stern, C.R., De Porras, M.E. & Maldonado, A. 2015. Tephrochronology of the upper Río Cisnes valley (44°S), southern Chile. *Andean Geology*, 42 (2), 173–189. https://doi.org/10.5027/andgeoV42n2-a02

Stern, C.R. 1992. Tephrochronology of Magallanes: new data and implications. *Anales del Instituto de la Patagonia* 21: 129-139.

Stern, C.R., 2008. Holocene tephrochronology record of large explosive eruptions in the southernmost Patagonian Andes. *Bulletin of Volcanology,* 70, 435–454. https://doi.org/10.1007/s00445-007-0148-z

Tagiri, M., Moreno, H., López-Escobar, L. & Notsu, K. 1993. Two magma types of the high-alumina basalt series of Osorno, Souther Andes (41°06'S)-plagioclase dilution effect. *Journal of Mineralogy, Petrology and Economic Geology*, 88 (7), 359–371. https://doi.org/10.2465/ganko.88.359

Villarosa, G., Outes, V., Hajduk, A., Crivelli Montero, E., Sellés, D., Fernández, M. & Crivelli, E. 2006. Explosive volcanism during the Holocene in the Upper Limay River Basin: The effects of ashfalls on human societies, Northern Patagonia, Argentina. *Quaternary International*, 158 (1), 44–57. https://doi.org/10.1016/j.quaint.2006.05.016

Wastegård, S., Veres, D., Kliem, P., Hahn, A., Ohlendorf, C., Zolitschka, B. 2013. Towards a late Quaternary tephrochronological framework for the southernmost part of South America – the Laguna Potrok Aike tephra record. *Quaternary Science Reviews*, 71, 81-90. https://doi.org/10.1016/j.quascirev.2012.10.019

Watt, S.F.L., Pyle, D.M. & Mather, T.A., 2011a. Geology, petrology and geochemistry of the dome complex of Huequi volcano, southern Chile. *Andean Geology,* 38 (2), 335–348. https://doi.org/10.5027/andgeov38n2-a05

Watt, S.F.L., Pyle, D.M., Naranjo, J.A., Rosqvist, G., Mella, M., Mather, T.A. & Moreno, H., 2011b. Holocene tephrochronology of the Hualaihue region (Andean southern volcanic zone, ~42° S), southern Chile. *Quaternary International*, 246 (1–2), 324–343. https://doi.org/10.1016/j.quaint.2011.05.029

Watt, S.F.L., Pyle, D.M. & Mather, T.A. 2013. Evidence of mid- to late-Holocene explosive rhyolitic eruptions from Chaitén Volcano, Chile. *Andean Geology,* 40 (2), 216–226. https://doi.org/10.5027/andgeoV40n2-a02

Weller, D., Miranda, C.G., Moreno, P.I., Villa-Martínez, R. & Stern, C.R. 2014. The large late-glacial Ho eruption of the Hudson volcano, southern Chile. *Bulletin of Volcanology*, 76, Article: 831. https://doi.org/10.1007/s00445-014-0831-9

Weller, D.J., Miranda, C.G., Moreno, P.I., Villa-Martínez, R. & Stern, C.R., 2015. Tephrochronology of the southernmost Andean Southern Volcanic Zone, Chile. *Bulletin of Volcanology*, 77, Article: 107. https://doi.org/10.1007/s00445-015-0991-2

Weller, D.J., De Porras, M.E., Maldonado, A., Méndez, C. & Stern, C.R., 2017. Holocene tephrochronology of the lower Río Cisnes valley, souhern Chile. *Andean Geology*, 44 (3), 229–248. https://doi.org/10.5027/andgeov44n3-a01

Weller, D.J., de Porras, M.E., Maldonado, A., Méndez & C., Stern, C.R., 2019. Petrology, geochemistry, and correlation of tephra deposits from a large early-Holocene eruption of Mentolat volcano, southern Chile. Journal of South American Earth Sciences, 90, 282–295. https://doi.org/10.1016/j.jsames.2018.12.020

3.8 Supplementary

Table S1. Summary of answers from the interviews with part of the tephrochronology community working or that has worked in the SVZ and AVZ. In bold is the information included in the data set and the issues address through the data set and the explorer.

Question	Summary of answers
Questions answered using tephrochronological data	.Reconstruct eruptive history (recurrence of volcanic activity, dispersion of its products and magnitude of the different eruptive events) of a particular volcanic center, or a volcanic area. This information is then used either for producing volcanic hazard maps, or to further the understanding of the mechanisms originating volcanic activity. .Ameliorating chronologies of marine archives and ideally synchronizing chronologies of different paleoenvironmental archives in order to study climate change.
Data used to answer these questions	.Geographic position of volcanic products. .Type of deposit. .Stratigraphic position of the deposit. .Thickness of the deposit. .Macroscopic description of the deposit. .Description of the lithic fraction. .Grain size of the deposit: maximum, minimum, mean and standard deviation. .Color of the deposit. .Name of the sample. .Date in which the sample was obtained. .Analyzed material. .Age constraints of the deposits: historical age, 14C age, Ar/Ar age. .Stratigraphic position of the dated material, i.e. whether the age estimate is maximum or minimum. .Microscopic (thin section) description. .Geochemical composition (major and trace elements ideally) of eruptive products. .Analytical technique employed to analyze the samples. .Secondary standards analyzed along with the samples: name of the secondary standard, mean analyzed value for each element, number of analyses performed, standard deviation.

	.Analytical conditions of the analyses: beam size, accelerating voltage, beam current. .Eruptive events known for the volcanic center of interest. .Uncertainties associated with the eruptive events, for example different names given to the same deposit. .Estimated eruptive volume of the event. .Height of the eruptive columns. .Magnitude and/or Volcanic Eplosivity Index estimations of the eruptive events. .Volume and thickness of lava flows. .Dispersion of the products by eruption. .Abbreviated citation of publication where the data was obtained from.
Where data is obtained from	.Scientific publications in peer reviewed journals. .Global Volcanism Pogram, Smithsonian Institute. .Geological maps from SERNAGEOMIN.
How data is organized and visualized	.The main tool for organizing the data are spreadsheets. Even though the interviewed people uses more and less the same information, the way of organizing it varies greatly. Some organize it first stratigraphically/chronologically, others by author or by volcanic center and eruption.
Problems when developing these tasks	.The information is sparse, dispersed. .The information is not standardized and thus it is difficult to integrate the information produced by different authors. .Different names given to same criteria. .Missing information (e.g. positon where the sample was obtained). .Different names given to the same eruption. .They don't know a priori if the data are comparable and establishing this can take a lot of time. .Ignorance of the existence of data. .Raw data is missing. .Changes in methodologies to calculate parameters over time. .Changes in the interpretation of data over time. .Differences in organizing criteria by different authors. .Difficulties organizing the amount of data in a highly dense volcanic area. .Biased tephrochronological archives.

Publications included in the dataset : publications in peer reviewed journals (Abarzúa & Moreno, 2008; Abarzúa et al., 2004; Alloway et al., 2015; Alloway et al., 2017a; Alloway et al., 2017b; Amigo et al., 2013; Bertrand et al., 2008; Bitschene et al., 1993; Bouvet de Maisonneuve et al., 2012; Brahm et al., 2018; Bucchi et al., 2015; Carel et al., 2011; Casati et al., 2019; Clapperton et al., 1995; Constantini et al., 2011; Del Carlo et al., 2018; D'Orazio et al., 2003; Fontijn et al., 2016; Futa & Stern, 1988; Geoffroy et al., 2018; Gerlach et al., 1988; Haberle & Lumley, 1998; Harambour, 1988; Heusser et al., 1989 Heusser et al., 2000; Hickey-Vargas et al., 1989; Jacques et al., 2014; Kilian et al., 2003; Kratzmann et al., 2008; Lara et al., 2004; Lara et al., 2006; Naranjo et al., 2017; Lohmar et al., 2012; López-Escobar et al., 1992; López-Escobar et al., 1993; López-Escobar et al., 1995; Martínez Fontaine et al., 2021; Mayr et al., 2019; Miranda et al., 2013; Weller et al., 2014; Moreno & León, 2003; Moreno et al., 2015; Moreno, 2004; Morgado et al., 2015; Morgado et al., 2019; Motoki et al., 2006; Naranjo & Moreno, 1991; Naranjo et al., 1993; Naranjo & Stern, 2004; Naranjo & Moreno, 2005; Naranjo & Stern, 1998; Naranjo et al., 2017; Pesce & Moreno, 2014; Rawson et al., 2015; Rawson et al., 2016; Reubi et al., 2011; Schindlbeck et al., 2014; Simmons et al., 2020; Singer et al., 2008; Singer et al., 2008; Naranjo et al., 2017; Smith et al., 2019; Stern et al., 2011; Stern et al., 2015; Stern, 1992; Stern, 2008; Tagiri et al., 1993; Villarosa et al., 2006; Wastegård et al., 2013; Watt et al., 2011a; Watt et al., 2011b; Watt et al., 2013; Weller et al., 2014; Weller et al., 2015; Weller et al., 2017; Weller et al., 2019); six publications from SERNAGEOMIN (Bertin et al., 2018; Lara et al., 2006; Moreno et al., 2010; Naranjo & Moreno, 2005; Naranjo & Stern, 1998; Sellés & Moreno, 2011); and two doctoral theses (Lohmar, 2008; Mella, 2008).

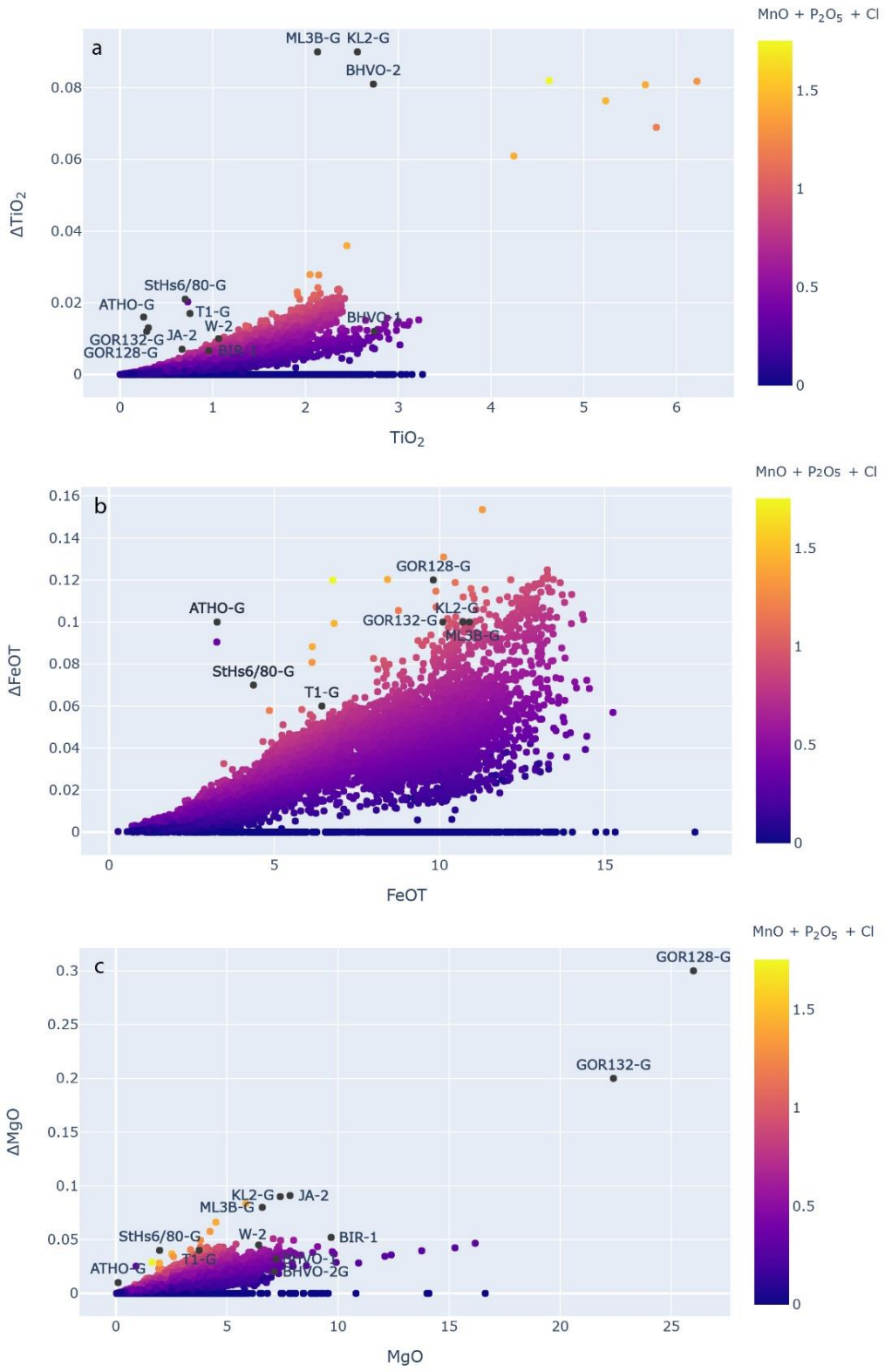

Figure S3.1. Assessment of the impact of normalizing by analytical totals considering different major elements. Δ= Normalized value considering the analytical total as the sum of all analyzed major elements – Normalized value considering the analytical total withouth Mn0, P_2O_5 and Cl. The composition of secondary standards analyzed along with the samples are also shown and indicated in the figure, the y value in this case corresponds to the 95%CL. Only secondary standards with certified values are shown: GOR128-G, GOR132-G, KL2-G, ML3B-G, T1-G, StHs6/80-G, ATHO-G (Jochum et al., 2006), NISTSRM610 (Jochum et al., 2011), AGV-2, BIR-1, BHVO-1, BHVO-2, BCR-2, JA-1, JA-2, W-2 (Jochum et al., 2016), S-Y, OREAS184, OREAS700.

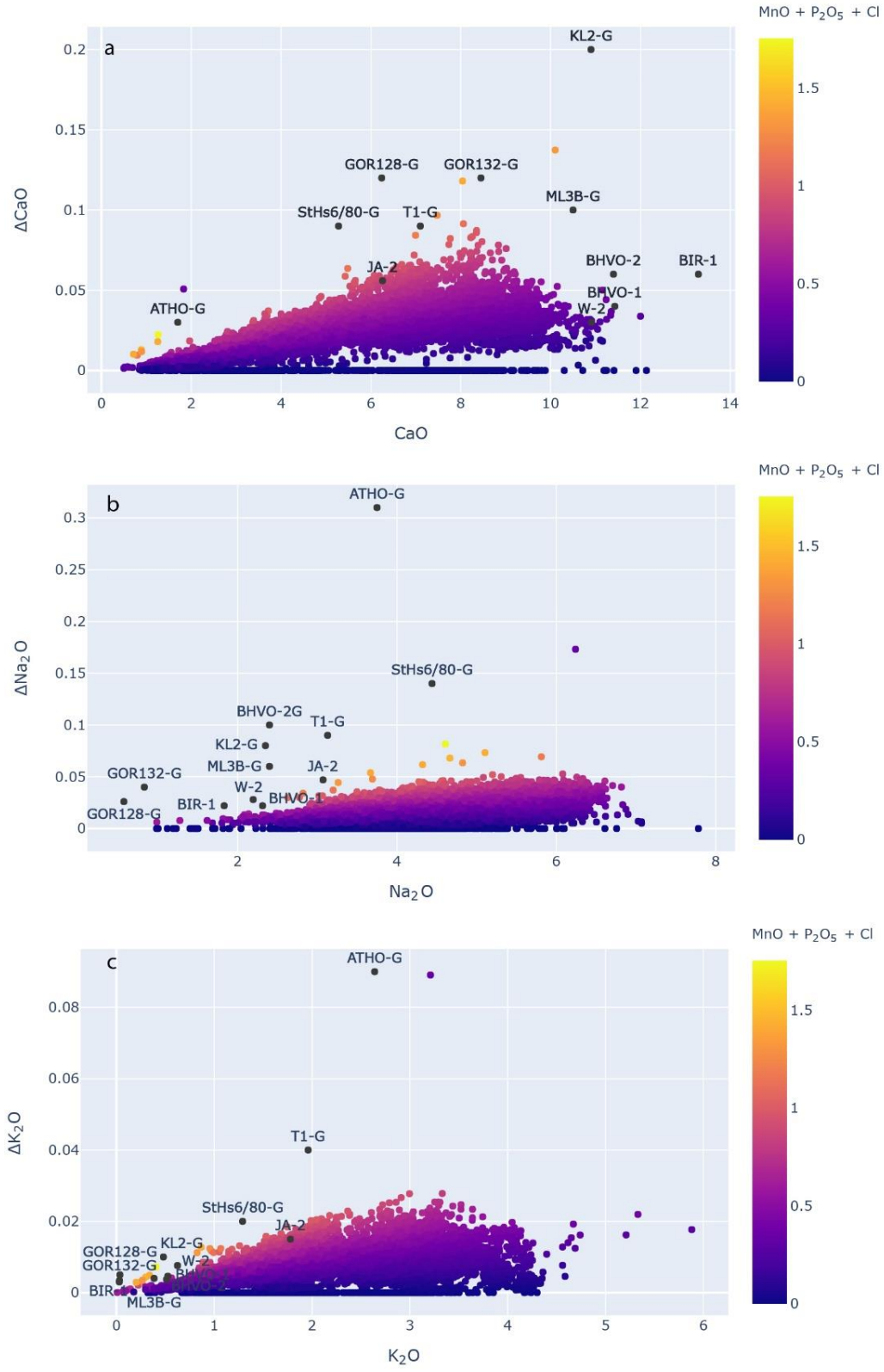

Figure S3.2. Assessment of the impact of normalizing by analytical totals considering different major elements. Δ= Normalized value considering the analytical total as the sum of all analyzed major elements – Normalized value considering the analytical total withouth Mn0, P_2O_5 and Cl. The composition of secondary standards analyzed along with the samples are also shown and indicated in the figure, the y value in this case corresponds to the 95%CL. Only secondary standards with certified values are shown: GOR128-G, GOR132-G, KL2-G, ML3B-G, T1-G, StHs6/80-G, ATHO-G (Jochum et al., 2006), NISTSRM610 (Jochum et al., 2011), AGV-2, BIR-1, BHVO-1, BHVO-2, BCR-2, JA-1, JA-2, W-2 (Jochum et al., 2016), S-Y, OREAS184, OREAS700.

Chapter 4: Post–glacial tephrochronology record off the Chilean continental margin (~41° S)

In Chapter 4, I describe the procedure for obtaining the tephrochronological records of marine sediment cores MD07-3098 and MD07-3100. For core MD07-3100, Giuseppe had already started the tephrochronological work, identifying the potential cryptotephras and analyzing their geochemical composition. For core MD07-3098 I developed this work. With this information I then proceeded to identify source of the cryptotephras and tephras in both cores. I then followed n analogous procedure for the tephrochronological record of core MD07-3081, described in chapter 5. This work is the base from which marine surface reservoir ages (Rs) in the studied area are later estimated in chapter 5, aiming to better constrain the chronologies of these cores. From this work, remains of eruptive activity were found in the whole studied interval of the marine sediment cores, highlighting the potential of using tephrochronology to improve the chronologies of cores in the Chilean Margin. One out of eight cryptotephras could be robustly correlated with eruptions on land in core MD07-3098; and 2 out of 17 in core MD07-1300; additionally, the volcanic source of 8 cryptotephras in core MD07-3100 were established. Cryptotephras that could not be robustly identified, can be determined in the future if trace elements are analyzed both in the marine sediment cores and on land; but also as more chronological constraints become available on land. Thus, the chronologies of these cores might be improved in the future by means of tephrochronology, building in the work here described.

The dataset and explorer described in chapter 3 were essential to robustly identify the source of the marine tephras, considering that most of them correspond to cryptotephras (remains of explosive eruptions not visible to the naked eye). This is relevant because cryptotephras can be transported from far away than tephras. Thus, the potential volcanic sources of the cryptotephras identified in the marine cores where around 30, many of which have had recurrent explosive activity during the last 20,000 years. The latter derived in an important bulk of data which I needed to understand in different dimensions (space, time, geochemistry), and the explorer was developed, in part, as a tool to help doing this.

In practice, chapter 4 corresponds a published article (Martínez Fontaine et al., 2021), and the full reference can be accessed in the supplementary material for this chapter.

Quaternary Science Reviews 261 (2021) 106928

Contents lists available at ScienceDirect

Quaternary Science Reviews

journal homepage: www.elsevier.com/locate/quascirev

Post–glacial tephrochronology record off the Chilean continental margin (~41° S)

Consuelo Martínez Fontaine [a, b, *], Giuseppe Siani [a], Guillaume Delpech [a], Elisabeth Michel [b], Gustavo Villarosa [c], Fatima Manssouri [b], Julius Nouet [a]

[a] Géosciences Paris-Saclay GEOPS/IPSL, UMR CNRS-Université Paris-Saclay 8148, Bat 504 - Université Paris-Saclay, 91405 Orsay Cedex, France
[b] Laboratoire des Sciences du Climat et de l'Environnement LSCE/IPSL, UMR CEA-CNRS-UVSQ 8212, Bat 714 - CEA Saclay, pièce 1034, Site de l'Orme des Merisiers Chemin de Saint Aubin - RD 128, F-91191 Gif sur Yvette Cedex, France
[c] Instituto Patagónico de Tecnologías Biológicas y Geoambientales IPATEC, CONICET-Universidad Nacional Del Comahue, Av De Los Pioneros 2350, 8400, San Carlos de Bariloche, Río Negro, Argentina

ARTICLE INFO

Article history:
Received 11 January 2021
Received in revised form
24 March 2021
Accepted 28 March 2021
Available online 26 April 2021

Handling Editor: I Hendry

Keywords:
Post–glacial
Quaternary
South America
Southern volcanic zone
Sedimentology-marine cores
Tephrochronology
Radiocarbon
Major and trace elements

ABSTRACT

The Southern Volcanic Zone of the Andes (~33–46° S) is a very active volcanic zone with several volcanic centers recording recurrent historical activity (e.g. Llaima, Villarrica, Puyehue-Cordón Caulle, Osorno, Calbuco and Hudson). Tephrochronology is a valuable tool to help better understand the eruptive history of volcanic centers, essential for producing volcanic hazard maps. Additionally, tephrochronology can also be very useful to synchronize stratigraphic records of different nature such as paleoclimatological, paleoceanographical and archaeological records on land, lakes, ice and the ocean. Here we present a (crypto) tephrochronological record from two marine sediment cores retrieved in the Chilean continental margin at ~41° S and ~41.6° S. The records display continuous sedimentation since the late glacial, as robustly constrained by planktonic foraminifera $\delta^{18}O$ and ^{14}C dates. During this period, twenty three cryptotephras were identified as glass shard peaks together with two ~25–30 cm–thick visible tephras (one in each core). The source of the (crypto) tephras was mainly constrained by major and trace element geochemistry of individual glass shards together with their stratigraphic position, since it is not possible to observe physical characteristics, such as color and grain size, when analyzing cryptotephras. From these, one cryptotephra was robustly correlated with the HW7 eruption from the Hudson volcano occurring in the Late Holocene at ~1.5 cal ka BP; and the two visible tephra layers were identified as distant correlatives of the Lepué tephra originating from Michinmahuida volcano and occurring in the Deglaciation/Holocene transition at around 11 cal ka BP. Additionally, eight cryptotephra occurring at ~3.6, 6.2, 7.0, 8.5, 9.6, 14.2, 15.9 and 18.2 cal ka BP were robustly identified as sourced from Michinmahuida volcano but where otherwise not correlated, providing novel evidence of pre Holocene activity of this volcanic center.

1. Introduction

Tephrochronology is a powerful tool not only to unveil the eruptive history of a territory, but to provide a robust chronological framework for its stratigraphic record. By identifying the pyroclastic remains of specific eruptions (tephra) in different sites, the eruptive history of a determined volcanic center can be reconstructed: its recurrence in time, the dispersion of its products and the magnitude of the different eruptive events. At the same time, the remains of the eruptions can be viewed as stratigraphic time markers, which provide regional chronological tie points for different records. When an explosive eruption occurs, the ejected pyroclastic material is deposited in different environments (land, lakes, ice caps, and the ocean) and by identifying its remains, the chronologies of paleoceanographic, paleoclimatological and archaeological records can be aligned, which is crucial when interpreting the evolution of complex systems, such as the climate.

The Southern Volcanic Zones of the Andes (SVZ) is a very active volcanic zone, composed of at least 60 active volcanic centers between 33° S and 46° S (Fig. 1), many of which have had recurrent

* Corresponding author.
E-mail addresses: consuelo.martinez-fontaine@universite-paris-saclay.fr, consuelola.m.f@gmail.com (C.M. Fontaine).

https://doi.org/10.1016/j.quascirev.2021.106928
0277-3791/

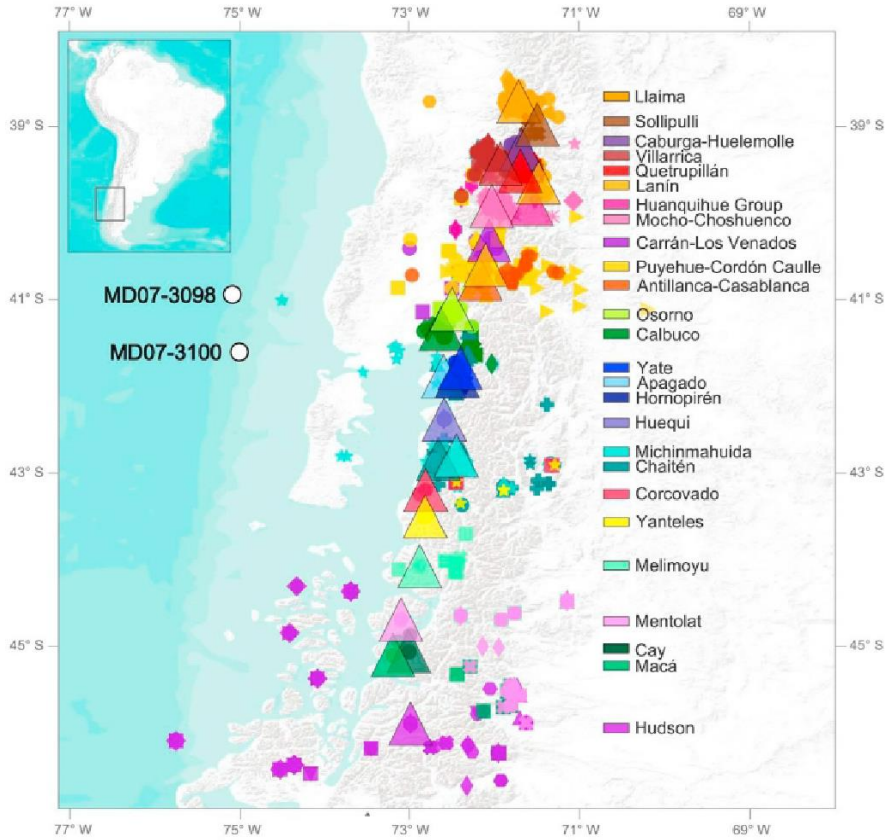

Fig. 1. Position of marine sediment cores MD07-3098 (-40.93° S, -75.03° W, 3055 m) and MD07-3100 (-41.60° S, -74.95° W, 1609 m), here studied. Additionally, volcanic centers of the Southern Volcanic Zone of the Andes which have been active since at least the late glacial are shown. Only volcanic centers between Llaima and Hudson volcanoes are considered, given the positon of the cores. Also shown are the position of tephrochronological samples which have been analyzed for geochemistry and/or dated. Each volcanic center and associated analyzed sample is assigned a particular color and each eruptive event a particular symbol (detailed legend and references in Fig. S16). (For interpretation of the references to color in this figure legend, the reader is referred to the Web version of this article.)

explosive volcanic activity in post–glacial times (~20 cal ka BP), such as Mocho-Choshuenco (Rawson et al., 2015), Chaitén (Alloway et al., 2017b; Amigo et al., 2013; Watt et al., 2013), Hudson (Haberle and Lumley 1998; Naranjo et al., 1993; Naranjo and Stern, 1998; Kratzmann et al., 2008; Carel et al., 2011; Weller et al., 2014, 2015); and/or in historical times, such as Llaima (Naranjo and Moreno, 1991, 2005; Reubi et al., 2011; Schindlbeck et al., 2014), Puyehue-Cordón Caulle (Alloway et al., 2015; Bertrand et al., 2014; Gerlach et al., 1988; Lara et al., 2006; Naranjo et al., 2017; Singer et al., 2008; Villarosa et al., 2006) and Calbuco (Morgado et al., 2019; Romero et al., 2016; Sellés and Moreno, 2011; Watt et al., 2011b). Since many of these volcanic centers are located nearby populated areas, volcanology together with tephrochronology become key in reconstructing their eruptive history, from which volcanic hazard maps are produced (e.g. Bertin et al., 2018; Moreno and Naranjo, 2002). At the same time, this recurrent explosive volcanic activity, together with the close proximity of the volcanic centers (Fig. 1), have produced a continuous and intricate tephrochronological record in the area (Fontijn et al., 2016), which is entangled within stratigraphic records on land, lakes, the ocean, peat bogs, etc. The latter has the potential of providing robust chronologies for paleo environmental records in Patagonia, crucial for understanding the behavior of global-scale climatic features thought to be important factors controlling glacial–interglacial transitions, such as the Southerly Westerly Winds (e.g. Menviel et al., 2018; Toggweiler et al., 2006) and upwelling in the Southern Ocean (e.g. Anderson et al., 2009; Siani et al., 2013).

In the last 40 years, the study of volcanology together with tephrochronology have increased importantly our understanding of the eruptive history of the SVZ since the late glacial period, revealing high recurrence and explosivity of previously thought to be much less active volcanic centers, such as Chaitén (Alloway et al., 2017b; Amigo et al., 2013; Iglesias et al., 2011; Moreno et al., 2014; Watt et al., 2013). However, it has also become apparent that there are still many volcanic centers in the area, such as Yate, Apagado, Hornopirén (Mella, 2008; Watt et al., 2011b), Yanteles and Corcovado (López-Escobar et al., 1993; Naranjo and Stern, 2004) for which the eruptive history is largely unknown. Efforts towards increasing our knowledge of the volcanic activity in the SVZ include undertaking field work in previously relatively less researched areas (Watt et al., 2011a, b) and increasing the research around specific particularly active volcanic centers such as Puyehue-Cordón Caulle (Alloway et al., 2015; Bertrand et al., 2014; Gerlach et al., 1988; Lara et al., 2006; Naranjo et al., 2017; Singer et al., 2008) and Hudson (Kratzmann et al., 2008; Naranjo et al., 1993; Naranjo and Stern, 1998; Weller et al., 2014). Understanding the eruptive history of this area has additionally benefited from the study of records such as peat (e.g. Stern, 2008; Weller et al., 2019), lake (Bertrand et al., 2008; Fontijn et al., 2014; Moreno et al., 2014; Watt et al., 2011b) and marine sediment cores (Carel et al., 2011). These records provide particularly relevant information in areas were the on land record of the eruptions is not available, either

because it is of difficult access, it is in a highly vegetated area (such as volcanoes south of ~42° S), or because it has been eroded, for example by the presence of the Patagonian Ice Sheet (PIS), which covered most of the SVZ south of ~38° S during the late glacial period (Davies et al., 2020). Additionally, if continuous sedimentation occurs, paleoenvironmental signals such as palynological or marine isotopic curves can be obtained from lake or sediment cores, which together with ^{14}C ages provide a more comprehensive context in which the tephras were deposited.

Because of the latter, marine sediment cores retrieved in the Chilean continental margin have great potential of providing relevant information to help complete the tephrochronological record in the area. However, as a result of the predominant wind pattern, it is expected that most eruptions leave rather thin ash deposits within marine sediments as opposed to potent tephra layers, which are routinely studied on land. Cryptotephrochronology identifies the remains of past volcanic eruptions which are invisible to the naked eye, and thus can be used to identify the remains of SVZ eruptions in the Chilean continental margin. Here we use both a tephrochronological and cryptotephrochronological approach to find evidence of past volcanic eruptions in two marine sediment cores retrieved in the Chilean continental margin (Fig. 1): core MD07-3098 (~40.93° S, ~75.03° W, 3055 m) and core MD07-3100 (~41.60° S, ~74.95° W, 1609 m). Since physical characteristics of tephras such as grain size, thickness and color, cannot be used in the identification of the volcanic source of the cryptotephras, their characterization is based on the geochemical composition (major and trace elements) of individual glass shards together with the stratigraphic position of the cryptotephras, given by planktonic foraminifera $\delta^{18}O$ and ^{14}C ages.

2. Volcanological context

The SVZ is one of the four volcanic zones that have been defined in the Andes (Northern (3–6° S), Central (15–27° S), Southern (33–46° S) and Austral (49–55° S); Stern, 2004), which, together with the northern and central zones, derive from the subduction of the Nazca plate under the South American plate. In particular, the SVZ corresponds to the volcanic activity between Tupungatito (~33° S) and Hudson (~46° S) volcanoes, where so far ~60 active volcanic centers have been identified, many of which have recorded recurrent explosive activity in post–glacial times (Global Volcanism Program, Smithsonian Institution). The volcanic products in the SVZ are characterized by a geochemical composition typical of subduction zones: calc–alkaline trends with medium to high–K, relatively high mobile incompatible element concentrations (Cs, Rb, K, Sr, Ba, Pb, Th, U), low REE and HFSE (Zr, Hf, Ta, Nb).

Among the more active and explosive volcanic centers in the area are Puyehue-Cordón Caulle, Calbuco, Michinmahuida and Hudson. Puyehue-Cordón Caulle, situated at ~40.6° S (Fig. 1), consists of the Puyehue volcano, which has been active since at least ~300 ka, and the Cordón Caulle fissure, active at least since ~170 ka (Singer et al., 2008). The products from Puyehue-Cordón Caulle range from basaltic to rhyolitic with medium/low–K to medium/high–K affinities (Alloway et al., 2015; Bertrand et al., 2014; Gerlach et al., 1988; Lara et al., 2006; Naranjo et al., 2017; Singer et al., 2008). The most recent explosive events of Puyehue-Cordón Caulle occurred in 1921–1922, 1960 and 2011, the last of which had a Volcanic Explosivity Index (VEI) of 5 (Naranjo et al., 2017), and all of which erupted mainly rhyolitic products. Other eruptive events of similar magnitude have been described in the literature during the Holocene, such as Mil Hojas, Puyehue 2/PCC2 and Puyehue 1/PCC1 (Fontijn et al., 2016; Lara et al., 2006; Naranjo et al., 2017; Singer et al., 2008); and many effusive products corresponding to deglacial times have been dated (Singer et al., 2008) although no explosive correlatives have been identified yet.

The Calbuco volcano, situated at ~41.3° S, has also recorded continuous volcanic activity since around 300 ka (Sellés and Moreno, 2011) and extensive historical activity (e.g. 1792, 1893, 1917, 1929, 1932, 1945, 1961, 1972, 2015) the last of which had a VEI of 4 (Romero et al., 2016). As with Puyehue-Cordón Caulle, Holocene tephras have been more thoroughly described (Watt et al., 2011b), but evidence of explosive activity during the Deglaciation has also been found and dated (Sellés and Moreno, 2011). Most products from Calbuco are andesites or basaltic andesites that have medium to low–K geochemical affinities (López-Escobar et al, 1992, 1995López-Escobar et al., 1995; Sellés and Moreno, 2011).

The Michinmahuida volcano is located at ~42.8° S in a little populated area and has no record of historical activity, however recurrent Holocene activity has been proposed in the literature (Amigo et al., 2013; Moreno et al., 2014). One of the most widespread tephra in the area is associated with Michinmahuida: the Amarillo Ignimbrite, also called the Lepué tephra (Alloway et al., 2017a; Amigo et al., 2013). The eruption that produced this tephra occurred at the beginning of the Holocene (~11 cal ka BP) and erupted bimodal products ranging from basaltic andesites to rhyolites with medium to high–K affinities and has been estimated to have had a VEI of 6 (Amigo et al., 2013).

The Hudson volcano is located at ~46° S in a little populated area difficult to access, as Michinmahuida volcano. Contrastingly, more information can be found about the Hudson volcano than for Michinmahuida, probably because of its highly explosive post–glacial and historical activity, notably, its 1991 eruption with a VEI 4 (Naranjo et al., 1993). Products of Hudson range from basaltic andesites to rhyolites with medium to high–K affinities (Carel et al., 2011; Haberle and Lumley, 1998; Kratzmann et al., 2008; López-Escobar et al., 1993; Naranjo et al., 1993; Naranjo and Stern, 1998; Weller et al., 2014, 2015) and at least 8 tephras have been described and dated in the literature (Ho, HW1, HW2, HW3, H1, H2, HW6 and HW7), the oldest one: Ho, occurred around ~17 cal ka BP with an estimated VEI of 6 and has been identified as far as ~900 km SE of the volcano (Weller et al., 2014).

The presence of the cryptotephra layers in marine cores, retrieved west of the volcanic centers can be somewhat counter-intuitive because the dispersion of volcanic ash in the SVZ is largely controlled by the prevailing Southerly Westerly Winds in the area. From what is observed in the literature, but also in modern eruptions such as Chaitén, 2008 (Watt et al., 2009) and Puyehue Cordón Caulle, 2011 (Bertrand et al., 2014), most of the ash produced by explosive eruptions in the central (37–42° S) and southern (42–46° S) zones of the SVZ are transported to the east by the Southerly Westerly Winds, the Subtropical jet and/or the Polar Front Jet (Gallego et al., 2005; Rahn and Garreaud, 2014). A lesser amount of the eruptions record a predominantly northward dispersion, which is associated with the southeast Pacific subtropical anticyclone transporting ashes to the north (Rahn and Garreaud, 2014). Among these, Cha1 from Chaitén (Watt et al., 2013; Fontijn et al., 2016), Neltume from Mocho-Choshuenco (Fontijn et al., 2016; Rawson et al., 2015) and the Hudson eruption in 1991 (Naranjo et al., 1993). Less frequently, winds to the south and to the west also occur as part of smaller scale phenomena, such as low pressure systems and changes associated to the Southern Hemisphere's baroclinic annular mode (Pérez-Santos et al., 2019), for example during the 2015 eruption of Calbuco (Romero et al., 2016). The latter might explain the less common occurrence of tephra deposits to the west and northwest of volcanoes, such as HW1–7 (Haberle and Lumley, 1998) and Lepué Tephra (Alloway et al., 2017a). Thus, even though ash transported by these short–lived wind directions might not be enough to deposit potent tephra in the ocean in most cases, they are enough to deposit thin ash layers and thus leave traces of

past volcanic eruptions identifiable via cryptotephrochronology.

3. Methods

3.1. Core retrieving

Marine sediment cores MD07-3098 (~40.93° S, ~75.03° W, 3055 m) and MD07-3100 (~41.60° S, ~74.95° W, 1609 m) are two CALYPSO cores retrieved by the French R/V Marion Dufresne during the PACHIDERME expedition in February 2007 (Kissel and The Shipboard Scientific Party, 2007). MD07-3098 is a 20.74 m long core composed mainly of silty clay with silty and sandy layers horizons, which also contains a visible tephra layer of ~30 cm between ~7.6 and 8 m labeled T6/98. MD07-3100 is a 29.8 m long core composed mainly of homogenous silty clays, which displays a visible tephra layer of ~25 cm between 7.25 and 7.5 m labeled T8/100. For this study, the first 13.5 m and 15 m from core MD07-3098 and MD07-3100 (respectively) have been analyzed, which correspond to the post–glacial portion of these sedimentary archives. Because of the difference in lithology given by the presence of the tephra, both cores present a ~25 cm gap in the upper part of the visible tephra (Fig. 2), which are corrected for in the age models.

3.2. Stable isotope stratigraphy

The stratigraphic constraint of the cores is provided by stable oxygen isotope data ($\delta^{18}O$) measured in planktonic foraminifera at the Laboratoire des Sciences du Climat et l'Environnement (LSCE) on Optima VG, GV Isoprime and Finnigan Delta + mass spectrometers. Isotopic measurements were made every 10 cm in one to thirty specimens of planktonic foraminifera *G. bulloides* (250–315 μm fraction) in both cores. This information allowed for a first order identification of the timeframe the cores span (Fig. 2). The measurements stopped where a stable late glacial isotopic signal was reached, at ~13.5 m in core MD07-3098 and ~15 m in core MD07-3100. Results from core MD07-3100 have already been published by Haddam et al. (2018) and those for core MD07-3098 are displayed in Table S1.

3.3. Tephra and cryptotephra identification

Cryptotephra layers were identified as peaks in the relative amount of glass shards and micro–pumice. The cores were sampled every 10 cm in 4 cc box samples, washed, sieved for the fraction>40 μm and rinsed in a 10% HCl solution to dilute the carbonated fraction and allow for the identification only of the detrital fraction. The percentage of glass shards and micro–pumice was obtained by counting the relative amount of glass shards, micro–pumice, crystals, lithics and other detrital material in the detrital fraction >40 μm in at least 300 particles per sample. Primary glass shards and micro–pumice were identified as having pristine angular morphologies with fragile tips and no remineralization coatings (Fig. S1). In most depths glass shards color range from a brown-honey color to white, with diverse degrees of vesicularity. The glass shard and micro–pumice peaks were considered where the percentage exceeded the background value at least three times. For core MD07-3100, 115 samples were counted each 10 cm between 60 and 1220 cm, the background was around 5% and sixteen glass shard and micro–pumice peaks were identified as cryptotephras and analyzed for geochemistry with peak values between 15 and 45%. For core MD07-3098, 86 samples were counted with a resolution between 10 and 20 cm, from 1 to 1321 cm depth, the background was 6% and seven glass shard peaks were identified as cryptotephras and analyzed for geochemistry with peak values between 18 and 27%.

In both cores, the visible tephras are recognized by an important change in lithology easily recognizable as a change from olive brown silty clay to black sand (Fig. 2). Both tephras present a sharp erosive contact at the base and graded at the top. Because of the graded upper contact, the upper limit of the tephras were identified as an important drop in the glass shard and micro–pumice count in both cores. Additionally, as mentioned in section 3.1, both cores present a gap in the upper part of the tephra deposits, thus the thickness of each tephra is estimated as the sum of the thickness above and below each gap.

3.4. Geochemistry

In order to characterize the geochemistry of the cryptotephras and visible tephras, individual glass shards from the identified layers were hand–picked and mounted in epoxy resin beads and polished on an automated polish wheel to avoid compositional variations due to surficial alteration processes. Major element where determined for each individual glass shard with a CAMECA-SX 100 Electron Microprobe (EPMA-CAMPARIS) at the University Paris VI (France). Ten elements were analyzed (Na, Mg, Si, Al, Cl, K, Ca, Ti, Mn and Fe) using an accelerating voltage of 15 KV, a current of 10 nA and a beam size of 5 μm to minimize loss of alkalis such as Na and the results are presented in Table S2. The instrument calibration was done using natural mineral standards (e.g. Na is calibrated from albite, K from Orthose, Si, Ca and Mg from diopside, Fe from hematite). Precisions on individual shards (1σ) were better than 0.6% for Si, ~1% for Al, 3% for Ca and Mg, 4% for Na, 5% for Fe, 6% for K, 10% for Ti and about 30% for Cl and Mn. The in-house glass standard Lipari was also analyzed as an unknown sample during the analytical sessions (Table S4) and display comparable values to published data (Jochum et al., 2007). As seen on Fig. S1, glass shards from different cryptotephra layers and even in a single layer (T8/100) might have very different aspects, such as highly vesiculated and microlite–rich glass shards coexist with non–vesiculated microlite–poor glass shards. Attention was paid to analyze glass shards with the less microlites possible and between ~10 and 30 analyses were acquired for each cryptotephra. Major element data obtained here, as well as those from the literature, were normalized to 100% before plotting in order to being able to compare the analyses.

Additionally, trace element concentrations were measured in ten of the sixteen depths in core MD07-3100 with a Laser Ablation High Resolution ICP-MS (LA-HR-ICPMS) at GEOPS laboratory (Paris-Saclay University). Results are presented in Table S2. For the ablation, a CETAC-Teledyne Excimer 193 nm laser system was connected to an Element XR HR-ICP-MS and the sample was transported to the torch using He gas. A frequency of 5 Hz and a fluence of 3.65 J/cm^2, for a spot size of 40 μm were used during analyses. The instrument was calibrated using the international glass standard NIST 612 as an external standard. In order to cover the large range of silica contents determined by EMPA for the glass shards, international glass standards of rhyolitic (ATHO-G; 75.6 wt% SiO_2) or basaltic (KL2-G; 50.3 wt% SiO_2) compositions were also run as unknown samples to control the quality of the measurements (Table S4). The reported values in Table S4 compare well with the preferred values from GEOREM (Jochum et al., 2007). For the purpose of the study, internal standards KL2-G and ATHO-G gave a precision (1σ) on La between 2.4 and 3.7%, between 2.7 and 5.2% for

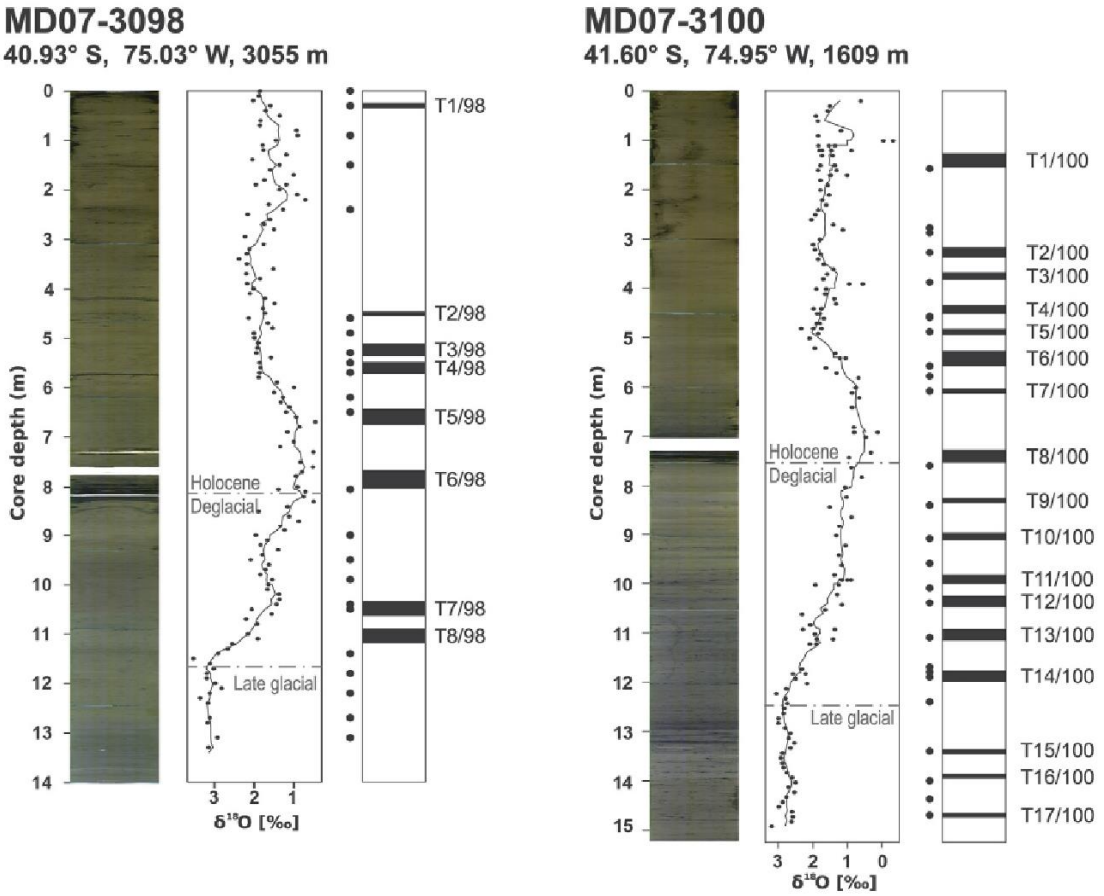

Fig. 2. Stratigraphy from cores MD07-3098 and MD07-3100. Left: Composite photograph of each core, showing the position of the visible tephras as a dark layer at around 8 m (T6/98 in MD07-3098) and 7.5 m (T8/100 in MD07-3100). Middle: $\delta^{18}O$ from planktonic foraminifera *G. bulloides*; dots indicate measurements every 10 cm, the curve corresponds to the three point moving average. Also indicated are climate intervals inferred from the observed changes in $\delta^{18}O$. Right: Depths considered as potential cryptotephra layers (relative glass shard peaks) labeled T1/98 to T8/98 (MD07-3098) and T1/100 to T17/100 (MD07-3100), together with the position where planktonic foraminifera ^{14}C ages where obtained as dark grey dots. Details for $\delta^{18}O$ and ^{14}C measurements in core M07-3098 in Tables S1 and S5 and for core MD07-3100 in Haddam et al. (2018).

Yb, between 3.2 and 3.7% for Zr and between 2 and 2.5% for Nb (Table S4).

3.5. Radiocarbon dating

After identifying the glass shard and micro–pumice peaks, planktonic foraminifera were picked either at the base or in the middle of the peak, according to foraminifera peak abundances. Radiocarbon dates for core MD07-3100 are published in Haddam et al. (2018) whereas new radiocarbon dates for core MD07-3098 are presented in Table S5. Either mono specific *G. bulloides* or mixed planktonic foraminifera were picked from the >150 μm fraction, samples >3 mg were measured at UMS-ARTEMIS (Pelletron 3 MV) AMS facilities (CNRS-CEA Saclay, France, Dumoulin et al., 2017; Moreau et al., 2013), whereas samples <3 mg were analyzed on the gas ion source ECHoMICADAS at the LSCE (Gif-Sur-Yvette, France) using coupling of cracker system to the gas handling system (Wacker et al., 2013; Tisnérat-Laborde et al., 2015). ^{14}C results are reported in conventional age BP according to the convention of Stuiver and Polach (1977), normalized to the base of $\delta^{13}C$ of −25.0‰ relative to the Pee Dee Belemnite (PDB) international standard, and corrected by the age of the background subtraction. The age model for the cores was then obtained with the software Undatable (Lougheed and Obrochta, 2019) with a depth uncertainty of 1 cm, corresponding to the sampling width, and calibrating according to SHCal20 curve (Hogg et al., 2020).

4. Results

4.1. Chronological framework

The obtained stable isotope stratigraphy (Table S1, Fig. 2) reveals that both studied cores cover at least the time interval between the late glacial and the Late Holocene and register similar variations and sedimentation rates since. The MD07-3100 $\delta^{18}O$ record displays steady values around 2.7‰ between ~12.5 and 15 m, which characterizes the late glacial in the core (Fig. 2). A deglacial decreasing trend is observed between ~12.5 and 7.5 m, when values decrease from ~2.7 to ~0.9‰ interrupted by two plateaus: around ~11 m and ~8–10 m. Minimum values of ~0.9‰ PDB are reached at ~7.5 m, coincident with the occurrence of the ~25 cm visible tephra (T8/100). Values characteristic of the Holocene are observed between ~7.5 m and the top. In particular: around 7 m $\delta^{18}O$ values reach its mean global minimum of around 0.9‰, followed by a steady increase until 2‰ between 6 and 5 m and finally, between ~5 and 0 m somewhat steady values of around 1.6‰ occur, with two intervals of lower values between ~3.6 and 4 and ~0.7–1 m.

The late glacial is observed in core MD07-3098 between ~13.5

and 11.7 m with steady values around 3‰ (Fig. 2). A deglacial decrease is observed between ~11.7 and 8.1 m. Between ~11.7 and 10.2 m values decrease until 1.5‰, a slight increase until 1.6‰ is observed between ~10.2 and 9 m, followed by a steady decrease until reaching minimum values of ~0.9‰ at 8.1 m, coincident with the presence of a ~30 cm thick tephra layer (T6/98). Minimum values of ~0.9‰ maintain until 6.6 m. Between ~6.6 and 5.6 m, values steadily increase until ~1.8‰ and are maintained at this value until ~3.2 m. From ~3.2 m to the core top values are relatively lighter and more variable.

The age model of core MD07-3098 was obtained from 27 planktonic ^{14}C ages (Table S5; Fig. S3), corrected by a mobile marine surface reservoir age (Rs), following the method by Haddam et al. (2018) for core MD07-3100. The similarity of the $\delta^{18}O$ curves of both cores versus their planktonic ^{14}C age (Fig. S2) suggests that they record variations of the same water mass (Subantarctic Water) in the studied time interval. Thus, we apply the same Rs correction used for MD07-3100 by Haddam et al. (2018) to the planktonic ^{14}C ages from core MD07-3098 (Table S5). The conventional radiocarbon ages were subsequently calibrated according to the SHCal20 curve (Hogg et al., 2020) and the age model was obtained with the software Undatable (Lougheed and Obrochta, 2019).

From the resulting age model (Table S1; Fig. S3, S4), core MD07-3098 has relatively high and nearly constant sedimentation rates during the Holocene and Deglaciation of ~70 cm/ky. Core MD07-3100 has nearly constant sedimentation rates of ~65 cm/ky during the whole studied interval (Haddam et al., 2018). The age model together with the stable isotope stratigraphy indicate that in the studied cores, the late glacial ends between 17 and 16.5 cal ka BP (Fig. S4), the Deglaciation occurs between ~17 and 16.5 and ~10.5 cal ka BP and the Holocene between ~10.5 cal ka BP and the present.

4.2. Cryptotephras

In core MD07-3100, sixteen depths where relative glass shard and micro–pumice peaks occurred were recognized as cyrypto-tephra layers labeled T1/100 to T17/100, in addition to T8/100 (Fig. 2, Table 1). From the stable isotope stratigraphy, cryptotephra T1/100 through T7/100 occur during the Holocene, T8/100 in the Holocene/Deglaciation transition, T9/100 to T14/100 during the Deglaciation and T15/100, T16/100 and T17/100 during the late glacial.

In core M07-3098, seven depths where relative glass shard and micro–pumice peaks occur were identified as cryptotephra layers labeled T1/98 to T8/98, in addition to the visible tephra layer T6/8 (Fig. 2, Table 1). T1/98 through T5/98 occur in the Holocene portion of the core, T6/98 in the Holocene/Deglaciation transition and T7/98 and T8/98 during the Deglaciation.

4.3. Geochemistry of the marine ash layers

All analyzed samples display major element composition belonging to the calc–alkaline series and most can be classified as medium–K to high–K, with rare glass shards of low-K affinity (Figs. 3–5, Table S2, 3). Major elements in all samples follow a trend, either bimodal or continuous, ranging from basaltic andesite (minimum value of 49.8 wt% SiO_2 in cryptotephra T8/100) to rhyodacite or rhyolite (maximum 77.8 wt% SiO_2 in cryptotephra T9/100).

Three groups can be defined based on the relative amount of K_2O versus SiO_2:

- Group 1 (Fig. 3, S5): samples with relatively high–K contents (0.7–3.9 wt% K_2O), with basaltic andesitic (52–56 wt% SiO_2), andesitic (56–63 wt% SiO_2) and dacitic composition (63–70 wt% SiO_2) plot along the boundary between medium and high-K fields (Peccerillo and Taylor, 1976) and points with rhyolitic composition in the high-K field (>70 wt% SiO_2). The two visible tephras T6/98 and T8/100 and eleven cryptotephras among the twenty three analyzed, fall in this group, notably T1/100 through T7/100, T12/100, T14/100, T15/100 and T17/100;
- Group 2 (Fig. 4, S6): samples with relatively lower K contents than Group 1 (0.4–4.21 wt% SiO_2). Basaltic andesitic and andesitic compositions plot in the medium–K field and sample points with dacitic and rhyolitic compositions at the boundary between medium–K and high–K. Eleven cryptotephras belong to this group: T1/98 through T5/98, T7/98, T9/100, T10/100, T11/100, T13/100, T16/100;
- Group 3 (Fig. 5, S7): restricted to cryptotephra T8/98, which has consistently lower K contents (0.7–1.3 wt% K_2O; with the exception of one outlier with high–K around 4.2 wt% K_2O), plotting near the low/medium–K field boundary, especially at dacitic and rhyolitic composition.

Additionally, nine cryptotephras from core MD07-3100 were analyzed for trace elements: T1/100, T2/100, T4/100, T5/100, T6/100, T7/100, T9/100, T12/100, T14/100 and T15/100 together with tephra T8/100. Overall these samples are relatively enriched in the most incompatible elements (Rb, Ba, Th, U), have lower HFSE (negative anomaly of Nb, Ta) and lower REE and Sr contents and display a positive anomaly in Pb. Three different behaviors are observed when analyzing the La/Yb versus Zr/Nb ratios of the samples (Figs. 3b and 4b): cryptotephra layers T2/100, T4/100, T5/100, T6/100, T7/100, T8/100, T12/100, T14/100 and T15/100 form a cluster with La/Yb values between ~4 and 7 and Zr/Nb between ~17 and 31; T1/100 has relatively higher La/Yb values between ~8 and 12 and Zr/Nb values between ~20 and 25; and T9/100 displays more dispersed values, with La/Yb between ~5 and 11 and Zr/Nb between ~18 and 30.

4.4. Correlations

For the identification of the potential source of the tephras and cryptotephras, we compared the geochemistry of the glass shards here analyzed with the geochemistry of both explosive and effusive products that were analyzed by both micro analytical and bulk geochemical methods from volcanic centers between Llaima and Hudson. The latter is achieved taking into account that for some of the volcanic centers in this area no micro analytical data were found in the literature (e.g. Yanteles and Corcovado by Naranjo and Stern (2004)) and that, especially for older eruptions, only effusive products were analyzed (e.g. Puyehue-Cordón Caulle by (Singer et al., 2008)). Additionally, previous work in the region has previously shown that a similar geochemical trend is followed by effusive and explosive products from the Hudson volcano (Carel et al., 2011), which is also observed in the literature here considered (Fig. S8, S9). Most of this literature corresponds to major element compositions, from which it can be observed that the major element signature of many volcanoes overlap (Fig. S10). Thus major element compositions cannot be used alone to pinpoint the volcanic source of the cryptotephras. Nevertheless, the potential volcanic sources can still be narrowed down based on their K_2O versus SiO_2 contents. With this in mind, in the following section, we organize the discussion regarding the potential source of the tephras and cryptotephras according to the three groups previously defined based on the relative amount of K_2O versus SiO_2 together with some key trace element ratios of the analyzed samples, when available (Figs. 3–5). The potential eruptive event is further constrained based on the stratigraphy and estimated age of the tephras

Table 1
Summary of identified tephras and cryptotephras in cores MD07-3098 and MD07-3100.

Cryptotephra	Core	Depth range (cm)	Calendar age median (years BP)	Calendar age 1σ range	Calendar age 2σ range	Group	Source	Potential correlative
T1/98	MD07-3098	25–35	294	445–132	747–62	Group 2		YA2?
T2/98	MD07-3098	445–455	6233	6410–5999	7053–5856	Group 1		
T3/98	MD07-3098	505–535	7633	7853–7320	8019–7027	Group 2		PCC2?
T4/98	MD07-3098	545–570	7928	8138–7738	8380–7639	Group 2		
T5/98	MD07-3098	645–675	9356	9581–9124	9916–8939	Group 2		PCC1?
T6/98	MD07-3098	764–801	10,512	10,702–10296	11,265–10050	Group 1	Michinmahuida	Lepué
T7/98	MD07-3098	1030–1060	13,965	14,387–13681	14,919–13546	Group 2		
T8/98	MD07-3098	1090–1120	15,472	15,778–15163	15,991–14596	Group 3		
T1/100	MD07-3100	130–160	1557	1410–1720	1315–1855	Group 1	Hudson	HW7
T2/100	MD07-3100	320–340	3635	3895–3382	4118–3141	Group 1	Michinmahuida	LTT-10?
T3/100	MD07-3100	370–385	4117	4342–3939	4424–3745	Group 1		
T4/100	MD07-3100	440–460	6170	6694–5716	6992–5122	Group 1	Michinmahuida	LTT14? LTT-15? MIC1?
T5/100	MD07-3100	485–495	7044	7214–6838	7520–6686	Group 1	Michinmahuida	LTT15? MIC1?
T6/100	MD07-3100	530–560	8514	8636–8364	8812–8228	Group 1	Michinmahuida	LTT20?
T7/100	MD07-3100	605–615	9603	9703–9478	9892–9318	Group 1	Michinmahuida	
T8/100	MD07-3100	728–755	10,616	10,706–10440	10,938–10348	Group 1	Michinmahuida	Lepué
T9/100	MD07-3100	825–835	12,163	12,464–11941	12,604–11760	Group 2		
T10/100	MD07-3100	895–915	12,839	12,966–12671	13,151–12575	Group 2		
T11/100	MD07-3100	980–1005	13,812	13,906–13672	14,047–13596	Group 2		
T12/100	MD07-3100	1025–1050	14,154	14,296–13950	14,533–13808	Group 1	Michinmahuida	
T13/100	MD07-3100	1125–1145	15,253	15,493–15048	15,701–14,777	Group 2		
T14/100	MD07-3100	1170–1190	15,930	16,063–15775	16,228–15649	Group 1	Michinmahuida	
T15/100	MD07-3100	1345–1355	18,226	18,422–18030	18,595–17870	Group 1	Michinmahuida	
T16/100	MD07-3100	1385–1395	19,386	19,709–19193	19,900–18758	Group 2		
T17/100	MD07-3100	1465–1475	20,448	20,638–20266	20,818–20080	Group 1		

and cryptotephras.

4.5. Group 1

The thirteen tephras and cryptotephras belonging to Group 1, with relatively higher K (0.7–3.9 wt% K_2O), especially at silica levels higher than ~68 wt% SiO_2 (Fig. 3a, S4), display a geochemical trend similar to volcanoes Michinmahuida (Alloway et al., 2017a; Amigo et al., 2013; Naranjo and Stern, 2004), Hudson (Carel et al., 2011; Del Carlo et al., 2018; Haberle and Lumley, 1998; Kratzmann et al., 2008; López-Escobar et al., 1993; Naranjo et al., 1993; Naranjo and Stern, 1998; Smith et al., 2019; Stern, 2008; Weller et al, 2014, 2015), Quetrupillán (Brahm et al., 2018; Fontijn et al., 2016; Hickey-Vargas et al., 1989; Rawson et al., 2016; Simmons et al., 2020) and Yate (López-Escobar et al., 1993; Mella, 2008; Watt et al., 2011b). These volcanic centers can be further discriminated by means of their trace element geochemistry, in particular, their Zr/Nb versus La/Yb ratios (Fig. 3b). From the thirteen tephras and cryptotephras in this group, one tephra and nine cryptotephras have been analyzed for trace elements: T1/100, T2/100, T4/100, T5/100, T6/100, T7/100, T8/100, T12/100, T14/100 and T15/100. When comparing their Zr/Nb versus La/Yb ratios, with the available information from Michinmahuida, Hudson, Quetrupillán and Yate, the tephra (T8/100) and eight of the nine cryptotephra layers (T2/100, T4/100, T5/100, T6/100, T7/100, T12/100, T14/100 and T15/100) display compositions similar to Michinmahuida and one cryptotephra (T1/100) displays compositions similar to Hudson. Similar behaviors are observed when looking at other trace elements (Fig. S11), such as Zr versus Y, La versus Tm and Th versus Nb, although the differences among the different volcanic centers are not as clear as in the case of La/Yb versus Zr/Nb.

In addition, one potential correlation among the marine sediment cores can be established.

In the following section we discuss the potential correlative of each cryptotephra based on its stratigraphic position, estimated calendar age and available geochemical information on land from the potential sources. Because many of the cryptotephras display a Michinmahuida signature, we discuss them together.

4.5.1. T1/100

The stratigraphic position of this cryptotephra corresponds to the Late Holocene, with an estimated mean calendar age at its base of ~1.6 (1σ: 1.7–1.4) cal ka BP (Table 1). Around this time, two of the volcanic centers associated with Group 1: Hudson and Quetrupillán, had eruptions recorded in the literature (Fig. 6): HW7 from Hudson (~1.5 cal ka BP; 1σ: 1.7–1.4; Haberle and Lumley, 1998), Quet5 (~1.7 cal ka BP; 1σ: 1.8–1.6) and Puesco (~1.9 cal ka BP; 1σ: 2–1.8; Fontijn et al., 2016) from Quetrupillán. Individual glass shard major element geochemistry has been obtained for all of these eruptions and therefore we can compare their geochemical fingerprints with those of the marine cryptotephras (Fig. 3c). From these, T1/100 displays values closer to HW7 (Carel et al., 2011; Haberle and Lumley, 1998), both of which follow a bimodal trend. In contrast Quet5 and Puesco only display more evolved products, between 65 and 68 wt% SiO_2, thus the less evolved part of the trend, observed in T1/100, is absent. Major and trace element data thus support the Hudson volcano as the source of the T1/100 cryptotephra (Fig. 3a, b, c, S7). We propose T1/100 as a distant correlative of the HW7 eruption of the Hudson volcano. The latter is consistent with prior information indicating a northwest dispersion of some Hudson volcano products (Fig. 6) such as eruptions HW2, HW3, HW6, HW1 and HW7, found in lake cores in Taitao peninsula and Chonos archipelago (Haberle and Lumley, 1998) as well as in marine sediment core MD07-3088 (Carel et al., 2011).

4.5.2. T3/100

Cryptotephra T3/100 occurs in the Late Holocene at an estimated calendar age of ~4.1 (1σ: 4.3–3.9) cal ka BP. During this time period, from the volcanoes in Group 1, only Hudson has a recorded eruption (Fig. 6): H2 at ~4 cal ka BP (Naranjo and Stern, 1998). From the comparison of the major element geochemistry, it is plausible that T3/100 corresponds to the eruption H2 (Fig. 3e), however H2 corresponds to fairly evolved products ranging from 64 to 70 wt% SiO_2 whereas T3/100 also presents a less evolved cluster between 54 and 56% SiO_2 not present in H2, as documented in the literature. As mentioned before, the major element geochemistry of T3/100 is also consistent with Yate, Michinmahuida and Quetrupillán

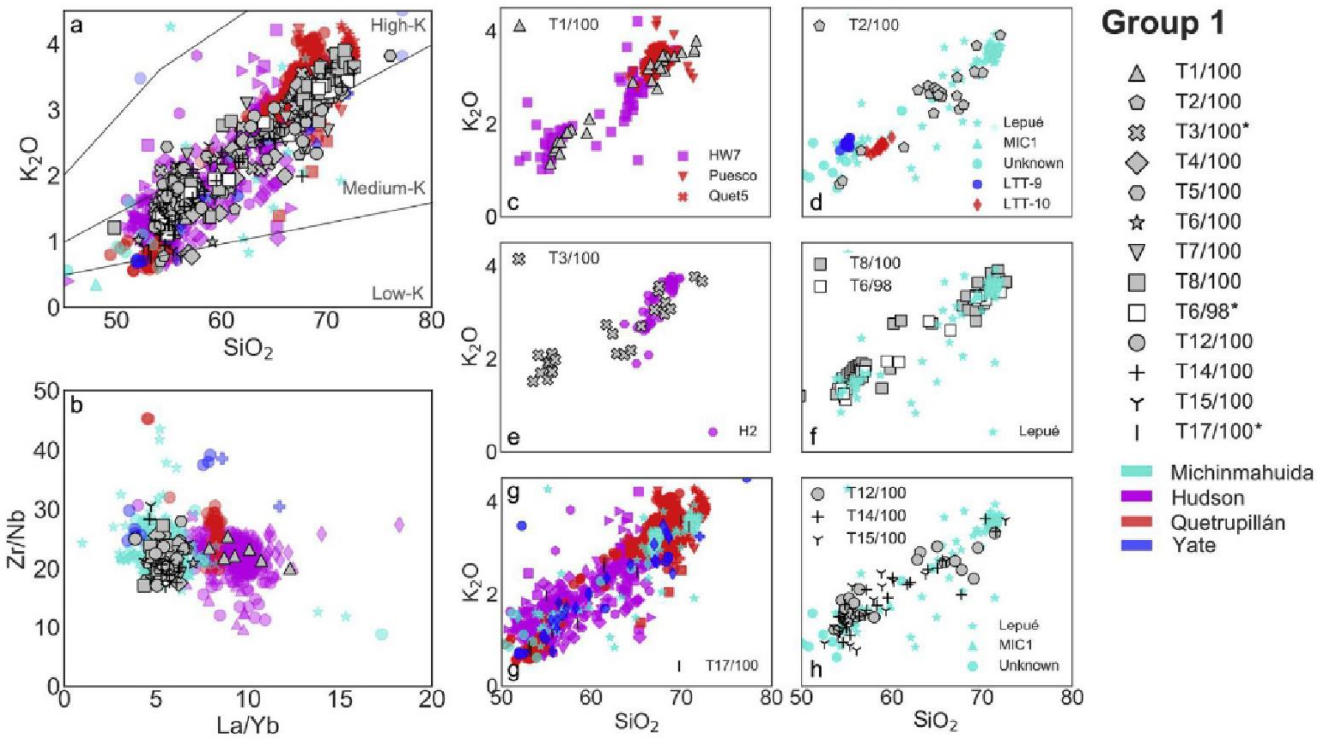

Fig. 3. Individual glass shard composition from the cryptotephra layers here studied corresponding to Group 1 (legend to the right). The latter are compared with available analyses of post–glacial deposits from volcanic centers displaying a similar behavior (color legend to the right): Michinmahuida (Alloway et al., 2017a; Amigo et al., 2013; López-Escobar et al., 1993; Naranjo and Stern, 2004), Hudson (Carel et al., 2011; Del Carlo et al., 2018; Haberle and Lumley, 1998; Kilian et al., 2003; Kratzmann et al., 2008; López-Escobar et al., 1993; Naranjo et al., 1993; Naranjo and Stern, 1998; Smith et al., 2019; Stern, 2008; Weller et al., 2014, 2015), Quetrupillán (Brahm et al., 2018; Fontijn et al., 2016; Hickey-Vargas et al., 1989; Rawson et al., 2016; Simmons et al., 2020) and Yate (López-Escobar et al., 1993; Mella, 2008; Watt et al., 2011b). "Unknown" corresponds to products not assigned to any particular eruption. a: All cryptotephras in Group 1 are plotted, lines separating areas with low–K, medium–K and high–K according to Peccerillo and Taylor (1976) are shown. b: Only tephra for which trace elements were analyzed are shown (cryptotephra without an asterisk in the legend to the right). c, d, e, f, g, h: Comparison of specific cryptotephra where a potential correlative could be identified on land with available geochemical analyses. c: HW7 (Haberle and Lumley, 1998), Puesco and Quet5 (Fontijn et al., 2016). d: LTT-9 and LTT-10 (Moreno et al., 2014) together with available post–glacial data from Michinmahuida (Lepué, MIC1 and Unknown). e: H2 (Haberle and Lumley, 1998; Naranjo and Stern, 1998; Smith et al., 2019; Weller et al., 2015). f: Lepué (Alloway et al., 2017a; Amigo et al., 2013). g: same as a. h: available post–glacial data from Michinmahuida (Lepué, MIC1 and Unknown). Major element data correspond to normalized volatile–free compositions. (For interpretation of the references to color in this figure legend, the reader is referred to the Web version of this article.)

(Fig. S8). The source of this cryptotephra could be further constrained by trace element analyses and future research around these volcanoes which might reveal other potential correlatives.

4.5.3. T17/100

T17/100, occurs in the Late glacial at an estimated age of ~20.5 (1σ: 20.6–20.3) cal ka BP. From the major elements alone is not possible to further narrow down among the volcanic centers in Group 1 as the possible source (Fig. 3g, S9). Additionally, little evidence for tephra deposits at this time exists on land because of the predominant presence of the PIS in the area until ~18 cal ka BP (Davies et al., 2020). From the volcanoes in Group 1, so far only volcanic products from Yate have been dated so far, by $^{40}Ar/^{39}Ar$ in 22 ± 7 cal ka BP (Mella, 2008), indicating volcanic activity during this time. No evidence for Michinmahuida, Hudson or Quetrupillán at this time exists so far, however because of the position of Quetrupillán north of the sediment core, which is opposite to the predominant winds in the area, it is less likely that T17/100 was emitted from this volcano.

4.5.4. Cryptotephras with michinmahuida signature

We now discuss the potential correlations of the tephra and cryptotephra layers which have geochemical compositions similar to the Michinmahuida volcano, as discussed above (T2/100, T4/100, T5/100, T6/100, T7/100, T8/100, T6/98, T12/100, T14/100 and T15/100).

4.5.4.1. T2/100. The younger cryptotephra with a geochemistry similar to Michinmahuida volcano is T2/100 (Fig. 3a, b, d) with an estimated age of ~3.6 cal ka BP (1σ: 3.9–3.4). In the literature, evidence for eruptive activity of this volcano at that time has been found in a lacustrine core.

~24 km southwest of Michinmahuida at Lago Teo (~42.9° S, ~72.7° W; Moreno et al., 2014) and in the Mallines section ~13 km southeast of it (~42.9° S, ~72.3° W; Amigo et al., 2013). In the Mallines section, Amigo et al. (2013) report a scoria deposit identified in the upper part of the section (3rd *scoria*), bracketed between ~5 and 1.3 cal ka BP, which they attribute to the Michinmahuida volcano. For this deposit, major and trace elements were analyzed in the bulk tephra, however the sample has been reported as altered (Amigo et al., 2013) so further robust correlation is not possible. At Lago Teo, on the other hand, four tephras with a Michinmahuida–like major element geochemistry have been identified between ~5 and 1.3 cal ka BP by Moreno et al. (2014). From these, the more likely correlatives to T2/100 correspond to LTT-9 and LTT-10 (Fig. 6), which have estimated calendar ages of ~3 (1σ: 3.2–2.9) and ~3.5 (1σ: 3.6–3.3) ka BP. However, it is not possible to establish a robust correlation because the majority of

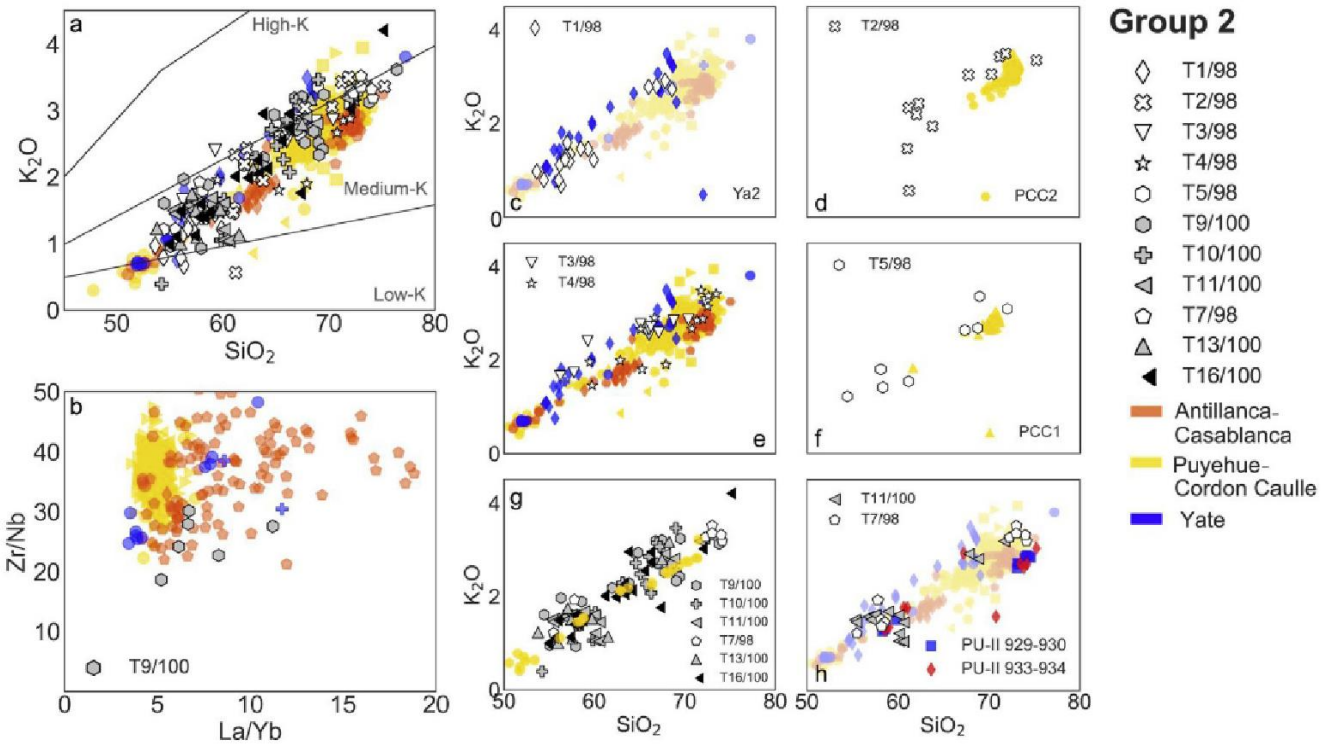

Fig. 4. Individual glass shard composition from the cryptotephra layers here studied corresponding to Group 2 (legend to the right). The latter are compared with available analyses of post–glacial deposits from volcanic centers (color legend to the right) displaying a similar behavior: Puyehue-Cordón Caulle (Alloway et al., 2015; Bertrand et al., 2008; Fontijn et al., 2016; Gerlach et al., 1988; Lara et al., 2006; Naranjo et al., 2017; Rawson et al., 2016; Singer et al., 2008). Antillanca-Casablanca (Fontijn et al., 2016; Geoffroy et al., 2018; Jacques et al., 2014; Naranjo et al., 2017; Rawson et al., 2016; Villarosa et al., 2006) and Yate (López-Escobar et al., 1993; Mella, 2008; Watt et al., 2011b). a: All cryptotephras in Group 2 are plotted, lines separating areas with low–K, medium–K and high–K according to Peccerillo and Taylor (1976) are shown. b: Trace element comparison between T9/100 and available information from volcanic centers in Group 2. c, d, e, f, g, h: Comparison of specific cryptotephras were a potential correlative could be identified on land with available geochemical analyses. c: Glass shards analyses from Ya2 (Watt et al., 2011b) are highlighted. d and f: Comparison with glass shard analyses of PCC2 and PPC1 by Fontijn et al. (2016) and bulk tephra by Singer et al. (2008), Rawson et al. (2016) and Naranjo et al. (2017). g: Comparison of deglacial and late glacial cryptotephras with deglacial products from Puyehue-Cordón Caulle, whole–rock analyses by Singer et al. (2008) dated by $^{40}Ar/^{39}Ar$ in 13.2 ± 2 and 18.7 ± 2.1 cal ka BP; post–glacial whole–rock analyses by Gerlach et al. (1988). h: comparison of T7/98 and T11/100 with tephra PU-II 929–930 and 933–934 cm (Bertrand et al., 2008). Major elements correspond to normalized volatile–free compositions. (For interpretation of the references to color in this figure legend, the reader is referred to the Web version of this article.)

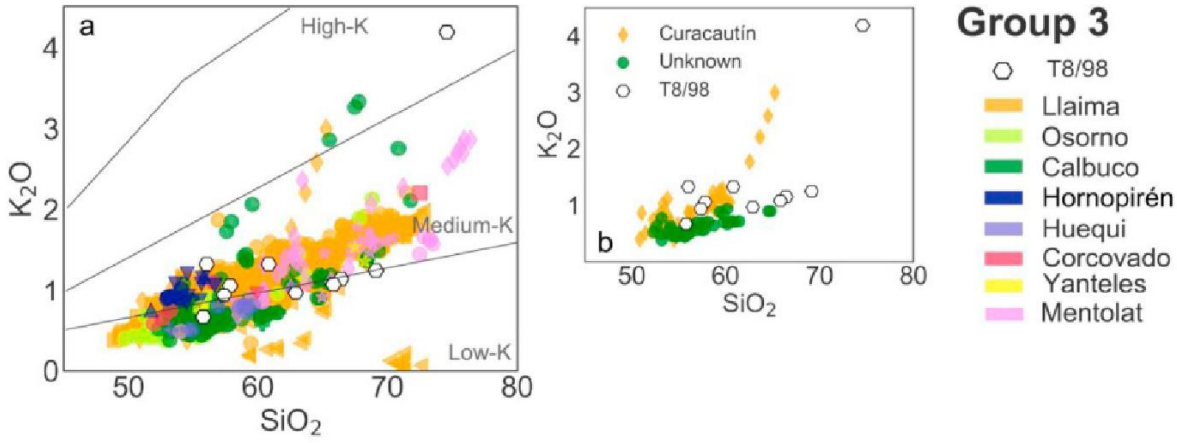

Fig. 5. Individual glass shard composition from the cryptotephra here studied corresponding to Group 3 (T8/98, legend to the right). T8/98 is compared with post–glacial analyses from volcanic centers (color legend to the right) displaying a similar behavior: Llaima (Bouvet de Maisonneuve et al., 2012; Naranjo and Moreno, 1991, 2005; Rawson et al., 2016; Reubi et al., 2011; Schindlbeck et al., 2014; Lohmar, 2008), Osorno (Bertrand et al., 2008; Jacques et al., 2014; López-Escobar et al., 1992, 1993; Moreno et al., 2010; Tagiri et al., 1993), Calbuco (López-Escobar et al, 1992, 1995López-Escobar et al., 1995; Morgado et al., 2019; Watt et al., 2011b; Sellés and Moreno, 2011), Huequi, Hornopirén (Watt et al., 2011a, 2011b), Mentolat (López-Escobar et al., 1993; Naranjo and Stern, 2004; Stern et al., 2015; Weller et al, 2015, 2017) Yanteles and Corcovado (López-Escobar et al., 1993; Naranjo and Stern, 2004). b: comparison with Curacautín tephra products: glass shards (Fontijn et al., 2016), matrix glass (Lohmar, 2008) and bulk tephra (Naranjo and Moreno, 2005; Lohmar, 2008; Schindlbeck et al., 2014) and eruptive products not assigned to any particular eruption from Calbuco, marked as "Unknown" (Sellés and Moreno, 2011). Major elements correspond to normalized volatile–free compositions. For tephras T6/98 and T8/100 since they display similar major element geochemistry and occur in a similar stratigraphic position (Fig. 2, 3f and 6). . (For interpretation of the references to color in this figure legend, the reader is referred to the Web version of this article.)

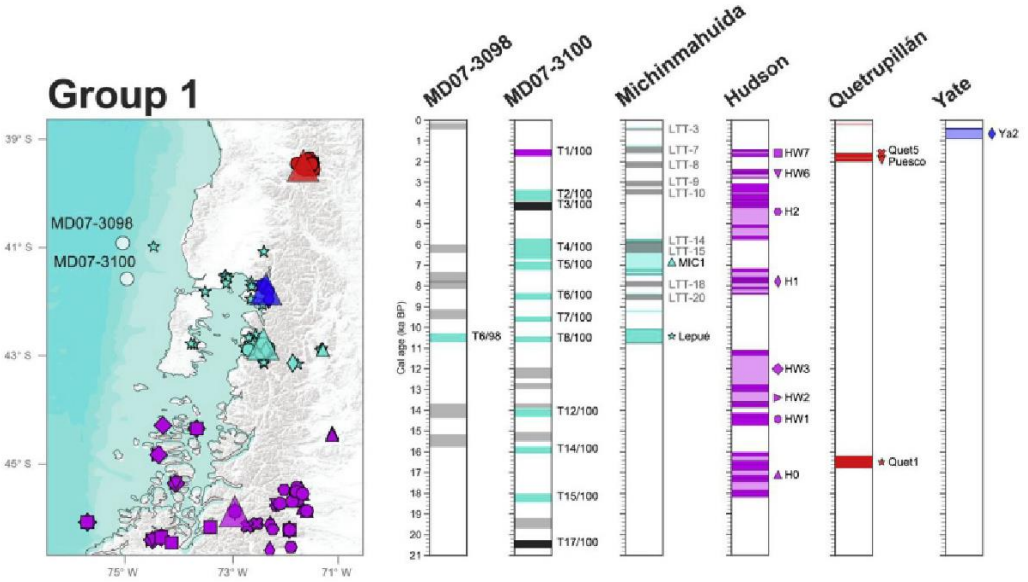

Fig. 6. Chronology for cores MD07-3098 and MD07-3100 highlighting the cryptotephras associated to Group 1, as described in the text, compared with the chronologies of explosive products from each volcanic center displaying a similar geochemical behavior (Fig. 3). Only known events dated by ^{14}C are plotted. To the left: position of the marine sediment cores here studied together with the position of each volcanic center associated to Group 1 indicated as a triangle, from north to south: Quetrupillán, Yate, Michinmahuida and Hudson. Also shown are the position of tephrochronological samples which have been analyzed for geochemistry and/or dated as smaller size symbols. Each symbol corresponds to a different eruptive event indicated in the respective volcanic center chronology (to the right). Pyroclastic deposits which have been dated but no correlation has been yet established are plotted in the chronology as colored rectangles of the corresponding volcanic center color, but they are unlabeled (no symbol or name is indicated to their right) and their position is indicated as a dot of the corresponding volcanic center color in the map. These samples are labeled "Unknown" in Table S6. Details on the chronologies of each volcanic center in Table S6. (For interpretation of the references to color in this figure legend, the reader is referred to the Web version of this article.)

the analyzed glass shards in T2/100 correspond to the more evolved part of the trend with dacitic and rhyolitic compositions, which are not present in LTT-9 and LTT-10.

4.5.4.2. T4/100 and T5/100. During the Middle Holocene, two cryptotephras with a Michinmahuida signature occur in the marine sediment cores: T4/100 and T5/100. T4/100 has a calibrated age of ~6.2 (1σ: 6.7–5.7) cal ka BP, whereas T5/100 has an age of ~7 (1σ: 7.2–6.8) cal ka BP.

At Lago Teo, two tephras occur in the Middle Holocene (LTT-14 and LTT-15), which have respectively estimated calendar ages of ~6.1 (1σ: 6.3–5.8) and ~6.2 (1σ: 6.4–6) cal ka BP (Moreno et al., 2014), and have been suggested to follow a geochemical trend similar to Michinmahuida. From these, LTT-14 displays values with lower K (Fig. 7a) than commonly reported for Michinmahuida, meanwhile the composition of LTT-15 is closer to Michinmahuida and to the less evolved part of the trend in both T4/100 and T5/100 (Fig. 7a). The estimated calendar ages of LTT-15 and LTT-14 overlap (Fig. 6) and they are both within error synchronous to T4/100, hence it is not possible to further correlate these deposits.

Additionally, both T4/100 and T5/100 could potentially be correlated to the MIC1 tephra from Michinmahuida volcano (Amigo et al., 2013; Naranjo and Stern, 2004). The MIC1 tephra was first identified as an andesitic pumice deposit ~90 km east of Michinmahuida volcano by Naranjo and Stern (2004). They obtained two ^{14}C ages from peat bracketing the MIC1 deposit, which indicate an age equal to or younger than ~7.2 and older than ~5.8 cal ka BP (Fig. 6, Table S6). A correlative of this tephra was later identified by Amigo et al. (2013) in the Mallines section, who dated the underlying paleosol at ~7.5 cal ka BP. However, a younger age was obtained in the same paleosol a few centimeter below, indicating this age altered by Amigo et al. (2013), thus a robust correlation based on geochemistry cannot be done. However, from the sole available analysis, major elements display similar values to T4/100 and T5/100 (Fig. 7a). Additional evidence for eruptive activity of Michinmahuida during this time is also provided by Alloway et al. (2017b), who describe the occurrence of a tephra layer in various sections (Pumalín-3, -4, -7, -2) in the area nearby Michinmahuida volcano occurring directly under Pumalín/Cha2 tephra, coincident with the position of MIC1 in the Mallines section. One trace element analysis in Pumalín-2 section (Pum 2–11) is provided by Alloway et al. (2017a) in bulk tephra, which displays a Michinmahuida–like geochemistry (Fig. 7b).

From a chronological point of view, it is possible that T4/100 is correlated to LTT-15 (and/or estimate might not be accurate. Unfortunately, only three geochemical data points identified as MIC1 are provided in the literature, all in bulk samples, two of which are thought to be LTT-14) and that T5/100 is correlated to MIC1. Additionally, because of the large uncertainty associated with the age of MIC1, it is also possible that LTT-15 and T4/100 are correlatives of MIC1 (Fig. 6) and that no correlative of LTT-15 has been identified.

4.5.4.3. T6/100. T6/100 occurs in the Early Holocene and has an estimated calendar age of ~8.5 cal ka BP (1σ: 8.6–8.3). Evidence of Michinmahuida activity around this time is again found in Lago Teo and in one section nearby the village of Chaitén (Casati et al., 2019). Casati et al. (2019) identified a Michinmahuida–sourced deposit dated in ~8.4 cal ka BP (1σ: 8.4–8.3) for which one geochemical analysis is available displaying La/Yb versus Zr/Nb ratios coincident with T6/100 (Sample P17-4CBd, Fig. 7d), thus we propose this deposit is a likely correlative of T6/100. In Lago Teo, two tephras identified as Michinmahuida occur during this period: LTT-18 and LTT-20 with calendar age estimates for tephra LTT-18 of ~7.9 cal ka BP (2σ: 8–7.8) and of ~8.5 cal ka BP (2σ: 8.6–8.4) for LTT-20. Thus, LTT-20 could correspond to T6/100. When comparing the major element geochemistry, LTT-20 represents a cluster around 68 wt% SiO_2, whereas T6/100 is rather bimodal with a wider range of

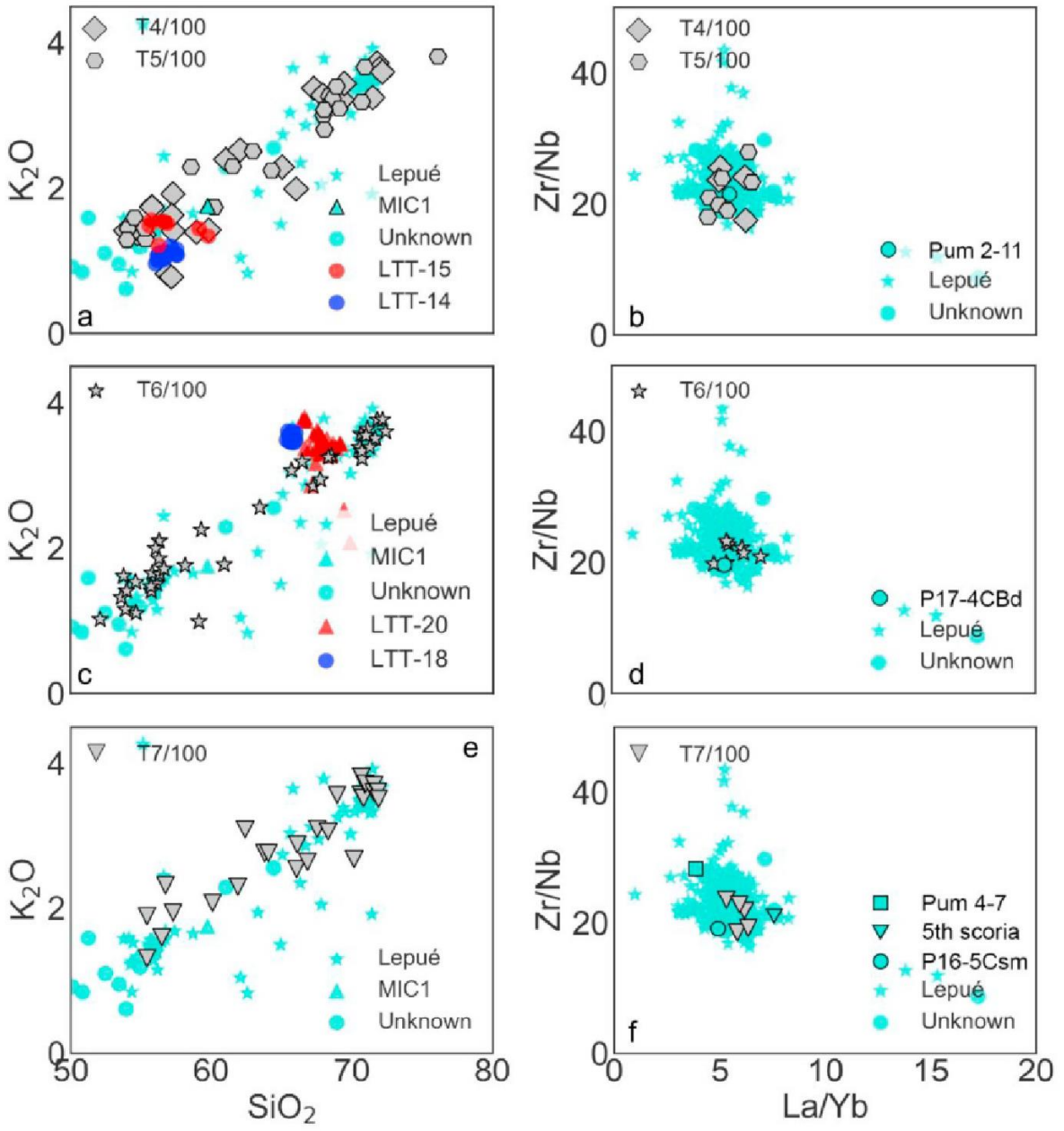

Fig. 7. Comparison of specific crytotephras belonging to Group 1 displaying a Michinmahuida signature with potential correlatives on land. In all cases all the available information from Michinmahuida is plotted as cyan symbols in the background (Alloway et al., 2017a; Amigo et al., 2013; López-Escobar et al., 1993; Naranjo and Stern, 2004) and specific correlatives are indicated in the legend. LTT-14, LTT-15, LTT-18 and LTT-20 (Moreno et al., 2014), MIC1 (Amigo et al., 2013; Naranjo and Stern, 2004), Pum 2–11 and Pum 4–7 (Alloway et al., 2017b), P17-4CBd and P16-5Csm (Casati et al., 2019), 5th scoria (Amigo et al., 2013), Lepué (Alloway et al., 2017a; Amigo et al., 2013), Unknown correspond to products not assigned to any particular eruption (Amigo et al., 2013; López-Escobar et al., 1993). Major elements correspond to normalized volatile–free compositions. (For interpretation of the references to color in this figure legend, the reader is referred to the Web version of this article.)

compositions, almost identical to Lepué tephra (Fig. 7c). However, they might still correspond to the same tephra, and further information might reveal in the future a wider compositional range for the eruption that formed LTT-20.

4.5.4.4. T7/100. T7/100 is the oldest cryptotephra that occurs in the Early Holocene, which has an estimated age of ~9.6 cal ka BP (1σ: 9.7–9.5). Evidence on land for Michinmahuida activity around this time is presented by Casati et al. (2019), who dated a deposit attributed to Michinmahuida at ~9.2 cal ka BP (1σ: 9.3–9.2), very similar to the estimated calendar age for T7/100 (Fig. 6). Amigo et al. (2013) identify one scoria deposit (5th *scoria* in the Mallines section) from Michinmahuida and bracket this event between ~7.6 and 10.3 cal ka BP. This deposit is positioned above Cha1 tephra, for which a calibrated age estimate ranging from ~9.5 to 10.5 cal ka BP has been proposed (Alloway et al., 2017b; Amigo et al., 2013; Fontijn et al., 2016; Naranjo and Stern, 2004; Watt et al., 2011b). A potential correlative of this deposit is also identified by Alloway et al. (2017b) in section Pumalín-4, which occurs above Cha1 as the 5th *scoria* from the Mallines section and is proposed to have a geochemical composition corresponding to Michinmahuida. A comparison of the element measurement for Pumalín-4 (Pum 4–7), the deposit

(P16-5Csm) identified by Casati et al. (2019) and the 5th *scoria*, display La/Yb versus Zr/Nb values close to those know for Michinmahuida and to T7/100 (Fig. 7f).

4.5.4.5. T6/98 and T8/100. T6/98 and T8/100 correspond to the only visible tephras in cores MD07-3098 and MD07-3100, respectively. Both tephras occur in the same stratigraphic position in each core at the Holocene-Deglaciation transition, and at synchronous calendar ages, within error, of ~10.6 (1σ: 10.7–10.4) for T8/100 and ~10.5 (1σ: 10.7–10.3) cal ka BP for T6/98 (Fig. 6). Additionally, they both have a thickness of ~25–30 cm and similar major element geochemistry (Fig. 3f), thus we propose that both tephras are correlatives. The major element compositions tend to be bimodal with two clusters at 54–57 and 68–73 wt% SiO_2 and both major and trace elements are consistent with volcanic deposits attributed to Michinmahuida, in particular the Lepué tephra (Fig. 3f).

So far, only one deposit from Michinmahuida volcano has been thoroughly described in the literature: the Amarillo Ignimbrite/Lepué Tephra. The Amarillo Ignimbrite was first described and dated by Amigo et al. (2013) in the vicinities of Michinmahuida volcano. However because of the lack of geochemical information they were not able to identify the fall deposit associated with the eruption. Later, Alloway et al. (2017a) identified and described the associated regional tephra and named it Lepué because of its occurrence in and around Lago Lepué on Chiloé island, northwest of the Michinmahuida volcano. This is a tephra with a bimodal composition with values ranging from ~54 to 72 wt% SiO_2 (Fig. 3f), with an estimated calendar age around 10.9 cal ka BP (Alloway et al., 2017a). The Lepué tephra has been identified in dozens of different sites, as far away as ~250 km northwest from the Michinmahuida volcano (Fig. 6), with a predominantly northern and northwestern dispersion (Alloway et al., 2017a). In particular, it has been identified on the Chilean continental margin at ODP-202 site 1233, located ~12 km southeast of marine core MD07-3098 and 50 km northeast of core MD07-3100. At ODP-202 site 1233, the Lepué tephra is ~30 cm thick and its age is bracketed between ~10 and 12.3 cal ka BP (Alloway et al., 2017a). The latter is consistent with the visible tephra layers of ~25–30 cm thick found in cores MD07-3100 and MD07-3098. Furthermore, when comparing their trace and major element geochemistry, both tephras in the studied cores are consistent with the Lepué Tephra products (Fig. 3b, f). Thus we identify the only visible tephra in the cores as the regional marker Lepué tephra.

4.5.4.6. T12/100, T14/100, T15/100. Cryptotephras T12/100, T14/100 and T15/100 have estimated calendar ages of ~14.2 (1σ: 14.3–14), ~15.9 (1σ: 16.1–15.8) and ~18.2 (1σ: 18.4–18) cal ka BP. No tephra with a geochemistry similar to Michinmahuida has been thoroughly described during the Deglaciation and late glacial and more particularly, none older than Lepué tephra. The lack of Michinmahuida tephras could be related to the presence of the PIS in the area proximal to the volcano in the last glacial period. However, a recent study in the La Zeta sequence located in the Argentina sector of the Andean complex has allowed to recover some tephras whose origin has been tentatively attributed to the Michinmahuida, however no geochemistry is available for further comparison (Alloway et al., 2017b). In particular, the JT1 tephra dated at ~18 cal ka BP (1σ: 18.2–17.8) has an age similar to that of the T15/100 event (~18.2 cal ka BP). Additionally, Alloway et al. (2017b) identify two other deposits, JT4 and JT5 with age estimates of 17.8 (1σ: 17.9–17.6) and 17.5 (1σ: 17.6–17.3) cal ka BP. These ages are not coincident with any of the marine cryptotephras here identified, however they represent an evidence of volcanic activity of the Michinmahuida volcano during deglacial period.

As a summary, it was possible to robustly identify two eruptions from the Group 1 tephras and cryptotephras: the Lepué tephra from Michinmahuida (T6/98 and T8/100), occurring at ~10.9 cal ka BP; and the HW7 tephra from the Hudson volcano (T1/100), occurring at ~1.5 cal ka BP. Both of which have been shown to record a northwestern dispersion (Fig. 6; Alloway et al., 2017a; Carel et al., 2011; Haberle and Lumley, 1998). Additionally, eight cryptotephras layers where identified as Michinmahuida–sourced (T2/100, T4/100, T5/100, T6/100, T7/100, T12/100, T14/100 and T15/100). These results are consistent with previous research around Michinmahuida volcano which had suggested recurrent volcanic activity during the Holocene (Amigo et al., 2013; Moreno et al., 2014). However, it is still hard to provide robust correlations among deposits, which in part is due to the paucity and accuracy of age/stratigraphic constraints, major and/or trace elements geochemistry. Additionally, the apparent high recurrence of Michinmahuida volcano can also be a source of uncertainty in the correlation since age estimates might not be precise enough to distinguish among eruptions, as in the case of LTT-14 and LTT-15 (Fig. 6). Here we combine age/stratigraphic constraints, major and/or trace elements geochemistry to provide robust correlatives for Michinmahuida–sourced tephras, in the ocean. The occurrence of tephras older than T8/100 (T2/100, T14/100 and T15/100, Fig. 6) is particularly interesting because it provides robust new evidence for recurrent activity of the Michinmahuida volcano since the late glacial period. This new information might be missing on land because of the highly vegetated area, less research around Michinmahuida because of its inactivity in historical times, or because of glacial erosion associated to the presence of the PIS. In many sites the Lepué tephra was found lying above glacial deposits (Alloway et al., 2017a), however in some other sites additional tephra deposits have been found between Lepué and glacial till and more so, organic matter directly above glacial deposits has been dated as old as ~17 cal ka BP. In fact, estimates of the PIS extent since the Last Glacial Maximum indicate that a rapid retreat would have begun in this area around 18 cal ka BP and that by 15 cal ka BP the ice was confined to the vicinities of the volcanoes (Davies et al., 2020), allowing for the deposition of deglacial tephras on land. Thus, it might be possible to find on land correlatives for the Michinmahuida cryptotephras discussed here. In particular, deposits tentatively associated with Michinmahuida have already been mentioned in the literature (Alloway et al., 2017a), which might be correlated if geochemical information becomes available.

4.6. Group 2

Cryptotephra layers T1/98, T2/98, T3/98, T4/98, T5/98, T9/100, T10/100, T11/100, T7/98, T13/100, T16/100 display a major element trend similar to that of volcanic centers Antillanca-Casablanca (Fontijn et al., 2016; Naranjo et al., 2017; Geoffroy et al., 2018; Villarosa et al., 2006), Puyehue-Cordón Caulle (Fig. 4, S5; Alloway et al., 2015; Bertrand et al., 2014; Fontijn et al., 2016; Gerlach et al., 1988; Lara et al., 2006; Naranjo et al., 2017; Singer et al., 2008; Villarosa et al., 2006) and Yate (López-Escobar et al., 1993; Mella, 2008; Watt et al., 2011b). T1/98 occurred in the Late Holocene; T2/98, T3/98, and T4/98 occurred in the Middle Holocene; T5/98 in the Early Holocene; T9/100, T10/100, T11/100, T7/98 and T13/100 during the Deglaciation; and T16/100 during the late glacial (Figs. 2 and 8).

Three eruptions sourced from Antillanca-Casablanca have been recognized so far in the literature: Nahuel Huapi (Fontijn et al., 2016; Naranjo et al., 2017), Rayhuen (Fontijn et al., 2016) and Playas Blanca-Negra (Fontijn et al., 2016; Geoffroy et al., 2018; Naranjo et al., 2017; Villarosa et al., 2006). All of them have been dated and occurred between ~1.3 and 3.5 cal ka BP (Fontijn et al., 2016; Naranjo et al., 2017; Villarosa et al., 2006) and cannot be

correlated with any of the cryptotephras studied here (Fig. 8). In the case of Puyehue-Cordón Caulle, five Holocene tephras deposits are described in the literature: Mil Hojas, North Cordón Caulle, Ranco, Puyehue2/PCC2 and Puyehue1/PCC1 (Fig. 8; Fontijn et al., 2016; Lara et al., 2006; Naranjo et al., 2017; Singer et al., 2008), and volcanic actvity during the Deglaciation has been identified by $^{40}Ar/^{39}Ar$ dating of some effusive products between 12 ± 2.8 and 18.7 ± 1.1 cal ka BP (Singer et al., 2008). Finally, two tephras of Yate volcano have been recognized in the literature: Ya1 and Ya2. Ya2 has been dated bracketed between ~0.4 and 0.9 cal ka BP, whereas Ya1 is thought to represent a Holocene eruption but its age is not constrained (Watt et al., 2011b). Additionally, $^{40}Ar/^{38}Ar$ dating together with the observation of volcanic products with and without evidence of glacial erosion have been identified and ascribed to the Yate volcano, suggesting a continuous activity since 122 ± 19 cal ka BP (Mella, 2008). Geochemically, some differences can be observed between these volcanic centers. When comparing glass shard major elements (Fig. 4, Fig. S8), Puyehue-Cordón Caulle products are mainly dacitic or rhyolitic (66–74 wt% SiO2) with relatively intermediate K (2.2–3.5 wt% K_2O (Alloway et al., 2015; Fontijn et al., 2016; Naranjo et al., 2017);) compared to the other volcanoes with similar silica concentration (Yate: 2.6–3.5 wt% K_2O; Antillanca-Casablanca: 2.2–3.2 wt% K_2O). Antillanca-Casablanca glass shards display a trend with relatively less evolved products (56–75 wt% SiO_2) than Puyehue-Cordón Caulle, from andesitic to rhyolitic compositions at relatively lower K than Puyehue-Cordón Caulle (Fontijn et al., 2016; Geoffroy et al., 2018; Naranjo et al., 2017; Villarosa et al., 2006). In the case of Yate, individual glass shards ranging from andesites to rhyolites have been erupted since the last glaciation (Mella, 2008; Watt et al., 2011b). The eruption with the most information corresponds to Ya2, which displays a continuous trend from basaltic andesite to rhyolite with relatively higher K than the two other volcanoes (Fig. 4a, c, e), particularly at andesitic compositions (Fig. 4c, e). For the three volcanic centers, whole–rock compositions (Gerlach et al., 1988; Jacques et al., 2014; Lara et al., 2006; López-Escobar et al., 1993; Mella, 2008; Naranjo et al., 2017; Rawson et al., 2016; Singer et al., 2008) record a more complete trend, from basalts and basaltic andesite to rhyolite, however andesites are rare in Puyehue-Cordón Caulle and Antillanca-Casablanca.

Additionally, these volcanic centers can be distinguished based on their trace elements. Notably, La/Yb values of Puyehue-Cordón Caulle are lower, plotting between 4 and 7 (Fig. 4b), with Zr/Nb values ranging between 22 and 50; meanwhile Antillanca-Casablanca displays very heterogeneous La/Yb values ranging between 4 and 21 and Zr/Nb values from 21 to 62; and Yate displays La/Yb values between 3 and 12 and Zr/Nb from 24 to 39. The latter helps discriminate between Puyehue-Cordón Caulle and the other two volcanic centers, however Antillanca-Casablanca and Yate cannot be distinguished based on these ratios. When looking at other trace elements, for example Th versus Zr, Th versus Nb or Ce versus Ta (Fig. S10) a similar behavior continues to be observed between Antillanca-Casablanca and Yate, thus at present a robust geochemical discrimination between them is not possible. In the following section, we discuss the potential source and correlative of each cryptotephra based on the available information, which for the moment is mainly associated with eruptions from the Puyehue-Cordón Caulle, however always keeping in mind that future work might reveal new tephras associated with Antillanca-Casablanca and/or Yate.

4.6.1. T1/98

The most recent cryptotephra layer from Group 2, T1/98, occurs in the Late Holocene and has an estimated age of ~0.3 cal ka BP (1σ: 0.4–0.1). T1/98 displays bimodal compositions with two clusters between 54–60 and 66–69 wt% SiO_2, and its major element geochemistry is more consistent with the available information from Yate than that of Puyehue-Cordón Caulle or Antillanca-Casablanca (Fig. 4c). Notably, andesitic compositions are frequent in the most primitive glass shards of T1/98, but are virtually absent or very rare in Puyehue-Cordón Caulle and Antillanca-Casablanca volcanic products. Therefore, tephra T1/98 could be a correlative of the most documented eruption from Yate volcano Ya2 (Fig. 8), bracketed between ~0.4 and ~0.9 cal ka BP. Additionally, although less likely, it could correspond to a Puyehue-Cordón Caulle eruption, for which many Late Holocene tephras have been described. In particular, the most recent described tephra from Puyehue-Cordón Caulle corresponds to the Mil Hojas eruption, for which an age estimate has been obtained by several authors between ~0.5 and ~1 cal ka BP (Fontijn et al., 2016; Lara et al., 2006; Naranjo et al., 2017; Singer et al., 2008), slightly older than T1/98. Additionally, two pyroclastic density current deposits associated with the Puyehue-Cordón Caulle and younger than Mil Hojas have age estimates of ~0.1 (1σ range: 0.1–0.06) and ~0.2 (1σ range: 0.2–0.1) cal ka BP (Table S6; Lara et al., 2006). At the same time, Naranjo et al. (2017) also recognize two tephra deposits associated to Puyehue-Cordón Caulle which are older than the historic eruption of 1921–1922 CE and younger than the Late Holocene Mil Hojas eruption. It is possible that these deposits are correlated with the pyroclastic density current dated by Lara et al. (2006) and T1/98. Unfortunately, there is no geochemistry available for either of these deposits and thus, a further correlation cannot be done. The most likely correlative of T1/98 would thus be the eruption Ya2 based on available information.

4.6.2. T2/98

T2/98 occurred during the Middle Holocene at an estimated calendar age of 6.2 cal ka BP (1σ: 6.4–6). Around this time, one eruption associated with Puyehue-Cordón Caulle has been described in the literature: Puyehue 2/PCC2, with estimated calendar ages ranging from 6.4 to 7.1 cal ka BP (Fontijn et al., 2016; Lara et al., 2006; Naranjo et al., 2017; Singer et al., 2008). The deposits corresponding to Puyehue 2/PCC2 were first ^{14}C dated by Lara et al. (2006) at ~6.7 (1σ: 6.7–6.6) cal ka BP (Fig. 8, Table S6). The same deposit is also described by Singer et al. (2008) who obtained bulk tephra geochemistry for the pyroclastic deposit and whole–rock geochemistry for its effusive correlative, a rhyolite lava dome named Pr2 and dated by $^{40}Ar/^{39}Ar$ in 6.4 ± 0.9 and 6.9 ± 1.6 cal ka BP. Additional information is provided by Fontijn et al. (2016), who obtained individual glass shard major element geochemistry for a likely correlative of this tephra (which they name PCC2), and provide a modelled age of ~6.4 cal ka BP. Finally, Naranjo et al. (2017) date the underlying sediment of this tephra in 7.1 cal ka BP (1σ: 7.2–7). From a chronological point of view it is possible that cryptotephra T2/98 is correlated to Puyehue2/PCC2. From a geochemical point of view, the most evolved cluster from T2/98, with values between ~70 and 75 wt% SiO_2 is consistent with analyses of PCC2 (Fig. 4d) but the marine tephra follows a more complete trend with SiO_2 values ranging from ~60 to 75 wt% SiO_2, whereas on land volcanic products are restricted to 70–73 wt% SiO_2. However, most of the available analyses were obtained by Fontijn et al. (2016), who mention that less evolved products were sampled but not analyzed because of the highly crystalline ground mass hampering major element measurements. Thus, the lack of less evolved products from Puyehue 2/PCC2 might be an analytical bias rather than a geochemical fingerprint of this eruption.

4.6.3. T3/98 and T4/98

T3/98 occurred during the Middle-Early Holocene with calendar age estimates of ~7.6 cal ka BP (1σ: 7.9–7.3). It displays bimodal

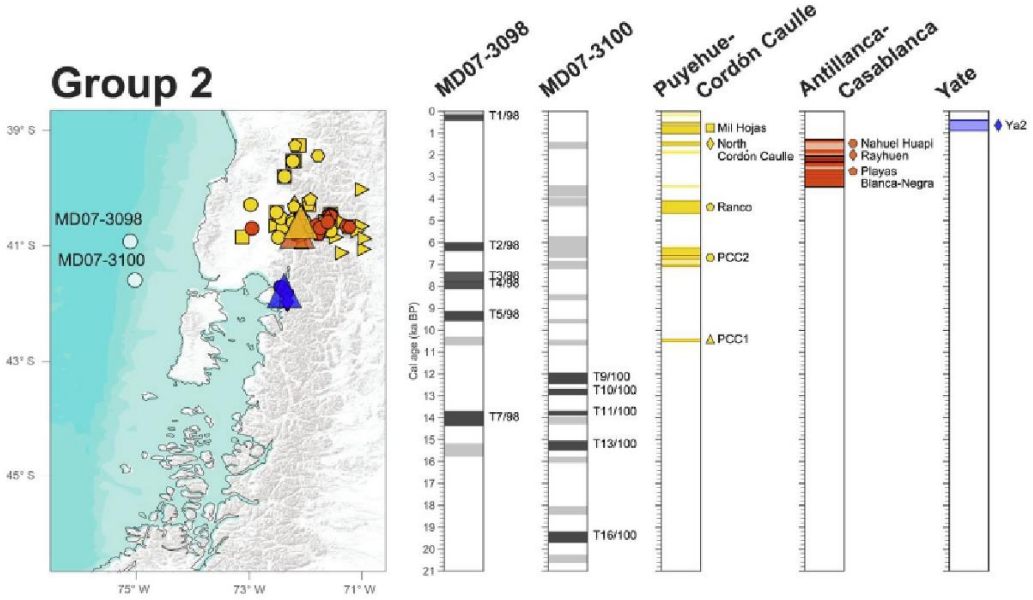

Fig. 8. Chronology for cores MD07-3098 and MD07-3100 highlighting the cryptotephra associated to Group 2, as described in the text, compared with the chronologies of explosive products from each volcanic center displaying a similar geochemical behavior (Fig. 4). Only events dated by ^{14}C are plotted. To the left: position of the marine sediment cores here studied together with the position of each volcanic center associated to Group 2 indicated as a triangle, from north to south: Puyehue-Cordón Caulle, Antillanca-Casablanca and Yate. Also shown are the position of tephrochronological samples associated with each volcanic center which have been analyzed for geochemistry and/or dated as smaller size symbols. Each symbol corresponds to a different eruptive event indicated to the right in the respective volcanic center chronology (to the right). Pyroclastic deposits which have been dated but no correlation has been stablished are plotted in the chronology but unlabeled and the position is indicated as a dot of the corresponding volcanic center color. Details on the chronologies of each volcanic center in Table S6. (For interpretation of the references to color in this figure legend, the reader is referred to the Web version of this article.)

compositions with two clusters between 56–59 and 65–72 wt% SiO_2 (Fig. 4e). T4/98 occurred during the Middle-Early Holocene at ~7.9 cal ka BP (1σ: 8.1–7.7). Glass shards in T4/98 display a continuous trend from 59 to 73 wt% SiO_2. During this time interval none of the volcanic centers in Group 2 has a recorded activity (Fig. 8), except for effusive products of Puyehue-Cordón Caulle dated at 6.9 ± 1.6 ka which have been correlated to the Puyehue2/PCC2 eruption (Singer et al., 2008). From the major elements alone it is not possible to further constrain the volcanic source of either of these two cryptotephra, thus future work might reveal potential correlatives for them.

4.6.4. T5/98

T5/98 occurs in the Early Holocene at ~9.4 cal ka BP (1σ: 9.6–9.1). It presents a bimodal geochemistry with values between 54–61 and 67–72 wt% SiO_2. The only described eruption from volcanoes in Group 2 during the Early Holocene corresponds to Puyehue 1/PCC1. Puyehue 1/PCC1 is a tephra found overlying moraine deposits or directly on rocks presenting glacial erosion (Naranjo et al., 2017), which has been dated by Singer et al. (2008), as part of unit Pr1, at ~10.5 cal ka BP (1σ: 10.5–10.4) and its whole–rock analysis corresponds to a dacitic composition. The estimated calendar ages of T5/98 and PCC1 do not coincide, notably the estimated calendar age of Puyehue 1/PCC1 is ~1000 years older than that of T5/98. When comparing the major element geochemistry of T5/98 and that of PCC1/Puyehue 1 (Fig. 4f), the most evolved part of the bimodal trend in the marine tephra is coincident with glass shard analyses by Fontijn et al. (2016) and whole–rock analyses by Singer et al. (2008). Additionally, one bulk tephra analysis (Rawson et al., 2016) has values similar to the less evolved part of the trend observed in T5/98, around 61 wt% SiO2 (Fig. 4f).

With the current age assessment for Puyehue 1/PCC1, it seems unlikely that T5/98 is the correlative of this tephra. However because so far only one age constraint is available, the estimated age of PCC1 might greatly vary in the future. As mentioned, for example, in the case of MIC1 in Section 5.1.4.2, for which the estimated age ranges between ~5.8 and 7.2 cal ka BP, age constraints for a tephra can greatly vary at different sites depending on the measured material and stratigraphic position of it, and thus the assessment of more dates could help further constraint the correlation between Puyehue 1/PCC1 and T5/98.

4.6.5. T9/100

Cryptotephra T9/100, occurring at ~12.2 cal ka BP (1σ: 12.5–11.9), is the only cryptotephra from Group 2 for which trace elements have been analyzed. As mentioned before, volcanoes in Group 2 can be further distinguished based in their La/Yb ratios. In particular, Puyehue-Cordón Caulle has very uniform and relatively low La/Yb values, around 5. In contrast, Antillanca-Casablanca and Yate volcanic centers display more heterogeneous La/Yb values ranging between ~3 and 21, similar to what is observed in T9/100 which presents values between ~5 and 12 (Fig. 4b). Surprisingly, when looking at other trace element concentrations, such as Th versus Zr or Nb, cryptotephra T9/100 seems to follow a Puyehue-Cordón Caulle trend (Fig. S14). From the latter, the geochemical signature from T9/100 is so far puzzling and a potential source is not yet identifiable.

4.6.6. Deglacial and late glacial cryptotephras21

According to our results, five cryptotephras from Group 2 occur during the Deglaciation and one during the late glacial period in addition to T9/100. Cryptotephra T10/100 occurs at ~12.8 cal ka BP (1σ: 13–12.7), T11/100 at ~13.8 cal ka BP (1σ: 13.9–13.7), T7/98 at ~14 cal ka BP (1σ: 14.4–13.7), T13/100 at ~15.3 cal ka BP (1σ: 15.5–15) and finally T16/100 at ~19.4 cal ka BP (1σ: 19.7–19.2).

From these, it is possible that T7/98 and T11/100 are correlated since they are within error synchronous and display similar major element trends (Fig. 4h, S15).

No tephra deposits have been robustly identified on land for the volcanic centers in Group 2 during the Deglaciation. As previously mentioned, Puyehue1/PCC1 (~10.5 cal ka BP (1σ: 10.5–10.4) is found deposited over moraine deposits or glaciated rocks (Naranjo et al., 2017), hence no older tephra deposit is known. However, Singer et al. (2008) dated effusive products of the Puyehue-Cordón Caulle by $^{40}Ar/^{39}Ar$ at 12 ± 2.8, 12.3 ± 1.9, 14.9 ± 2.9, 18.7 ± 1.1 cal ka BP. Unfortunately, the higher error associated with the $^{40}Ar/^{39}Ar$ method relative to ^{14}C dating does not allow a direct correlation with these products. However, this information demonstrates that Puyehue-Cordón Caulle was active during the Deglaciation and late glacial and thus it is a plausible source for the marine cryptotephras. Additionally, the effusive products from Puyehue-Cordón Caulle follow a wide range from basalts to rhyolites, coherent with the compositional variations found in cryptotephras from Group 2 (Fig. 4g).

Further information on the volcanic activity of volcanic centers in Group 2 during the Deglaciation might be found in a lake core record from Lago Puyehue (Pu-II; Bertrand et al., 2008), where two tephra layers with similar geochemistry (PU-II 929–930 and 933–934 cm) have an estimated age slightly older than 13.8 cal ka BP. Bertrand et al. (2008) propose a Puyehue-Cordón Caulle source for PU-II 933–934 cm and suggest a more distant source for PU-II 929–930, however no exact volcanic center is indicated. When observing their major element geochemistry, they both present a bimodal trend with the more evolved part of the trend plotting very closely to the more evolved products from Antillanca-Casablanca and Puyehue-Cordón Caulle (Fig. 4h). On the other hand, the less evolved part of the trend could correspond to either of the volcanic centers in Group 2. When comparing these tephras with T11/100 and T7/98, dated at ~13.8 and ~14 cal ka BP respectively, both cryptotephras and tephras on land represent bimodal trends with geochemical similarities around the less evolved clusters at ~60 wt % SiO_2. However, at higher silica values the comparison between products becomes less consistent, the on land tephras having higher SiO_2 contents for lower K_2O. Thus it is unlikely that they correspond to correlatives.

As a summary for Group 2, eleven cryptotephras were identified as either Puyehue-Cordón Caulle, Antillanca-Casablanca or Yate sourced. However, the paucity of literature information did not enable us to correlate with robustness any of these cryptotephras. We suggest that T1/98 might be correlated to Ya2, and that more on land chronological constraints together with trace element analyses could help further constrain this correlation and better discriminate it from Puyehue-Cordón Caulle activity at this time. Additionally we suggest that T2/98 might be correlated to PCC2/Puyehue 2, if less evolved products from the latter are analyzed; and T5/98 to PCC1/Puyehue 1, if more age constraints on land become available. Regarding the remaining cryptotephras in this group, no tentative correlations could be established. However the data presented here supports previous evidence for volcanic activity of Puyehue-Cordón Caulle and Yate during Holocene, deglacial and late glacial periods for which the marine tephras might represent the distant evidence of this explosive volcanic activity. A better correlation with the on land information however requires more geochronological and geochemical data, for example Ya1 eruption so far no age constraint exits and only two geochemical bulk analyses of the tephra are available (Watt et al., 2011b). Additionally, most deglacial evidence potentially correlated to the cryptotephra here analyzed corresponds to $^{40}Ar/^{39}Ar$ dating in effusive products which does not allow for a correlation because of the high errors associated with $^{40}Ar/^{39}Ar$ dating relative to ^{14}C dating.

4.7. Group 3

Cryptotephra layer T8/98 occurs at the beginning of the Deglaciation and has an estimated calibrated age of ~15.5 cal ka BP (1σ: 15.8–15.2). The major element geochemistry of this cryptotephra is unique in both cores analyzed here, with much lower K_2O values ranging between ~0.5 and 1.3 wt% at variable SiO_2 contents (Figs. 5a, 3a and 4a for comparison). This particular geochemical fingerprint is shared by eight volcanic centers dispersed between 39 and 45° S along the SVZ (Fig. 1): Llaima (Bouvet de Maisonneuve et al., 2012; Naranjo and Moreno, 1991, 2005; Rawson et al., 2016; Reubi et al., 2011; Schindlbeck et al., 2014; Lohmar, 2008), Osorno (Bertrand et al., 2008; Jacques et al., 2014; López-Escobar et al., 1992, 1993; Moreno et al., 2010; Tagiri et al., 1993), Calbuco (López-Escobar et al. 1992, 1995López-Escobar et al., 1995; Morgado et al., 2019; Watt et al., 2011b; Sellés and Moreno, 2011), Hornopirén (Watt et al., 2011b), Huequi (Watt et al., 2011a), Corcovado, Yanteles (López-Escobar et al., 1993; Naranjo and Stern, 2004) and Mentolat (López-Escobar et al., 1993; Naranjo and Stern, 2004; Stern et al., 2015; Weller et al. 2015, 2017, 2019).

Among these volcanoes, one eruption from the Llaima volcano has been well described and dated with a similar age to T8/98 (~15.5 cal ka BP). The Curacautín Ignimbrite, resulting from this eruption, is proposed to have occurred in two phases based on ^{14}C ages populations and field observations (Lohmar, 2008): Curacautín 1 (Table S6) with a mean age of ~16.1 cal ka BP and Curacautín 2 with a mean age ~15 cal ka BP (Fig. 9). A direct geochemical comparison of individual glass shards major element geochemistry between T8/98 and Curacautín products indicates similar values below 60 wt% SiO_2 (Fig. 5b), however the more evolved values observed in T8/98 with low K_2O are not present in Curacautín, for which glass shards with higher silica values display much higher K than tephra T8/98. The geochemical trend displayed by T8/98 seems more consistent with a poorly described pyroclastic deposit from the Calbuco volcano, dated at ~14.4 cal ka BP (Sellés and Moreno, 2011). For this deposit no geochemical data have been reported and the stratigraphic position of the charcoal used for ^{14}C dating is unknown, hampering further robust correlation. Regarding the remaining volcanoes, no deposits have been identified during this time interval (Fig. 9) and the Osorno volcano is thought to be a volcano with a dominant effusive activity (Moreno et al., 2010), it might thus be a less likely possible source for T8/98.

From the latter, it is plausible that the cryptotephra T8/98 is correlated to either Curacautín1, 2 or the unknown event from Calbuco volcano. Given the wind configuration in the area and the position of the volcanic centers relative to core MD07-3098, Calbuco volcano would be the more likely source of the cryptotephra (Fig. 1). However, given the chaotic nature of atmospheric circulation as described in section 2, a Llaima source is not impossible.

Further information, especially regarding the volcanic activity of Calbuco could help clarify.

4.8. General comment

As mentioned in the previous sections, all the cryptotephra and tephra layers analyzed here represent a trend, either bimodal or continuous, from basaltic andesite to dacite or rhyolite, which is in contrast with many records on land which represent clusters. This was also observed by Carel et al. (2011) when comparing marine tephra layers and on land tephras from the Hudson volcano. This difference, which is observed in the case of T2/100 versus LTT-9 and LTT-10, T3/100 versus H2 (Fig. 3d, e), T4/100 or T5/100 versus LTT-14 and LTT-15, LTT-20 compared to T6/100 (Fig. 7a, c), T2/98 versus

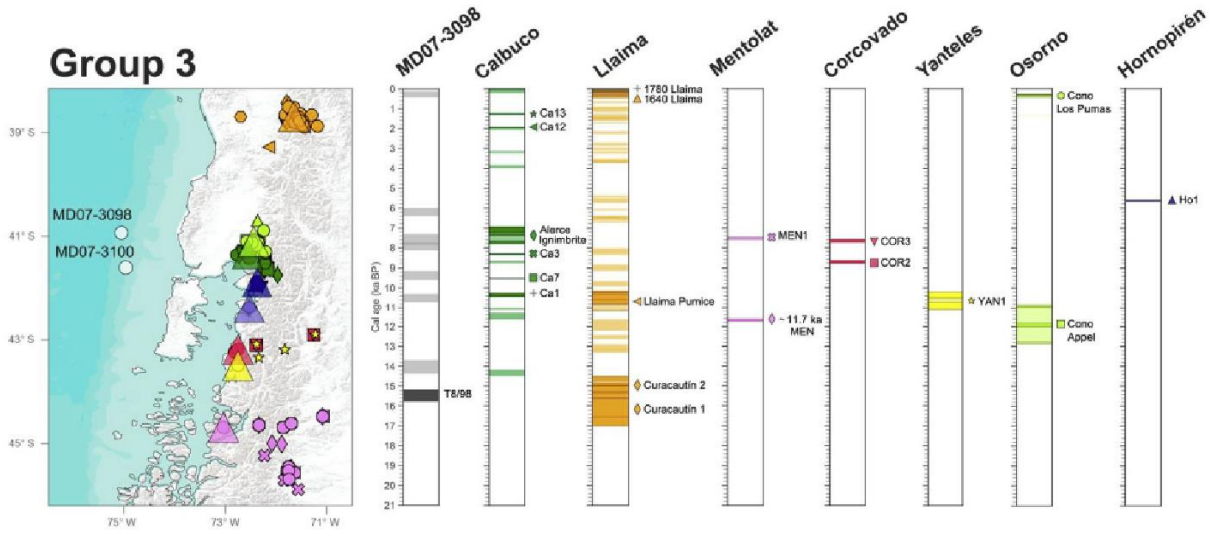

Fig. 9. Chronology for cores MD07-3098 and MD07-3100 highlighting the one cryptotephra associated to Group 3 (T8/98), as described in the text, compared with the chronologies of explosive products from each volcanic center displaying a similar geochemical behavior (Fig. 6). Only events dated by ^{14}C are plotted. To the left: position of the marine sediment cores here studied together with the position of each volcanic center associated to Group 3 indicated as a triangle, from north to south: Llaima, Osorno, Calbuco, Hornopirén, Huequi (no eruptive events have been dated for Huequi so far), Corcovado, Yanteles and Mentolat. Also shown are the position of tephrochronological samples associated with each volcanic center which have been analyzed for geochemistry and/or dated, as smaller size symbols. Each symbol corresponds to a different eruptive event indicated in the respective volcanic center chronology (to the right). Pyroclastic deposits which have been dated but no correlation has been stablished are plotted but unlabeled in the chronology and the position is indicated as a dot of the corresponding volcanic center color. Details on the chronologies of each volcanic center in Table S6. This possible correlation in the future. . (For interpretation of the references to color in this figure legend, the reader is referred to the Web version of this article.)

Puyehue 2/PCC2 (Fig. 4d) might indicate either that the deposits on land and the ocean arise from different eruptive events or it could also arise from biases associated to the dispersion of the ashes and/or measuring techniques. For example, it has been mentioned in the literature that analytical biases arise by the increased difficulty in analyzing glass shards with microlites, which are more abundant in less evolved melts (e.g. Alloway et al., 2017a; Fontijn et al., 2016). The latter could explain the lack of less evolved products in LTT-20 compared to T6/100 (Fig. 7c), however it would not explain the differences observed in T2/100 versus LTT-9 and LTT/10 (Fig. 3d) and T4/100 or T5/100 versus LTT-14 and LTT-15 (Fig. 7a).

An interesting situation regarding this point is observed in both identified eruptions in this study: HW7 and Lepué tephra. For both these tephras a number of different sections have been analyzed for geochemistry on land for which different sections display different geochemistry. In particular, in the case of Lepué tephra, none of the analyzed sections on land represent the whole trend (Alloway et al., 2017a; Amigo et al., 2013), however all marine tephras do, including ODP-202 site 1233 and both tephras here analyzed (Fig. 10). In addition, a similar situation is observed for tephra HW7, however in this case two of the studied sections on land: "Laguna Marcelo" and "Laguna Stibnite" also display the full trend (Haberle and Lumley, 1998), as do cryptotephra T1/100 and cryptotephra at 160 cm in core MD07-3088 (Carel et al., 2011), all of them located to the west of Hudson volcano. It is difficult to pinpoint what give rise to the different geochemical compositions in the different sections as this probably arises from a sum of different biases. For example: bias associated with the depositional environment; bias associated with the analytical techniques; biases associated with the very nature of the eruption i.e. its explosiveness and/or duration; and finally, biases associated with the dispersal conditions of their products, such as wind direction at the moment of the eruption. For these various reasons, marine cryptotephra might have the capacity of recording a more complete geochemical trend from a single volcano than on land tephras. Although the reasons are still unclear, this would mean that marine tephras/cryptotephras can thus serve as robust compositional reference for further correlations because they would be less geochemically biased. In addition to the robust stratigraphic constraints here provided for each tephra and cryptotephra, the geochemistry of the marine tephras/cryptotephras constitute robust tephrochronological constraints to disentangle the complex tephrochronological record in the SVZ.

5. Conclusion

Here we present a continuous marine (crypto) tephrochronological record associated with the SVZ, derived from two marine sediment cores retrieved in the Chilean continental margin. From the twenty five tephras and cryptotephras analyzed: one cryptotephra was correlated with tephra HW7 from Hudson volcano previously identified by Carel et al. (2011) and Haberle and Lumley (1998); and the Lepué tephra (Alloway et al., 2017a; Amigo et al., 2013), associated with Michinmahuida volcano, was identified in both studied cores as a ~25–30 cm–thick visible tephra layer. The latter constitutes an important tie point to align not only the chronologies of cores MD07-3098 and MD07-3100, but also the chronologies of other available paleoceanographic record in the area, such as ODP-202 site 1233 (Lamy et al., 2004, 2015) and MD07-3088 (Carel et al., 2011; Siani et al., 2013). Thus representing a step forward towards producing a chronologically robust paleoceanographic record in the area.

Additionally, eight cryptotephra were identified as Michinmahuida sourced based on major and trace elements for which robust stratigraphic constraints are provided. The latter is in agreement with previous records suggesting continuous Holocene activity of Michinmahuida (Amigo et al., 2013; Moreno et al., 2014), and provides new and robust evidence for its deglacial and late glacial activity. Eleven cryptotephra were identified as sourced either from Puyehue-Cordón Caulle, Antillanca-Casablanca or Yate, even though no robust correlation could be established at this

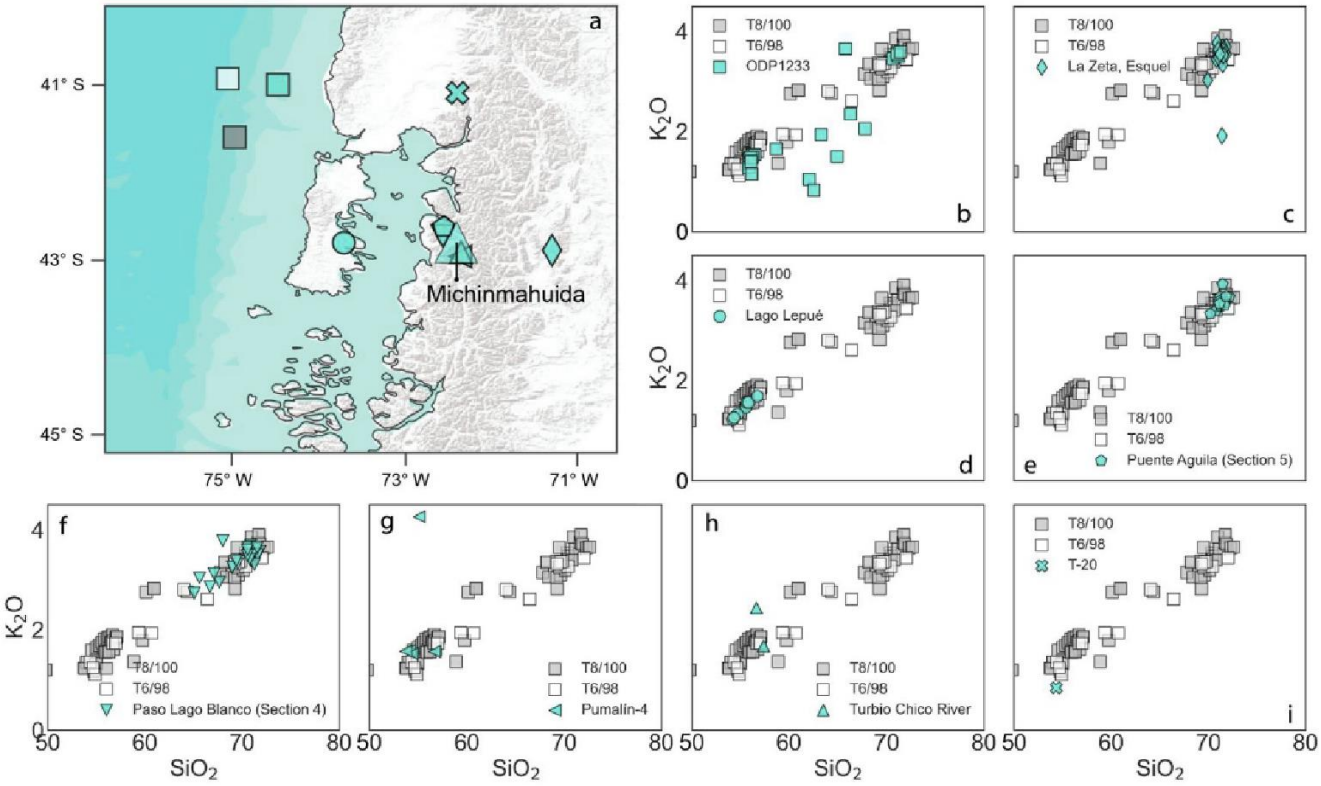

Fig. 10. SiO_2 vs K_2O and position (a) of deposits correlated with Lepué tephra), indicated in the legend (b–i) are the given name for each section in which the Lepué tephra was identified and analyzed. b–g deposits analyzed by Alloway et al. (2017a); i: Analyzes of Amarillo ignimbrite, correlative of Lepué tephra (Amigo et al., 2013); h: Analysis of Lepué correlative analyzed by Naranjo and Stern (2004), who initially identified this deposit as COR1.

stage. Nevertheless, they represent evidence for late glacial and deglacial explosive activity of either of these volcanic centers, for which evidence on land has only been previously identified by Bertrand et al. (2008). The latter complements previous information from Puyehue-Cordón Caulle (Singer et al., 2008) and Yate (Mella, 2008) for which effusive products have been dated indicating late glacial and deglacial ages and provides further chronological constraints for the Puyehue-Cordón Caulle activity.

Overall, the marine sediment cores here studied provide robust geochemical and stratigraphic evidence for a continuous volcanic activity in the SVZ since the late glacial (~20 cal ka BP). In the future, this information, together with an increased geochemical and chronological on land database, might help further unveil the volcanic activity of the different volcanic centers and provide additional tie points to synchronize different paleo environmental records in the area.

Declaration of competing interest

The authors declare that they have no known competing financial interests or personal relationships that could have appeared to influence the work reported in this paper.

Acknowledgements

We thank the captains and the crew of the R/V Marion Dufresne during the PACHIDERME cruise for their help retrieving cores MD07-3098 and MD07-3100. We would also like to thank the French INSU-LEFE-IMAGO SEPORA project 2016 (2016–2018), the French/Chilean ECOS SUD-CONICYT project C15U04 2016–2019 and the Chilean National Agency of Research and Development (ANID) for their financial support through Becas Chiles, Doctorado en el Extranjero Convocatoria 2017. We are thankful to the French ^{14}C AMS facility ARTEMIS and EchoMicadas for the chemical preparation and measurements of the ^{14}C samples. We also thank Frédéric Haurine for his assistance during laser ablation ICP-MS. Finally we very sincerely thank Brent Alloway, Derek Weller, Karen Fontijn, Sebastian Watt and the people from the Chilean Geological Service (SERNAGEOMIN), especially Álvaro Amigo and Virginia Toloza for kindly facilitating details on their published data and/or whose comments helped improve the manuscript.

Appendix A. Supplementary data

Supplementary data to this article can be found online at https://doi.org/10.1016/j.quascirev.2021.106928

Author contributions

Consuelo Martínez Fontaine: Conceptualization, Methodology, Investigation, Writing – original draft, Visualization, Giuseppe Siani: Conceptualization, Methodology, Investigation, Resources, Writing – review & editing, Project administration, Funding acquisition, Guillaume Delpech: Methodology, Investigation, Writing – review & editing, Elisabeth Michel: Resources, Writing – review & editing, Gustavo Villarosa: Conceptualization, Fatima Manssouri: Methodology, Julius Nouet: Methodology.

References

Alloway, B.V., Moreno, P.I., Pearce, N.J.G., De Pol-Holz, R., Henríquez, W.I., Pesce, O.H., Sagredo, E., Villarosa, G., Outes, V., 2017a. Stratigraphy, age and correlation of Lepué Tephra: a widespread c. 11 000 cal a BP marker horizon sourced from the Chaitén Sector of southern Chile. J. Quat. Sci. 32, 795–829. https://doi.org/10.1002/jqs.2976.

Alloway, B.V., Pearce, N.J.G., Moreno, P.I., Villarosa, G., Jara, I., De Pol-Holz, R., Outes, V., 2017b. An 18,000 year-long eruptive record from Volcán Chaitén, northwestern Patagonia: paleoenvironmental and hazard-assessment implications. Quat. Sci. Rev. 168, 151–181. https://doi.org/10.1016/j.quascirev.2017.05.011.

Alloway, B.V., Pearce, N.J.G., Villarosa, G., Outes, V., Moreno, P.I., 2015. Multiple melt bodies fed the AD 2011 eruption of Puyehue-Cordón Caulle, Chile. Sci. Rep. 5 https://doi.org/10.1038/srep17589.

Amigo, Á., Lara, L.E., Smith, V.C., 2013. Holocene record of large explosive eruptions from Chaitén and Michinmahuida Volcanoes, Chile. Andean Geol. 40, 227–248. https://doi.org/10.5027/andgeov40n2-a03.

Anderson, R.F., Ali, S., Bradtmiller, L.I., Nielsen, S.H.H., Fleisher, M.Q., Anderson, B.E., Burckle, L.H., 2009. Wind-driven upwelling in the Southern Ocean and the deglacial rise in atmospheric CO_2. Science 323, 1443–1448. https://doi.org/10.1126/science.1167441.

Bertin, L., Moreno, H., Becerril, L., 2018. Peligros del Campo Volcánico Carrán-Los Venados, Región de los Ríos. Servicio Nacional de Geología y Minería, Carta Geológica de Chile. Ser. Geol. Ambient. 33, 1–90 (Santiago).

Bertrand, S., Castiaux, J., Juvigné, E., 2008. Tephrostratigraphy of the late glacial and Holocene sediments of Puyehue lake (southern volcanic zone, Chile, 40°S). Quat. Res. 70, 343–357. https://doi.org/10.1016/j.yqres.2008.06.001.

Bertrand, S., Daga, R., Bedert, R., Fontijn, K., 2014. Deposition of the 2011-2012 Cordón Caulle tephra (Chile, 40°S) in lake sediments: implications for tephrochronology and volcanology. J. Geophys. Res. Earth Surf. 119, 2555–2573. https://doi.org/10.1002/2014JF003321.

Bouvet de Maisonneuve, C., Dungan, M.A., Bachmann, O., Burgisser, A., 2012. Insights into shallow magma storage and crystallization at volcán Llaima (andean southern volcanic zone, Chile). J. Volcanol. Geoth. Res. 211–212, 76–91. https://doi.org/10.1016/j.jvolgeores.2011.09.010.

Brahm, R., Parada, M.A., Morgado, E., Contreras, C., McGee, L.E., 2018. Origin of Holocene trachyte lavas of the Quetrupillán volcanic complex, Chile: examples of residual melts in a rejuvenated crystalline mush reservoir. J. Volcanol. Geoth. Res. 357, 163–176. https://doi.org/10.1016/j.jvolgeores.2018.04.020.

Carel, M., Siani, G., Delpech, G., 2011. Tephrostratigraphy of a deep-sea sediment sequence off the south Chilean margin: new insight into the Hudson volcanic activity since the last glacial period. J. Volcanol. Geoth. Res. 208, 99–111. https://doi.org/10.1016/j.jvolgeores.2011.09.011.

Casati, E., D'Amico, M., Šefrna, L., Trombino, L., Tunesi, A., Previtali, F., 2019. Geopedological contribution to the reconstruction of Holocene activity of Chaitén volcano (Patagonia, Chile). J. South Am. Earth Sci. 94 https://doi.org/10.1016/j.jsames.2019.102222.

Davies, B.J., Darvill, C.M., Lovell, H., Bendle, J.M., Dowdeswell, J.A., Fabel, D., García, J.L., Geiger, A., Glasser, N.F., Gheorghiu, D.M., Harrison, S., Hein, A.S., Kaplan, M.R., Martin, J.R.V., Mendelova, M., Palmer, A., Pelto, M., Rodés, Á., Sagredo, E.A., Smedley, R.K., Smellie, J.L., Thorndycraft, V.R., 2020. The evolution of the Patagonian Ice Sheet from 35 ka to the present day (PATICE). Earth Sci. Rev. 204 https://doi.org/10.1016/j.earscirev.2020.103152.

Del Carlo, P., Di Roberto, A., D'Orazio, M., Petrelli, M., Angioletti, A., Zanchetta, G., Maggi, V., Daga, R., Nazzari, M., Rocchi, S., 2018. Late Glacial-Holocene tephra from southern Patagonia and Tierra del Fuego (Argentina, Chile): a complete textural and geochemical fingerprinting for distal correlations in the Southern Hemisphere. Quat. Sci. Rev. 195, 153–170. https://doi.org/10.1016/j.quascirev.2018.07.028.

Dumoulin, J.-P., Comby-Zerbino, C., Delqué-Količ, E., Moreau, C., Caffy, I., Hain, S., Perron, M., Thellier, B., Setti, V., Berthier, B., Beck, L., 2017. Status report on sample preparation protocols developed at the LMC14 laboratory, Saclay, France: from sample collection to 14C AMS measurement. Radiocarbon 59, 713–726. https://doi.org/10.1017/RDC.2016.116.

Fontijn, K., Lachowycz, S.M., Rawson, H., Pyle, D.M., Mather, T.A., Naranjo, J.A., Moreno-Roa, H., 2014. Late Quaternary tephrostratigraphy of southern Chile and Argentina. Quat. Sci. Rev. 89, 70–84. https://doi.org/10.1016/j.quascirev.2014.02.007.

Fontijn, K., Rawson, H., Van Daele, M., Moernaut, J., Abarzúa, A.M., Heirman, K., Bertrand, S., Pyle, D.M., Mather, T.A., De Batist, M., Naranjo, J.A., Moreno, H., 2016. Synchronisation of sedimentary records using tephra: a postglacial tephrochronological model for the Chilean Lake District. Quat. Sci. Rev. 137, 234–254. https://doi.org/10.1016/j.quascirev.2016.02.015.

Gallego, D., Ribera, P., Garcia-Herrera, R., Hernandez, E., Gimeno, L., 2005. A new look for the Southern Hemisphere jet stream. Clim. Dynam. 24, 607–621. https://doi.org/10.1007/s00382-005-0006-7.

Geoffroy, C.A., Alloway, B.V., Amigo, Á., Parada, M.A., Gutierrez, F., Castruccio, A., Pearce, N.J.G., Morgado, E., Moreno, P.I., 2018. A widespread compositionally bimodal tephra sourced from Volcán Melimoyu (44°S, Northern Patagonian Andes): insights into magmatic reservoir processes and opportunities for regional correlation. Quat. Sci. Rev. 200, 141–159. https://doi.org/10.1016/j.quascirev.2018.09.034.

Gerlach, D.C., Frey, F.A., Moreno-Roa, H., López-Escobar, L., 1988. Recent volcanism in the puyehue–cordon Caulle region, southern Andes, Chile (40.5°S): petrogenesis of evolved lavas. J. Petrol. 29, 333–382. https://doi.org/10.1093/petrology/29.2.333.

Haberle, S.G., Lumley, S.H., 1998. Age and origin of tephras recorded in postglacial lake sediments to the west of the southern Andes, 44°S to 47°S. J. Volcanol. Geoth. Res. 84, 239–256. https://doi.org/10.1016/S0377-0273(98)00037-7.

Haddam, N.A., Siani, G., Michel, E., Kaiser, J., Lamy, F., Duchamp-Alphonse, S., Hefter, J., Braconnot, P., Dewilde, F., Isgüder, G., Tisnerat-Laborde, N., Thil, F., Durand, N., Kissel, C., 2018. Changes in latitudinal sea surface temperature gradients along the Southern Chilean margin since the last glacial. Quat. Sci. Rev. 194, 62–76. https://doi.org/10.1016/j.quascirev.2018.06.023.

Hickey-Vargas, R.L., Moreno Roa, H., López-Escobar, L., Frey, F.A., 1989. Geochemical variations in Andean basaltic and silicic lavas from the Villarrica-Lanin volcanic chain (39.5° S): an evaluation of source heterogeneity, fractional crystallization and crustal assimilation. Contrib. Mineral. Petrol. 103, 361–386. https://doi.org/10.1007/BF00402922.

Hogg, A.G., Heaton, T.J., Hua, Q., Palmer, J.G., Turney, C.S.M., Southon, J., Bayliss, A., Blackwell, P.G., Boswijk, G., Bronk Ramsey, C., Pearson, C., Petchey, F., Reimer, P., Reimer, R., Wacker, L., 2020. SHCal20 southern Hemisphere calibration, 0-55,000 Years cal BP. Radiocarbon 62, 759–778. https://doi.org/10.1017/RDC.2020.59.

Iglesias, V., Whitlock, C., Bianchi, M.M., Villarosa, G., Outes, V., 2011. Holocene climate variability and environmental history at the Patagonian forest/steppe ecotone: Lago Mosquito (42°29'37.89"S, 71°24'14.57"W) and Laguna del Cóndor (42°20'47.22"S, 71°17'07.62"W). Holocene 22, 1297–1307. https://doi.org/10.1177/0959683611427330.

Jacques, G., Hoernle, K., Gill, J., Wehrmann, H., Bindeman, I., Lara, L.E., 2014. Geochemical variations in the Central Southern Volcanic Zone, Chile (38–43°S): the role of fluids in generating arc magmas. Chem. Geol. 371, 27–45. https://doi.org/10.1016/j.chemgeo.2014.01.015.

Jochum, K.P., Nohl, U., Herwig, K., Lammel, E., Stoll, B., Hofmann, A.W., 2007. GeoReM: a new geochemical database for reference materials and isotopic standards. Geostand. Geoanal. Res. 29, 333–338. https://doi.org/10.1111/j.1751-908X.2005.tb00904.x.

Kilian, R., Hohner, M., Biester, H., Wallrabe-Adams, H.J., Stern, C.R., 2003. Holocene peat and lake sediment tephra record from the southernmost Chilean Andes (53-55°S). Rev. Geol. Chile 30, 47–64. https://doi.org/10.4067/S0716-02082003000100002.

Kissel, C., 2007. MD 159-PACHIDERME IMAGES XV, Cruise Report 06.02.07-28.02.07, vol. 1. PlouzanÉ inst. polaire français Paul Émile Victor, p. 84.

Kratzmann, D.J., Carey, S., Scasso, R., Naranjo, J.A., 2008. Compositional variations and magma mixing in the 1991 eruptions of Hudson volcano, Chile. Bull. Volcanol. 71, 419–439. https://doi.org/10.1007/s00445-008-0234-x.

Lamy, F., Arz, H.W., Kilian, R., Lange, C.B., Lembke-Jene, L., Wengler, M., Kaiser, J., Baeza-Urrea, O., Hall, I.R., Harada, N., Tiedemann, R., 2015. Glacial reduction and millennial-scale variations in Drake Passage throughflow. Proc. Natl. Acad. Sci. U.S.A. 112, 13496–13501. https://doi.org/10.1073/pnas.1509203112.

Lamy, F., Kaiser, J., Ninnemann, U., Hebbeln, D., Arz, H.W., Stoner, J., 2004. Antarctic timing of surface water changes off Chile and Patagonian ice sheet response. Science 80 (304), 1959–1962. https://doi.org/10.1126/science.1097863.

Lara, L.E., Moreno, H., Naranjo, J.A., Matthews, S., Pérez de Arce, C., 2006. Magmatic evolution of the puyehue-cordón Caulle volcanic complex (40° S), southern andean volcanic zone: from shield to unusual rhyolitic fissure volcanism. J. Volcanol. Geoth. Res. 157, 343–366. https://doi.org/10.1016/j.jvolgeores.2006.04.010.

Lohmar, 2008. Pétrologie des grands dépôts d'ignimbrites des volcans Villarrica (Licán et Pucón) et Llaima (Ignimbrite Curacautín), dans les Andes du Sud (Chili). PhD Thesis, Université Blause Pascal - Clermont Ferrand II, France.

López-Escobar, L., Kilian, R., Kempton, P.D., Tagiri, M., 1993. Petrography and geochemistry of quaternary rocks from the southern volcanic zone of the Andes between 41°30′ and 46°00′S, Chile. Rev. Geol. Chile 20, 33–55. https://doi.org/10.5027/andgeoV20n1-a04.

López-Escobar, L., Parada, M.A., Hickey-Vargas, R.L., Frey, F.A., Kempton, P.D., Moreno, H., 1995. Calbuco Volcano and minor eruptive centers distributed along the Liquiñe-Ofqui Fault Zone, Chile (41°–42° S): contrasting origin of andesitic and basaltic magma in the Southern Volcanic Zone of the Andes. Contrib. Mineral. Petrol. 119, 345–361. https://doi.org/10.1007/BF00286934.

López-Escobar, L., Parada, M.A., Moreno, H., Frey, F.A., Hickey-Vargas, R.L., 1992. A contribution to the petrogenesis of Osorno and Calbuco volcanoes, Southern Andes (41°00'-41°30'S): a comparative study. Rev. Geol. Chile 19, 211–226.

Lougheed, B.C., Obrochta, S.P., 2019. A rapid, deterministic age-depth modeling routine for geological sequences with inherent depth uncertainty. Paleoceanogr. Paleoclimatol. 34, 122–133. https://doi.org/10.1029/2018PA003457.

Menviel, L., Spence, P., Yu, J., Chamberlain, M.A., Matear, R.J., Meissner, K.J., England, M.H., 2018. Southern Hemisphere westerlies as a driver of the early deglacial atmospheric CO_2 rise. Nat. Commun. 9, 1–12. https://doi.org/10.1038/s41467-018-04876-4.

Mella, M., 2008. Petrogêneses Do Complexo Vulcânico Yate (42, 30°S), Andes Do Sul, Chile. Tese de Doutorado, Instituto de Geociências, Universidade de São Paulo, São Paulo. https://doi.org/10.11606/T.44.2009.tde-04032009-091537.

Moreau, C., Caffy, I., Comby, C., Delqué-Količ, E., Dumoulin, J.-P., Hain, S., Quiles, A., Setti, V., Souprayen, C., Thellier, B., Vincent, J., 2013. Research and development of the artemis 14C AMS facility: status report. Radiocarbon 55 (Issue 2), 331–337. https://doi.org/10.1017/S0033822200057441.

Moreno, P.I., Alloway, B.V., Villarosa, G., Outes, V., Henríquez, W.I., Pol-Holz, R. De,

Pearce, N.J.G., 2014. A past-millennium maximum in postglacial activity from Volcán Chaitén, southern Chile. Geology 43, 47–50. https://doi.org/10.1130/G36248.1.

Moreno, H., Lara, L., Orozco, G., 2010. Geología del Volcán Osorno, Región de Los Lagos. Servicio Nacional de Geología y Minería, Carta Geológica de Chile. Ser. Geol. Básica 126, 1–31, (Santiago).

Moreno, H., Naranjo, J., 2002. Mapa de Peligros del Volcán Llaima, Región de La Araucanía. Servicio Nacional de Geología y Minería, Carta Geológica de Chile, vol. 7. Serie Geología Ambiental, Santiago. https://doi.org/10.13140/RG.2.1.1844.3124.

Morgado, E., Morgan, D.J., Harvey, J., Parada, M.Á., Castruccio, A., Brahm, R., Gutiérrez, F., Georgiev, B., Hammond, S.J., 2019. Localised heating and intensive magmatic conditions prior to the 22–23 April 2015 Calbuco volcano eruption (Southern Chile). Bull. Volcanol. 81 https://doi.org/10.1007/s00445-019-1280-2.

Naranjo, J.A., Moreno, H., 1991. Actividad explosiva postglacial en el volcan Llaima, Andes del Sur (38° 45'S). Rev. Geol. Chile 18, 69–80. https://doi.org/10.5027/andgeoV18n1-a06.

Naranjo, J.A., Moreno, H., Banks, N.G., 1993. La erupción del volcán Hudson en 1991 (46°S), Región XI, Aisén, Chile. Serv. Nac. Geol. Miner. Bol. 44, 1–50.

Naranjo, J.A., Moreno, H., 2005. Geología del Volcán Llaima, Región de la Araucanía. Servicio Nacional de Geología y Minería, Carta Geológia de Chile. Ser. Geol. Básica 88, 1–33. Escala 1:50.000, Santiago.

Naranjo, J.A., Singer, B.S., Jicha, B.R., Moreno, H., Lara, L.E., 2017. Holocene tephra succession of Puyehue-Cordón Caulle and Antillanca/Casablanca volcanic complexes, southern Andes (40–41°S). J. Volcanol. Geoth. Res. 332, 109–128. https://doi.org/10.1016/j.jvolgeores.2016.11.017.

Naranjo, J.A., Stern, C.R., 2004. Holocene tephrochronology of the southernmost part (42°30'-45°S) of the andean southern volcanic zone. Rev. Geol. Chile 31, 225–240. https://doi.org/10.4067/S0716-02082004000200003.

Naranjo, J.A., Stern, C.R., 1998. Holocene explosive activity of Hudson volcano, southern Andes. Bull. Volcanol. 59, 291–306. https://doi.org/10.1007/s004450050193.

Peccerillo, A., Taylor, S.R., 1976. Geochemistry of eocene calc-alkaline volcanic rocks from the kastamonu area, northern Turkey. Contrib. Mineral. Petrol. 58, 63–81. https://doi.org/10.1007/BF00384745.

Pérez-Santos, I., Seguel, R., Schneider, W., Linford, P., Donoso, D., Navarro, E., Amaya-Cárcamo, C., Pinilla, E., Daneri, G., 2019. Synoptic-scale variability of surface winds and ocean response to atmospheric forcing in the eastern austral Pacific Ocean. Ocean Sci. 15, 1247–1266. https://doi.org/10.5194/os-15-1247-2019.

Rahn, D.A., Garreaud, R.D., 2014. A synoptic climatology of the near-surface wind along the west coast of South America. Int. J. Climatol. 34, 780–792. https://doi.org/10.1002/joc.3724.

Rawson, H., Keller, T., Fontijn, K., Pyle, D.M., Mather, T.A., Smith, V.C., Naranjo, J.A., 2016. Compositional variability in mafic arc magmas over short spatial and temporal scales: evidence for the signature of mantle reactive melt channels. Earth Planet Sci. Lett. 456, 66–77. https://doi.org/10.1016/j.epsl.2016.09.056.

Rawson, H., Naranjo, J.A., Smith, V.C., Fontijn, K., Pyle, D.M., Mather, T.A., Moreno, H., 2015. The frequency and magnitude of post-glacial explosive eruptions at Volcán Mocho-Choshuenco, southern Chile. J. Volcanol. Geoth. Res. 299, 103–129. https://doi.org/10.1016/j.jvolgeores.2015.04.003.

Reubi, O., Bourdon, B., Dungan, M.A., Koornneef, J.M., Sellés, D., Langmuir, C.H., Aciego, S., 2011. Assimilation of the plutonic roots of the Andean arc controls variations in U-series disequilibria at Volcan Llaima, Chile. Earth Planet Sci. Lett. 303, 37–47. https://doi.org/10.1016/j.epsl.2010.12.018.

Romero, J.E., Morgavi, D., Arzilli, F., Daga, R., Caselli, A., Reckziegel, F., Viramonte, J., Díaz-Alvarado, J., Polacci, M., Burton, M., Perugini, D., 2016. Eruption dynamics of the 22–23 april 2015 Calbuco volcano (southern Chile): analyses of tephra fall deposits. J. Volcanol. Geoth. Res. 317, 15–29. https://doi.org/10.1016/j.jvolgeores.2016.02.027.

Schindlbeck, J.C., Freundt, A., Kutterolf, S., 2014. Major changes in the post-glacial evolution of magmatic compositions and pre-eruptive conditions of Llaima Volcano, Andean Southern Volcanic Zone, Chile. Bull. Volcanol. 76, 1–22. https://doi.org/10.1007/s00445-014-0830-x.

Sellés, D., Moreno, H., 2011. Geología del Volcán Calbuco. Servicio Nacional de Geología y Minería, Carta Geológica de Chile. Ser. Geol. Básica 130. Escala 1:50.000, Santiago.

Siani, G., Michel, E., De Pol-Holz, R., DeVries, T., Lamy, F., Carel, M., Isguder, G., Dewilde, F., Lourantou, A., 2013. Carbon isotope records reveal precise timing of enhanced Southern Ocean upwelling during the last deglaciation. Nat. Commun. 4 https://doi.org/10.1038/ncomms3758.

Singer, B.S., Jicha, B.R., Harper, M.A., Naranjo, J.A., Lara, L.E., Moreno, H., 2008. Eruptive history, geochronology, and magmatic evolution of the Puyehue-Cordón Caulle volcanic complex, Chile. Bull. Geol. Soc. Am. 120, 599–618. https://doi.org/10.1130/B26276.1.

Simmons, I.C., McGarvie, D., Cortés, J.A., Calder, E.S., Pavez, A., 2020. Holocene volcanism at the Quetrupillán volcanic complex (39°30' S, 71°43' W), southern Chile. Volcania 3 (1), 115–137. https://doi.org/10.30909/vol.03.01.115137.

Smith, R.E., Smith, V.C., Fontijn, K., Gebhardt, A.C., Wastegård, S., Zolitschka, B., Ohlendorf, C., Stern, C., Mayr, C., 2019. Refining the late quaternary tephrochronology for southern south America using the laguna potrok aike sedimentary record. Quat. Sci. Rev. 218, 137–156. https://doi.org/10.1016/j.quascirev.2019.06.001.

Stern, C.R., 2004. Active Andean volcanism: its geologic and tectonic setting. Rev. Geol. Chile 31, 161–206. https://doi.org/10.4067/S0716-02082004000200001.

Stern, C.R., 2008. Holocene tephrochronology record of large explosive eruptions in the southernmost Patagonian Andes. Bull. Volcanol. 70, 435–454. https://doi.org/10.1007/s00445-007-0148-z.

Stern, C.R., De Porras, M.E., Maldonado, A., 2015. Tephrochronology of the upper Río Cisnes valley (44°S), southern Chile. Andean Geol. 42, 173–189. https://doi.org/10.5027/andgeoV42n2-a02.

Stuiver, M., Polach, H.A., 1977. Discussion: reporting of 14C data. Radiocarbon 19, 355–363. https://doi.org/10.1017/S0033822200003672.

Tagiri, M., Moreno, H., López-Escobar, L., Notsu, K., 1993. Two magma types of the high-alumina basalt series of Osorno, Souther Andes (41°06'S)-plagioclase dilution effect. J. Min. Petr. Econ. Geol. 88, 359–371. https://doi.org/10.2465/ganko.88.359.

Tisnérat-Laborde, N., Thil, F., Synal, H.-A., Cersoy, S., Hatté, C., Gauthier, C., Massault, M., Michelot, J.-L., Noret, A., Siani, G., et al., 2015. ECHoMICADAS: a new compact AMS system to measuring 14C for environment, climate and human sciences. In: Paper Presented at the 22nd International Radiocarbon Conference. Dakar, Senegal, pp. 16–20.

Toggweiler, J.R., Russell, J.L., Carson, S.R., 2006. Midlatitude westerlies, atmospheric CO_2, and climate change during the ice ages. Paleoceanography 21. https://doi.org/10.1029/2005PA001154.

Villarosa, G., Outes, V., Hajduk, A., Crivelli Montero, E., Sellés, D., Fernández, M., Crivelli, E., 2006. Explosive volcanism during the Holocene in the upper limay river basin: the effects of ashfalls on human societies, northern Patagonia, Argentina. Quat. Int. 158, 44–57. https://doi.org/10.1016/j.quaint.2006.05.016.

Wacker, L., Fahrni, S.M., Hajdas, I., Molnar, M., Synal, H.A., Szidat, S., Zhang, Y.L., 2013. A versatile gas interface for routine radiocarbon analysis with a gas ion source. Nucl. Instrum. Methods Phys. Res. Sect. B Beam Interact. Mater. Atoms 294, 315–319. https://doi.org/10.1016/j.nimb.2012.02.009.

Watt, S.F.L., Pyle, D.M., Mather, T.A., 2013. Evidence of mid- to late-Holocene explosive rhyolitic eruptions from Chaitén Volcano, Chile. Andean Geol. 40, 216–226. https://doi.org/10.5027/andgeoV40n2-a02.

Watt, S.F.L., Pyle, D.M., Mather, T.A., 2011a. Geology, petrology and geochemistry of the dome complex of Huequi volcano, southern Chile. Andean Geol. 38, 335–348. https://doi.org/10.5027/andgeov38n2-a05.

Watt, S.F.L., Pyle, D.M., Mather, T.A., Martin, R.S., Matthews, N.E., 2009. Fallout and distribution of volcanic ash over Argentina following the May 2008 explosive eruption of Chaitén, Chile. J. Geophys. Res. Solid Earth 114, 1–11. https://doi.org/10.1029/2008JB006219.

Watt, S.F.L., Pyle, D.M., Naranjo, J.A., Rosqvist, G., Mella, M., Mather, T.A., Moreno, H., 2011b. Holocene tephrochronology of the Hualaihue region (Andean southern volcanic zone, ~42° S), southern Chile. Quat. Int. 246, 324–343. https://doi.org/10.1016/j.quaint.2011.05.029.

Weller, D., Miranda, C.G., Moreno, P.I., Villa-Martínez, R., Stern, C.R., 2014. The large late-glacial Ho eruption of the Hudson volcano, southern Chile. Bull. Volcanol. 76, 1–18. https://doi.org/10.1007/s00445-014-0831-9.

Weller, D.J., de Porras, M.E., Maldonado, A., Méndez, C., Stern, C.R., 2019. Petrology, geochemistry, and correlation of tephra deposits from a large early-Holocene eruption of Mentolat volcano, southern Chile. J. South Am. Earth Sci. 90, 282–295. https://doi.org/10.1016/j.jsames.2018.12.020.

Weller, D.J., De Porras, M.E., Maldonado, A., Méndez, C., Stern, C.R., 2017. Holocene tephrochronology of the lower Río Cisnes valley, southern Chile. Andean Geol. 44, 229–248. https://doi.org/10.5027/andgeov44n3-a01.

Weller, D.J., Miranda, C.G., Moreno, P.I., Villa-Martínez, R., Stern, C.R., 2015. Tephrochronology of the southernmost andean southern volcanic zone, Chile. Bull. Volcanol. 77, 1–24. https://doi.org/10.1007/s00445-015-0991-2.

4.2 Supplementary material – Figures

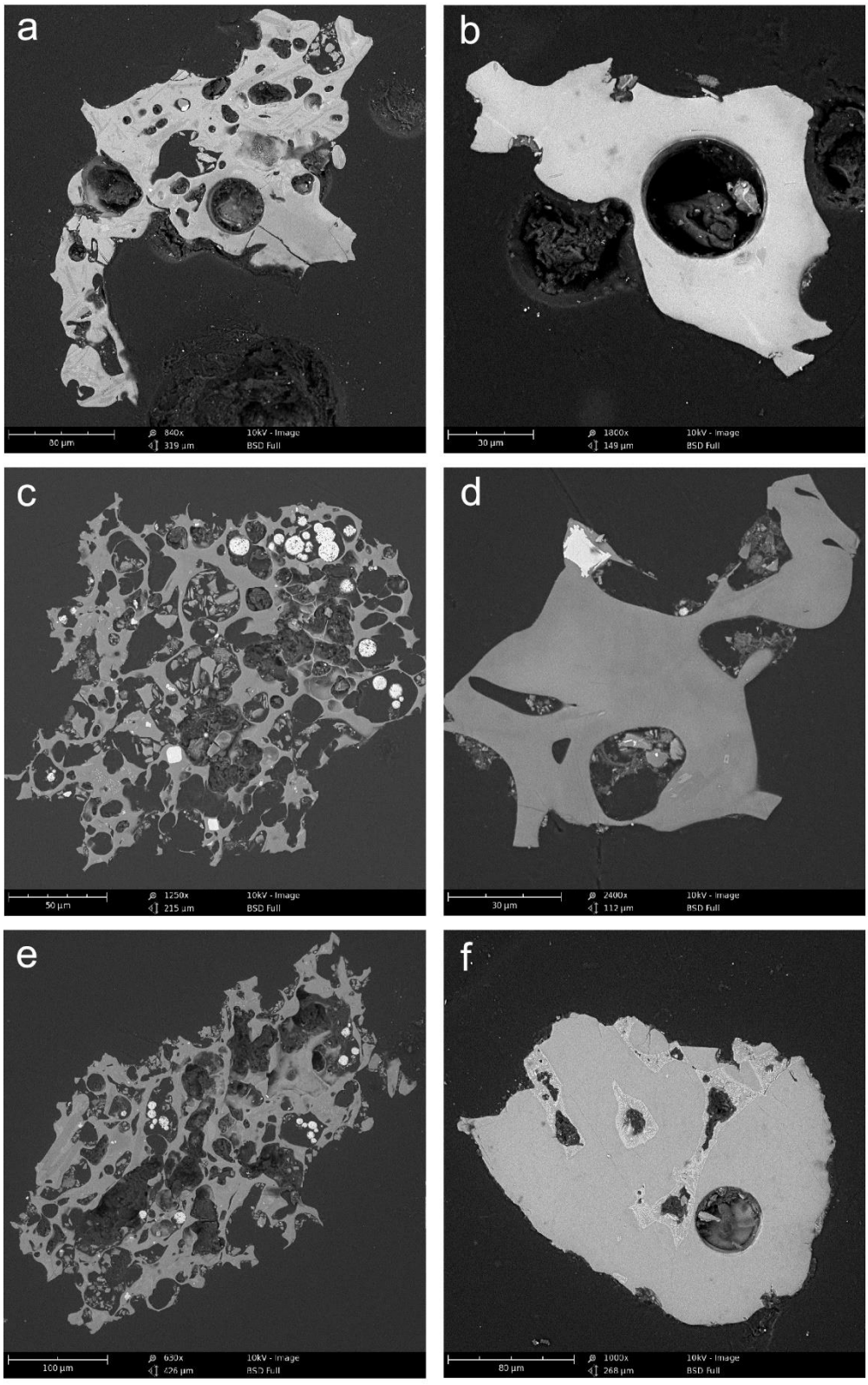

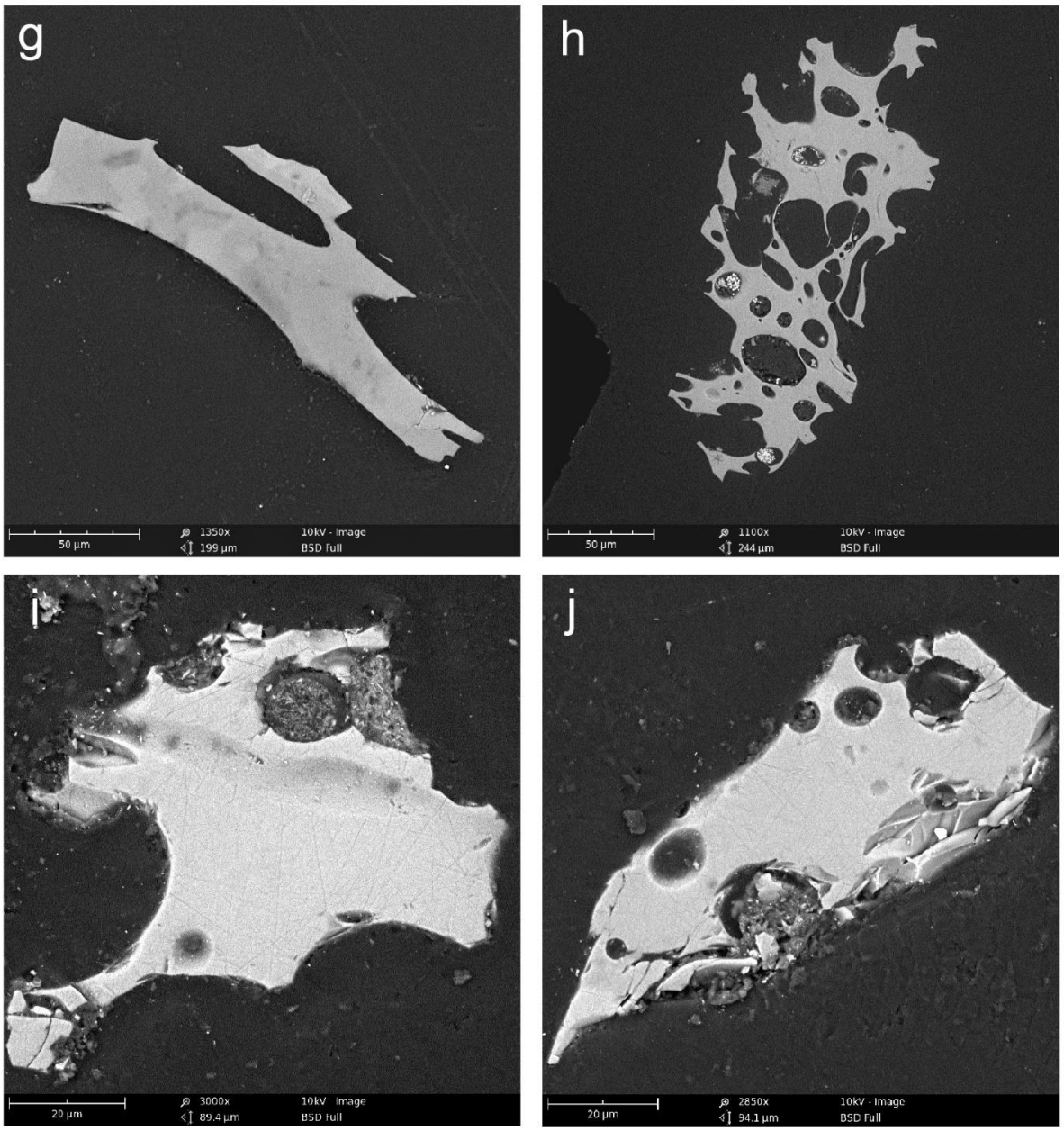

Figure S1. Scanning Electron Microscope individual glass shard images showing pristine morphologies of analyzed glass shards. a–f correspond to tephra T8/100, a and e are microlitic whereas b, c, d and f are microlitic–poor or free shards. g and h: cryptotephra T1/100. i and j: cryptotephra T16/100.

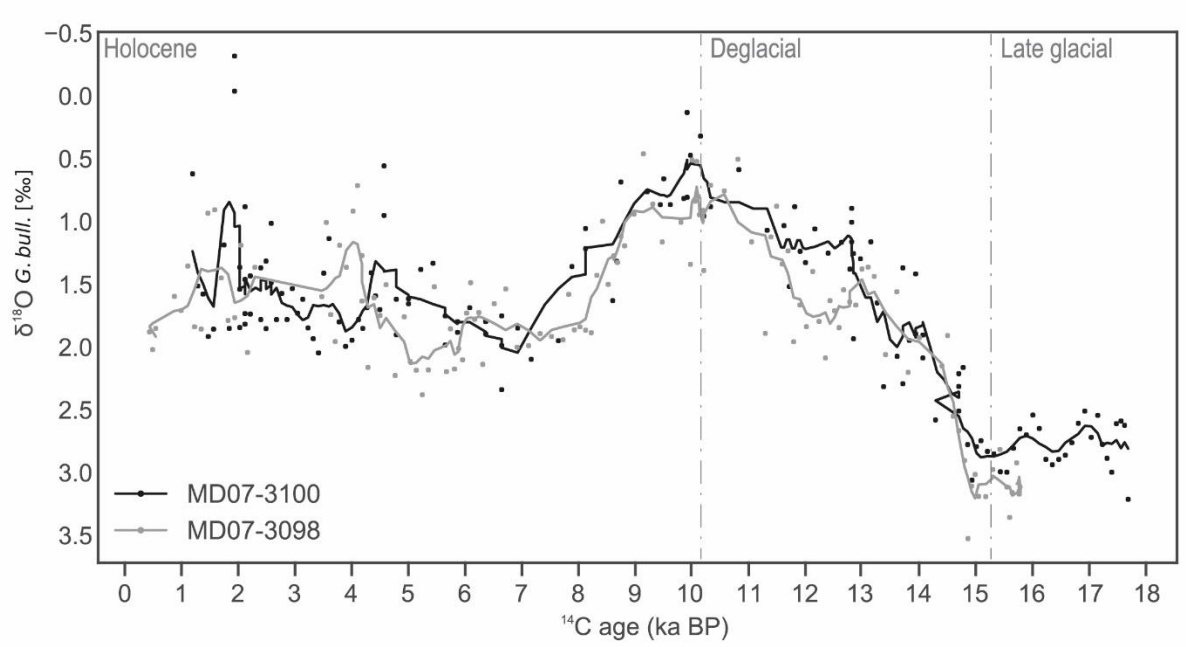

Figure S2. Comparison of planktonic foraminifera *G. bulloides* $\delta^{18}O$ versus interpolated planktonic foraminifera ^{14}C age from cores MD07-3100 (Haddam et al., 2018) and MD07-3098 (Table S1, S3). Points indicate measurements every 10 cm, the lines correspond to the respective three point moving average. Also indicated are climate intervals inferred from the observed changes in $\delta^{18}O$.

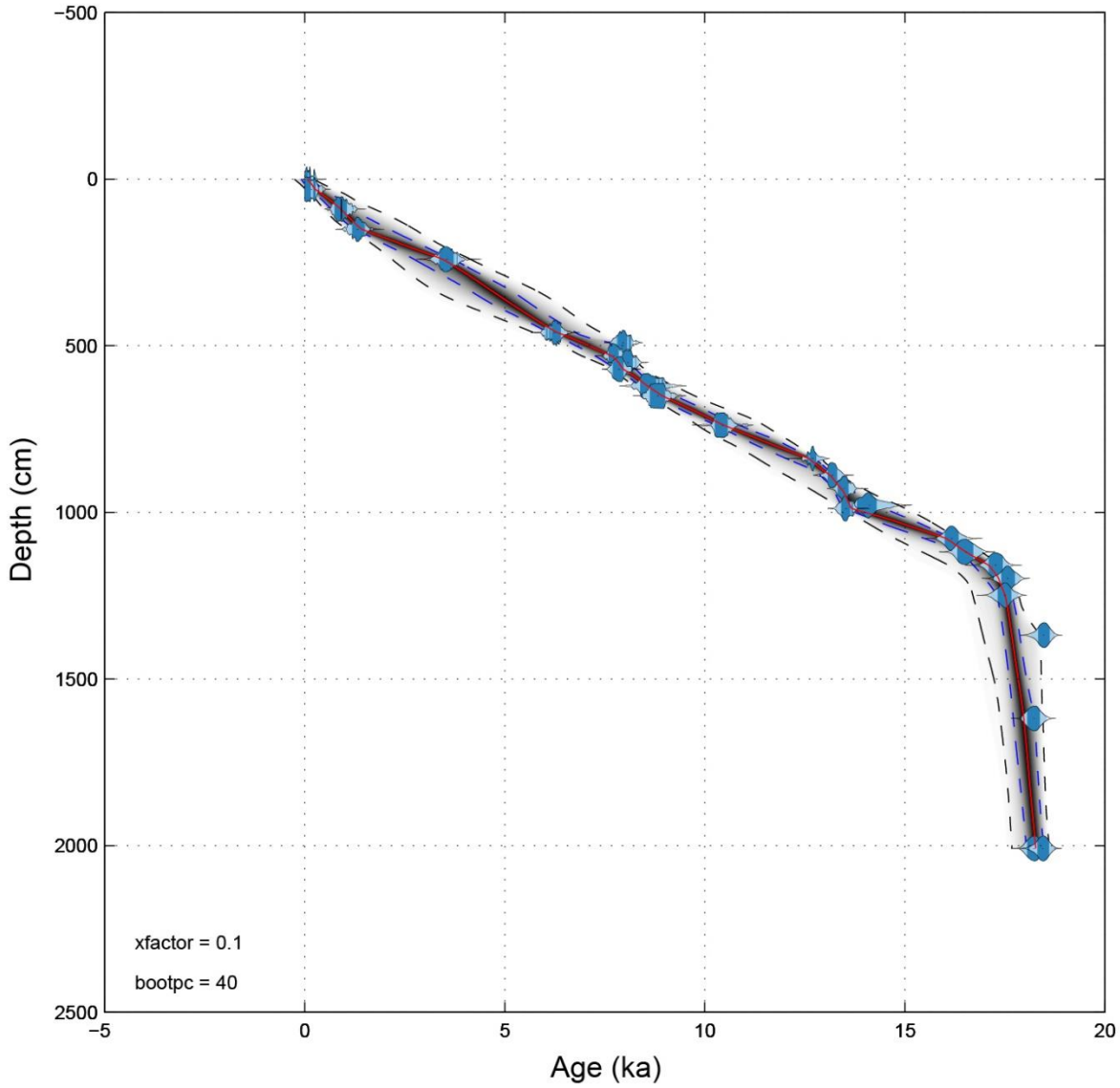

Figure S3. Age model from core MD07-3098 produced from 27 planktonic foraminifera ^{14}C ages corrected by a mobile marine surface reservoir age as described in the text and indicated in Table S5. The age model was produced using the Undatable software (Lougheed and Obrochta, 2019), calibrating with the SHCal20 curve (Hogg et al., 2020). Each calibrated age distribution is plotted in light blue, the red line corresponds to the age–depth model median calendar age, the blue dotted and black dotted lines correspond to the 1σ range and 2σ envelopes, respectively.

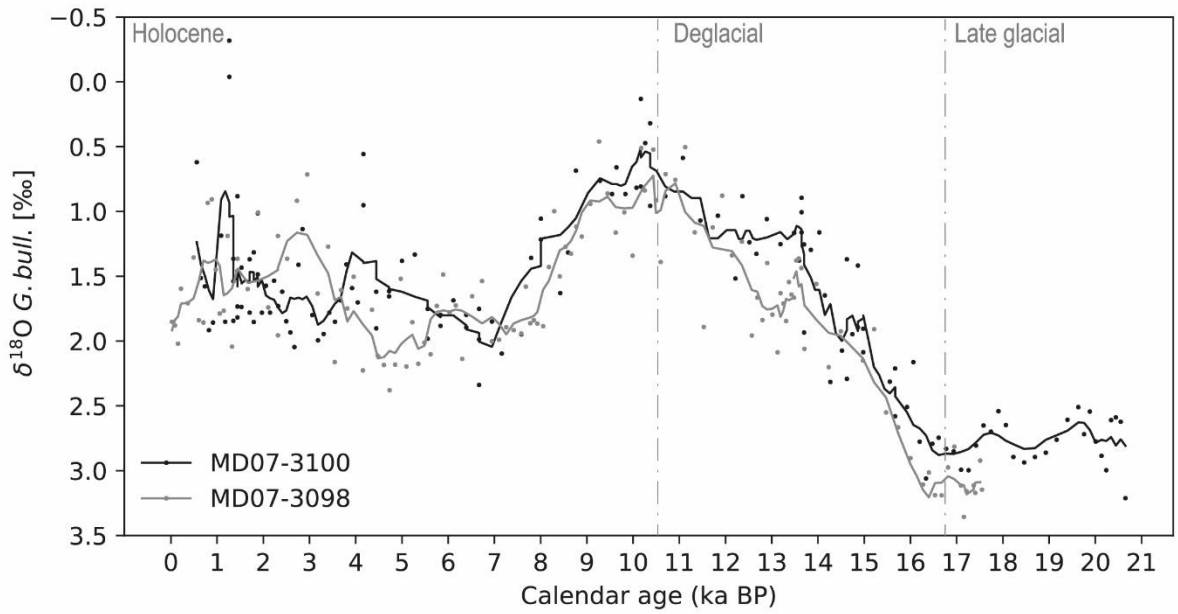

Figure S4. Comparison of planktonic foraminifera *G. bulloides* $\delta^{18}O$ versus estimated calendar ages from cores MD07-3100 (Haddam et al., 2018) and MD07-3098 (Table S1). Points indicate measurements every 10 cm, the lines correspond to the respective three point moving average. Also indicated are climate intervals inferred from the observed changes in $\delta^{18}O$.

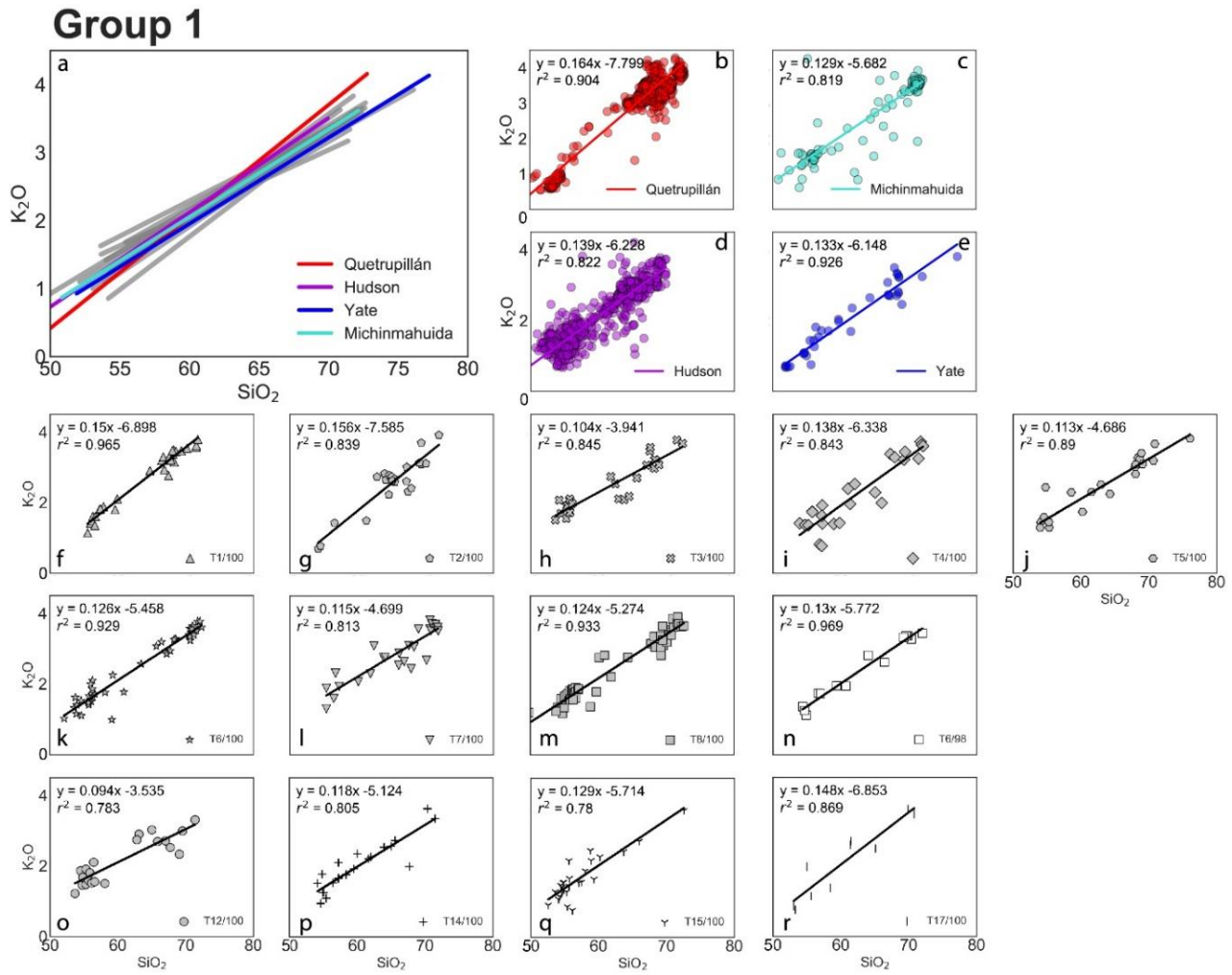

Figure S5. Linear regression for products associated with Group 1. a: The linear regression from each volcanic center and cryptotephra (in grey) associated to Group 1 are plotted together for comparison. Also plotted are lines separating areas with Low-K, Medium-K and High-K according to Peccerillo and Taylor (1976). b, c, d, e: Linear regressions for each volcanic center associated to Group 1 together with the available geochemical information on land from both effusive and explosive products and both micro analytical and bulk analyses. Michinmahuida (Alloway et al., 2017a; Amigo et al., 2013; Casati et al., 2019; López-Escobar et al., 1993; Naranjo and Stern, 2004), Hudson (Bitschene et al., 1993; Carel et al., 2011; Del Carlo et al., 2018; Haberle and Lumley, 1998; Kilian et al., 2003; Kratzmann et al., 2008; López-Escobar et al., 1993; Naranjo et al., 1993; Naranjo and Stern, 1998; Smith et al., 2019; Stern, 2008; Weller et al., 2014, 2019, 2015), Quetrupillán (Brahm et al., 2018; Fontijn et al., 2016; Hickey-Vargas et al., 1989; Rawson et al., 2016; Simmons et al., 2020), Yate (López-Escobar et al., 1993; Mella, 2008; Watt et al., 2011b). f to r: Linear regression for each cryptotephra in Group 1 together with the corresponding glass shard analyses at each depth. Major elements correspond to normalized volatile–free compositions.

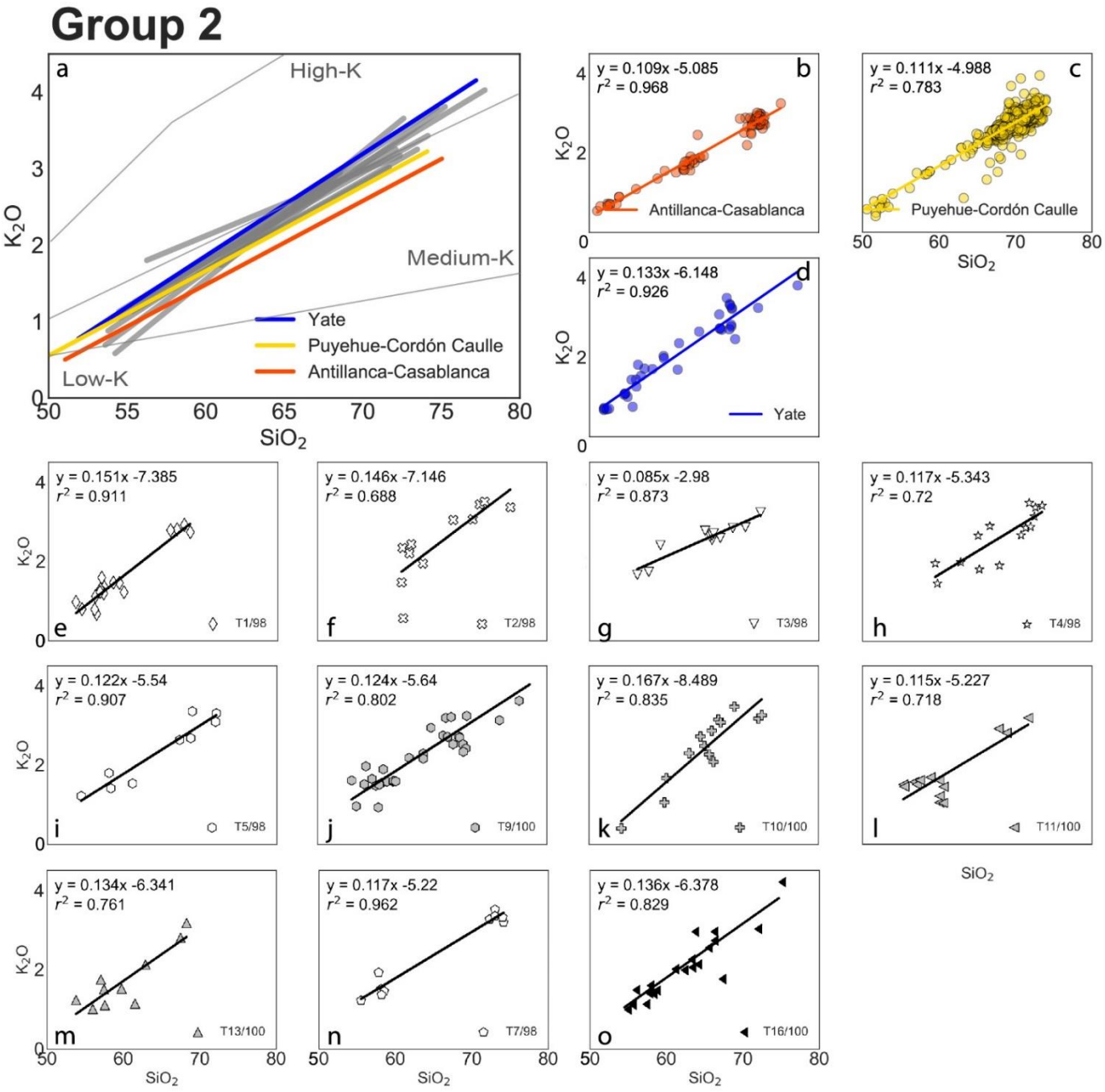

Figure S6. Linear regression for products associated with Group 2. a: The linear regression from each volcanic center and cryptotephra (in grey) associated to Group 2 are plotted together for comparison. Also plotted are lines separating areas with Low-K, Medium-K and High-K according to Peccerillo and Taylor (1976). b, c, d: Linear regressions for each volcanic center associated to Group 2 together with the available geochemical information on land from both effusive and explosive products and both micro analytical and bulk analyses. Puyehue-Cordón Caulle (Alloway et al., 2015; Bertrand et al., 2008; Fontijn et al., 2016; Gerlach et al., 1988; Lara et al., 2006; Naranjo et al., 2017; Rawson et al., 2016; Singer et al., 2008), Antillanca-Casablanca (Fontijn et al., 2016; Geoffroy et al., 2018; Jacques et al., 2014; Naranjo et al., 2017; Rawson et al., 2016; Villarosa et al., 2006) and Yate (López-Escobar et al., 1993; Mella, 2008; Watt et al., 2011b). e to o: Linear regression for each cryptotephra in Group 2 together with the corresponding glass shards analyses at each depth. Major elements correspond to normalized volatile–free compositions.

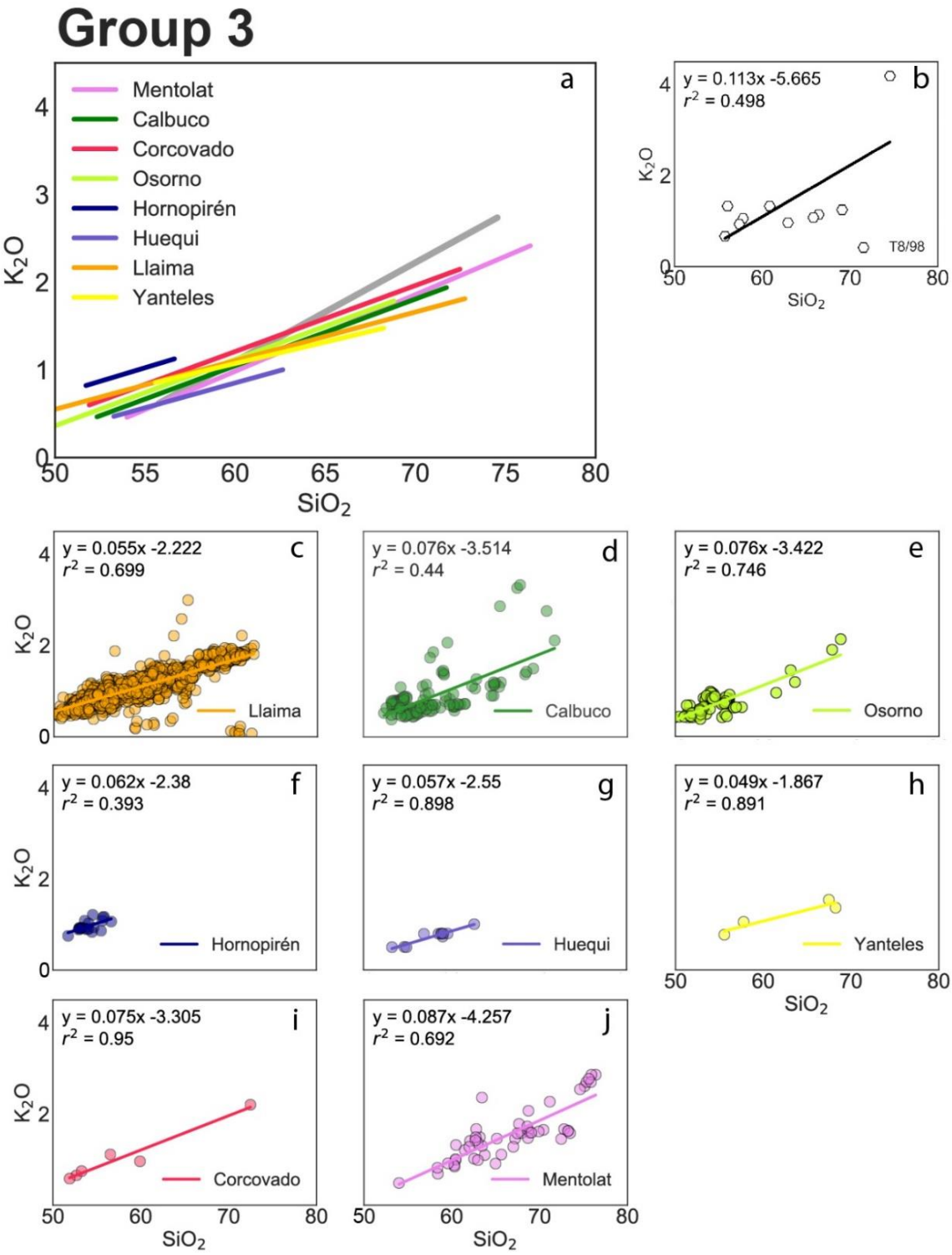

Figure S7. Linear regression for products associated with Group 3. a: The linear regression from each volcanic center and cryptotephra T8/98 (in grey), associated to Group 3. c to j: Linear regressions for each volcanic center associated to Group 3 together with the available geochemical information on land from both effusive and explosive products and both micro analitical and bulk analyses. Llaima (Bouvet de Maisonneuve et al., 2012; Lohmar, 2008; Naranjo and Moreno, 1991, 2005; Rawson et al., 2016; Reubi et al., 2011; Schindlbeck et al., 2014), Osorno (Bertrand et al., 2008; Jacques et al., 2014; López-Escobar et al., 1993, 1992; Moreno et al., 2010; Tagiri et al., 1993), Calbuco (López-Escobar et al., 1995, 1992; Morgado et al., 2019; Sellés and Moreno, 2011; Watt et al., 2011b), Huequi (Watt et al., 2011a), Hornopirén (Watt et al., 2011b), Mentolat (López-Escobar et al., 1993; Naranjo and Stern, 2004; Stern et al., 2015; Weller et al., 2017, 2015) Yanteles and Corcovado (López-Escobar et al., 1993; Naranjo and Stern, 2004). Major elements correspond to normalized volatile–free compositions.

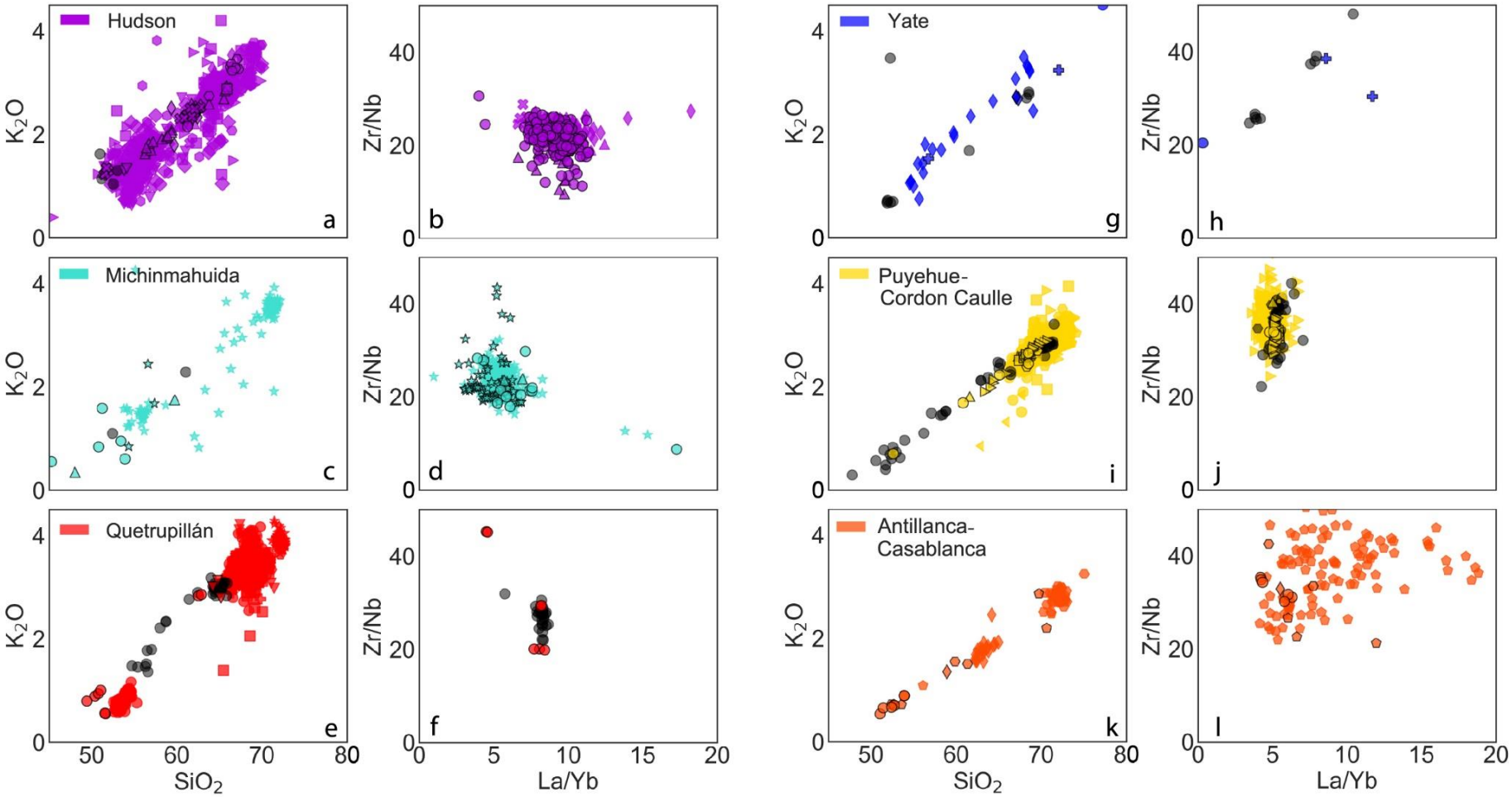

Figure S8. Comparison of the geochemical composition of the different types of analyzed products for volcanoes in Group 1 (a–h) and 2 (g–l). For all plots: analyses of lavas correspond to black markers, bulk tephra correspond to colored markers with black edges and glass shard analyses correspond to colored markers with colored edges. Hudson (Bitschene et al., 1993; Carel et al., 2011; Del Carlo et al., 2018; Haberle and Lumley, 1998; Kilian et al., 2003; Kratzmann et al., 2008; López-Escobar et al., 1993; Naranjo et al., 1993; Naranjo and Stern, 1998; Smith et al., 2019; Stern, 2008; Weller et al., 2014, 2019, 2015), Michinmahuida (Alloway et al., 2017a; Amigo et al., 2013; Casati et al., 2019; López-Escobar et al., 1993; Naranjo and Stern, 2004), Quetrupillán (Brahm et al., 2018; Fontijn et al., 2016; Hickey-Vargas et al., 1989; Rawson et al., 2016; Simmons et al., 2020), Yate (López-Escobar et al., 1993; Mella, 2008; Watt et al., 2011b), Puyehue-Cordón Caulle (Alloway et al., 2015; Bertrand et al., 2008; Fontijn et al., 2016; Gerlach et al., 1988; Lara et al., 2006; Naranjo et al., 2017; Rawson et al., 2016; Singer et al., 2008), Antillanca-Casablanca (Fontijn et al., 2016; Geoffroy et al., 2018; Jacques et al., 2014; Naranjo et al., 2017; Rawson et al., 2016; Villarosa et al., 2006).

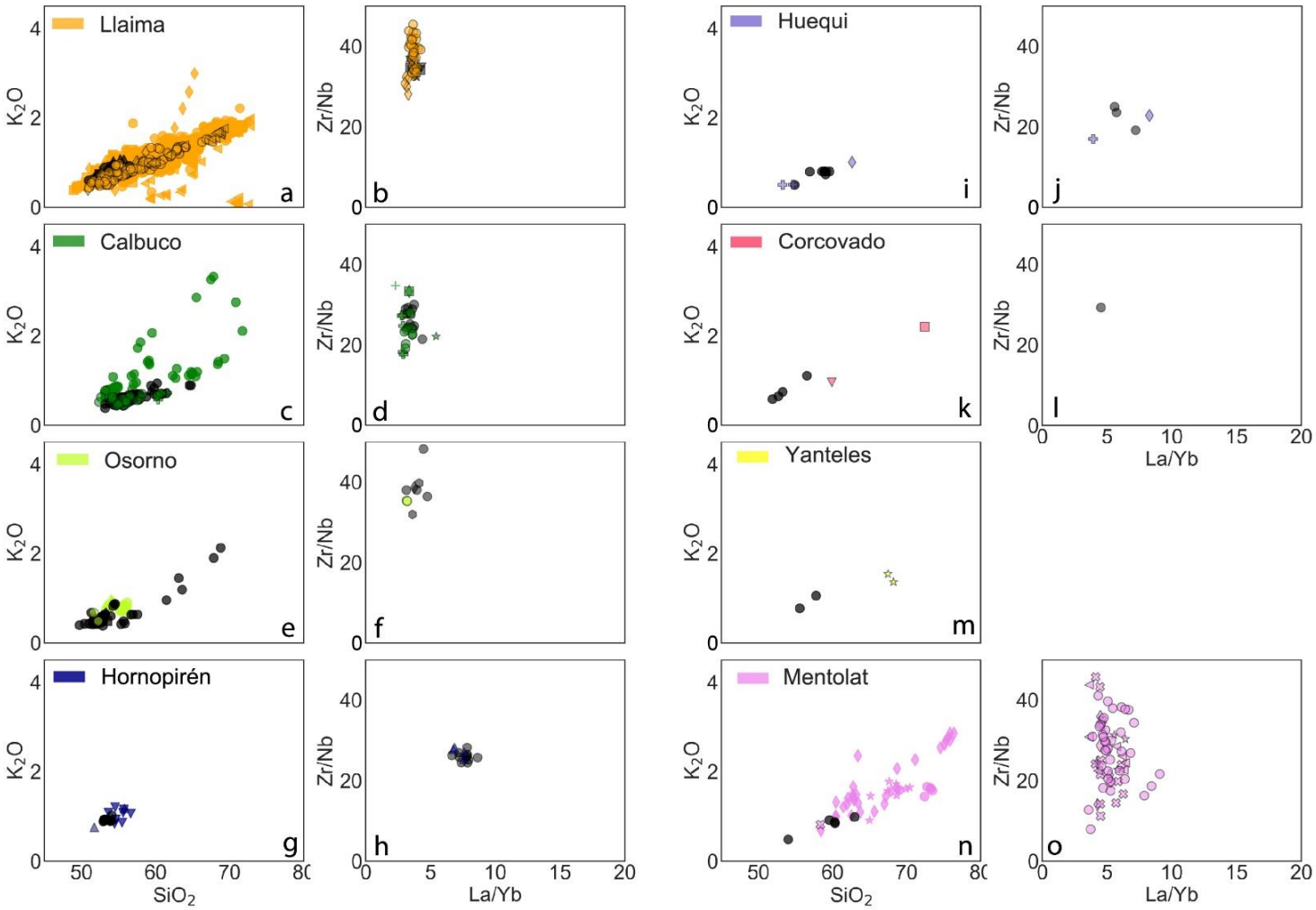

Figure S9. Comparison of the geochemical composition of the different types of analyzed products for volcanoes in Group 3. For all plots: analyses of lavas correspond to black markers, bulk tephra correspond to colored markers with black edges and glass shard analyses correspond to colored markers with colored edges. Llaima (Bouvet de Maisonneuve et al., 2012; Naranjo and Moreno, 1991, 2005; Rawson et al., 2016; Reubi et al., 2011; Schindlbeck et al., 2014; Lohmar, 2008), Osorno (Bertrand et al., 2008; Jacques et al., 2014; López-Escobar et al., 1993, 1992; Moreno et al., 2010; Tagiri et al., 1993), Calbuco (López-Escobar et al., 1995, 1992; Morgado et al., 2019; Watt et al., 2011b; Sellés and Moreno, 2011), Huequi (Watt et al., 2011a), Hornopirén (Watt et al., 2011b), Mentolat (López-Escobar et al., 1993; Naranjo and Stern, 2004; Stern et al., 2015; Weller et al., 2017, 2015) Yanteles and Corcovado (López-Escobar et al., 1993; Naranjo and Stern, 2004). Major elements correspond to normalized volatile–free compositions.

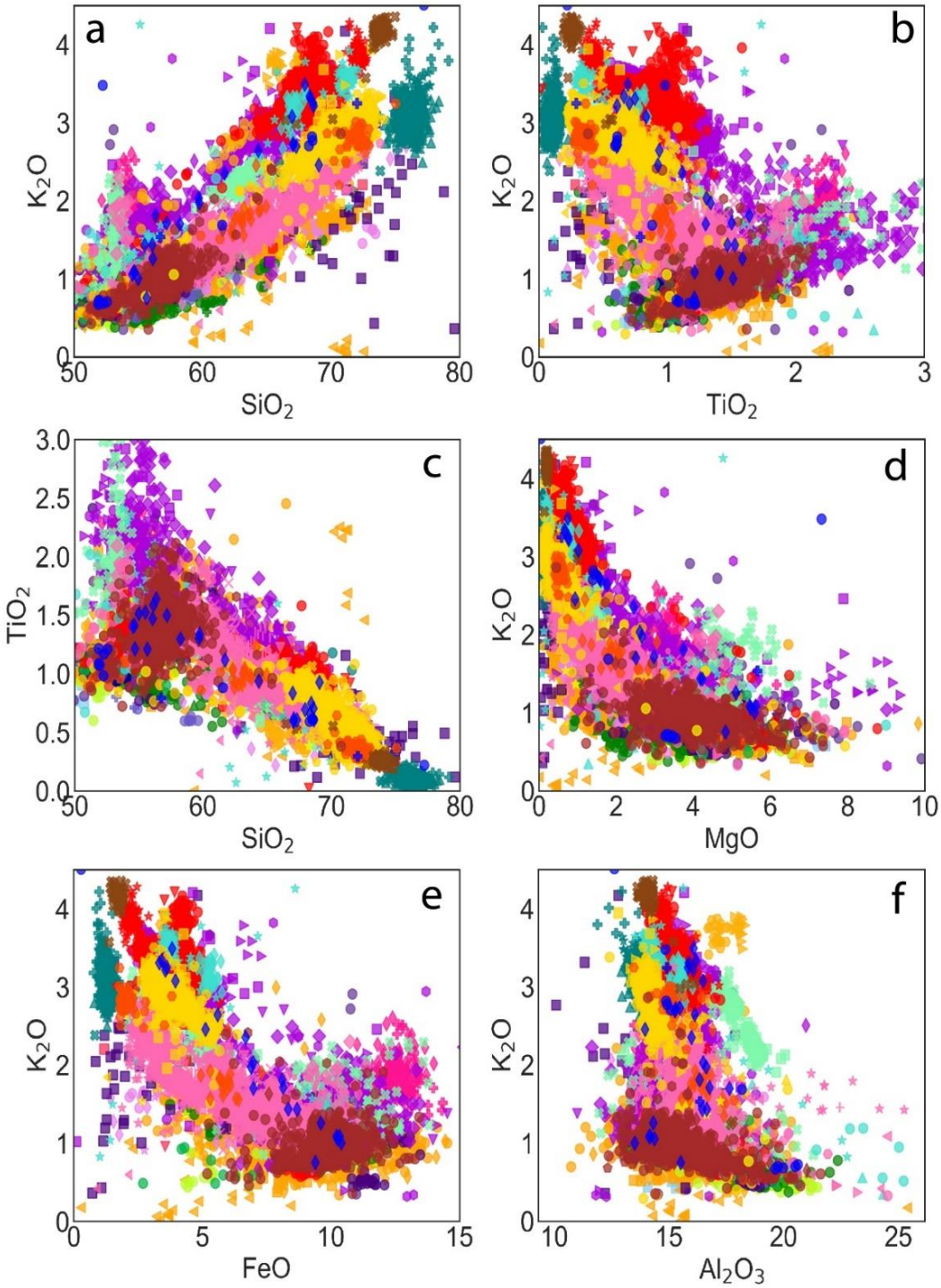

Figure S10. Major element comparison of effusive and explosive data from volcanic center between Llaima and Hudson here consider as potential sources of the cryptotephra and tephra in marine sediment cores MD07-3100 and MD07-3098. Major elements correspond to normalized volatile–free compositions. Detailed legend and references in Figure S16.

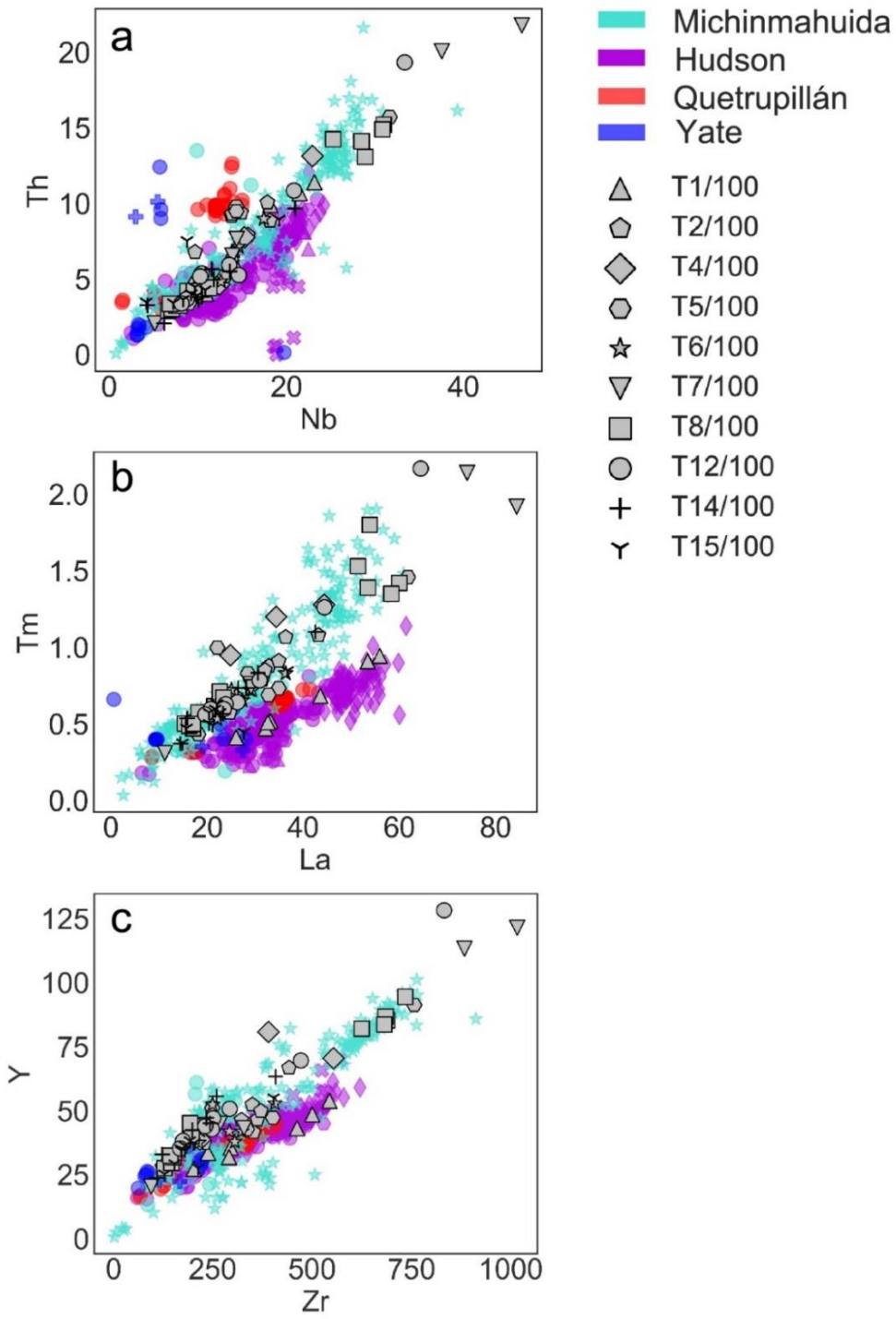

Figure S11. Comparison of trace element from products associated with Group 1. All cryptotephra belonging to Group 1 with available trace elements are plotted in a, b and c and indicated in the legend to the right. Trace element data from Michinmahuida (Alloway et al., 2017a; Amigo et al., 2013; Casati et al., 2019; López-Escobar et al., 1993; Naranjo and Stern, 2004), Hudson (Bitschene et al., 1993; Del Carlo et al., 2018; Kratzmann et al., 2008; López-Escobar et al., 1993; Naranjo and Stern, 1998; Stern, 2008; Weller et al., 2014, 2015), Quetrupillán (Brahm et al., 2018; Hickey-Vargas et al., 1989; Rawson et al., 2016; Simmons et al., 2020) and Yate (López-Escobar et al., 1993; Mella, 2008; Watt et al., 2011b).

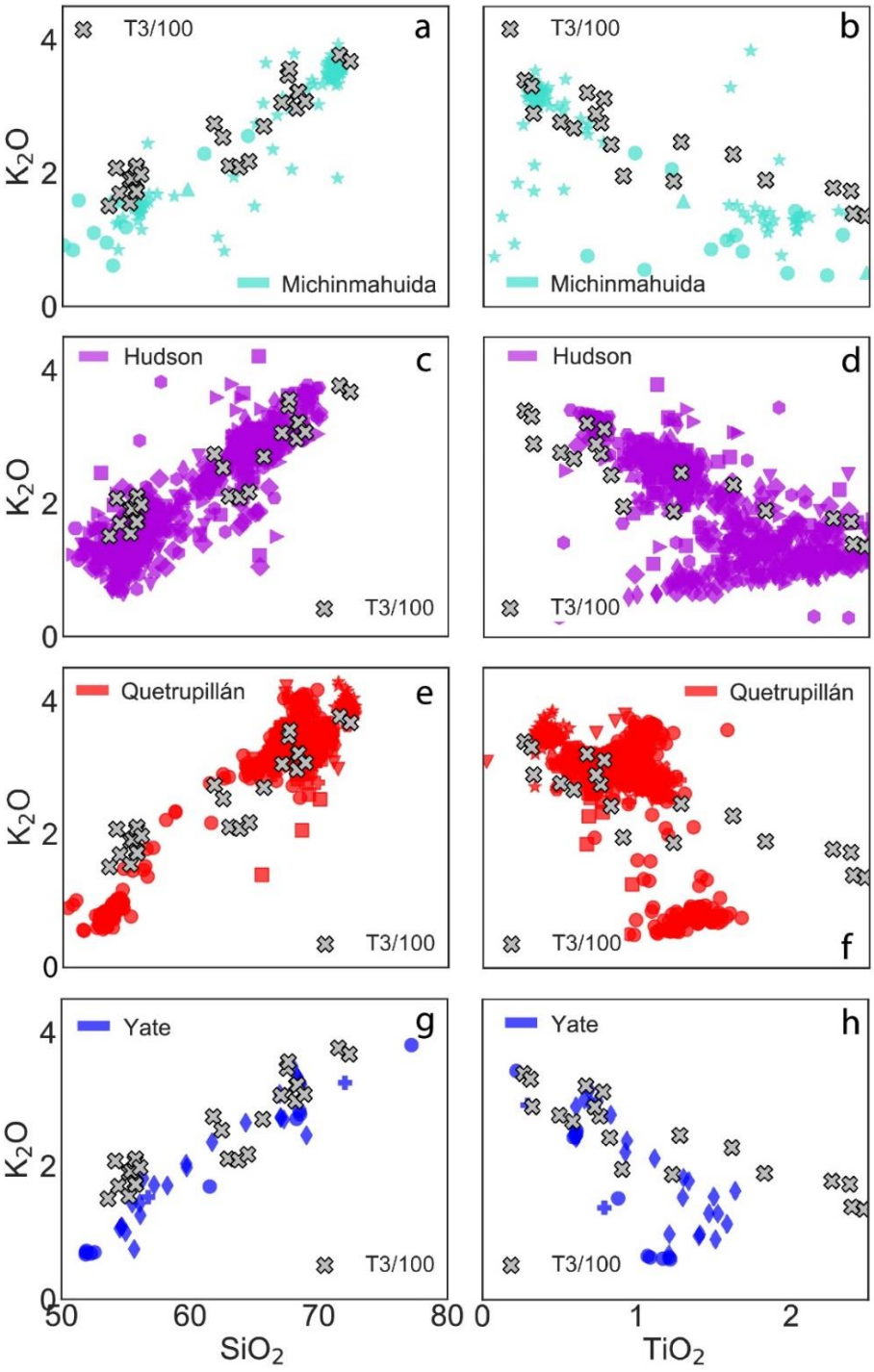

Figure S12. Comparison of individual glass shard geochemistry from crytotephra T3/100 with available information on land of each volcanic center in Group 1. a and b: Michinmahuida (Alloway et al., 2017a; Amigo et al., 2013; Casati et al., 2019; López-Escobar et al., 1993; Naranjo and Stern, 2004),c and d: Hudson (Bitschene et al., 1993; López-Escobar et al., 1993; Naranjo et al., 1993; Naranjo and Stern, 1998; Haberle and Lumley, 1998; Kilian et al., 2003; Kratzmann et al., 2008; Stern, 2008; Carel et al., 2011; Weller et al., 2014, 2015, 2019; Del Carlo et al., 2018; Smith et al., 2019), e and f: Quetrupillán (Brahm et al., 2018; Hickey-Vargas et al., 1989; Fontijn et al., 2016; Rawson et al., 2016; Simmons et al., 2020), g and h: Yate (López-Escobar et al., 1993; Mella, 2008; Watt et al., 2011b). Major elements correspond to normalized volatile–free compositions.

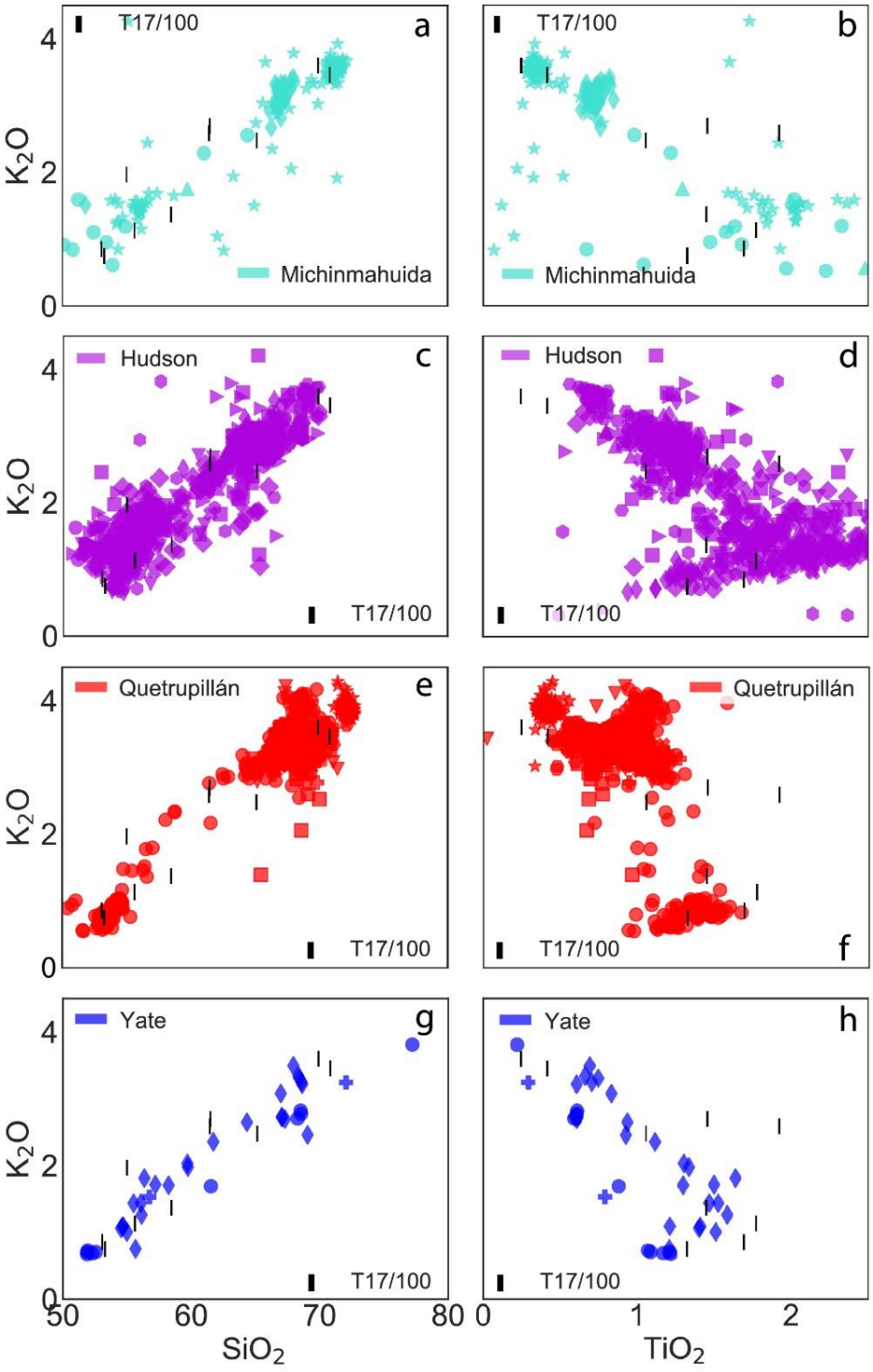

Figure S13. Comparison of individual glass shard geochemistry from crytotephra T17/100 with available information on land of each volcanic center in Group 1. a and b: Michinmahuida (López-Escobar et al., 1993; Naranjo and Stern, 2004; Amigo et al., 2013; Alloway et al., 2017a, b), c and d: Hudson (Bitschene et al., 1993; López-Escobar et al., 1993; Naranjo et al., 1993; Naranjo and Stern, 1998; Haberle and Lumley, 1998; Kilian et al., 2003; Kratzmann et al., 2008; Stern, 2008; Carel et al., 2011; Weller et al., 2014, 2015, 2019; Del Carlo et al., 2018; Smith et al., 2019), e and f: Quetrupillán (Brahm et al., 2018; Hickey-Vargas et al., 1989; Fontijn et al., 2016; Rawson et al., 2016; Simmons et al., 2020), g and h: Yate (López-Escobar et al., 1993; Mella, 2008; Watt et al., 2011b). Major elements correspond to normalized volatile–free compositions.

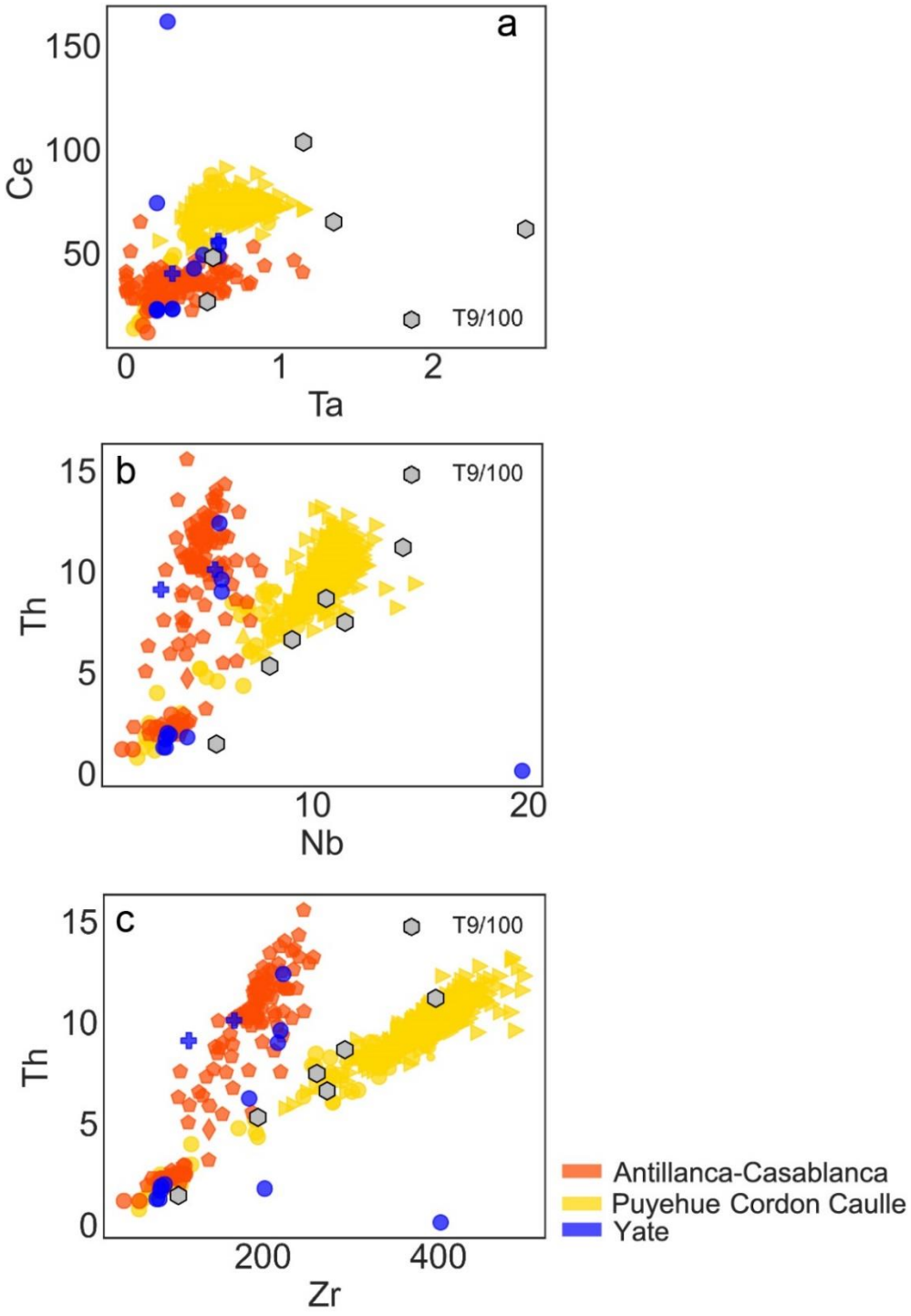

Figure S14. Comparison of individual glass shard geochemistry from crytotephra T9/100 with available information on land of each volcanic center in Group 2. Trace element data from Puyehue-Cordón Caulle (Alloway et al., 2015; Gerlach et al., 1988; Lara et al., 2006; Naranjo et al., 2017; Rawson et al., 2016; Singer et al., 2008), Antillanca-Casablanca (Geoffroy et al., 2018; Jacques et al., 2014; Naranjo et al., 2017; Rawson et al., 2016; Villarosa et al., 2006) and Yate (López-Escobar et al., 1993; Mella, 2008; Watt et al., 2011b).

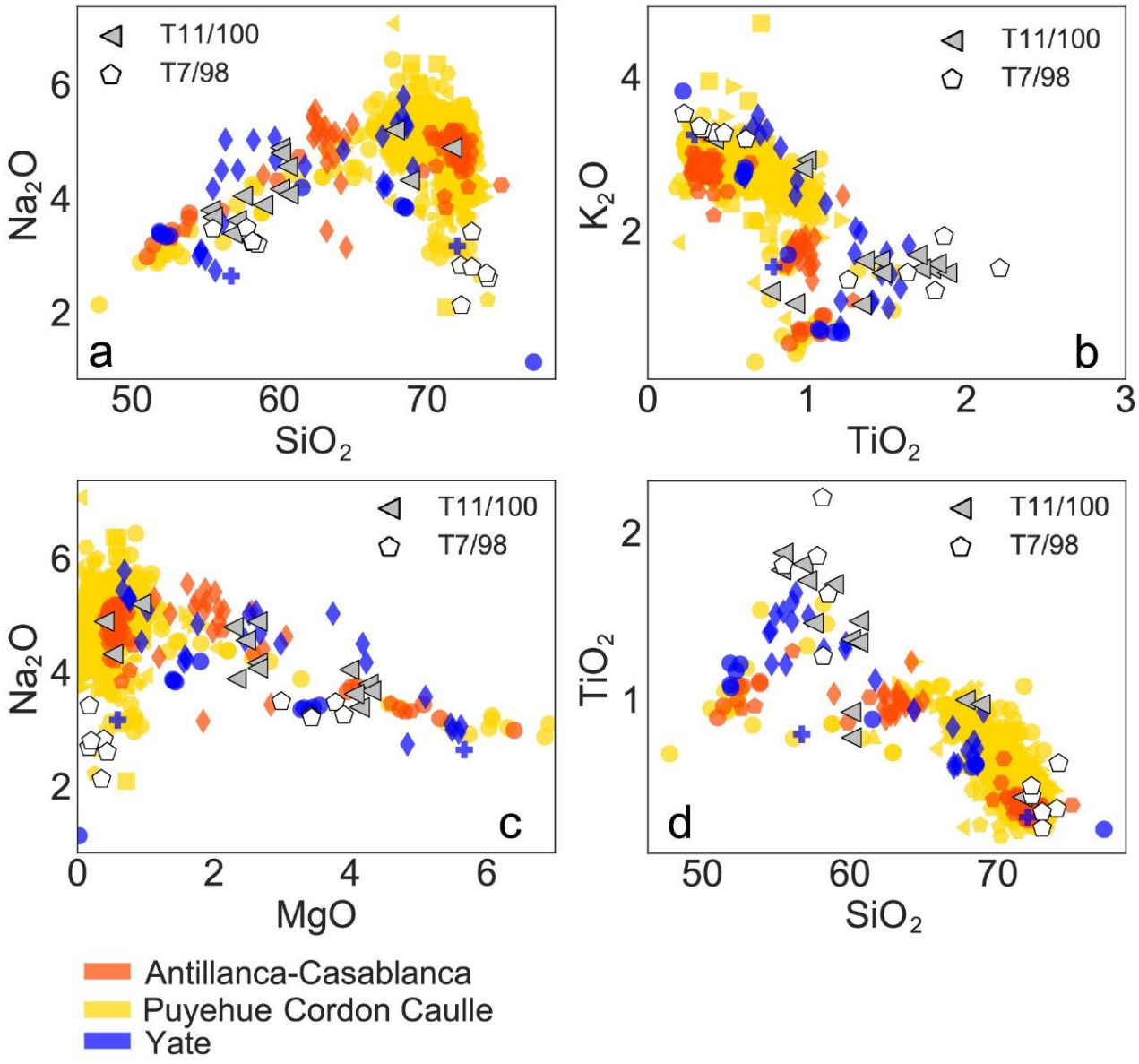

Figure S15. Comparison of major element glass shards composition from cryptotephras T11/100 and T7/98 which have a similar stratigraphic position an estimated calendar age, as indicated in the text. Also shown are composition from products associated with volcanic centers in Group 2: Puyehue-Cordón Caulle (Alloway et al., 2015; Bertrand et al., 2008; Fontijn et al., 2016; Gerlach et al., 1988; Lara et al., 2006; Naranjo et al., 2017; Rawson et al., 2016; Singer et al., 2008), Antillanca-Casablanca (Fontijn et al., 2016; Geoffroy et al., 2018; Jacques et al., 2014; Naranjo et al., 2017; Rawson et al., 2016; Villarosa et al., 2006) and Yate (López-Escobar et al., 1993; Mella, 2008; Watt et al., 2011b). Major elements correspond to normalized volatile–free compositions.

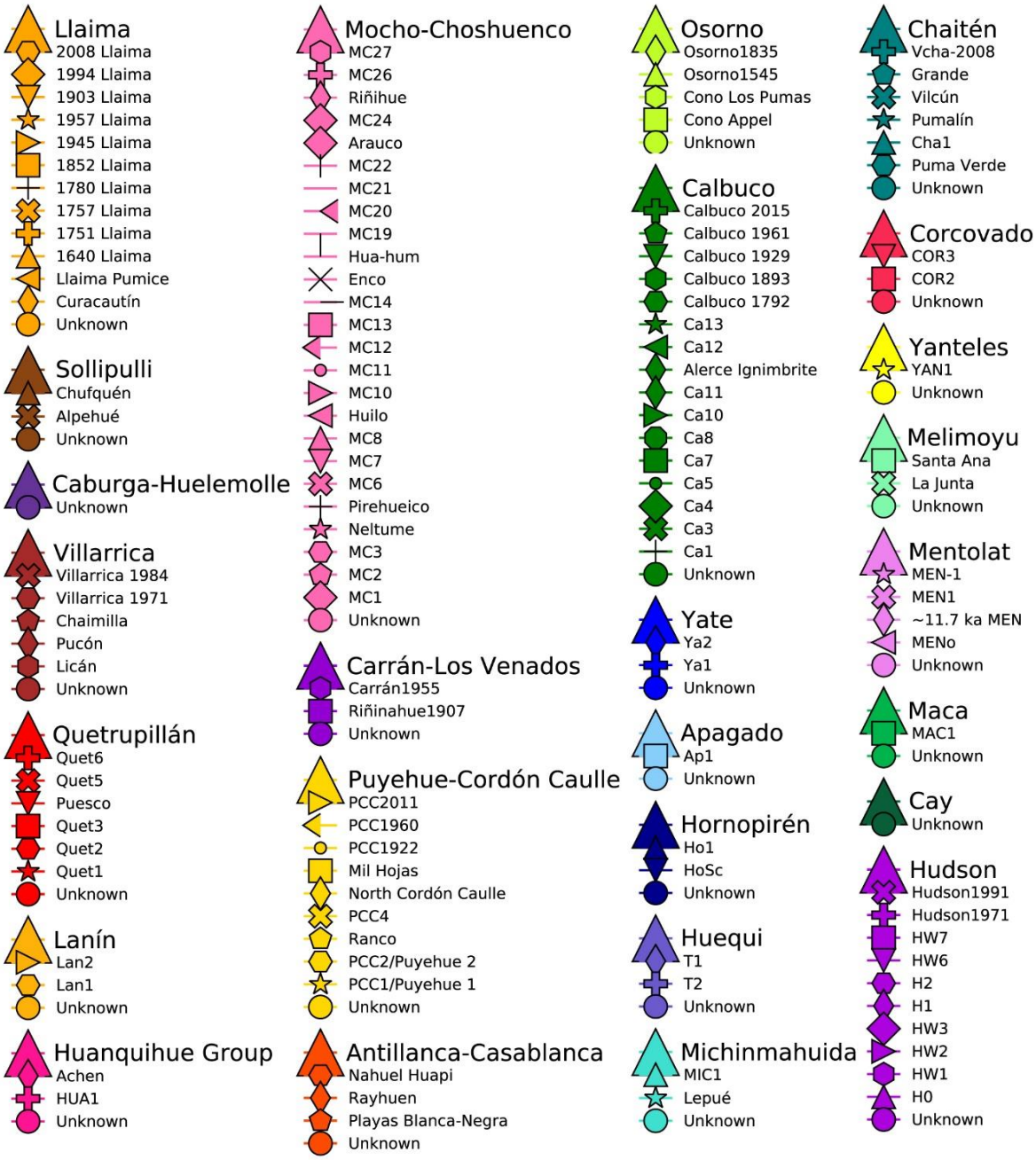

Figure S16. Detailed legend for Figure 1 and S10. "Unknown" correspond to products associated with a volcanic center but which are not yet associated with any particular eruption. The complete legend from which the latter was compiled is detailed below.

Llaima (Bouvet de Maisonneuve et al., 2012; Fontijn et al., 2016; Jacques et al., 2014; Lohmar, 2008; Naranjo and Moreno, 1991, 2005; Rawson et al., 2016; Reubi et al., 2011; Schindlbeck et al., 2014)

Sollipulli (Fontijn et al., 2014; Naranjo et al., 1993b)

Caburga-Huelemolle (Fontijn et al., 2016; Hickey-Vargas et al., 1989; Jacques et al., 2014; Morgado et al., 2015; Rawson et al., 2016)

Villarrica (Costantini et al., 2011; Fontijn et al., 2016; Hickey-Vargas et al., 1989; Jacques et al., 2014; Lohmar et al., 2012; Rawson et al., 2016)

Quetrupillán (Brahm et al., 2018; Fontijn et al., 2016; Hickey-Vargas et al., 1989; Rawson et al., 2015; Simmons et al., 2020)

Lanín (Fontijn et al., 2016; Hickey-Vargas et al., 1989; Lara et al., 2004)

Huanquqihue Group (Fontijn et al., 2016; Rawson et al., 2016)

Mocho-Choshuenco (Fontijn et al., 2016; Jacques et al., 2014; Rawson et al., 2016, 2015)

Carrán-Los Venado (Bertrand et al., 2008; Bucchi et al., 2015; Fontijn et al., 2016; Singer et al., 2008)

Puehue-Cordón Caulle (Alloway et al., 2015; Bertrand et al., 2008; Fontijn et al., 2016; Gerlach et al., 1988; Lara et al., 2006; Naranjo et al., 2017; Rawson et al., 2016; Singer et al., 2008)

Antillanca-Casablanca (Fontijn et al., 2016; Geoffroy et al., 2018; Jacques et al., 2014; Lara et al., 2006; Naranjo et al., 2017; Rawson et al., 2016; Singer et al., 2008; Villarosa et al., 2006)

Osorno (Bertrand et al., 2008; Fontijn et al., 2016; Jacques et al., 2014; López-Escobar et al., 1992; Moreno, 2010; Tagiri et al., 1993)

Calbuco (Fontijn et al., 2016; López-Escobar et al., 1995, 1992; Morgado et al., 2019; Rawson et al., 2016; Sellés and Moreno, 2011; Watt et al., 2011b)

Yate, Apagado, Hornopirén (López-Escobar et al., 1993; Mella, 2008; Watt et al., 2011b)

Huequi (López-Escobar et al., 1993; Watt et al., 2011a)

Michinmahuida (Alloway et al., 2017a, 2017b; Amigo et al., 2013; Casati et al., 2019; López-Escobar et al., 1993; Naranjo and Stern, 2004)

Chaitén (Alloway et al., 2017b; Amigo et al., 2013; Casati et al., 2019; Fontijn et al., 2016; López-Escobar et al., 1993; Moreno et al., 2015; Naranjo and Stern, 2004; Watt et al., 2013, 2011b)

Corcovado (Casati et al., 2019; López-Escobar et al., 1993; Naranjo and Stern, 2004)

Yanteles (López-Escobar et al., 1993; Naranjo and Stern, 2004)

Melimoyu (Geoffroy et al., 2018; López-Escobar et al., 1993; Naranjo and Stern, 2004, 1998; Stern et al., 2015; Weller et al., 2017)

Mentolat (López-Escobar et al., 1993; Naranjo and Stern, 2004; Stern et al., 2015; Weller et al., 2019, 2017, 2015)

Maca (D'Orazio et al., 2003; López-Escobar et al., 1993; Naranjo and Stern, 2004; Weller et al., 2015)

Cay (D'Orazio et al., 2003; López-Escobar et al., 1993; Naranjo and Stern, 1998)

Hudson (Carel et al., 2011; Del Carlo et al., 2018; Haberle and Lumley, 1998; Haddam et al., 2018; Kilian et al., 2003; Kratzmann et al., 2008; López-Escobar et al., 1993; Naranjo et al., 1993a; Naranjo and Stern, 1998; Smith et al., 2019; Stern, 2008; Weller et al., 2014, 2019, 2015)

4.2.1 References

Alloway, B. V., Moreno, P.I., Pearce, N.J.G., De Pol-Holz, R., Henríquez, W.I., Pesce, O.H., Sagredo, E., Villarosa, G., Outes, V., 2017a. Stratigraphy, age and correlation of Lepué Tephra: a widespread c. 11 000 cal a BP marker horizon sourced from the Chaitén Sector of southern Chile. J. Quat. Sci. 32, 795–829. https://doi.org/10.1002/jqs.2976

Alloway, B. V., Pearce, N.J.G., Moreno, P.I., Villarosa, G., Jara, I., De Pol-Holz, R., Outes, V., 2017b. An 18,000 year-long eruptive record from Volcán Chaitén, northwestern Patagonia: Paleoenvironmental and hazard-assessment implications. Quat. Sci. Rev. 168, 151–181. https://doi.org/10.1016/j.quascirev.2017.05.011

Alloway, B. V., Pearce, N.J.G., Villarosa, G., Outes, V., Moreno, P.I., 2015. Multiple melt bodies fed the AD 2011 eruption of Puyehue-Cordón Caulle, Chile. Sci. Rep. 5. https://doi.org/10.1038/srep17589

Amigo, Á., Lara, L.E., Smith, V.C., 2013. Holocene record of large explosive eruptions from Chaitén and Michinmahuida Volcanoes, Chile. Andean Geol. 40, 227–248. https://doi.org/10.5027/andgeov40n2-a03

Bertrand, S., Castiaux, J., Juvigné, E., 2008. Tephrostratigraphy of the late glacial and Holocene sediments of Puyehue Lake (Southern Volcanic Zone, Chile, 40°S). Quat. Res. 70, 343–357. https://doi.org/10.1016/j.yqres.2008.06.001

Bertrand, S., Daga, R., Bedert, R., Fontijn, K., 2014. Deposition of the 2011-2012 Cordón Caulle tephra (Chile, 40°S) in lake sediments: Implications for tephrochronology and volcanology. J. Geophys. Res. Earth Surf. 119, 2555–2573. https://doi.org/10.1002/2014JF003321

Bouvet de Maisonneuve, C., Dungan, M.A., Bachmann, O., Burgisser, A., 2012. Insights into shallow magma storage and crystallization at Volcán Llaima (Andean Southern Volcanic Zone, Chile). J. Volcanol. Geotherm. Res. 211–212, 76–91. https://doi.org/10.1016/j.jvolgeores.2011.09.010

Brahm, R., Parada, M.A., Morgado, E., Contreras, C., McGee, L.E., 2018. Origin of Holocene trachyte lavas of the Quetrupillán volcanic complex, Chile: Examples of residual melts in a rejuvenated crystalline mush reservoir. J. Volcanol. Geotherm. Res. 357, 163–176. https://doi.org/10.1016/j.jvolgeores.2018.04.020

Bucchi, F., Lara, L.E., Gutiérrez, F., 2015. The Carrán-Los Venados volcanic field and its relationship with coeval and nearby polygenetic volcanism in an intra-arc setting. J. Volcanol. Geotherm. Res. 308, 70–81. https://doi.org/10.1016/j.jvolgeores.2015.10.013

Carel, M., Siani, G., Delpech, G., 2011. Tephrostratigraphy of a deep-sea sediment sequence off the south Chilean margin: New insight into the Hudson volcanic activity since the last glacial period. J.

Volcanol. Geotherm. Res. 208, 99–111. https://doi.org/10.1016/j.jvolgeores.2011.09.011

Casati, E., D'Amico, M., Šefrna, L., Trombino, L., Tunesi, A., Previtali, F., 2019. Geo-pedological contribution to the reconstruction of Holocene activity of Chaitén volcano (Patagonia, Chile). J. South Am. Earth Sci. 94. https://doi.org/10.1016/j.jsames.2019.102222

Costantini, L., Pioli, L., Bonadonna, C., Clavero, J., Longchamp, C., 2011. A Late Holocene explosive mafic eruption of Villarrica volcano, Southern Andes: The Chaimilla deposit. J. Volcanol. Geotherm. Res. 200, 143–158. https://doi.org/10.1016/j.jvolgeores.2010.12.010

Del Carlo, P., Di Roberto, A., D'Orazio, M., Petrelli, M., Angioletti, A., Zanchetta, G., Maggi, V., Daga, R., Nazzari, M., Rocchi, S., 2018. Late Glacial-Holocene tephra from southern Patagonia and Tierra del Fuego (Argentina, Chile): A complete textural and geochemical fingerprinting for distal correlations in the Southern Hemisphere. Quat. Sci. Rev. 195, 153–170. https://doi.org/10.1016/j.quascirev.2018.07.028

D'Orazio, M., Innocenti, F., Manetti, P., Tamponi, M., Tonarini, S., González-Ferrán, O., Lahsen, A., Omarini, R., 2003. The Quaternary calc-alkaline volcanism of the Patagonian Andes close to the Chile triple junction: geochemistry and petrogenesis of volcanic rocks from the Cay and Maca volcanoes (~45°S, Chile). J. South Am. Earth Sci. 16, 219–242. https://doi.org/10.1016/S0895-9811(03)00063-4

Fontijn, K., Rawson, H., Van Daele, M., Moernaut, J., Abarzúa, A.M., Heirman, K., Bertrand, S., Pyle, D.M., Mather, T.A., De Batist, M., Naranjo, J.A., Moreno, H., 2016. Synchronisation of sedimentary records using tephra: A postglacial tephrochronological model for the Chilean Lake District. Quat. Sci. Rev. 137, 234–254. https://doi.org/10.1016/j.quascirev.2016.02.015

Geoffroy, C.A., Alloway, B.V., Amigo, Á., Parada, M.A., Gutierrez, F., Castruccio, A., Pearce, N.J.G., Morgado, E., Moreno, P.I., 2018. A widespread compositionally bimodal tephra sourced from Volcán Melimoyu (44°S, Northern Patagonian Andes): Insights into magmatic reservoir processes and opportunities for regional correlation. Quat. Sci. Rev. 200, 141–159. https://doi.org/10.1016/j.quascirev.2018.09.034

Gerlach, D.C., Frey, F.A., Moreno-Roa, H., López-Escobar, L., 1988. Recent Volcanism in the Puyehue–Cordon Caulle Region, Southern Andes, Chile (40.5°S): Petrogenesis of Evolved Lavas. J. Petrol. 29, 333–382. https://doi.org/10.1093/petrology/29.2.333

Haberle, S.G., Lumley, S.H., 1998. Age and origin of tephras recorded in postglacial lake sediments to the west of the southern Andes, 44°S to 47°S. J. Volcanol. Geotherm. Res. 84, 239–256. https://doi.org/10.1016/S0377-0273(98)00037-7

Haddam, N.A., Siani, G., Michel, E., Kaiser, J., Lamy, F., Duchamp-Alphonse, S., Hefter, J., Braconnot, P.,

Dewilde, F., Isgüder, G., Tisnerat-Laborde, N., Thil, F., Durand, N., Kissel, C., 2018. Changes in latitudinal sea surface temperature gradients along the Southern Chilean margin since the last glacial. Quat. Sci. Rev. 194, 62–76. https://doi.org/10.1016/j.quascirev.2018.06.023

Hickey-Vargas, R.L., Frey, F.A., Gerlach, D.C, 1986. Multiple sources for basaltic arc rocks from the Southern Volcanic Zone of the Andes (34°–41°S): trace element and isotopic evidence for contributions from subducted oceanic crust, mantle, and continental crust. J. Geophys. Res. 91, 5963–5983. https://doi.org/10.1029/JB091iB06p05963

Hickey-Vargas, R.L., Moreno Roa, H., López-Escobar, L., Frey, F.A., 1989. Geochemical variations in Andean basaltic and silicic lavas from the Villarrica-Lanin volcanic chain (39.5° S): an evaluation of source heterogeneity, fractional crystallization and crustal assimilation. Contrib. to Mineral. Petrol. 103, 361–386. https://doi.org/10.1007/BF00402922

Hogg, A.G., Heaton, T.J., Hua, Q., Palmer, J.G., Turney, C.S.M., Southon, J., Bayliss, A., Blackwell, P.G., Boswijk, G., Bronk Ramsey, C., Pearson, C., Petchey, F., Reimer, P., Reimer, R., Wacker, L., 2020. SHCal20 Southern Hemisphere Calibration, 0-55,000 Years cal BP. Radiocarbon 62, 759–778. https://doi.org/10.1017/RDC.2020.59

Jacques, G., Hoernle, K., Gill, J., Wehrmann, H., Bindeman, I., Lara, L.E., 2014. Geochemical variations in the Central Southern Volcanic Zone, Chile (38–43°S): The role of fluids in generating arc magmas. Chem. Geol. 371, 27–45. https://doi.org/10.1016/j.chemgeo.2014.01.015

Kilian, R., Hohner, M., Biester, H., Wallrabe-Adams, H.J., Stern, C.R. 2003. Holocene peat and lake sediment tephra record from the southernmost Chilean Andes (53-55°S). Rev. Geol. Chile 30, 47–64. https://dx.doi.org/10.4067/S0716-02082003000100002

Kratzmann, D.J., Carey, S., Scasso, R., Naranjo, J.A., 2008. Compositional variations and magma mixing in the 1991 eruptions of Hudson volcano, Chile. Bull. Volcanol. 71, 419–439. https://doi.org/10.1007/s00445-008-0234-x

Lara, L.E., Moreno, H., Naranjo, J.A., Matthews, S., Pérez de Arce, C., 2006. Magmatic evolution of the Puyehue-Cordón Caulle Volcanic Complex (40° S), Southern Andean Volcanic Zone: From shield to unusual rhyolitic fissure volcanism. J. Volcanol. Geotherm. Res. 157, 343–366. https://doi.org/10.1016/j.jvolgeores.2006.04.010

Lara, L.E., Naranjo, J.A., Moreno, H., 2004. Lanín volcano (39.5°S), Southern Andes: geology and morphostructural evolution. Rev. Geol. Chile 31, 241–257. https://doi.org/10.4067/S0716-02082004000200004

Lohmar, 2008. Pétrologie des grands dépôts d'ignimbrites des volcans Villarrica (Licán et Pucón) et

Llaima (Ignimbrite Curacautín), dans les Andes du Sud (Chili). PhD Thesis, Université Blause Pascal - Clermont Ferrand II, France.

Lohmar, S., Parada, M., Gutiérrez, F., Robin, C., Gerbe, M.C., 2012. Mineralogical and numerical approaches to establish the pre-eruptive conditions of the mafic Licán Ignimbrite, Villarrica Volcano (Chilean Southern Andes). J. Volcanol. Geotherm. Res. 235–236, 55–69. https://doi.org/10.1016/j.jvolgeores.2012.05.006

López-Escobar, L., Kilian, R., Kempton, P.D., Tagiri, M., 1993. Petrography and geochemistry of Quaternary rocks from the Southern Volcanic Zone of the Andes between 41°30′ and 46°00′S, Chile. Rev. Geol. Chile 20, 33–55. https://doi.org/10.5027/andgeoV20n1-a04

López-Escobar, L., Parada, M.A., Hickey-Vargas, R.L., Frey, F.A., Kempton, P.D., Moreno, H., 1995. Calbuco Volcano and minor eruptive centers distributed along the Liquiñe-Ofqui Fault Zone, Chile (41°–42° S): contrasting origin of andesitic and basaltic magma in the Southern Volcanic Zone of the Andes. Contrib. to Mineral. Petrol. 119, 345–361. https://doi.org/10.1007/BF00286934

López-Escobar, L., Parada, M.A., Moreno, H., Frey, F.A., Hickey-Vargas, R.L., 1992. A contribution to the petrogenesis of Osorno and Calbuco volcanoes, Southern Andes (41°00'-41°30'S): a comparative study. Rev. Geol. Chile 19, 211–226.

Lougheed, B.C., Obrochta, S.P., 2019. A Rapid, Deterministic Age-Depth Modeling Routine for Geological Sequences With Inherent Depth Uncertainty. Paleoceanogr. Paleoclimatology 34, 122–133. https://doi.org/10.1029/2018PA003457

Martínez Fontaine, C., Siani, G., Delpech, G., Michel, E., Villarosa, G., Manssouri, F., Nouet, J. Post–glacial tephrochronology record off the Chilean continental margin (~41° S). Quaternary Science Reviews. Quaternary Science Reviews 261, 106928. https://doi.org/10.1016/j.quascirev.2021.106928

Mella, M, 2008. Petrogêneses do complexo vulcânico Yate (42, 30ºS), Andes do Sul, Chile. Tese de Doutorado, Instituto de Geociências, Universidade de São Paulo, São Paulo. https://doi.org/10.11606/T.44.2009.tde-04032009-091537

Moreno, P.I., Alloway, B. V., Villarosa, G., Outes, V., Henríquez, W.I., Pol-Holz, R. De, Pearce, N.J.G., 2014. A past-millennium maximum in postglacial activity from Volcán Chaitén, southern Chile. Geology 43, 47–50. https://doi.org/10.1130/G36248.1

Moreno, H., Lara, L., Orozco, G., 2010. Geología del Volcán Osorno, Región de Los Lagos. Servicio Nacional de Geología y Minería, Carta Geológica de Chile, Serie Geológica Básica, 126, 1–31, Santiago.

Moreno, H., Naranjo, J., 2002. Mapa de Peligros del Volcán Llaima, Región de La Araucanía. Servicio Nacional de Geología y Minería, Carta Geológica de Chile, Serie Geología Ambiental 7. Santiago.

https://doi.org/10.13140/RG.2.1.1844.3124

Morgado, E., Morgan, D.J., Harvey, J., Parada, M.Á., Castruccio, A., Brahm, R., Gutiérrez, F., Georgiev, B., Hammond, S.J., 2019. Localised heating and intensive magmatic conditions prior to the 22–23 April 2015 Calbuco volcano eruption (Southern Chile). Bull. Volcanol. 81. https://doi.org/10.1007/s00445-019-1280-2

Morgado, E., Parada, M.A., Contreras, C., Castruccio, A., Gutiérrez, F., McGee, L.E., 2015. Contrasting records from mantle to surface of Holocene lavas of two nearby arc volcanic complexes: Caburgua-Huelemolle Small Eruptive Centers and Villarrica Volcano, Southern Chile. J. Volcanol. Geotherm. Res. 306, 1–16. https://doi.org/10.1016/j.jvolgeores.2015.09.023

Naranjo, J.A., Moreno, H., 1991. Actividad explosiva postglacial en el volcan Llaima, Andes del Sur (38° 45'S). Rev. geol. Chile 18, 69–80. https://doi.org/10.5027/andgeoV18n1-a06

Naranjo, J.A., Moreno, H., Banks, N.G., 1993a. La erupción del volcán Hudson en 1991 (46°S), Región XI, Aisén, Chile. Serv. Natl. Geológico Minería Bol. 44, 1–50.

Naranjo, J.A., Moreno, H., Emparan, C., Murphy, M., 1993b. Volcanismo explosivo reciente Sollipulli la caldera del volcán Sollipulli, Andes del Sur (39°S). Rev. Geol. Chile 20, 167–191.

Naranjo, J.A., Moreno, H., 2005. Geología del Volcán Llaima, Región de la Araucanía. Servicio Nacional de Geología y Minería, Carta Geológia de Chile, Serie Geología Básica, 88, 1-33, Escala 1:50.000, Santiago.

Naranjo, J.A., Singer, B.S., Jicha, B.R., Moreno, H., Lara, L.E., 2017. Holocene tephra succession of Puyehue-Cordón Caulle and Antillanca/Casablanca volcanic complexes, southern Andes (40–41°S). J. Volcanol. Geotherm. Res. 332, 109–128. https://doi.org/10.1016/j.jvolgeores.2016.11.017

Naranjo, J.A., Stern, C.R., 2004. Holocene tephrochronology of the southernmost part (42°30'-45°S) of the Andean Southern Volcanic Zone. Rev. Geol. Chile 31, 225–240. https://doi.org/10.4067/S0716-02082004000200003

Naranjo, J.A., Stern, C.R., 1998. Holocene explosive activity of Hudson Volcano, southern Andes. Bull. Volcanol. 59, 291–306. https://doi.org/10.1007/s004450050193

Peccerillo, A., Taylor, S.R., 1976. Geochemistry of Eocene Calc-Alkaline Volcanic Rocks from the Kastamonu Area, Northern Turkey. Contrib. to Mineral. Petrol. 58, 63–81. https://doi.org/10.1007/BF00384745

Rawson, H., Keller, T., Fontijn, K., Pyle, D.M., Mather, T.A., Smith, V.C., Naranjo, J.A., 2016. Compositional variability in mafic arc magmas over short spatial and temporal scales: Evidence for the signature

of mantle reactive melt channels. Earth Planet. Sci. Lett. 456, 66–77. https://doi.org/10.1016/j.epsl.2016.09.056

Rawson, H., Naranjo, J.A., Smith, V.C., Fontijn, K., Pyle, D.M., Mather, T.A., Moreno, H., 2015. The frequency and magnitude of post-glacial explosive eruptions at Volcán Mocho-Choshuenco, southern Chile. J. Volcanol. Geotherm. Res. 299, 103–129. https://doi.org/10.1016/j.jvolgeores.2015.04.003

Reubi, O., Bourdon, B., Dungan, M.A., Koornneef, J.M., Sellés, D., Langmuir, C.H., Aciego, S., 2011. Assimilation of the plutonic roots of the Andean arc controls variations in U-series disequilibria at Volcan Llaima, Chile. Earth Planet. Sci. Lett. 303, 37–47. https://doi.org/10.1016/j.epsl.2010.12.018

Schindlbeck, J.C., Freundt, A., Kutterolf, S., 2014. Major changes in the post-glacial evolution of magmatic compositions and pre-eruptive conditions of Llaima Volcano, Andean Southern Volcanic Zone, Chile. Bull. Volcanol. 76, 1–22. https://doi.org/10.1007/s00445-014-0830-x

Sellés, D., Moreno, H., 2011. Geología del Volcán Calbuco. Servicio Nacional de Geología y Minería, Carta Geológica de Chile, Serie Geológica Básica, 130, Escala 1:50.000, Santiago.

Siani, G., Michel, E., De Pol-Holz, R., DeVries, T., Lamy, F., Carel, M., Isguder, G., Dewilde, F., Lourantou, A., 2013. Carbon isotope records reveal precise timing of enhanced Southern Ocean upwelling during the last deglaciation. Nat. Commun. 4. https://doi.org/10.1038/ncomms3758

Simmons, I.C., McGarvie, D., Cortés, J.A., Calder, E.S., Pavez, A. 2020. Holocene volcanism at the Quetrupillán Volcanic Complex (39°30' S, 71°43' W), southern Chile. Volcania, 3(1), pp. 115–137. https://doi.org/10.30909/vol.03.01.115137

Singer, B.S., Jicha, B.R., Harper, M.A., Naranjo, J.A., Lara, L.E., Moreno, H., 2008. Eruptive history, geochronology, and magmatic evolution of the Puyehue-Cordón Caulle volcanic complex, Chile. Bull. Geol. Soc. Am. 120, 599–618. https://doi.org/10.1130/B26276.1

Smith, R.E., Smith, V.C., Fontijn, K., Gebhardt, A.C., Wastegård, S., Zolitschka, B., Ohlendorf, C., Stern, C., Mayr, C., 2019. Refining the Late Quaternary tephrochronology for southern South America using the Laguna Potrok Aike sedimentary record. Quat. Sci. Rev. 218, 137–156. https://doi.org/10.1016/j.quascirev.2019.06.001

Stern, C.R., 2008. Holocene tephrochronology record of large explosive eruptions in the southernmost Patagonian Andes. Bull. Volcanol. 70, 435–454. https://doi.org/10.1007/s00445-007-0148-z

Stern, C.R., De Porras, M.E., Maldonado, A., 2015. Tephrochronology of the upper Río Cisnes valley (44°S), southern Chile. Andean Geol. 42, 173–189. https://doi.org/10.5027/andgeoV42n2-a02

Tagiri, M., Moreno, H., López-Escobar, L., Notsu, K. 1993. Two magma types of the high-alumina basalt

series of Osorno, Souther Andes (41°06'S)-plagioclase dilution effect. J. Min. Petr. Econ. Geol. 88, 359–371. https://doi.org/10.2465/ganko.88.359

Villarosa, G., Outes, V., Hajduk, A., Crivelli Montero, E., Sellés, D., Fernández, M., Crivelli, E., 2006. Explosive volcanism during the Holocene in the Upper Limay River Basin: The effects of ashfalls on human societies, Northern Patagonia, Argentina. Quat. Int. 158, 44–57. https://doi.org/10.1016/j.quaint.2006.05.016

Watt, S.F.L., Pyle, D.M., Mather, T.A., 2013. Evidence of mid- to late-Holocene explosive rhyolitic eruptions from Chaitén Volcano, Chile. Andean Geol. 40, 216–226. https://doi.org/10.5027/andgeoV40n2-a02

Watt, S.F.L., Pyle, D.M., Mather, T.A., 2011a. Geology, petrology and geochemistry of the dome complex of Huequi volcano, southern Chile. Andean Geol. 38, 335–348. https://doi.org/10.5027/andgeov38n2-a05

Watt, S.F.L., Pyle, D.M., Naranjo, J.A., Rosqvist, G., Mella, M., Mather, T.A., Moreno, H., 2011b. Holocene tephrochronology of the Hualaihue region (Andean southern volcanic zone, ~42° S), southern Chile. Quat. Int. 246, 324–343. https://doi.org/10.1016/j.quaint.2011.05.029

Weller, D., Miranda, C.G., Moreno, P.I., Villa-Martínez, R., Stern, C.R., 2014. The large late-glacial Ho eruption of the Hudson volcano, southern Chile. Bull. Volcanol. 76, 1–18. https://doi.org/10.1007/s00445-014-0831-9

Weller, D.J., de Porras, M.E., Maldonado, A., Méndez, C., Stern, C.R., 2019. Petrology, geochemistry, and correlation of tephra deposits from a large early-Holocene eruption of Mentolat volcano, southern Chile. J. South Am. Earth Sci. 90, 282–295. https://doi.org/10.1016/j.jsames.2018.12.020

Weller, D.J., De Porras, M.E., Maldonado, A., Méndez, C., Stern, C.R., 2017. Holocene tephrochronology of the lower Río Cisnes valley, souhern Chile. Andean Geol. 44, 229–248. https://doi.org/10.5027/andgeov44n3-a01

Weller, D.J., Miranda, C.G., Moreno, P.I., Villa-Martínez, R., Stern, C.R., 2015. Tephrochronology of the southernmost Andean Southern Volcanic Zone, Chile. Bull. Volcanol. 77, 1–24. https://doi.org/10.1007/s00445-015-0991-

Chapter 5: Oceanic circulation of the Southeast Pacific during the last 20,000 years

Finally, in chapter 5, the main aim of this work is tackled and the previous work is integrated. First, the tephrochronology work developed in cores MD07-3098, MD07-3100 and MD07-3081 is used to estimate Rs variations at 41° and 49° S during the last 20,000 years. Because not every depth where planktic foraminifera radiocarbon ages have been analyzed has a corresponding Rs estimate, assumptions regarding how Rs might have varied in the past have to be made in order to calibrate them. In this chapter I describe the strategy used to this aim. In particular, I compared the stable isotope stratigraphies of cores MD07-3098, MD07-3100, and MD07-3081 in a 14C age, rather than calendar age, from which changes in surface waters and their Rs at different latitudes in the Chilean continental margin are inferred. To complement the newly produced information, I compared it to previously published Rs and stable isotope stratigraphy in core MD07-3088, retrieved off the Chilean continental margin at ~46°S (Siani et al., 2013). From this, important latitudinal variations in surface water distribution and Rs in the SEP during the last 20,000 years are inferred. This procedure is an improvement from the strategy followed in chapter 2 to estimate Rs variations at ~31° S and ~36° S, as it incorporates new Rs estimates, and a more complete stable isotope stratigraphy is available for the cores. However, it still holds a lot of uncertainty: associated with the Rs estimates, which could change in time as new chronological and stratigraphic constrains for on land tephra becomes available; or as more cryptotephra are identified, allowing to better understand the mechanisms controlling Rs variations in the area. With the high uncertainties in chronologies in mind, I calculated the variation in bottom water Δ14C at each core retrieving site together with the 95.4 Confidence Interval of these estimations. However big, these uncertainties are kept in mind when interpreting ventilation changes in the SEP, as future improvements in marine core chronologies might greatly change the mean Δ14C estimates. In spite of the big uncertainties, important circulation variations are observed during the last ~20,000 years in the Southeast Pacific.

Oceanic circulation of the Southeast Pacific during the last 20,000 years

Consuelo Martínez Fontaine[a, b*], Elisabeth Michel[b], Giuseppe Siani[a], Ricardo de Pol-Holz[c]

[a]Géoscience Paris Saclay (GEOPS) Université Paris-Saclay, CNRS UMR 8148, 91405 Orsay, France

[b]Laboratoire des Sciences du Climat et de l'Environnement (LSCE), Laboratoire mixte CNRS-CEA, Avenue de la Terrasse, 91198 Gif-sur-Yvette Cedex, France

[c]Centro de Investigación GAIA-Antárctica (CIGA) and Network for Extreme Environments Research (NEXER), Universidad de Magallanes, Punta Arenas, Chile

*Corresponding author: Consuelo Martínez Fontaine, Geoscience Paris Sud (GEOPS) Université Paris-Saclay, CNRS UMR 8148, 91405 Orsay, France; E-mail: consuelo.martinez-fontaine@universite-paris-saclay.fr

5.1 Introduction

The ocean is though to have an important role in glacial–interglacial cycles by having the capacity of storing CO_2 during glacial periods and release it to the atmosphere during interglacials periods. During the last important transition from a glacial to an interglacial state, the last deglaciation (~18-11 cal ka BP), atmospheric reconstructions indicate that pCO_2 concentrations rose from 190 ppm to 270 ppm. At the same time, as atmtospheric $\Delta^{14}CO_2$ reconstructions indicate that values decreased ~270‰ during the same period (Reimer et al., 2020), which is more than can be accounted for by the variability in ^{14}C production rates in the atmosphere (Broecker and Barker, 2007; Hain et al., 2014). This evidence had led to the hypothesis that during the Last Glacial Maximum carbon accumulated in different areas of the global deep ocean, and that during the deglaciation this carbon would be release to the atmosphere as CO_2 via the Southern Ocean and Equatorial Pacific Ocean. Because the climatic system is very complex and an intricate series of feedbacks interplay, there is still a lot of work to be done to disentangle the mechanisms leading to this carbon transfer. Among the possible mechanisms: changes in deep ocean ventilation associated with the extension of sea ice around Antarctica; variations in the latitudinal position of the Southerly Westerly Winds; changes in the formation of North Atlantic Deep Water, which in the modern ocean helps ventilate deep waters in the Southern Ocean. Here we present new ^{14}C data on four marine sediment cores retrieved at depths between ~1,600–3,300 m in the South East Pacific, between ~41–49° S. By integrating this new information with five previously published records of five marine sediment cores in the SEP (De Pol-Holz et al., 2010; Martínez Fontaine et al., 2019; Siani et al., 2013) we obtain a detailed transect between 31–49° S and 500–3,300 m depth constraining the ventilation of AAIW, PDW and CDW during the last ~22 cal ka BP.

5.2 Methodology

5.2.1 Core retrieving

Marine sediment cores MD07-3098 (40.93° S, 75.03° W, 3055 m), MD07-3100 (41.60° S, 74.95° W, 1609 m) and MD07-3081 (49.42° S, 76.96° W, 3273 m), correspond to three CALYPSO cores retrieved by the French R/V Marion Dufresne during the PACHIDERME expedition in February 2007 (Kissel and The Shipboard Scientific Party, 2007). Cores MD07-3098 and MD07-3100 are described by Martínez Fontaine et al. (2021), corresponding to chapter 4 of this thesis and by Haddam et al. (2018), respectively. Briefly, core MD07-3098 is a 20.74 m long core composed mainly of silty clay with silty and sandy layers horizons, which contains a visible tephra layer of ~30 cm between ~7.6 and 8 m; MD07-3100 is a 29.8 m long core composed mainly of homogenous silty clays, which displays a visible tephra layer of ~25 cm between 7.25 and 7.5 m; meanwhile core MD07-3081 corresponds to a 16.22 m–long core composed of olive to gray silty clay interbedded with sandy layers (Figure 5.1).

5.2.2 Stable isotope stratigraphy

The stratigraphic constraints of the cores here studied are given by planktonic foraminifera *G. bulloides* and benthic foraminifera *Cibicides wuellerstorfi*, *Cibicides* spp or *Uvigerina peregrina* stable oxygen isotope data ($\delta^{18}O$, $\delta^{13}C$). The latter are used to identify relevant climatic periods in the cores, which aid in the identification of cryptotephras, Rs estimates, and age model production (Section 5.2.4). Both planktonic and benthic foraminifera are employed taking into consideration that both type of records have their own biases. On the one hand, the signal recorded by *G. bulloides* can be affected by local processes such as fresh water inputs and front migration (e.g. Haddam et al., 2018), making it sometimes difficult to correlate even nearby records. At the same time, benthic foraminifera are expected to represent the more stable $\delta^{18}O$ signal of deep waters, helping better constrain climatic periods in the cores. However, the deglaciation signal might not be the same at the different water depths, the cores being retrieved in different water masses that underwent a different history. Thus both planktic and benthic records have been used for this stratigraphy purpose. The latter is true for epifaunal *Cibicides* species here analyzed (cores MD07-3100), which have been observed to calcify in equilibrium with ambient bottom waters in the SEP (Reyes-Macaya et al., *in preparation*). However, infaunal *U. peregrina* might not reflect the $\delta^{18}O$ of bottom sea water as it lives in the sediment interface and so can be affected by pore water micro habitats. Nevertheless, a comparison of ambient bottom water and *U. peregrina* $\delta^{18}O$ in the modern SEP indicates that *U. peregrina* is consistenly more enriched than bottom water in ~ 1‰ throughout the water column (Reyes-Macaya et al., *in preparation*). For the two deeper cores (MD07-3098 and MD07-3100) no *Cibicides* curve could be obtained and thus these benthic stratigraphies can be aided by observing changes in *G. bulloides*.

G. bulloides results from cores MD07-3100 and MD07-3098 have already been published by Haddam et al. (2018) and Martínez Fontaine et al. (2021), respectively. For core MD07-3081, isotopic measurements were made every 10 cm, between 20 cm and 830 cm depth, and with irregular spacing between 5 and 120 cm, between 830 cm and 1620 cm (Table S5.1). Analyses were performed in 1 to 30 specimens at each depth (picked from the 250–315 µm fraction) at the Laboratoire des Sciences du Climat et l'Environnement (LSCE) on Optima VG and GV Isoprime mass spectrometers.

Regarding the benthic foraminifera, because of its low availability, in core MD07-3100, no monospecific *Cibicides* species though to calcify in equilibrium with ambient bottom water could be picked for the whole interval of interest and thus a curve was build integrating analyses performed in *Cibicides bradyi*, *Cibicides kullenberghi*, *Cibicides pachyderma* (corrected by -0.5‰) and *Cibicides wuellerstorfi*. Results from cores MD07-3100 and MD07-3119 have already been published by Haddam et al. (2020). For cores MD07-3098 and MD07-3081 *Cibicides* availabilities throughout the cores were too low to build a curve and thus *U. peregrina* was picked instead. In core MD07-3098, between 3 and 12 specimens were analyzed every 10–20 cm between 0 and 1340 cm; and in core MD07-3081, between 6 and 1 specimens

every 10 cm between 20 cm and 830 cm depth, and with irregular spacing between 5 and 120 cm in the rest of the core (Table S5.1).

This stable oxygen stratigraphy allowed for a first order identification of the time frame the cores span in order to concentrate the work in the portion of the cores since the LGM. In cores MD07-3098, MD07-3100 this corresponds to the first ~14 m of the cores, whereas in core MD07-3081, it corresponds to the whole core (Figure 5.1).

5.2.3 Radiocarbon dating

Radiocarbon dating in planktic and benthic foraminifera were performed in all the cores in order to obtain their chronologies (planktic foraminifera) and to interpret changes in ventilation of deep waters (benthic foraminifera). Results are shown in Table S5.2. Planktic foraminifera radiocarbon ages for core MD07-3100 and MD07-3098 have already been published by Haddam et al. (2018) and Martínez Fontaine et al. (2021), respectively. Mixed benthic foraminifera were analyzed in thirty depths between 0 and 2070 cm in core MD07-3098, twenty-eight of which have been analyzed for planktic foraminifera as well. Because of relatively lower benthic foraminifera abundances, samples <3 mg were analyzed on the gas ion source ECHoMICADAS at the LSCE (Gif-Sur-Yvette, France) using a coupling of cracker system to the gas handling system (Wacker et al., 2013; Tisnérat-Laborde et al., 2015); whereas samples >3 mg were measured at UMS-ARTEMIS (Pelletron 3 MV) AMS facilities (CNRS-CEA Saclay, France, Dumoulin et al., 2017; Moreau et al., 2013). In core MD07-3100, fourteen depths between 160 and 1340 cm were analyzed for benthic foraminifera at the UMS-ARTEMIS AMS facilities, twelve of which have been analyzed for planktic foraminifera as well.

For core MD07-3081, paired planktic and benthic foraminifera were analyzed in seventeen out of twenty-one depth analyzed in total. In the four remaining depths only planktic foraminifera were analyzed. Because of the overall lower foraminifera abundances, mainly mixed planktonic and mixed benthic foraminifera were analyzed, except for four depths where mono specific *G. bulloides* were analyzed. In general, benthic foraminifera were less abundant in this core and thus samples <2 mg were analyzed on the gas ion source ECHoMICADAS at the LSCE, whereas samples >2 mg were measured at UMS-ARTEMIS AMS facilities. Radiocarbon results are reported in conventional ages before present (BP) according to the convention of Stuiver and Polach (1977), normalized to the base of $\delta^{13}C$ of –25.0‰ relative to the Pee Dee Belemnite (PDB) international standard, and corrected by the age of the background subtraction.

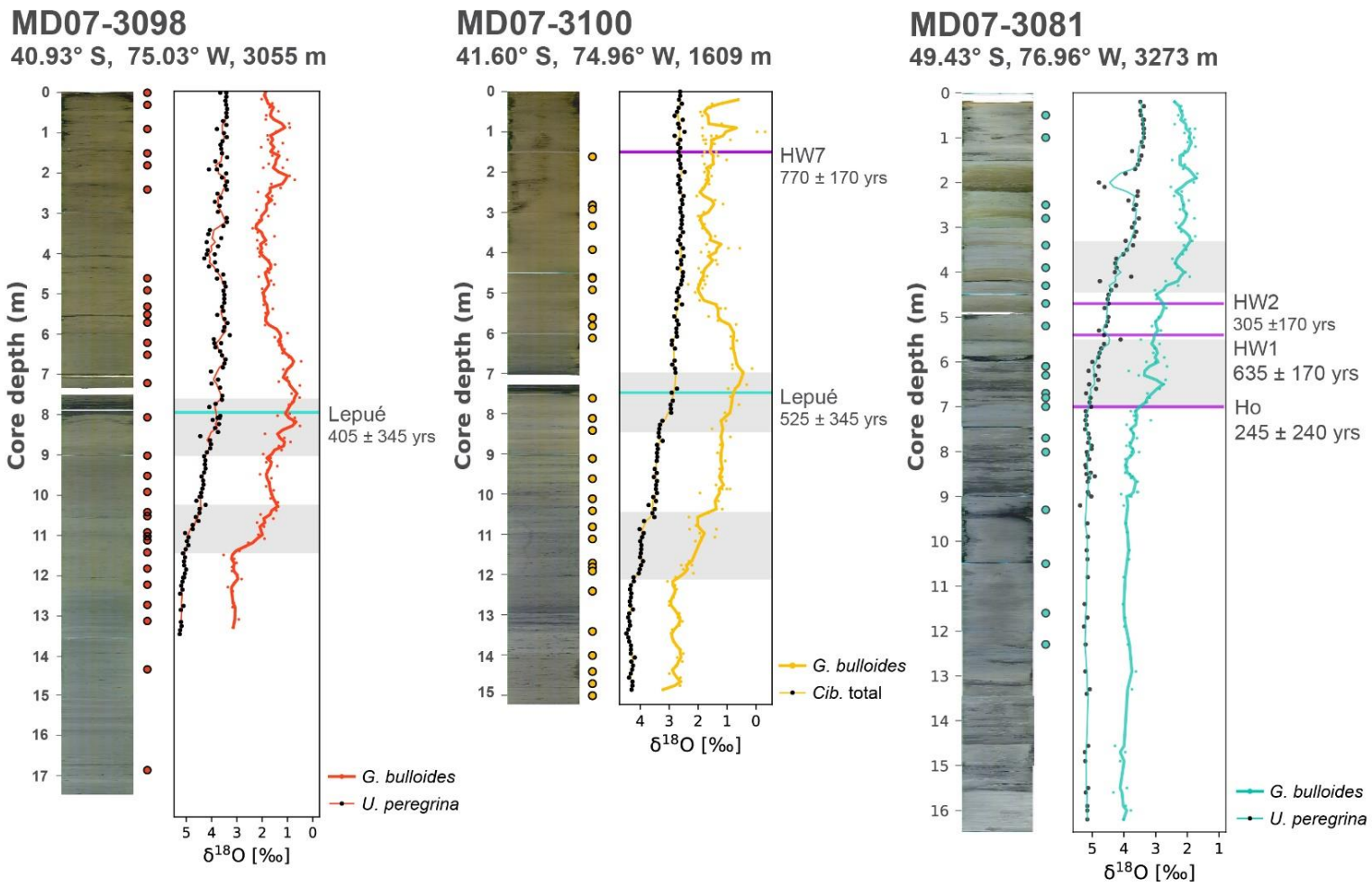

Figure 5.1 $\delta^{18}O$ stratigraphy for the cores for which new benthic foraminifera ^{14}C data is presented in this study. In each core, to the left: composite picture of the core, to the right: *G.bulloides* (color) and benthic foraminifera (black) $\delta^{18}O$. For core MD07-3098 and MD07-3081 *U. peregrina* was analyzed, in core MD07-3100 different *Cibicides* species, and in core MD07-3119 *Cibicides wuellerstorfi.* Depths where ^{14}C ages were obtained are indicated as dots of the corresponding core color next to the composite photo. The depth of the identified tephras and cryptotephras in the cores are also indicated as horizontal lines together with the name of the tephra (e.g Lepué). For cores MD07-3098 and MD07-3100, tephras are identified in Martínez Fontaine et al. (2021), for core MD07-3081 the details are in the supplementary.

5.2.4 Age models

The age models for the marine sediment cores, i.e. assigning a calendar age estimate to different depths of the marine sediment cores, are obtained using the software Undatable (Lougheed and Obrochta, 2019). Undatable uses the planktonic foraminifera ^{14}C ages analyzed at different depths of the marine sediment cores to estimate calendar ages every 1 cm. To do this, the user provides a number X of ((age, uncertainty), (depth, uncertainty)) pairs for constraining the chronologies of the cores. In this case, these correspond to the X planktonic foraminifera radiocarbon ages analyzed at each core, with its corresponding analytical error, and the depth at which they were analyzed. For core MD07-3098, 29 ^{14}C ages were analyzed in 28 depths; in core MD07-3100, 42 ^{14}C ages where analyzed in 31 depths; and 20 ^{14}C ages where obtained in 20 depths in core MD07-3081. The uncertainty assigned to the depths of the radiocarbon dating was 1 cm, which corresponds to the sampling width (except for four depths in core MD07-3100 where the sampling widths were between 2 and 4cm). With this information, Undatable calibrated the ^{14}C ages by SHCal20 curve (Hogg et al., 2020) and produced a number *nsim* (in this case 100,000) of age–depth curves. Each age—depth curve is constructed by random sampling from the calibrated age and depth distributions from the X ((age, uncertainty), (depth, uncertainty)) pairs of each core. Then, a calendar age estimate is produced every 1 cm, which corresponds to the mean, median, 68.2% and 95.4% confidence intervals (CI) of the nsim age–depth curves at that particular depth.

In order to correctly calibrate the planktic foraminifera ^{14}C ages for obtaining the age models of each core, they must first be corrected by appropriate marine surface reservoir ages (Rs). In the Southeast Pacific, Rs vary latitudinally, because of different regimes of coastal upwelling in the Chilean margin (Merino et al., 2018), bringing more or less ^{14}C–depleted ESSW to the surface. In particular, either seasonal or permanent coastal upwelling occurs north of ~39° S and modern Rs estimates are relatively high, whereas south of ~39° S, upwelling is generally impeded by the SWW, and Rrs are relatively low. The position of the SWW is thought to have changed in the past, and in particular they are hypothesized to have reached its southernmost position during the early Holocene (Gray et al. *submitted*). Thus, the upwelling regime at the core retrieving sites may have been different in the past. Additionally, previous Rs estimates in the study area, at ~46° S, indicate important variations during the deglaciation (Siani et al., 2013). Here we use tephrochronology to estimate Rs variations in cores MD07-3098, MD07-3100 and MD07-3081 (section 5.2.4.1) since the late glacial. Because not every depth where planktonic foraminifera were dated has a corresponding Rs estimate, assumptions regarding the variations of Rs in the past have to be made (section 5.2.4.2).

From this, new age models for cores MD07-3098 and MD07-3081 are produced, and the age model for core MD07-3100 is pudated from Haddam et al. (2018) by incorporating new Rs (see below) and calibrating by SHCal20 curve. Additionally, the age models of marine cores with previously published ^{14}C records in the area are updated using SHCal20 curve. These cores correspond to MD07-3088 (Haddam

et al., 2018; Siani et al., 2013), GeoB 7163-7, GeoB 7162-6, GeoB 717-6, GeoB 71494-2 (Martínez Fontaine et al., 2019) and core SO161-22SL (from now on 22SL, de Pol-Holz et al., 2010; Martínez Fontaine et al., 2019).

5.2.4.1 Reservoir ages estimates

In order to estimate Rs variations in the past in the study area, here we use the identification of tephras and cryptotephras in the marine cores as a reference for the contemporary atmospheric ^{14}C age. The principle behind this is that, if tephras and/or cryptotephras identified in the marine sediment cores can be robustly correlated with tephras on land, which have been independently dated by ^{14}C, then Rs can be estimated as:

$$Rs = {}^{14}C_{\text{tephra in marine core}} - {}^{14}C_{\text{tephra on land}}$$

For cores MD07-3098 and MD07-3100, cryptotephra and tephra identification is described in Martínez Fontaine et al. (2021). In core MD07-3098 one tephra is robustly correlated with Lepué tephra (Figure 5.1, 5.2), sourced in Michinmahuida volcano (~43° S), which occurred at ~11 ka cal BP (Amigo et al., 2013; Alloway et al., 2017; Martínez Fontaine et al., 2021). In core MD07-3100, one tephra is also correlated with Lepué tephra, and one cryptotephra is correlated with HW7 tephra, sourced in Hudson volcano, which occurred at ~1.5 ka cal BP (~46° S; Haberle & Lumley, 1998; Carel et al., 2011). For core MD07-3081, an analogous approach was followed to identify source of the identified cryptotephras in it, and is described in the supplementary material. From the latter it was possible to robustly identify three cryptotephras in core MD07-3081, corresponding to eruptions HW2, HW1 (Haberle & Lumley, 1998; Carel et al., 2011) and Ho (Bendle et al., 2019; Van Daele et al., 2016; Weller et al., 2014), all three sourced in Hudson volcano, occurring around 13.7, 14.5 and 17.4 ka cal BP, respectively. After the identification of the tephras and cryptotephras in the marine sediment cores, the Rs were estimated as the difference between the planktonic ^{14}C age at the midpoint between base of the cryptotephra and its peak, and the estimated ^{14}C age of the tephra on land. To estimate the ^{14}C ages of the tephras on land, the available ^{14}C dates in the literature were collected for each tephra (Table S5.5), this information was then filtered following certain criteria, described below.

The products of volcanic eruptions (e.g. lava or tephra) cannot be directly dated by ^{14}C, because they don't contain a measurable amount of it, they are ^{14}C–dead. Instead, organic matter *associated* with deposits of explosive eruptions (tephra) are dated, which give a reference of the time the eruptions occurred. Depending on the material analyzed and its stratigraphic position with respect to the tephra, the ^{14}C ages estimates are thought to be more or less accurate in representing the actual age of the eruption. For example, when an explosive eruption occurs, a portion of the pyroclastic material ejected from the volcanic center interior is transported down the slopes of the volcanic center by pyroclastic currents. When this occurs in vegetated areas, these very hot pyroclastic currents burn the organic matter growing

nearby the volcanic centers. Then, if pieces of charcoal are found within the pyroclastic curent deposits, it is expected that they represent the ^{14}C of the atmosphere at the time of the eruption. This is an ideal case, however, many times it is not possible to identify charcoal or burnt material within tephra deposits. When this is the case, generally organic matter found below and/or above the tephra is dated, which gives an idea of the maximum/minimum age of an eruption. In this case, however, additional attention must be given to the material dated. For example, in some cases soil developed above or below a tephra is dated, as soil is formed by the decomposition of organic matter over time, this ^{14}C will corresponds to the mean of the ^{14}C ages of the materials composing it, which can differ greatly from the age of the eruption. Additionally, depending on the rate of accumulation of sediment in different environments, the distance of the sampled material from the tephra deposition is also relevant. Ideally, organic matter obtained directly below the tephra would be dated, because its age is expected to be closer to the *real* age of the tephra. Analogously, when organic matter sampled above the tephra deposit is dated, there is no certainty on how long after the tephra it was deposited, and so it constitutes a minimum age. Because of all of the above, we collected information in the stratigraphic position and analyzed material of the ^{14}C estimates available for the eruptions identified in the marine sediment cores. When available, ^{14}C ages of macro rests (e.g. charcoal or wood remains) rertrieved from within the tephra deposit or directly below it, were preferred over bulk organic matter found above or below it (details below). An additional filter employed was selecting only ^{14}C ages associated to deposits for which geochemical analyzes where available. The latter is done taking into account that the Southern Volcanic Zone of the Andes, from which the cryptotephras and tephras identified in the marine cores originate, is highly active and thus it is not unlikely that two eruption from different volcanic center occurred closely spaced in the stratigraphic record on land. Thus, the geochemical composition of the deposits is used to differentiate among potentially contemporaneous eruptions.

From the identified eruptions, Lepué tephra, identified in cores MD07-3100 and MD07-3098, corresponds to a widespread ignimbrite. Around twenty ^{14}C ages analyzes performed in different outcrops and lake sediment cores identified as Lepué tephra are available in the literature (Table S5.5; Alloway et al., 2017 and references therein; Amigo et al., 2013). From these, seven ^{14}C ages correspond to deposits analyzed for geochemistry, from which only one ^{14}C age was performed in a charcoal found within the tephra, corresponding to 9960 ± 330 years. Because of the relatively high error of this ^{14}C estimate, we included four other ^{14}C performed in bulk organic matter sampled directly below the lower contact of the tephra in order to evaluate if the ^{14}C age could be better constrained. The mean ^{14}C ages of the five ages is 9,800 ± 340 ^{14}C years BP, which is within error the same as considering the one charcoal date. Taking this into consideration, the ^{14}C age considered for Lepué tephra is the latter (Table S5.5). In cores MD07-3100 and MD07-3098, planktonic foraminifera at the base of Lepué tephra have been dated in 10,325±40 and 10,205±40 ^{14}C years, resulting in Rs estimates of 530 ± 340 and 400 ± 345, respectively.

For HW7, identified in core MD07-3100, two ^{14}C age are available in the literature (Habele & Lumley, 1998), both of which are associated with deposits analyzed for geochemistry and correspond to macrorest of organic matter found within the tephras. From these, the estimated ^{14}C on land for HW7 is 1,720 ± 160 ^{14}C years. In core MD07-3100, the base of HW7 was dated in 2,490 ± 60, resulting in a Rs of ~770 ± 170 years.

For HW2, identified in core MD07-3081, three ^{14}C age are available in the literature (Habele & Lumley, 1998), all of which are associated with deposits analyzed for geochemistry. From these, two ^{14}C ages correspond to macrorest of organic matter within the tephras and one to bulk sediment above the tephra. The two age estimates within the tephra are used for estimating the ^{14}C age of HW2, resulting in an age of 11,910 ± 110 ^{14}C years. HW2 has been identified in core MD07-3081 and dated at is base in 12,215 ± 60 ^{14}C years, resulting in a Rs of 310 ± 120 years.

For HW1 identified in core MD07-3081, two ^{14}C age are available in the literature (Habele & Lumley, 1998), both of which are associated with deposits analyzed for geochemistry and correspond to macrorest of organic matter within the tephras. From these, the estimated ^{14}C on land for HW1 is 12,435 ± 110 ^{14}C years. In core MD07-3081, the base of HW1 was dated at ~13,070 ± 60, resulting in a Rs of ~640 ± 130 years.

Finally, for tephra Ho, eight ^{14}C ages estimates are available in the literature (Weller et al., 2014), from which six are associated to deposited analyzed for geochemistry. All of the six ages were performed in bulk organic matter deposited either above or below Ho. From these, we've selected the dates for samples obtained below the tephra, as they were stratigraphically closer to Ho (Table S5.5). Taking into account those ages, the mean estimate for Ho is 14,610 ± 240 years. Because of what was mentioned above, this age must be consideried as a maximum age, and thus, the Rs estimated from this value should be considered as minimum values. In core MD07-3081, the base of Ho was dated in 14,850 ± 60, resulting in a minimum Rs of 245 ± 240.

5.2.4.2 Rs variations in the Chilean margin (40-49° S) since the late glacial

In order to produce the age models for the cores, each planktonic foramnifera ^{14}C age has to be corrected by a Rs. Because not every depth where planktonic foraminifera were dated has a corresponding Rs estimate, assumptions regarding how Rs might have varied in the past have to be made. At present, surface waters at the retrieving sites of cores MD07-3098, MD07-3100 and MD07-3081 are all bathed by SAAW, which is present from the surface to ~100 m depth. SAAW is transported east by the Antarctic Circumpolar Current (ACC) around Antarctica and in its way from the Pacific to the Atlantic Ocean, *bumps into* South America at ~46° S. From there a portion is transported north by the Humboldt current or Peru-Chile current until ~30° S, *reaching* cores MD07-3100 and MD07-3098; and a portion is transported south and into the Atlantic Ocean by the Cape horn current, reaching core MD07-3081. Modern Rs

estimates obtained between 41–43° S yield a mean value of 440 ± 100 years, whereas further south, between 51–53° S, Rs are relatively lower, with a mean value of 355 ± 80 years (Merino et al., 2018). As already mentioned, north of ~39° S, the northward flowing SAAW is modified by mixing with ESSW, brought to the surface by coastal upwelling and Rs are relatively higher.

The available modern Rs information in the Chilean continental margin, indicate overall lower values at higher latitudes (Merino et al., 2018 and references therein). This latitudinal variation in Rs has been associated with different upwelling regimes in the region, largely controlled by the coastal line together with the southeast Pacific subtropical anticyclone and the latitudinal position of the SWW (Strub et al., 1998). The coastal line of the Chilean continental margin together with the presence of the southeast Pacific subtropical anticyclone favor the development of strong northward winds parallel to the coast, which induce offshore Ekman pumping and thus, coastal upwelling (Strub et al., 1998). This phenomenon is responsible for yearlong coastal upwelling north of ~30° S. Between 30–39° S, coastal upwelling occurs in austral summer, whereas in austral winter the northward migration of the easterly blowing SWW, impedes coastal upwelling. South of ~40° S, coastal upwelling is for the most part impeded by the permanent presence of the SWW. However, evidence of favorable upwelling condition between ~40 and 46° S has been found (Narváez et al., 2019), which might explain the relatively higher Rs between 42–43° S with respect to ~51–53° S. As already mentioned, coastal upwelling is thought to have an important impact in Rs in the SEP because it brings relatively ^{14}C–depleted ESSW to the surface. ESSW flows south from the equator until ~39° S between ~200 and 400 m, underneath SAAW. In areas where strong coastal upwelling occurs, characteristics of the ESSW can be identified in the first 50 m of the water column (Figure S5.4, Reyes-Macaya et al., *submitted*). Although little modern ^{14}C information in the continental margin exists to characterize ESSW, the off shore section at 87°W, where ESSW can still be identified, indicates even lower ^{14}C contents than AAIW (Figure 1.2). Thus, its upwelling should modify importantly the Rs in the SEP. Even though the core of ESSW reaches ~39° S, between ~39–46° S, a mixing zone with SAAW is identified below 100 m until ~46° S (Reyes-Macaya et al., *submitted*; Silva et al., 2009).

From the latter, if a similar configuration maintained in the past, Rs are expected to be fairly similar at the three core retrieving sites, although they may be slightly lower in core MD07-3081, as modern estimates indicate. However, because of important changes during the deglaciation (e.g. migrations in the position of the SWW), this configuration might have changed in the past. To evaluate this, we compare the stable isotope ($\delta^{18}O$ and $\delta^{13}C$) curves of cores MD07-3098, MD07-3100 and MD07-3081, versus their planktonic foraminifera ^{14}C ages. By comparing the stable isotope curves in a ^{14}C age, if important differences in Rs occurred at different latitudes, it should be visible as a lagged timing of the transitions between climatic periods (late glacial, deglaciation, ACR). Additionally, we evaluate if coastal upwelling or some other process occurred in the past, bringing *old* ESSW to the surface at the core retieving sites by comparing their planktonic foraminifera $\delta^{13}C$ curves. Because ESSW and SAAW have very contrasting

$\delta^{13}C$ values (Reyes-Macaya et al., *submitted*), it is possible to identify upwelling hotspots in the Chilean continental margin by looking at its latitudinal variation at the surface (e.g. as in Martínez Fontaine et al., 2019). We complement the information here provided with previous information (Rs estimates, $\delta^{18}O$ and $\delta^{13}C$) in core MD07-3088 retrieved at ~46° S (Siani et al., 2013), this record provides six additional Rs estimates in the core of SAAW and thus it is expected to present similar conditions to those at ~41°S and ~46° S.

From the comparison in Figure 5.2, during the late glacial and deglaciation, two different behaviours are observed: cores MD07-3098, MD07-3100 and MD07-3088 display similar $\delta^{13}C$ and $\delta^{18}O$ values, whereas MD07-3081 has higher $\delta^{13}C$ and $\delta^{18}O$ values, especially during the deglaciation. Additionally during the deglaciation and late glacial, Rs estimates in core MD07-3081 are consistently lower than in core MD07-3088, by ~500-600 years, at depths where the same eruptions have been identified. During the early Holocene, $\delta^{13}C$ in core MD07-3088 displays more variability than the other cores, oscillating between lower values similar to cores MD07-3098 and MD07-3100, and higher values similar to core MD07-3081. In this period, Rs estimates for cores MD07-3098, MD07-3100 and MD07-3088 are available. However, the error of the Rs estimates in cores MD07-3098 and MD07-3100 is very large (~345 years), and thus it is difficult to make an inference respect to wether the Rs at ~41° S and 46° S are different or not. After ~8 ka ^{14}C BP, all four cores display similar isotopic values. In this period, eruptiton HW7 has been identified in cores MD07-3100 and MD07-30088, and Rs estimates are similar. From the latter, it seems that surface waters at ~41 and 46° S have had similar characteristics and Rs since the late glacial, whereas surface waters at 49° S had different characteristics and lower Rs. The lower $\delta^{13}C$ values in the northermost cores during the deglaciation might be indicative of more presence of ESSW at the surface during this period. One explanation of for this is that the position of the SWW had been further south during that period favoring coastal upwelling in this area. This is unlikely during the ACR as palynological information indicates that SWW might be close to 46° S (Montade et al., 2019) as paleoclimatological information in land indicates the presence of the SWW at ~ 41° S during this period, as seen in the prevalence eof cold/wet conditions at this latitude (Moreno, 2004). However during the two warming episodes of the deglaciation the subtropical front might have migrated far South favoring coastal upwelling at the location of cores retrieved at 40 and 46° S). Another possible explanation can be inferred taking into account the planktonic foraminifera $\delta^{18}O$ curves. During the deglaciation and until the early Holocene, planktonic foraminifera $\delta^{18}O$ in cores MD07-3098, MD07-3100 and MD07-3088 are relative lower than in core MD07-3081. The latter has been interpreted as more important influence of fresh water input at ~41° S and ~46° S with respect to ~49°S, derived from the melt of Patagonian ice sheet (Haddam et al., 2018), which dramatically reduced its extension during the deglaciation (Davies et al., 2020). The $\delta^{18}O$ curve mirrors the changes in $\delta^{13}C$, which since the late glacial, but especially during the deglaciation are ~1‰ lower than at ~49°S. We hypothesize that the big discharge of fresh water to the

coast would have destabilized the surface water, inducing mixing with sub surface ESSW during this time and increasing Rs at ~41°S and ~46°S and decreasing the surface waters $\delta^{13}C$.

From the latter, we consider that surface water conditions, and in particular Rs, where similar at ~41° S and ~46° S since the late glacial. Thus, for the climatic periods where no Rs are available in core MD07-3098 and MD07-3100 (deglaciation and late glacial), we assign the Rs estimates at 46°S. For core MD07-3081, evidence indicates that surface waters were different than at 41° S and 46° S, and in particular Rs were lower. And thus, for core MD07-3081 we assign its Rs estimates for the deglaciation and late glacial. For the Holocene we assign the modern value.

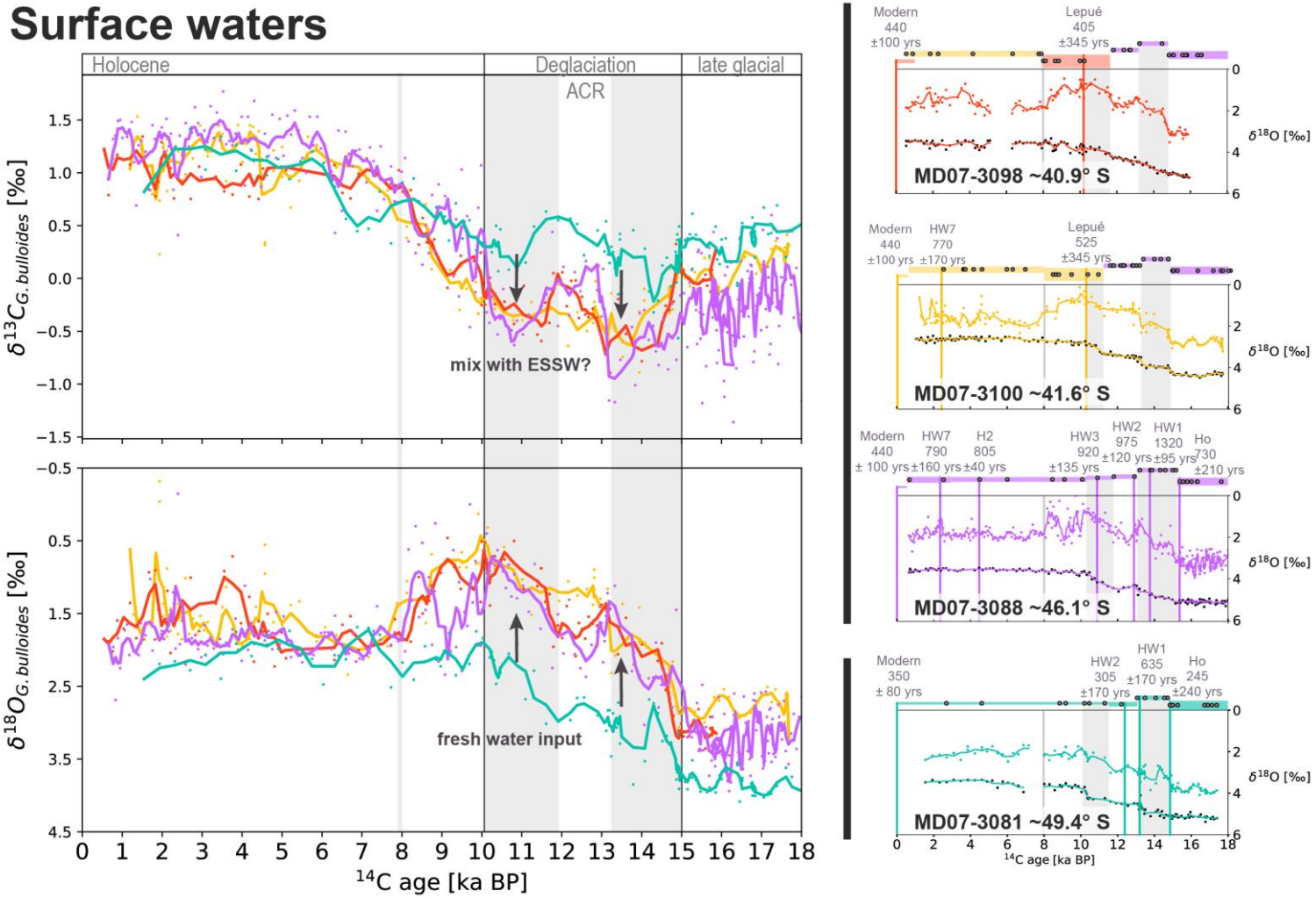

Figure 5.2. To the left: omparison of the *G.bulloides* stable carbon and oxygen isotope of cores in this study and core MD07-3088 (Carel et al., 2011; Siani et al., 2013), versus linealy interpolated planktonic ^{14}C ages. As detailed in the text, this comparison is interpreted in terms of water mass present at the surface and Rs at ~41° S, ~46° S and ~49° S. To the right individual plots for each core showing: *G.bulloides* $\delta^{18}O$ plotted as colored curves and dots, benthic foraminifera $\delta^{18}O$ as colored curve with black dots, the identified tephras and cryptotephras in the cores as a vertical lines together with the name given to the tephra and the estimated Rs. Rs estimates for core MD07-3088 from Siani et al. (2013). To the right are additionally plotted, the planktonic ^{14}C ages obtained in each core as grey dots. As indicated in the text, constant Rs were applied to planktonic ^{14}C to each climatic period (i.e. late glacial, HS1, ACR, YD, Holocene), which in the figure are indicated as rectangles of different colors corresponding to the error and height corresponding to the mean value. For example, in core MD07-3098, an Rs estimated in core MD07-3100 was applied to planktonic foraminifera ^{14}C in the Holocene portion of the core, whereas for the deglaciation, Rs estimated in core MD07-3088 were applied.

5.2.5 Δ14C estimation

In order to interpret changes in ventilation of deep waters in the SEP since the late glacial, we obtain the $\Delta^{14}C$ of deep waters, corresponding to the deviation from the modern atmosphere, following the expression by Adkins and Boyle (1997) derived from Stuiver and Polach (1977):

$$\Delta^{14}C = \left(\frac{e^{-\frac{^{14}C\ age}{8,033}}}{e^{-\frac{cal\ age}{8,266}}} - 1 \right) 1000‰$$

Because of the dependence of $\Delta^{14}C$ from calendar ages, it is important to communicate the error associated with the age models and its impact in $\Delta^{14}C$ estimation. In order to account for this uncertainty, the 68.2 and 95.4%Confidence Intervals (CI) are estimated by calculating the Δ14C value over the last 1,000 Monte Carlo simulations of the nsim iterations produced by Undatable for each age model. Additionally, to account for the analytical uncertainty in benthic foraminifera ^{14}C ages, the ^{14}C age in each $\Delta^{14}C$ calculation is randomly drawn from a normal distribution with mean equal to the reported benthic foraminifera ^{14}C age, and a standard deviation equal to the analytical error. The 68.2 and 95.4 % CI are reported in Table S5.2 and all the simulations in the 95.4% CI are visualized in Figures 5.3, 5.4, S5.7.

5.3 Results

From the benthic and planktic $\delta^{18}O$ stratigraphy and chronology, all cores cover at least from the late glacial to the late Holocene. A steady signal between ~3 and 4‰ $\delta^{18}O$ in *G. bulloides*, and between 4 and 5‰ $\delta^{18}O$ for benthtic foraminifera is observed until ~17 ka cal BP (95.4% CI 16.3–17.7) in core MD07-3100; ~16.5 ka cal BP (95.4% CI 15.5–17.3) in core MD07-3098; and ~17.5 ka cal BP (95.4% CI 16.8–18.2) in core MD07-3081 (Figue S5). A trend to lighter values is then observed until ~13.8 ka cal BP (95% CI 13.3–14.3) in core MD07-3100; until ~13.8 ka cal BP (95.4% CI 13.2–14.6) in core MD07-3098; and until ~14.8 ka cal BP (95% CI 13.8—15.7) in core MD07-3081. An ACR–like trend, with either constant or heavier values, is observed until 12.2 ka cal BP (95.4% CI 11.4–13.2) in core MD07-3100; ~12.7 ka cal BP (95.4% CI 12–13.1) in core MD07-3098; and ~13 ka cal BP (95.4% CI 12.4–13.5) in core MD07-3081. Subsequently, all cores display decreasing trends reaching their lighter values in *G. bulloides* and Holocene–like values in benthic foraminifera at: ~11 ka cal BP (95.4% CI 10.3–12.1) in core MD07-3100; ~11 ka cal BP (95.4% CI 10.2–11) in core MD07-3098; and 11.1 ka cal BP (95% CI 10.3–11.6) in core MD07-3081. Taking into account all these variations, we define the late glacial/deglacial transition in these cores at ~ 17 ka cal BP, the ACR between

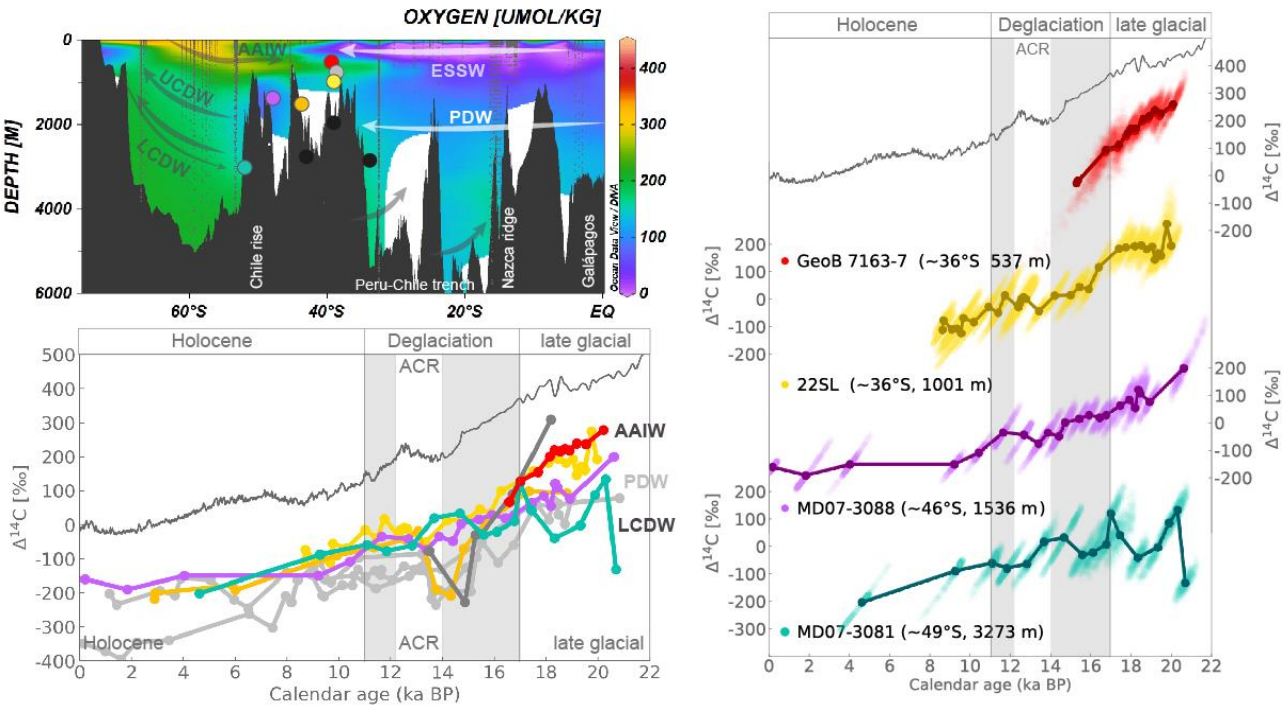

Figure 5.3 $\Delta^{14}C$ in the SEP for cores in group a, as described in the text. Core GeoB 7163-7 and 22SL (De Pol-Holz et al., 2010; Martínez Fontaine et al., 2019), MD07-3088 (Siani et al., 2013) and MD07-3081, here described. Cores MD07-3100 and GeoB 7162, also belonging to group a, are plotted separatedly in figure 5.4 and together tcores in group in the plot to the bottom left. The darker dots indicate mean values, whereas values in the 95.4% CI are plotted as lighter dots. Also indicated are the position of the cores in the water column, together with cores in group b as black dots.

14 and 12.5 ka cal BP and the Holocene starting at ~11 ka cal BP. These are the intervals plotted in Figures 5.3, 5.4 and S5.6.

Regarding the ventilation of deep waters, during the late glacial core MD07-3100 (~41.6° S, ~1609 m), displays more or less steady values. At ~18.8 ka cal BP (95.4% CI 19.3–18.1), mean values of ~90‰ $\Delta^{14}C$ (95.4% CI -3–173) are observed, meanwhile ~100‰ $\Delta^{14}C$ (95.4% CI -52–197) at ~17.3 ka cal BP (95.4% CI 18.1–16.8). From there, a decreasing trend is observed reaching a mean value of ~-210‰ $\Delta^{14}C$ (95.4% CI -278–-127) at ~14.3 ka cal BP (95.4% CL 15.1, 13.6), the minimum value of the whole studied interval. Relatively low values of ~-189‰ $\Delta^{14}C$ (95.4% CI -233–125) continue at ~13.7 ka cal BP (95.4% CI 13.3–4.4). After this, $\Delta^{14}C$ values increase abruptly, reaching ~-19‰ $\Delta^{14}C$ (95.4% CI -85–44) at ~13.1 ka cal BP (95.4% CI 12.5–13.6). From there, a decreasing trend with more or less constant slope is observed until ~2.9 ka cal BP (95.4% CI 2.5–3.4), when mean values reach -220‰ $\Delta^{14}C$ (95.4% CI -258–-175).

During the late glacial, core MD07-3098 (~41° S, 3055 m) displays more or less constant values around 40‰ $\Delta^{14}C$, between ~19 and ~17 ka cal BP. During this period, values oscilate from maximum values ~77‰ $\Delta^{14}C$ (95.4% CI 80–144) at ~19 ka cal BP (95.4% CI 19.5–18.4) and minimum values ~2‰ $\Delta^{14}C$ (95.4% CI -64–71) at 18.7 ka cal BP (95.4% CI 18.6–17.2). After this, a decreasing trend is observed

starting at ~17.6 ka cal BP (95.4% CI 18.4–16.6) with values f ~61‰ $\Delta^{14}C$ (95.4% CI -71–171), until 16.1 ka cal BP (95.4% 17.1–15.1) when values reach -111‰ $\Delta^{14}C$ (95.4% CI -221–-6). A increase is observed at ~15.5 ka cal BP (95.4% CI 16.9–14.2), with values of ~-52‰ $\Delta^{14}C$ (95.4% CI -190–115). An abrupt decreasing trend is then observed, reaching values of ~-196‰ $\Delta^{14}C$ (95.4% CI -334–-18) at15.1 ka cal BP (95.4% CI 16.8–13.6). Low values maintain until ~13.6 ka cal BP (95.4% CI 14.9–12.6), when values are ~-218‰ $\Delta^{14}C$. An abrupt increase to ~-108‰ $\Delta^{14}C$ (95.4% CI -223–47) occurres at ~13.4 ka cal BP (95.4% CI 14–12.3). From then until ~9 ka cal BP (95.4% CI 9.9–8.3), when values are ~124‰ $\Delta^{14}C$ (95.4% CI -199–-31), values are variable but more or less steady. From ~9 ka cal BP, a decreasing trend reachng minimum values of ~-303‰ $\Delta^{14}C$ (95.4% CI -401–-238) at ~7.4 ka cal BP (95.4% CI 8.2–6.2), is observed. From then until the present, values continue to decrease with a slope similar to that of the atmosphere. Minimum values of ~-396‰ $\Delta^{14}C$ (95.4% CI -436–-308) are reached at ~1.6 ka cal BP (95.4% CI 2.7–1.1).

From the cores here studied, core MD07-3081 (~49.5° S, 3273 m) reaches further back, until ~20.7 ka cal BP (95.4% 21.3–20.1), where its values are the most depleted with respect to the contemporary atmosphere, reaching ~130‰ $\Delta^{14}C$ (95.4% CI -196–-64). After this, values increase fast to ~134‰ $\Delta^{14}C$ (95.4% CI 50–217) at ~20.3 ka cal BP (95.4% CI 20.8–19.7). From then, a decreasing trend is observed until ~18.3 ka cal BP (95.4% CI 18.8–17.7) when values are ~-39‰ $\Delta^{14}C$ (-117–33). After this, an increasing trend is observed from ~18.3 ka cal BP until ~17 ka cal BP (95.4% CI 17.7–16.4), reaching values of ~122‰ $\Delta^{14}C$ (95.4% CI 33–222). Again values decrease fast to ~10‰ $\Delta^{14}C$ (95.4% CI -111–104) at ~16.8 ka cal BP (95.4% CI 17.5–15.7), and continue to slightly decrease to -29‰ $\Delta^{14}C$ (-112–92) until ~ 15.6 ka cal BP (95.4% CI 16.5–14.9). Values again increase to 33‰ $\Delta^{14}C$ (95.4% CI -105–150) at ~14.7 ka cal BP (95.4% CI 15.6–13.5).From then, values decease with a moe or less steady slope until ~4.6 ka cal BP (95.4% CI 6.1–3.5), when values aer ~-202‰ $\Delta^{14}C$ (95.4% CI -306–-51). Slightly lower values of ~-62‰ $\Delta^{14}C$ (95.4% CI -150–8) and ~-78‰ $\Delta^{14}C$ (95.4% CI -137–28) at ~12.8 ka cal BP (95.4% CI 13.5–12.1) and ~11.8 ka cal BP (95.4% CI 12.7–11.3), respectively (Figure 5.4, S5.7). The latter is observed with the exception of a decresing trend reaching exceptionally low values of -216‰ Δ14C (95.4% CI -273 – -148) at ~14.2 ka cal BP (95.4% CI 14.9–13.6) and -206‰ Δ14C (95.4% CI -274– -152) at ~13.6 ka cal BP (95.4% CI 14.1–12.9). Uncertainties in calendar ages are minimum in the late Holocene with ~2σ of 300 years, and maximum at the deglacial/Holocene transition, with ~2σ of ~1000 years. Uncertainties in Δ14C are minimum in the late Holocene, with estimated ~2σ of ~40‰ Δ14C and ~80‰ Δ14C in the rest of the core.

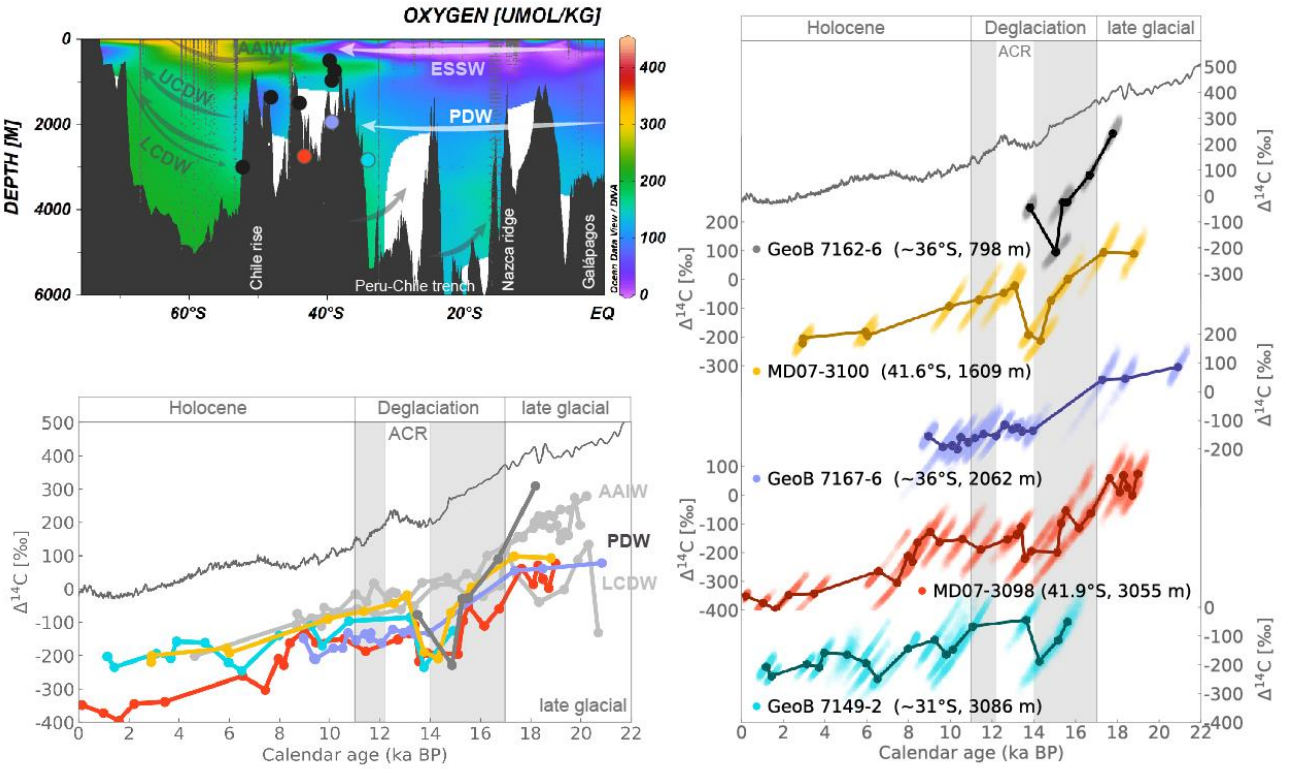

Figure 5.4 $\Delta^{14}C$ in the SEP for cores in group b, as described in the text: GeoB 7167-6, GeoB 7149-2 (Martínez Fontaine et al., 2019) and MD07-3098 here described. Also plotted are cores GoeB 762-6 (Martínez Fontaine et al., 2019) and MD07-3100, here described, for comparion of the timing of the important ^{14}C drop described in section 5.4.2.3. The darker dots indicate mean values, whereas values in the 95.4% CI are plotted as lighter dots. Also indicated are the position of the cores in the water column, together with cores in group a as black dots.

Core MD07-3098 (~41° S, 3055 m) displays values between -10 and 60‰ Δ14C during the late glacial. At around 17 ka cal BP, a fast drop to -71‰ Δ14C (95.4% CI -132 –63) is observed, and values continue to be as or more depleted in 14C with respect to the respective contemporary atmosphere througout the deglaciation (Figure 5.4, S5.7). Minimum values during the deglaciation of -231‰ Δ14C (95.4% CI -324– -136) are reached at ~14.7 ka cal BP (95.4% CI 15.7–13.7) and -217‰ Δ14C (95.4% CI -277 – -94) at ~13.6 ka cal BP (95.4% CI 14.7–12.9). Better ventilated values are observed during the early Holocene between -167‰ Δ14C (95.4% CI -217– -108) and -267‰ Δ14C (95.4% CI -321– -140), at ~10.5 ka cal BP (95.4% CI 11.5–9.4) and ~6.5 ka cal BP (95.4% CI 7.8–5.9), respectively. During the Holocene, especially low values of –335‰ Δ14C (95.4% CI -403– -254) are observed at ~7 ka cal BP (95.4% CI 8.1–6.1); of -355‰ Δ14C (95.4% CI -389– -366) at ~1.2 ka cal BP (95.4% CI 1.7–0.7); and of -350‰ Δ14C (95.4% CI -363 – -336) at ~0.1 ka cal BP (95.4% CI 0.2– 0.0). Mean uncertainties in calendar age estimates are ~2σ 850 years, and ~150‰ in Δ14C; minimum uncertainties correspond to the late Holocene, with ~2σ between ~130 and 300 years in calendar ages and ~60‰ in Δ14C, whereas maximum uncertainties are reached between ~17.9 and 14.7 ka cal BP, with ~2σ of ~1200 years, with corresponding ~2σ in Δ14C of 135‰.

Core MD07-3119 (~46° S, 2523 m) displays overall similar deviations from the contemporary atmosphere of ~-200‰ throughout the record (Figure 5.4, S5.7), with the exception of better ventilated waters with Δ14C vlaues of 137‰ (95.4% CI -3 – 200) at ~17.8 ka cal BP (95.4% CI 18.2– 16.7) and relatively less ventilated waters between ~16.1 ka cal BP (95.4% CI 17.2–15.8) and ~15.1 ka cal BP (95.4% CI 15.6–14.1), with values of -70‰ Δ14C (95% CI -152– 52) and -83‰ Δ14C (95% CI -189– -15), respectively. Mean uncertainties in calendar age estimates of ~2σ are ~530 years and ~60 ‰ in Δ14C; minimum uncertanties are reached in the core top, where ~2σ values are ~150 years and ~15‰ Δ14C; whereas maximum uncertainties are reached at ~ 7.2 ka cal BP, with ~2σ of ~1650 years and ~140‰ Δ14C.

Core MD07-3081 (~49.5° S, 3273 m) displays the most depleted values during the late glacial, between -147‰ Δ14C (95.4% CI -202– -88) at ~20.6 ka cal BP (95.4% CI 21 – 20) and -22‰ Δ14C (95.4% CI -141– 115) at ~ 19.1 ka cal BP (95.4% CI 20.2–18.1), interrupted by a period of relativey better ventilated values of 113‰ Δ14C (95.4% CI 34–192) and 67‰ Δ14C (95% CI 163– -29) at 20.2 ka cal BP (95.4% CI 20.7–19.6) and 19.7 ka cal BP (95.4% CI 20.4–18.9), respectively. Relatively better ventilated values are reached at around ~17.1 ka cal BP (95.4% CI 17.4–16.6). Again, relatively better ventilated values are observed between ~14.5 ka cal BP (95.4% CI 15.2–13.4) and ~9.3 ka cal BP (95% CI 9.7–7.6), of 13‰ Δ14C (95% CI -114– 105) and -88‰ Δ14C (95% CI -259– -34), respectively. Mean uncertainties in calendar ages are ~600 years and 80‰ Δ14C (~2σ); minimum uncertainties in the late glacial ~250 years and ~40‰ Δ14C and maximum in the late Holocene of ~1000 years and 70‰ Δ14C.

5.4 Discussion

In order to characterize changes in the ventilation of intermediate and deep waters in the Southeast Pacific during the last 20,000 years, we compare the new $\Delta^{14}C$ records here described for cores MD07-3100, MD07-3098 and MD07-3081, with previously published $\Delta^{14}C$ records for cores MD07-3088 (46.07° S, 75.68° W, 1536 m; Siani et al., 2013), GeoB 7149-2 (31.48° S, 72.00° W, 3086 m), GeoB 7163-7 (36.43°S, 73.59° W, 537 m), GeoB 7162-6 (36.54° S, 73.67° W, 798 m), GeoB 7167-6 (36.45° S, 73.93° W, 2061 m; Martínez Fontaine et al., 2019) and SO161-22SL (36.22° S, 73.68° W, 1001 m; De Pol-Holz et al., 2010; Martínez-Fontaine et al., 2019). From these, cores GeoB 7163-7, Geob 7162-6 and 22SL were retrieved in the upper, core and lower modern boundaries of the AAIW, respectively (Figures 5.3 and 5.4); cores MD07-3100 and MD07-3088 were retrieved in the boundary between AAIW and PDW; GeoB 7167-6 in the core of PDW; GeoB 7149-2 and MD07-3098 in the lower boundary of PDW, nearby the influence of CDW; and finally, MD07-3081 was retrieved in the boundary between PDW and LCDW. Together, these records allow us to characterize variations on the ventilation of the main intermediate and deep water masses in the Southeast Pacific.

5.4.1 Late glacial

During the late glacial portion here presented, corresponding to ~22–17 ka cal BP, the available ^{14}C information in the SEP indicates that depths today bathed by AAIW (GeoB 7163-6, GeoB 7162-6 and 22L) had higher $\Delta^{14}C$ contents than deeper depths between AAIW and PDW (Figure 5.3; MD07-3100, MD07-3088) and in the core (GeoB 7167-6) and bottom boundary of PDW (MD07-3098). Additionally, depths between AAIW and PDW display $\Delta^{14}C$ within error equal to PDW, and waters today in the boundary between LCDW and PDW (MD07-3081) were the least ventilated of the transect here presented. In particular, during this time interval, estimated mean $\Delta^{14}C$ values in the upper boundary of AAIW (GeoB 7163-7) go from ~280 to ~150‰ $\Delta^{14}C$; in the core of AAIW, at ~800 m, the only available value corresponds to ~300‰ $\Delta^{14}C$ (GeoB 7162-6); in the lower boundary of AAIW values go from ~190 to ~160‰ (22SL); in the boundary between AAIW and UCDW, at ~1500 m (MD07-3100 and MD07-3088), mean values range between ~200–60‰ $\Delta^{14}C$; at the core of PDW, at~2000 m depth (GeoB 7167-6) between 80–50‰ $\Delta^{14}C$; and in the boundary between LCDW and PDW, at ~3300 m (MD07-3098) values are more variable and go from ~-131‰ to 134‰ $\Delta^{14}C$.

Particularly contrasting with the modern ocean, are the relatively low ^{14}C values observed in core MD07-3081, with respect to sites bathed by PDW, between ~22–18 ka cal BP. As mentioned before, this core was retrieved in the boundary between PDW and LCDW (Figure 5.3, S5.4). In the modern scenario, the lower ^{14}C contents in the global ocean correspond to depths bathed by PDW, which in the study area has values of ~-215‰ $\Delta^{14}C$ (Lauvset et al, *in preparation*). In contrast, in the SEP, LCDW has relatively more ventilated values, around -130‰ $\Delta^{14}C$ (Figure 1.2). Thus, if a configuration similar to that of the present day would have been in place during the late glacial, we would expect that the record of MD07-3081 had ^{14}C contents higher than that of cores GeoB 7167-6 and MD07-3098, which is not the case. Today, LCDW is thought to derive from the mixing of well–ventilated North Atlantic Deep Water (NADW) –*entering* the ACC at the Atlantic sector of the Southern Ocean (as seen in its relative high salinity, Figure S5.4)– with recently formed AABW, as it sinks to the abyssal ocean and is transported to lower latitudes (Carter et al., 2008; Talley et al., 2013). Evidence of NADW formation in the North Atlantic indicates that between ~20–18 the production of NADW was relatively high, and decreases importantly from ~18–15 ka cal BP (McManus et al., 2004). From the latter, the observed ventilation changes in the SEP cannot be explained by changes in NADW ventilatin depths bathed by LCDW. In this scenario, the variation in the ventilation observed at the coree retrieving site of MD07-3081could be explained by changes in the formation of AABW and other less dense deep waters in the Southern Ocean, which help ventilate these depths at present. Today, southward flowing UCDW and LCDW upwell at the surface in the Southern Ocean. There, a portion of the upwelled deep waters move south to form AABW and sink to the abyssal circumpolar ocean. In this trajectory, UCDW and LCDW exchange gases with the atmosphere, which results in relatively higher oxygen and ^{14}C contents of AABW with respect to its precursors UCDW and LCDW

(Figure S5.4). Thus, during the late glacial the mechanism of formation of AABW should have changed to explain the observed ^{14}C values in the SEP. In particular, decreasing considerably the amount of sea–air gas exchange between the atmosphere and deep waters flowing south, resulting in waters at ~3,000 m depth being older than their precursor PDW or UCDW.

As already mentioned, the late glacial $\Delta^{14}C$ values observed in core MD07-3081, are consistent with deep water $\Delta^{14}C$ records from the South Atlantic (3770 m; Skinner et al., 2010) and South Indian Ocean (3615 m; Gottschalk et al., 2020), but also in the South West Pacific (2060 m, 4339 m; Ronge et al., 2016; 1600–3500 m, Sikes et al., 2016) and Equatorial East Pacific (2730 m, Umling & Thunell, 2017; 2921 m; De la Fuente et al., 2015). These relatively ^{14}C–depleted deep waters, together with records of lower oxygenation in the South Indian, South Atlantic and Equatorial East Pacific (Gottschalk et al., 2016; Umling & Thunell, 2018; Gottschalk et al., 2020; Anderson et al., 2019), lower $\delta^{13}C$ in deep waters in the Atlantic and Pacific oceans (Curry et al., 1987; Rosenthal et al.1997; Matsumoto & Lynch-Stieglitz, 1999; Duplessy et al., 2002; Sikes et al., 2017) and CO_3^{2-} reconstructions in the SWP (Allen et al., 2015), have been interpreted as a signal of a higher amount of respired CO_2 being stored in the deep glacial ocean with respect to the Holocene. From what is observed in the SEP, it seems as at least the LCDW was more isolated from the atmosphere than at present, thus probably accumulating more carbon. To explain this increase in respired carbon in the glacial deep ocean, changes in ventilation of deep waters in the SO are primarily invoked in the literature, in line with what is observed in the SEP. Among these, an increase in sea ice extent (Gersonde et al. 2005) has been hypothesized to translate in: i) decreased gas exchange of deep waters with the atmosphere because of a bigger portion of these upwelling under sea ice (e.g. Stephens and Keeling, 2000; Ferrari et al. 2014); ii) changes in the formation mechanisms of AABW (Rosenthal et al., 1997; Watson and Naveira Garabato, 2006) producing denser AABW, in turn increasing stratification of deep waters in the SO and decreasing both diapycnal mixing with less ventilated deep waters and isopycnal mixing with better ventilated NADW (Adkins, 2015). In this context, the deep SO would slowly fill with denser, less ventilated waters. Additionally, the intensity and position of the SWW has also been invoked to explain changes in deep water ventilation in the SO (e.g. Toggweiler et al., 2006; Anderson et al., 2009; Denton et al., 2010), as today they are related with the amount of deep waters effectively surfacing in the SO and thus exchanging gas with the atmosphere. During the late glacial, reconstructions indicate a ~5° northern position of the SWW (Moreno et al., 1999; Gray et al. *submitted*), which is thought to reduce the amount and depth of deep waters upwelling to the surface in the SO. Today, a southern position of the SWW is associated with increased wind–driven Ekman divergence and thus deep water upwelling. In contrast, when SWW are located further north, the Ekman divergence is opposed by stronger eddies occurring at lower latitudes.

On the other hand, the relative higher ^{14}C content at depths bathed by AAIW with respect to depths bathed by UCDW or PDW, indicates that the process producing AAIW and ventilating intermediate depths at

present, continuous to be in place during the late glacial. Although, this process might have been in part modified, as seen from cores located at present in the boundary between AAIW/UCDW (MD07-3088 and MD07-3100), which display ^{14}C contents closer to PDW than at present. The latter is consistent with previous studies in the SEP (Haddam et al., 2020) indicating lower oxygenation of bottom waters in core MD07-3088 and MD07-3100 during the late glacial, with respect to the present, i.e. less AAIW influence at those depths. Haddam et al (2020) have interpreted these and other records in the SEP (Martínez-Méndez et al., 2013; Muratli et al., 2010) as a northern displacement of the formation zone of the AAIW during the late glacial. Because the formation processes of AAIW at present are not clearly understood, it is unclear what would produce this northward displacement of the AAIW formation zone. However, it is known that AAIW derives from the upwelling of UCDW and LCDW in the Southern Ocean, from where a portion is transported to the north, and circulates around Antarctica until for some unclear process, it sinks to intermediate depths. Thus, the upwelling in the SO continues to occur, with a norther branch effectively ventilating deep waters and forming AAIW, which ventilates intermediate depths as at present; and a southern branch where waters for either of the hypothesis already described, become less ventilated. From the results here presented, at least during the late last glacial, the SEP does not show evidence for a extremely isolated deep glacial ocean. Instead, the evidence here presented argues in favor of slight circulation changes in the Southern Ocean which result in aging and probably carbon accumulation of deep waters there. Meanwhile PDW seem to be as or slightly less ventilated than at present.

5.4.2 Deglaciation

Entering the deglaciation, the relative contents of ^{14}C observed during the late glacial, changes. Broadly two groups can be defined, which we will call groups a and b. Group a corresponds to cores that at the beginning of the deglaciation all display similar and relatively higher ^{14}C contents: core GeoB 7162-6, GeoB 7163-7, 22SL, MD07-3100, MD07-3088 and MD07-3081. Whereas group b corresponds to cores displaying overall less ventilated waters: GeoB 7167-6, MD07-3098 and GeoB 1749-2. In the following we describe both groups separately. Additionally, cores belonging to both groups, display an important drop in ^{14}C between ~15 and 13.5 ka cal BP. This drop is identified in cores bathed by PDW (MD0-3098 and GeoB 7149-2), AAIW (GeoB 162-6), and in the boundary between AAIW and PDW (MD07-3100), but not all cores expected to be bathed by the same water mass display this drop. Because of the latter, this feature seems to be independent of water mass formation, and more so, it seems to be over imposed to the overall behavior of cores in groups a and be. This is discussed separately at the end of this section.

5.4.2.1 Group a

In group a (Figure 5.3), at the beginning of the deglaciation, cores GeoB 1763-7 (537m, upper boundary of the AAIW), GeoB 7162-6 (798 m, core of AAIW) and 22SL (1001 m, lower boundary of AAIW), become less ventilated with respect to the late glacial, reaching values of ~130‰ $\Delta^{14}C$; whereas cores MD07-3088

(1536 m, boundary AAIW/PDW), MD07-3100 (1609 m, boundary AAIW/PDW) continue to have similar ^{14}C values to the late glacial, around 100‰ $\Delta^{14}C$; and core MD07-3081 (3273 m, boundary between PDW and LCDW), becomes better ventilated, reaching values of ~120‰ $\Delta^{14}C$ at ~17 ka cal BP. All these cores reach similar values with the onset of the deglaciation and continue to have similar values throughout the deglaciation and until ~8 ka cal BP. From then, data (especially at depths bathed by AAIW) becomes sparse and the records cannot be further compared.

From the latter it is inferred that, whichever they are, the mechanisms responsible for the aging of deep waters in the SO during the late glacial change, initiating their ventilation. As mentioned before, today the waters bathing the retrieving site of core MD07-3081 is ventilated by the intrusion of NADW in the ACC, together with the formation of deep and bottom waters in the Southern Ocean, south of the Polar Front (Carter et al., 2008; Talley et al., 2013). At the onset of the deglaciation, the production of NADW is still suppressed (MacManus et al., 2004), and thus cannot be invoked to explain the increased ventilation observed in core MD07-3081. Thus, a change in the formation of deep waters in the SO must be in place to explain the observed values. As mentioned before, AAIW and AABW originate from the same process, the upwelling of deep waters in the SO. When this occurs, some of the recently upwelled water is transported north to form AAIW, whereas some of it is transported south to form AABW. In contrast to what is observed during the late glacial, with the onset of the deglaciation it seems that the southern upwelling branch began to effectively ventilate deep waters at this time. Because the increase in ventilation in MD07-3081 is rather fast, we hypothesize that waters bathing these depths begin to effectively exchange gas with the atmosphere before sinking to deeper depths, unlike during the late glacial. A possible explanation for this is the upwelling of deep waters in ice–free conditions, as has been proposed by Ferrari et al. (2014), among others.

Additional information to understand the mechanisms behind the change in circulation observed in the SEP with the onset of the deglaciation, is given by cores retrieved at intermediate depths. As mentioned before, cores bathed by AAIW and cores in the boundary between AAIW and PDW, go from a difference of ~100‰ $\Delta^{14}C$ during the late glacial, to homogeneous values at ~17 ka cal BP (Figure 5.3). Additional information to interpret these changes in the area, corresponds to bottom water oxygenation reconstructions in cores MD07-3088, MD07-3100 and MD07-3082 (1792 m, ~49.2° S; Haddam et al., 2020), and at depths bathed by AAIW (Muratli et al., 2020), including ODP site 1234, retrieved nearby core 22SL. These records indicate a transition to more oxygenated values with the onset of the deglaciation in cores MD07-3088, MD07-3100 and MD07-3082, and to lower oxygenation in cores retrieved in the upper and lower boundaries of the AAIW at ~36°°S. This information has been interpreted as a southward displacement of the formation area of AAIW at the beginning of the deglaciation, together with a vertical expansion near its formation site (southernmost cores). The latter is consistent with the ^{14}C records here produced. We thus interpret the similar values at depths bathed

by AAIW and cores MD07-3088 and MD07-3100 as a vertical expansion of the AAIW, reaching deeper depths at least in cores south of ~40° S. Even though AAIW production in the modern ocean is not yet well understood (Bostock et al., 2013; McCartney, 1977; Sloyan et al., 2010; Piola & Goron 1989), model simulations indicate that an intensification of SWW during the last deglaciation would result in more AAIW and AABW production (Menviel et al., 2018). The latter would result in steeper isopycnas in the SO, upwelling deeper waters to the ocean surface, and resulting in a deeper convection of the AAIW. Additionally, a southern position of the SWW, would additionally favor the upwelling of deeper waters, as the wind–driven Ekman transport would be less opposed by eddy circulation. The timing of the observed changes at the beginning of the deglaciation is consistent with reconstructions of the position of the SWW, indicating the beginning of a southward shift which continues throughout the deglaciation, reaching maximum values of ~5° a at ~11 ka cal BP (Gray et al., submitted). Thus, although more information regarding the formation of AAIW could help clarify this issue, it is likely that the observed changes in intermediate water ventilation in the SEP are regulated by changes in the position and/or intensity of the SWW. In this scenario, it is plausible that a southward position of the SWW at the beginning of the deglaciation, together with a hypothesized retreat of sea ice extent, would result in the upwelling of more and deeper waters in to an ice–free surface. This water would then sink to deeper depths, ventilating –previously isolated– deep waters in the SO. A similar transition from less to better ventilated values is observed in deep waters in the South Indian Ocean, today bathed by LCDW (Gottschalk et al., 2020); the SWP (Ronge et al., 2016), at depths bathed by UCDW and AABW. These records have been interpreted as ventilation of the deep SO by a combination of the effects of decreased sea ice extent, increased vertical mixing, changes in the formation processes of AABW and/or SWW shifts modulating Ekman pumping of deep waters.

After the important ventilation change observed in core MD07-3081 at ~17 ka cal BP, less ventilated values are again observed between 16.7 and 15.6 ka cal BP, but which are within error equal to values observed in cores MD07-3100, MD07-3088, GeoB 7162-6 and 22SL. At ~15 ka cal BP, core MD07-3081 becomes again more ventilated. This change is within error synchronous with changes to better ventilated and oxygenated deep waters in the South Indian Ocean (3615 m; Gottschalk et al., 2020), the South Atlantic (3770 m; Skinner et al., 2010; Gottschalk et al., 2016) and the EEP (2921 m; de la Fuente et al., 2015; 2730 m ;Umling & Thunell, 2017; Umling & Thunell, 2018). This increased ventilation is synchronous with the acceleration of the AMOC (McNannus et al., 2004), and in the SA and South Indian Ocean, it has been interpreted as the signal of NADW entering the ACC (Gottschalk et al., 2020). Since core MD07-3081 is today bathed by LCDW, partially sourced in the NADW, the better ventilated values at ~15 ka cal BP are consistent with this interpretation. Additionally, changes observed in the EEP might also be associated with the reinvigoration of NADW, as below ~3,000-3,500 m, the Paicific Ocean is bathed by a mix of Pacific Deep water transported south, with southern–sourced deep waters (AABW, NADW, LCDW)

transported north. Thus, it is not unlikely that during the late glacial, imore and more dense southern sourced deep waters filled the deep Pacific Ocean. Thus, the fact that deep cores in the EEP display better ventilated values ~15 ka cal BP might be reflecting the reinvigoration of NADW, ventilating these depths.

5.4.2.2 Group b

In contrast to cores in group a, another group of cores can be defined which, during the deglaciation, follow a different trend (Figure 5.4). In this group are included cores which display overall less ventilated values with respect to cores in group a during the deglaciation: cores GeoB 7167-6, MD07-3098 and core GeoB 7149-2. The Δ^4C content in core GeoB 7149-2, oscillates between values close to those observed in cores in group a, and more ^{14}C–depleted values, similar to cores in group b. As mentioned before, during the late glacial, cores MD07-3098 and GeoB 767-6, display more or less constant values of ~50‰ $\Delta^{14}C$ and are relatively better ventilated than the record from core MD07-3081. With the onset of the deglaciation, a fast decrease in ^{14}C is observed in core MD07-3098, reaching ~-60‰ $\Delta^{14}C$ (Figure 5.4) at 16.7 ka cal BP. From there and throughout the deglaciation (with the exception of the period between ~15–13.5 ka cal BP, discussed below), MD07-3098 continues to be depleted in ~50-100‰ Δ ^{14}C, with respect to cores in group a. One exception is observed 15.5 ka cal BP, when ^{14}C values in core MD07-3098 are similar to those observed in group a, around -50‰ $\Delta^{14}C$. Between ~14 and 9 ka cal BP, core GeoB 767-6 closely follows the values of MD07-3098. Meanwhile, during the deglaciation GeoB 7149-2 displays intermediate values between those in cores GeoB 767-7 and MD07-3098 and values in cores in group a. As mentioned before, core GeoB 767-6 was retrieved at ~2,000 m depth and ~36° S, in the core of PDW. On the other hand, cores MD07-3098 and GeoB 7149-2 were retrieved in deeper waters ~3,000 m depth, near the influence of CDW as it is transported from the Southern Ocean to the North Pacific at depths >3,000 m. From what is observed here, core MD07-3098 is bathed by PDW during the deglaciation and late glacial, whereas GeoB 7149-2 seems to be more influenced by CDW, resulting in intermediate values between cores in group a and b.

From the latter, PDW in the SEP does not display important changes in its ^{14}C content during the late glacial or deglaciation. Instead, important changes in the ventilation of water masses in the SEP are dominated by changes occurring in the SO, i.e. variations in the formation of AAIW and SO deep waters (i.e. AABW and other less dense deep water which mix with LCDW).

5.4.2.3 ^{14}C drop between ~15–13.5 ka cal BP

As mentioned before, some of the cores in groups a and b, display important drops in their ^{14}C content, which are superimposed to the deglacial trends described in sections 4.2.1 and 4.2.2. All these cores experiment drops in their $\Delta^{14}C$ of between ~120–200‰ and which occur between ~15–13.5 ka cal BP (Figure 5.4). In particular, core GeoB 7162-6 reaches minimum values of ~-230‰ $\Delta^{14}C$ at ~14.8 ka cal BP; MD07-3100 displays low values around -~200‰ $\Delta^{14}C$ between ~13.7 and ~14.3 ka cal BP; core

MD07-3098 displays values between ~-200 and ~-220‰ $\Delta^{14}C$ between ~13.5 and 15 ka cal BP; and core GeoB 7149-2, a value of ~-235‰ $\Delta^{14}C$ at ~14 ka cal BP. From these cores, and from what was previously dicussed, during the deglaciation GeB 7162-7 and MD07-3100 are bathed by AAIW, cores MD07-3098 by PDW and GeoB 7149-2 by a mixture of PDW and CDW.

One possibility to explain the relatively low ^{14}C values observed in these cores, is that this signal represents changes in PDW and that this water mass reaches MD07-3100 during that period but no MD07-3088 (which continuous to have relatively well ventilated values during that time). However, this feature is not present at core sites today bathed by PDW in the EEP (~2900 m, de la Fuente et al., 2015; ~2,700 m, Umling & Thunell, 2017), the NP (~3,600 m, Galbraith et al., 2007; Rae et al., 2014), or the SWP (2066 m, Ronge et al., 2016), which during that time are better ventilated and present values similar to cores in group a. As previously described, for the EEP cores the latter might be due to a more important presence of southern–sourced waters in those sites at that time, thus they might not represent PDW as today. However, cores in the NP and SWP are thought to represent changes in PDW during that time. Extremely ^{14}C–depleted values of ~-600‰ have been identified in deep waters the East Pacific Rise (EPR, 3,600 m) at ~46°S and in the SWP (2,500 m; Ronge et al., 2016). However, these waters get ventilated at around ~15 ka cal BP, before the observed drop in ^{14}C in the SEP. Additionally, bottom water oxygenation reconstructions and benthic foraminifera $\delta^{13}C$ values in core MD07-3100 (Haddam et al., 2020) at that time are relatively high. These characteristics are consistent with well–ventilated deep waters, in this case AAIW, and not with PDW, which is characterized by low oxygen levels and $\delta^{13}C$ values (Lauvset et al., *in preparation*). Thus, it is unlikely that this signal represents changes in PDW ventilation. In addition, because cores in group a are also relatively better ventilated during this time, southern–sourced deep waters are not a plausible source for the ^{14}C drop either.

Records of waters with a similar ^{14}C depletion during the deglaciation have been produced in intermediate waters in Baja California (~700 m, Marchitto et al., 2007; Lindsay et al., 2016) and in the EEP (~600 m, Bova et al., 2018; Stott et al., 2007). On the one hand, records in Baja California displaying minimum $\Delta^{14}C$ values of ~-180‰ $\Delta^{14}C$ during the HS1, and of ~-320‰ $\Delta^{14}C$ during the YD, have been interpreted as EqPIW laterally advecting a signal of deep ^{14}C–depleted water, likely sourced in the SO or the Pacific Ocean (Marchitto et al., 2007; Lindsay et al., 2016). On the other hand, extremely ^{14}C–depleted records in EEP have been interpreted as either purely hydrothermally–sourced (Stott et al., 2007; Stott and Timmerman, 2011); as a mixture of hydrothermally–sourced together with ^{14}C–depleted waters from a deep carbon pool, likely in the NP (Bova et al., 2018); and/or as a result of hydrothermal fluids in pore waters, but not representative of bottom waters conditions (Chen et al.2020). Even though some of these authors indicate a deep ocean source for the ^{14}C–depleted values observed in Baja California and the EEP, evidence of deep waters depleted enough to account for the values observed in these sites, has not yet been identified. The latter, however, does not necessarily mean that this water did not exist, and

for example, in the SEP remnants of the deep late glacial ^{14}C–depleted waters could be stored in the Perú-Chile trench (~6–39° S, Figure 5.4) where bathymetry is much deeper, reaching depths ~8000 m. The latter could be especially true if the late glacial waters are much denser and thus they do not mix with the less dense SO abyssal waters hypothetically being produced at the beginning of the deglaciation. Thus, a possible explanation for the relatively low ^{14}C values in the SEP between ~15–13 ka cal BP is that this water was effectively ventilated during this period entering the PDW in the SEP. However, evidence for this is yet to be found.

If we rule out that the low ^{14}C signal represents the ventilation of –previously isolated– deep waters, another likely explanation for it would be a hydrothermal source injecting ^{14}C–dead CO_2 to deep and intermediate waters, either locally or regionally. At present, hydrothermal activity in the ocean can be tracked very clearly by the δ^3He content of water (Jenkins et al., 2019). From the latter, most hydrothermal activity in the modern ocean is concentrated in the Pacific Ocean (Figure S5.6), where it is possible to identify prominent hydrothermal plumes with maximum values between 30–40% δ^3He. Such plumes are found in the EPR, both north and south of the equator (Lupton & Craig, 1981; Lupton, 1998; Jenkins et al., 2017), in the French Polynesia (Jenkins et al., 2015), in the Juan de Fuca Ridge (Lupton, 1998) and in Tonga–Fiji region (Lupton et al., 2004). Most these plumes display maximum δ^3He values at ~2000–2500 m depth and extend for thousands of kilometers away from the main vents. For example, in the SEP, a plume can be identified as a ~25 % δ^3He contour extending eastward between ~2000–3000 m depth from the main vent, located in the EPR at ~26°S, as seen from maximum values around 30% δ^3He (Figure S5.7). Baja California and the EEP, on the other hand, are influenced by another prominent plume sourced in the EPR at ~11° N, also between ~2000–3000 m. Thus, it is plausible that during the deglaciation these sites are influenced by hydrothermal activity. However, for the ^{14}C values observed to have a hydrothermal source, the submarine volcanic activity should have been enhanced and/or different in composition than today. In the modern Pacific Ocean, even though ^{14}C–dead CO_2 is a hydrothermal product, the ^{14}C content of deep waters are mainly controlled by the remineralization of organic matter, as seen in the coupling between the lowest ^{14}C values in the ocean with low oxygen and high nutrient contents in the NP (Lauvset et al., *in preparation*). However, in some areas, as the Tonga-Fiji region, local minimum ^{14}C contents might be hydrothermally sourced. Thus, for the observed signal to be sourced in hydrothermal vents, the eruption rate would have to be higher and/or the composition would have to contain more ^{14}C–dead CO_2, than vents in the modern ocean.

Even though the timing and magnitude of the changes observed in Baja California, the EEP and the SEP between ~15–13 ka cal BP are similar, it is difficult to reconcile a common source for all the observed depths and latitudes, especially considering records of relatively well–ventilated deep and intermediate waters in the EEP during the deglaciation (Chen et al., 2020; Bova et al., 2018; Zhao and Keigwin, 2018; Umling and Thunell, 2017; de la Fuente et al., 2015). However, it is still plausible that the observed drops

in ^{14}C are hydrothermal, but represent more local signals of intensified activity. For example the SEP could be influenced, as today, by an eastward flowing plume coming from the EPR, or alternatively from volcanic activity in the Chile rise or Sala y Gomez ridge. However, for the observe drop to reach depths of ~800 (core GeoB 7162-6) and ~1000 m (core MD07-3100) in the SEP, the hydrothermal activity would have to correspond to one or several event plumes. These correspond to massive releases of hydrothermal fluid into the water column which can reach ~1000 m above the venting depth (e.g. Baker et al., 1987). It is not unlikely that this is the case as there is evidence of enhanced hydrothermal activity in the EPR during this time (Lund et al., 2016). More so, Lund et al. (2016) document peaks in hydrothermal activity in the EPR last two deglaciations, and interpret it as a lagged response to minimum sea levels during the LGM. Thus, in this scenario, it is plausible that the signals in Baja California, the EEP and the SEP correspond to separate plumes given by enhanced volcanic activity due to sea level drop during the LGM.

Regardless of whether or not the hypothesized intensified volcanic activity between 15-13 ka cal BP carried a high CO_2 signal, it might still have had an influence in the CO_2 budget. In the modern ocean, prominent hydrothermal plumes in the South Pacific, have an impact in oceanic circulation, accelerating an anticyclonic circulation at mid depths (Lupton & Craig, 1981; Stommel, 1982; Hautala & Riser, 1983). In fact, model simulations evaluating the effect of including δ^3He in large–scale deep ocean global circulation, found that including it reduces the time of re-exposure of Pacific bottom water by ~50–150 years (DeVries & Holzer, 2019). Thus, an intensified hydrothermal activity in the deglacial would potentially dynamize the circulation in the SEP, maybe even aiding the ventilation of extremely depleted ^{14}C waters found in the EPR and SWP, estimated to have happened around ~15 ka cal BP. Around 14.8 ka cal BP, an abrupt increase (10–15 ppm in 100–200 years) in atmospheric pCO_2 occurred in Antarctica (Marcott et al., 2014), within error synchronous with a drop in 30‰ in 100 years atmospheric $\Delta^{14}C$ followed by a relatively slower drop of 30‰ in 300 years (Reimet et al., 2021). Because at present oceanic records do not have the resolution and accuracy of atmospheric records, it is difficult to identify the exact source or mechanisms responsible for atmospheric changes in pCO_2. In fact, as already mentioned, around the same time records in the Atlantic Ocean register the reinvigoration of AMOC, which together with increased ventilation in the deep SA and SI are interpreted as NADW entering the circumpolar circulation, consistent with ventilation changes observed here in core MD07-3081. The latter has been indicated as a likely source of the atmospheric changes in pCO_2 around 14.8 ka cal BP (Gottschalk et al., 2020). Thus, the observed changes in atmospheric pCO_2 are difficult to attribute to a specific event. However, the records here presented might indicate that is worthwhile testing the effects of including variations in hydrothermal activity in climatic models, not only because of the CO_2 input but because of its effect in deep ocean circulation.

Another explanation that has been put forward to explain the extremely ^{14}C–depleted values found in EEP is that they would actually corresponds to the signal of the pore–water microhabitat in which the infaunal foraminifera often picked for ^{14}C dating live (e.g. *U. peregrina*). Chen et al. (2020) propose that hydrothermal activity could explain the ^{14}C values in the EEP but that it would not be injected in bottom waters but stay restricted to pore waters. There is abundant evidence for gas-hydrate occurrences along the Chilean margin (Bangs et al., 1993; Froelich et al., 1995; Morales, 2003; Grevemeyer et al., 2003; Vargas-Cordero et al., 2010a, b; Vargas-Cordero et al., 2016; Villar-Muñoz et al., 2019), thus it is not unlikely that this is the case for cores in the SEP. However, even if it is, there should still be increased hydrothermal activity in the area between ~15-13 ka cal BP to explain the observed values.

5.4.3 Holocene

During the Holocene, cores in group a continue to be relatively well ventilated and their ^{14}C content is within error the same. With respect to cores in group b, at the beginning of the Holocene, all three cores display relatively less ventilated waters with respect to cores in group a, and in particular core GeoB 749-2 displays values that are closer to cores MD07-3098 and GeoB 767-7, which might represent more presence of PDW at the core retrieving site (~3,300 m, 31° S). At ~9 ka cal BP, all three cores become more ventilated, reaching values similar to cores in group a. After this, core GeoB 749-2 displays values similar to cores in group a, with the exception of one value of -245 ‰ at ~6.9 ka cal BP, which might indicate again more influence of PDW at that time. Between ~9 ka cal BP and the present, no $\Delta^{14}C$ estimates for GeoB 7167-6 are available. Regarding core MD07-3098, after displaying values similar to cores in group a at ~9 ka cal BP, it presents a decreasing trend, reaching a local minimum of ~-300‰ $\Delta^{14}C$ at ~7.4 ka cal BP. At ~6.5 ka cal BP, it becomes better ventilated with values ~-260‰ $\Delta^{14}C$, similar to values observed in core GeoB 7149-2. After this, between ~3.4–0.1 ka cal BP, core MD07-3098 displays relatively depleted ^{14}C contents between ~-340 and -400‰ $\Delta^{14}C$. With the information here provided, it is unclear if this signal represent a PDW signal or a local signal, however the values presented in core MD07-3098 are lower than anywhere in the modern ocean, thus it is unlikely that they represent changes in PDW formation.

5.5 References

Amigo, Á., Lara, L.E., Smith, V.C., 2013. Holocene record of large explosive eruptions from Chaitén and Michinmahuida Volcanoes, Chile. *Andean Geology*, 40, 227–248. https://doi.org/10.5027/andgeov40n2-a03

Alloway, B. V., Moreno, P.I., Pearce, N.J.G., De Pol-Holz, R., Henríquez, W.I., Pesce, O.H., Sagredo, E., Villarosa, G., Outes, V., 2017. Stratigraphy, age and correlation of Lepué Tephra: a widespread c. 11 000 cal a BP marker horizon sourced from the Chaitén Sector of southern Chile. *J. Quat. Sci*. 32, 795–829. https://doi.org/10.1002/jqs.2976

Allen, K. A., Sikes, E. L., Hönisch, B., Elmore, A. C., Guilderson, T. P., Rosenthal, Y., & Anderson, R. F. 2015. Southwest Pacific deep water carbonate chemistry linked to high southern latitude climate and atmospheric CO2 during the Last Glacial Termination. *Quaternary Science Reviews*, 122, 180–191. https://doi.org/10.1016/j.quascirev.2015.05.007

Anderson, R. F., Sachs, J. P., Fleisher, M. Q., Allen, K. A., Yu, J., Koutavas, A., & Jaccard, S. L. 2019. Deep-sea oxygen depletion and ocean carbon sequestration during the last ice age. *Global Biogeochemical Cycles*, 33, 301– 317. https://doi.org/10.1029/2018GB006049

Anderson, R. F., Ali, S., Bradtmiller, L. I., Nielsen, S. H. H., Fleisher, M. Q., Anderson, B. E. & Burckle, L. H. 2009. Wind–Driven Upwelling in the Southern Ocean and the Deglacial Rise in Atmospheric CO_2. *Science*, 323 (5920), 1443–1448. https://doi.og/10.1126/science.1167441

Bangs, N. L., Sawyer, D. S. & Golovchenko, X. 1993. Free gas at the base of the gas hydrate zone in the vicinity of the Chile triple junction. *Geology* **21**, 905–908. https://doi.org/10.1130/0091-7613(1993)021<0905:FGATBO>2.3.CO;2

Baker, E., Massoth, G. & Feely, R. 1987. Cataclysmic hydrothermal venting on the Juan de Fuca Ridge. Nature 329, 149–151. https://doi.org/10.1038/329149a0

Bendle, J.M., Palmer, A.P., Thorndycraft, V.R. *et al.* 2019. Phased Patagonian Ice Sheet response to Southern Hemisphere atmospheric and oceanic warming between 18 and 17 ka. *Sci Rep* **9,** 4133. https://doi.org/10.1038/s41598-019-39750-w

Bostock, H., Sutton, P., Williams, M., & Opdyke, B. 2013. Reviewing the circulation and mixing of Antarctic Intermediate Water in the South Pacific using evidence from geochemical tracers and Argo float trajectories. *Deep Sea Research, Part I*, 73, 84–98. https://doi.org/10.1016/j.dsr.2012.11.007

Bova, S. C., Herbert, T. D., & Altabet, M. A. 2018. Ventilation of northern and southern sources of aged carbon in the eastern equatorial Pacific during the Younger Dryas rise in atmospheric CO2. *Paleoceanography and Paleoclimatology*, 33, 1151–1168. https://doi.org/10.1029/2018PA003386

Burke, A. & Robinson, L.F. 2012. The Southern Ocean's Role in Carbon Exchange During the Last Deglaciation. *Science*, 335, 557–561. https://doi.org/10.1126/science.1208163

Carel, M., Siani, G., Delpech, G., 2011. Tephrostratigraphy of a deep-sea sediment sequence off the south Chilean margin: New insight into the Hudson volcanic activity since the last glacial period. *J. Volcanol. Geotherm. Res.* 208, 99–111. https://doi.org/10.1016/j.jvolgeores.2011.09.011

Chen, T., Robinson, L. F., Burke, A., Southon, J., Spooner, P., Morris, P. J. & Hong Chin, N. 2015. Synchronous centennial abrupt events in the ocean and atmosphere during the last deglaciation. *Science*, 349 (6255), 1537–1541. https://doi.org/10.1126/science.aac6159

Chen, T., Robinson, L.F., Burke, A. et al. Persistently well-ventilated intermediate-depth ocean through the last deglaciation. *Nat. Geosci.* 13, 733–738 (2020). https://doi.org/10.1038/s41561-020-0638-6

Curry, W.B., Crowley, T.J., 1987. The $\delta^{13}C$ of equatorial Atlantic surface waters: implications for ice age pCO_2 levels. *Paleoceanography*, 2, 489–517. https://doi.org/10.1029/PA002i005p00489

Denton, G.H., Anderson, R.F., Toggweiler, J.R., Edwards, R.L, Schaefer, J.M. & Putnam, A.E. 2010. The Last Glacial Termination. *Science,* 328, 1652–1656. https://doi.org/10.1126/science.1184119

De la Fuente, M., Skinner, L., Calvo, E., Pelejero, C. & Cacho, I. 2015. Increased reservoir ages and poorly ventilated deep waters inferred in the glacial Eastern Equatorial Pacific. *Nature Communications*, 6:7420. https://doi.org/10.1038/ncomms8420

De Pol–Holz, R., Keigwin, L., Southon, J., Hebbeln, D. & Mohtadi, M. 2010. No signature of abyssal carbon in intermediate waters off Chile during deglaciation. *Nature Geoscience*, 3 (3), 192–195. https://doi.org/10.1038/NGEO745

DeVries, T., & Holzer, M. 2019. Radiocarbon and helium isotope constraints on deep ocean ventilation and mantle-3He sources. Journal of Geophysical Research: Oceans, 124, 3036–3057. https://doi.org/10.1029/2018JC014716

Ferrari, R., Jansen, M. F., Adkins, J. F., Burke, A., Stewart, A.L. & Thompson, A.F. 2014. Antarctic sea ice control on ocean circulation in present and glacial climates. *Proceedings of the National Academy Sciences of the United States of America*, 111 (24), 8753–8758. https://doi.org/10.1073/pnas.1323922111.

Frowlich, P., Kvenvolden, K., Torres, M., Waseda, A., Didyk, B., & Lorenson, T. 1995. Geochemical evidence for gas hydrate in sediment near the Chile Triple Junction. *Proceedings of the Ocean Drilling Program, Scientific Results*, 141, 186-279. https://www.doi.org/10.2973/odp.proc.sr.141.019.1995

Galbraith, E. D., Jaccard, S. L., Pedersen, T. F., Sigman, D. M., Haug, G. H., Cook, M., et al. 2007. Carbon dioxide release from the North Pacific Abyss during the last deglaciation. Nature, 449(7164), 890–893. https://doi.org/10.1038/nature06227

Gersonde, R., Crosta, X., Abelmann, A. & Armand, L. 2005. Sea-surface temperature and sea ice distribution of the Southern Ocean at the EPILOG Last Glacial Maximum– a circum-Antarctic view based on siliceous microfossil records. *Quaternary Science Reviews*, 24 (7–9), 869–896. https://doi.org/10.1002/2014GB004929

Gottschalk, J., Michel, E., Thöle, L.M. *et al.* 2020. Glacial heterogeneity in Southern Ocean carbon storage abated by fast South Indian deglacial carbon release. *Nat Commun* **11,** 6192. https://doi.org/10.1038/s41467-020-20034-1

Gottschalk, J., Skinner, L., Lippold, J. *et al.* 2016. Biological and physical controls in the Southern Ocean on past millennial-scale atmospheric CO_2 changes. *Nat Commun* **7,** 11539. https://doi.org/10.1038/ncomms11539

Grevemeyer, I., Diaz-Naveas, J. L., Ranero, C. R. & Villinger, H. W. 2003. Heat flow over the descending Nazca plate in central Chile, 32 S to 41 S: observations from ODP Leg 202 and the occurrence of natural gas hydrates. *Earth Planet. Sci. Lett.* **213**, 285–298. https://doi.org/10.1016/S0012-821X(03)00303-0

Hain, M. P., Sigman, D. M. & Haug, G. H. 2014. Distinct roles of the Southern Ocean and North Atlantic in the deglacial atmospheric radiocarbon decline. Earth and Planetary Science Letters, 394, 198–208. https://doi.org/10.1016/j.epsl.2014.03.020

Haberle, S.G., Lumley, S.H., 1998. Age and origin of tephras recorded in postglacial lake sediments to the west of the southern Andes, 44°S to 47°S. *J. Volcanol. Geotherm. Res.* 84, 239–256. https://doi.org/10.1016/S0377-0273(98)00037-7

S.G. Haberle, K.D. Bennett, 2004. Postglacial formation and dynamics of North Patagonian Rainforest in the Chonos Archipelago, Southern Chile, *Quaternary Science Reviews*, Volume 23, Issues 23–24, Pages 2433-2452. https://doi.org/10.1016/j.quascirev.2004.03.001

Haddam, N. A., Michel, E., Siani, G., Licari, L., & Dewilde, F. 2020. Ventilation and expansion of intermediate and deep waters in the Southeast Pacific during the last termination. Paleoceanography and Paleoclimatology, 35, Articles: e2019PA003743. https://doi.org/10.1029/2019PA003743

Haddam, N.A., Siani, G., Michel, E., Kaiser, J., Lamy, F., Duchamp-Alphonse, S., Hefter, J., Braconnot, P., Dewilde, F., Isgüder, G., Tisnerat-Laborde, N., Thil, F., Durand, N., Kissel, C., 2018. Changes in

latitudinal sea surface temperature gradients along the Southern Chilean margin since the last glacial. *Quat. Sci. Rev*. 194, 62–76. https://doi.org/10.1016/j.quascirev.2018.06.023

Hautala, S. L., & Riser, S. C. 1993. A nonconservative β-spiral determination of the deep circulation in the Eastern South Pacific. Journal of Physical Oceanography, 23 (9), 1975–2000.

Hogg, A.G., Heaton, T.J., Hua, Q., Palmer, J.G., Turney, C.S.M., Southon, J., Bayliss, A., Blackwell, P.G., Boswijk, G., Bronk Ramsey, C., Pearson, C., Petchey, F., Reimer, P., Reimer, R., Wacker, L., 2020. SHCal20 Southern Hemisphere Calibration, 0-55,000 Years cal BP. *Radiocarbon*, 62, 759–778. https://doi.org/10.1017/RDC.2020.59

Holzer, M., DeVries, T. & de Lavergne, C. 2021. Diffusion controls the ventilation of a Pacific Shadow Zone above abyssal overturning. *Nat Commun*, **12,** 4348. https://doi.org/10.1038/s41467-021-24648-x

Jenkins, W., Lott, D., Longworth, B., Curtice, J., & Cahill, K. 2015. The distributions of helium isotopes and tritium along the US GEOTRACES North Atlantic sections (GEOTRACES GAO3). *Deep Sea Research Part II: Topical Studies in Oceanography*, 116, 21–28. https://doi.org/10.1016/j.dsr2.2014.11.017

Jenkins, W., Doney, S., Fendrock, M., Fine, R., Gamo, T., Jean-Baptiste, P., Key, R., Klein, B., Lupton, J., Rhein, M., Roether, W., Sano, Y., Schlitzer, R., Schlosser, P., Swift, J. 2019, A comprehensive global oceanic dataset of helium isotope and tritium measurements, Earth Syst. Sci. Data, 11, 441-454, https://doi.org/10.5194/essd-11-441-2019

Jenkins, W. J., Lott, D. E., German, C. R., Cahill, K. L., Goudreau, J., & Longworth, B. 2017. The deep distributions of helium isotopes, radiocarbon, and noble gases along the U.S. GEOTRACES East Pacific Zonal Transect (GP16). *Marine Chemistry*, 201, 167–182. https://doi.org/10.1016/j.marchem.2017.03.009

Kissel, C., 2007. MD 159-PACHIDERME IMAGES XV, cruise report 06.02.07-28.02.07. PlouzanÉ inst. polaire français Paul Émile Victor 1, 84.

Lindsay, C. M., Lehman, S. J., Marchitto, T. M., Carriquiry, J. D., & Ortiz, J. D. 2016. New constraints on deglacial marine radiocarbon anomalies from a depth transect near Baja California. *Paleoceanography,* 31, 1103–1116. https://doi.org/10.1002/2015pa002878

Lund, D. C., Asimow, P. D., Farley, K. A., Rooney, T. O., Seeley, E., Jackson, E. W., Durham, Z. M. 2016. Enhanced East Pacific Rise hydrothermal activity during the last two glacial terminations. Durham *Science,* 29, 478-482. https://doi.org/10.1126/science.aad4296

Lupton, J. E., & Craig, H. 1981. A major helium-3 source at 15◦S on the East Pacific Rise. Science, 214 (4516), 13–18. https://doir.org/10.1126/science.214.4516.13

Lupton, J. 1998. Hydrothermal helium plumes in the Pacific Ocean. Journal of Geophysical Research, 103(C8), 15,853–15,868. https://doi.org/10.1029/98JC00146

Lupton, J. E., Pyle, D. G., Jenkins, W. J., Greene, R., & Evans, L. 2004. Evidence for an extensive hydrothermal plume in the Tonga-Fiji region of the South Pacific. *Geochemistry, Geophysics, Geosystems*, 5, Article: Q01003. https://doi.org/10.1029/2003GC000607

Marchitto, T., Scott, J., Ortiz, J., Flückiger, J. & van Green, A. 2007. Marine Radiocarbon Evidence for the Mechanism of Deglacial Atmospheric CO_2 Rise. *Science*, 316 (5830), 1456–1461. https://doi.org/10.1126/science.1138679

Marcott, S. A., Bauska, T. K., Buizert, C., Steig, E. J., Rosen, J. L., Cuffey, K. M., et al. 2014. Centennial-scale changes in the global carbon cycle during the last deglaciation. *Nature*, 514(7524), 616–619. https://doi.org/10.1038/nature13799

Martínez Fontaine, C., Siani, G., Delpech, G., Michel, E., Villarosa, G., Manssouri, F., Nouet, J. 2021. Post–glacial tephrochronology record off the Chilean continental margin (~41° S). *Quaternary Science Reviews* 261, Article : 106928. https://doi.org/10.1016/j.quascirev.2021.106928

Martínez Fontaine, C., De Pol-Holz, R., Michel, E., Siani, G., Reyes-Macaya, D., Martínez-Méndez, G., DeVries, T., Stott, L., Southon, J., Mohtadi, M., Hebbeln, D. 2019. Ventilation of the Deep Ocean Carbon Reservoir During the Last Deglaciation: Results From the Southeast Pacific. *Paleoceanogr. Paleoclimatology* 34, 2080–2097. https://doi.org/10.1029/2019PA003613

Matsumoto, K., Lynch-Stieglitz, J., 1999. Similar glacial and Holocene deep water circulation inferred from southeast Pacific benthic foraminiferal carbon isotope composition. *Paleoceanography and Paleoclimatology,* Volume 14, Issue 2, pp 149-163. https://doi.org/10.1029/1998PA900028

McCartney, M. S. 1977. Subantarctic mode water. *Deep-Sea Research*, 24, 103–119.

McManus, J. F., François, R., Gherardi, J. & Keigwin, L. D. 2004. Collapse and rapid resumption of Atlantic meridional circulation linked to deglacial climate changes. *Nature*, 428, 834–837. https://doi.org/10.1038/nature02494

Menviel, L., Spence, P., Yu, J., Chamberlain, M. A., Matear, R. J., Meissner, K. J., & England, M. H. 2018. Southern Hemisphere westerlies as a driver of the early deglacial atmospheric CO2 rise. *Nature Communications*, 9(1), 2503. https://doi.org/10.1038/s41467-018-04876-4

Merino–Campos, V., De Pol-Holz, R., Southon, J., Latorre, C. & Collado-Fabbri, S. 2019 Marine radiocarbon reservoir age along the chilean continental margin. *Radiocarbon*, 61 (1), 1–16. https://doi.org/10.1017/RDC.2018.81

Montade, V., Peyron, O., Favier, C., Francois, J. P. & Haberle, S., G. 2019. A pollen–climate calibration from western Patagonia for palaeoclimatic reconstructions. *Journal of Quaternary Science*, 34 (1), 76–86. https://doi.org/10.1002/jqs.3082

Morales, G. 2003. Methane hydrates in the Chilean continental margin. *Electron. J. Biotechnol.* **6**, 80–84. https://doi.org/10.4067/S0717-34582003000200002

Moreno, P. I. 2004. Millennial-scale climate variability in northwest Patagonia over the last 15 000 yr. Journal of Quaternary Science, 19 (1), 35–47. https://doi.org/10.1002/jqs.813

Moreno, P.I., Lowell, T.V., Jacobson Jr., G.L. & Denton, G.H. 1999. Abrupt vegetation and climate changes during the Last Glacial Maximum and last termination in the Chilean Lake District: A case study from Canal de la Puntilla (41° S). *Geografiska Annaler*, 81 (A), 285–311. https://doi.org/10.1111/j.0435-3676.1999.00059.x

Narváez, D. A., Vargas, C. A., Cuevas, L. A., García-Loyola, S. A., Lara, C., Segura, C., Tapia, F. J. & Broitman, B. R. 2019. Dominant scales of subtidal variability in coastal hydrography of the Northern Chilean Patagonia. Journal of Marine Systems, 193, 59–73. https://doi.org/10.1016/j.jmarsys.2018.12.008

Piola, A. R., & Gordon, A. I. 1989. Intermediate water in the southwestern South Atlantic. *Deep-Sea Research*, 36 (1), 1–16. https://doi.org/10.1016/0198-0149(89)90015-0

Rae, J. W. B., Sarnthein, M., Foster, G. L., Ridgwell, A., Grootes, P. M., & Elliott, T. 2014. Deep water formation in the North Pacific and deglacial CO2 rise. *Paleoceanography*, 29, 645–667. https://doi.org/10.1002/2013PA002570

Reimer, P., Austin, W., Bard, E., Bayliss, A., Blackwell, P., Bronk Ramsey, C., . . . Talamo, S. 2020. The IntCal20 Northern Hemisphere Radiocarbon Age Calibration Curve (0–55 cal kBP). *Radiocarbon*, 62(4), 725-757. https://doi.org/10.1017/RDC.2020.41

Ronge, T. A., Steph, S., Tiedemann, R., Prange, M., Merkel, U., Nürnberg, D., & Kuhn, G. 2015. Pushing the boundaries: Glacial/interglacial variability of intermediate and deep waters in the southwest Pacific over the last 350,000 years. *Paleoceanography,* 30, 23–38. https://doi.org/10.1002/2014PA002727

Ronge, T., Tiedemann, R., Lamy, F., Köhler, P., Allway, B.V., De Pol-Holz, et al. (2016). Radiocarbon constraints on the extent ad evolution of the South Pacific glacial carbon pool. *Nature Communications*, 7:11487. https://doi.org/10.1038/ncomms11487

Rosenthal, Y., Boyle, E. A., and Labeyrie, L. (1997), Last Glacial Maximum paleochemistry and deepwater circulation in the Southern Ocean: Evidence from foraminiferal cadmium, *Paleoceanography*, 12(6), 787– 796, https://doi.org/10.1029/97PA02508

Siani, G., Michel, E., De Pol-Holz, R., DeVries, T., Lamy, F., Carel, M. et al. 2013. A Carbon isotope records reveal precise timing of enhanced Southern Ocean upwelling during the last deglaciation. *Nature Communications*, 4: 2758. https://doi.org/10.1038/ncomms3758

Sikes, E. L., Cook, M. S. & Guilderson, T. P. 2016. Reduced Deep Ocean Ventilation in the Southern Pacific Ocean During the Last Glaciation Persisted into the Deglaciation. *Earth and Planetary Science Letters*, 438, 130–138. https://doi.org/10.1016/j.epsl.2015.12.039

Sikes, E.L, Allen, K.A. & Lund, D. 2017. Enhanced δ13C and δ18O differences between the South Atlantic and South Pacific during the last glaciation: The deep gateway hypothesis. *Paleoceanography,* 32, 1000–1017. https://doi.org/10.1002/2017PA003118.

Skinner, L., Fallon, S., Waelbroeck, C., Michel, E., & Barker, S. 2010. Ventilation of the deep Southern Ocean and deglacial CO2 rise. *Science*, 328 (5982), 1147–1151. https://doi.org/10.1126/science.1183627

Sloyan, B. M., Talley, L. D., Chereskin, K., Fine, R., & Holte, J. 2010. Antarctic intermediate water and subantarctic mode water formation in the Southeast Pacific: The role of turbulent mixing. *Journal of Physical Oceanography*, 40, 1558–1574. https://doi.org/10.1175/2010JPO4114.1

Stephens, B.S. & Keeling, R.F. 2000. The influence of Antarctic sea ice in glacial–interglacial CO_2 variations. *Nature,* 404 (6774), 171–174. https://doi.rg/10.1038/35004556

Stott, L., Southon, J., Timmermann, A., & Koutavas, A. 2009. Radiocarbon age anomaly at intermediate water depth in the Pacific Ocean during the last deglaciation. Paleoceanography, 24, Artclie: PA2223. https://doi.org/10.1029/2008PA001690

Stott, L. D., & Timmermann, A. 2011. *Hypothesized link between glacial/interglacial atmospheric CO2 cycles and storage/release of CO2-rich fluids from deep-sea sediments*. In R. Harunur, L. Polyak, & E. Mosley-Thompson (Eds.), Abrupt climate change: Mechanisms, patterns, and impacts geophysical monograph series, (Vol. 193, pp. 123–138). United States of America: American Geophysical Union. https://doi.org/10.1029/2010GM001052

Stommel, H. 1982. Is the South Pacific helium-3 plume dynamically active? *Earth and Planetary Science Letters*, 61 (1), 63–67. https://doi.org/10.1016/0012-821X(82)90038-3

Toggweiler, J.R., Russell, J. L. & Carson, S. R. 2006. Midlatitude westerlies, atmospheric CO_2, and climate change during the ice ages. *Paleoceanography*, 21 (2), PA2005, https://doi.org/10.1029/2005PA001154

Umling, N.E. & Thunell, R.C. 2017. Synchronous deglacial thermocline and deep water ventilation in the eastern equatorial Pacific. *Nature Communications*, 8: 14203, 2017. https://doi.org/10.1038/ncomms14203

Umling, N. E. & Thunell, R. C. 2018. Mid-depth respired carbon storage and oxygenation of the eastern equatorial Pacific over the last 25,000 years. Quat. Sci. Rev. 189, 43–56. https://doi.org/10.1016/j.quascirev.2018.04.002

Van Daele, M., Bertrand, S., Meyer, I., Moernaut, J., Vandoorne, W., Siani, G., Tanghe, N., Ghazoui, Z., Pino, M., Urrutia, R., De Batist, M. 2016. Late Quaternary evolution of Lago Castor (Chile, 45.6°S): Timing of the deglaciation in northern Patagonia and evolution of the southern westerlies during the last 17 kyr, *Quaternary Science Reviews*, 133, 130-146, https://doi.org/10.1016/j.quascirev.2015.12.021.

Vargas-Cordero, I., Tinivella, U., Accaino, F., Loreto, M. F. & Fanucci, F. 2010. Thermal state and concentration of gas hydrate and free gas of Coyhaique, Chilean Margin (44° 30′ S). *Mar. Petrol. Geol.* **27**, 1148–1156. https://doi.org/10.1016/j.marpetgeo.2010.02.011

Vargas-Cordero, I. et al. 2010. Analyses of bottom simulating reflections offshore Arauco and Coyhaique (Chile). *Geo-Mar. Lett.* **30**, 271–281. https://doi.org/10.1007/s00367-009-0171-5

Vargas-Cordero, I., Tinivella, U., Villar Muñoz, L. & Giustiniani, M. 2016. Gas hydrate and free gas estimation from seismic analysis offshore Chiloé island (Chile). *Andean Geol.* **43**, 263–274. https://doi.org/10.5027/andgeoV43n3-a02

Vargas-Cordero, I., Tinivella, U. & Villar-Muñoz, L. 2017. Gas hydrate and free gas concentrations in two sites inside the Chilean Margin (Itata and Valdivia Offshores). *Energies* 10, 2154–2165. https://doi.org/10.3390/en1012215

Villar-Muñoz, L. *et al.* 2019. Gas hydrate estimate in an area of deformation and high heat flow at the Chile triple junction. *Geosciences* **9**, 28. https://doi.org/10.3390/geosciences9010028

Watson, A.J. & Naveira Garabato, A.C. 2006. The role of Southern Ocean mixing and upwelling in glacial-interglacial atmospheric CO_2 change. *Tellus Series B-Chemical and Physical Meteorology*, 58(1), 73–87. https://doi.org/10.1111/j.1600-0889.2005.00167.x

Weller, D., Miranda, C.G., Moreno, P.I., Villa-Martínez, R., Stern, C.R., 2014. The large late-glacial Ho eruption of the Hudson volcano, southern Chile. *Bull. Volcanol*. 76, 1–18. https://doi.org/10.1007/s00445-014-0831-9

Weller, D.J., Miranda, C.G., Moreno, P.I., Villa-Martínez, R., Stern, C.R., 2015. Tephrochronology of the southernmost Andean Southern Volcanic Zone, Chile. *Bull. Volcanol*. 77, 1–24. https://doi.org/10.1007/s00445-015-0991-2

Skinner, L., Fallon, S., Waelbroeck, C., Michel, E. & Barker, S. 2010. Ventilation of the Deep Southern Ocean and Deglacial CO_2 Rise. *Science*, 328 (5982), 1147–1151. https://doi.org/10.1126/science.1183627

Zhao, N., & Keigwin, L. D. 2018. An atmospheric chronology for the glacial-deglacial Eastern Equatorial Pacific. Nature Communications, 9(1), 3077. https://doi.org/10.1038/s41467-018-05574-x

5.6 Supplementary material

5.6.1 Cryptotephra identification

In core MD07-3081, glass shard percentages were obtained following the methodology by Carel et al. (2011), from which thirteen glass shard peaks were identified between 270 cm (early Holocene) and 1340 cm (late glacial). From these, individual glass shards were analyzed for major element geochemistry in ten depths, using a CAMECA-SX 100 Electron Microprobe (EPMA-CAMPARIS) at the University Paris VI (France). These depths correspond to: one cryptotephra occuring in the late Holocene (270 cm), one in the Holocene/Younger Dryas transition (330 cm), three in the deglaciation (470 cm, 550 cm and 650 cm), two in the Heinrich Stadial 1/late glacial transition (700 cm and 750 cm) and four during the late glacial (910 cm, 1040 cm, 1140 cm and 1220 cm). All ten cryptotephra present similar major element chemistry consistent with products from volcanic sources Yate (~42.8° S), Michinmahuida (~43.8° S) and Hudson (~45.9° S; Table S5.3; Figure S5.2). From these volcanic centers, Michinmahuida and Hudson present activity during the Younger Dryas/Holocene transition, corresponding to Lepué (Amigo et al., 2013; Alloway et al., 2017; Martínez Fontaine et al., 2021) and HW3 (Haberle & Lumley, 1998; Haberle & Bennet, 2004) eruptions, respectively. When comparing the geochemistry of these eruptions with the cryptotephra identified at 330 cm, its geochemical composition is consistent with both eruptions (Figure S5.3a, b). However, taking into account the available on land information, estimated Rs would be ~150 ± 100 years if the cryptotephra corresponded to HW3, which is very unlikely. If the cryptotephra was sourced in Lepué eruption, Rs would be 295 ± 280 years, which is more plausible. However with the available information it is not possible to distinguish between these eruptions and thus none of these Rs is taking into consideration for the age model of core MD07-3081.

Regarding older cryptotephras, Hudson is the only volcanic center with similar geochemistry for which deglacial and late glacial activity has been robustly described and dated on land (Haberle and Lumley, 1998; Weller et al., 2014; Weller et al., 2015): HW2, HW1 and Ho. HW2 has been dated in 11910 ± 110 14C years BP; HW1 in 12435 ± 110 14C years BP and occurs in the Heinrich Stadial 1/Antarctic Cold Reversal transition according to pollen records (Haberle and Bennett, 2004). Cryptotephras at 470 cm and 550 cm can be correlated with HW2 and HW1, resulting in Rs of 480 ± 120 and 770 ± 130 years, respectively (Figure S5.3 c–f).

Ho has been identified in Lago General Carrera/Buenos Aires (FCMC17; Bendle et al., 2019) and a record obtained from Lago Castor (Van Daele et al., 2016). From these two records Ho occurs in the Heinrich Stadial 1/late glacial transition, as cryptotephras at 700 and 750 cm. Additionally, Ho has been dated by radiocarbon above and below the tephra deposit in 14583 ± 210 14C years BP (Table S5.5). From the geochemical composition, either the cryptotephra at 700 cm or at 750 cm (Figure S3 g, h) could correspond to Ho, even maybe both since Ho is thought to have been a massive eruption with an estimated magnitude of 6 (Weller et al., 2014). Cryptotephras at 700 cm and 750 cm have similar ages of

14850 ± 60 and 14960 ± 60 14C years BP, resulting in Rs of 270 ± 220 years and 380 ± 220 years, respectively. Thus, since with the available information is not possible to further discriminate these two cryptoteprhas, we tentatively correlate cryptotephra 750 cm to MD07-3081 as it result in more plausible Rs, similar to modern (Merino-Campos et al., 2019).

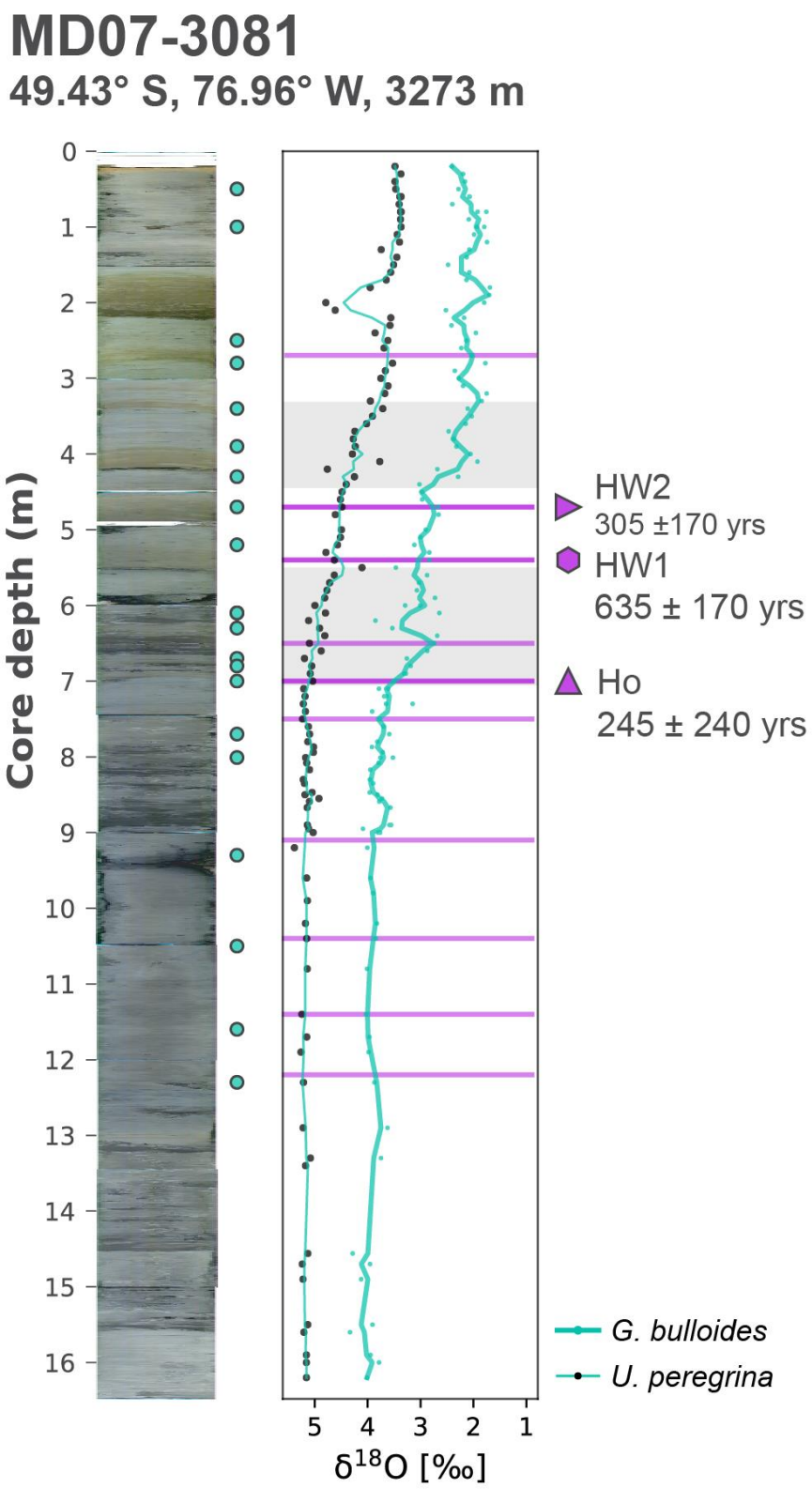

Figure S5.1. Stratigraphic position of cryptotephras in core MD07-3081. As described in the supplementary, all cryptotephras have a Hudson–like geochemistry. Cryptotephras correlated with on land information are shown in a more opaque purple and the name of the tephra correlative is indicated.

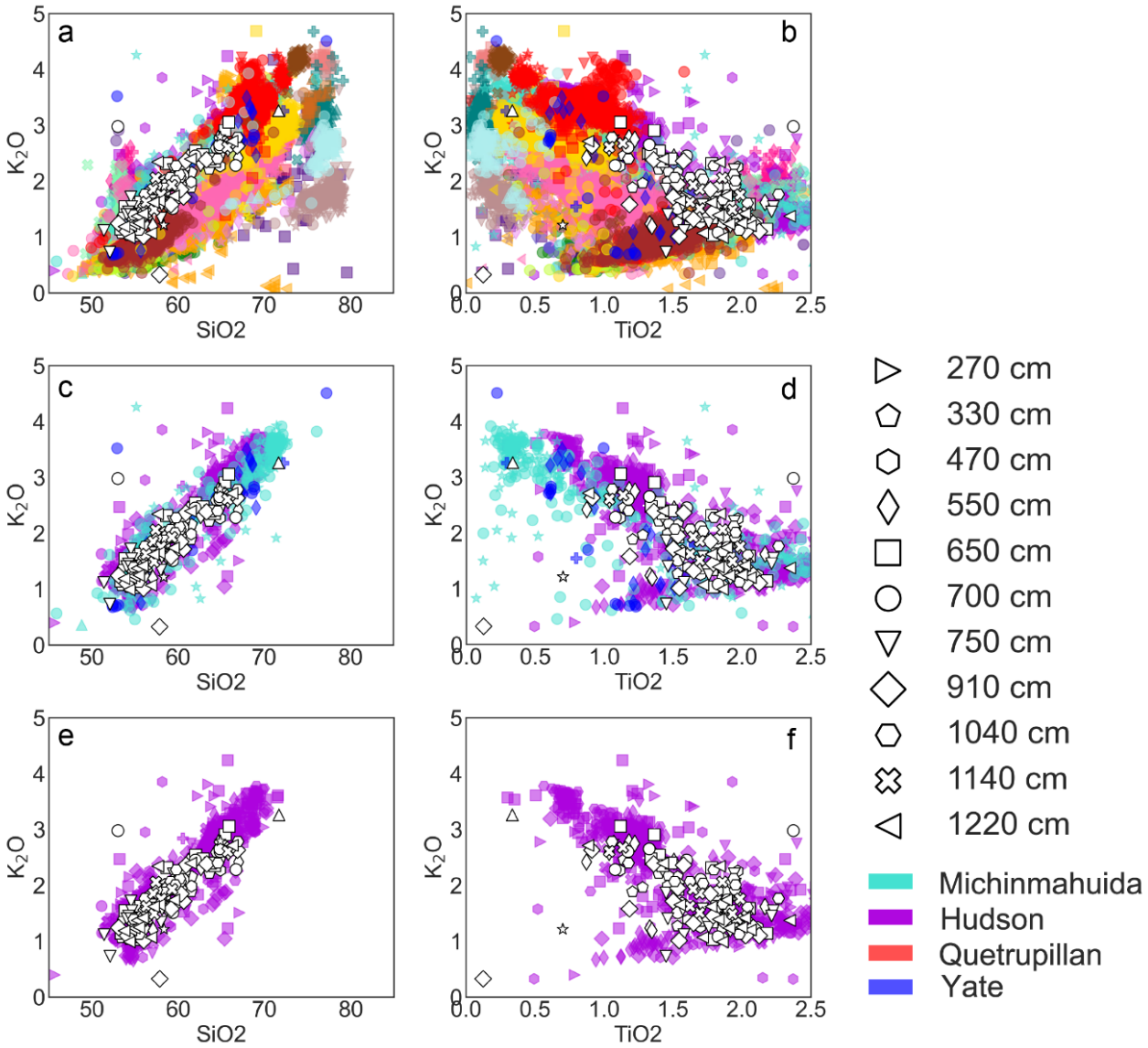

Figure S5.2.- Geochemistry of the cryptotephras identified in core MD07-3081, compared with information on land from volcanic centers in the Southern and Austral volcanic zones of the Andes from the Teprha Database (Chapter 3 of this thesis, Martínez Fontaine et al., *in prep*). a and b) comparison with all available information from the Tephra Database, c and d) comparison only with volcanic centers displaying similar values, e and f comparison only with Hudson volcano.

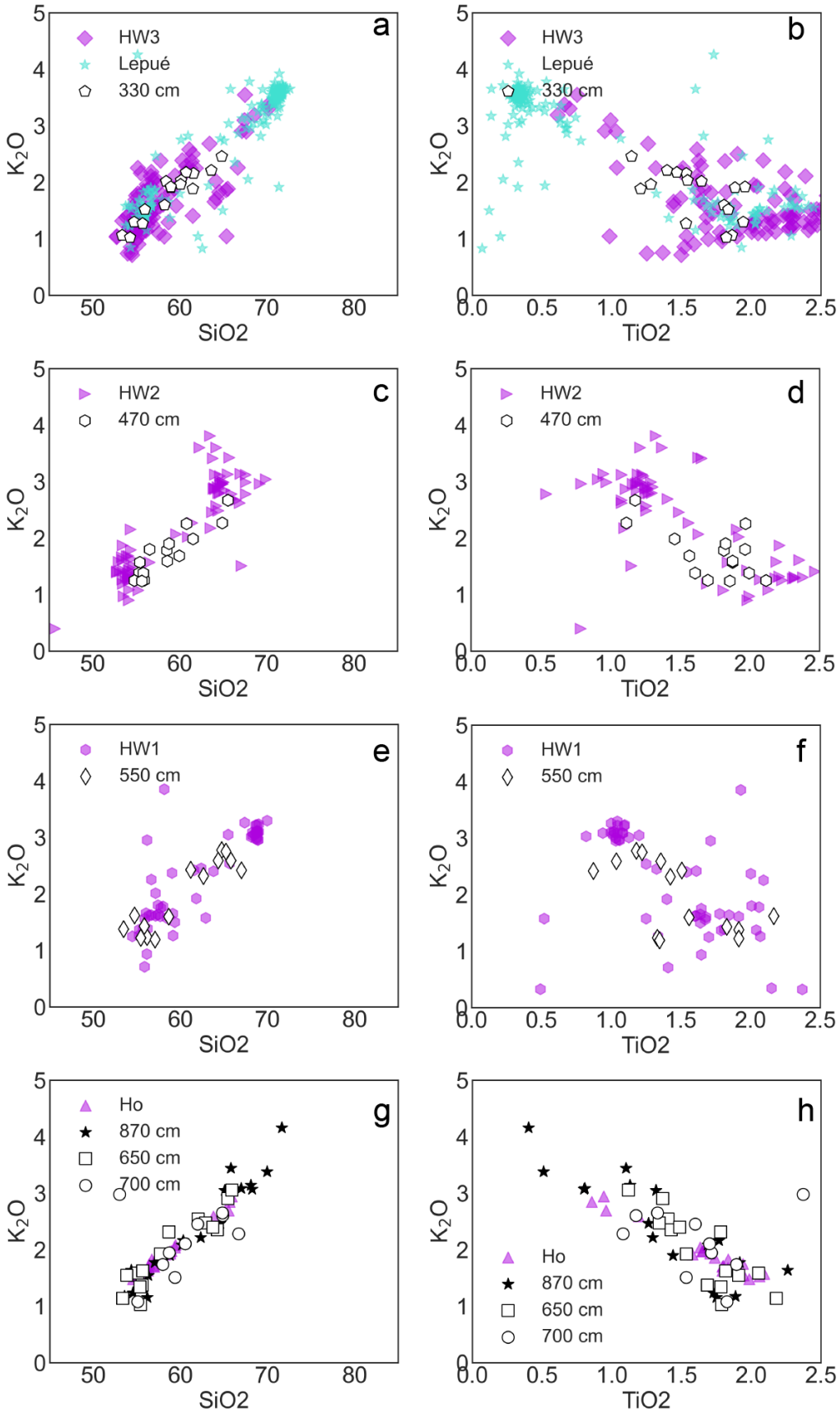

Figure S5.3. Comparison of specific cryptotephras in core MD07-3081 with potential correlatives on land, as described in the supplementary.

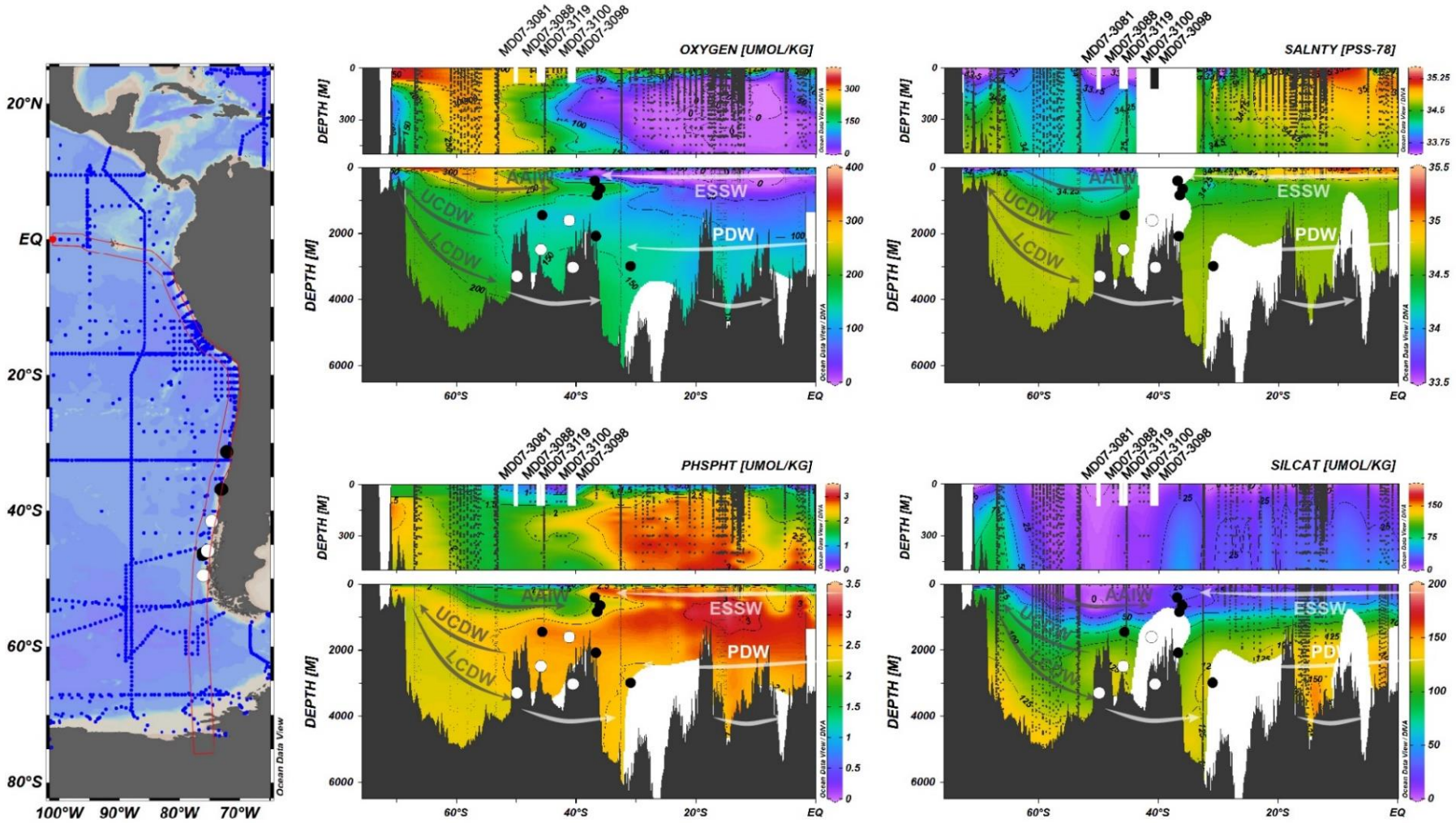

Figura S5.4 Position of the cores in this study and other cores with available $\Delta^{14}C$ in the SEP, discussed in the main text, in oceanic profiles of Oxygen, Salinity, Phosphate and Silicate. Also indicated are the main water masses in the region and its transport and main bathymetric features. In each section a Zoom of the first 500 m is also shown in order to better visualize surface waters. Data from GLODAP v2 2021 (ref) and Reyes-Macaya et al. (*submitted*), plotted in ODV (Schlitzer, Reiner, Ocean Data View, https://odv.awi.de, 2021).

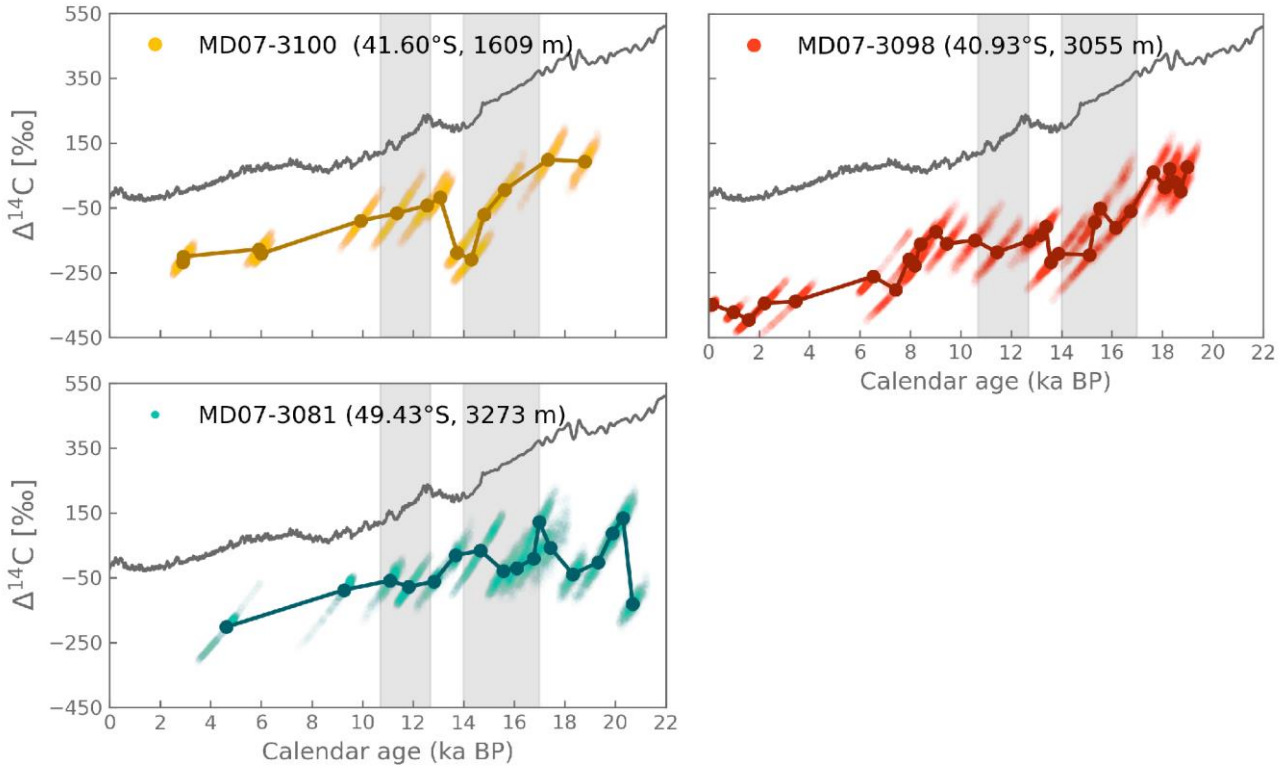

Figure S5.6 $\Delta^{14}C$ results for cores in this study. The darker dots indicate mean values, whereas values in the 95.4% CI are plotted as lighter dots.

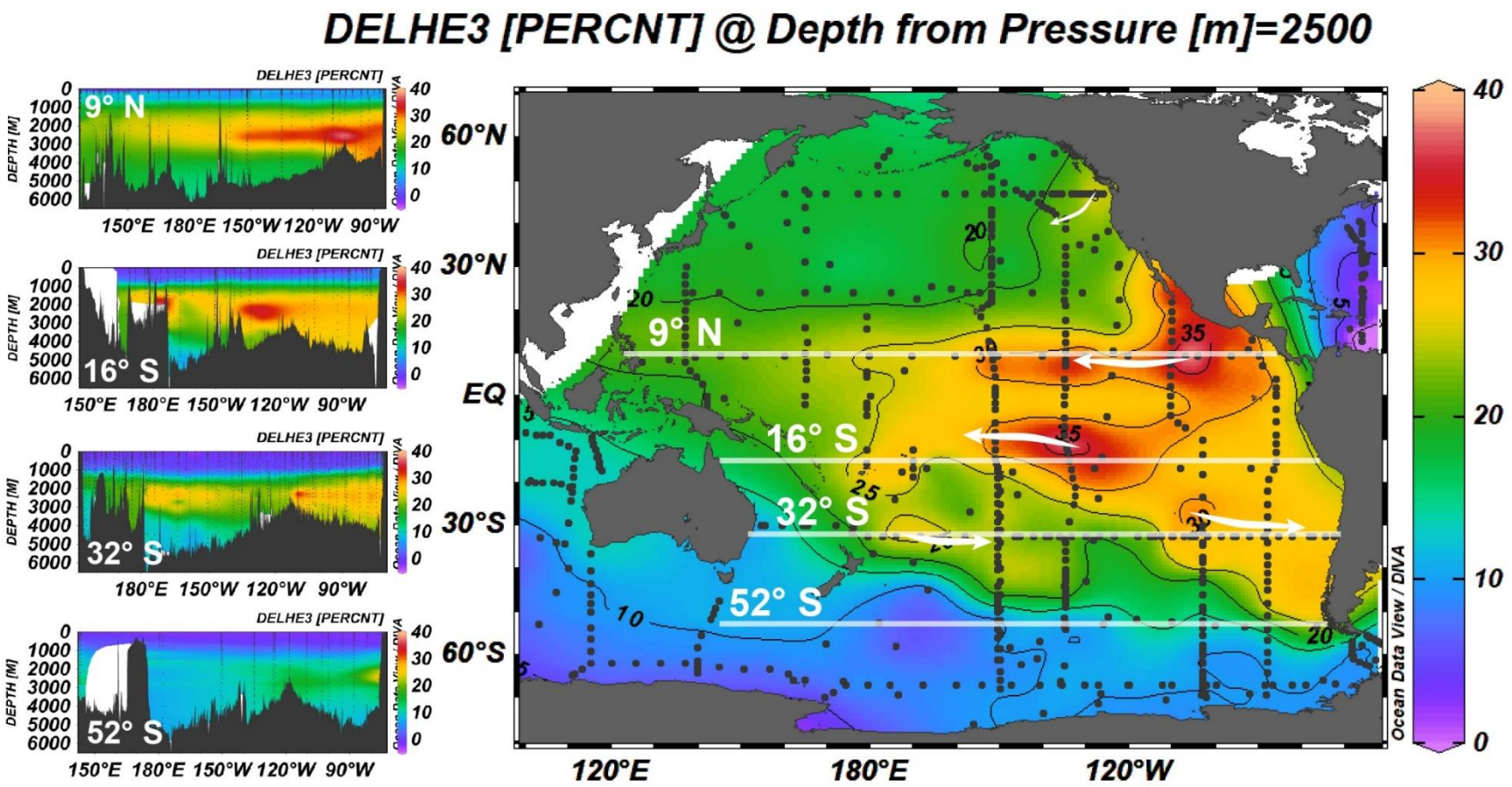

Figura S5.7 δ^3He distribution in the Pacific Ocean showing the most prominent hydrothermal plumes and their directions (white arrows). Data from GLODAP v2 2021 and Jenkins et al. (2019), plotted in ODV (Schlitzer, Reiner, Ocean Data View, https://odv.awi.de, 2021).

6 Conclusion and perspectives

The main aim of this work was to help better constrain the circulation changes in intermediate and deep waters in the Southeast Pacific Ocean during the last 20,000 years. In particular, to provide information that will help better understand the role of the ocean during the last deglaciation. Here I provide new ^{14}C records in seven marine sediment cores in the Southeast Pacific Ocean. These new records, together with previous ^{14}C records in two marine sediment cores in the area (de Pol-Holz et al., 2010; Siani et al., 2013), comprehend a detailed transect constraining the ventilation of AAIW, PDW and LCDW in the Southeast Pacific during the last 20,000 years. Constraining the ventilation of deep waters using ^{14}C requires accurate chronologies of marine sediment cores. To this purpose I complemented planktonic foraminifera radiocarbon dating with stable isotope stratigraphy and tephrochronology.

The tephrochronological work I developed in cores MD07-3098, MD07-3100 and MD07-3081 resulted in the robust identification of between 1 and 3 tephras (eruptions) in each core. From this, I estimated six new Rs in the Southeast Pacific Ocean since the late glacial, at ~40° S and ~49° S. These, together with the stable isotope stratigraphy of each core, and previous Rs estimates in the area (Siani et al.,2013), revealed that during the deglaciation, Rs between ~40–46° S, were consistently higher by ~500 years than Rs at ~49° S. This result stresses the importance of having references on how the Rs of the surface waters at the core retrieving sites may have varied when producing marine core chronologies by calibrating planktonic foraminifera ^{14}C ages. The new Rs I estimated provide reference values for future paleoceanographic research in the area. Taking into account the spatial variability of Rs in the area, future works should use the stable isotope stratigraphy of the marine sediment cores as a reference to evaluate if the same surface water is present in the site of interest.

Regardless of the fact that the new Rs I estimated here aid the understanding of how Rs vary in the Southeast Pacific Ocean, the errors associated with the Rs estimates, and consequently the chronologies of the marine sediment cores, are still very big (from hundreds to a thousand years). As mentioned in the introduction, chronologies with errors of this magnitude do not allow for a proper integration of the paleoceanographic and paleoclimatic data produced in different parts of the ocean and on land, as their chronologies are not comparable. In order to better constrain Rs variations in the Southeast Pacific Ocean using tephrochronology, it is necessary that the age of on land tephras are better constrained. The Southern and Austral Volcanic Zones of the Andes are two very active volcanic zones, where many active volcanic centers are located close to each other. This results in a statigraphic record in which the remains of explosive eruptions of many different volcanic centers are intertwined. In order to robustly identify tephras in this area, ideally

geochemistry and robust stratigraphic constrains, such as palynological records together with radiocarbon ages, need to be more routinely reported. This will in turn help to better constrain the ages of specific eruptions (tephra). In this regard, the marine tephrochronological record I produced provides robust geochemical and stratigraphically evidence of continuous activity of Michinmahuida volcano since the late glacial. This volcano is located in a highly vegetated area of difficult access and an important portion of the volcanic edifice is currently covered by ice. Because of the latter, and the presence of the Patagonian Ice Sheet during the late glacial in this area, robust evidence for late glacial and deglacial activity of this volcano had not been identified before this work. The tephrochronological work I developed in this thesis highlights the value of marine tephrochronology for unveiling the eruptive history of the Southern and Austral Volcanic Zones of the Andes. As more information to robustly constrain the tephrochronological record in the area becomes available in the future, tephrochronology can help better constrain chronologies in the Southeast Pacific. This new information could, for instance help identify the cryptotephras analyzed in the marine sediment cores here studied for which the source and/or specific event cannot be determined at the moment.

Additionally, the database I assembled is a step forward in unveiling the tephrochronological record in the Southern and Austral Volcanic Zones of the Andes, as it integrates tephrochronological and volcanological data on 130 different eruptive events of 32 active volcanic centers, retrieved from 80 scientific publications. Additionally, the explorer of the database provides tools to explore the database in its multidimensionality (geochemical composition of the tephras, time of the eruptions, geographical distribution of the tephras), which can help improve the efficiency of the tephrochronological work in the area. Because the database provides a structure to standardize and integrate tephrochronological and volcanological information produced by heterogeneous groups of researchers, it has the potential of growing in time, integrating new information as it is published. Future efforts regarding this work correspond to finding the platforms which allow for the growth of the database in time, i.e. a community and/or service which can integrate new data according to community–based data quality criteria, maintain the online services in time, and ideally provide a platform for the evolution of the exploration tools as new information is integrated.

After this work, and once the chronology of the cores was constrained, the ^{14}C information here provided indicates that during the late glacial period, two main differences in the ventilation of the Southeast Pacific Ocean are observed, with respect to the deglaciation:

- Depths bathed today by AAIW were relatively well ventilated, with a ^{14}C depletion with respect to their contemporary atmosphere that was similar to the present. The latter suggests that the mechanisms leading to its formation at present, were also in place during the late glacial.

- Waters at ~1,500 m between ~40–49° S, today located at the boundary of AAIW and PDW, had ^{14}C contents within error homogeneous with PDW during this period. This information is in line with previous paleoceanographic records in the area (Haddam et al., 2020), indicating a shallower convection of the AAIW during this period, at least with respect to the deglaciation.
- Deep waters, at present located at the boundary between LCDW and PDW, were less ventilated than depths bathed by PDW during the late glacial. As PDW feeds the formation of LCDW, the latter is evidence for a change in the water mass formation in the Southern Ocean at this time, in which the ventilation of deep waters formed in the there is importantly decreased.

During the deglaciation, important circulation changes are inferred from the ^{14}C transect in the Southeast Pacific with respect to the late glacial period:

- With the onset of the deglaciation and throughout it, $\Delta^{14}C$ records in cores retrieved at sites bathed at present by AAIW, in the boundary between PDW and AAIW, and in the boundary between PDW and LCDW, all become homogeneous within error. The latter represents an important change in water mass ventilation with respect to the late glacial period, which importantly augments the ventilation of deep waters in the Southern Ocean.
- Waters bathed today by PDW continue to be as depleted from the contemporary atmosphere as during the glacial, which indicate no important ventilation change of this water mass during this period.

During the deglaciation, additionally:

- Waters bathed by different water masses in the Southeast Pacific present an important drop in $\Delta^{14}C$ contents between ~15 and 13.5 ka cal BP, which likely does not derive from water mass formation processes. With the information here provided, however, it is not yet possible to discriminate what is the origin of this signal and whether it is regional or local.

During the Holocene:

- The ventilation of waters in the upper boundary of PDW between 40–46° S, between LCDW and PDW at ~49° S and of PDW and CDW at ~31° S continues to be homogeneous within error.
- No information of waters bathed by AAIW is available during this period.
- It is unclear if core MD07-3098 represents changes in PDW during the deglaciation or rather a local ^{14}C–depleted signal, for example from hydrothermal sources.

Overall, the information here provided indicates that no extremely ^{14}C–depleted carbon reservoir existed in the Southeast Pacific in waters above 3300 m depth during the last 20,000 years. However, it is still plausible

that during the Last Glacial Maximum deep waters in the Southern Ocean where more isolated than in the studied interval, as observed in the South West Pacific, South Indian and South Atlantic Oceans.

In order to better interpret what the water mass ventilation changes here presented represent in terms of variations in oceanic circulation and the mechanisms responsible for these changes (e.g. variations in the position or intensity of the SWW or in the extension of sea–ice around Antarctica), future work might concentrate in better constraining the ventilation of AAIW during the Holocene. At present, the "natural" $\Delta^{14}C$ content of AAIW has been modified by the bomb effect and thus it is difficult to understand if the circulation observed during the deglaciation is different from modern or not. This might help to better understand what are the mechanisms controlling this water mass formation and how they have changed in the past.

Additionally, in order to understand the origin of the low ^{14}C signal observed in four of the five marine sediment cores I studied, and whether or not it has an important effect in the carbon cycle, future work should concentrate in finding proxies which allow to trace if this signal has an hydrothermal origin, and whether is local or not.

7 Résumé en français

L'océan joue un rôle important dans les cycles glaciaires-interglaciaires, en régulant la quantité de CO2 dans l'atmosphère. En particulier, pendant le dernier maximum glaciaire (~23 000-19 000 années civiles avant le présent (années cal. BP)), on pense que l'océan profond a accumulé du CO2, le libérant dans l'atmosphère pendant la dernière déglaciation (~18 000-11 000 années cal. BP). La quantité de CO2 stockée/libérée, les zones de l'océan où cela se produirait et les mécanismes menant à ce stockage/libération, sont actuellement discutés et des informations sont produites dans le monde entier dans ce but. Dans cette thèse, je produis de nouveaux enregistrements sur les changements de ventilation des eaux intermédiaires et profondes dans le Pacifique Sud-Est (SEP) au cours des ~22 000 dernières années. En utilisant les âges 14C de foraminifères benthiques et planctoniques appariés dans neuf carottes de sédiments marins dans un transect entre ~500-3,300 m et ~31-49° S, j'interprète les changements de la circulation océanique pendant la dernière déglaciation.

Le chapitre 2 de cette thèse correspond à un travail qui a commencé avant le début de cette thèse, mais qui a été développé en grande partie, et publié, pendant les deux premières années de ce doctorat. Il correspond à l'étude de cinq carottes de sédiments prélevées dans la marge continentale chilienne par le navire allemand R/V Sonne, dans lequel mon ancien superviseur : Ricardo de Pol-Holz, avait participé. Les carottes GeoB 7149-2, GeoB 7163-7, GeoB 7162-6, SO161-22SL et GeoB 7167-6 entre 13 et 6° S et ~500-3000 m de profondeur. Les foraminifères planctoniques et benthiques ont été prélevés et préparés pour la datation au radiocarbone et l'analyse des isotopes stables, par Dharma Reyes-Macaya et Ricardo. Les datations au radiocarbone ont été effectuées au Keck Carbon Cycle Accelerator Mass Spectrometer facility de l'Université de Californie, Irvine UCI-AMS. Comme ces informations étaient déjà disponibles, mon étude de premier cycle consistait à les utiliser pour mieux comprendre les changements de la circulation océanique dans les eaux intermédiaires et profondes du Pacifique Sud-Est au cours des 20 000 dernières années. Dans le cadre de ce travail, un problème très important que j'ai rencontré était l'obtention de chronologies robustes pour les carottes de sédiments marins. En particulier parce qu'aucun travail antérieur sur les variations de Rs n'était disponible pour les latitudes où les carottes ont été récupérées. Dans cette zone, les variations de Rs peuvent être très importantes, en raison de la remontée des eaux côtières qui dépend de la position latitudinale du SWW, dont on pense qu'elle a changé dans le passé (détails dans le chapitre 2, section "4. Modèles d'âge"). Dans le deuxième chapitre de cette thèse, j'explore comment la stratigraphie des isotopes stables (δ13C), ainsi que les âges 14C des foraminifères planctoniques peuvent nous donner des informations sur la variation passée de Rs dans des zones où aucune estimation de Rs n'est disponible. Ensuite, de multiples chronologies et les Δ14C correspondants sont produits pour chaque carotte, en prenant en considération la

gamme de Rs possibles donnée par les informations disponibles dans la zone. Ce travail a mis en avant le fait qu'idéalement une certaine référence des variations de Rs in situ doit être disponible pour produire des chronologies robustes. En particulier, comme dans le Pacifique Sud-Est, Rs varie latitudinalement en raison des différents régimes de remontée d'eau à différentes latitudes qui amènent à la surface des eaux de subsurface plus ou moins anciennes ; et parce que la distribution latitudinale de ces régimes de remontée d'eau a probablement aussi varié dans le temps.

Comme mentionné précédemment, une conclusion importante du travail développé dans le chapitre deux est que pour mieux contraindre les chronologies des carottes de sédiments marins dans le Pacifique Sud-Est, il est important d'estimer les variations de Rs dans le passé. La téphrochronologie est un outil qui a déjà été utilisé par Siani et al. (2013) pour estimer les variations de Rs à 46° S. En raison de la présence des zones volcaniques australe et méridionale des Andes, adjacentes à la marge continentale chilienne - qui sont deux zones volcaniques très actives actuellement - la téphrochronologie a un grand potentiel pour améliorer les chronologies dans la zone d'étude. Comme je connaissais très peu le volcanisme de la région et pratiquement rien de la téphrochronologie, le premier travail que j'ai développé a été de rassembler des informations sur la téphrochronologie dans la région. En particulier, quels volcans avaient eu des éruptions au cours des 20 000 dernières années, combien d'éruptions avaient-ils eu, si ces éruptions étaient datées ou non, analysées par géochimie ou non, etc. Tout cela dans le but d'identifier les volcans et les éruptions particulières responsables des cendres volcaniques trouvées dans les carottes de sédiments marins. En développant cette tâche, j'ai rencontré divers obstacles, tels que des noms différents donnés à un même événement éruptif, des données non standardisées, l'impossibilité d'accéder aux données brutes, des informations manquantes, par exemple la position des échantillons, etc. Avec l'aide de Chiara Marmo, ingénieure de recherche au laboratoire GEOPS, j'ai compris qu'il s'agissait d'un problème largement répandu dans la science, et j'ai pu lui donner un nom : les données téphrochronologiques n'étaient pas FAIR (Findable, Accesible, Interoperable, Reusable ; Wilkinson et al., 2016).

Le chapitre 3 correspond à la description du jeu de données que j'ai compilé afin de pouvoir identifier la source des restes volcaniques trouvés dans les carottes de sédiments marins. Il comprend des informations téphrochronologiques et volcanologiques sur 32 centres volcaniques actifs des zones volcaniques australe et méridionale des Andes, entre les volcans Llaima (~38,7° S) et Mount Burney (~52,3° S), recueillies à partir de soixante-treize publications scientifiques publiées dans des revues à comité de lecture, six publications de SERNAGEOMIN et deux thèses de doctorat. Au total, elle contient des informations sur ~16 500 analyses d'échantillons, ce qui correspond à ~130 événements éruptifs différents identifiés et à de nombreux autres encore non corrélés avec d'autres gisements. Mais il ne s'agit pas seulement d'un ensemble de données. Le problème de la loyauté des données m'a vraiment intéressé, et j'ai pris à cœur d'essayer d'aider à progresser

dans ce domaine. Ainsi, pour ce faire, en collaboration avec Chiara Marmo et Vanessa Araya, ancienne post-doc et actuelle professeure à l'INRIA, nous avons commencé à développer une application web dans le but de créer des visualisations qui aideront les futurs utilisateurs du jeu de données à lui donner un sens, favorisant ainsi la découverte d'informations ; et qui aideront au téléchargement personnalisé du jeu de données. Ce travail est en cours et vous pouvez accéder à l'explorateur à l'adresse suivante : http://varaya.cl:3001/. Vous y apprendrez, nous l'espérons, quelque chose sur la téphrochronologie et le volcanisme dans la zone d'étude. Ce travail a été réalisé en collaboration avec l'agence chilienne de géologie et des mines : SERNAGEOMIN par le biais du département du Réseau national de vigilance volcanique. L'idée est qu'à l'avenir, le jeu de données et l'explorateur soient gérés par SERNAGEOMIN, et que de nouvelles informations puissent y être ajoutées, afin de rendre ces données plus équitables.

Parallèlement au jeu de données, j'ai réalisé le travail décrit au chapitre quatre, qui correspond à la procédure et aux résultats des enregistrements téphrochronologiques dans les carottes de sédiments marins MD07-3098 et MD07-3100. Une procédure analogue a été suivie pour la carotte MD07-3081, qui est décrite dans le chapitre 5. Ce travail constitue la base à partir de laquelle les R sont estimés ultérieurement dans le chapitre 5 et utilisés pour établir les chronologies des carottes. Grâce à ce travail, des restes d'activité éruptive ont été trouvés dans tout l'intervalle étudié des carottes de sédiments marins, soulignant le potentiel de l'utilisation de la téphrochronologie pour améliorer les chronologies des carottes dans la marge chilienne. Parmi ceux-ci, 1 téphra sur 8 a pu être identifié de manière robuste dans la carotte MD07-3098 et 2 sur 17 dans la carotte MD07-1300. De plus, huit cryptotéphras apparaissant à ~3,6, 6,2, 7,0, 8,5, 9,6, 14,2, 15,9 et 18,2 cal ka BP ont été identifiés de manière robuste comme provenant du volcan Michinmahuida, mais n'ont pas été corrélés par ailleurs, fournissant une nouvelle preuve de l'activité pré-holocène de ce centre volcanique. Les téphras qui n'ont pas pu être identifiés de manière robuste pourront l'être à l'avenir si les éléments traces sont analysés à la fois dans les carottes de sédiments marins et sur terre, mais aussi lorsque davantage de contraintes chronologiques seront disponibles sur terre. Ainsi, les chronologies de ces carottes peuvent continuer à être améliorées au moyen de la téphrochronologie.

L'ensemble de données et l'explorateur décrits au chapitre 3 étaient essentiels pour identifier de manière robuste la source des téphras marins, étant donné que la plupart d'entre eux correspondent à des cryptotephras (couches très fines de matériel pyroclastique). Ceci est pertinent parce que les cryptotephras peuvent être transportés de loin et donc les sources volcaniques potentielles dans la région étaient environ 30, dont beaucoup ont eu une activité explosive récurrente au cours des 20.000 dernières années. Dans le même temps, le développement des enregistrements téphrochronologiques marins a contribué à améliorer l'ensemble des données. Ce faisant, les informations nécessaires pour corréler de manière robuste les

téphras marins ont été ajoutées à l'ensemble de données, et en même temps, la visualisation nécessaire pour donner un sens à la masse de données a été développée.

Enfin, dans le chapitre cinq, l'objectif principal de ce travail est abordé et les travaux précédents sont intégrés. Tout d'abord, les travaux de téphrochronologie développés dans les carottes MD07-3098, MD07-3100 et MD07-3081 sont utilisés pour estimer les variations de Rs à 41° et 49° S au cours des 20 000 dernières années. Ceci s'avère être un problème en soi, comme par exemple, même lors de l'identification robuste d'une éruption volcanique, comme c'est le cas de l'identification du téphra de Lepué dans les carottes MD07-3098 et MD07-3100. Dans ce cas, les dates de radiocarbone sur les terrains associés de manière robuste au téphra de Lépué (par exemple par l'analyse géochimique du téphra), sont très rares et dispersées. Ainsi, l'erreur pour le Rs estimé est relativement importante (~350 ans). De plus, étant donné que chaque profondeur où les âges radiocarbone des foraminifères planctoniques ont été analysés n'a pas une estimation Rs correspondante, des hypothèses concernant les variations doivent être faites afin de les calibrer. Ici, j'intègre les nouveaux âges Rs avec les précédents Rs obtenus dans la marge continentale chilienne à ~46°S (Siani et al., 2013), et les stratigraphies d'isotopes stables des carottes MD07-3098, MD07-3100, MD07-3119 et MD07-3081, pour estimer les variations de Rs aux différents sites de carottes. Cette procédure comporte encore d'importantes incertitudes, dont une partie est quantifiée et communiquée dans les graphiques. Il en ressort que Rs au cours de la dernière déglaciation semble avoir été plus vieux d'environ 400 ans à ~41° et 46° S qu'à ~49° S. Ce dernier phénomène est probablement associé à un mélange accru de SAAW avec des ESSW relativement anciennes, en raison d'un apport accru d'eau de fonte provenant de la fonte de la calotte glaciaire de Patagonie (chapitre 5).

L'interprétation des variations de la circulation des eaux intermédiaires et profondes dans le SEP est ensuite faite en intégrant les nouveaux enregistrements Δ14C décrits dans le chapitre 5, avec les enregistrements Δ14C décrits dans le chapitre 2. Considérant le fait qu'il y a encore un niveau important d'incertitude dans les chronologies des carottes de sédiments marins, les interprétations des changements de circulation sont faites en prenant en compte uniquement les variations de Δ14C en dehors de l'intervalle de 2σ. Néanmoins, d'importantes variations de circulation sont observées pendant la déglaciation, dont certaines sont déroutantes et nécessitent des recherches plus approfondies afin de comprendre les mécanismes qui les sous-tendent et s'ils ont un rôle dans la déglaciation ou non. Les informations fournies ici indiquent que :

- Au cours de la dernière période glaciaire tardive, les masses d'eau baignant l'océan Pacifique Sud-Est (AAIW, PDW et CDW) avaient des valeurs de 14C plus hétérogènes qu'actuellement. L'AAIW était relativement mieux ventilé par rapport à l'UCDW/PDW qu'aujourd'hui, alors que l'LCDW était moins

ventilé par rapport au PDW qu'actuellement. Ce dernier résultat est cohérent avec un océan glaciaire plus stratifié, les eaux profondes de l'océan Austral étant plus isolées de l'atmosphère qu'aujourd'hui.

Pendant la déglaciation, d'importants changements de circulation sont observés, les masses d'eau suivant l'un ou l'autre de deux comportements principaux :

- Le premier comportement est observé dans les sites baignés actuellement par des eaux de source méridionale : AAIW (GeoB 7163-6, 22SL), UCDW (MD07-3088 ; Siani et al., 2013) et LCDW (MD07-3081). Dans ces sites, AAIW et UCDW deviennent moins ventilés, tandis que LCDW devient plus ventilé, tous les derniers atteignant des valeurs similaires (dans l'erreur) à environ 17 ka cal BP. Ce dernier phénomène est interprété comme une rupture de la stratification dans l'océan Austral, qui entraînerait la ventilation du LCDW précédemment isolé, et en même temps une convection plus profonde du AAIW. Ces observations sont cohérentes avec les enregistrements de 14C dans l'Atlantique Sud (Skinner et al., 2010), l'océan Indien Sud (Gottschalk et al., 2020), le Pacifique Sud-Ouest (Ronge et al., 2016 ; Sikes et al., 2016) et le Pacifique Est équatorial (Umling & Thunell, 2017 ; De la Fuente et al., 2015) et l'augmentation de l'upwelling (Anderson et al., 2009 ; Siani et al., 2013) et de la pCO2 dans l'océan Austral (Martínez-Botí et al., 2015). Bien que le mécanisme exact à l'origine de cette rupture de stratification reste à déterminer, nos observations sont cohérentes avec un déplacement vers le sud du SWW, ce qui pourrait expliquer la remontée d'eaux profondes - auparavant isolées - et a été associé à une convection plus profonde du AAIW (Haddam et al., 2020 ; Ronge et al., 2015).
- Le second comportement observé ici correspond à des carottes extraites dans des sites aujourd'hui baignés principalement par des PDW (GeoB 7149-2, GeoB 7167-6, MD07-3098, MD07-3100 et MD07-3119), et à la carotte GeoB 7162-6, baignée par des AAIW. Pendant la déglaciation, toutes ces carottes présentent des valeurs anormalement appauvries en 14C, similaires à ce qui est observé dans les eaux intermédiaires et profondes du Pacifique Est équatorial (Bova et al., 2018 ; Stott et al., 2007) et de la Basse Californie (Lindsay et al., 2016 ; Marchitto et al., 2007). J'émets l'hypothèse que ce signal pourrait être hydrothermal, car il n'est pas partagé par les enregistrements de PDW dans le Pacifique Nord, le Pacifique Est équatorial ou le Pacifique Sud-Ouest ; et parce que la zone d'étude est influencée aujourd'hui par un panache hydrothermal provenant de l'EPR (par exemple Jenkins et al., 2019 ; Lupton, 1998), et par une activité hydrothermale locale (par exemple Bangs et al., 1993 ; Froelich et al., 1995ref). Avec les informations fournies ici, il n'est cependant pas encore possible de discriminer si le signal observé dans le SEP est régional ou local.

Des travaux futurs pourraient se concentrer sur la production d'enregistrements dans les carottes présentant le faible signal 14C, ce qui pourrait aider à discriminer : i) si le signal est hydrothermal ou non ; ii) si ce signal est local ou régional. A partir de là, il faut également déterminer si cette activité hydrothermale hypothétique a un effet sur l'augmentation du CO2 de l'atmosphère et/ou sur la relance de la circulation océanique profonde, aidant à ventiler l'océan profond.

8 Annexes

8.1 Supplementary Tables Chapter 2

Table S1 Planktonic and benthonic radiocarbon dates for all cores, calendar and Δ14C obtained according to the text.

Core	Depth (cm)	IGSN	Lab Code	Species	^{14}C age (years BP)	Error	Calendar Age (years BP)	σ1	Δ^{14}C (‰)
GeoB 7149-2	3	IECMF0001	UCIAMS-123855	*N. dutertrei*	1,880	20	1032	122	
GeoB 7149-2	8	IECMF0002	UCIAMS-114575	*N. pachyderma*	1570	70	1151	134	
GeoB 7149-2	8	IECMF0003	UCIAMS-114574	*Uvigerina*	2945	35	1151	134	-203
GeoB 7149-2	13	IECMF0004	UCIAMS-123857	*N. pachyderma*	1980	20	1353	150	
GeoB 7149-2	13	IECMF0005	UCIAMS-123856	*Uvigerina*	3530	80	1353	150	-241
GeoB 7149-2	28	IECMF0006	UCIAMS-123858	*N. pachyderma*	2730	25	2146	142	
GeoB 7149-2	28	IECMF0007	UCIAMS-123859	*N. dutertrei*	2670	55	2146	142	
GeoB 7149-2	43	IECMF0008	UCIAMS-123860	*N. dutertrei*	3510	20	3132	152	
GeoB 7149-2	43	IECMF0009	UCIAMS-123861	*N. pachyderma*	3585	25	3132	152	
GeoB 7149-2	43	IECMF000A	UCIAMS-123862	*Uvigerina*	4750	60	3132	152	-191
GeoB 7149-2	53	IECMF000B	UCIAMS-114577	*N. pachyderma*	4100	30	3686	136	
GeoB 7149-2	53	IECMF000C	UCIAMS-114576	*Uvigerina*	5435	30	3686	136	-206
GeoB 7149-2	58	IECMF000D	UCIAMS-123865	*N. dutertrei*	4085	20	3866	117	
GeoB 7149-2	58	IECMF000E	UCIAMS-123864	*G. bulloides*	4115	25	3866	117	
GeoB 7149-2	58	IECMF000F	UCIAMS-123866	*N. pachyderma*	4120	70	3866	117	
GeoB 7149-2	58	IECMF000G	UCIAMS-123863	Mixed Benthic Foraminifera	5180	90	3866	117	-162
GeoB 7149-2	78	IECMF000H	UCIAMS-123867	N. dutertrei	5000	30	4995	188	
GeoB 7149-2	78	IECMF000I	UCIAMS-123869	*N. pachyderma* (dextral)	4960	240	4995	188	
GeoB 7149-2	78	IECMF000J	UCIAMS-123868	*Uvigerina*	6330	190	4995	188	-168
GeoB 7149-2	98	IECMF000K	UCIAMS-114578	*Uvigerina*	7810	70	5917	267	-226
GeoB 7149-2	98	IECMF000L	UCIAMS-114579	Infaunal	7190	25	5917	267	-164
GeoB 7149-2	108	IECMF000M	UCIAMS-123871	*N. pachyderma* (dextral)	6040	80	6370	223	
GeoB 7149-2	108	IECMF000N	UCIAMS-123870	*Uvigerina*	8590	100	6370	223	-258
GeoB 7149-2	133	IECMF000O	UCIAMS-114581	Mixed Planktonic Foraminifera	7945	50	8025	203	

GeoB 7149-2	133	IECMF000P	UCIAMS-114580	*Uvigerina*	8975	50	8025	203	-136
GeoB 7149-2	168	IECMF000Q	UCIAMS-123875	*N. pachyderma* (dextral)	8750	60	9212	178	
GeoB 7149-2	168	IECMF000R	UCIAMS-123874	*N. dutertrei*	8515	25	9212	178	
GeoB 7149-2	173	IECMF000U	UCIAMS-123878	*N. dutertrei*	9495	35	9501	151	
GeoB 7149-2	173	IECMF000V	UCIAMS-123877	*G. bulloides*	9220	200	9501	151	
GeoB 7149-2	173	IECMF000W	UCIAMS-123879	*N. pachyderma* (dextral)	8830	35	9501	151	
GeoB 7149-2	173	IECMF000X	UCIAMS-123876	Mixed Benthic Foraminifera	10940	130	9501	151	-191
GeoB 7149-2	178	IECMF000Y	UCIAMS-114582	*G. bulloides*	10510	240	9883	160	
GeoB 7149-2	178	IECMF000Z	UCIAMS-123883	*G. bulloides*	12780	290	9883	160	
GeoB 7149-2	178	IECMF0010	UCIAMS-123750	*G. bulloides*	11950	220	9883	160	
GeoB 7149-2	178	IECMF0011	UCIAMS-123880	*N. pachyderma* (dextral)	10125	45	9883	160	
GeoB 7149-2	178	IECMF0012	UCIAMS-123881	*N. dutertrei*	9380	230	9883	160	
GeoB 7149-2	178	IECMF0013	UCIAMS-123749	*N. dutertrei*	9205	45	9883	160	
GeoB 7149-2	178	IECMF0014	UCIAMS-114584	*N. pachyderma* (dextral)	9590	340	9883	160	
GeoB 7149-2	178	IECMF0015	UCIAMS-123748	*N. pachyderma* (dextral)	9880	70	9883	160	
GeoB 7149-2	178	IECMF0016	UCIAMS-114583	*Uvigerina*	10790	70	9883	160	-137
GeoB 7149-2	178	IECMF0017	UCIAMS-123882	*Uvigerina*	11420	630	9883	160	-202
GeoB 7149-2	218	IECMF0018	UCIAMS-123747	*G. bulloides*	10420	120	10938	159	
GeoB 7149-2	218	IECMF0019	UCIAMS-114585	*G. bulloides*	10390	130	10938	159	
GeoB 7149-2	218	IECMF001A	UCIAMS-114587	*N. pachyderma* (dextral)	9750	120	10938	159	
GeoB 7149-2	218	IECMF001B	UCIAMS-123745	*N. pachyderma* (dextral)	10410	130	10938	159	
GeoB 7149-2	218	IECMF001C	UCIAMS-123746	*N. dutertrei*	9935	35	10938	159	
GeoB 7149-2	218	IECMF001D	UCIAMS-114586	*Uvigerina*	11290	90	10938	159	-79
GeoB 7149-2	253	IECMF001E	UCIAMS-123744	*G. bulloides*	10910	50	11712	165	
GeoB 7149-2	253	IECMF001F	UCIAMS-123743	*N. pachyderma* (dextral)	10820	55	11712	165	
GeoB 7149-2	278	IECMF001G	UCIAMS-123740	*G. bulloides*	12040	60	12461	170	
GeoB 7149-2	278	IECMF001H	UCIAMS-123742	*N. pachyderma* (dextral)	11910	45	12461	170	
GeoB 7149-2	278	IECMF001I	UCIAMS-123741	*N. dutertrei*	11610	200	12461	170	
GeoB 7149-2	303	IECMF001J	UCIAMS-114588	*G. bulloides*	12260	120	13319	158	
GeoB 7149-2	303	IECMF001K	UCIAMS-123738	*G. bulloides*	12445	50	13319	158	
GeoB 7149-2	303	IECMF001L	UCIAMS-114590	*N. pachyderma* (dextral)	12200	240	13319	158	
GeoB 7149-2	303	IECMF001M	UCIAMS-123739	*N. pachyderma* (dextral)	12810	100	13319	158	
GeoB 7149-2	303	IECMF001N	UCIAMS-114591	*G. inflata*	12570	120	13319	158	
GeoB 7149-2	303	IECMF001O	UCIAMS-114589	Infaunal	13580	170	13319	158	-76

GeoB 7149-2	328	IECMF001P	UCIAMS-114592	*G. bulloides*	13090	80	14055	219	
GeoB 7149-2	328	IECMF001Q	UCIAMS-123736	*G. bulloides*	13450	90	14055	219	
GeoB 7149-2	328	IECMF001R	UCIAMS-114594	*N. pachyderma* (dextral)	12740	310	14055	219	
GeoB 7149-2	328	IECMF001S	UCIAMS-123737	*N. pachyderma* (dextral)	13290	190	14055	219	
GeoB 7149-2	328	IECMF001T	UCIAMS-114595	*G. inflata*	13400	160	14055	219	
GeoB 7149-2	328	IECMF001U	UCIAMS-114593	Infaunal	15520	160	14055	219	-207
GeoB 7149-2	348	IECMF001V	UCIAMS-123735	*G. bulloides*	13710	60	14624	201	
GeoB 7149-2	348	IECMF001W	UCIAMS-123734	*N. pachyderma* (dextral)	13580	100	14624	201	
GeoB 7149-2	363	IECMF001X	UCIAMS-114612	*G. bulloides*	13470	110	15002	212	
GeoB 7149-2	363	IECMF001Y	UCIAMS-114613	*G. inflata*	10440	290	15002	212	
GeoB 7149-2	373	IECMF001Z	UCIAMS-114596	*G. bulloides*	13850	130	15242	243	
GeoB 7149-2	373	IECMF0020	UCIAMS-114611	Infaunal	15700	370	15242	243	-105
GeoB 7149-2	403	IECMF0021	UCIAMS-114614	*G. bulloides*	13520	100	15989	302	
GeoB 7149-2	403	IECMF0022	UCIAMS-123733	*N. pachyderma* (dextral)	14060	210	15989	302	
GeoB 7149-2	403	IECMF0023	UCIAMS-114615	Infaunal	15580	180	15989	302	-5
GeoB 7163-7	273	IECMF0024	UCIAMS-123726	Mixed Planktonic Foraminifera	15570	570	16938	170	
GeoB 7163-7	273	IECMF0025	UCIAMS-113881	*G. inflata*	14870	460	16938	170	
GeoB 7163-7	273	IECMF0026	UCIAMS-113880	*G. bulloides*	15050	140	16938	170	
GeoB 7163-7	273	IECMF0027	UCIAMS-113879	*Uvigerina & Boli?*	15600	260	16938	170	113
GeoB 7163-7	278	IECMF0028	UCIAMS-123725	Mixed Planktonic Foraminifera	15430	90	16996	149	
GeoB 7163-7	288	IECMF0029	UCIAMS-114491	*G. bulloides*	15370	70	17105	160	
GeoB 7163-7	288	IECMF002A	UCIAMS-114492	*G. inflata*	15330	220	17586	160	
GeoB 7163-7	288	IECMF002B	UCIAMS-113882	*Uvigernina*	15570	170	17501	160	196
GeoB 7163-7	303	IECMF002C	UCIAMS-114493	*G. bulloides*	15460	140	17287	144	
GeoB 7163-7	328	IECMF002D	UCIAMS-114495	*G. bulloides*	15580	80	17558	145	
GeoB 7163-7	328	IECMF002E	UCIAMS-114494	*Uvigerina & Boli?*	16040	320	17558	145	136
GeoB 7163-7	353	IECMF002F	UCIAMS-114497	*G. bulloides*	15950	90	17805	136	
GeoB 7163-7	353	IECMF002G	UCIAMS-114498	*G. inflata*	15820	60	17805	136	
GeoB 7163-7	353	IECMF002H	UCIAMS-114496	*Uvigerina*	16170	80	17805	136	151
GeoB 7163-7	383	IECMF002I	UCIAMS-114500	*G. bulloides*	15700	180	18084	156	
GeoB 7163-7	383	IECMF002J	UCIAMS-114501	*G. inflata*	16080	90	18084	156	
GeoB 7163-7	383	IECMF002K	UCIAMS-114499	*Uvigerina*	16220	70	18084	156	184

GeoB 7163-7	408	IECMF002L	UCIAMS-114503	*G. bulloides*	16190	70	18332	169	
GeoB 7163-7	408	IECMF002M	UCIAMS-114504	*G. inflata*	14720	450	18332	169	
GeoB 7163-7	408	IECMF002N	UCIAMS-114502	*Uvigerina & Boli?*	16460	140	18332	169	184
GeoB 7163-7	433	IECMF002O	UCIAMS-114506	*G. bulloides*	16530	90	18632	169	
GeoB 7163-7	433	IECMF002P	UCIAMS-114507	*G. inflata*	16310	180	18632	169	
GeoB 7163-7	433	IECMF002R	UCIAMS-114505	*Uvigerina*	16590	60	18632	169	208
GeoB 7163-7	463	IECMF002S	UCIAMS-114510	*G. bulloides*	16410	150	18930	184	
GeoB 7163-7	463	IECMF002T	UCIAMS-114509	*Uvigerina*	16790	80	18930	184	221
GeoB 7163-7	498	IECMF002U	UCIAMS-114512	*G. bulloides*	16760	170	19284	196	
GeoB 7163-7	498	IECMF002V	UCIAMS-114511	*Uvigerina*	16930	90	19284	196	253
GeoB 7163-7	523	IECMF002W	UCIAMS-114514	*G. bulloides*	16890	90	19543	212	
GeoB 7163-7	523	IECMF002X	UCIAMS-114515	*G. inflata*	16990	90	19543	212	
GeoB 7163-7	523	IECMF002Y	UCIAMS-114513	*Uvigerina*	17290	70	19543	241	236
GeoB 7163-7	543	IECMF002Z	UCIAMS-114572	*G. bulloides*	17560	90	19772	241	
GeoB 7163-7	543	IECMF0030	UCIAMS-114573	*G. inflata*	17430	500	19772	241	
GeoB 7163-7	543	IECMF0031	UCIAMS-114571	*Uvigerina*	17680	70	19772	241	211
GeoB 7167-6	163	IECMF0032	UCIAMS-178123	Mixed planktonic foraminifera	8860	35	9064	231	
GeoB 7167-6	163	IECMF0033	UCIAMS-123885	Mixed Benthic Foraminifera	9980	110	9064	231	-136
GeoB 7167-6	163	IECMF0034	UCIAMS-178122	Mixed Benthic Foraminifera	10005	20	9064	231	-138
GeoB 7167-6	213	IECMF0035	UCIAMS-178126	Mixed planktonic foraminifera	9780	350	10,208	191	
GeoB 7167-6	213	IECMF0036	UCIAMS-178124	Mixed Benthic Foraminifera	11015	35	10,208	191	-127
GeoB 7167-6	213	IECMF0037	UCIAMS-178125	Mixed Benthic Foraminifera	11100	90	10,208	191	-137
GeoB 7167-6	223	IECMF0038	UCIAMS-178128	Mixing planktonic foraminifera	9800	90	10,445	168	
GeoB 7167-6	223	IECMF0039	UCIAMS-178127	Mixed Benthic Foraminifera	11425	35	10,445	168	-147
GeoB 7167-6	228	IECMF003A	UCIAMS-178130	Mixing planktonic foraminifera	10430	70	10,597	149	
GeoB 7167-6	228	IECMF003B	UCIAMS-178129	Mixed Benthic Foraminifera	11800	45	10,597	149	-171
GeoB 7167-6	233	IECMF003C	UCIAMS-178132	Mixing planktonic foraminifera	10440	100	10,728	141	
GeoB 7167-6	233	IECMF003D	UCIAMS-178131	Mixed Benthic Foraminifera	11570	45	10,728	141	-133
GeoB 7167-6	248	IECMF003E	UCIAMS-178134	Mixed planktonic foraminifera	10490	30	11,076	127	
GeoB 7167-6	248	IECMF003F	UCIAMS-178133	Mixed Benthic Foraminifera	12070	25	11,076	127	-150

GeoB 7167-6	258	IECMF003G	UCIAMS-178136	Mixed planktonic foraminifera	10880	25	11,371	145	
GeoB 7167-6	258	IECMF003H	UCIAMS-178135	Mixed Benthic Foraminifera	12250	30	11,371	145	-139
GeoB 7167-6	268	IECMF003I	UCIAMS-178138	Mixed planktonic foraminifera	10910	110	11,668	167	
GeoB 7167-6	268	IECMF003J	UCIAMS-178141	Mixed planktonic foraminifera	10790	140	11,668	167	
GeoB 7167-6	268	IECMF003K	UCIAMS-178137	Mixed Benthic Foraminifera	12460	100	11,668	167	-130
GeoB 7167-6	268	IECMF003L	UCIAMS-178139	Mixed Benthic Foraminifera	12575	30	11,668	167	-143
GeoB 7167-6	278	IECMF003M	UCIAMS-178143	Mixed planktonic foraminifera	11780	25	12,101	190	
GeoB 7167-6	278	IECMF003N	UCIAMS-178142	Mixed Benthic Foraminifera	13160	25	12,101	190	-160
GeoB 7167-6	288	IECMF003O	UCIAMS-178145	Mixed planktonic foraminifera	12125	35	12,558	139	
GeoB 7167-6	288	IECMF003P	UCIAMS-178144	Mixed Benthic Foraminifera	13195	30	12,558	139	-116
GeoB 7167-6	298	IECMF003Q	UCIAMS-178147	Mixed planktonic foraminifera	12580	30	13,152	143	
GeoB 7167-6	298	IECMF003R	UCIAMS-178146	Mixed Benthic Foraminifera	13690	30	13,152	143	-107
GeoB 7167-6	308	IECMF003S	UCIAMS-178149	Mixde planktonic foraminifera	12855	40	13,458	115	
GeoB 7167-6	308	IECMF003T	UCIAMS-178148	Mixed Benthic Foraminifera	13875	25	13,458	115	-94
GeoB 7167-6	318	IECMF003U	UCIAMS-178151	Mixed planktonic foraminifera	12975	20	13,705	120	
GeoB 7167-6	318	IECMF003V	UCIAMS-178150	Mixed Benthic Foraminifera	14210	30	13,705	120	-105
GeoB 7167-6	328	IECMF003W	UCIAMS-123756	Mixed Planktonic Foraminifera	13340	120	14,028	163	
GeoB 7167-6	328	IECMF003X	UCIAMS-123757	Mixed Benthic Foraminifera	14700	120	14,028	163	-124
GeoB 7167-6	398	IECMF003Y	UCIAMS-178153	Mixed planktonic foraminifera	15105	40	16,551	206	
GeoB 7167-6	398	IECMF003Z	UCIAMS-178152	Mixed Benthic Foraminifera	16460	90	16,551	206	-46
GeoB 7167-6	438	IECMF0040	UCIAMS-178155	Mixed planktonic foraminifera	15965	35	17,844	187	
GeoB 7167-6	438	IECMF0041	UCIAMS-178154	Mixed Benthic Foraminifera	17490	100	17,844	187	-18
GeoB 7167-6	538	IECMF0045	UCIAMS-178157	Mixed planktonic foraminifera	18030	60	20,426	584	
GeoB 7167-6	538	IECMF0046	UCIAMS-178156	Mixed Benthic Foraminifera	19640	70	20,426	584	26

GepB 7162-6	252	IECMF004C	OS- 72168	Mixed *N. pachyderma*	13100	65	14684	201	
GepB 7162-6	252	IECMF004D	OS- 72177	*Uvigerina*	13750	95	14684	201	66
GepB 7162-6	316	IECMF004E	OS- 72169	Mixed Planktonic Foraminifera	14400	70	15385	125	
GepB 7162-6	316	IECMF004F	OS- 72172	*Uvigerina*	16550	80	15385	125	-180
GepB 7162-6	344	IECMF004G	OS- 72024	Mixed Planktonic Foraminifera	14350	80	15658	113	
GepB 7162-6	344	IECMF004H	OS- 72178	*Uvigerina*	15100	100	15658	113	15
GepB 7162-6	356	IECMF004I	OS- 72171	Mixed Planktonic Foraminifera	14350	75	15778	113	
GepB 7162-6	356	IECMF004J	OS- 72179	*Uvigerina*	15300	110	15778	113	5
GepB 7162-6	372	IECMF004K	OS- 72030	Mixed Planktonic Foraminifera	14550	75	15982	132	
GepB 7162-6	398	IECMF004L	OS- 72170	Mixed Planktonic Foraminifera	15050	70	16321	133	
GepB 7162-6	398	IECMF004M	OS- 72138	*Uvigerina*	15550	75	16321	133	43
GepB 7162-6	416	IECMF004N	OS- 72754	*Uvigerina*	15520	75	16539	155	119
GepB 7162-6	416	IECMF004O	OS- 72135	Mixed Planktonic Foraminifera	15550	150	16539	155	
22SL	202	IECMF004P	UCIAMS-96737	Mixed Benthonic Foraminifera	9340	20	9354	131	-31
22SL	203	IECMF004Q	UCIAMS-64328	*Brizalina*	9090	80	9367	130	2
22SL	218	IECMF004R	UCIAMS-96738	Mixed Benthonic Foraminifera	9775	20	9558	137	-59
22SL	234	IECMF004S	UCIAMS-96739	Mixed Benthonic Foraminifera	9990	20	9830	156	-53
22SL	250	IECMF004T	UCIAMS-96740	Mixed Benthonic Foraminifera	10360	20	10115	153	-64
22SL	253	IECMF004U	UCIAMS-64329	Mixed Planktonic Foraminifera	9160	380	10170	155	
22SL	253	IECMF004V	UCIAMS-64330	*Brizalina*	9970	60	10170	155	-11
22SL	268	IECMF004W	UCIAMS-96741	Mixed Benthonic Foraminifera	10600	20	10492	170	-49
22SL	278	IECMF004X	UCIAMS-64331	Mixed Planktonic Foraminifera	10510	200	10686	156	
22SL	292	IECMF004Y	UCIAMS-97369	Mixed Benthonic Foraminifera	10845	30	10978	165	-22

22SL	293	IECMF004Z	UCIAMS-64332	Mixed Planktonic Foraminifera	10470	150	10997	162	
22SL	310	IECMF0050	UCIAMS-96742	Mixed Benthonic Foraminifera	11480	20	11335	172	-56
22SL	321	IECMF0051	OS-69278	Mixed Planktonic Foraminifera	11050	55	11556	172	
22SL	321	IECMF0052	OS-69322	*Uvigerina* spp	11300	55	11556	172	-9
22SL	345	IECMF0053	OS-69545	Mixed Planktonic Foraminifera	11700	100	12018	183	
22SL	345	IECMF0054	OS-69273	Mixed Planktonic Foraminifera	12300	80	12018	183	-74
22SL	350	IECMF0055	UCIAMS-64333	Mixed Benthic Foraminifera	12240	210	12119	192	-56
22SL	356	IECMF0056	UCIAMS-97361	Mixed Benthonic Foraminifera	12185	45	12228	200	-37
22SL	364	IECMF0057	UCIAMS-96743	Mixed Benthonic Foraminifera	12245	25	12373	205	-27
22SL	374	IECMF0058	UCIAMS-97362	Mixed Benthonic Foraminifera	12400	45	12557	211	-24
22SL	425	IECMF0059	OS-66960	Mixed Planktonic Foraminifera	13050	100	13503	190	
22SL	425	IECMF005A	OS-66829	*Uvigerina* spp	13400	60	13503	190	-34
22SL	491	IECMF005B	OS-66830	Mixed Planktonic Foraminifera	13450	65	14378	192	
22SL	491	IECMF005C	OS-66827	Mixed Benthic Foraminifera	13700	60	14378	192	35
22SL	540	IECMF005D	OS-71076	Mixed Planktonic Foraminifera	14050	90	15084	147	
22SL	540	IECMF005E	OS-71081	Mixed Benthic Foraminifera	14450	90	15084	147	26
22SL	565	IECMF005F	OS-71077	Mixed Planktonic Foraminifera	14200	75	15434	135	
22SL	565	IECMF005G	OS-71082	*Uvigerin*a spp	14650	90	15434	135	44
22SL	588	IECMF005H	OS-69280	Mixed Planktonic Foraminifera	14650	65	15784	126	
22SL	588	IECMF005I	OS-69274	*Uvigerina* spp	15150	85	15784	126	24
22SL	619	IECMF005J	OS-66828	Mixed Planktonic Foraminifera	14800	75	16177	118	
22SL	619	IECMF005K	OS-66865	*Uvigerina* spp	15050	75	16177	118	87
22SL	665	IECMF005L	OS-66831	Mixed Planktonic Foraminifera	15100	75	16756	127	

22SL	665	IECMF005M	OS-66864	*Uvigerina* spp	15550	100	16756	127	96
22SL	685	IECMF005N	OS-69318	*G bulloides*	15350	70	17031	123	
22SL	685	IECMF005O	OS-69277	*Uvigerina* spp	15850	75	17031	123	91
22SL	725	IECMF005P	OS-69282	*G bulloides*	15700	80	17610	121	
22SL	725	IECMF005Q	OS-69279	*Uvigerina* spp	16250	85	17610	121	114
22SL	760	IECMF005R	OS-69319	*G bulloides*	16000	65	18044	126	
22SL	760	IECMF005S	OS-69323	*Uvigerina* spp	16550	75	18044	126	131
22SL	785	IECMF005T	OS-69320	*G bulloides*	16100	75	18431	125	
22SL	785	IECMF005U	OS-69321	*G inflata*	16450	75	18431	125	
22SL	785	IECMF005V	OS-69324	*Uvigerina* (Benthic)	16900	70	18431	125	134
22SL	808	IECMF005W	OS- 72023	Mixed Planktonic Foraminifera	16600	70	18827	113	
22SL	808	IECMF005X	OS-72174	*Uvigerina* (Benthic)	17100	90	18827	113	161
22SL	818	IECMF005Y	OS-72167	Mixed Planktonic Foraminifera	16850	75	18993	109	
22SL	818	IECMF005Z	OS-72025	*Uvigerina* (Benthic)	17550	75	18993	109	120
22SL	833	IECMF0060	OS- 72026	Mixed Planktonic Foraminifera	16800	110	19200	115	
22SL	833	IECMF0061	OS-72136	*Uvigerina* (Benthic)	17550	90	19200	115	148
22SL	843	IECMF0062	OS- 71924	Mixed Planktonic Foraminifera	16900	85	19330	117	
22SL	843	IECMF0063	OS-72137	*Uvigerina* (Benthic)	17750	85	19330	117	138
22SL	868	IECMF0064	OS- 71925	Mixed Planktonic Foraminifera	17400	70	19642	129	
22SL	868	IECMF0065	OS- 72556	*Uvigerina* (Benthic)	17250	330	19642	129	257
22SL	883	IECMF0066	OS- 71926	Mixed Planktonic Foraminifera	17300	70	19804	135	
22SL	883	IECMF0067	OS-72028	*Uvigerina* (Benthic)	18000	100	19804	135	168

Table S2 $\delta^{13}C$ measurements presented in Figure S2. Ages marked with an * correspond to the original 14C ages, whereas the rest are the extrapolated ages.

Core	Depth (cm)	Species	$\delta^{13}C$ (‰)	Extrapolated ^{14}C age (years BP)
GeoB 7149-2	13	*N. dutertrei*	2.02	1980*
GeoB 7149-2	18	*N. dutertrei*	2.13	2220
GeoB 7149-2	23	*N. dutertrei*	-0.60	2460
GeoB 7149-2	28	*N. dutertrei*	1.85	2700*
GeoB 7149-2	33	*N. dutertrei*	1.78	2983
GeoB 7149-2	38	*N. dutertrei*	1.85	3265
GeoB 7149-2	43	*N. dutertrei*	1.98	3548*
GeoB 7149-2	48	*N. dutertrei*	2.01	3824
GeoB 7149-2	53	*N. dutertrei*	2.05	4100*
GeoB 7149-2	58	*N. dutertrei*	1.95	4107*
GeoB 7149-2	63	*N. dutertrei*	2.13	4337
GeoB 7149-2	68	*N. dutertrei*	1.88	4555
GeoB 7149-2	73	*N. dutertrei*	2.13	4774
GeoB 7149-2	78	*N. dutertrei*	1.91	4992*
GeoB 7149-2	83	*N. dutertrei*	1.60	5157
GeoB 7149-2	98	*N. dutertrei*	1.69	5687
GeoB 7149-2	108	*N. dutertrei*	1.62	6040*
GeoB 7149-2	113	*N. dutertrei*	1.74	6421
GeoB 7149-2	123	*N. dutertrei*	1.77	7183
GeoB 7149-2	126	*N. dutertrei*	1.62	7564
GeoB 7149-2	133	*N. dutertrei*	1.35	7945*
GeoB 7149-2	138	*N. dutertrei*	1.72	8040
GeoB 7149-2	143	*N. dutertrei*	1.60	8134
GeoB 7149-2	173	*N. dutertrei*	1.09	9182*
GeoB 7149-2	178	*N. dutertrei*	1.18	10092*
GeoB 7149-2	183	*N. dutertrei*	1.13	10103
GeoB 7149-2	188	*N. dutertrei*	1.72	10114
GeoB 7149-2	193	*N. dutertrei*	1.63	10126
GeoB 7149-2	198	*N. dutertrei*	1.22	10137
GeoB 7149-2	203	*N. dutertrei*	1.49	10148
GeoB 7149-2	208	*N. dutertrei*	1.43	10159
GeoB 7149-2	213	*N. dutertrei*	1.33	10170
GeoB 7149-2	218	*N. dutertrei*	1.76	10181*
GeoB 7149-2	223	*N. dutertrei*	1.14	10279
GeoB 7149-2	228	*N. dutertrei*	1.55	10377
GeoB 7149-2	233	*N. dutertrei*	1.38	10475
GeoB 7149-2	243	*N. dutertrei*	1.60	10670
GeoB 7149-2	248	*N. dutertrei*	1.48	10768
GeoB 7149-2	253	*N. dutertrei*	1.03	10865*
GeoB 7149-2	258	*N. dutertrei*	0.93	11063
GeoB 7149-2	263	*N. dutertrei*	1.25	1121
GeoB 7149-2	278	*N. dutertrei*	1.47	11854*
GeoB 7149-2	283	*N. dutertrei*	0.92	11975
GeoB 7149-2	288	*N. dutertrei*	1.45	12095

GeoB 7149-2	293	*N. dutertrei*	0.78	12216
GeoB 7149-2	298	*N. dutertrei*	1.04	12337
GeoB 7149-2	308	*N. dutertrei*	1.27	12589
GeoB 7149-2	338	*N. dutertrei*	1.51	13381
GeoB 7149-2	343	*N. dutertrei*	1.20	13513
GeoB 7149-2	348	*N. dutertrei*	1.93	13645*
GeoB 7149-2	353	*N. dutertrei*	1.70	13686
GeoB 7149-2	378	*N. dutertrei*	1.31	13885
GeoB 7149-2	383	*N. dutertrei*	0.73	13920
GeoB 7149-2	403	*N. dutertrei*	1.65	14060*
GeoB 7149-2	13	*G. bulloides*	-0.09	1980*
GeoB 7149-2	18	*G. bulloides*	-0.36	2220
GeoB 7149-2	23	*G. bulloides*	-0.96	2460
GeoB 7149-2	33	*G. bulloides*	-0.60	2700
GeoB 7149-2	43	*G. bulloides*	0.26	2982.5*
GeoB 7149-2	48	*G. bulloides*	0.26	3265
GeoB 7149-2	53	*G. bulloides*	0.28	3548*
GeoB 7149-2	58	*G. bulloides*	0.11	3824*
GeoB 7149-2	63	*G. bulloides*	0.18	4100
GeoB 7149-2	68	*G. bulloides*	0.21	4107
GeoB 7149-2	78	*G. bulloides*	0.07	4337*
GeoB 7149-2	83	*G. bulloides*	0.06	4555
GeoB 7149-2	88	*G. bulloides*	-0.42	4773
GeoB 7149-2	98	*G. bulloides*	-0.22	4992
GeoB 7149-2	123	*G. bulloides*	-0.37	5157
GeoB 7149-2	126	*G. bulloides*	-0.38	5333
GeoB 7149-2	133	*G. bulloides*	-0.43	5687*
GeoB 7149-2	138	*G. bulloides*	-0.50	6040
GeoB 7149-2	143	*G. bulloides*	-1.00	6421
GeoB 7149-2	173	*G. bulloides*	-0.63	7183*
GeoB 7149-2	183	*G. bulloides*	-0.68	7564
GeoB 7149-2	188	*G. bulloides*	-0.93	7945
GeoB 7149-2	193	*G. bulloides*	-1.09	8039
GeoB 7149-2	198	*G. bulloides*	-0.22	8134
GeoB 7149-2	203	*G. bulloides*	-0.92	9182
GeoB 7149-2	208	*G. bulloides*	-0.39	10091
GeoB 7149-2	213	*G. bulloides*	-0.44	10103
GeoB 7149-2	218	*G. bulloides*	-0.15	10114*
GeoB 7149-2	223	*G. bulloides*	-0.61	10125
GeoB 7149-2	233	*G. bulloides*	-0.71	10136
GeoB 7149-2	243	*G. bulloides*	-0.60	10147
GeoB 7149-2	248	*G. bulloides*	-0.44	10159
GeoB 7149-2	253	*G. bulloides*	-0.51	10170*
GeoB 7149-2	258	*G. bulloides*	-0.73	10181
GeoB 7149-2	263	*G. bulloides*	-0.80	10279
GeoB 7149-2	268	*G. bulloides*	-1.32	10376
GeoB 7149-2	273	*G. bulloides*	-0.60	10474
GeoB 7149-2	278	*G. bulloides*	-0.47	10670*
GeoB 7149-2	283	*G. bulloides*	-0.63	10767
GeoB 7149-2	288	*G. bulloides*	-0.65	10865

GeoB 7149-2	293	*G. bulloides*	-0.52	11063
GeoB 7149-2	298	*G. bulloides*	-0.44	11260
GeoB 7149-2	303	*G. bulloides*	-0.58	11458*
GeoB 7149-2	308	*G. bulloides*	-0.81	11656
GeoB 7149-2	313	*G. bulloides*	-0.78	11853
GeoB 7149-2	318	*G. bulloides*	-0.77	11974
GeoB 7149-2	323	*G. bulloides*	-0.81	12095
GeoB 7149-2	328	*G. bulloides*	-0.94	12216
GeoB 7149-2	333	*G. bulloides*	-0.74	12337
GeoB 7149-2	338	*G. bulloides*	-0.86	12457
GeoB 7149-2	343	*G. bulloides*	-0.87	12589
GeoB 7149-2	348	*G. bulloides*	-0.79	12721*
GeoB 7149-2	353	*G. bulloides*	-1.30	12853
GeoB 7149-2	358	*G. bulloides*	-1.21	12985
GeoB 7149-2	363	*G. bulloides*	-1.09	13117*
GeoB 7149-2	368	*G. bulloides*	-1.19	13249
GeoB 7149-2	373	*G. bulloides*	-1.18	13381*
GeoB 7149-2	378	*G. bulloides*	-1.23	13513
GeoB 7149-2	383	*G. bulloides*	-1.04	13645
GeoB 7149-2	388	*G. bulloides*	-1.14	13686
GeoB 7149-2	393	*G. bulloides*	-1.08	13727
GeoB 7149-2	398	*G. bulloides*	-1.08	13768
GeoB 7149-2	403	*G. bulloides*	-1.00	13809*
GeoB 7149-2	408	*G. bulloides*	-1.36	13850
GeoB 7149-2	413	*G. bulloides*	-1.48	13885
GeoB 7163-7	273	*G. bulloides*	-0.48	15163*
GeoB 7163-7	278	*G. bulloides*	-0.01	15172
GeoB 7163-7	283	*G. bulloides*	0.26	15180
GeoB 7163-7	288	*G. bulloides*	-0.09	15188
GeoB 7163-7	293	*G. bulloides*	-0.16	15361
GeoB 7163-7	298	*G. bulloides*	-0.82	15411
GeoB 7163-7	303	*G. bulloides*	-0.09	15460*
GeoB 7163-7	308	*G. bulloides*	0.08	15484
GeoB 7163-7	318	*G. bulloides*	0.06	15532
GeoB 7163-7	323	*G. bulloides*	-0.43	15556
GeoB 7163-7	328	*G. bulloides*	0.22	15580*
GeoB 7163-7	333	*G. bulloides*	0.03	15604
GeoB 7163-7	338	*G. bulloides*	-0.19	15702
GeoB 7163-7	343	*G. bulloides*	-0.22	15763
GeoB 7163-7	348	*G. bulloides*	-0.79	15824
GeoB 7163-7	353	*G. bulloides*	-1.31	15885*
GeoB 7163-7	358	*G. bulloides*	0.28	15886
GeoB 7163-7	363	*G. bulloides*	0.04	15887
GeoB 7163-7	368	*G. bulloides*	-0.69	15888
GeoB 7163-7	373	*G. bulloides*	-0.24	15889
GeoB 7163-7	383	*G. bulloides*	0.27	15890*
GeoB 7163-7	388	*G. bulloides*	-0.44	16006
GeoB 7163-7	393	*G. bulloides*	-0.33	16052
GeoB 7163-7	398	*G. bulloides*	-0.18	16098
GeoB 7163-7	403	*G. bulloides*	-0.44	16144

GeoB 7163-7	408	*G. bulloides*	-0.15	16190*
GeoB 7163-7	413	*G. bulloides*	-0.04	16236
GeoB 7163-7	418	*G. bulloides*	-0.09	16282
GeoB 7163-7	423	*G. bulloides*	-0.31	16328
GeoB 7163-7	428	*G. bulloides*	-0.12	16374
GeoB 7163-7	433	*G. bulloides*	0.37	16420*
GeoB 7163-7	438	*G. bulloides*	0.07	16446
GeoB 7163-7	443	*G. bulloides*	-0.62	16472
GeoB 7163-7	448	*G. bulloides*	-0.36	16498
GeoB 7163-7	458	*G. bulloides*	-0.37	16550
GeoB 7163-7	463	*G. bulloides*	-0.15	16576
GeoB 7163-7	468	*G. bulloides*	0.28	16603
GeoB 7163-7	473	*G. bulloides*	0.21	16629
GeoB 7163-7	478	*G. bulloides*	-0.01	16655
GeoB 7163-7	483	*G. bulloides*	-0.36	16681
GeoB 7163-7	488	*G. bulloides*	0.05	16707
GeoB 7163-7	493	*G. bulloides*	-0.07	16733
GeoB 7163-7	498	*G. bulloides*	-0.38	16760*
GeoB 7163-7	503	*G. bulloides*	0.03	16796
GeoB 7163-7	513	*G. bulloides*	0.04	16868
GeoB 7163-7	523	*G. bulloides*	0.29	16940*
GeoB 7163-7	528	*G. bulloides*	-0.32	17079
GeoB 7163-7	533	*G. bulloides*	-0.32	17218
GeoB 7163-7	538	*G. bulloides*	0.11	17356
GeoB 7163-7	543	*G. bulloides*	0.39	17495*
GeoB 7167-6	128	*G. bulloides*	-3.42	8216
GeoB 7167-6	153	*G. bulloides*	-0.49	8676
GeoB 7167-6	163	*G. bulloides*	-0.95	8860*
GeoB 7167-6	168	*G. bulloides*	0.40	8952
GeoB 7167-6	248	*G. bulloides*	-0.80	10490*
GeoB 7167-6	253	*G. bulloides*	-0.61	10685
GeoB 7167-6	258	*G. bulloides*	-0.80	10880*
GeoB 7167-6	263	*G. bulloides*	-0.95	10910*
GeoB 7167-6	273	*G. bulloides*	-0.60	11285
GeoB 7167-6	308	*G. bulloides*	-0.41	12855*
GeoB 7167-6	313	*G. bulloides*	-0.72	12915
GeoB 7167-6	318	*G. bulloides*	-0.91	12975*
GeoB 7167-6	323	*G. bulloides*	-1.28	13158
GeoB 7167-6	328	*G. bulloides*	-1.14	13340*
GeoB 7167-6	333	*G. bulloides*	-1.31	13466
GeoB 7167-6	338	*G. bulloides*	-1.39	13592
GeoB 7167-6	343	*G. bulloides*	-1.42	13718
GeoB 7167-6	348	*G. bulloides*	-1.34	13844
GeoB 7167-6	353	*G. bulloides*	-0.85	13970
GeoB 7167-6	358	*G. bulloides*	-1.31	14096
GeoB 7167-6	363	*G. bulloides*	-1.49	14223
GeoB 7167-6	368	*G. bulloides*	-1.06	14349
GeoB 7167-6	373	*G. bulloides*	-1.28	14475
GeoB 7167-6	378	*G. bulloides*	-0.81	14601
22SL	122	*G. bulloides*	-0.38	2086

22SL	168	*G. bulloides*	-1.15	4570
22SL	176	*G. bulloides*	-0.37	5002
22SL	178	*G. bulloides*	-0.62	5110
22SL	196	*G. bulloides*	-1.50	6082
22SL	206	*G. bulloides*	-0.29	6622
22SL	208	*G. bulloides*	-0.96	6730
22SL	210	*G. bulloides*	-0.54	6838
22SL	254	*G. bulloides*	-0.23	9214
22SL	260	*G. bulloides*	-0.73	9538
22SL	264	*G. bulloides*	-0.49	9754
22SL	268	*G. bulloides*	-0.42	9970
22SL	270	*G. bulloides*	-0.36	10078
22SL	272	*G. bulloides*	-0.63	10186
22SL	274	*G. bulloides*	-0.84	10294
22SL	276	*G. bulloides*	-0.35	10402
22SL	278	*G. bulloides*	-0.80	10510*
22SL	280	*G. bulloides*	-0.67	10535
22SL	282	*G. bulloides*	-1.14	10560
22SL	284	*G. bulloides*	-0.96	10585
22SL	286	*G. bulloides*	-0.62	10610
22SL	288	*G. bulloides*	-1.03	10636
22SL	290	*G. bulloides*	-0.94	10660
22SL	292	*G. bulloides*	-1.36	10686
22SL	294	*G. bulloides*	-0.98	10711
22SL	296	*G. bulloides*	-1.52	10736
22SL	298	*G. bulloides*	-0.90	10761
22SL	300	*G. bulloides*	-0.99	10786
22SL	302	*G. bulloides*	-0.81	10811
22SL	304	*G. bulloides*	-1.20	10837
22SL	306	*G. bulloides*	-0.72	10862
22SL	308	*G. bulloides*	-1.51	10887
22SL	310	*G. bulloides*	-0.79	10912
22SL	312	*G. bulloides*	-0.88	10937
22SL	314	*G. bulloides*	-1.27	10962
22SL	316	*G. bulloides*	-0.99	10987
22SL	318	*G. bulloides*	-1.21	11012
22SL	320	*G. bulloides*	-0.87	11037
22SL	324	*G. bulloides*	-1.95	11131
22SL	328	*G. bulloides*	-1.52	11240
22SL	332	*G. bulloides*	-1.46	11348
22SL	334	*G. bulloides*	-1.92	11402
22SL	338	*G. bulloides*	-1.50	11510
22SL	340	*G. bulloides*	-1.70	11565
22SL	342	*G. bulloides*	-1.53	11619
22SL	344	*G. bulloides*	-1.24	11673
22SL	346	*G. bulloides*	-1.27	11717
22SL	348	*G. bulloides*	-1.64	11751
22SL	350	*G. bulloides*	-1.08	11784
22SL	352	*G. bulloides*	-1.41	11818
22SL	366	*G. bulloides*	-1.06	12054

22SL	372	*G. bulloides*	-1.25	12156
22SL	374	*G. bulloides*	-1.09	12189
22SL	376	*G. bulloides*	-1.23	12223
22SL	380	*G. bulloides*	-0.92	12291
22SL	384	*G. bulloides*	-0.49	12358
22SL	386	*G. bulloides*	-0.85	12392
22SL	394	*G. bulloides*	-0.80	12527
22SL	396	*G. bulloides*	-0.74	12560
22SL	398	*G. bulloides*	-0.99	12594
22SL	400	*G. bulloides*	-0.77	12628
22SL	402	*G. bulloides*	-1.23	12662
22SL	404	*G. bulloides*	-1.03	12696
22SL	406	*G. bulloides*	-1.18	12729
22SL	410	*G. bulloides*	-1.24	12797
22SL	412	*G. bulloides*	-1.14	12831
22SL	414	*G. bulloides*	-0.67	12864
22SL	416	*G. bulloides*	-0.77	12898
22SL	418	*G. bulloides*	-0.62	12932
22SL	422	*G. bulloides*	-0.48	12999
22SL	424	*G. bulloides*	-1.17	13033
22SL	426	*G. bulloides*	-0.86	13056
22SL	428	*G. bulloides*	-0.60	13068
22SL	432	*G. bulloides*	-1.17	13092
22SL	434	*G. bulloides*	-0.70	13105
22SL	436	*G. bulloides*	-0.59	13117
22SL	438	*G. bulloides*	-0.91	13129
22SL	440	*G. bulloides*	-1.06	13141
22SL	442	*G. bulloides*	-1.31	13153
22SL	444	*G. bulloides*	-1.47	13165
22SL	446	*G. bulloides*	-1.71	13177
22SL	448	*G. bulloides*	-1.00	13189
22SL	450	*G. bulloides*	-1.58	13202
22SL	452	*G. bulloides*	-1.10	13214
22SL	454	*G. bulloides*	-0.92	13226
22SL	456	*G. bulloides*	-1.35	13238
22SL	458	*G. bulloides*	-1.13	13250
22SL	460	*G. bulloides*	-1.54	13262
22SL	462	*G. bulloides*	-1.03	13274
22SL	464	*G. bulloides*	-1.29	13286
22SL	466	*G. bulloides*	-1.40	13298
22SL	468	*G. bulloides*	-1.22	13311
22SL	470	*G. bulloides*	-1.15	13323
22SL	472	*G. bulloides*	-1.07	13335
22SL	474	*G. bulloides*	-1.35	13347
22SL	476	*G. bulloides*	-1.28	13359
22SL	478	*G. bulloides*	-1.41	13371
22SL	480	*G. bulloides*	-1.71	13383
22SL	482	*G. bulloides*	-1.55	13395
22SL	484	*G. bulloides*	-1.57	13408
22SL	486	*G. bulloides*	-0.99	13420

22SL	488	*G. bulloides*	-1.83	13432
22SL	490	*G. bulloides*	-1.73	13444
22SL	492	*G. bulloides*	-1.37	13462
22SL	494	*G. bulloides*	-1.34	13487
22SL	496	*G. bulloides*	-1.14	13511
22SL	498	*G. bulloides*	-1.49	13536
22SL	500	*G. bulloides*	-1.35	13560
22SL	502	*G. bulloides*	-1.40	13585
22SL	504	*G. bulloides*	-1.12	13609
22SL	506	*G. bulloides*	-1.36	13634
22SL	508	*G. bulloides*	-1.40	13658
22SL	510	*G. bulloides*	-1.37	13683
22SL	512	*G. bulloides*	-1.38	13707
22SL	514	*G. bulloides*	-1.02	13732
22SL	516	*G. bulloides*	-1.53	13756
22SL	518	*G. bulloides*	-1.10	13781
22SL	520	*G. bulloides*	-0.70	13805
22SL	522	*G. bulloides*	-1.12	13830
22SL	524	*G. bulloides*	-1.40	13854
22SL	526	*G. bulloides*	-1.53	13879
22SL	528	*G. bulloides*	-1.23	13903
22SL	530	*G. bulloides*	-0.87	13928
22SL	532	*G. bulloides*	-1.07	13952
22SL	534	*G. bulloides*	-1.02	13977
22SL	536	*G. bulloides*	-1.44	14001
22SL	538	*G. bulloides*	-1.34	14026
22SL	540	*G. bulloides*	-1.13	14050*
22SL	542	*G. bulloides*	-1.09	14062
22SL	544	*G. bulloides*	-1.05	14074
22SL	546	*G. bulloides*	-1.14	14086
22SL	548	*G. bulloides*	-1.27	14098
22SL	550	*G. bulloides*	-1.47	14110
22SL	552	*G. bulloides*	-0.86	14122
22SL	554	*G. bulloides*	-1.40	14134
22SL	556	*G. bulloides*	-1.48	14146
22SL	558	*G. bulloides*	-1.34	14158
22SL	560	*G. bulloides*	-1.31	14170
22SL	562	*G. bulloides*	-1.23	14182
22SL	564	*G. bulloides*	-1.25	14194
22SL	566	*G. bulloides*	-1.46	14220
22SL	568	*G. bulloides*	-1.12	14259
22SL	570	*G. bulloides*	-1.35	14298
22SL	572	*G. bulloides*	-1.02	14337
22SL	574	*G. bulloides*	-1.21	14376
22SL	576	*G. bulloides*	-1.16	14415
22SL	580	*G. bulloides*	-0.75	14493
22SL	582	*G. bulloides*	-1.09	14533
22SL	584	*G. bulloides*	-1.48	14572
22SL	586	*G. bulloides*	-1.01	14611
22SL	588	*G. bulloides*	-1.15	14650*

22SL	590	*G. bulloides*	-0.93	14660
22SL	592	*G. bulloides*	-0.98	14669
22SL	594	*G. bulloides*	-0.85	14679
22SL	596	*G. bulloides*	-0.72	14689
22SL	598	*G. bulloides*	-0.92	14698
22SL	600	*G. bulloides*	-1.02	14708
22SL	602	*G. bulloides*	-0.77	14718
22SL	604	*G. bulloides*	-0.81	14727
22SL	606	*G. bulloides*	-1.41	14737
22SL	608	*G. bulloides*	-1.00	14747
22SL	610	*G. bulloides*	-0.91	14756
22SL	612	*G. bulloides*	-1.00	14766
22SL	614	*G. bulloides*	-1.09	14776
22SL	616	*G. bulloides*	-0.62	14785
22SL	618	*G. bulloides*	-0.74	14795
22SL	620	*G. bulloides*	-0.66	14807
22SL	622	*G. bulloides*	-1.04	14820
22SL	624	*G. bulloides*	-1.15	14833
22SL	626	*G. bulloides*	-1.15	14846
22SL	628	*G. bulloides*	-1.13	14859
22SL	630	*G. bulloides*	-0.75	14872
22SL	632	*G. bulloides*	-0.92	14885
22SL	634	*G. bulloides*	-0.59	14898
22SL	636	*G. bulloides*	-0.65	14911
22SL	638	*G. bulloides*	-0.89	14924
22SL	640	*G. bulloides*	-0.78	14937
22SL	642	*G. bulloides*	-0.85	14950
22SL	644	*G. bulloides*	-0.50	14963
22SL	646	*G. bulloides*	-0.30	14976
22SL	648	*G. bulloides*	-0.46	14989
22SL	650	*G. bulloides*	-0.62	15002
22SL	652	*G. bulloides*	-0.24	15015
22SL	654	*G. bulloides*	-0.68	15028
22SL	656	*G. bulloides*	-0.66	15041
22SL	658	*G. bulloides*	-0.43	15054
22SL	660	*G. bulloides*	-0.75	15067
22SL	662	*G. bulloides*	-0.20	15080
22SL	664	*G. bulloides*	-0.21	15093
22SL	666	*G. bulloides*	-0.29	15113
22SL	668	*G. bulloides*	0.45	15138
22SL	670	*G. bulloides*	-0.55	15163
22SL	672	*G. bulloides*	-0.09	15188
22SL	674	*G. bulloides*	0.11	15213
22SL	676	*G. bulloides*	0.14	15238
22SL	678	*G. bulloides*	-0.29	15263
22SL	680	*G. bulloides*	-0.12	15288
22SL	682	*G. bulloides*	0.12	15313
22SL	684	*G. bulloides*	-0.46	15338
22SL	686	*G. bulloides*	0.04	15359
22SL	688	*G. bulloides*	0.28	15376

22SL	690	*G. bulloides*	-0.26	15394
22SL	692	*G. bulloides*	0.20	15411
22SL	694	*G. bulloides*	-0.19	15429
22SL	696	*G. bulloides*	0.18	15446
22SL	698	*G. bulloides*	0.24	15464
22SL	700	*G. bulloides*	-0.24	15481
22SL	702	*G. bulloides*	0.27	15499
22SL	704	*G. bulloides*	-0.29	15516
22SL	706	*G. bulloides*	-0.08	15534
22SL	708	*G. bulloides*	-0.12	15551
22SL	710	*G. bulloides*	-0.13	15569
22SL	712	*G. bulloides*	-0.10	15586
22SL	714	*G. bulloides*	-0.11	15604
22SL	716	*G. bulloides*	-0.23	15621
22SL	718	*G. bulloides*	-0.06	15639
22SL	720	*G. bulloides*	0.33	15656
22SL	722	*G. bulloides*	-0.25	15674
22SL	724	*G. bulloides*	-0.09	15691
22SL	726	*G. bulloides*	-0.15	15709
22SL	728	*G. bulloides*	0.17	15726
22SL	730	*G. bulloides*	0.01	15743
22SL	732	*G. bulloides*	-0.56	15760
22SL	734	*G. bulloides*	0.13	15777
22SL	736	*G. bulloides*	0.20	15794
22SL	738	*G. bulloides*	-0.21	15811
22SL	740	*G. bulloides*	0.14	15829
22SL	742	*G. bulloides*	-0.09	15846
22SL	744	*G. bulloides*	0.01	15863
22SL	746	*G. bulloides*	-0.11	15880
22SL	748	*G. bulloides*	0.44	15897
22SL	750	*G. bulloides*	0.37	15914
22SL	752	*G. bulloides*	0.35	15931
22SL	754	*G. bulloides*	0.06	15949
22SL	756	*G. bulloides*	0.19	15966
22SL	758	*G. bulloides*	0.11	15983
22SL	760	*G. bulloides*	0.07	16000*
22SL	762	*G. bulloides*	-0.23	16022
22SL	764	*G. bulloides*	-0.04	16044
22SL	766	*G. bulloides*	0.25	16066
22SL	770	*G. bulloides*	0.10	16110
22SL	772	*G. bulloides*	-0.43	16132
22SL	774	*G. bulloides*	0.13	16154
22SL	776	*G. bulloides*	0.20	16176
22SL	778	*G. bulloides*	-0.43	16198
22SL	780	*G. bulloides*	0.35	16220
22SL	782	*G. bulloides*	0.27	16242
22SL	784	*G. bulloides*	0.24	16264
22SL	786	*G. bulloides*	0.34	16289
22SL	788	*G. bulloides*	0.37	16317
22SL	790	*G. bulloides*	0.55	16346

22SL	792	*G. bulloides*	0.16	16374
22SL	794	*G. bulloides*	0.24	16403
22SL	796	*G. bulloides*	0.22	16430
22SL	800	*G. bulloides*	0.34	16487
22SL	802	*G. bulloides*	0.52	16515
22SL	804	*G. bulloides*	0.21	16543
22SL	806	*G. bulloides*	0.15	16572
22SL	808	*G. bulloides*	-0.14	16600*
22SL	810	*G. bulloides*	-0.87	16650
22SL	812	*G. bulloides*	0.25	16700
22SL	814	*G. bulloides*	0.11	16750
22SL	816	*G. bulloides*	-0.04	16800
22SL	818	*G. bulloides*	0.44	16850*
22SL	820	*G. bulloides*	-0.28	16854
22SL	822	*G. bulloides*	0.24	16858
22SL	824	*G. bulloides*	0.46	16862
22SL	826	*G. bulloides*	0.46	16866
22SL	828	*G. bulloides*	0.12	16870
22SL	830	*G. bulloides*	0.34	16874
22SL	832	*G. bulloides*	0.03	16878
22SL	834	*G. bulloides*	-0.05	16882
22SL	836	*G. bulloides*	0.13	16886
22SL	838	*G. bulloides*	0.18	16890
22SL	840	*G. bulloides*	-0.12	16894
22SL	842	*G. bulloides*	0.26	16898
22SL	844	*G. bulloides*	0.11	16920
22SL	846	*G. bulloides*	-0.01	16960
22SL	848	*G. bulloides*	0.28	17000
22SL	850	*G. bulloides*	0.15	17040
22SL	852	*G. bulloides*	0.24	17080
22SL	854	*G. bulloides*	0.27	17120
22SL	856	*G. bulloides*	-0.16	17160
22SL	858	*G. bulloides*	-0.18	17200
22SL	860	*G. bulloides*	-0.50	17240
22SL	862	*G. bulloides*	-0.20	17280
22SL	864	*G. bulloides*	-0.01	17320
22SL	866	*G. bulloides*	-0.30	17360
22SL	868	*G. bulloides*	-0.20	17400*
22SL	870	*G. bulloides*	-0.41	17440
22SL	872	*G. bulloides*	-0.20	17480
22SL	874	*G. bulloides*	0.02	17520
22SL	876	*G. bulloides*	-0.21	17560
22SL	878	*G. bulloides*	-0.33	17600
22SL	880	*G. bulloides*	-0.50	17640
22SL	882	*G. bulloides*	-0.12	17680
22SL	884	*G. bulloides*	-0.14	17720
22SL	886	*G. bulloides*	-0.10	17760
22SL	888	*G. bulloides*	0.20	17800
22SL	890	*G. bulloides*	0.32	17840

*Indicates the original radiocarbon dates

Table S3 Cores location

Core	Latitude	Longitude	Depth (m)
GeoB 7149-2	31°29.14'S	72°00.00'W	3086
GeoB 7163-7	36°25.54'S	73°35.73'W	537
GeoB 7167-6	36°27.19'S	73°55.50'W	2062
GeoB 7162-6	36°32.52'S	73°40.02'W	798
22SL	36°13.26'S	73°40.50'W	1001

Table S4 Reservoir ages used in different age models described in the text.

Age model	**>13 ka 14C**	**13-11 ka 14C**	**<11 ka 14C**
a	Rs from MD07-3088	Rs from MD07-3088	Rs from MD07-3088
b	Rs from MD07-3088	Rs from TR163-23	Rs from MD07-3088
c	Rs modern	Rs modern	Rs modern
d (core GeoB 7149-2)	Rs from TR163-23	Rs from TR163-23	Rs from ~32° S
Age model	**>13 ka 14C**	**13-11 ka 14C**	**<11 ka 14C**
a	Rs from MD07-3088	Rs from MD07-3088	Rs from MD07-3088
b	Rs from MD07-3088	Rs from TR163-23	Rs from MD07-3088
c	Rs modern	Rs modern	Rs modern
d (core GeoB 7149-2)	Rs from TR163-23	Rs from TR163-23	Rs from ~32° S

8.2 Supplementary Tables Chapter 3

Table S2. Sample of the TephraDatabaSet. Because of its size, only a sample is shown below. The full dataset can be accessed at https://github.com/consuelola/TephraDataBase/

Volcano	Event	Vei	Magnitude	SampleID	SampleObservationID	Location	Latitude	Longitude	Authors	TypeOfRegister	TypeOfAnalysis	AnalyticalTechnique	AnalyzedMaterial
Aguilera	A1			CH1 380 cm	CH1 380 cm	Lago Chandler	-52.7833	-72.9333	Kilian et al., 2003	Organic matter	Micro Analytical	Accelerator Mass Spectrometry	Organic macrofossil
Aguilera	A1			PROXAVZ1-A1-93-03	PROXAVZ1-A1-93-03_10	Lago Roca	-50.3667	-72.75	Smith et al., 2019	Pyroclastic material	Micro Analytical	EMP	Glass shards
Aguilera	A1			PROXAVZ1-A1-93-03	PROXAVZ1-A1-93-03_11	Lago Roca	-50.3667	-72.75	Smith et al., 2019	Pyroclastic material	Micro Analytical	EMP	Glass shards
Aguilera	A1			PROXAVZ1-A1-93-03	PROXAVZ1-A1-93-03_13	Lago Roca	-50.3667	-72.75	Smith et al., 2019	Pyroclastic material	Micro Analytical	EMP	Glass shards
Aguilera	A1			PROXAVZ1-A1-93-03	PROXAVZ1-A1-93-03_14	Lago Roca	-50.3667	-72.75	Smith et al., 2019	Pyroclastic material	Micro Analytical	EMP	Glass shards
Aguilera	A1			PROXAVZ1-A1-93-03	PROXAVZ1-A1-93-03_15	Lago Roca	-50.3667	-72.75	Smith et al., 2019	Pyroclastic material	Micro Analytical	EMP	Glass shards
Aguilera	A1			PROXAVZ1-A1-93-03	PROXAVZ1-A1-93-03_16	Lago Roca	-50.3667	-72.75	Smith et al., 2019	Pyroclastic material	Micro Analytical	EMP	Glass shards
Aguilera	A1			PROXAVZ1-A1-93-03	PROXAVZ1-A1-93-03_17	Lago Roca	-50.3667	-72.75	Smith et al., 2019	Pyroclastic material	Micro Analytical	EMP	Glass shards
Aguilera	A1			PROXAVZ1-A1-93-03	PROXAVZ1-A1-93-03_18	Lago Roca	-50.3667	-72.75	Smith et al., 2019	Pyroclastic material	Micro Analytical	EMP	Glass shards
Aguilera	A1			PROXAVZ1-A1-93-03	PROXAVZ1-A1-93-03_19	Lago Roca	-50.3667	-72.75	Smith et al., 2019	Pyroclastic material	Micro Analytical	EMP	Glass shards
Aguilera	A1			PROXAVZ1-A1-93-03	PROXAVZ1-A1-93-03_2	Lago Roca	-50.3667	-72.75	Smith et al., 2019	Pyroclastic material	Micro Analytical	EMP	Glass shards
Aguilera	A1			PROXAVZ1-A1-93-03	PROXAVZ1-A1-93-03_21	Lago Roca	-50.3667	-72.75	Smith et al., 2019	Pyroclastic material	Micro Analytical	EMP	Glass shards
Aguilera	A1			PROXAVZ1-A1-93-03	PROXAVZ1-A1-93-03_22	Lago Roca	-50.3667	-72.75	Smith et al., 2019	Pyroclastic material	Micro Analytical	EMP	Glass shards
Aguilera	A1			PROXAVZ1-A1-93-03	PROXAVZ1-A1-93-03_23	Lago Roca	-50.3667	-72.75	Smith et al., 2019	Pyroclastic material	Micro Analytical	EMP	Glass shards
Aguilera	A1			PROXAVZ1-A1-93-03	PROXAVZ1-A1-93-03_24	Lago Roca	-50.3667	-72.75	Smith et al., 2019	Pyroclastic material	Micro Analytical	EMP	Glass shards
Aguilera	A1			PROXAVZ1-A1-93-03	PROXAVZ1-A1-93-03_27	Lago Roca	-50.3667	-72.75	Smith et al., 2019	Pyroclastic material	Micro Analytical	EMP	Glass shards

Table S3. Sample of the MeasurementRuns file. Because of its size, only a sample is shown below. The full dataset can be accessed at https://github.com/consuelola/TephraDataBase/

MeasurementRun	StandardID	n	SiO2	SD_SiO2	RSD_SiO2	TiO2	SD_TiO2	RSD_TiO2	Al2O3	SD_Al2O3	RSD_Al2O3
Rawson2016	AGV-2	Not reported	60.09			1.05			17.22		
100415	ATHO-G	18	74.91	0.43	0.57	0.26	0.02	9.09	12.20	0.12	0.94
220115	ATHO-G	10	74.76	0.30	0.40	0.24	0.03	10.82	12.18	0.08	0.64
230115	ATHO-G	18	74.98	0.29	0.39	0.25	0.02	8.77	12.25	0.07	0.61
mr060912	ATHO-G	5	74.93156000	1.09501804	1.46	0.24300000	0.03460455	14.24	12.10698000	0.15265539	1.26
mr070912	ATHO-G	8	75.24642500	0.29533485	0.39	0.24396250	0.02601527	10.66	12.24655000	0.12302982	1.00
100912	ATHO-G	5	75.33524000	0.21156783	0.28	0.24066000	0.03956018	16.44	12.27026000	0.11874196	0.97
11112	ATHO-G	4	75.75340000	0.42429769	0.56	0.24807500	0.03633349	14.65	12.17170000	0.01331090	0.11
021112	ATHO-G	13	75.52461538	0.66728873	0.88	0.23826923	0.02167469	9.10	12.22366923	0.15541588	1.27
61112	ATHO-G	3	74.39310000	0.13248592	0.18	0.23963333	0.01866181	7.79	12.21066667	0.05688737	0.47
081112	ATHO-G	4	74.21940000	0.17714602	0.24	0.27410000	0.03268771	11.93	12.20840000	0.10204022	0.84
40413	ATHO-G	7	74.90948750	0.21453349	0.29	0.24588750	0.02910141	11.84	12.29621250	0.11144529	0.91
050413	ATHO-G	5	74.73658000	0.24933248	0.33	0.25424000	0.03168474	12.46	12.26250000	0.09604830	0.78
080713	ATHO-G	4	75.43860000	0.38049166	0.50	0.23635000	0.01753558	7.42	12.34242500	0.12633821	1.02
100713	ATHO-G	6	75.48293333	0.18470976	0.24	0.25023333	0.01218042	4.87	12.40908333	0.11891872	0.96
120713	ATHO-G	7	75.31630000	0.20007101	0.27	0.25217143	0.02571262	10.20	12.37018571	0.11457257	0.93
211013	ATHO-G	5	75.04326000	0.19305565	0.26	0.24156000	0.02156057	8.93	12.50240000	0.10798419	0.86
221013	ATHO-G	4	74.53330000	0.84505291	1.13	0.22640000	0.01421290	6.28	12.20265000	0.10012780	0.82
131213	ATHO-G	20	74.70665500	0.93061307	1.25	0.24835500	0.03592943	14.47	12.09372500	0.19329040	1.60
210114	ATHO-G	3	75.07866667	0.30050268	0.40	0.23543333	0.02285636	9.71	12.59426667	0.09137102	0.73
220114	ATHO-G	3	75.58473333	0.18786432	0.25	0.26936667	0.01446732	5.37	12.57163333	0.13527458	1.08
140214	ATHO-G	6	75.37331667	0.41669608	0.55	0.25465000	0.02557035	10.04	12.36903333	0.10362067	0.84
190314	ATHO-G	14	75.23771429	0.54851764	0.73	0.24114286	0.04712970	19.54	12.13885714	0.13518811	1.11
200314	ATHO-G	14	76.05907143	0.70295710	0.92	0.22457143	0.03690677	16.43	12.22864286	0.15813899	1.29
210314	ATHO-G	29	75.38658621	0.97448113	1.29	0.24103448	0.04599261	19.08	12.12586207	0.23940428	1.97

Table S4. Sample of the Reference file. Because of its size, only a sample is shown below. The full dataset can be accessed at https://github.com/consuelola/TephraDataBase/

Standard	Color	Comentarios	Authors	error	SiO2	σ_SiO2	RSD_SiO2	TiO2	σ_TiO2	RSD_TiO2
OREAS184	y		https://www.oreas.com/crm/oreas-184/	SD	42.19	0.81	1.91	0.06	0.00	6.90
GOR132-G	xkcd:vibrant purple		Jochum et al., 2006	95%CL	45.5	0.40	0.88	0.31	0.01	4.25
GOR128-G	deepskyblue		Jochum et al., 2006	95%CL	46.1	0.10	0.22	0.29	0.01	4.17
OREAS700	gold		https://www.oreas.com/crm/oreas-700/	SD	47.3	0.51	1.08	0.32	0.01	3.13
BIR-1	darkviolet		Jochum et al., 2016	95%CL	47.79	0.16	0.33	0.96	0.01	0.69
BHVO-2G	violet			SD	49.3	0.10	0.20	2.79	0.02	0.72
BHVO-2	rebeccapurple		Jochum et al., 2016	95%CL	49.6	0.14	0.28	2.73	0.08	2.97
BHVO-1	red		Jochum et al., 2016	95%CL	49.79	0.12	0.24	2.74	0.01	0.44
SY-4	saddlebrown		https://www.nrcan.gc.ca/our-natural-resources/minerals-mining/mining-resources/sy-4-diorite-gneiss/8025	95%CL	49.9	0.10		0.29	0.00	
KL2-G	xkcd:saffron		Jochum et al., 2006	95%CL	50.3	0.30	0.60	2.56	0.09	3.52
ML3B-G	teal		Jochum et al., 2006	95%CL	51.4	0.60	1.17	2.13	0.09	4.23
W-2	darkgreen		Jochum et al., 2016	95%CL	52.57	0.32	0.61	1.06	0.01	0.94
BCR-2	khaki		Jochum et al., 2016	95%CL	54	0.20	0.37	2.27	0.02	1.06
BCR-2G	palegreen			SD	54.4	0.40	0.74	2.27	0.04	1.76
JA-2	deeppink		Jochum et al., 2016	95%CL	56.39	0.23	0.41	0.67	0.01	1.05
T1-G	turquoise		Jochum et al., 2006	95%CL	58.6	0.40	0.68	0.76	0.02	2.25
AGV-2	lightcoral		Jochum et al., 2016	95%CL	59.14	0.58	0.98	1.05	0.02	2.19
CFA-47	xkcd:red pink	Not in GeoRem but published by the authors			61.63			0.42		
StHs6/80-G	Paleturquoise		Jochum et al., 2006	95%CL	63.7	0.50	0.78	0.70	0.02	2.99
JA-1	darkblue		Jochum et al., 2016	95%CL	64.43	0.31	0.48	0.85	0.02	2.12
NIST2711	xkcd:seafoam	Compiled values			65.11			0.51		
NIST610	xkcd:shamrock			95%CL	69.7	0.50	0.72			
NCS DC70009 (GBW07241)	hotpink		NACIS (http://www.ncsstandard.com/upload/file/201606088392.pdf)	71.27			0.04			
GBW 07113	teal	Compiled values	GeoRem		72.78			0.30		

8.3 Supplementary Tables Chapter 4

Table S1.- Globigerina bulloides δ18O and the resulting age model for core MD07-3098 with its respective 1σ and 2σ envelopes.

Depth MD07-3098 (cm)	δ18O *G. bull.* (‰)	Moving three point average δ18O *G. bull.*	Calendar age mean (ka BP)	1σ range (years)	2σ range (years)
0	1.85	1.92	24	139--136	255--288
10	1.88	1.84	88	219--72	333--182
20	2.02	1.81	153	289--3	462--78
30	1.60	1.71	219	380–59	606–5
40	1.71	1.70	365	519–193	879–108
50	1.35	1.67	491	690–296	1036–187
60	1.84	1.54	603	839–386	1138–258
70	1.86	1.38	705	952–472	1226–323
80	0.93	1.40	798	1040–555	1333–389
90	0.91	1.39	885	1116–637	1487–463
100	1.45	1.37	970	1185–718	1654–541
110	1.79	1.42	1056	1254–805	1828–621
120	1.77	1.65	1143	1326–898	2004–697
129	1.19	1.63	1226	1403–985	2163–776
139	2.04	1.59	1324	1500–1077	2331–892
150	1.36	1.44	1443	1660–1182	2506–1021
160	1.60	1.55	1662	1870–1405	2646–1240
170	1.01	1.53	1885	2158–1603	2778–1403
180	1.74	1.50	2106	2445–1785	2918–1546
190	1.96	1.45	2316	2684–1958	3061–1677
190	1.19	1.43	2316	2684–1958	3061–1677
200	1.36	1.23	2516	2878–2138	3200–1806
210	0.92	1.16	2727	3063–2356	3346–1938
220	0.71	1.18	2950	3257–2624	3504–2067
230	1.63	1.34	3176	3470–2904	3680–2186
240	1.27	1.48	3403	3714–3149	3908–2302
250	2.16	1.68	3545	3852–3302	4047–2416
260	1.61	1.66	3682	3990–3437	4209–2529
270	1.75	1.85	3818	4131–3565	4399–2641
280	1.50	1.77	3953	4277–3687	4597–2757
295	2.23	1.87	4154	4506–3857	4899–2932
310	1.76	1.96	4352	4737–4019	5183–3116
320	2.12	2.13	4481	4887–4123	5348–3252
330	2.18	2.12	4608	5029–4229	5497–3396
340	2.38	2.08	4731	5159–4336	5637–3559
350	2.18	2.09	4852	5274–4446	5783–3744
360	1.52	2.03	4973	5382–4563	5928–3936
370	2.20	1.99	5096	5485–4692	6063–4124
380	1.85	1.95	5223	5588–4836	6186–4307
390	2.17	2.06	5352	5690–4991	6301–4493
400	2.01	2.04	5485	5791–5153	6414–4687

410	2.10	1.83	5618	5894–5317	6527–4892
420	1.73	1.77	5754	6000–5480	6640–5105
430	1.49	1.76	5890	6109–5640	6754–5323
440	1.78	1.77	6027	6222–5792	6871–5544
450	1.72	1.76	6164	6344–5932	6991–5759
460	2.14	1.77	6302	6481–6064	7121–5931
470	1.65	1.81	6518	6753–6284	7272–6107
480	1.54	1.86	6732	7040–6463	7528–6251
490	2.00	1.81	6946	7237–6622	7888–6384
500	1.99	1.87	7099	7371–6777	7931–6512
510	1.89	1.95	7255	7504–6951	7953–6644
520	1.92	1.86	7417	7655–7123	7974–6778
530	1.94	1.84	7581	7814–7256	7998–6934
540	1.58	1.83	7680	7897–7384	8068–7123
550	1.86	1.82	7775	7997–7513	8243–7316
560	1.84	1.81	7851	8069–7639	8310–7496
570	1.87	1.78	7928	8138–7738	8380–7639
580	1.89	1.60	8053	8226–7887	8460–7785
590	1.43	1.54	8178	8345–8013	8555–7893
600	1.00	1.42	8293	8462–8124	8667–7989
610	1.50	1.30	8413	8592–8238	8801–8092
620	1.27	1.27	8537	8740–8343	8975–8190
630	1.33	1.23	8656	8847–8465	9113–8320
640	1.12	1.14	8770	8962–8567	9276–8429
650	1.19	1.01	8889	9106–8658	9455–8510
660	0.94	0.91	9075	9281–8855	9639–8706
670	0.46	0.92	9263	9477–9038	9823–8866
680	0.86	0.89	9448	9684–9206	10012–9008
690	1.16	0.97	9623	9869–9365	10207–9140
710	1.01	0.98	9810	10048–9551	10453–9298
720	1.34	0.97	9989	10206–9752	10693–9487
730	0.51	0.84	10176	10370–9962	10922–9722
750	0.84	0.80	10251	10438–10042	11009–9809
760	0.52	0.72	10437	10621–10226	11197–9991
800	0.91	1.01	10493	10682–10276	11248–10035
805	1.39	0.99	10597	10786–10387	11331–10112
810	0.71	0.84	10703	10901–10492	11412–10193
820	0.76	0.78	10915	11157–10683	11583–10366
830	0.50	1.00	11127	11412–10860	11782–10542
840	1.16	1.09	11334	11652–11036	11974–10709
850	1.89	1.11	11529	11854–11212	12127–10867
860	1.12	1.28	11723	12029–11409	12261–11018
870	0.88	1.29	11927	12200–11649	12396–11178
880	1.34	1.31	12139	12374–11920	12537–11336
890	1.23	1.41	12353	12557–12185	12702–11491
900	1.96	1.61	12568	12765–12411	12918–11666
910	1.67	1.62	12686	12863–12540	12988–11867
920	1.84	1.73	12798	12966–12666	13076–12075
930	1.40	1.76	12902	13056–12785	13166–12279
940	1.80	1.75	13013	13157–12902	13263–12446

950	2.09	1.72	13125	13276–13002	13393–12608
960	1.63	1.81	13189	13328–13078	13436–12746
970	1.71	1.76	13250	13384–13141	13499–12846
980	1.85	1.67	13310	13444–13196	13590–12912
990	1.54	1.69	13371	13522–13240	13701–12967
1000	1.64	1.67	13426	13594–13271	13821–13033
1010	1.67	1.51	13479	13681–13299	13994–13101
1020	1.38	1.46	13531	13773–13330	14168–13167
1030	1.36	1.58	13585	13886–13361	14354–13227
1040	1.44	1.56	13641	13998–13393	14559–13274
1050	2.06	1.72	13707	14193–13423	14735–13309
1060	1.56	1.84	13965	14387–13681	14919–13546
1070	2.20	1.94	14231	14613–13916	15128–13737
1080	1.92	1.96	14493	14889–14136	15340–13905
1100	2.15	2.13	14972	15364–14572	15678–14224
1110	1.91	2.32	15215	15568–14842	15830–14402
1120	2.55	2.44	15472	15778–15163	15991–14596
1130	2.67	2.71	15734	16005–15473	16183–14809
1140	2.90	2.95	16000	16270–15705	16445–15061
1150	3.53	3.04	16140	16372–15899	16529–15355
1160	3.11	3.15	16270	16480–16074	16636–15659
1170	3.01	3.21	16399	16595–16223	16758–15952
1180	3.19	3.10	16532	16742–16343	16902–16188
1190	3.19	3.09	16675	16864–16502	17011–16317
1200	2.98	3.04	16813	17001–16629	17154–16407
1210	2.82	3.07	16949	17149–16745	17292–16482
1220	3.11	3.11	17093	17333–16834	17478–16549
1230	3.36	3.11	17157	17381–16914	17517–16613
1240	3.16	3.18	17215	17427–16988	17563–16675
1270	3.11	3.14	17368	17573–17149	17768–16896
1280	3.17	3.09	17402	17595–17199	17780–16982
1310	2.92	3.09	17509	17682–17333	17832–17179
1330	3.15	3.03	17547	17715–17376	17864–17223

Table S2. Inividual glass shard analyses in core MD07-3100. Major elements analyzed by EPMA.

Cryptotephra	Core Depth	IGSN	SiO2 (wt.%)	TiO2 (wt.%)	Al2O3 (wt.%)	FeO (wt.%)	MnO (wt.%)	MgO (wt.%)	CaO (wt.%)	Na2O (wt.%)	K2O (wt.%)	Cl (wt.%)	P2O5 (wt.%)	Total (wt.%)
T1/100	150 cm	IECMF0068	55.06	1.6	16.4	8.07	0.17	3.94	7.47	4.23	1.4	0.09		98.44
T1/100	150 cm	IECMF0069	53.44	1.41	15.99	7.72	0.18	3.59	7.14	4.12	1.42	0.14		95.14
T1/100	150 cm	IECMF006A	53.74	1.29	15.79	7.16	0.19	3.97	7.29	4.4	1.54	0.11		95.47
T1/100	150 cm	IECMF006B	53.98	1.5	15.97	7.43	0.1	3.65	6.84	4.18	1.54	0.08		95.28
T1/100	150 cm	IECMF006C	54.91	1.53	15.83	7.81	0.08	3.19	6.03	4.67	1.73	0.09		95.86
T1/100	150 cm	IECMF006D	58.12	1.25	15.91	6.55	0.18	2.63	5.6	5.42	1.76	0.13		97.55
T1/100	150 cm	IECMF006E	63.03	1.16	14.04	7.34	0.21	1.03	3.36	4.17	2.83	0.23		97.4
T1/100	150 cm	IECMF006F	63.99	0.82	15.61	3.96	0.18	1	2.39	5.12	3.08	0.17		96.31
T1/100	150 cm	IECMF006G	65.09	0.76	15.9	3.53	0.16	0.82	2.46	5.53	3.21	0.16		97.63
T1/100	150 cm	IECMF006H	65.02	0.81	15.1	3.51	0.23	0.99	2.34	5.59	2.67	0.15		96.42
T1/100	150 cm	IECMF006I	64.88	0.64	15.36	3.43	0.19	0.69	1.97	4.82	3.24	0.17		95.39
T1/100	150 cm	IECMF006J	65.98	0.76	15.75	3.36	0.16	0.78	1.92	4.69	3.27	0.21		96.89
T1/100	150 cm	IECMF006K	65.64	0.69	15.54	3.45	0.12	0.67	1.76	4.88	3.36	0.15		96.27
T1/100	150 cm	IECMF006L	65.27	0.78	15.86	3.35	0.13	0.72	1.77	4.5	3.01	0.19		95.58
T1/100	150 cm	IECMF006M	66.79	0.69	15.59	3.53	0.11	0.67	2.03	4.46	3.36	0.19		97.43
T1/100	150 cm	IECMF006N	65.81	0.75	15.59	3.11	0.07	0.68	1.92	3.51	3.28	0.18		94.92
T1/100	150 cm	IECMF006O	67.88	0.34	13.73	3.23	0.17	0.21	1.88	5.75	3.42	0.17		96.77
T1/100	150 cm	IECMF006P	69.08	0.29	14.46	3.6	0.04	0.21	1.39	3.93	3.45	0.19		96.62
T1/100	150 cm	IECMF006Q	69.34	0.49	13.88	3.35	0.04	0.31	1.85	3.94	3.5	0.21		96.9
T1/100	150 cm	IECMF006S	57.43	1.21	15.83	7.13	0.19	2.49	4.93	4.46	2.02	0.24		95.92
T1/100	150 cm	IECMF006T	68.62	0.76	15.96	3.42	0.14	0.86	2.05	6.14	3.36	0.22		101.53
T1/100	150 cm	IECMF006U	58.11	1.48	16.95	8.02	0.17	3.17	6.51	4.85	1.85	0.14		101.26
T1/100	150 cm	IECMF006W	68.62	0.71	16.02	3.63	0.11	0.7	1.83	6.17	3.24	0.17		101.2
T1/100	150 cm	IECMF006X	67.12	0.74	15.87	3.27	0.25	0.65	1.96	5.19	3.42	0.19		98.67
T1/100	150 cm	IECMF006Y	67.42	0.82	16.27	3.74	0.13	1.07	2.91	5.45	2.96	0.15		100.91
T2/100	330 cm	IECMF006Z	52.99	1.58	15.53	9.98	0.2	4.98	8.28	3.56	0.68	0.05		97.82
T2/100	330 cm	IECMF0070	52.52	1.37	15.31	9.83	0.16	4.96	8.03	3.37	0.75	0.06		96.34
T2/100	330 cm	IECMF0071	61.43	1.36	14.69	6.97	0.32	1.34	4.13	4.62	2.67	0.21		97.74
T2/100	330 cm	IECMF0072	62.51	0.98	15.6	6.09	0.16	1.26	3.57	4.65	2.76	0.16		97.73

T2/100	330 cm	IECMF0073	62.17	1	15.27	6.62	0.12	1.15	3.62	4.28	2.56	0.14	96.93
T2/100	330 cm	IECMF0074	63.47	0.47	17.65	3.87	0.17	0.61	4.7	5.01	2.19	0.12	98.26
T2/100	330 cm	IECMF0075	62.76	1.02	15.44	5.65	0.21	1.19	3.6	4.31	2.69	0.18	97.06
T2/100	330 cm	IECMF0076	62.57	0.93	15.39	5.82	0.15	1.15	3.6	3.94	2.55	0.15	96.26
T2/100	330 cm	IECMF0077	63.06	0.97	15.48	5.99	0.25	1.25	3.63	3.6	2.65	0.1	96.98
T2/100	330 cm	IECMF0078	62.12	0.99	14.95	5.59	0.18	1.24	3.74	3.98	2.48	0.17	95.45
T2/100	330 cm	IECMF0079	64.1	1.05	15.39	6.01	0.11	1.18	3.59	4.19	2.56	0.1	98.27
T2/100	330 cm	IECMF007A	63.39	0.99	15.15	6	0.15	1.25	3.67	3.53	2.59	0.15	96.86
T2/100	330 cm	IECMF007C	65.4	0.64	15.19	4.68	0.21	0.88	3.06	4.52	2.24	0.18	97
T2/100	330 cm	IECMF007E	68.47	0.51	15.34	3.48	0.07	0.54	2	4.18	3.04	0.14	97.77
T2/100	330 cm	IECMF007F	70.1	0.17	13.47	3.18	0.13	0.15	1.12	4.98	3.81	0.25	97.37
T2/100	330 cm	IECMF007G	66.76	0.52	15.61	4.73	0	0.78	3.39	5.53	2.99	0.27	100.57
T2/100	330 cm	IECMF007H	68.7	0.55	15.57	3.6	0.14	0.6	2.27	4.66	3.11	0.19	99.38
T2/100	330 cm	IECMF007I	67.93	0.25	17.72	2.18	0.21	0.16	2.89	6.06	2.41	0.21	100.02
T2/100	330 cm	IECMF007J	60.95	0.89	19.17	4.67	-0.03	1.16	6.28	4.69	1.48	0.17	99.46
T2/100	330 cm	IECMF007K	63.47	1.02	15.03	5.46	-0.03	1.08	3.45	4.79	2.5	0.12	96.92
T2/100	330 cm	IECMF007L	63.66	1	15.05	5.95	0.14	1.32	3.7	4.14	2.56	0.24	97.77
T2/100	330 cm	IECMF007M	65.93	0.73	15.18	4.59	0.05	0.92	2.64	5.3	2.55	0.25	98.14
T2/100	330 cm	IECMF007N	68.72	0.3	15.4	3.03	0.17	0.22	2.04	5.22	3.65	0.3	99.06
T2/100	330 cm	IECMF007O	55.68	2.49	13.72	10.82	0.2	3.53	6.72	3.75	1.4	0.1	98.41
T3/100	380 cm	IECMF007Q	53.13	2.78	13.96	12.5	0.32	2.08	6.32	3.84	2.03	0.15	0.94	98.07
T3/100	380 cm	IECMF007R	54.53	2.7	13.05	14.29	0.1	2.92	5.2	4.52	1.7	0.17	1	100.17
T3/100	380 cm	IECMF007S	53.54	2.32	14.27	11.16	0.31	3.09	6.48	3.39	1.5	0.11	0.75	96.91
T3/100	380 cm	IECMF007T	54.03	2.68	13.65	11.19	0.26	3.24	6.98	2.88	1.86	0.12	0.88	97.76
T3/100	380 cm	IECMF007U	53.97	2.32	12.91	12.13	0.27	3.26	6.64	3.19	1.88	0.07	0.75	97.38
T3/100	380 cm	IECMF007V	56.05	2.89	13.12	12.75	0.23	2.82	6.37	3.58	1.76	0.11	0.91	100.6
T3/100	380 cm	IECMF007W	55.77	2.86	13.84	10.42	0.29	3.37	7.3	3.24	2.07	0.11	0.83	100.09
T3/100	380 cm	IECMF007X	53.73	2.67	11.4	12.06	0.24	3.54	6.82	2.67	2.03	0.18	1.02	96.36
T3/100	380 cm	IECMF007Y	53.86	2.65	13.83	11.59	0.16	2.9	6.5	3.34	1.66	0.09	96.59
T3/100	380 cm	IECMF007Z	55.94	2.26	13.26	11.76	0.29	3.5	5.9	3.83	1.97	0.1	0.9	99.71
T3/100	380 cm	IECMF0080	55.34	1.98	17.62	8.19	0.17	1.44	6.63	4.22	1.36	0.11	0.8	97.87
T3/100	380 cm	IECMF0081	60.23	1.25	15.05	7.7	0.28	1.56	4.42	4.16	2.67	0.17	97.47

T3/100	380 cm	IECMF0082	59.83	1.55	14.43	7.24	0.29	1.79	4.46	3.62	2.43	0.16	95.79
T3/100	380 cm	IECMF0083	61.05	1.77	12.85	8.99	0.24	2.01	4.23	3.65	2.04	0.15	96.99
T3/100	380 cm	IECMF0085	61.57	0.86	15.3	5.6	0.19	1.67	4.07	3.99	2.07	0.14	95.47
T3/100	380 cm	IECMF0086	64.53	0.81	14.98	5.96	0.26	1.1	3.23	4.4	2.65	0.19	0.19	98.31
T3/100	380 cm	IECMF0087	64.73	0.73	14.81	4.96	0.09	0.97	3.14	3.96	2.95	0.21	96.54
T3/100	380 cm	IECMF0088	66.02	0.76	15.06	5.07	0.09	0.67	2.48	3.99	3.38	0.23	97.75
T3/100	380 cm	IECMF008A	66.46	0.57	15.72	3.71	0.07	0.69	2.36	4.76	2.89	0.21	97.45
T3/100	380 cm	IECMF008B	66.01	0.7	15.23	4.16	0.14	0.65	2.29	4.24	3.1	0.17	96.68
T3/100	380 cm	IECMF008C	66.86	0.32	15.7	3.87	0.19	0.65	2.24	4.68	3.14	0.17	97.82
T3/100	380 cm	IECMF008D	67.3	0.49	15.69	4.05	0.03	0.61	2.38	4.02	3	0.14	97.71
T3/100	380 cm	IECMF008E	68.53	0.26	13.77	3.67	0.12	0.21	1.4	4.03	3.61	0.2	95.79
T3/100	380 cm	IECMF008F	70.05	0.3	13.74	3.77	0.17	0.27	1.74	2.87	3.56	0.19	0.14	96.79
T4/100	450 cm	IECMF008G	52.23	1.72	15.57	9.33	0.2	3.87	7.3	3.83	1.31	0.1	95.46
T4/100	450 cm	IECMF008H	52.78	1.65	15.79	9.36	0.22	3.61	7.21	3.61	1.3	0.09	95.61
T4/100	450 cm	IECMF008I	53.76	1.72	15.44	9.86	0.26	3.2	6.6	3.71	1.68	0.17	96.39
T4/100	450 cm	IECMF008J	54.45	1.97	15.46	10.02	0.15	3.21	6.98	3.61	1.7	0.08	97.63
T4/100	450 cm	IECMF008K	56.59	1.52	14.68	10.08	0.22	4.25	7.89	3.4	0.82	0.07	99.51
T4/100	450 cm	IECMF008L	55.67	1.16	14.28	9.62	0.29	4.24	7.99	3.3	0.75	0.09	97.39
T4/100	450 cm	IECMF008M	55.48	1.92	14.93	9.57	0.19	3.09	6.1	3.64	1.86	0.12	96.9
T4/100	450 cm	IECMF008N	57.63	1.55	14.18	11.53	0.17	3.03	4.31	3.93	1.36	0.09	97.78
T4/100	450 cm	IECMF008O	58.64	0.87	15.26	7.69	0.2	1.92	4.81	4.22	2.3	0.17	96.08
T4/100	450 cm	IECMF008Q	61	1.03	16.4	6.73	0.13	1.4	4.88	4.15	2.48	0.13	98.33
T4/100	450 cm	IECMF008R	64.48	0.72	16.83	5.21	0.15	1.1	4.49	3.81	2.27	0.09	99.15
T4/100	450 cm	IECMF008S	65.59	0.12	19.64	2.09	0.04	0.13	3.79	5.88	1.98	0.1	99.34
T4/100	450 cm	IECMF008T	65.04	0.72	14.54	5.17	0.24	0.79	2.62	4.12	3.26	0.16	96.66
T4/100	450 cm	IECMF008U	66.18	0.68	14.38	5.13	0.18	1.25	2.05	4.25	3.2	0.14	97.44
T4/100	450 cm	IECMF008V	67.14	0.6	15.63	3.51	0.22	0.77	2.49	3.22	3.12	0.18	96.88
T4/100	450 cm	IECMF008W	67.54	0.31	15.24	3.39	0.1	0.2	2.05	4.88	3.35	0.18	97.25
T4/100	450 cm	IECMF008X	68.41	0.37	14.12	3.39	0.03	0.2	1.54	3.55	3.55	0.2	95.35
T4/100	450 cm	IECMF008Y	69.61	0.33	14.07	3.44	0.18	0.19	1.43	3.8	3.53	0.22	96.81
T4/100	450 cm	IECMF008Z	69.26	0.22	13.61	3.31	0.11	0.23	1.58	4	3.46	0.24	96.03
T4/100	450 cm	IECMF0090	67.72	0.33	14.85	3.42	0.05	0.22	1.55	5.23	3.19	0.16	96.73

T4/100	450 cm	IECMF0091	51.7	1.88	12.37	10.85	0.31	6.19	10.97	2.8	1.16	0.13	98.35
T4/100	450 cm	IECMF0092	67.13	0.57	14.73	4.67	0.17	0.53	2.17	5.65	2.86	0.17	98.66
T4/100	450 cm	IECMF0093	56.74	1.96	15.27	9.78	0.19	3.16	6.24	3.73	1.9	0.12	99.1
T4/100	450 cm	IECMF0094	70.98	0.44	14.25	3.51	0.09	0.24	1.45	4.96	3.23	0.21	99.34
T4/100	450 cm	IECMF0095	59.48	1.09	17.49	6.96	0.34	1.68	6.62	4.25	1.42	0.12	99.44
T4/100	450 cm	IECMF0096	55.14	1.5	15.5	8.91	0.12	3.09	6.11	4.36	1.57	0.11	96.41
T5/100	490 cm	IECMF0097	51.91	2.31	14.8	11.01	0.17	3.33	7.48	3.54	1.38	0.1	96.03
T5/100	490 cm	IECMF0098	52.04	2.24	13.21	12.49	0.24	4.15	6.07	3.3	1.52	0.15	95.41
T5/100	490 cm	IECMF009A	53.38	2.47	14.24	12.44	0.14	3	6.28	3.2	1.25	0.08	96.49
T5/100	490 cm	IECMF009B	55.8	1.88	14.99	8.6	0.24	2.53	5.04	3.88	2.18	0.13	95.28
T5/100	490 cm	IECMF009C	59.52	1.18	14.72	8.15	0.08	2.19	4.63	3.95	2.22	0.11	96.74
T5/100	490 cm	IECMF009D	61.1	1.08	14.97	6.89	0.06	1.95	4.47	4.01	2.43	0.09	97.06
T5/100	490 cm	IECMF009E	65.25	0.64	15.55	4.21	0.11	0.67	2.39	4.14	2.88	0.15	95.99
T5/100	490 cm	IECMF009F	66.07	0.54	15.76	4.07	0.08	0.6	2.27	3.94	3.15	0.16	96.63
T5/100	490 cm	IECMF009G	66.63	0.4	15.39	3.6	0.15	0.73	2.44	4.52	3.1	0.25	97.21
T5/100	490 cm	IECMF009H	66.21	0.67	15.58	3.45	0.13	0.67	2.37	4.09	3.12	0.17	96.46
T5/100	490 cm	IECMF009I	66.66	0.71	14.44	3.77	0.15	0.57	2.07	4.86	3.29	0.2	96.73
T5/100	490 cm	IECMF009J	66.91	0.48	15.37	3.7	0.07	0.69	2.16	4.27	3	0.18	96.82
T5/100	490 cm	IECMF009K	68.48	0.2	13.93	3.88	0.13	0.33	1.84	4.08	3.54	0.19	96.6
T5/100	490 cm	IECMF009L	73.08	0.21	12.62	1.35	0	0.21	1.3	3.4	3.67	0.21	96.05
T5/100	490 cm	IECMF009M	69.22	0.59	16.52	3.89	0.13	0.65	2.22	5.21	3.13	0.19	101.75
T5/100	490 cm	IECMF009N	72.12	0.2	15.7	3.04	0.13	0.22	1.87	5.33	3.25	0.19	102.06
T5/100	490 cm	IECMF009O	67.01	0.65	15.53	3.87	0.13	0.65	2.28	5.27	2.77	0.33	98.48
T5/100	490 cm	IECMF009P	59.06	0.85	17.49	5.69	0	2.03	6.66	4.44	1.7	0.17	98.1
T5/100	490 cm	IECMF009Q	54.62	2.42	16.54	11.6	0.11	3.11	6.94	4.47	1.3	0.08	101.18
T5/100	490 cm	IECMF009R	55.61	2.22	14.53	10.62	0.33	3.68	8.12	3.95	1.46	0.12	100.63
T6/100	550 cm	IECMF009T	52.3	2.38	13.96	12.98	0.35	3.82	7.13	3.23	1.29	0.13	97.57
T6/100	550 cm	IECMF009U	53.46	2.16	12.87	13.66	0.21	4.34	6.4	3.14	1.5	0.12	97.88
T6/100	550 cm	IECMF009V	54.23	2.07	16.57	8.6	0.2	2.83	7.67	3.7	1.37	0.04	97.29
T6/100	550 cm	IECMF009W	54.29	2.09	14.94	10.09	0.24	2.7	7.45	3.34	1.46	0.15	96.75
T6/100	550 cm	IECMF009X	54.95	2.52	13.88	11.21	0.21	2.68	6.43	3.63	2.05	0.06	97.61
T6/100	550 cm	IECMF009Y	56.38	1.49	15.54	8.52	0.2	3.1	6.02	3.89	1.71	0.13	96.99

T6/100	550 cm	IECMF009Z	58.43	1.2	16.67	8.12	0.21	2.66	6.08	4.31	0.98	0.18	98.83
T6/100	550 cm	IECMF00A0	60.91	0.86	11.97	7.84	0.25	2.88	4.92	3.74	2.45	0.15	95.99
T6/100	550 cm	IECMF00A1	63.68	0.86	14.52	5.95	0.13	1.05	3.22	4.33	2.98	0.19	96.92
T6/100	550 cm	IECMF00A2	63.22	0.81	14.56	5.29	0.16	1.03	2.96	3.85	3.03	0.18	95.1
T6/100	550 cm	IECMF00A3	66.13	0.63	14.17	4.96	0.26	0.86	2.26	3.81	3.16	0.21	96.46
T6/100	550 cm	IECMF00A4	67.66	0.28	14.38	3.79	0.1	0.26	1.64	4.35	3.25	0.23	95.95
T6/100	550 cm	IECMF00A5	67.22	0.3	14.14	3.7	0.14	0.2	1.53	4.35	3.39	0.21	95.19
T6/100	550 cm	IECMF00A6	68.12	0.39	13.75	3.81	0.16	0.27	1.37	4.31	3.49	0.19	95.87
T6/100	550 cm	IECMF00A7	68.72	0.25	14.1	3.31	0	0.25	1.56	4.16	3.37	0.21	95.93
T6/100	550 cm	IECMF00A9	68.7	0.28	13.48	3.36	0.16	0.22	1.22	4	3.59	0.23	95.23
T6/100	550 cm	IECMF00AA	67.18	0.34	14.35	3.14	0.07	0.28	1.6	5.1	2.87	0.22	95.16
T6/100	550 cm	IECMF00AB	52.65	0.63	19.15	5	0.01	3.94	10.17	3.78	0.44	0.02	95.81
T6/100	550 cm	IECMF00AC	67.15	0.26	14.21	3.76	0.07	0.21	1.45	4.64	3.07	0.18	95.01
T6/100	550 cm	IECMF00AD	67.15	0.26	14.21	3.76	0.07	0.21	1.45	4.64	3.07	0.18	95.01
T6/100	550 cm	IECMF00AE	67.9	0.43	14.15	3.61	0.08	0.18	1.44	4.93	3.21	0.16	96.09
T6/100	550 cm	IECMF00AF	54.18	1.78	15.9	8.97	0.18	3.44	6.98	4.31	1.43	0.12	97.28
T6/100	550 cm	IECMF00AG	60.79	1.02	19.33	4.92	0.18	0.87	5.55	5.26	1.77	0.1	99.78
T6/100	550 cm	IECMF00AH	52.33	1.63	15.3	10.73	0.26	3.61	8.33	3.68	1.12	0.09	97.07
T6/100	550 cm	IECMF00AI	64.48	0.66	15	4.7	0.11	0.79	2.67	4.55	2.73	0.2	95.88
T6/100 (base)	580 cm	IECMF00AJ	53.88	3	14.68	13.27	0.16	2.82	6.06	3.79	1.62	0.11	0.85	100.23
T6/100 (base)	580 cm	IECMF00AK	53.59	2.42	14.29	11.19	0.19	3.63	7.76	3.79	1.4	0.12	0.88	99.28
T6/100 (base)	580 cm	IECMF00AL	54.48	2.01	15.98	9.47	0.25	3.27	8.72	3.58	1.1	0.07	0.74	99.68
T6/100 (base)	580 cm	IECMF00AM	54.47	1.87	15.01	10.77	0.25	3.21	6.17	3.54	1.62	0.15	0.57	97.64
T6/100 (base)	580 cm	IECMF00AN	55.21	2.51	12.81	10.72	0.27	4.06	6.82	3.28	1.97	0.11	0.74	98.51
T6/100 (base)	580 cm	IECMF00AO	55.38	2.81	12.6	12.72	0.32	2.99	5.52	3.17	1.83	0.21	0.85	98.41
T6/100 (base)	580 cm	IECMF00AP	54.56	1.78	15.71	8.82	0.17	3.2	6.61	3.64	1.59	0.15	0.61	96.84
T6/100 (base)	580 cm	IECMF00AQ	55.42	1.61	15.79	8.77	0.17	3.01	6.45	4.27	1.68	0.11	0.55	97.83

T6/100 (base)	580 cm	IECMF00AR	58.03	1.49	14.85	9.21	0.26	2.39	5.37	3.34	2.2	0.2	0.52	97.88
T6/100 (base)	580 cm	IECMF00AS	65.31	0.52	14.36	5.15	0.17	1.01	2.98	3.44	2.84	0.2	0.4	96.38
T6/100 (base)	580 cm	IECMF00AT	66.5	0.92	14.28	5.08	0.18	0.78	2.89	2.91	3.17	0.18	0.45	97.35
T6/100 (base)	580 cm	IECMF00AU	69.16	0.5	14.53	3.97	0.16	0.51	1.98	2.91	3.46	0.15	0.11	97.45
T6/100 (base)	580 cm	IECMF00AV	69.29	0.66	13.84	4.26	0.16	0.67	2.17	2.66	3.3	0.16	0.09	97.26
T7/100	610 cm	IECMF00AX	53.11	2.08	13.23	12.35	0.24	3.09	6.42	3.43	1.81	0.12		95.88
T7/100	610 cm	IECMF00AY	53.38	2.38	13.13	10.74	0.16	4.42	7.24	3.51	1.26	0.13		96.34
T7/100	610 cm	IECMF00AZ	53.8	1.55	15.45	9.16	0.13	3.34	6.48	3.72	1.53	0.11		95.25
T7/100	610 cm	IECMF00B0	55.4	3.03	14.48	12.07	0.28	0.99	4.82	4.18	2.26	0.15		97.67
T7/100	610 cm	IECMF00B1	57.88	1.25	14.76	8.48	0.36	2.36	4.98	4.11	2	0.14		96.32
T7/100	610 cm	IECMF00B2	59.58	1.29	15.03	7.31	0.18	2.07	4.57	3.89	2.21	0.14		96.27
T7/100	610 cm	IECMF00B3	59.88	1.08	14.32	6.49	0.13	1.33	5.77	3.83	2.97	0.17		95.97
T7/100	610 cm	IECMF00B4	60.8	1.11	13.51	6.78	0.17	2.49	3.88	3.79	2.63	0.14		95.3
T7/100	610 cm	IECMF00B5	62.11	0.75	14.62	6.71	0.13	1.52	3.72	4.61	2.68	0.12		96.97
T7/100	610 cm	IECMF00B6	64.07	0.6	16.48	4.18	0.18	0.81	3.61	4.41	2.47	0.18		96.98
T7/100	610 cm	IECMF00B7	62.83	0.86	14.8	5.24	0.18	1.1	2.96	4.15	2.74	0.16		95.02
T7/100	610 cm	IECMF00B9	66.22	0.41	15.71	4.05	0.16	0.47	2.67	4.09	2.97	0.19		96.94
T7/100	610 cm	IECMF00BA	67.51	0.2	15.22	3.01	0.18	0.12	2.21	5.06	2.58	0.17		96.24
T7/100	610 cm	IECMF00BB	67.82	0.25	14.1	3.78	0.09	0.15	1.4	4.52	3.67	0.2		95.97
T7/100	610 cm	IECMF00BC	67.59	0.23	13.64	3.92	0.14	0.24	1.39	4.44	3.53	0.22		95.33
T7/100	610 cm	IECMF00BD	67.97	0.39	13.95	3.45	0.2	0.27	1.58	4.24	3.56	0.19		95.81
T7/100	610 cm	IECMF00BE	69.09	0.35	13.94	3.87	0.11	0.19	1.41	3.98	3.48	0.19		96.6
T7/100	610 cm	IECMF00BF	68.81	0.24	13.98	3.77	0.18	0.26	1.3	3.91	3.56	0.2		96.2
T7/100	610 cm	IECMF00BG	68.7	0.31	13.96	2.97	0.11	0.23	1.5	4.23	3.45	0.18		95.64
T7/100	610 cm	IECMF00BH	69.59	0.5	13.81	3.58	0.12	0.21	1.32	4.11	3.4	0.2		96.84
T7/100	610 cm	IECMF00BJ	70.96	0.27	14.37	3.78	0.3	0.24	1.34	5.24	3.53	0.2		100.23
T7/100	610 cm	IECMF00BK	69.54	0.52	15.02	4.18	0.06	0.5	2.13	5.05	3.6	0.25		100.84
T7/100	610 cm	IECMF00BL	66.77	0.84	14.87	5.42	0.13	1.15	3.07	4.77	2.64	0.23		99.88
T7/100	610 cm	IECMF00BM	55.87	1.69	15.85	8.19	0.22	2.99	6.56	4.15	1.89	0.13		97.54

T8/100	700 cm (top)	IECMF00BN	52.12	2.23	11.67	12.08	0.38	5.98	9.18	2.86	1.03	0.04	0.71	98.28
T8/100	700 cm (top)	IECMF00BO	53.55	2.47	14.24	11.1	0.26	3.15	6.91	3.82	1.48	0.11	0.74	97.83
T8/100	700 cm (top)	IECMF00BP	54.83	2.5	14.25	11.1	0.27	2.21	6.4	3.52	1.52	0.08	0.74	97.41
T8/100	700 cm (top)	IECMF00BQ	58.71	1.29	15.88	7.38	0.2	2.35	5.66	4.52	1.76	0.13	0.4	98.28
T8/100	700 cm (top)	IECMF00BR	61.47	1.01	14.5	6.21	0.33	1.43	3.59	3.76	2.64	0.17	0.4	95.5
T8/100	700 cm (top)	IECMF00BS	67.03	0.34	14.62	4.07	0.16	0.57	2.39	3.94	2.98	0.18	0.05	96.32
T8/100	700 cm (top)	IECMF00BT	67.96	0.25	13.76	3.85	0.14	0.33	1.6	5	3.42	0.2	0.12	96.64
T8/100	700 cm (top)	IECMF00BU	68.15	0.3	14.18	2.91	0.18	0.15	1.69	5.48	3.35	0.18	0.12	96.72
T8/100	700 cm (top)	IECMF00BV	68.92	0.45	14.12	3.57	0.09	0.28	1.62	4.03	3.5	0.16	0.13	96.88
T8/100	740 cm (top)	IECMF00BW	52.67	2.21	15.75	10.07	0.24	3.59	6.99	3.42	1.53	0.09		96.56
T8/100	740 cm (top)	IECMF00BY	55.25	1.87	17.24	9.22	0.14	3.19	7.6	4.46	1.34	0.16		100.48
T8/100	740 cm (top)	IECMF00BZ	52.41	2.54	12.55	10.98	0.22	3.64	7.21	3.34	1.57	0.11	0.67	95.24
T8/100	740 cm (top)	IECMF00C0	53.37	2.2	15.17	10.09	0.19	3.73	6.9	3.08	1.63	0.11		96.47
T8/100	740 cm (top)	IECMF00C2	54.68	2.4	14.13	9.57	0.24	4.66	7.3	3.47	1.52	0.08		98.05
T8/100	740 cm (top)	IECMF00C3	53.82	2.52	13.53	11.42	0.22	3.24	6.95	2.81	1.76	0.11		96.4
T8/100	740 cm (top)	IECMF00C5	53.88	2.22	15.83	9.09	0.23	2.83	6.18	3.63	1.78	0.13		95.79
T8/100	740 cm (top)	IECMF00C6	54.49	2.09	16.17	8.46	0.14	3.17	6.56	3.6	1.8	0.11		96.6
T8/100	740 cm (top)	IECMF00C7	55.2	2.31	15.73	9.23	0.21	3.25	6.36	3.57	1.71	0.1		97.67
T8/100	740 cm (top)	IECMF00C8	54.76	1.98	15.55	9.25	0.29	3	6.14	3.72	1.84	0.11		96.62
T8/100	740 cm (top)	IECMF00C9	54.95	2.08	15.62	9.06	0.24	3.08	6.2	3.77	1.73	0.12		96.85

T8/100	740 cm (top)	IECMF00CA	55.73	1.69	15.96	9.4	0.23	3.13	6.3	3.99	1.58	0.19	98.21
T8/100	740 cm (top)	IECMF00CB	54.27	1.79	13.34	8.33	0.09	3.84	7.62	3.93	1.76	0.12	95.08
T8/100	740 cm (top)	IECMF00CC	54.67	1.51	12.29	11.15	0.35	4.49	6.02	3.29	1.79	0.15	95.72
T8/100	740 cm (top)	IECMF00CD	56.03	1.34	16.57	6.76	0.15	2.9	6.44	3.59	1.3	0.11	95.2
T8/100	740 cm (top)	IECMF00CE	58.13	2.05	14.58	8.37	0.18	1.88	4.7	3.96	2.66	0.15	96.67
T8/100	740 cm (top)	IECMF00CG	65.94	0.72	14.49	4.8	0.12	0.84	2.77	4.36	3.06	0.17	97.27
T8/100	740 cm (top)	IECMF00CH	66.53	0.66	14.96	4.83	0.15	0.69	2.61	4.06	2.89	0.18	97.55
T8/100	740 cm (top)	IECMF00CI	65.51	0.61	14.38	4.4	0.15	0.73	2.62	4.18	3.22	0.19	96
T8/100	740 cm (top)	IECMF00CJ	65.14	0.6	14.49	4.43	0.21	0.71	2.54	4.02	2.91	0.2	95.24
T8/100	740 cm (top)	IECMF00CK	66.47	0.56	14.43	4.25	0.05	0.66	1.89	4.15	3.23	0.13	0.21	96.04
T8/100	740 cm (top)	IECMF00CM	66.69	0.63	14.4	3.9	0.15	0.42	1.8	4.25	3.5	0.22	95.97
T8/100	740 cm (top)	IECMF00CO	68.65	0.13	14.83	3.62	0.18	0.19	1.54	4.04	3.06	0.16	96.41
T8/100	740 cm (top)	IECMF00CP	68.18	0.38	13.59	3.51	0.18	0.21	1.28	3.95	3.56	0.28	95.13
T8/100	740 cm (top)	IECMF00CR	69.19	0.21	13.84	3.68	0.14	0.22	1.42	3.78	3.58	0.25	96.3
T8/100	740 cm (top)	IECMF00CS	69.44	0.33	14.05	3.21	0.11	0.2	1.4	3.54	3.49	0.27	96.04
T8/100	740 cm (top)	IECMF00CT	69.55	0.13	13.92	3.04	0.09	0.17	1.35	3.77	3.5	0.23	95.75
T8/100	740 cm (top)	IECMF00CU	54.33	2.16	15.05	10.2	0.03	2.92	6.64	3.44	1.5	0.25	96.53
T8/100	740 cm (top)	IECMF00CV	56.42	2.35	16.12	10.37	0.3	2.49	6.72	4.43	1.57	0.11	100.86
T8/100	740 cm (top)	IECMF00CW	61.41	1.67	14.98	8.19	0.22	2.19	4.66	4.42	2.84	0.2	100.78
T8/100	740 cm (top)	IECMF00CX	68.21	0.33	15.02	3.73	0.14	0.34	1.96	5.58	3	0.18	98.49

T8/100	740 cm (top)	IECMF00CY	66.88	0.23	15.99	2.98	0.15	0.17	2.15	5.03	2.72	0.25	96.55
T8/100	740 cm (top)	IECMF00CZ	67.05	0.39	14.59	3.63	0.12	0.26	1.57	5.51	3.13	0.2	96.46
T8/100	740 cm (top)	IECMF00D0	66.79	0.28	14.25	3.72	0.11	0.23	1.53	5.08	3.04	0.21	95.24
T8/100	740 cm (top)	IECMF00D1	69.58	0.39	14.67	3.5	0.16	0.26	1.47	4.69	3.33	0.27	98.33
T8/100	740 cm (top)	IECMF00D3	53.65	1.89	15.93	10.44	0.05	4.8	8.13	3.55	1.23	0.05	99.73
T8/100	740 cm (top)	IECMF00D5	54.72	1.77	15.73	8.97	0.39	4.21	8.19	3.98	1.38	0.19	99.53
T8/100	740 cm (top)	IECMF00D6											
T9/100	830 cm	IECMF00D7	51.71	1.78	13.69	9.92	0.16	4.59	8.32	3.1	1.53	0.15	94.96
T9/100	830 cm	IECMF00D8	52.44	1.34	14.1	10.01	0.2	4.71	8.3	3.22	0.91	0	95.24
T9/100	830 cm	IECMF00D9	55.29	1.77	15.61	8.25	0.36	3.2	6.56	4.08	1.6	0.11	96.83
T9/100	830 cm	IECMF00DA	57.16	1.43	15.7	9.67	0.14	3.21	6.58	3.77	1.47	0.05	99.18
T9/100	830 cm	IECMF00DB	56.08	1.3	15.14	9.03	-0.04	3.37	7	3.89	0.9	0.1	96.77
T9/100	830 cm	IECMF00DC	56.9	1.6	15.21	8.86	0.16	3.19	6.55	3.47	1.5	0.12	97.56
T9/100	830 cm	IECMF00DD	56.67	1.73	15.13	8.43	0.22	2.89	6.14	3.55	1.82	0.11	96.7
T9/100	830 cm	IECMF00DE	57.1	1.4	15.39	8.02	0.09	3.09	6.43	3.48	1.53	0.12	96.64
T9/100	830 cm	IECMF00DF	59.03	1.6	14.67	8.72	0.21	2.75	6.02	3.92	1.56	0.12	98.61
T9/100	830 cm	IECMF00DG	57.59	1.28	14.69	8.39	0.19	2.56	5.93	3.88	1.54	0.05	96.09
T9/100	830 cm	IECMF00DH	58.9	1.26	14.86	8.21	0.14	2.63	5.88	4.24	1.55	0.13	97.8
T9/100	830 cm	IECMF00DI	60.4	1.34	15.12	7.3	0.27	2.25	5.01	3.49	2.12	0.14	97.45
T9/100	830 cm	IECMF00DJ	62.3	0.99	15.6	6.11	0.04	1.68	4.48	4.09	2.23	0.1	97.62
T9/100	830 cm	IECMF00DK	63.84	1.35	14.33	7.91	0.23	1.79	4.71	3.59	2.16	0.11	100.03
T9/100	830 cm	IECMF00DL	62.46	1.31	14.44	5.98	0.13	1.72	4.08	3.27	2.83	0.11	96.33
T9/100	830 cm	IECMF00DM	65.66	0.72	16.23	3.96	0.11	0.83	2.83	5.7	2.7	0.13	98.86
T9/100	830 cm	IECMF00DN	64.86	0.92	15.2	4.71	0.13	1.28	3.23	3.58	3.1	0.14	97.13
T9/100	830 cm	IECMF00DO	64.03	1.21	15.1	4.39	0.22	1.27	3.16	2.31	3.05	0.17	94.92
T9/100	830 cm	IECMF00DP	66.97	0.9	15.17	4.7	0.08	1	2.76	3.51	2.68	0.15	97.9
T9/100	830 cm	IECMF00DQ	66.55	0.65	14.8	4.2	0.11	0.71	2.48	4.76	2.61	0.16	97.04
T9/100	830 cm	IECMF00DS	68.9	0.74	14.37	4.89	0.22	0.66	2.65	4.29	2.4	0.16	99.28

T9/100	830 cm	IECMF00DT	67.97	0.7	15.38	3.78	0.1	0.76	2.23	3.52	3.17	0.16	97.79
T9/100	830 cm	IECMF00DU	69.59	0.35	13.79	2.2	0.07	0.3	1.1	3.74	2.96	0.2	94.3
T9/100	830 cm	IECMF00DX	53.91	2.09	13.55	11.34	0.24	2.59	6.38	3.59	1.88	0.16	95.73
T9/100	830 cm	IECMF00DY	64.4	1.1	15	3.48	0.11	0.93	2.4	5.11	2.4	0.17	95.1
T9/100	830 cm	IECMF00DZ	67.98	0.81	14.4	5.18	0.14	0.72	2.42	4.34	2.3	0.16	98.43
T9/100	830 cm	IECMF00E0	66.49	0.96	15.39	4.66	0.16	0.97	2.64	5.18	2.69	0.11	99.24
T9/100	830 cm	IECMF00E1	54.55	1.73	15.93	9.16	0.18	3.23	6.83	4	1.47	0.12	97.2
T9/100	830 cm	IECMF00E2	57.13	1.57	15.61	8.84	0.22	3.08	6.34	3.96	1.48	0.16	98.38
T10/100	900 cm	IECMF00E3	54	0.75	17.78	7.16	0.1	5.7	10.04	3.63	0.39	0.03	99.58
T10/100	900 cm	IECMF00E4	57.48	1.03	18.1	5.86	0.11	1.32	6.76	4.3	1.01	0.07	96.04
T10/100	900 cm	IECMF00E5	60.05	1.57	14.99	8.35	0.13	2.87	6.55	3.63	1.66	0.09	99.9
T10/100	900 cm	IECMF00E6	60.9	1.5	14.5	7.24	0.24	1.66	4.32	3.72	2.22	0.2	96.5
T10/100	900 cm	IECMF00E7	62.81	1.04	15.05	5.38	0.13	1.56	3.73	4.81	2.64	0.11	97.25
T10/100	900 cm	IECMF00E8	63.97	1.35	14.71	7.02	0.21	1.42	4.11	2.94	2.43	0.11	98.27
T10/100	900 cm	IECMF00E9	65.07	1.42	14.18	7.21	0.11	1.14	3.82	3.7	2.24	0.12	99.02
T10/100	900 cm	IECMF00EA	63.73	0.86	14.63	5.32	0.1	1.23	3.39	4.36	2.76	0.11	96.5
T10/100	900 cm	IECMF00EC	64.63	1.07	14.97	3.73	0.17	0.85	2.69	5.26	3.04	0.19	96.59
T10/100	900 cm	IECMF00ED	65.83	0.84	15.7	3.66	0.24	0.86	2.18	5.41	3	0.19	97.9
T10/100	900 cm	IECMF00EE	67.27	0.86	14.71	3.18	0.06	0.7	2.13	5.02	3.38	0.16	97.47
T10/100	900 cm	IECMF00EF	71.59	0.53	14.57	2.42	0.1	0.43	1.18	5.01	3.15	0.22	99.2
T10/100	900 cm	IECMF00EG	71.94	0.25	14.25	2.21	0.1	0.37	1.16	5.41	3.22	0.18	99.11
T11/100	990 cm	IECMF00EH	53.44	1.72	14.98	9.39	0.12	4.12	7.65	3.66	1.46	0.06	96.59
T11/100	990 cm	IECMF00EI	53.26	1.8	14.58	9.32	0.16	4.13	7.7	3.53	1.4	0.14	96
T11/100	990 cm	IECMF00EJ	55.38	1.77	14.54	9.48	0.23	4.03	7.17	3.3	1.53	0.07	97.48
T11/100	990 cm	IECMF00EK	56.01	1.68	14.83	9.05	0.34	3.98	7.1	3.55	1.48	0.08	98.09
T11/100	990 cm	IECMF00EL	56.52	1.43	14.55	9.03	0.23	3.91	6.99	3.97	1.59	0.05	98.28
T11/100	990 cm	IECMF00EM	58.15	1.67	15.03	9.94	0.08	2.3	6.01	3.83	1.67	0.06	98.73
T11/100	990 cm	IECMF00EN	57.95	1.31	14.46	8.57	0.13	2.55	5.83	4.02	1.56	0.13	96.52
T11/100	990 cm	IECMF00EO	59.38	0.91	17.89	6.04	0.1	2.61	6.01	4.83	1.04	0.05	98.86
T11/100	990 cm	IECMF00EP	58.08	0.74	17.45	6.05	0.19	2.21	6.11	4.63	1.17	0.02	96.65
T11/100	990 cm	IECMF00EQ	59.24	1.31	15.76	7.54	0.1	2.41	5.83	4.46	1.02	0.16	97.84
T11/100	990 cm	IECMF00ER	59.32	1.44	15.36	7.82	0.07	2.59	5.79	3.98	1.42	0.1	97.88

T11/100	990 cm	IECMF00ES	65.4	0.96	14.75	3.99	0.09	0.9	2.37	5.01	2.81	0.16		96.45
T11/100	990 cm	IECMF00ET	66.57	0.94	14.46	4.18	0.1	0.5	2.92	4.18	2.72	0.14		96.71
T11/100	990 cm	IECMF00EU	68.65	0.4	13.26	3.48	0.06	0.37	1.64	4.68	3.05	0.19		95.77
T12/100	1030 cm	IECMF00EV	52.72	1.85	11.29	11.73	0.32	6.99	8.44	3.01	1.2	0.02	0.68	98.26
T12/100	1030 cm	IECMF00EW	53.18	2.35	13.13	12.18	0.32	3.16	6.96	3.58	1.82	0.08	0.84	97.6
T12/100	1030 cm	IECMF00EX	53.29	2.28	12.57	11.36	0.25	3.9	8.09	3.35	1.42	0.14	0.74	97.39
T12/100	1030 cm	IECMF00EY	53.64	2.62	13.29	11.65	0.26	3.45	7.14	3.26	1.64	0.11	0.81	97.86
T12/100	1030 cm	IECMF00EZ	53.63	2.52	13.21	11.9	0.19	3.12	6.74	2.75	1.86	0.12	0.99	97.03
T12/100	1030 cm	IECMF00F1	53.35	2.58	13.27	11.96	0.26	2.49	6.58	2.8	1.53	0.1	0.96	95.88
T12/100	1030 cm	IECMF00F2	54.16	2.45	14.03	9.83	0.29	2.77	6.92	3.87	1.75	0.12	0.77	96.96
T12/100	1030 cm	IECMF00F3	55.12	2.18	11.82	12.42	0.37	3.76	6.29	3.21	2.05	0.11	0.36	97.68
T12/100	1030 cm	IECMF00F4	60.93	1.06	15.16	6	0.22	1.05	3.64	4.77	2.8	0.28	0.65	96.56
T12/100	1030 cm	IECMF00F5	62.47	0.9	14.67	5.68	0.28	1.21	3.09	4.4	2.9	0.15	0.35	96.09
T12/100	1030 cm	IECMF00F6	63.97	0.84	14.63	5.58	0.14	1.28	3.86	3.89	2.61	0.13	0.2	97.15
T12/100	1030 cm	IECMF00F7	68.68	0.29	14.17	3.49	0.2	0.37	2.11	3.47	3.18	0.16	0.11	96.22
T12/100	1030 cm	IECMF00F8	53.05	2.15	14.59	11.5	0.26	3.01	7.38	3.35	1.2	0.09		96.57
T12/100	1030 cm	IECMF00F9	67.21	0.3	15.01	4.37	0.12	0.61	2.13	4.79	2.86	0.2		97.6
T12/100	1030 cm	IECMF00FA	64.83	0.74	15.56	5.36	0.1	1.14	3.53	4.86	2.65	0.26		99.02
T12/100	1030 cm	IECMF00FB	54.73	1.9	14.41	11.07	0.27	5.69	6.53	3.72	1.37	0.09		99.77
T12/100	1030 cm	IECMF00FD	56.66	1.81	18.29	7.62	-0.03	2.23	8.02	4.17	1.37	0.19		100.36
T12/100	1030 cm	IECMF00FE	53.34	0.86	18.57	5.99	0.19	4.84	11.19	3.7	0.71	0.2		99.59
T12/100	1030 cm	IECMF00FF	66.74	0.31	14.23	3.69	0.05	0.59	2.19	5.19	2.88	0.14		96
T12/100	1030 cm	IECMF00FG	54.96	2.72	14.32	11.79	0.2	2.25	5.78	3.44	1.51	0.16		97.14
T13/100	1130 cm	IECMF00FI	51.28	2.36	13.92	11.27	0.1	3.69	7.87	3.63	1.18	0.05		95.34
T13/100	1130 cm	IECMF00FJ	54.47	1.53	15.09	9.44	0.3	3.87	8.11	3.42	0.98	0.07		97.29
T13/100	1130 cm	IECMF00FK	55.04	1.72	14.59	9.43	0.17	3.54	6.77	3.46	1.69	0.07		96.47
T13/100	1130 cm	IECMF00FL	55.21	2.17	13.25	10.5	0.16	3.32	6.5	3.48	1.44	0.1		96.12
T13/100	1130 cm	IECMF00FM	56.75	1.16	16.95	7.91	0.19	2.97	7.83	3.68	1.09	0.07		98.6
T13/100	1130 cm	IECMF00FN	58.23	1.54	15.1	8.55	0.11	2.53	5.8	3.98	1.48	0.12		97.45
T13/100	1130 cm	IECMF00FO	60.33	1.19	16.04	7.22	0.12	1.36	5.51	5.01	1.12	0.18		98.08
T13/100	1130 cm	IECMF00FP	60.93	0.83	15.58	6.3	0.01	2.02	4.82	4.23	2.06	0.14		96.93
T13/100	1130 cm	IECMF00FQ	64.09	1.07	13.23	4.92	0.28	1.87	2.67	4.1	2.66	0.1		94.98

T13/100	1130 cm	IECMF00FR	65.26	0.71	14.77	3.61	0.13	0.77	2.35	4.82	3.03	0.13	95.59
T14/100	1180 cm	IECMF00FS	52.96	2.58	13.25	12.22	0.25	3.36	7.08	3.04	1.71	0.12	96.57
T14/100	1180 cm	IECMF00FT	54.72	1.72	15.19	10.28	0.2	3.97	7.44	4.04	1.08	0.11	98.74
T14/100	1180 cm	IECMF00FU	55.63	1.69	15.68	8.51	0.28	3.11	6.47	4.1	1.61	0.1	97.17
T14/100	1180 cm	IECMF00FV	55.34	1.51	15.81	7.39	0.03	2.47	6.5	3.95	1.67	0.13	94.81
T14/100	1180 cm	IECMF00FW	59.32	1.54	15.01	8.97	0.15	2.32	4.73	4.31	2.32	0.13	98.8
T14/100	1180 cm	IECMF00FX	61.6	1.16	14.1	7.77	0.32	3.48	5.21	3.97	2.2	0.08	99.88
T14/100	1180 cm	IECMF00FY	60.22	1.36	14.86	7.24	0.27	1.82	4.51	4.44	2.19	0.18	97.08
T14/100	1180 cm	IECMF00FZ	62.72	0.88	15.34	4.48	0.12	1.19	2.91	5.27	2.6	0.11	95.63
T14/100	1180 cm	IECMF00G1	69.31	0.41	14.27	3.73	0.08	0.35	2.13	4.46	3.57	0.19	98.51
T14/100	1180 cm	IECMF00G2	69.01	0.26	13.97	3.37	0.2	0.21	1.5	4.55	3.23	0.21	96.51
T14/100	1180 cm	IECMF00G4	52.86	1.65	14.25	10.14	0.26	4.14	7.39	4.15	1.2	0.15	96.19
T14/100	1180 cm	IECMF00G5	54.47	2.03	17.72	8.67	0.17	2.52	7.9	4.12	1.24	0.11	98.95
T14/100	1180 cm	IECMF00G6	52.92	1.75	16.69	9.47	0.12	3.43	7.68	3.83	0.91	0.07	96.86
T14/100	1180 cm	IECMF00G7	55.64	1.95	16.47	8.39	0.06	2.92	6.68	4.85	1.5	0.14	98.6
T14/100	1180 cm	IECMF00G8	52.76	2.28	14.75	10.5	0.09	3.23	8.13	4.02	1.47	0.17	97.4
T14/100	1180 cm	IECMF00G9	57.43	1.36	14.87	7.28	0.16	2.66	5.79	4.91	1.85	0.18	96.49
T15/100	1340 cm	IECMF00GA	51.24	1.86	14.36	11.91	0.16	4.86	8.45	3.66	0.89	0.09	97.48
T15/100	1340 cm	IECMF00GB	52.42	2.47	14.01	11.03	0.16	3.54	7.22	3.97	1.42	0.12	96.37
T15/100	1340 cm	IECMF00GC	53.38	2.19	14.74	10.24	0.14	4.36	7.44	3.77	1.39	0.09	97.74
T15/100	1340 cm	IECMF00GD	54.57	2.5	14.18	11.72	0.17	3.5	7.52	3.76	1.54	0.11	99.58
T15/100	1340 cm	IECMF00GE	53.73	1.66	16.13	8.68	0.1	4	7.5	4.6	1.53	0.07	97.99
T15/100	1340 cm	IECMF00GF	54.14	1.65	16.67	9.36	0.22	2.6	7.72	4.19	1.26	0.11	97.91
T15/100	1340 cm	IECMF00GG	54.16	1.53	13.19	10.91	0.25	4.77	8.4	3.61	0.85	0.13	97.78
T15/100	1340 cm	IECMF00GH	54.63	2.4	14.17	10.9	0.23	3.16	6.76	3.7	2.13	0.13	98.19
T15/100	1340 cm	IECMF00GI	54.5	1.99	14.91	9.51	0.27	3.87	6.96	4.35	1.42	0.13	97.92
T15/100	1340 cm	IECMF00GJ	53.75	2.36	15.55	9.51	0.16	2.64	6.82	3.99	1.6	0.12	96.49
T15/100	1340 cm	IECMF00GK	54.45	1.38	13.64	10.06	0.22	4.64	8.25	3.55	0.74	0.08	97.01
T15/100	1340 cm	IECMF00GL	55.89	1.41	14.73	9.31	0.22	3.54	6.49	4.02	1.52	0.14	97.27
T15/100	1340 cm	IECMF00GM	57.11	1.44	14.65	9.6	0.32	3.09	6.04	4.28	1.85	0.06	98.44
T15/100	1340 cm	IECMF00GN	57.81	1.72	14.67	9.03	0.15	2.74	5.81	3.92	2.13	0.16	98.15
T15/100	1340 cm	IECMF00GO	63.57	0.82	14.4	7.52	0.21	2	4.32	4.43	2.42	0.12	99.82

T15/100	1340 cm	IECMF00GP	69.53	0.5	13.73	1.74	0.13	0.24	0.95	5.36	3.44	0.14	95.77
T15/100	1340 cm	IECMF00GQ	54.83	2.15	14.35	12.62	0.16	6.12	6.44	3.14	1.17	0.08	101.06
T15/100	1340 cm	IECMF00GR	54.26	1.48	18.59	8.28	0.2	3.59	7.69	3.92	1.25	0.15	99.42
T15/100	1340 cm	IECMF00GS	59.79	1.66	15.94	9.38	0.13	2.52	5.37	4.25	2.5	0.15	101.68
T15/100	1340 cm	IECMF00GT	54.92	2.09	15.37	10.69	0.11	4.28	7.81	3.4	1.35	0.12	100.13
T15/100	1340 cm	IECMF00GU	52.33	2.4	15.92	10.97	0.16	3.18	7.42	3.86	1.26	0.15	97.64
T15/100	1340 cm	IECMF00GV	53.09	1.48	16.36	9.87	0.16	5.53	7.21	3.36	1.06	0.08	98.18
T15/100	1340 cm	IECMF00GW	57.68	1.49	14.94	8.58	0.17	3.18	5.75	3.72	1.6	0.12	97.24
T15/100	1340 cm	IECMF00GX	62.57	0.89	15.17	4	0.3	1.12	2.85	5.16	2.57	0.18	94.82
T15/100	1340 cm	IECMF00GY	57.86	2.33	14.06	11.74	0.14	3.6	6.9	3.05	1.56	0.16	101.4
T15/100	1340 cm	IECMF00GZ	60.46	1.36	15.57	8.12	0	2.76	5.38	4.39	2.28	0.13	100.46
T16/100	1390 cm	IECMF00H0	52.86	1.33	15.22	9.53	0.22	4.8	8.44	3.53	0.96	0.09	96.98
T16/100	1390 cm	IECMF00H1	53.09	1.72	15.08	10.27	0.19	3.53	7.21	3.97	1.07	0.09	96.22
T16/100	1390 cm	IECMF00H2	53.16	1.82	13.61	10.05	0.28	4.55	7.09	3.57	1.42	0.05	95.59
T16/100	1390 cm	IECMF00H3	54.96	1.16	13.25	10.13	0.14	5.71	6.77	3.24	1.09	0.08	96.53
T16/100	1390 cm	IECMF00H4	55.18	1.6	12.85	10.23	0.24	4.56	6.66	3.47	1.35	0.08	96.21
T16/100	1390 cm	IECMF00H5	56.06	1.6	15.04	9.24	0.21	2.97	6.47	4.26	1.56	0.12	97.53
T16/100	1390 cm	IECMF00H6	56.02	1.29	15.16	8.94	0.19	3.11	6.54	4.07	1.35	0.09	96.76
T16/100	1390 cm	IECMF00H7	56.92	1.19	14.95	9.38	0.17	2.89	6.29	4.27	1.44	0.07	97.57
T16/100	1390 cm	IECMF00H8	58.26	1.81	14.12	8.07	0.31	2.15	5.12	4.09	1.93	0.08	95.93
T16/100	1390 cm	IECMF00H9	59.29	1.12	14.79	7.25	0.22	2.02	4.84	4.12	1.9	0.15	95.71
T16/100	1390 cm	IECMF00HA	59.84	1.35	15.14	5.65	0.14	1.77	4.14	4.9	2.15	0.1	95.19
T16/100	1390 cm	IECMF00HB	60.19	1.53	14.15	7.19	0.21	1.85	4.76	3.65	1.97	0.12	95.62
T16/100	1390 cm	IECMF00HC	60.91	1.16	14.56	6.3	0.12	1.77	4	4.35	2.84	0.16	96.18
T16/100	1390 cm	IECMF00HD	61.04	1.21	14.76	5.87	0.14	1.71	4.57	4.26	2.04	0.13	95.74
T16/100	1390 cm	IECMF00HE	63.02	1.31	14.92	5	0.08	1.57	3.7	4.57	2.47	0.15	96.78
T16/100	1390 cm	IECMF00HF	62.53	1.04	14.67	4.8	0.05	1.15	2.95	4.84	2.81	0.15	94.98
T16/100	1390 cm	IECMF00HG	63.19	0.98	14.65	4.61	0.18	1.19	3.08	5.24	2.62	0.19	95.94
T16/100	1390 cm	IECMF00HI	68.84	0.51	13.65	3.12	0.23	0.43	1.66	4.56	2.91	0.26	96.17
T16/100	1390 cm	IECMF00HJ	71.46	0.27	13.24	0.68	0.1	0.08	1.1	4.6	4.02	0.09	95.65
T17/100	1470 cm	IECMF00HK	51.88	1.66	17.47	9	0.24	3.71	8.71	4.24	0.84	0.04	97.79
T17/100	1470 cm	IECMF00HL	51.8	1.29	14.89	9.95	0.18	5.88	8.8	3.63	0.73	0.07	97.22

T17/100	1470 cm	IECMF00HM	52.76	2.45	13.72	12.37	0.22	3.05	6.11	3.27	1.89	0.11	95.94
T17/100	1470 cm	IECMF00HN	53.54	1.71	14.55	10.35	0.25	3.57	7.14	3.99	1.09	0.09	96.28
T17/100	1470 cm	IECMF00HO	56.46	1.4	14.6	8.86	0.15	3.07	6.3	4.34	1.32	0.09	96.57
T17/100	1470 cm	IECMF00HP	59.23	1.85	14.18	8.16	0.21	1.54	4.16	4.36	2.49	0.21	96.41
T17/100	1470 cm	IECMF00HQ	59.54	1.41	15.69	6.26	0.23	2.21	4.31	4.41	2.61	0.16	96.84
T17/100	1470 cm	IECMF00HR	62.76	1.02	15.3	4.78	0.32	1.52	3.6	4.56	2.39	0.13	96.36
T17/100	1470 cm	IECMF00HS	67.49	0.24	13.85	3.98	0.16	0.31	1.75	5.13	3.47	0.17	96.54
T17/100	1470 cm	IECMF00HT	67.49	0.4	13.59	3.67	0.12	0.27	1.58	4.75	3.29	0.14	95.29

Table S2. Inividual glass shard analyses in core MD07-3100. Ttrace elements analyzed by LA-ICP-MS.

Cryptotephra	Core Depth	IGSN	Zr (ppm)	Nb (ppm)	Ba (ppm)	La (ppm)	Ce (ppm)	Pr (ppm)	Nd (ppm)	Sm (ppm)	Eu (ppm)	Gd (ppm)	Tb (ppm)	Dy (ppm)	Ho (ppm)	Er (ppm)	Tm (ppm)	Yb (ppm)	Lu (ppm)	Hf (ppm)	Ta (ppm)	Pb (ppm)	Th (ppm)	U (ppm)
T1/100	150 cm	IECMF006S	294.23	13.79	568.15	33.14	83.77	9.71	34.38	7.35	1.58	6.52	0.9	5.23	1.16	3.85	0.52	3.09	0.61	7.06	0.87	12.96	6.7	1.07
T1/100	150 cm	IECMF006T	543.21	23.14	1011.62	55.86	119.4	12.92	56.24	10.16	2.11	9.32	1.31	10.44	1.82	6.41	0.95	7.08	1.35	13.76	1.72	25.04	11.39	2.53
T1/100	150 cm	IECMF006U	238.04	10.91	454.96	32.63	65.58	8.44	38.38	7.4	1.44	5.4	0.82	6.02	1.19	3.5	0.51	3.75	0.5	4.54	0.62	9.9	4.03	1.05
T1/100	150 cm	IECMF006W	500.38	21.5	978.56	53.37	113.59	13.32	54.73	9.53	2	7.24	1.54	9.31	1.87	5.48	0.91	5.3	1.11	12.64	1.42	23.49	10.67	2.81
T1/100	150 cm	IECMF006X	461.91	18.17	807.19	43.52	109.86	11.25	46.71	7.15	1.94	7	1.3	7.96	1.66	5.15	0.68	4.89	0.97	10.16	#N/A	36.38	9.91	2.63
T1/100	150 cm	IECMF006Y	290.8	14.49	526.62	32.2	67.98	8.3	30.25	8.09	0.92	3.89	0.75	5.56	1.2	3.27	0.47	2.62	0.44	5.54	1.51	11.9	5.64	1.31
T2/100	330 cm	IECMF007H	352.31	13.79	633.5	31.42	67.95	8.54	35.53	7.53	1.52	6.48	0.98	7.22	1.58	4.95	0.79	5.72	0.86	8.89	1.36	30.21	9.17	3.04
T2/100	330 cm	IECMF007I	370.64	18.12	839.42	36.3	85.52	10.59	42.58	8.42	3.15	8.52	1.34	8.91	2	4.98	1.07	6.42	0.86	9.5	1.15	25.28	8.85	2.82
T2/100	330 cm	IECMF007J	441.31	17.83	591.38	43.13	91.8	11.72	53.92	10.31	2.7	11.53	2.03	13.35	2.63	7.19	1.08	6.86	1.22	10.68	#N/A	30.04	10.06	2.87
T2/100	330 cm	IECMF007K	321.95	13.85	576.04	32.86	67.59	8.53	40.07	9.49	1.83	8.05	1.26	7.98	1.75	4.51	0.88	4.92	0.78	7.86	0.73	19.81	9.29	2.85
T2/100	330 cm	IECMF007L	348.55	14.89	621.96	34.87	77.21	9.76	43.27	9.26	1.97	7.94	1.23	9.48	1.66	5.06	0.91	6.17	1.05	8.15	0.99	20.56	9.39	2.56
T2/100	330 cm	IECMF007M	227.93	9.67	491.31	24.68	53.82	7	29	5.49	1.18	6.32	0.79	7.18	1.33	3.71	0.57	4.16	0.69	5.4	0.75	16.93	6.78	1.96
T2/100	330 cm	IECMF007N	361.77	15.62	609.05	32.06	72.7	8.69	33.85	5.92	1.92	5.99	1.09	6.88	1.79	4.77	0.85	4.9	0.8	7.68	0.87	18.85	7.89	2.13
T2/100	330 cm	IECMF007O	122.69	7.04	238.16	16.89	38.36	4.98	22.4	5.18	1.48	4.82	0.75	5.75	1.24	2.74	0.52	3.34	#N/A	2.79	#N/A	11.51	2.85	1.09
T4/100	450 cm	IECMF0093	389.47	15.23	464.48	34.35	89.3	11.65	53.73	14.44	3.13	13.43	2.38	17.57	3.44	7.59	1.2	6.82	1.52	10.26	#N/A	23.23	7.76	2.16

T4/100	450 cm	IECMF0094	553.27	22.91	735.9	44.34	106.73	13.51	46.5	11.56	1.75	11.65	1.67	10.74	2.65	7.59	1.28	7.15	1.33	12.24	1.94	25.38	13.13	3.63
T4/100	450 cm	IECMF0095	231.26	9.77	426.79	24.81	79.41	6.3	27.43	7.48	1.44	9.35	1.26	6.84	1.86	4.05	0.95	4.98	0.61	5.53	0.92	14.91	4.3	1.24
T4/100	450 cm	IECMF0096	218.06	12.43	385.47	25.88	58.24	7.91	32.42	9.32	1.94	6.88	1.07	7.12	1.43	3.67	0.67	4.15	0.69	5.1	1.26	13.74	4.65	1.55
T5/100	490 cm	IECMF009M	400.8	14.35	687.51	34.88	79.56	9.18	38.74	8.41	1.99	6.88	1.19	7.13	1.75	6.38	0.73	5.48	0.91	9.56	#N/A	26.61	9.78	3.16
T5/100	490 cm	IECMF009N	756.39	31.63	993.71	61.77	139.01	17.13	72.03	13.89	1.78	12.92	2.25	16.37	3.27	11.01	1.46	12.07	1.95	17.82	2.17	40.56	15.7	5.28
T5/100	490 cm	IECMF009O	335.15	14.35	648.56	32.75	74.23	8.44	37.6	7.65	1.75	6.89	1.15	6.79	1.85	4.57	0.69	5.01	0.69	9	1.35	24.32	9.49	2.79
T5/100	490 cm	IECMF009P	204.47	9.74	363.61	22.12	54.02	7.02	35.46	6.3	1.88	8.32	1.29	7.97	1.42	4.99	1	4.89	0.87	5.42	0.62	16.65	4.74	1.5
T5/100	490 cm	IECMF009Q	162.13	8.99	307.22	18.19	49.97	6.76	27.16	8.28	1.7	6.56	1.13	6.6	1.34	3.95	0.43	4.08	0.54	4.29	0.56	14.13	3.39	1.35
T5/100	490 cm	IECMF009R	195.53	9.85	359.48	22.88	56.56	7.04	31.67	7.66	2.11	7.8	1.22	7.52	1.66	4.1	0.59	4.61	0.59	4.43	0.74	12.41	3.84	0.98
T6/100	550 cm	IECMF00AC	322.48	14.18	627.38	28.89	67.15	8.47	33.64	7.16	1.74	7.02	1.01	6.82	1.55	4.54	0.72	5.25	0.83	7.38	1.59	17.29	6.83	1.79
T6/100	550 cm	IECMF00AD	304.82	14.59	574.07	30.7	70.67	8.31	35.53	7.53	2.07	5.64	0.94	6.73	1.42	5.54	0.78	4.37	0.95	8.05	#N/A	19.07	7.14	1.85
T6/100	550 cm	IECMF00AE	405.38	17.43	678.24	36.35	87.13	10.13	43.11	9.22	1.83	8.22	1.29	9.07	2.05	4.72	0.83	6.72	1.06	8.76	1.24	22.68	8.98	2.51
T6/100	550 cm	IECMF00AF	218.14	10.92	375.37	25.01	56.86	7.54	34.15	7.92	2.34	7.68	1.2	8.32	1.67	4.36	0.72	4.63	0.68	5.82	0.66	12.92	4.62	1.2
T6/100	550 cm	IECMF00AG	214.77	9.65	363.42	22.1	50.7	6.34	25.47	7.23	1.59	6.77	0.9	6.71	1.32	3.72	0.53	3.6	0.63	5.53	0.71	13.02	4.54	1.45
T6/100	550 cm	IECMF00AH	248.75	12.59	450.63	29.32	69.61	9.82	44.61	9.17	3.08	10.39	1.45	10.19	2.08	5.06	0.72	6.1	0.87	5.53	1.23	14.35	4.83	1.38
T6/100	550 cm	IECMF00AI	291.12	13.59	423.13	27.37	62.08	7.49	31.49	6.94	1.08	6.93	0.89	7.06	1.58	4.38	0.66	4.4	0.69	6.52	1.07	17.66	6	1.58
T7/100	610 cm	IECMF00BJ	327.82	14.37	446.23	29.16	66.95	8.09	31.57	6.32	1	6.44	1.04	6.76	1.69	4.06	0.74	4.93	0.72	7.68	0.83	28.52	7.64	2.25
T7/100	610 cm	IECMF00BK	883.27	37.52	1144.82	74.07	169.62	22.09	89.66	19.34	2.55	16.61	3.09	18.94	4.62	11.59	2.14	13.98	1.85	21.78	3.11	46.05	20.07	6.08
T7/100	610 cm	IECMF00BL	267.59	13.9	563.7	29.01	68.26	9.18	34.38	7.45	2.03	7.7	1.23	7.41	1.76	4.92	0.76	4.58	0.68	6.37	0.7	23.63	6.54	2.1
T7/100	610 cm	IECMF00BM	95.07	5.13	173.46	11.22	29.03	3.86	16.18	4.36	1.13	3.79	0.52	3.52	0.69	2.34	0.31	1.93	0.34	2.29	0.33	6.81	2.05	0.71
T8/100	740 cm (top)	IECMF00CU	150.97	7.96	287.22	18.25	44.88	5.67	25.49	6.19	1.77	6.03	0.97	5.72	1.39	3.68	0.58	3.23	0.53	4.14	0.58	10.69	3.22	1.02
T8/100	740 cm (top)	IECMF00CV	145.95	7.09	297.32	17.13	39.27	5.47	24.67	5.05	1.7	5.32	1.12	6.11	1.41	3.04	0.47	2.81	0.64	3.36	0.55	9.22	2.99	1.04
T8/100	740 cm (top)	IECMF00CW	128.31	6.69	229.36	15.38	36.21	4.69	23.16	5.11	1.42	5.18	0.75	5.09	0.99	3.42	0.5	2.95	0.45	3.61	0.44	7.08	2.89	0.91

T8/100	740 cm (top)	IECMF00CX	684.54	28.89	917.35	60.01	126.69	14.94	72.45	10.86	3.05	11.08	2.69	15.7	3.45	8.05	1.42	12.82	1.93	15.2	2.18	40.11	13.06	5.17
T8/100	740 cm (top)	IECMF00CY	688.88	25.28	804.1	53.44	115.43	14.74	59.5	14.03	1.63	12.77	1.97	14.37	2.78	9.35	1.39	9.92	1.61	15.4	#N/A	32.12	14.22	3.54
T8/100	740 cm (top)	IECMF00CZ	733.91	30.82	905.39	58.31	127.38	17.62	63.56	19.32	2.42	9.54	2.07	15.31	2.95	9.12	1.35	10.5	1.4	15.72	2.04	39.16	14.88	4.52
T8/100	740 cm (top)	IECMF00D0	625.1	28.48	823.44	51.41	118.91	14.72	56.24	15.28	1.87	11.31	1.85	16.07	2.92	9.36	1.53	9.08	1.62	15.27	1.68	34.13	14.1	3.54
T8/100	740 cm (top)	IECMF00D1	681.14	30.96	931.34	53.81	135.36	15.89	64.43	13.19	1.81	11.77	2.16	17.82	3.02	10.25	1.8	11.2	1.6	14.45	2.36	38.69	15.19	5.1
T8/100	740 cm (top)	IECMF00D3	193.44	11.32	326.19	23.44	55.49	7.08	35.8	9.68	2.42	7.71	1.26	8.96	1.88	4.56	0.67	5.37	0.76	5.53	0.68	13.11	4.41	1.05
T8/100	740 cm (top)	IECMF00D5	196.88	9.58	388.41	22.65	52.24	7.09	36.27	8.1	2.07	7.13	1.15	7.08	1.47	3.91	0.71	4.26	0.47	4.82	0.65	11.08	4.18	1.06
T8/100	740 cm (top)	IECMF00D6	143.77	6.88	251.28	17.1	40.2	5.31	26.29	6.67	1.67	6.85	0.98	6.49	1.41	3.23	0.5	3.19	0.58	3.61	0.46	9.24	3.36	0.92
T9/100	830 cm	IECMF00DX	103.59	5.56	238.11	11.43	26.79	3.79	14.42	4.36	1.07	1.63	0.57	3.83	0.68	1.51	0.27	2.2	0.28	1.85	0.53	6.18	1.46	0.59
T9/100	830 cm	IECMF00DY	260.88	11.5	684.44	31.64	65.04	7.71	34.15	7.63	1.76	6.03	0.94	6.19	1.43	3.57	0.55	3.81	0.61	6.92	1.35	25.22	7.49	2.52
T9/100	830 cm	IECMF00DZ	272.84	9.05	611.39	27.58	61.58	8	30.85	7.25	1.4	6.71	0.87	7.43	1.37	4.22	0.69	4.12	0.94	6.48	2.6	21.91	6.63	1.88
T9/100	830 cm	IECMF00E0	292.84	10.64	680.83	30.81	63.22	7.28	33.77	6.44	1.21	6.39	0.86	5.83	1.48	3.81	0.57	2.75	0.75	6.1	#N/A	20.35	8.67	1.89
T9/100	830 cm	IECMF00E1	396.41	14.18	852.64	47.99	103.64	14.53	65.14	15.46	3.95	15.39	2.17	14.2	2.82	8.85	1.31	7.22	1.28	10.66	1.15	35.9	11.2	3.43
T9/100	830 cm	IECMF00E2	193.96	8.03	365.55	22.19	47.96	6.45	27.41	6.35	2.15	5.07	0.92	6.54	0.94	3.34	0.57	3.61	0.45	4.47	0.56	9.44	5.32	1.41
T12/100	1030 cm	IECMF00FA	471.08	20.84	701.2	44.4	105.13	13.34	53.04	11.89	2.37	10.77	1.75	12.88	2.52	7.58	1.26	8.55	1.27	11.1	3.85	29.08	10.84	3.25
T12/100	1030 cm	IECMF00FB	174.89	8.74	340.04	20.76	48.53	6.12	30.18	7.26	1.74	6.62	1.09	7.01	1.54	3.6	0.6	3.69	0.7	4.1	0.57	10.5	3.67	1.15
T12/100	1030 cm	IECMF00FD	250.68	14.63	386.2	26.3	60.21	7.94	34.15	9.37	2.19	8.35	1.22	9.73	1.84	4.77	0.64	5.21	0.73	5.66	#N/A	27.12	5.25	1.46
T12/100	1030 cm	IECMF00FE	247.11	10.44	426.41	23.83	53.63	6.86	30.37	6.95	1.71	6.77	1.05	7.27	1.3	4.47	0.63	4.4	0.68	5.76	2.71	15.96	5.37	1.39
T12/100	1030 cm	IECMF00FF	831.7	33.31	947.79	64.39	163.14	20.51	84.21	22.38	2.99	20.29	3.5	23.41	4.86	14.41	2.17	16.64	2.41	21.92	2.37	33.42	19.33	5.65
T12/100	1030 cm	IECMF00FG	167.83	8.16	327.72	19.64	44.45	6.1	28.4	7.16	1.71	6.45	1.1	6.28	1.34	3.32	0.56	3.64	0.58	4	0.97	14.35	3.37	0.87
T14/100	1180 cm	IECMF00G4	122.84	4.34	322.64	15.88	35.69	4.74	23.83	4.96	1.62	6.39	0.82	6.04	1.44	3.87	0.54	3.41	0.61	3.48	0.28	11.78	3.25	0.92

T14/100	1180 cm	IECMF00G5	109.74	6.22	250.02	14.44	33.31	4.08	18.78	4.36	1.52	4.84	0.74	4.36	0.91	2.28	0.37	2.36	0.39	2.52	0.41	8.17	2.06	0.71
T14/100	1180 cm	IECMF00G6	259.08	13.6	430.16	30.57	73.8	10.3	45.94	11.37	2.51	11.07	1.79	10.41	2.06	5.98	0.83	5.78	0.87	6.06	0.99	15.36	5.49	1.52
T14/100	1180 cm	IECMF00G7	233.6	11.61	425.02	28.17	69.66	7.94	35.71	8.13	2.29	8.22	1.23	9.35	1.83	4.36	0.73	4.47	0.71	5.78	0.78	15.82	5.64	1.79
T14/100	1180 cm	IECMF00G8	198.27	10.48	368.75	23.35	58.31	7.51	34.05	8.45	2.16	7.9	1.25	8.87	1.57	4.96	0.57	4.07	0.63	5.25	0.64	11.81	3.8	1.51
T14/100	1180 cm	IECMF00G9	408.09	20.96	631.17	42.56	97.86	12.02	53.85	11.15	2.5	12.17	2.01	10.57	2.2	7.28	1.1	6.85	1.02	9.41	1.31	29.03	9.66	2.69
T15/100	1340 cm	IECMF00GQ	170.67	10.08	304.21	20.41	51.61	6.9	29.4	6.48	2.16	6.6	0.88	5.14	1.23	3.8	0.5	3.7	0.48	4.62	1.27	13.87	3.58	1.48
T15/100	1340 cm	IECMF00GR	191.89	10.85	340.82	22.7	54.52	7.03	31.74	7.02	2.17	7.05	1.11	7.13	1.48	4.08	0.58	3.96	0.6	4.45	1.23	11.62	4.29	1.04
T15/100	1340 cm	IECMF00GS	402.59	19.18	630.33	36.75	84.8	10.42	43.03	9.09	1.96	9.46	1.4	10.02	1.89	5.86	0.85	6.41	0.94	9.32	1.07	20.12	8.96	2.74
T15/100	1340 cm	IECMF00GT	202.25	9.67	306.24	21.69	49.94	6.58	28.54	7.03	1.65	7.23	0.95	7.29	1.38	3.87	0.6	4.1	0.66	4.95	0.61	11.8	4.47	1.21
T15/100	1340 cm	IECMF00GU	169.73	8.34	316.57	20.4	45.54	6.08	28.46	6.51	1.72	6.18	1.02	7.55	1.37	4.1	0.58	4.16	0.57	4.53	0.78	13.52	3.64	1.05
T15/100	1340 cm	IECMF00GV	179.17	9.26	332.96	21.13	48.07	6.22	30.09	7.1	2.02	6.07	1.16	6.91	1.36	3.52	0.49	3.79	0.5	4.53	#N/A	11.82	4.02	1.13
T15/100	1340 cm	IECMF00GW	128.09	4.19	310.87	14.84	33.04	4.47	19.93	4.22	1.2	5.57	0.85	4.81	0.99	2.95	0.38	3.15	0.36	3.17	0.34	12.44	3.48	1.13
T15/100	1340 cm	IECMF00GX	213.44	8.79	636.49	27.68	54.66	6.25	25.82	5.98	1.9	3.9	0.99	5.91	1.33	3.04	0.45	4.08	0.49	6.51	1.03	18.95	7.55	2.03
T15/100	1340 cm	IECMF00GY	179.65	9.88	339.34	22.07	51.09	6.63	28.98	6.35	1.83	6.77	0.95	7.09	1.39	4.5	0.63	4.71	0.8	4.23	1.45	14.74	3.91	1.01
T15/100	1340 cm	IECMF00GZ	153.59	7.23	229.53	15.69	36.28	4.81	22.13	5.93	1.33	5.65	0.83	5.81	1.2	3.76	0.48	3.62	0.49	3.71	0.57	8.1	3.43	0.89

Cryptotephra	Core Depth	IGSN	SiO2 (wt.%)	TiO2 (wt.%)	Al2O3 (wt.%)	FeO (wt.%)	MnO (wt.%)	MgO (wt.%)	CaO (wt.%)	Na2O (wt.%)	K2O (wt.%)	Cl (wt.%)	Total (wt.%)
T1/98	30 cm	IECMF00IL	55.69	1.42	15.43	8.41	0.21	3.88	7.15	3.6	1.31	0.11	97.21
T1/98	30 cm	IECMF00IM	55.24	1.11	16.13	8.1	0.08	3.37	7.48	3.78	1.15	0.1	96.54
T1/98	30 cm	IECMF00IN	55.6	1.08	13.74	10.15	0.24	6.26	7.63	3.17	1.11	0.07	99.05
T1/98	30 cm	IECMF00IO	67.72	0.65	16.65	3.33	0.06	0.65	1.76	6.02	2.92	0.17	99.93
T1/98	30 cm	IECMF00IP	64.9	0.52	16.3	3.92	0.19	0.73	1.93	5.67	2.72	0.24	97.11
T1/98	30 cm	IECMF00IQ	55.72	1.47	15.49	8.32	0.16	3.95	7.61	4.03	1.27	0.12	98.15
T2/98	450 cm	IECMF00IR	71.89	0.26	15.36	1.2	0.06	0.17	0.66	2.56	3.21	0.19	95.56
T2/98	450 cm	IECMF00IT	59.55	1.38	15.66	7.42	0.28	1.93	4.73	4.09	2.28	0.1	97.41
T2/98	450 cm	IECMF00IU	61.96	1.19	15.88	6.9	0.2	1.83	4.65	4.36	2.42	0.14	99.54

T2/98	450 cm	IECMF00IV	60.96	1.1	14.84	8.04	0.26	2.08	4.84	3.87	2.16	0.12	98.28
T2/98	450 cm	IECMF00IW	65.35	0.59	15.27	4.29	0.13	0.73	2.48	4.48	2.94	0.2	96.46
T2/98	450 cm	IECMF00IX	62.03	1.2	15.2	6.26	0.09	1.83	3.45	5.18	1.89	0.13	97.27
T2/98	450 cm	IECMF00IY	69.71	0.37	14.22	3.92	0.19	0.24	1.32	4.33	3.36	0.24	97.89
T2/98	450 cm	IECMF00IZ	69.33	0.31	13.88	3.25	0.09	0.27	1.13	4.66	3.38	0.19	96.49
T2/98	450 cm	IECMF00J0	69.52	0.79	14.76	3.1	0.1	0.72	1.83	4.88	3.02	0.17	98.9
T2/98	450 cm	IECMF00J1	58.85	0.86	17.6	4.69	0	1.48	5.71	5.79	1.42	0.1	96.5
T3/98	530 cm	IECMF00J2	66.3	0.8	14.26	6.13	0.1	1.7	3.98	4.43	2.55	0.17	100.4
T3/98	530 cm	IECMF00J3	66.17	0.9	14.5	6.93	0.02	1.75	3.96	3.59	2.65	0.17	100.66
T3/98	530 cm	IECMF00J4	70.78	0.35	14.07	3.48	0.21	0.24	1.6	3.73	3.16	0.18	97.81
T3/98	530 cm	IECMF00J5	68.13	0.39	16.22	2.98	-0.03	0.31	2.62	5.49	2.82	0.14	99.1
T3/98	530 cm	IECMF00J6	57.7	1.39	15.96	9.06	0.13	1.34	4.68	4.63	2.34	0.13	97.37
T3/98	530 cm	IECMF00J7	64.61	0.4	10.96	7.43	0.38	1.63	4.76	3.45	2.49	0.15	96.28
T3/98	530 cm	IECMF00J8	70.57	0.4	14.09	4.06	0.23	0.81	2.39	4.69	2.87	0.17	100.29
T3/98	530 cm	IECMF00J9	55.79	1.7	15.19	8.33	0.17	2.97	6.36	4.36	1.68	0.07	96.62
T3/98	530 cm	IECMF00JA	61.96	0.96	14.07	6.91	0.19	1.19	3.82	3.22	2.64	0.2	95.16
T3/98	530 cm	IECMF00JB	63.69	0.84	13.78	6.26	0.02	1.22	3.86	4.01	2.55	0.2	96.44
T3/98	530 cm	IECMF00JC	54.94	1.76	15.72	9.07	0.11	3.27	6.97	4.07	1.62	0.15	97.68
T3/98	530 cm	IECMF00JD	64.97	0.84	14.47	5.43	0.11	1.28	3.69	4.51	2.66	0.15	98.11
T4/98	550 cm	IECMF00JE	71.23	0.2	13.8	3.42	0.14	0.25	1.39	3.04	3.31	0.17	96.96
T4/98	550 cm	IECMF00JF	67.57	0.18	18.55	1.88	0.03	0.09	3.55	5.69	1.9	0.09	99.52
T4/98	550 cm	IECMF00JG	68.88	0.38	15.4	3.41	0.15	0.7	2.23	2.5	2.76	0.16	96.57
T4/98	550 cm	IECMF00JH	68.66	0.38	15.78	3.47	0.09	0.67	2.45	2.76	2.59	0.2	97.04
T4/98	550 cm	IECMF00JI	68.64	0.46	14.4	3.7	0.14	0.42	1.73	2.58	3.33	0.2	95.61
T4/98	550 cm	IECMF00JJ	68.85	0.27	14.12	3.54	0.16	0.24	1.63	2.94	2.98	0.22	94.95
T4/98	550 cm	IECMF00JK	58.93	1.6	14.41	9.17	0.31	3.11	6.38	3.04	1.94	0.14	99.04
T4/98	550 cm	IECMF00JL	69.63	0.32	14.3	3.55	0.06	0.21	1.42	2.93	3.24	0.25	95.9
T4/98	550 cm	IECMF00JM	70	0.15	15.16	3.12	0.2	0.17	1.83	3.63	2.8	0.18	97.24
T4/98	550 cm	IECMF00JN	63.59	1.44	14.9	6.5	0.28	1.17	3.66	3.4	2.6	0.11	97.66
T4/98	550 cm	IECMF00JO	57.58	1.4	14.85	7.6	0.08	3.64	6.36	3.25	1.4	0.17	96.35
T4/98	550 cm	IECMF00JP	63.75	0.81	14.7	5.37	0.11	1.03	3.32	3.6	2.78	0.19	95.65
T4/98	550 cm	IECMF00JQ	62.74	1.07	15.06	6.2	0.13	1.74	4.13	3.22	1.74	0.1	96.12

T4/98	550 cm	IECMF00JR	61.86	1.38	15.49	6.56	0.24	1.62	4.81	4.37	1.96	0.13	98.41
T5/98	670 cm	IECMF00JS	66.58	0.75	14.82	5.63	0.18	0.93	2.8	4.52	2.6	0.14	98.95
T5/98	670 cm	IECMF00JU	57.8	1.47	16.31	7.68	0.16	3.53	6.97	3.7	1.4	0.17	99.18
T5/98	670 cm	IECMF00JV	53.56	1.85	15.93	10.79	0.27	3.77	7.17	3.86	1.2	0.04	98.45
T5/98	670 cm	IECMF00JW	66.57	0.75	15.54	3.37	0.13	0.83	2.14	3.81	3.24	0.18	96.56
T5/98	670 cm	IECMF00JX	67.96	0.87	15.14	5.4	0.14	1.13	3.1	2.33	2.65	0.18	98.9
T5/98	670 cm	IECMF00JY	57.69	1.65	14.44	8.01	0.15	2.67	5.5	2.73	1.45	0.11	94.39
T5/98	670 cm	IECMF00JZ	71.7	0.36	14.55	3.74	0.21	0.61	2.28	2.92	3.08	0.18	99.63
T5/98	670 cm	IECMF00K0	56.21	1.68	16.2	8.2	0.11	2.67	6.06	3.82	1.74	0.13	96.82
T6/98	800 cm	IECMF00K1	52.99	1.87	15.91	9.8	0.23	3.68	6.94	3.97	1.07	0.1	96.55
T6/98	800 cm	IECMF00K2	54.77	1.7	15.55	9.61	0.27	2.89	6.06	4.01	1.67	0.13	96.64
T6/98	800 cm	IECMF00K3	56.36	1.72	16.2	9.09	0.25	3.17	6.13	4.12	1.71	0.11	98.85
T6/98	800 cm	IECMF00K4	52.78	1.82	15.85	10.29	0.15	3.44	7.01	4.33	1.32	0.09	97.07
T6/98	800 cm	IECMF00K5	68.75	0.27	14.49	3.79	0.15	0.17	1.41	5.26	3.19	0.23	97.69
T6/98	800 cm	IECMF00K6	53.32	2.03	16.12	9.59	0.23	3.53	7.26	4.1	1.21	0.15	97.54
T6/98	800 cm	IECMF00K7	67.98	0.32	14.56	3.65	0.13	0.38	1.67	5.17	3.28	0.21	97.35
T6/98	800 cm	IECMF00K8	57.24	1.19	15.14	7.9	0.25	2.67	5.36	4.7	1.88	0.1	96.44
T6/98	800 cm	IECMF00K9	68.36	0.48	14.75	3.54	0.15	0.24	1.5	5.64	3.3	0.25	98.2
T6/98	800 cm	IECMF00KA	58.44	1.28	15.42	6.22	0.15	2.21	5.78	4.67	1.86	0.19	96.23
T6/98	800 cm	IECMF00KB	61.52	0.93	15	6.39	0.15	1.19	3.86	4.19	2.7	0.13	96.07
T6/98	800 cm	IECMF00KC	65.81	0.74	15.31	5.23	0.16	0.94	3.23	4.84	2.59	0.21	99.07
T6/98	800 cm	IECMF00KD	69.49	0.48	15.2	3.8	0.19	0.22	1.59	5.82	3.33	0.17	100.31
T6/98	800 cm	IECMF00KE	70.01	0.26	13.96	3	0.09	0.21	1.19	4.93	3.34	0.18	97.18
T7/98	1050 cm	IECMF00KF	68.7	0.4	14.79	3.88	0.17	0.33	1.41	2.02	3.11	0.19	95.01
T7/98	1050 cm	IECMF00KG	54.44	1.77	16.1	9.91	0.13	3.71	7.32	3.4	1.2	0.12	98.1
T7/98	1050 cm	IECMF00KH	69.77	0.46	14.33	3.62	0.18	0.37	1.67	2.72	3.15	0.24	96.52
T7/98	1050 cm	IECMF00KI	56.01	2.13	14.66	9.08	0.18	3.3	6.31	3.11	1.46	0.1	96.34
T7/98	1050 cm	IECMF00KJ	56.18	1.81	14.51	10.01	0.24	2.9	6.22	3.39	1.88	0.09	97.22
T7/98	1050 cm	IECMF00KK	70.34	0.58	14.36	2.56	0.1	0.41	0.81	2.47	3.03	0.21	94.87
T7/98	1050 cm	IECMF00KL	58.07	1.62	14.98	9.38	0.18	3.4	6.9	3.18	1.44	0.07	99.23
T7/98	1050 cm	IECMF00KM	70.02	0.22	14.4	2.78	0.15	0.17	1.18	3.27	3.37	0.33	95.89
T7/98	1050 cm	IECMF00KN	71.14	0.33	13.58	3.5	0.11	0.16	1.29	2.58	3.19	0.24	96.12

T7/98	1050 cm	IECMF00KO	71.15	0.32	14.2	3.67	0.19	0.19	1.49	2.72	3.27	0.25	97.44
T7/98	1050 cm	IECMF00KP	56.31	1.22	14.66	9.66	0.2	3.78	6.35	3.14	1.32	0.15	96.78
T8/98	1110 cm	IECMF00KQ	68.19	0.93	14.9	5.68	0.13	1.5	4.17	1.78	1.24	0.16	98.68
T8/98	1110 cm	IECMF00KR	53.84	1.7	14.98	8.93	0.28	4.91	7.64	2.47	1.28	0.07	96.11
T8/98	1110 cm	IECMF00KS	71.23	0.32	14.55	1.57	0.05	0.28	0.83	2.47	4	0.27	95.56
T8/98	1110 cm	IECMF00KT	56.03	1.6	15.97	8.67	0.29	3.38	6.68	3.15	1.03	0.1	96.89
T8/98	1110 cm	IECMF00KU	60.24	1.56	16.16	7.41	0.13	2.57	5.74	3.81	1.32	0.1	99.03
T8/98	1110 cm	IECMF00KV	62.88	1.41	15.35	7.84	0.21	2.49	5.58	3.08	0.97	0.14	99.95
T8/98	1110 cm	IECMF00KW	56.37	1.58	14.88	8.86	0.22	4.06	7.54	3.76	0.92	0.06	98.25
T8/98	1110 cm	IECMF00KX	65.12	1.01	15.03	5.57	0.12	1.77	4.78	3.36	1.13	0.17	98.04
T8/98	1110 cm	IECMF00KY	54.88	1.38	9.28	13.52	0.33	9.59	6.54	2.2	0.66	0.06	98.43
T8/98	1110 cm	IECMF00KZ	65.75	0.94	15.86	5.76	0.08	1.49	4.83	3.9	1.08	0.2	99.88

Table S4. Internal standards used to control the measurements, analyzed as unknowns. Major elements measured by EPMA and trace elements by LA-ICP-MS

Standard (EMP)			SiO2	TiO2	Al2O3	FeO	MnO	MgO	CaO	Na2O	K2O	Cl	Total
Lipari	This study	Mean (n=8)	74.17	0.11	13.13	1.74	0.09	0.04	0.69	4.17	4.86	0.34	99.34
		1SD	1.11	0.09	0.48	0.55	0.05	0.02	0.13	0.19	0.34	0.06	
	GEOREM compilation	Mean (n=36)	74.53	0.10	13.00	1.52	0.08	0.04	0.76	4.06	5.11	0.38	99.58
		1SD	0.56	0.14	0.44	0.10	0.07	0.01	0.04	0.17	0.10	0.01	

Standard (LA-ICPMS)			Rb	Sr	Y	Zr	Nb	Ba	La	Ce	Pr	Nd	Sm	Eu	Gd	Tb	Dy	Ho	Er	Tm	Yb	Lu	Hf	Ta	Pb	Th	U
KL2-G	This study	Mean (n=10)	9.5	350	24.3	138	14	122	13.2	33.9	4.5	21.8	5.52	1.88	5.93	0.85	5.22	0.980	2.55	0.336	2.2	0.29	3.82	0.93	2.11	1.00	0.52
		1SD	0.4	17	1.1	5	0.3	5	0.3	1.6	0.2	1.3	0.54	0.13	0.33	0.05	0.32	0.073	0.11	0.032	0.1	0.02	0.20	0.05	0.17	0.07	0.02
	GEOREM Recommended values		8.7	356	25.4	152	15	123	13.1	32.4	4.6	21.6	5.54	1.92	5.92	0.89	5.22	0.961	2.54	0.331	2.1	0.29	3.93	0.96	2.07	1.02	0.55
		1SD	0.4	8	1.1	5	1	5	0.2	0.7	0.1	0.4	0.09	0.04	0.20	0.03	0.12	0.022	0.07	0.009	0.05	0.01	0.14	0.02	0.10	0.03	0.02
		Measured v/s Ref	1.09	0.98	0.96	0.91	0.96	0.99	1.01	1.05	0.98	1.01	1.00	0.98	1.00	0.95	1.00	1.02	1.00	1.02	1.02	1.00	0.97	0.96	1.02	0.98	0.94
ATHO-G	This study	Average (n=9)	65.3	94.0	94.3	482	56.1	540	56.5	123	14.5	61.4	14.2	2.59	14.5	2.39	16.9	3.51	10.3	1.54	10.8	1.61	13.4	3.8	5.59	7.4	2.35
		1SD	2.4	4.0	3.6	16	1.4	21	2.1	5	0.7	2.6	0.6	0.22	0.7	0.10	0.8	0.16	0.6	0.09	0.3	0.11	0.7	0.2	0.25	0.2	0.11
	GEOREM Recommended values		65.3	94.1	94.5	512	62.4	547	55.6	121	14.6	60.9	14.2	2.76	15.3	2.51	16.2	3.43	10.3	1.52	10.5	1.54	13.7	3.9	5.67	7.4	2.37
		1SD	3.0	2.7	3.5	20	2.6	16	1.5	4	0.4	2	0.4	0.1	0.7	0.08	0.7	0.11	0.5	0.07	0.4	0.05	0.5	0.2	0.62	0.27	0.12
		Measured v/s Ref	1.00	1.00	1.00	0.94	0.90	0.99	1.02	1.02	0.99	1.01	1.00	0.94	0.95	0.95	1.04	1.02	1.00	1.02	1.03	1.05	0.98	0.97	0.99	1.00	0.99

Table S5.- Planktonic foraminifera radiocarbon ages from core MD07-3098 and the respective marine surface reservoir age correction applied (Rs) in the calibration.

Depth MD07-3098 (cm)	Laboratory code	Species	^{14}C age (years BP)	1σ (years)	Rs (years)	1σ (years)
0	ECHo 3294	Mixed planktonic foraminifera	520	50	790	160
30	SacA54466	Mixed planktonic foraminifera	875	30	790	160
90	SacA57395	Mixed planktonic foraminifera	1830	30	790	160
150	ECHo 3295	Mixed planktonic foraminifera	2260	50	805	140
240	ECHo 3296	*G. bulloides*	4150	80	805	140
460	SacA54471	Mixed planktonic foraminifera	6310	30	805	140
490	SacA54473	*G. bulloides*	7980	35	805	140
530	SacA54475	*G. bulloides*	7725	30	805	140
550	SacA54477	*G. bulloides*	8095	30	805	140
570	SacA57397	*G. bulloides*	7875	40	805	140
620	SacA57398	*G. bulloides*	8620	150	805	140
650	SacA57399	*G. bulloides*	8810	40	805	140
805	SacA54480	Mixed planktonic foraminifera	10205	40	805	140
900	SacA57401	Mixed planktonic foraminifera	11790	50	920	135
950	SacA57402	*G. bulloides*	12350	60	975	120
990	SacA57403	*G. bulloides*	12670	50	975	120
1040	SacA57404	*G. bulloides*	13210	60	975	120
1050	SacA54485	*G. bulloides*	12710	50	975	120
1140	SacA57406	*G. bulloides*	14800	70	1320	95
1180	SacA57407	*G. bulloides*	15050	70	1320	95
1220	SacA57408	*G. bulloides*	15550	70	1320	95
1270	SacA57409	*G. bulloides*	15780	70	1320	95
1310	SacA57410	Mixed planktonic foraminifera	15720	70	1320	95
1430	SacA57411	Mixed planktonic foraminifera	16570	80	1320	95
1680	SacA57412	*G. bulloides*	16360	80	1320	95
2070	SacA57413	*G. bulloides*	16360	80	1320	95
2070	SacA57414	*G. inflata*	16550	80	1320	95

Table S6. Radiocarbon ages obtained for deposits of the volcanic centers discussed in the text and plotted in Figures 6, 8 and 9. Because the 14C calibration curves have evolved since the publication of these data, they were re-claibrated by the SHCal20 curve (Hogg et al., 2020) using the software Calib 8.2 (Stuiver et al., 2020).

In the case where a modelled age estimate was provided in the original publication, that age was plotted instead (Fontijn et al., 2016; Moreno et al., 2014; Alloway et al., 2017a).

Volcano	Eruptive Event	Reference	Measured Material	Sample ID		1σ (years)	Calendar age median (years BP)	1σ range (years)	2σ range (years)	Modelled median (cal years BP)	Modelled 1σ (years)	Modelled 2σ range (years)
Hudson	HW7	Haberle and Lumley, 1998	Bulk sediment	Q-2835	1635	40	1479	1530–1449	1401–1568			
Hudson	HW7	Haberle and Lumley, 1998	Bulk sediment	AA-10296	1830	75	1710	1750–1611	1538–1880			
Hudson	HW7	Haberle and Lumley, 1998	Bulk sediment	AA-10300	1605	55	1454	1523–1408	1348–1564			
Hudson	HW6	Haberle and Lumley, 1998	Bulk sediment	AA-10295	2600	60	2624	2594–2513	2420–2780			
Hudson	HW6	Haberle and Lumley, 1998	Bulk sediment	AA-10299	2560	55	2588	2600–2495	2416–2752			
Hudson	HW6	Haberle and Lumley, 1998	Bulk sediment	Q-2962	2470	40	2492	2496–2360	2352–2545			
Hudson	HW6	Haberle and Lumley, 1998	Bulk sediment	Q-2976	2710	35	2786	2789–2750	2739–2860			
Hudson	H2	Naranjo and Stern, 1998	Charred wood	94T-39	3670	70	3956	4002–3847	3819–4153			
Hudson	H2	Naranjo and Stern, 1998	Peat	93-48B	3485	100	3711	3839–3574	3454–3934			
Hudson	H2	Naranjo and Stern, 1998	Peat	94T-49B	3740	60	4046	4101–3971	3942–4240			
Hudson	H2	Naranjo and Stern, 1998	Charred wood	94T-1C	3790	80	4124	4239–4059	3901–4317			
Hudson	H2	Naranjo and Stern, 1998	Soil Organic matter	93-38A	3495	105	3725	3849–3573	3452–3985			
Hudson	H2	Naranjo and Stern, 1998	Soil Organic matter	93-38B	4980	105	5694	5756–5587	5471–5920			
Hudson	H2	Naranjo and Stern, 1998	Soil Organic matter	93-41B	3155	185	3305	3494–3067	2851–3726			
Hudson	H2	Naranjo and Stern, 1998	Charcoal	94T-42	4590	70	5191	5192–5052	4972–5335			
Hudson	H1	Del Carlo et al., 2018	Soil Organic matter	AR-1E	7325	46	8102	8171–8078	8003–8188			
Hudson	H1	Del Carlo et al., 2018	Soil Organic matter	EO-1A	7294	71	8084	8172–8069	7934–8204			
Hudson	H1	Del Carlo et al., 2018	Soil Organic matter	EO-2E	7026	49	7821	7867–7777	7695–7883			

Hudson	H1	Naranjo and Stern, 1998	Peat	94T-49E	6330	90	7205	7322–7157	6985–7370
Hudson	H1	Kilian et al., 2003	Organic macrofossil	GC2 116 cm	6915	40	7714	7755–7668	7614–7797
Hudson	H1	Naranjo and Stern, 1998	Peat	94T-49G	6840	90	7653	7731–7574	7485–7841
Hudson	H1	Naranjo and Stern, 1998	Charcoal	94T-44D	7010	40	7805	7854–7741	7690–7872
Hudson	H1	Kilian et al., 2003	Organic macrofossil	GC2 144 cm	7635	40	8399	8424–8368	8334–8488
Hudson	HW3	Haberle and Lumley, 1998	Bulk sediment	AA-10298	9930	85	11355	11353–11202	11179–11639
Hudson	HW3	Haberle and Lumley, 1998	Bulk sediment	Beta-107815	9830	90	11203	11311–11093	11064–11361
Hudson	HW3	Haberle and Lumley, 1998	Bulk sediment	Q-2838	11005	75	12897	12933–12775	12773–13074
Hudson	HW2	Haberle and Lumley, 1998	Bulk sediment	AA-10293	11965	100	13803	13869–13739	13594–14045
Hudson	HW2	Haberle and Lumley, 1998	Bulk sediment	AA-10297	11855	120	13685	13794–13582	13912–14021
Hudson	HW2	Haberle and Lumley, 1998	Bulk sediment	Q-2959	11145	105	13022	13115–12922	12776–13183
Hudson	HW1	Haberle and Lumley, 1998	Bulk sediment	Beta-107813	12480	100	14606	14735–14332	14161–15043
Hudson	HW1	Haberle and Lumley, 1998	Bulk sediment	Beta-107816	12390	120	14471	14569–14139	14059–14971
Hudson	H0	Miranda et al., 2013; Weller et al., 2014	Bulk organic matter	1,419–1,420 cm	13430	50	16127	16219–16034	15941–16310
Hudson	H0	Miranda et al., 2013; Weller et al., 2014	Bulk organic matter	1,423–1,424 cm	13720	45	16542	16634–16432	16345–16756
Hudson	H0	Miranda et al., 2013; Weller et al., 2014	Bulk organic matter	1,348–1,349 cm	13810	110	16704	16914–16537	16359–17024
Hudson	H0	Miranda et al., 2013; Weller et al., 2014	Bulk organic matter	1,664–1,665 cm	14220	45	17229	17312–17123	17081–17382
Hudson	H0	Miranda et al., 2013; Weller et al., 2014	Bulk organic matter	1,517–1,518 cm	14345	45	17396	17465–17316	17259–17547
Hudson	H0	Miranda et al., 2013; Weller et al., 2014	Bulk organic matter	1,452–1,453 cm	14670	45	17951	18051–17847	17768–18168
Hudson	H0	Miranda et al., 2013; Weller et al., 2014	Macro plant remains	1,685–1,686 cm	14735	30	18039	18135–17957	17872–18186
Hudson	H0	Miranda et al., 2013; Weller et al., 2014	Bulk organic matter	1,457–1,458 cm	14800	90	18076	18207–17985	17844–18248
Michinmahuida	Lepué	Amigo et al., 2013	Charred wood	LL230409-1 (age)	9260	50	10387	10434–10291	10247–10514

Michinmahuida	Lepué	Alloway et al., 2017a	Charcoal	UCIAMS-145938	9960	330				10909	228	10714–10080
Michinmahuida	Lepué	Moreno and León, 2003	Wood	NSRL-12478	9030	60				10994	124	
Michinmahuida	Lepué	Moreno and León, 2003	Wood	ETH-18856	9415	80				10994	124	
Michinmahuida	Lepué	Moreno and León, 2003	Wood	AA23236	9635	85				10994	124	
Michinmahuida	Lepué	Abarzúa and Moreno, 2008	Terrestrial macrofossil		9105	70				10994	124	
Michinmahuida	Lepué	Moreno and León, 2003	Bulk gytja	ETH-20386	9695	90				10994	124	
Michinmahuida	Lepué	Moreno and León, 2003	Bulk gytja	ETH-188857	9545	70				10994	124	
Michinmahuida	Lepué	Moreno and León, 2003	Bulk gytja	ETH-24476	9830	75				10994	124	
Michinmahuida	Lepué	Moreno, 2004	Bulk gytja	A8070	9680	85				10994	124	
Michinmahuida	Lepué	Moreno, 2004	Bulk gytja	A8069	10060	80				10994	124	
Michinmahuida	Lepué	Moreno, 2004	Bulk gytja	A8068	11265	65				10994	124	
Michinmahuida	Lepué	Abarzúa et al., 2004		GX28215	8990	110				10994	124	
Michinmahuida	Lepué	Abarzúa et al., 2004	Bulk gytja	NSRL-12473	10150	50				10994	124	
Michinmahuida	Lepué	Abarzúa and Moreno, 2008	Bulk gytja	CAMS-115814	10000	40				10994	124	
Michinmahuida	Lepué	Pesce and Moreno, 2014	Bulk gytja	ETH-25451	8965	65				10994	124	
Michinmahuida	Lepué	Pesce and Moreno, 2014	Bulk gytja	UCIAMS-125915	10360	40				10994	124	
Michinmahuida	Lepué	Amigo et al., 2013	Organic sediment	AA040311-1S	9510	50	10729	10777–10650	10572–10831			
Michinmahuida	Lepué	Alloway et al., 2017a	Bulk carbonac. Muds	LLNL-158290	9560	35				10909	228	10714–10080
Michinmahuida	Lepué	Alloway et al., 2017a	Bulk Higly carbonac. Muds	LLNL-123029	9570	30				10909	228	10714–10080
Michinmahuida	Lepué	Alloway et al., 2017a	Bulk carbonac. Muds	LLNL-123032	9635	35				10909	228	10714–10080
Michinmahuida	MIC1	Naranjo and Stern, 2004	Peat	170299-1G	6350	60	7233	7285–7165	7156–7341			
Michinmahuida	MIC1	Naranjo and Stern, 2004	Peat	170299-1i	5120	80	5816	5920–5733	5649–5954			
Michinmahuida	MIC1	Amigo et al., 2013	Organic sediment	AA040311-1J	6590	30	7466	7489–7426	7422–7517			
Michinmahuida	Unknown	Amigo et al., 2013	Wood	AA280110-3B	390	40	401	375–327	320–493			
Michinmahuida	Unknown	Amigo et al., 2013	Charred wood	AA040311-1E	1310	30	1217	1268–1204	1176–1274			
Michinmahuida	Unknown	Casati et al., 2019	Organic matter	P16-5Csm	8230	60	9161	9267–9174	9006–9314			

Michinmahuida	Unknown	Casati et al., 2019	Organic matter	P17-4CBd	7670	60	8434	8465–8374	8341–8552			
Quetrupillán	Quet5	Fontijn et al., 2016	Charcoal	CLD177C	1860	37				1695	48	1790–1587
Quetrupillán	Puesco	Fontijn et al., 2016	Charcoal	CLD164B	2012	35				1915	35	1987–1850
Quetrupillán	Puesco	Fontijn et al., 2016	Charcoal	CLD166A	2442	37				1915	35	1987–1850
Quetrupillán	Puesco	Fontijn et al., 2016	Charcoal	CLD167B	2171	35				1915	35	1987–1850
Quetrupillán	Puesco	Fontijn et al., 2016	Charcoal	CLD177A	2088	37				1915	35	1987–1850
Quetrupillán	Quet1	Fontijn et al., 2016	Charred wood	CLD168O	10515	43				16492	154	16784–16189
Quetrupillán	Unknown	Fontijn et al., 2016	Charcoal	CLD168A	233	37	196	218–147	138–231			
LTT-3	LTT-3	Moreno et al., 2014	Gyttja	LTT-3	470	25				471		404-508
LTT-7	LTT-7	Moreno et al., 2014	Gyttja	LTT-7	1765	35				1554		1281-1599
LTT-8	LTT-8	Moreno et al., 2014	Gyttja	LTT-8	2285	35				2194		20022284
LTT-9	LTT-9	Moreno et al., 2014	Gyttja	LTT-9	2955	25				2980		2939-3200
LTT-10	LTT-10	Moreno et al., 2014	Gyttja	LTT-10	3315	35				3508		3338-3593
LTT-14	LTT-14	Moreno et al., 2014	Gyttja	LTT-14	–	–				6059		5821-6266
LTT-15	LTT-15	Moreno et al., 2014	Gyttja	LTT-15	5815	35				6195		5984-6409
LTT-18	LTT-18	Moreno et al., 2014	Gyttja	LTT-18	–	–				7901		7777-8044
LTT-20	LTT-20	Moreno et al., 2014	Gyttja	LTT-20	7620	30				8488		8411-8664
LTT-20	LTT-20	Moreno et al., 2014	Gyttja	LTT-20	7990	30				8488		8411-8664
Yate	Ya2	Watt et al., 2011b	Organic macrofossil	LV-1	980	35	851	905–876	786–924			
Yate	Ya2	Watt et al., 2011b	Organic mud	03-1E	319	35	378	440–400	348–451			
Antillanca-Casablanca	Nahuel Huapi	Singer et al., 2008; Naranjo et al., 2017	Charcoal	PU-05-06	1740	30	2295	2336–2288	2268–2364			
Antillanca-Casablanca	Nahuel Huapi	Lara et al., 2006; Naranjo et al., 2017	Charcoal	171297-6	1520	60	1370	1412–1307	1290–1517			
Antillanca-Casablanca	Rayhuen	Fontijn et al., 2016	Charcoal	CLD246B	1952	37				1849	37	1766–1915

Antillanca-Casablanca	Playas Blanca-Negra	Villarosa et al., 2006	Charcoal	612 IIA	2215	85	2169	2159–2056	1944–2350			
Antillanca-Casablanca	Playas Blanca-Negra	Villarosa et al., 2006	Paleosol	612 IIIN1	2750	250	2830	3164–2668	2301–3402			
Antillanca-Casablanca	Playas Blanca-Negra	Villarosa et al., 2006	Paleosol	612 IIIN4	3100	180	3239	3449–3026	2842–3641			
Antillanca-Casablanca	Playas Blanca-Negra	Villarosa et al., 2006	Charcoal	LJ-5130	2230	40	2229	2309–2231	2090–2334			
Antillanca-Casablanca	Playas Blanca-Negra	Villarosa et al., 2006	Charcoal	LJ-5131	2720	40	2798	2796–2754	2739–2876			
Antillanca-Casablanca	Playas Blanca-Negra	Villarosa et al., 2006	Charcoal	Beta 62499	2190	60	2121	2149–2043	2002–2184			
Antillanca-Casablanca	Playas Blanca-Negra	Villarosa et al., 2006	–	Beta 54771	2200	60	2143	2152–2055	2007–2184			
Antillanca-Casablanca	Playas Blanca-Negra	Villarosa et al., 2006	–	Beta 54772	2220	50	2141	2151–2082	2011–2182			
Antillanca-Casablanca	Playas Blanca-Negra	Naranjo et al., 2017	Charcoal	240198-3N	2260	80	2218	2332–2191	2003–2365			
Antillanca-Casablanca	Playas Blanca-Negra	Naranjo et al., 2017	Charcoal	240198-4L	2430	80	2463	2518–2339	2310–2722			
Antillanca-Casablanca	Playas Blanca-Negra	Fontijn et al., 2016	Charcoal	CLD238L	2266	37				2244	22	2283–2233
Antillanca-Casablanca	Playas Blanca-Negra	Fontijn et al., 2016	Charcoal	CLD244B	2272	37				2244	22	2283–2233
Antillanca-Casablanca	Playas Blanca-Negra	Singer et al., 2008	Charcoal	PU-04-04-B	2750	75	2832	2881–2752	2719–3007			
Puyehue-Cordón Caulle	Mil Hojas	Singer et al., 2008; Naranjo et al., 2017	Charcoal	PU-04-04-D	575	75	548	562–502	463–662			
Puyehue-Cordón Caulle	Mil Hojas	Singer et al., 2008	Charcoal	110299-5C	830	60	712	740–666	635–800			
Puyehue-Cordón Caulle	Mil Hojas	Lara et al., 2006	Charcoal	070599-1B	830	60	712	740–666	635–800			
Puyehue-Cordón Caulle	Mil Hojas	Naranjo et al., 2017	Charcoal	250198-7	950	60	823	820–763	723–928			
Puyehue-Cordón Caulle	Mil Hojas	Naranjo et al., 2017	Charcoal	250306-0A1	1180	35	1022	1034–978	958–1099			
Puyehue-Cordón Caulle	Mil Hojas	Fontijn et al., 2016	Charcoal	CLD248G	1074	37				840	88	1015–672
Puyehue-Cordón Caulle	North Cordón Caulle	Lara et al., 2006; Naranjo et al., 2017	Charcoal	050699-1	1630	60	1475	1537–1409	1350–1591			
Puyehue-Cordón Caulle	North Cordón Caulle	Lara et al., 2006	Charcoal	060300-3	2400	40	1501	1564–1432	1400–1592			
Puyehue-Cordón Caulle	North Cordón Caulle	Lara et al., 2006; Naranjo et al., 2017	Charcoal	100295-1	2400	60	1491	1577–1406	1358–1598			

Puyehue-Cordón Caulle	Ranco	Fontijn et al., 2016	Charcoal	CLD154F	3820	43				4353	163	1987–1850
Puyehue-Cordón Caulle	Ranco	Fontijn et al., 2016	Charcoal	CLD154G	4166	35				4353	163	1987–1850
Puyehue-Cordón Caulle	Ranco	Fontijn et al., 2016	Charcoal	CLD249B	5543	38				4353	163	1987–1850
Puyehue-Cordón Caulle	PCC2	Lara et al. 2006; Singer et al., 2008	Charcoal	240198-3D	5890	70	6667	6598–6748	6486–6854			
Puyehue-Cordón Caulle	PCC2	Fontijn et al., 2016	Charcoal	CLD244D	5946	39				6419	82	1987–1850
Puyehue-Cordón Caulle	PCC2	Fontijn et al., 2016	Charcoal	CLD247C	5975	39				6419	82	1987–1850
Puyehue-Cordón Caulle	PCC2	Naranjo et al., 2017; Singer et al., 2008	Charcoal	PU-04-04-A	6260	40	7108	7122–7021	6995–7141			
Puyehue-Cordón Caulle	PCC1	Singer et al., 2008; Naranjo et al., 2017	Charcoal	PU-05-36	9310	45	10449	10521–10378	10270–10580			
Puyehue-Cordón Caulle	Unknown	Lara et al., 2006	Charcoal	XM0064	180	50	146	116–59	165–282			
Puyehue-Cordón Caulle	Unknown	Lara et al., 2006	Charcoal	XM0065	240	50	200	222–142	126–325			
Puyehue-Cordón Caulle	Unknown	Lara et al., 2006	Charcoal	070399-2	1970	80	1873	1934–1812	1700–2059			
Puyehue-Cordón Caulle	Unknown	Singer et al., 2008	Charcoal	PU-04-04-C	1980	35	1889	1926–1864	1820–1936			
Puyehue-Cordón Caulle	Unknown	Lara et al., 2006	Charcoal	070599-1A	3270	60	3449	3489–3377	3335–3593			
Puyehue-Cordón Caulle	Unknown	Lara et al., 2006	Charcoal	110299-5B	5470	70	6225	6307–6180	6107–6351			
Calbuco	Unknown	Sellés and Moreno, 2011	Wood	XG0119C	130	60	112	75–18	0–154			
Calbuco	Unknown	Sellés and Moreno, 2011	Charcoal	201297-2B	150	50	115	142–56	0–154			
Calbuco	Unknown	Sellés and Moreno, 2011	Wood	201297-1	230	60	216	220–143	132–230			
Calbuco	Unknown	Sellés and Moreno, 2011	Charred wood	XG0118	1310	60	1187	1272–1188	1058–1299			
Calbuco	Ca13	Watt et al., 2011b	Charcoal	23-2B	1378	37	1244	1296–1264	1178–1252			
Calbuco	Ca12	Watt et al., 2011b	Charcoal	25-5j	2075	37	1991	1973–1928	1919–2091			
Calbuco	Unknown	Sellés and Moreno, 2011	Charcoal	201297-3A	2070	60	1987	2057–1923	1866–2131			
Calbuco	Unknown	Sellés and Moreno, 2011	Organic silt	SCA-076	3030	40	3175	3238–3136	3054–3271			
Calbuco	Unknown	Sellés and Moreno, 2011	Charcoal	CAJ-17F	3640	50	3916	3983–3837	3822–4087			

Calbuco	Ca11	Watt et al., 2011b	Charcoal	25-5F	6166	52	7019	7034–6942	6854–7165
Calbuco	Alerce Ignimbrite	Sellés and Moreno, 2011	Charcoal	CAJ-9	6550	40	7424	7388–7334	7324–7509
Calbuco	Alerce Ignimbrite	Sellés and Moreno, 2011	Charcoal	050399-1B	6250	130	7097	7261–6951	6793–7360
Calbuco	Alerce Ignimbrite	Sellés and Moreno, 2011	Charcoal	CAJ-12A-2	6910	80	7718	7790–7653	7578–7864
Calbuco	Ca3	Watt et al., 2011b	Charcoal	130398-2B	7510	40	8285	8351–8290	8189–8373
Calbuco	Unknown	Sellés and Moreno, 2011	Organic matter	SCA-070	7970	40	8782	8781–8644	8636–8987
Calbuco	Ca7	Watt et al., 2011b	Charcoal	803-4A	8559	39	9511	9516–9489	9464–9548
Calbuco	Ca1	Watt et al., 2011b	Charcoal	25-5B	9246	78	10385	10429–10256	10233–10574
Calbuco	Unknown	Sellés and Moreno, 2011	Charcoal	CAJ-10A	9610	60	10929	11079–10987	10707–11163
Calbuco	Unknown	Sellés and Moreno, 2011	Charcoal	XBD-3B	10040	90	11504	11634–11306	11242–11777
Calbuco	Unknown	Sellés and Moreno, 2011	Charcoal	XBD-3A	12380	70	14408	14490–14163	14089–14640
Llaima	1780 Llaima	Naranjo and Moreno, 2005	Charcoal	240498-2A	160	80	141	147–54	0–293
Llaima	1780 Llaima	Naranjo and Moreno, 2005	Charcoal	240498-3B	160	50	123	121–57	0–154
Llaima	1780 Llaima	Naranjo and Moreno, 2005	Charcoal	180198-1A	170	70	143	151–56	0–285
Llaima	1780 Llaima	Naranjo and Moreno, 2005	Wood	220498-9	170	50	134	119–58	0–155
Llaima	1780 Llaima	Naranjo and Moreno, 2005	Charcoal	141287-2	220	50	187	227–140	56–310
Llaima	1640 Llaima	Naranjo and Moreno, 2005	Soil Organic matter	LT-3E	280	60	291	216–149	240–467
Llaima	1640 Llaima	Naranjo and Moreno, 2005	Charcoal	220498-5B	300	50	322	328–281	266–455
Llaima	1640 Llaima	Naranjo and Moreno, 2005	Charcoal	230498-3	320	50	371	442–362	277–472
Llaima	Unknown	Naranjo and Moreno, 2005	Charcoal	060487-4	410	90	405	412–323	277–549
Llaima	Unknown	Naranjo and Moreno, 2005	Peat	160190-3	410	60	412	496–439	307–507
Llaima	Unknown	Naranjo and Moreno, 2005	Charcoal	230498-1B	770	70	668	725–637	556–766
Llaima	Unknown	Naranjo and Moreno, 2005	Charcoal	171089-1	1080	100	942	998–898	737–1116
Llaima	Unknown	Naranjo and Moreno, 2005	Charcoal	261089-1	1160	70	1027	1073–956	905–1178
Llaima	Unknown	Naranjo and Moreno, 2005	Charcoal	190198-1B	1280	60	1148	1168–1070	1052–1283
Llaima	Unknown	Naranjo and Moreno, 2005	Charcoal	LT-3G	1460	90	1324	1408–1266	1176–1531

Llaima	Unknown	Naranjo and Moreno, 2005	Charcoal	010694-B	1610	70	1459	1532–1402	1311–1588			
Llaima	Unknown	Naranjo and Moreno, 2005	Charcoal	LT-3K	1690	90	1548	1612–1426	1351–1744			
Llaima	Unknown	Naranjo and Moreno, 2005	Charcoal	180198-1B	1840	50	1722	1750–1697	1587–1833			
Llaima	Unknown	Naranjo and Moreno, 2005	Charcoal	150897-i	2290	70	2233	2265–2144	2054–2371			
Llaima	Unknown	Naranjo and Moreno, 2005	Charcoal	010694-E	2680	70	2765	2858–2717	2682–2941			
Llaima	Unknown	Naranjo and Moreno, 2005	Charcoal	080487-2B	2940	60	3046	3084–2959	2862–3223			
Llaima	Unknown	Schindlbeck et al., 2014	Charcoal	JK210	3045	25	3199	3249–3152	3074–3268			
Llaima	Unknown	Naranjo and Moreno, 2005	Charcoal	211289-1	3440	100	3654	3728–3559	3440–3903			
Llaima	Unknown	Naranjo and Moreno, 2005	Charcoal	150897-H	3460	70	3676	3727–3574	3485–3853			
Llaima	Unknown	Naranjo and Moreno, 2005	Charcoal	010694-M	4630	70	5297	5462–5377	5039–5479			
Llaima	Unknown	Naranjo and Moreno, 2005	Charcoal	150897-F	5000	80	5708	5752–5496	5573–5908			
Llaima	Unknown	Naranjo and Moreno, 2005	Charcoal	JK211	5320	25	6079	6117–6044	5988–6128			
Llaima	Unknown	Naranjo and Moreno, 2005	Charcoal	LT-2C	5690	90	6448	6504–6386	6291–6656			
Llaima	Unknown	Naranjo and Moreno, 2005	Charcoal	010694-P	5770	90	6534	6639–6441	6389–6736			
Llaima	Unknown	Naranjo and Moreno, 2005	Charcoal	JK209b	5940	30	6724	6748–6671	6644–6798			
Llaima	Unknown	Naranjo and Moreno, 2005	Charcoal	070487-1A	7420	180	8194	8357–8027	7913–8544			
Llaima	Unknown	Naranjo and Moreno, 2005	Charcoal	150897-E	8110	90	8969	9127–8856	8643–9153			
Llaima	Unknown	Naranjo and Moreno, 1991	Charcoal	Río Truful-D-1	8830	80	9838	9920–9666	9555–9969			
Llaima	Llaima Pumice	Schindlbeck et al., 2014	Charcoal	JK229	9005	30	10156	10223–10147	10116–10232			
Llaima	Llaima Pumice	Naranjo and Moreno, 2005	Charcoal	150190-1	9360	250	10571	10805–10233	9892–11238			
Llaima	Llaima Pumice	Fontijn et al., 2016	Charred wood	CLD296F	9385	41				10450	67	1987–1850
Llaima	Llaima Pumice	Naranjo and Moreno, 2005	Charcoal	150897-B	9400	260	10627	10815–10248	9890–11269			

Llaima	Llaima Pumice	Schindlbeck et al., 2014	Charcoal	JK256b	9420	100	10615	10759–10487	10269–10823
Llaima	Llaima Pumice	Schindlbeck et al., 2014	Charcoal	JK287	9750	35	11154	11203–11110	11073–11234
Llaima	Unknown	Naranjo and Moreno, 2005	Charcoal	230191-1B	10270	230	11950	12210–11628	11248–12621
Llaima	Unknown	Naranjo and Moreno, 2005	Charcoal	010200-1B	10530	100	12413	12628–12435	12019–12699
Llaima	Unknown	Naranjo and Moreno, 1991	Charcoal	Río Truful-C-1	11240	230	13113	13313–12899	12735–13503
Llaima	Unknown	Naranjo and Moreno, 2005	Charcoal	JK288	11300	35	13170	13186–13154	13101–13244
Llaima	Curacautín 2	Lohmar, 2008	–	LL24B	12510	40	14656	14711–14503	14328–14744
Llaima	Curacautín 2	Lohmar, 2008	–	LL25	12650	140	14942	15251–14818	14262–15419
Llaima	Curacautín 2	Lohmar, 2008	–	LL9	12730	90	15130	15266–14996	14829–15477
Llaima	Curacautín 2	Naranjo and Moreno, 2005	Charcoal	261089-2A	12760	130	15163	15392–14956	14802–15617
Llaima	Curacautín 1	Naranjo and Moreno, 1991	Charcoal	040487-7	13200	150	15800	16029–15583	15330–16232
Llaima	Curacautín 1	Lohmar, 2008	–	LL13	13230	330	15838	16311–15328	14843–16963
Llaima	Curacautín 1	Naranjo and Moreno, 1991	Charcoal	190190-1BC	13260	200	15886	16190–15607	15282–16459
Llaima	Curacautín 1	Naranjo and Moreno, 1991	Charcoal	041189-1A	13460	400	16173	16796–15614	15003–17358
Llaima	Curacautín 1	Lohmar, 2008	–	LL24A	13850	150	16749	16997–16551	16263–17131
Osorno	Cono Los Pumas	Moreno et al., 2010	Charcoal	LL040210-2	350	40	389	444–359	299–470
Osorno	Cono Los Pumas	Moreno et al., 2010	Charcoal	LL171008-3	240	40	281	315–273	260–330
Osorno	Unknown	Fontijn et al., 2016	Charcoal	CLD329C	1523	35	1360	1375–1343	1301–1426
Osorno	Cono Appel	Moreno et al., 2010	Charcoal	LL090710-3	10960	50	12836	12852–12768	12748–12930
Osorno	Cono Appel	Moreno et al., 2010	Charcoal	LL050210-1	10260	60	11907	11998–11833	11712–12099
Osorno	Cono Appel	Moreno et al., 2010	Charcoal	LL090710-8	9650	40	10944	10965–10863	10768–10979
Corcovado	COR2	Naranjo and Stern, 2004	Peat	T-20D	7980	100	8800	8810–8645	8537–9030

Corcovado	COR3	Naranjo and Stern, 2004	Peat	T-20B	6870	90	7680	7750–7582	7564–7863
Yanteles	YAN1	Naranjo and Stern, 2004	Wood	T-23	9560	60	10859	11071–10697	10650–11105
Yanteles	YAN1	Naranjo and Stern, 2004	Charcoal	T-25	9190	130	10346	10501–10206	10114–10687
Mentolat	MEN1	Naranjo and Stern, 2004	Soil Organic matter	T-58A	6690	60	7528	7579–7478	7428–7618
Mentolat	~11.7 ka MEN	Weller et al., 2019	Sediment	D-AMS 017353	10109	34	11634	11734–11622	11610–11773
Hornopirén	Ho1	Watt et al., 2011b	Plant Stem	801-1F	4977	46	5669	5665–5600	5587–5754

8.4 Supplementary Tables Chapter 5

Table S5.1.1. Benthic foraminifera *Uvigerina peregrine* $\delta^{18}O$ for core MD07-3098

Depth [cm]	$\delta^{18}O_{U. peregrina}$ [‰]	$\delta^{18}O_{U. peregrina}$ three point moving average [‰]
0	3.47	3.58
0	3.70	3.54
10	3.47	3.56
20	3.50	3.48
30	3.48	3.47
40	3.44	3.46
50	3.47	3.46
60	3.46	3.51
70	3.59	3.51
80	3.47	3.63
90	3.82	3.62
100	3.56	3.61
110	3.45	3.54
120	3.62	3.59
129	3.69	3.65
139	3.66	3.66
150	3.63	3.58
160	3.44	3.65
170	3.88	3.67
180	3.68	3.80
190	3.82	3.88
190	4.13	3.81
200	3.47	3.74
210	3.63	3.52
220	3.44	3.53
230	3.50	3.47
240	3.45	3.59
250	3.80	3.64
260	3.67	3.79
270	3.90	3.77
280	3.72	3.80
295	3.78	3.66
310	3.46	3.56
320	3.45	3.50
330	3.58	3.71
340	4.09	3.94
350	4.15	3.97
360	3.66	4.01
370	4.21	3.88
380	3.78	4.05
390	4.17	4.05
400	4.21	4.09

400	3.91	4.14
410	4.30	4.03
420	3.90	4.11
430	4.13	3.95
440	3.82	3.84
450	3.59	3.74
460	3.82	3.65
470	3.54	3.62
480	3.50	3.54
490	3.58	3.54
500	3.55	3.56
510	3.55	3.55
520	3.55	3.57
530	3.63	3.59
540	3.58	3.67
550	3.81	3.64
560	3.54	3.59
570	3.43	3.50
580	3.54	3.52
590	3.59	3.49
600	3.34	3.62
610	3.94	3.73
620	3.92	3.84
620	3.66	3.82
630	3.88	3.75
640	3.70	3.74
650	3.63	3.61
660	3.50	3.56
670	3.54	3.55
680	3.60	3.73
690	4.05	3.81
710	3.78	3.95
720	4.03	3.84
730	3.71	3.79
750	3.62	3.65
760	3.63	3.71
770	3.87	3.87
778	4.11	3.89
800	3.70	3.87
805	3.80	3.74
805	3.72	3.84
810	3.98	3.82
820	3.75	3.88
830	3.90	3.81
840	3.78	4.04
850	4.45	4.11
860	4.09	4.19
870	4.05	4.07
880	4.07	4.11
890	4.20	4.19

900	4.31	4.26
910	4.26	4.28
920	4.28	4.26
930	4.25	4.28
940	4.31	4.32
950	4.41	4.35
960	4.34	4.36
970	4.33	4.35
980	4.37	4.37
990	4.42	4.42
1000	4.47	4.44
1000	4.42	4.50
1010	4.60	4.42
1020	4.25	4.44
1030	4.48	4.40
1040	4.48	4.53
1050	4.62	4.54
1060	4.52	4.63
1070	4.73	4.66
1080	4.74	4.83
1090	5.02	4.88
1100	4.89	4.95
1110	4.95	4.91
1120	4.90	4.95
1130	5.00	5.00
1140	5.10	5.04
1150	5.03	5.06
1160	5.06	5.05
1170	5.06	5.03
1180	4.98	5.02
1190	5.03	5.03
1200	5.06	5.06
1200	5.10	5.09
1210	5.12	5.13
1220	5.17	5.14
1230	5.12	5.17
1240	5.21	5.14
1270	5.08	5.16
1280	5.18	5.15
1310	5.18	5.17
1320	5.16	5.18
1330	5.21	5.20
1340	5.23	5.22

Table S5.1.2. Planktic foraminifera Globigerina bulloides $\delta^{18}O$ for core MD07-3081

Depth [cm]	$\delta^{18}O_{G.\ bulloides}$ [‰]	$\delta^{18}O_{G.\ bulloides}$ three point moving average [‰]
20	2.40	2.25
30	2.19	2.26
40	2.16	2.22
50	2.28	2.15
60	2.07	2.19
60	2.07	2.15
70	2.40	2.04
80	1.92	2.04
80	1.75	1.99
90	2.08	1.89
100	1.79	1.91
100	1.93	1.91
110	1.99	1.90
120	1.74	1.97
130	2.07	2.08
140	2.12	2.10
150	2.47	2.17
160	2.07	2.10
170	2.13	2.01
180	1.69	1.88
190	1.70	1.96
200	1.79	1.97
210	2.52	2.12
220	2.17	2.17
230	2.41	2.24
240	1.95	2.18
250	2.13	2.15
260	2.23	2.02
270	2.03	2.10
280	1.77	2.13
290	2.35	2.12
300	2.27	2.07
310	2.19	2.08
320	1.75	2.03
330	1.84	1.98
340	2.10	1.97
350	2.03	2.12
360	2.14	2.22
370	2.47	2.26
380	2.37	2.27
390	2.32	2.22
400	2.05	2.27
410	1.92	2.25
420	2.68	2.39

430	2.29	2.57
440	3.02	2.78
450	2.97	2.78
460	2.97	2.85
470	2.66	2.83
480	2.65	2.83
500	2.90	2.86
510	2.99	2.90
520	3.11	2.93
530	2.83	3.05
540	2.83	3.02
550	3.46	3.00
560	2.87	3.05
570	3.03	3.03
580	3.07	2.94
590	2.72	3.02
600	3.00	2.94
600	3.29	3.10
610	2.64	3.26
620	3.85	3.20
630	3.53	3.09
640	2.68	3.13
650	2.73	3.01
660	2.87	2.94
670	3.25	3.06
680	3.18	3.18
690	3.27	3.30
690	3.30	3.41
700	3.51	3.49
710	3.78	3.57
710	3.61	3.64
720	3.64	3.67
720	3.68	3.55
730	3.65	3.61
730	3.15	3.63
740	3.91	3.64
750	3.77	3.62
760	3.70	3.76
770	3.59	3.76
780	3.81	3.75
787	3.91	3.76
794	3.71	3.74
801	3.76	3.74
801	3.52	3.74
808	3.79	3.79
817	3.95	3.82
830	3.95	3.91
835	3.89	3.91
847	3.96	3.87
850	3.81	3.83

855	3.72	3.77
859	3.78	3.69
867	3.56	3.64
890	3.55	3.71
890	3.58	3.71
895	4.08	3.75
900	3.76	3.84
900	3.80	3.91
920	4.00	3.87
960	3.94	3.94
980	3.89	3.88
1020	3.82	3.85
1040	3.84	3.89
1080	4.01	3.96
1140	4.03	4.00
1170	3.96	3.96
1190	3.98	3.86
1230	3.87	3.83
1290	3.62	3.80
1330	3.74	3.88
1456	4.28	4.02
1470	3.95	4.06
1490	4.12	4.12
1550	3.90	4.05
1560	4.33	4.01
1590	3.94	3.99
1600	3.78	4.01
1620	4.01	3.91

Table S5.1.3 Benthic foraminifera *Uvigerina peregrine* $\delta^{18}O$ for core MD07-3081

Depth [cm]	$\delta^{18}O_{U. peregrina}$ [‰]	$\delta^{18}O_{U. peregrina}$ three point moving average [‰]
20	3.48	3.42
30	3.37	3.44
40	3.48	3.44
50	3.46	3.44
60	3.36	3.41
60	3.39	3.38
70	3.40	3.38
80	3.36	3.38
80	3.37	3.37
90	3.37	3.37
100	3.36	3.39
110	3.44	3.40
120	3.39	3.52
130	3.74	3.53
140	3.45	3.56
150	3.50	3.50
160	3.56	3.57
170	3.64	3.72
180	3.95	4.13
200	4.79	4.45
210	4.61	4.32
220	3.56	3.91
230	3.57	3.66
240	3.86	3.68
250	3.61	3.72
260	3.69	3.61
280	3.53	3.62
290	3.66	3.64
300	3.75	3.67
310	3.61	3.68
320	3.67	3.74
330	3.94	3.77
340	3.71	3.85
350	3.90	3.88
360	4.02	4.05
370	4.24	4.17
380	4.27	4.25
390	4.23	4.26
400	4.28	4.09
410	3.77	4.27
420	4.76	4.26
430	4.25	4.47
440	4.40	4.38
450	4.48	4.46

460	4.51	4.49
470	4.48	4.53
480	4.61	4.53
500	4.49	4.54
510	4.51	4.52
520	4.57	4.62
530	4.78	4.66
540	4.63	4.50
550	4.10	4.45
560	4.63	4.48
570	4.71	4.70
580	4.77	4.76
590	4.81	4.86
600	4.99	4.86
610	4.79	4.97
620	5.11	4.94
630	4.90	4.94
640	4.81	4.94
650	5.10	4.93
660	4.87	5.05
670	5.19	5.04
680	5.05	5.11
690	5.08	5.06
700	5.03	5.11
710	5.21	5.14
720	5.18	5.20
730	5.21	5.19
740	5.17	5.20
750	5.23	5.17
760	5.12	5.14
770	5.09	5.11
780	5.13	5.08
787	5.02	5.06
794	5.02	5.07
801	5.17	5.11
808	5.15	5.14
817	5.09	5.15
830	5.21	5.17
835	5.19	5.15
847	5.05	5.14
850	5.18	5.05
855	4.92	5.06
859	5.10	5.05
867	5.14	5.12
890	5.14	5.13
895	5.11	5.09
900	5.03	5.17
920	5.38	5.19
960	5.15	5.22
990	5.13	5.15

1020	5.17	5.15
1040	5.15	5.15
1080	5.14	5.17
1140	5.24	5.17
1170	5.15	5.21
1190	5.26	5.20
1230	5.21	5.23

Table S5.2.1 Benthic foraminifera ^{14}C ages and corresponding calendar age and deep water $\Delta^{14}C$ estimates, for core MD07-3100.

Depth [cm]	Laboratory code	Analyzed species	^{14}C age [years BP]	error ^{14}C age [years BP]	0.025 Cal Age [cal years BP]	0.16 Cal Age [cal years BP]	0.84 Cal Age [cal years BP]	0.975 Cal Age [cal years BP]	Calendar age mean [cal years BP]	0.025 $\Delta^{14}C$ [‰]	0.16 $\Delta^{14}C$ [‰]	0.84 $\Delta^{14}C$ [‰]	0.975 $\Delta^{14}C$ [‰]	Mean $\Delta^{14}C$ [‰]
279	SacA43904	Mixed benthic foraminifera	4800	30	2647	2780	3003	3130	**2890**	-244	-230	-208	-196	**-219**
280	SacA43905	Mixed benthic foraminifera	4630	40	2671	2799	3010	3135	**2903**	-227	-212	-190	-176	**-202**
459	SacA43906	Mixed benthic foraminifera	7310	40	5341	5648	6166	6402	**5891**	-232	-203	-152	-126	**-179**
460	SacA43907	Mixed benthic foraminifera	7550	40	5657	5821	6196	6414	**6000**	-228	-211	-173	-151	**-192**
610	SacA43911	Mixed benthic foraminifera	10420	45	8996	9334	9885	10113	**9616**	-188	-154	-95	-70	**-125**
760	SacA36224	Mixed benthic foraminifera	11620	60	10429	10795	11737	12397	**11274**	-166	-131	-27	53	**-78**
840	SacA36228	Mixed benthic foraminifera	12560	70	11496	12049	13136	13390	**12529**	-157	-102	25	59	**-45**
910	SacA43915	Mixed benthic foraminifera	12860	60	12526	12749	13333	13540	**13062**	-80	-56	13	40	**-20**
1010	SacA36233	Mixed benthic foraminifera	15050	80	12867	13354	13809	14088	**13573**	-275	-230	-182	-153	**-206**
1080	SacA43917	Mixed benthic foraminifera	15800	70	13625	13837	14605	14936	**14226**	-273	-253	-181	-148	**-217**
1110	SacA43920	Mixed benthic foraminifera	15000	60	14114	14476	15144	15338	**14820**	-145	-111	-34	-10	**-71**
1180	SacA43919	Mixed benthic foraminifera	15160	80	15187	15335	15958	16432	**15639**	-55	-32	46	103	**6**
1240	SacA43922	Mixed benthic foraminifera	16120	70	16248	16998	17720	17941	**17322**	-43	47	146	177	**94**
1340	SacA36240	Mixed benthic foraminifera	17560	100	18149	18605	19035	19293	**18799**	10	63	126	163	**92**

Table S5.2.2 Benthic foraminifera ^{14}C ages and corresponding calendar age and deep water $\Delta^{14}C$ estimates, for core MD07-3098.

Depth [cm]	Laboratory code	Analyzed species	^{14}C age [years BP]	error ^{14}C age [years BP]	0.025 $\Delta^{14}C$ [‰]	0.16 $\Delta^{14}C$ [‰]	0.84 $\Delta^{14}C$ [‰]	0.975 $\Delta^{14}C$ [‰]	Mean $\Delta^{14}C$ [‰]	0.025 Cal Age [cal years BP]	0.16 Cal Age [cal years BP]	0.84 Cal Age [cal years BP]	0.975 Cal Age [cal years BP]	Calendar age mean [cal years BP]
0	Echo 3293	Mixed benthic foraminifera	3580	50	-363	-358	-343	-336	**-351**	-3	27	232	262	**113**
90	SacA 57418	Mixed benthic foraminifera	4705	30	-389	-366	-347	-313	**-355**	761	1077	1308	1727	**1210**
460	SacA 54472	Mixed benthic foraminifera	8805	35	-321	-292	-235	-141	**-267**	5871	6218	6855	7792	**6478**
490	SacA 54474	Mixed benthic foraminifera	10140	40	-403	-370	-291	-254	**-335**	6181	6621	7589	8007	**7043**
530	SacA 54476	Mixed benthic foraminifera	9625	40	-300	-270	-219	-192	**-239**	6945	7309	7839	8126	**7646**
550	SacA 54478	Mixed benthic foraminifera	10035	35	-305	-282	-238	-220	**-260**	7332	7583	8081	8263	**7833**
570	SacA 57423	Mixed benthic foraminifera	9600	40	-230	-221	-179	-153	**-203**	7733	7823	8255	8493	**7998**
620	SacA 57424	Mixed benthic foraminifera	9830	70	-217	-189	-145	-108	**-167**	8092	8410	8799	9187	**8597**
650	SacA 57425	Mixed benthic foraminifera	10600	70	-248	-232	-178	-112	**-206**	8607	8727	9267	9909	**8984**
720	Echo 3298	Mixed benthic foraminifera	11590	107	-272	-225	-108	-66	**-167**	9291	9804	10957	11302	**10391**
805	SacA 54481	Mixed benthic foraminifera	12790	90	-283	-245	-157	-109	**-202**	10457	10851	11760	12117	**11279**
900	Echo 3299	Mixed benthic foraminifera	13680	129	-244	-194	-104	-70	**-148**	11775	12326	13143	13366	**12740**
950	SacA 57426	Mixed benthic foraminifera	13960	90	-208	-151	-114	-93	**-134**	12473	13055	13338	13548	**13171**
990	SacA 57427	Mixed benthic foraminifera	13930	60	-216	-125	-88	-54	**-109**	12287	13259	13565	13881	**13371**
1040	SacA 57428	Mixed benthic foraminifera	15170	60	-278	-260	-161	-94	**-217**	12924	13125	14153	14764	**13570**
1050	SacA 54486	Mixed benthic foraminifera	15210	60	-250	-236	-144	-74	**-198**	13308	13431	14364	14991	**13816**

1090	SacA 57429	Mixed benthic foraminifera	16470	70	-324	-284	-182	-136	**-233**	13700	14198	15269	15742	**14739**
1100	SacA 57430	Mixed benthic foraminifera	15710	70	-258	-187	-82	-28	**-133**	13731	14450	15462	15946	**14965**
1110	SacA 54488	Mixed benthic foraminifera	15540	80	-214	-139	-37	24	**-87**	14018	14786	15663	16137	**15216**
1140	SacA 57431	Mixed benthic foraminifera	16650	80	-255	-181	-94	-67	**-134**	14689	15505	16305	16526	**15928**
1180	SacA 57432	Mixed benthic foraminifera	16770	70	-132	-107	-36	63	**-72**	16135	16323	16941	17727	**16629**
1220	SacA 57433	Mixed benthic foraminifera	16680	90	-78	-23	110	137	**50**	16483	16966	18000	18194	**17553**
1270	SacA 57434	Mixed benthic foraminifera	17490	80	-91	-35	32	57	**0**	17197	17714	18251	18424	**17986**
1310	SacA 57435	Mixed benthic foraminifera	17230	80	-1	30	79	102	**53**	17804	17987	18346	18488	**18151**
1430	Echo 3301	Mixed benthic foraminifera	17740	110	-47	-20	36	90	**9**	17911	18130	18505	18949	**18327**
1680	SacA 57436	Mixed benthic foraminifera	18180	90	-71	-44	17	44	**-13**	18123	18363	18828	19030	**18594**
2070	SacA 57437	Mixed benthic foraminifera	17860	80	5	34	87	114	**60**	18450	18665	19051	19256	**18856**

Table S5.2.3 Benthic foraminifera ^{14}C ages and corresponding calendar age and deep water $\Delta^{14}C$ estimates, for core MD07-3119.

Depth [cm]	Laboratory code	Analized species, benthic foraminifera	^{14}C age [years BP]	error ^{14}C age [years BP]	0.025 Cal Age [cal years BP]	0.16 Cal Age [cal years BP]	0.84 Cal Age [cal years BP]	0.975 Cal Age [cal years BP]	Calendar age mean [cal years BP]	0.025 Δ14C [‰]	0.16 Δ14C [‰]	0.84 Δ14C [‰]	0.975 Δ14C [‰]	Mean Δ14C [‰]
2	SacA35743	Mixed benthtic foraminifera	2725	30	717	787	955	1024	**870**	-224	-217	-200	-192	**-209**
165	SacA35744	Mixed benthtic foraminifera	9010	50	4339	6110	7744	7905	**7045**	-453	-320	-167	-152	**-230**
265	SacA35745	Mixed benthtic foraminifera	10705	50	8628	9500	10021	10364	**9715**	-248	-169	-112	-76	**-144**
292	SacA35746	Mixed benthtic foraminifera	11045	40	9798	10110	10654	11221	**10382**	-173	-141	-81	-17	**-111**
361	SacA35747	Mixed benthtic foraminifera	12570	60	11204	11784	12344	12562	**12036**	-189	-131	-68	-43	**-102**
401	SacA35748	Mixed benthtic foraminifera	13410	50	12032	12708	13042	13166	**12844**	-190	-125	-86	-69	**-109**
431	SacA35749	Mixed benthtic foraminifera	13720	60	12709	13117	13447	14049	**13278**	-151	-116	-77	-3	**-96**
461	SacA35750	Mixed benthtic foraminifera	14250	60	13483	13614	14329	14811	**13936**	-136	-120	-42	21	**-84**
491	SacA35751	Mixed benthtic foraminifera	15340	70	14080	14653	15390	15637	**15055**	-190	-127	-45	-15	**-84**
531	SacA35752	Mixed benthtic foraminifera	16270	60	15382	15821	16507	17168	**16130**	-152	-107	-30	53	**-70**
561	SacA35753	Mixed benthtic foraminifera	16720	70	16185	16694	17755	17949	**17276**	-117	-59	70	96	**10**
591	SacA35754	Mixed benthtic foraminifera	16260	80	16658	17529	18101	18223	**17780**	-4	99	182	204	**137**
641	SacA35755	Mixed benthtic foraminifera	17110	70	17517	17985	18306	18541	**18146**	-16	46	91	121	**68**
682	SacA35756	Mixed benthtic foraminifera	17570	80	17933	18181	18532	18678	**18343**	-16	9	58	82	**33**
712	SacA35757	Mixed benthtic foraminifera	17360	70	18280	18347	18701	18794	**18517**	44	59	108	123	**82**

Table S5.2.4 Planktic and benthic foraminifera ^{14}C ages and corresponding calendar age and deep water $\Delta^{14}C$ estimates, for core MD07-3081.

Depth [cm]	Laboratory code	Analized species, planktic foraminifera	^{14}C age [years BP]	error ^{14}C age [years BP]	Laboratory code	Analized species, benthic foraminifera	^{14}C age [years BP]	error ^{14}C age [years BP]	0.025 Cal Age [cal years BP]	0.16 Cal Age [cal years BP]	0.84 Cal Age [cal years BP]	0.975 Cal Age [cal years BP]	Calendar age mean [cal years BP]	0.025 Δ14C [‰]	0.16 Δ14C [‰]	0.84 Δ14C [‰]	0.975 Δ14C [‰]	Mean Δ14C [‰]
50	SacA 62139	Mixed planktic foraminifera	2700	30														
100	SacA 61334	*G. bulloides*	4620	30	SacA 62140	Mixed benthic foraminifera	6325	30	3438	3948	4926	5781	4607	-312	-265	-174	-81	-204
250	SacA 62141	Mixed planktic foraminifera	8860	35	SacA 62142	Mixed benthic foraminifera	9765	50	7632	8972	9531	9740	9275	-260	-123	-57	-35	-88
280	SacA 61335	Mixed planktic foraminifera	9180	40														
340	SacA 61336	Mixed planktic foraminifera	10200	40	Echo 3830.1.1	Mixed benthic foraminifera	11280	110	10100	10796	11383	11680	11130	-168	-94	-21	14	-55
390	SacA 62143	*G. bulloides*	10465	35	SacA 62144	Mixed benthic foraminifera	12160	50	11346	11512	12191	12601	11833	-133	-114	-38	14	-78
430	SacA 62145	*G. bulloides*	11305	40	Echo 3829.1.1	Mixed benthic foraminifera	12980	90	12046	12610	13007	13324	12806	-149	-87	-38	0	-64
470	SacA 61337	Mixed planktic foraminifera	12215	40	Echo 3828.1.1	Mixed benthic foraminifera	13150	120	12666	13443	13828	14183	13630	-103	-15	45	87	13
520	SacA 62146	*G. bulloides*	13070	60	SacA 62147	Mixed benthic foraminifera	14010	50	13390	14040	15014	15211	14509	-114	-44	75	105	13
610	SacA 62148	Mixed planktic foraminifera	13500	50	Echo 3827.1.1	Mixed benthic foraminifera	15390	110	14624	15039	15809	16222	15383	-141	-96	-3	55	-53
610	SacA 62149	Mixed planktic foraminifera	14910	60														
630	SacA 62150	Mixed planktic foraminifera	14080	50	Echo 3826.1.1	Mixed benthic foraminifera	15820	110	15186	15655	16201	16524	15927	-129	-76	-7	35	-41
670	SacA 62151	Mixed planktic foraminifera	14730	50	Echo 3825.1.1	Mixed benthic foraminifera	16230	110	15966	16303	16887	17164	16595	-89	-51	24	64	-13
680	SacA 62152	Mixed planktic foraminifera	14550	70	SacA 62153	Mixed benthic foraminifera	15600	100	16273	16509	16995	17239	16755	21	55	123	159	89
700	SacA 61338	Mixed planktic foraminifera	14850	60	Echo 3824.1.1	Mixed benthic foraminifera	16620	270	16640	16846	17278	17440	17071	-85	-44	38	81	-4
770	SacA 62154	Mixed planktic foraminifera	15000	60														
801	SacA 62155	Mixed planktic foraminifera	15270	60	Echo 3823.1.1	Mixed benthic foraminifera	18140	140	17528	17816	18481	18661	18139	-138	-103	-22	13	-62
930	SacA 62156	Mixed planktic foraminifera	16900	70	Echo 3822.1.1	Mixed benthic foraminifera	18820	130	18096	18625	19817	20225	19153	-141	-88	58	116	-23

1050	SacA 62157	Mixed planktic foraminifera	16730	130	Echo 3821.1.1	Mixed benthic foraminifera	18660	120	18967	19362	20100	20403	19737	-29	19	116	163	68
1160	SacA 62158	Mixed planktic foraminifera	17130	100	Echo 3820.1.1	Mixed benthic foraminifera	18730	120	19600	19874	20423	20659	20153	34	74	152	192	113
1230	SacA 62159	Mixed planktic foraminifera	17390	100	Echo 3819.1.1	Mixed benthic foraminifera	21240	140	20035	20242	20781	21002	20527	-203	-179	-117	-88	-147

Table S5.3 Inividual glass shard geochemical analyses in potential cryptotephras identified as glass shard peaks in core MD07-3081. Major elements analyzed by EPMA.

Core	Core depth	Volcanic source	Correlative	SiO2	TiO2	Al2O3	FeOT	MnO	MgO	CaO	Na2O	K2O	Cl	Total
MD07-3081	470 cm	Hudson	HW2	53.84	1.64	16.70	8.38	0.24	3.86	7.72	2.68	1.21	0.07	96.31
MD07-3081	470 cm	Hudson	HW2	55.28	1.87	16.93	8.80	0.19	3.58	7.10	4.37	1.57	0.10	99.78
MD07-3081	470 cm	Hudson	HW2	52.92	1.54	16.09	7.46	0.24	3.88	8.47	3.64	1.32	0.12	95.70
MD07-3081	470 cm	Hudson	HW2	59.23	1.55	16.44	6.71	0.14	2.68	5.74	4.50	1.66	0.18	98.83
MD07-3081	470 cm	Hudson	HW2	65.53	1.18	16.76	4.40	0.07	1.41	3.08	4.71	2.67	0.19	99.99
MD07-3081	470 cm	Hudson	HW2	60.27	1.43	16.65	6.21	0.25	2.33	4.80	3.94	1.94	0.17	97.99
MD07-3081	470 cm	Hudson	HW2	61.33	1.99	15.43	7.90	0.24	2.30	4.97	4.29	2.28	0.19	100.90
MD07-3081	470 cm	Hudson	HW2	58.36	1.81	15.75	8.01	0.24	2.78	5.72	5.22	1.78	0.10	99.77
MD07-3081	470 cm	Hudson	HW2	64.52	1.11	16.38	4.49	0.19	1.39	3.26	5.68	2.26	0.18	99.47
MD07-3081	470 cm	Hudson	HW2	53.84	2.08	15.14	9.23	0.19	4.24	8.02	4.24	1.23	0.11	98.32
MD07-3081	470 cm	Hudson	HW2	54.52	1.95	15.43	8.90	0.19	3.39	7.48	4.42	1.35	0.08	97.71
MD07-3081	470 cm	Hudson	HW2	57.80	1.80	14.94	8.56	0.24	3.03	5.96	4.01	1.87	0.15	98.37
MD07-3081	470 cm	Hudson	HW2	57.19	1.83	15.67	6.98	0.32	2.94	6.15	4.86	1.56	0.18	97.69
MD07-3081	470 cm	Hudson	HW2	54.82	1.83	15.19	9.20	0.11	3.76	7.67	4.65	1.22	0.09	98.53
MD07-3081	470 cm	Hudson	HW2	55.33	1.92	15.65	8.57	0.26	3.25	6.32	4.69	1.76	0.13	97.88
MD07-3081	540 cm	Hudson	HW1	53.28	2.18	15.74	10.72	0.19	4.55	7.87	4.01	1.13	0.18	99.84
MD07-3081	540 cm	Hudson	HW1	54.76	2.04	16.52	8.48	0.38	3.73	7.64	4.10	1.58	0.13	99.36
MD07-3081	540 cm	Hudson	HW1	57.05	1.73	16.51	7.36	0.19	2.61	5.27	4.15	2.25	0.14	97.26
MD07-3081	540 cm	Hudson	HW1	55.46	1.81	15.72	9.32	0.08	3.90	7.46	4.12	1.62	0.14	99.62
MD07-3081	540 cm	Hudson	HW1	61.22	1.38	15.78	6.63	0.26	1.58	4.02	5.13	2.51	0.17	98.69
MD07-3081	540 cm	Hudson	HW1	63.28	1.40	16.49	4.73	0.24	1.39	3.15	5.33	2.32	0.19	98.51
MD07-3081	540 cm	Hudson	HW1	55.28	1.68	16.85	9.03	0.15	3.82	7.23	3.97	1.37	0.05	99.44
MD07-3081	540 cm	Hudson	HW1	55.04	1.77	15.85	9.28	0.26	4.00	7.37	4.45	1.33	0.10	99.46
MD07-3081	540 cm	Hudson	HW1	51.90	1.84	15.70	8.63	0.23	4.07	7.90	4.51	1.49	0.14	96.41
MD07-3081	540 cm	Hudson	HW1	55.07	1.78	15.08	10.21	0.25	3.75	8.12	4.00	1.02	0.12	99.41
MD07-3081	540 cm	Hudson	HW1	65.06	1.36	15.95	5.28	0.13	1.17	2.44	5.00	2.89	0.15	99.41
MD07-3081	540 cm	Hudson	HW1	56.46	1.50	15.39	8.28	0.11	3.36	6.48	4.16	1.88	0.24	97.87
MD07-3081	540 cm	Hudson	HW1	62.79	1.34	16.88	5.23	0.16	1.72	3.94	5.18	2.47	0.15	99.85

MD07-3081	540 cm	Hudson	HW1	63.59	1.48	16.19	5.26	0.16	1.65	3.64	5.28	2.39	0.17	99.81
MD07-3081	540 cm	Hudson	HW1	65.78	1.12	15.64	5.47	0.15	0.94	2.04	5.55	3.05	0.07	99.80
MD07-3081	700 cm	Hudson	Ho	54.17	1.79	16.60	8.96	0.20	3.70	7.80	3.96	1.06	0.08	98.32
MD07-3081	700 cm	Hudson	Ho	64.48	1.17	17.05	4.23	0.13	1.48	3.06	5.21	2.59	0.07	99.47
MD07-3081	700 cm	Hudson	Ho	56.88	1.66	15.81	7.32	0.15	2.99	5.44	4.64	1.88	0.12	96.90
MD07-3081	700 cm	Hudson	Ho	57.09	1.87	16.04	8.27	0.31	2.93	5.68	4.54	1.71	0.09	98.52
MD07-3081	700 cm	Hudson	Ho	58.58	1.64	15.84	7.44	0.21	2.26	4.43	4.10	2.04	0.23	96.77
MD07-3081	700 cm	Hudson	Ho	62.99	1.29	15.56	5.11	0.16	1.54	3.24	4.56	2.58	0.17	97.19
MD07-3081	700 cm	Hudson	Ho	61.58	1.59	16.23	7.00	0.12	1.81	3.66	4.88	2.44	0.07	99.36
MD07-3081	700 cm	Hudson	Ho	51.91	2.32	16.04	10.55	0.31	2.97	6.02	4.66	2.92	0.25	97.95
MD07-3081	700 cm	Hudson	Ho	64.71	1.05	15.76	5.27	0.07	1.30	3.16	3.37	2.21	0.15	97.05
MD07-3081	700 cm	Hudson	Ho	57.46	1.48	16.42	7.12	0.07	3.04	6.14	3.49	1.46	0.10	96.79

Table S5.4 Marine surface reservoir ages (Rs) estimates for cores in this study. The details on the 14C age estimates for tephras on land can be accessed in Table "OnlandTephraAges".

Core	Depth base/medio tephra/criptotephra [cm]	^{14}C age [years BP]	error ^{14}C age [years BP]	Volcanic source	Eruption	^{14}C age mean [years BP]	error ^{14}C age [years BP]	Rs	error Rs
MD07-3100	160	2490	60	Hudson	HW7	1718	159	**773**	**170**
MD07-3100	760	10325	40	Michinmahuida	Lepué	9801	343	**524**	**345**
MD07-3098	805	10205	40	Michinmahuida	Lepué	9801	343	**404**	**345**
MD07-3081	330	10200	40	Hudson	HW3	9959	90	**241**	**185**
MD07-3081	330	10200	40	Michinmahuida	Lepué	9759	285	**441**	**288**
MD07-3081	460	12215	40	Hudson	HW2	11910	110	**305**	**161**
MD07-3081	510*	13070	60	Hudson	HW2	11910	110	**1160**	**167**
MD07-3081	510*	13070	60	Hudson	HW1	12435	110	**635**	**167**
MD07-3081	670	14730	50	Hudson	Ho	14638	202	125	240
MD07-3081	700	14850	60	Hudson	Ho	14638	202	245	242
MD07-3081	770*	15000	60	Hudson	Ho	14638	202	**395**	**242**

*Depths where 14C ages where interpolated

Table S5.5 Radiocarbon ages obtained for deposits of Lepué tephra identified in cores MD07-3098 and MD07-3100, and of eruptions of Hudson volcano potentially correlated with cryptotephras in core MD07-3081 (Figure S1, S2).

Volcanic source	Eruption	Reference	Type of archive	Site name	Sample	^{14}C Laboratory code	^{14}C age [years BP]	error ^{14}C age [years BP]	Analyzed material	Stratigraphic position	Comments geochemistry
Michinmahuida	**Lepué**	Abarzúa & Moreno, 2008		Lago Meli	818-819 cm		9105	70	Terrestrial macrofossil	~20 cm above Lepué tephra correlative.	
Michinmahuida	**Lepué**	Abarzúa et al., 2004		Laguna Tahui	891-895cm	GX28215	8990	110	Bulk gyttja	~20 cm above Lepué tephra correlative.	
Michinmahuida	**Lepué**	Moreno, 2004	Lacustrine core	Lago Condorito	PM10, 685-688 cm	A8070	9680	85	Bulk gyttja	~40 cm above Lepué tephra correlative.	
Michinmahuida	**Lepué**	Moreno, 2004	Lacustrine core	Lago Condorito	PM10, 821-824 cm	A8068	11265	65	Bulk gyttja	~100 cm below Lepué tephra correlative.	
Michinmahuida	**Lepué**	Pesce & Moreno, 2014	Lacustrine core	Lago Lepué	0201 DT8, 786cm		8965	65	Bulk gyttja	~40 cm above Lepué tephra correlative.	Analized for geochemistry
Michinmahuida	**Lepué**	Pesce & Moreno, 2014	Lacustrine core	Lago Lepué	0201 DT9, 904cm	CAMS-125915	10360	40	Bulk gyttja	~30 cm below Lepué tephra correlative.	Analized for geochemistry
						Mean	**9727.5**				
						Desvesta	**925**				
						Error of the mean	**185**				
Michinmahuida	**Lepué**	Abarzúa et al., 2004		Lago Meli	934-936cm	NSRL-12473	10150	50	Bulk gyttja	2 cm below Lepué tephra correlative.	
Michinmahuida	**Lepué**	Abarzúa & Moreno, 2008		Lago Meli	844 cm	CAMS-115814	10000	40	Bulk gyttja	Directly below Lepué tephra correlative.	
Michinmahuida	**Lepué**	Alloway et al., 2017b	Outcrop	Pte Pichileufú	LLNL-123032	LLNL-123032	9635	35	Bulk carbonac. Muds	Immediately below lower contact.	analized for geochemistry
Michinmahuida	**Lepué**	Alloway et al., 2017b	Outcrop	Puelche	LLNL-123029	LLNL-123029	9570	30	Bulk Higly carbonac. Muds	Immediately below lower contact.	analized for geochemistry
Michinmahuida	**Lepué**	Alloway et al., 2017b	Outcrop	Section 12	ETH-20386	LLNL-158290	9560	35	Bulk carbonac. Muds	Immediately below lower contact.	

Michinmahuida	**Lepué**	Alloway et al., 2017b	Outcrop	Section 12		LLNL-158291	9970	35	Wood in growth position	Immediately below lower contact.	
Michinmahuida	**Lepué**	Moreno & León, 2003	Sediment core	Lago Condorito	901B-601A	ETH-20386	9695	90	Bulk gyttja	Basal contact	
Michinmahuida	**Lepué**	Moreno & León, 2003	Sediment core	Lago Condorito	901B-601A	ETH-18856	9415	80	Wood	Basal contact	
Michinmahuida	**Lepué**	Moreno & León, 2003	Sediment core	Lago Condorito	901B-601A	AA23236	9635	85	Wood	Basal contact	
Michinmahuida	**Lepué**	Moreno & León, 2003	Sediment core	Lago Condorito	901B-601A	ETH-188857	9545	70	Bulk gyttja	Basal contact	
Michinmahuida	**Lepué**	Moreno & León, 2003	Sediment core	Lago Condorito	901B-601A	ETH-24476	9830	75	Bulk gyttja	Basal contact	
Michinmahuida	**Lepué**	Amigo et al. 2013	Outcrop		AA040311-1S		9510	50	Organic sediment	Paleosol 1-2 cm above deposit.	analized for geochemistry
Michinmahuida	**Lepué**	Alloway et al., 2017b	Outcrop		Section 9	LLNL-158125	10330	40	Bulk carbonac. Muds	Immediately below lower contact.	analized for geochemistry

Mean	9757
Desvesta	277
Error of the mean	212

Michinmahuida	**Lepué**	Amigo et al., 2013	Outcrop		LL230409-1		9260	50	Charred wood	Within deposit.	
Michinmahuida	**Lepué**	Alloway et al., 2017b	Outcrop	Pumalín-1	Pumalín-1	LLNL-122960	9785	30	Charcoal	Within pyroclastic deposit (co-eruptive correlative).	
Michinmahuida	**Lepué**	Moreno, 2004	Lacustrine core	Lago Condorito	PM10, 710-713 cm	A8069	10060	80	Bulk gyttja	Within Lepué tephra correlative.	
Michinmahuida	**Lepué**	Alloway et al., 2017b	Outcrop	Secion 4	UCIAMS-145938	UCIAMS-145938	9960	330	Charcoal	Within-surge deposit (co-eruptive correlative).	analized for geochemistry
						Mean wood/charcoal	9766	356			
						Mean wood/charcoal and directly below	9759	285			

						Mean everything	9751	504			
						Mean analyzed for geochemistry	**9801**				
						Desvesta	343				
						Error of the mean	339				
Hudson	**HW7**	Haberle & Lumley, 1998	Lacustrine core	Laguna Stibnite	Stb-4	AA-10296	1830	75	" organics associated with tephras".	direct AMS dating of organics associated with tephras	analized for geochemistry
Hudson	**HW7**	Haberle & Lumley, 1998	Lacustrine core	Laguna Ssix minutes	Six-4	AA-10300	1605	55	" organics associated with tephras".	direct AMS dating of organics associated with tephras	analized for geochemistry
						Mean macrorests	1718				
						Desvesta	159				
						Error of the mean	93				
Hudson	**HW3**	Haberle & Lumley, 1998	Lacustrine core		Beta-107815	Beta-107815	9830	90	" organics associated with tephras".	direct AMS dating of organics associated with tephras	analized for geochemistry
Hudson	**HW3**	Haberle & Lumley, 1998	Lacustrine core		AA-10298	AA-10298	9930	85	" organics associated with tephras".	direct AMS dating of organics associated with tephras	analized for geochemistry
Hudson	**HW3**	Haberle & Lumley, 1998	Lacustrine core		Beta-107812	Beta-107812	10080	100			analized for geochemistry
Hudson	**HW3**	Haberle & Lumley, 1998	Lacustrine core		AA-10294	AA-10294	9995	85			analized for geochemistry
						Mean macrorests	**9959**				
						Desvesta	**106**				

					Error of the mean	**90**				
Hudson	**HW2**	Haberle & Lumley, 1998	Lacustrine core		Q-2959	Q-2959	11145	105	Bulk sediment	Bracketing tephra	analized for geochemistry
Hudson	**HW2**	Haberle & Lumley, 1998	Lacustrine core		AA-10297	AA-10297	11855	120	" organics associated with tephras".	direct AMS dating of organics associated with tephras	analized for geochemistry
Hudson	**HW2**	Haberle & Lumley, 1998	Lacustrine core		AA-10293	AA-10293	11965	100	" organics associated with tephras".	direct AMS dating of organics associated with tephras	analized for geochemistry
					Mean macrorests	**11910**				
					Desvesta	**78**				
					Error of the mean	**110**				
Hudson	**HW1**	Haberle & Lumley, 1998	Lacustrine core		Beta-107813	Beta-107813	12480	100	" organics associated with tephras".	direct AMS dating of organics associated with tephras	analized for geochemistry
Hudson	**HW1**	Haberle & Lumley, 1998	Lacustrine core		Beta-107816	Beta-107816	12390	120	" organics associated with tephras".	direct AMS dating of organics associated with tephras	analized for geochemistry
					Mean macrorests	**12435**				
					Desvesta	**64**				
					Error of the mean	**110**				
Hudson	**Ho**	Miranda et al., 2013; Weller et al., 2014	Lacustrine core		T8 1,423-1,424 cm	CAMS-159614	13720*	45	Bulk organic matter	~25 cm Above Ho.	analized for geochemistry
Hudson	**Ho**	Miranda et al., 2013; Weller et al., 2014	Lacustrine core		T8 1,419-1,420 cm	UCIAMS-122978	13430*	50	Bulk organic matter	~30 cm Above Ho.	analized for geochemistry
Hudson	**Ho**	Miranda et al., 2013; Weller et al., 2014	Lacustrine core		T6 1,348-1,349 cm	CAMS-159606	13810*	110	Bulk organic matter	~ 40 cm Above Ho.	analized for geochemistry

Hudson	**Ho**	Miranda et al., 2013; Weller et al., 2014	Lacustrine core	T10 1,664-1,665 cm	CAMS-159607	14220*	45	Bulk organic matter	~ 90 cm Above Ho.	
Hudson	**Ho**	Miranda et al., 2013; Weller et al., 2014	Lacustrine core	T9 1,517-1,518 cm	CAMS-159613	14345	45	Bulk organic matter	~20 cm Below Ho.	
Hudson	**Ho**	Miranda et al., 2013; Weller et al., 2014	Lacustrine core	T7 1,457-1,458 cm	UCIAMS-123030	14800	90	Bulk organic matter	~ 10 cm Below Ho.	~analized for geochemistry
Hudson	**Ho**	Miranda et al., 2013; Weller et al., 2014	Lacustrine core	T9 1,685-1,686 cm	CAMS-154860	14735	30	Macro plant remains	~10 cm Below Ho.	~analized for geochemistry
Hudson	**Ho**	Miranda et al., 2013; Weller et al., 2014	Lacustrine core	T7 1,452-1,453 cm	UCIAMS-122999	14670	45	Bulk organic matter	~ 5 cm Below Ho.	Comments geochemistry

Mean	**14638**
Desvesta	**202**
Error of the mean	**114**

université PARIS-SACLAY | ÉCOLE DOCTORALE Sciences mécaniques et énergétiques, matériaux et géosciences (SMEMAG)

Titre : Utilisation du radiocarbone et de la téphrochronologie pour contraindre la circulation océanique dans l'Océan Pacifique Sud-est depuis les dernières 20,000 années

Mots clés : Paléocéanographie – Radiocarbone – Téphrochronologie – Pacifique Sud-est –Zone volcanique sud des Andes – Déglaciation

Résumé : L'océan joue un rôle important dans les cycles glaciaires-interglaciaires, en régulant la quantité de CO2 dans l'atmosphère. En particulier, pendant le dernier maximum glaciaire (~23 000–19 000 années calendaires avant le présent (années cal. BP)), l'océan profond avait accumulé du CO2, le libérant dans l'atmosphère pendant la dernière déglaciation (~18,000–11,000 années cal. BP). La quantité de CO2 stockée/libérée, les zones de l'océan qui aurait dégazé le CO2 et les mécanismes menant à ce stockage/libération, sont actuellement discutés et analysés par la communauté scientifique. Dans cette thèse, je présente de nouveaux enregistrements sur les changements de ventilation des eaux intermédiaires et profondes dans le Pacifique Sud-Est (SEP) au cours des ~22,000 dernières années. En utilisant les âges 14C des couples de foraminifères planctoniques et benthiques dans neuf carottes de sédiments marins sur un transect entre ~500–3,300 m de profondeur et ~31–49° S, les changements de la circulation océanique pendant la dernière déglaciation sont interprétés. Un défi important en paléocéanographie consiste à établir des chronologies robustes pour les carottes de sédiments marins, ce qui est essentiel pour intégrer les informations fournies par les enregistrements paléoenvironnementaux dans différentes zones de l'océan, mais aussi à terre et dans des calottes glaciaires. Afin d'explorer comment améliorer les chronologies des carottes étudiées ici, une étude téphrochronologique dans trois des carottes selectionnées a permis d'identifier des éruptions volcaniques dans chaque carotte, en améliorant ainsi la robustesse de leurs chronologies. D'après les enregistrements produits, la circulation dans le SEP au cours des 20,000 dernières années révèle un océan glaciaire plus stratifié, les eaux les plus appauvries en 14C se trouvant dans l'océan Austral profond. Pendant la déglaciation, d'importants changements de circulation sont observés, indiquant une convection plus vigoureuse et une meilleure ventilation des eaux profondes dans l'océan Austral. De plus, des valeurs anormalement appauvries en 14C sont observées pendant la déglaciation à des profondeurs baignées par les eaux profondes du Pacifique, ce qui pourrait indiquer l'influence d'une possible source hydrothermale.

université PARIS-SACLAY | ÉCOLE DOCTORALE Sciences mécaniques et énergétiques, matériaux et géosciences (SMEMAG)

Title : Utilisation of radiocarbon and tephrochronology to constrain the oceanic circulation in the Southeast Pacific Ocean during the last 20,000 years

Keywords : Paleoceanography – Radiocarbon – Tephrochronology – Southeast Pacific – Southern Volvanic Zone of the Andes – Deglaciation

Abstract : The ocean is thought to have an important role in glacial–interglacial cycles, by regulating the amount of CO2 in the atmosphere. In particular, during the Last Glacial Maximum (~23,000–19,000 calendar years before present (cal years BP)), the deep ocean is thought to have accumulated CO2, releasing it to the atmosphere during the last deglaciation (~18,000–11,000 cal years BP). The amount of CO2 stored/released, the areas of the ocean where this would take place and the mechanisms leading to this storing/release, are currently being discussed and information worldwide is being produced to this aim. In this thesis I produce new records on ventilation changes of intermediate and deep waters in the Southeast Pacific (SEP) during the last ~22,000 years. Using 14C ages of paired benthic and planktic foraminifera in nine marine sediment cores in a transect between ~500–3,300 m and ~31–49° S, changes in oceanic circulation during the last deglaciation are interpreted. An important challenge in paleoceanograhy at the time is establishing robust chronologies for marine sediment cores, which is essential to integrate the information provided by paleoenvironmental records in different areas of the ocean, but also on land and ice caps. In order to explore how to improve the chronologies in the cores here studied, a tephrochronological record is produced in three of the cores. This study allowed to identify between one and three tephras (eruptions) in each core, aiding the robustness of their chronologies. From the produced records, the circulation in the SEP during the last 20,000 years reveals a more stratified glacial ocean, with the most 14C–depleted waters found in the deep Southern Ocean. During the deglaciation, important circulation changes are observed, indicating a more vigorous convection and the ventilation of deep waters in the Southern Ocean. Additionally, anomalously 14C–depleted values are observed during the deglaciation at depths bathed by Pacific Deep Waters, which might indicate the influence of potential hydrothermal sources.